The Turbulent Separating Boundary Layer and Downstream Wake

Brian Edward Thompson
B.A.Sc.(Mech. Eng.)

Thesis submitted for the degree of Doctor of Philosophy
in the Faculty of Engineering University of London
and for the
Diploma of Membership of
Imperial College

Imperial College of Science and Technology
Department of Mechanical Engineering
Fluids Section, London. SW7 2BX

December, 1983

To my mum, dad and Juliet

ABSTRACT

Measurements and calculations of the pressure and velocity characteristics of a two-dimensional separating boundary layer and its downstream wake are presented and compared. A combination of impact, hot-wire and flying hot-wire probes has been used to quantify the flow in the vicinity of a trailing flap whose angle of incidence results in turbulent boundary-layer separation, a large region of recirculating flow and a curved downstream wake. A flying hot-wire arrangement has been developed for the measurement of velocity characteristics in the region where negative values of instantaneous velocity occur; the mechanism and signal processing equations are described and appraised by comparing stationary and flying wire measurements. The results indicate that the effects of streamline curvature are important in the boundary-layer and separated flow regions, and that the inviscid-viscous interaction is strong near separation. The dominant feature of the separated region is the shear layer associated with the streamline dividing forward and reverse flow where generation of and transport by turbulence are large and solution of the cross-stream momentum equation is required.

The calculated results were obtained by numerically solving time-averaged transport equations in their potential, boundary-layer and elliptic forms. The Laplace equations for potential flow were solved, in finite-difference form, to obtain the co-ordinates of the intersections of iso-velocity potential and iso-stream function lines; the potential velocity and pressure distribution were subsequently obtained and used as boundary conditions for a finite-difference solution of the boundary-layer equations with a turbulence model based on transport equations for the Reynolds stresses. A two-dimensional form of the Reynolds-averaged

equations was solved using a two-equation turbulence model on an orthgonal curvilinear mesh obtained from the potential-flow solution. The general flow patterns are in close accord with measurements in some regions of the flow. In others, including the near-wall region and near wake, significant discrepancies exist and the influences of numerical features are quantified to separate errors due to numerical, turbulence-model and wall-function assumptions.

ACKNOWLEDGEMENTS

I am most grateful to Professor J.H. Whitelaw whose supervision, insight, criticisms and counsel were fundamental to the prosperous execution of this research.

I am glad to acknowledge support from the Ministry of Defence, and am grateful to Mr. K.G. Winter and Dr. B.R. Williams of the Royal Aircraft Establishment and Mr. D.J. Butter of British Aerospace for their very useful advice.

Professor M.M. Ribeiro, of the Institute Superior Technico in Lisbon, who was responsible for the initial design of the flying-wire and Messrs. J.R. Laker and O. Vis contributed greatly to development of its mechanical and electrical hardware. Mr. D. Adair assisted me in the laboratory phase of the flying-wire measurements. I am very pleased to acknowledge their contributions.

I also wish to express my thanks to my colleagues as follows: Dr. J.J. McGuirk, who gave generously of his time and knowledge, for advice in many discussion on calculations; Dr. A.D. Gosman and Dr. P.S. Harvey for support and encouragement with the calculations in orthogonal curvilinear co-ordinates; Dr. M.M. Gibson and Mr. B.A. Younis for assistance with the boundary-layer calculations; Dr. A.M.K.P. Taylor, Dr. N.S. Vlachos, Dr. W.P. Jones and Dr. R.I. Issa for many interesting and informative discussions; and, Dr. J.B. Medley, Dr. A.B. Strong and Dr. G.D. Raithby of the University of Waterloo, Canada.

The support of the technical staff of Imperial College was essential to the experimental research program: Messrs. N. Frost, M. Roper, F. King and the late R. Church were particularly helpful.

I wish to thank Ms. C. Maxwell, Mr. F. King and Mr. A. Craig for assistance in the preparation of this text.

Finally, I deeply appreciate the love and support of my wife, Juliet, and my parents.

TABLE OF CONTENTS

		Page
ABSTRACT		ii
ACKNOWLEDGEMENTS		iv
LIST OF TABLES		vii
LIST OF FIGURES		ix
CHAPTER 1	THETIC INTRODUCTION	1
1.1	Objectives	3
1.2	Review of Related Work	4
1.3	Present Contribution	18
CHAPTER 2	EXPERIMENTAL TECHNIQUES	41
2.1	Flow visualization	41
2.2	Pressure Measurements	47
2.3	Hot-Wire Anemometry	56
2.4	Flying Hot-Wire Anemometry	69
2.5	Summary	81
Appendix 2.A	Approximate Hot-Wire Response Equations	113
CHAPTER 3	EXPERIMENTAL INVESTIGATION	121
3.1	Description of the Flow Configuration	122
3.2	Mean Flow Results	127
3.3	Turbulence Results	135
3.4	Discussion	145
3.5	Concluding Remarks	156

		Page
CHAPTER 4	CONSERVATION EQUATIONS, TURBULENCE MODELS AND CALCULATION PROCEDURES	207
4.1	Transport Equations and Turbulence Models	208
4.2	Inviscid Flow Calculation Procedure	227
4.3	Viscous-Inviscid Interactive Calculation Procedure	242
4.4	Procedure for Solving Elliptic Transport Equations in Orthogonal Curvilinear Co-ordinates	256
4.5	Viscous Flow Boundary Conditions	283
4.6	Summary	294
CHAPTER 5	COMPUTATIONAL INVESTIGATIONS AND COMPARISONS WITH EXPERIMENTAL RESULTS	314
5.1	Inviscid Flow	315
5.2	Boundary-Layer Flow and the Viscous-Inviscid Interaction	320
5.3	Separated and Wake Flow	329
5.4	Discussion and Conclusions	342
CHAPTER 6	CLOSURE	369
NOMENCLATURE		383
REFERENCES		391

LIST OF TABLES

TABLE NUMBER	TITLE	PAGE
1.1	Summary of separated flow calculations with the viscid-inviscid interaction	22
1.2	Summary of separated flow calculations with time-averaged Navier-Stokes equations	28
1.3	Summary of the relevant wake calculations	33
1.4	Summary of detailed experiments in turbulent separating boundary layers and downstream wakes	35
2.1	Constants of five-hole impact probe	83
2.2	Maximum uncertainties for pressure probes	84
2.3	Sample hot-wire calibration	85
2.4	Probe orientations and sensitivity coefficients of hot wires	86
2.5	Maximum uncertainties for stationary hot-wire anemometry	87
2.6	Essential details of the flying hot-wire anemometer	88
3.1	Mean and variance of the free-stream velocity	158
3.2	Reference parameters	159
3.3	Maximum values of Reynolds stresses and comparison with other experiments	160
3.4	Parameters of the mean flow development	161
4.1	The k-ϵ turbulence model constants	297
4.2	Reynolds stress turbulence model constants	297
4.3	Source terms for orthogonal curvilinear form of transport equations	298

		PAGE
4.4	Under-relaxation parameters	300
4.5	Convection, diffusion and source terms of momentum and turbulence kinetic energy balance equations	301
4.6	Summary of boundary conditions	304
5.1	Comparison of recirculation length and detachment point	348
5.2	Comparison of the effects of different wall boundary conditions in the separated region	349

LIST OF FIGURES

FIGURE NUMBER	TITLE	PAGE
2.1	Helium bubble visualizations	89
2.2	Surface oil flow visualization of separation point	90
2.3	Surface oil flow around a circular cylinder	91
2.4	Diagram of five-hole impact probe	92
2.5	Orientation of hot-wire	92
2.6	Trajectory of flying hot-wire	93
2.7	Flying hot-wire mechanism and instrumentation	94
2.8	Cooling velocity on the flying hot-wire probe	96
2.9	Velocity characteristics of the attached boundary-layer flow at s/c of 0.78	97
2.10	Velocity characteristics of the separated boundary-layer flow at s/c of 0.90	103
2.11	Velocity characteristics of the wake at x/c of 0.66	108
3.1	Flow configuration	164
3.2	Flow control vanes	165
3.3	Total pressure contours in the plane of the trailing-edge	166
3.4	Surface flow visualization of the upstream boundary-layer	167
3.5	Surface flow visualization of curved boundary-layer and separated region	167
3.6	Parameters of mean flow development	168
3.7	Profiles of static pressure coefficient	174
3.8	Mean velocity vector in the vicinity of separation	175

		PAGE
3.9	Streamlines and probability of downstream flow in the vicinity of separation	176
3.10	Profiles of mean velocity	178
3.11	Profiles of flow angle	181
3.12	Clauser charts	184
3.13	Profiles of Reynolds stresses approaching separation	186
3.14	Profiles of Reynolds stresses in the vicinity of separation	191
3.15	Profiles of Reynolds stresses in the wake	199
4.1	Orthogonal curvilinear co-ordinate system	307
4.2	Two-dimensional plane of orthogonal curvilinear co-ordinates	308
4.3	Numerical mesh for stream function - vorticity solution	308
4.4	Streamline solution mesh	309
4.5	s-n Boundary-layer co-ordinate system	310
4.6	Schematic of viscous-inviscid interaction procedure	311
4.7	Comparison of boundary-cell representation	312
4.8	Schematic of solution domain	313
5.1	Stream-function and velocity-potential lines around a cylinder	350
5.2	Surface pressure distribution on a cylinder	350
5.3	Comparison of measured and calculated non-dimensional longitudinal pressure gradient on the upper surface of the plate and flap	351
5.4	Calculated and measured distributions of momentum thickness, shape factor and skin friction in the vicinity of separation	352

		PAGE
5.5	Calculated and measured profiles of mean velocity and Reynolds stresses in the boundary-layer approaching separation.	352
5.6	Potential flow mesh with the calculated displacement thickness added to the surface of the plate and flap	358
5.7	Calculation domain and scalar cell faces	359
5.8	Calculated mean velocity vectors	359
5.9	Calculated mean streamlines	361
5.10	Experimental and calculated distributions of free-stream velocity, surface static-pressure and skin-friction coefficient	362
5.11	Profiles of calculated and experimental mean velocity	365
5.12	Profiles of calculated and experimental turbulence kinetic energy	368

CHAPTER 1

THETIC INTRODUCTION

This thesis is concerned with the aerodynamic characteristics of the subsonic flow around airfoils with turbulent trailing-edge separation associated with high lift and large angles of attack. Aircrafts must operate at low speeds and use high angles of attack to provide lift, for example during take-off and landing, although most of the flight cycle is at cruise conditions where low angles of attack minimize drag forces. Airfoils at large angles of attack can have a region of sustained adverse pressure gradients over the downstream portion of their surface and this leads to boundary-layer separation with recirculating flow near the trailing edge. This separation can appreciably effect the high-lift performance and stall characteristics of airfoils, wings and aircraft and leads to a reduction in lift and an increase in drag. The importance of these separation effects makes it desirable to improve understanding of their occurrence and effects, and to develop theoretical procedures to account for them. This dissertation is concerned with these requirements.

The ability to predict separation in the trailing-egde region of wings would aid design and possibly assist in the avoidance of stall and spin, caused by separation, which are a major cause of avionic accidents, see Anderson (1979). Viscous effects on airfoils are significant, even under attached flow conditions, and proper treatment of the trailing-edge region, including wake curvature, normal pressure gradients, and viscous-inviscid interactions, is necessary to obtain

satisfactory predictions of lift and drag (Melnik and Grossman, 1981 and Olson et al, 1978). The numerical solution of boundary-layer and potential-flow equations has already been applied to simple airfoil and wing configurations as described, for example, by McDonald and Briley (1983), Cebeci, Stewartson and Whitelaw (1983), Lock (1980) and Melnik (1980). Most methods involve interactive viscous-inviscid calculations which satisfactorily account for viscous effects through the boundary-layer displacement thickness distribution over the surface and in the near wake, see LeBalleur (1982), even with small regions of recirculating flow at the trailing-edge, see McDonald and Briley (1983). These approaches are extended here to include the calculation of large trailing-edge regions of turbulent separation which, at least for engineering purposes, depends on satisfactory modelling of the turbulence and strong viscous-inviscid interactions. The ability to calculate the mean turbulent flow, and consequently displacement thickness, is not satisfactory in the separated region and the major deficiencies have been inadequacy of the turbulence model and solution of overly-simplified transport equations. The primary purpose of this dissertation is to study a large-scale separated flow on a relatively simple configuration with the view to understanding the basic aerodynamic features and to improve flow modelling.

1.1 Objectives

Experimental and computational investigations have been undertaken with the following specific objectives:

1. To improve understanding of flow phenomena associated with turbulent boundary-layer separation in the vicinity of the trailing-edge of airfoils by the application of experimental and calculation methods.
2. To develop and appraise prediction techniques for the external flow around the trailing edge of airfoils at high angles of incidence.
3. To develop measurement techniques and obtain results which will assist physical understanding and may be used for the verification of the prediction techniques and, specifically, of the equations, numerical assumptions, boundary conditions and turbulence model which they require.

The proposed calculation method is based on the numerical solution of conservative transport equations in differential form. The two-dimensional form of the time-averaged Navier-Stokes equations has been solved in the region of recirculating flow together with equations which represent the transport of turbulence kinetic energy and its dissipation rate. Upstream of the region of recirculating flow, boundary-layer and potential-flow equations have been solved and coupled through boundary conditions which represent the viscous-inviscid interaction. This pattern of solution implies numerical, turbulence-model and boundary-condition approximations which require experimental support. As a consequence, the corresponding

measurement program is extensive and has involved the development of instrumentation as well as measurements in the regions of inviscid, boundary-layer, recirculating and wake flow. The choice of flow configuration and of instrumentation can be justified by reference to the review of the following section.

1.2 Review of Related Work

This section briefly describes previous investigations relevant to the formulation and assessment of the present contribution. Theoretical developments, including calculation methods for separated flows, are examined first to emphasize the recent trends toward their use in engineering design. The second part of this section reports on experimental investigations with separation and provides physical understanding with which calculated results can be compared and evaluated. Experimental techniques are also discussed to provide background for the choices of the present work.

A complete review of aerodynamic literature is not attempted and the reader is referred to the recent texts of Chang (1970, 1976), Kuchemann (1978), Cebeci and Smith (1974), Bradshaw et al (1981) and to the reviews of McDonald and Briley (1983), Cebeci et al (1983), Hess (1981), Melnik (1980), Lock (1980), Lynch (1978), Fernholz (1976) and Smetana et al (1975). Reference to specific methodology or topics which are are the subject of the following chapters, and not considered here, are introduced in the relevant parts of the text.

Theoretical investigations. The need for improvements to computational fluid dynamic techniques for aeronautical design of high-lift components has been identified, for example by Liebeck (1978), Lynch (1978), and Hunt et al (1981). The general opinion appears to be that advanced computational methods can result in improved levels of aerodynamic technology and efficiency, and reduce design costs and time by decreasing the amount of wind-tunnel testing required. At present, the benefits obtained from using calculation methods in high-lift design are limited and one limitation is the inability to predict the onset of turbulent boundary-layer separation including the properties of the downstream recirculation region and its wake.

The flow around airfoils can be divided into different regions and those which are presently of interest are as follows: the potential flow, the attached turbulent boundary-layer flow upstream of separation, the turbulent recirculating flow and the downstream wake flow. In each region, a different level of approximation for transport equations, turbulence modelling and numerical schemes may be appropriate and calculation methods have been developed to treat these regions either independently or collectively.

Most methods for calculating the flow around airfoils make use of a combination of inviscid and boundary-layer equations (Cebeci, Stewartson and Whitelaw, 1983) since viscous effects are important to lift and, especially, to drag (Olson et al, 1978). Potential flow solutions, which have been obtained with methods such as those reviewed by Hess (1975, 1980) or Hunt et al (1981), are interacted with solutions of boundary-layer equations, through appropriate boundary conditions and have been used for high speed flows and cruise conditions, but

without separation, for sometime (see Melnik, 1980 and Smetana et al, 1975). The solutions of boundary-layer equations up to separation were considered in the 1968 Stanford Conference (Coles and Hurst, 1968) and some further work is referred to by Cebeci and Smith (1974), Cebeci and Bradshaw (1977), Le Balleur et al (1980), Melnik (1980), Bradshaw et al (1981), Kline et al (1981) and Cebeci et al (1983).

In trailing-edge flows, turbulent boundary-layer separation occurs gradually over a region of the suction-side surface and the following review is restricted to this type of separation which is initiated by an adverse pressure gradient. In contrast, separation can be initiated at a surface discontinuity, such as at a corner, and for this the reader is referred to the reviews of Taylor and Whitelaw (1983), Taylor (1981) and Eaton and Johnston (1981). The prediction of turbulent boundary-layer separation has been obtained with empirically-based correlations, often using simplified forms of the integral momentum equation; for examples see Smith (1972), Chang (1970) and Thwaites (1955). Such methods were reasonably effective at alerting designers to the possibility of separation, but were of less value in remedying the situation.

It is now widely recognized that steady boundary-layer equations can be used to predict small regions of separation when the interaction with the outer inviscid flow is represented (McDonald and Briley, 1983). Inverse boundary-layer procedures are necessary where the angle of incidence is large enough to cause upper surface separation as discussed, for example, by Carter (1975) and Cebeci (1976) for finite-difference solutions to the boundary-layer equations, and by Kuhn and Nielsen (1973) and East, Smith and Merryman (1977) for integral boundary-layer calculations. The viscid-inviscid interaction

in the vicinity of separation is reviewed by Le Balleur (1982, 1983), McDonald and Briley (1983) and Cebeci, Stewartson and Whitelaw (1983) and these authors refer to a number of calculations of small regions of recirculation with interactive techniques. Those shown on table 1.1 are of particular interest to the present study in that they demonstrate that integral methods are often to be preferred for practical applications, including three-dimensional flows, because they are comparatively economic. They do, however, require appropriate velocity-profile assumptions which, although they have been applied to a range of attached flows (see Kline et al, 1968), need to be obtained or extended to include reversed flow (Swafford, 1983). Further, methods for solving the boundary-layer or integral-momentum equations can be used to treat small regions of recirculation but, where the region of recirculation exceeds a size which remains to be established, the boundary-layer approximations cease to apply and the Navier-Stokes equations are required.

A consequence of a large region of recirculation is that the inviscid flow field is significantly altered and the flow exhibits a strong viscous-inviscid interaction. One way to deal with strong interactions is to solve time-averaged Navier-Stokes equations over the entire flow domain. Attempts have been made to obtain complete solutions for attached flows over airfoils with the Navier-Stokes equations, for example see Wu et al (1977), Steger (1978), Shamroth and Gibeling (1980), Hegna (1982) and Rhie and Chow (1982), but numerical difficulties and extra expense make them undesirable alternatives where the simpler and cheaper methods discussed above can be used. Regions of recirculation have been calculated with elliptic transport equations to characterize the recirculating flow; for example see Bradshaw et al (1981), Simpson (1981), Cebeci et al (1983) and those shown on table 1.2 which

are relevant to the present study. The last few on this table deal with separation in confined flows and were selected to indicate the likelihood of success near recirculation with the present approach to calculations. The problems associated with the calculation of separated flows are associated with boundary-condition, numerical and turbulence-model assumptions (Whitelaw, 1981). Reasonable representation of the mean flow has been achieved where numerical truncation errors were sufficiently reduced and the indication is that closure with two-equation or higher order turbulence models is required for recirculating flows, see Gosman et al (1969), Mellor and Herring (1973), Wadcock (1980), Bradshaw et al (1981) and Marvin (1982), as opposed to the simpler models recommended for attached aerodynamic flows, for instance by Cebeci and Meier (1980).

Calculation of the wake is also important, for example in determing drag, and the relevant wake studies are shown on table 1.3. The results suggest that the mean flow fields of symmetric and asymmetric near wakes can be predicted with satisfactory accuracy, but that the agreement between experiment and prediction deteriorates with distance from the trailing edge: it is dependent on turbulence model assumptions. It is worth noting that the inaccurate representation of the flow in the vicinity of separation can propagate into the wake and that prediction of the wake thereafter depends on the accuracy of the solution in the upstream part of the wake (Durst and Rastogi, 1979) and to a lesser degree on turbulence models (McGuirk, Taylor and Whitelaw, 1981). Accordingly, the present calculations emphasize the requirements for predicting the recirculating flow near the trailing-edge and presume, initially, that they are adequate in the wake.

Experimental investigations. Measurements are needed to provide physical insight into the flow in and around regions of turbulent boundary-layer separation near a trailing-edge. In addition they guide the choice of equations and turbulence models which are required to represent the flow.

Turbulent separation has been the subject of experimental studies in many engineering flows including the bluff-body separated flows reviewed by Simpson (1981), Taylor (1981), and reattaching flows of Eaton and Johnston (1981). Laminar boundary-layer separation has also been investigated and the studies by Gault (1949), Tani (1964), Arena and Mueller (1980), van den Berg (1981), Mueller and Batill (1982) and the theoretical work of Smith (1983) are noteworthy since they provide understanding of certain separation processes and help to identify turbulent trailing-edge separation as different from the types of separation associated with laminar bubbles.

There is little reliable information of the flow structure for turbulent separating boundary layers and this is indicated in the references of table 1.4. Results in recirculating regions have been obtained with hot-wire, flying hot-wire and laser-Doppler anemometry and discussion of the relative advantages and disadvantages of these techniques appears in the next subsection. The flows of Nakayama (1983) and Coles and Wadcock (1979) are closest to the interests of the present study in that they were obtained near the trailing-edge of lifting airfoils with turbulent separation: the former study, with a combination of hot-wires and laser-Doppler anemometry, has a smaller region of separation than that of present interest, and the latter study with flying hot-wire anemometry is at maximum lift but does not include detailed near-wall measurements. These results together

with those of Simpson et al (1981) in the vicinity of detachment and of Hastings and Moreton (1982), both obtained with laser-Doppler anemometry in turbulent separating boundary-layers, are compared to the present experimental results in chapter 3.

The above experiments indicate that velocity characteristics of the flow in the vicinity of turbulent separation are significantly different from those of attached turbulent boundary layers. For example, mean reverse velocities up to a maximum of 20 per cent of the free stream velocity have been found close to the wall (Simpson et al, 1977). Also, intermittent reverse velocities have been found upstream of mean streamline detachment across the boundary-layer to about the location where the streamwise turbulence intensity is a maximum (Simpson et al, 1981) and downstream of the trailing-edge in the wake (Nakayama, 1983). Production of and diffusion by turbulence are very large around separation and, since the flow is also highly anisotropic, this implies turbulence modelling is not straightforward. Also in contrast to attached flows, the viscous-inviscid interaction is strong in the vicinity of separation since normal pressure gradients and Reynolds normal stresses are large and are important to the mean flow field (Nakayama, 1983).

It is evident that information about the near-wall region of the backflow is lacking in the results of Coles and Wadcock (1979) and is uncertain in the flows of Simpson et al (1981) and Hasting and Moreton (1982). It is difficult to establish a two-dimensional separated region and the flows of Nakayama (1983), Hastings and Moreton (1982), Simpson et al (1981, 1977) and Wadcock (1980) all report relatively good two-dimensional mean flow upstream of separation, but with less

certainty further downstream. There are also uncertainties associated with the experimental techniques used to obtain the measurements; for example, Coles and Wadcock (1979) report interference due to their mounting of the flying-wire motor inside the wind-tunnel and the laser-Doppler measurements suffer from difficulties associated with seeding and resolution in the backflow and near-wall regions.

There are also difficulties in comparing the available measurements with calculations. In the case of Simpson et al (1981), the downstream boundary has to be located part way through the recirculating flow and, in the case of Coles and Wadcock (1979), interference of the motor and probe on the surface pressure and backflow, respectively, introduce unacceptable uncertainties. Also, the upstream flow is unknown since there are no measurements near the leading edge. Nakayama (1983) and Viswanath and Brown (1983) have, perhaps, reported the most satisfactory sets of results but their separations are small and it is probable that boundary-layer equations may be appropriate if solved in an inverse mode. In the case of Hastings and Moreton (1982), the lack of potential flow above the boundary layer downstream of detachment, and the resulting interference with the tunnel-roof boundary-layer, causes unncessary complications for calculations.

A few of the recent experimental studies of table 1.4 have included the wake downstream of recirculation and are relevant to the present study. The wakes of flat plates have also been investigated experimentally with emphasis on the turbulence structure, since the viscid-inviscid interaction is small, see for example Chevray and Kovasznay (1969), Pot (1979), Andreopoulos and Bradshaw (1980), Ramaprian et al (1982), MacLennan and Vincent (1982) and Wood and

Bradshaw (1982). It is clear that the ability to predict these wakes, and those of lifting airfoils, is related to the turbulence structure (Hah and Lakshminarayama, 1982) which is significantly different in separated wakes. Airfoil wakes have been the subject of the experiments of Nakayama (1983), Hah and Lakshminarayama (1982), Yu (1981), Viswanath et al (1980) and Preston et al (1945) and these investigations provide information of the wakes of lifting and non-lifting aerofoils with attached boundary layers at the trailing edge. Information of the development of the very-near wake, pressure-side mixing layer and far wake are not available for the flow downstream of a large region of recirculation caused by turbulent boundary-layer separation near the trailing-edge.

Measurement techniques for separated flows. Measurements of velocity characteristics in subsonic flow with velocity reversals have been obtained with the following: pressure-sensing methods, i.e. with impact probes; convection cooling techniques, i.e. with stationary or moving hot-wires; time-of-flight measurements with thermal or other tracers, i.e. pulsed-wire anemometry; and optical techniques, i.e. laser-Doppler velocimetry. Flow visualization can also be used to obtain the flow patterns in separated flow, see Chang (1976), but it is not practical for measuring velocity in highly turbulent recirculating flow.

Measurements in recirculation regions with stationary probes introduce uncertainties which are difficult to assess because the wake of the probe and its supports is retained, at least temporarily, within the recirculating flow and affects the regional flow properties. For example with impact, hot-wire and pulsed-wire probes, there will

be some instances where at least instantaneous measurements will be obtained in the probe wake since reversing flows do not have a preferred direction with which to align the probe.

Impact probes have been primarily used to obtain mean values of pressure and velocity in both two- and three-dimensional mean flows, for example see Coles and Hurst (1968), Chang (1970), Cook et al (1979) and Mattick and Stollery (1981), and various back-to-back Pitot tubes have been used for mean velocities in very large regions of recirculating flow, for example see Rodgers, Seetharam and Wentz (1979). There are, however, large uncertainties in velocity characteristics obtained with pressure-probes in regions with flow reversals for the following reasons: the flow does not have a preferential direction so the probe cannot be aligned, even approximately, with the flow direction and it measures inaccurately at large flow angles; the probe interferes with the local, and possibly overall, flow patterns as discussed above; mean readings of static and total pressure that are used to derive velocity values are affected by velocity fluctuations, which are large in the vicinity of separation and are also distorted by the probe, and this gives large relative errors in mean-velocity values especially in regions of recirculating flow where velocities tend to be small; and, lastly, large gradients of mean and instantaneous values of velocity and pressure that are associated with separation can cause significant errors in the response of impact probes. In conclusion, pressure probes are not very useful in separated flow.

Stationary hot-wires suffer from rectification around zero velocity because they respond to the rate of convective cooling,

i.e. forced convection, rather than directly to velocity. Directionally-sensitive hot-wire probes have been developed but are subject to restrictions which, as shown below, make them inappropriate for the turbulent separated flow of the present study. Downing (1972) and Fairlie and Perry (1975) made use of two additional resistance thermometers, i.e. fine-wire sensors, to locate the thermal wake of a hot-wire and, thus, to determine the flow direction. These probes are unable to measure in flows with large tangential velocities and their frequency response is limited to fluctuations less than about 50 Hz because of ambiguities associated with the time required for the heated wake to pass from the hot-wire to the previously-upstream thermal sensor. Uncertainties resulting from these restrictions are unacceptable for the present purposes.

In a similar fashion, the shielded dual-wire probe of Cook and Redfearn (1976) is capable of measuring the mean and fluctuating components of velocity in reversing flow. It uses two hot-wire sensors to measure the one-dimensional flow through the central hole of a disc-shaped shield and detects the flow direction by identifying the thermal wake on the downstream wire. Unfortunately, the probe is insensitive to flow direction when the wake misses the downstream wire and this is prevalent in low turbulence-intensity flow. Also, its use is limited to velocities between about 0.3 and 10 m/s and to velocity fluctuations with frequencies less than about 100 Hz and these factors, plus the large size of the probe, make it inappropriate for the present recirculating flow.

Split hot-film probes, which measure the heat transfer from heated strips which are located 180 degrees (2 sensors) or 120 degrees

(3 sensors) from one another on the surface of a cylindrical fibre, have been developed by Wentz and Seetharam (1977) and Jorgensen (1981), respectively. Split-film anemometry uses the variation of heat transfer with position around a two-dimensional cylinder to identify the velocity vector. Major sources of error can arise from uncertainties in the response of the individual hot-film strips. First, different combinations of instantaneous fluctuating velocity components may not be uniquely related to the voltage output levels, and, second, the response to velocity components parallel to the hot-film axis is uncertain which is of particular consequence to measurements of quantities involving fluctuating transverse velocities. Split-films have to be calibrated for variations in both flow speed and direction, which is expensive considering the large number of constants involved (see Jorgensen, 1981). Also, calibration needs to be repeated frequently because of time-dependent change in the thermal resistance of the surface above each hot-film sensor which is mainly caused by non-uniform particle deposition over the surface. Measurements with these multi-sensor probes incur uncertainties, which include those associated with interference effects of a stationary probe in recirculating flow discussed above, that are unacceptable for the present purposes and, although further investigation into their use is required, they are not considered here.

Pulsed-wire anemometry has been discussed by Castro and Cheun (1982) and Bradbury (1976) and it can be used to obtain mean and fluctuating components of velocity. It measures the time of flight of a tracer of heated air to one of two parallel sensing-wires

which act as resistance thermometers and are located perpendicular to, and on either side of, a pulsed heat-generating wire. Bradbury (1976) recommends its use in highly turbulent or reversing flow far away from walls. Pulsed-wire measurements of lateral turbulence intensity and turbulence shear stress are unsatisfactory for turbulence intensities less than about 10 per cent because the thermal tracers miss the sensing-wires. For turbulence levels above this, the largest sources of error in pulse-wire measurements are a direct consequence of its yaw response. There are two main effects: zero velocity is measured for instantaneous velocities at an angle greater than about 70^{o} to the axis perpendicular to both sensor and heat-generating wires and, second, thermal diffusion prevents the wire from having an ideal cosine-law response. The resulting errors are dependent on characteristics of the turbulence field and are discussed by Castro and Cheun (1982). In their analysis of a typical, practical pulsed-wire in homogeneous turbulence, it is shown that components of the Reynolds stress tensor have errors greater than 20% of their values for the turbulence intensity ranges as follows: for longitudinal Reynolds stress, $\langle u^2 \rangle$, above 50 per cent turbulence intensity; for lateral turbulence intensity, $\langle v^2 \rangle$ or $\langle w^2 \rangle$, below 25 per cent turbulence intensity, assuming the wire is rotated 90 degrees from the first case; and for Reynolds shear stress, $\langle uv \rangle$, below 25 per cent and above 80 per cent turbulence intensities. Pulsed-wires have acceptable accuracy for all of the Reynolds stresses between about 25 and 50 per cent turbulence intensity and this restriction, plus those that are a consequence of its dimensions, make it inadequate for the present purposes.

Laser-Doppler velocimetry (LDV) is a non-obtrusive optical technique which measuresthe velocity of particles moving in the fluid and has been used, with frequency shift, to measure velocity characteristics in recirculating flows, see Durst, Melling and Whitelaw (1981) and, for airfoil flows, see table 1.4. LDV requires optical access and is expensive of time and money because the instrumentation is complex and difficult to use. In air flows, there are unresolved uncertainties associated with light-scattering particles which may result in substantial errors in recirculation regions. For example, the correlation between velocity and particle number may cause high readings of mean velocity depending on the turbulence intensity (Habib, 1980). The number of particles found in the recirculation region can be up to an order of magnitude less than in the free stream as shown by Young, Meyer and Hoad (1978) and the related uncertainties are discussed by Simpson et al (1981) and Nakayama (1983). There are also uncertainties associated with the size and location of the measuring volume, particularly close to walls, and these are discussed by Olson and Orloff (1982) who propose an expensive remedy using mirrored surface and telescopes to improve the signal-to-noise ratio and to focus the crossed laser-beams, respectively.

Flying hot-wire anemometry has been used by Coles and Wadcock (1979) to measure velocity characterisitcs in the recirculating flow resulting from turbulent boundary-layer separation on a NACA 4412 airfoil at high angle of attack. It was developed to shift the rectification effect associated with stationary wires to negative velocities equal to the probe speed. Moving the probe can be of further advantage since the flying-wire motion can be arranged so that the probe arrives in the region of interest before it has disturbed the

local flow and then waits, before returning, at some inconspicuous location in the external or far-downstream flow until any disturbances associated with the probe wake have been dissipated from the region of interest and the flow there returns to its undisturbed state. Flying-wire calibration is similar to that for stationary hot-wires and, although the probe velocity must be obtained, the flying-wire can be calibrated using the known probe velocity for values less than the maximum possible probe speed. Flying hot-wire anemometry represents an alternative to laser-Doppler velocimetry rather than a directly justifiable choice for the present flow. In contrast to LDV, flying-wire anemometry is an extension of a well-developed technique with known uncertainties. Since it appears to be a promising approach, it was developed for use in the present region of turbulent trailing-edge separation and is discussed in chapter 2.

1.3 Present Contribution

The review of the previous section indicates that the lack of detailed experimental information on velocity and pressure characteristics in and around the recirculating flow near the trailing-edge has prevented evaluation and inhibited development of current prediction procedures. It is also clear that the use of flying hot-wire anemometry may be able to provide accurate measurements of the velocity characteristics and,

in particular, to quantify the properties of the recirculation region. There is a need for an experimental investigation of a trailing-edge flow with substantial recirculation resulting from turbulent boundary-layer separation which includes measurements that will allow the evaluation of calculation methods but without ambiguities arising from the boundary conditions.

The contributions of this thesis include experimental and computational investigations of the flow in the vicinity of the trailing flap shown on figure 3.1, whose angle of incidence results in turbulent boundary-layer separation, a large region of recirculation and a curved downstream wake. The experimental investigations quantify the pressure and velocity characteristics of this flow, particularly in and around recirculation, and the results are sufficiently complete to allow the evaluation and development of calculation procedures and turbulence models. The computational investigation is divided into three parts which consider the regions of inviscid flow, boundary-layer flow approaching suction-side separation, and the separated flow including its downstream wake. The relative importance of assumptions contained in numerical methods, boundary conditions, turbulence models and approximate forms of transport equations are investigated.

The present flow configuration was selected to improve understanding of phenomena associated with turbulent trailing-edge separation without the complicating effects associated with the flow around the leading edge of airfoils.

The remainder of this treatise is dividied into five chapters. Chapter 2 describes the experimental methodology used to affect the measurements reported in chapter 3. Flow visualization was used to

describe the flow patterns and to identify the region of two-dimensional mean flow. Pressure-measuring instruments were used to obtain the mean pressure distributions on the model surface and in the external flow where there were no velocity reversals. Velocity characteristics were quantified with a combination of impact, hot-wire and flying hot-wire probes and the associated instrumentation, equations and procedures are described: flying hot-wire anemometry was required where instantaneous flow reversals occur and was developed for this application.

In chapter 3, measurements of pressure and velocity characteristics in the flow of the trailing-edge configuration shown on figure 3.1, are reported and were obtained with the experimental techniques of chapter 2. Mean values of pressure and velocity, and the four non-zero Reynolds stresses in two-dimensional flow are presented in the regions of potential, boundary-layer, recirculating and wake flow. Mean velocity distributions were investigated in the near-wall flow, including the backflow, because of their importance to the calculation methods of chapter 4. The two-dimensional nature of the mean flow was visualized and then quantified by velocity and pressure measurements which included the use of flying-wire anemometry in the recirculation region. Physical implications of mean-flow and turbulence results are discussed in relation to calculation methods for recirculation flows.

Calculation methods are the subject of chapter 4 which presents the conservation equations representing transport of mass, momentum and turbulence quantities in their differential and finite-difference forms appropriate for potential, boundary-layer and recirculating flows. Two turbulence models, based on the k-ε model and on modelling transport equations for the Reynolds stresses are described. The former was

used in the recirculation region and the latter in the upstream boundary layer. Numerical procedures for solving inviscid, boundary-layer and elliptic transport equations are described and a procedure for interacting the inviscid and boundary-layer equations is presented. The implementation of boundary conditions appropriate to each method is explained.

Chapter 5 presents results obtained with the calculation procedures of chapter 4. The inviscid flow was calculated around the present trailing-edge configuration after verifying the inviscid procedure in the flow around an infinite cylinder. Solutions to the boundary-layer equations with a Reynolds-stress transport turbulence model are presented in the region approaching separation. The wall boundary condition first included the measured pressure distribution to test the validity of the boundary-layer equations approaching separation and then the viscous-inviscid interaction was subsequently modelled to predict the wall pressure. Elliptic transport equations with the k-ε turbulence model were solved in orthogonal curvilinear co-ordinates to represent the regions of potential, curved boundary-layer, separated and wake flow. The results are compared with the measurements of chapter 3.

Finally, chapter 6 reviews the achievements of this research and provides recommendations for improvements and future work.

TABLE 1.1

SUMMARY OF SEPARATED FLOW CALCULATIONS WITH THE VISCID-INVISCID INTERACTIONS

Author(s)	Flow and Method	Findings/Comments
Street (1982)	Supercritical airfoil. 8 ft. Supercritical wing and body. 3-D Integral boundary-layer method. Full potential code. Wake strip method.	Good agreement with experiment. Calculates small region of recirculation. Acceptable computation times. 3-D Wing body effects need to be calculated with a 3-D boundary-layer code rather than a strip 2-D method.
Olson et al (1978)	Joukowski airfoil. NACA 4412 with flap. 2-D Finite-difference boundary-layer method. Panel method. 2-layer eddy viscosity model. Automatic grid generation.	Drag acceptably calculated for single airfoils up to incipient separation and for multi-elements between lift coefficients of 0.6 and 2.2. Recommend comparisons of mean velocity and Reynolds stresses with experiment particularly for multi-element case.
Seebohm and and Newman (1975)	NACA 4418 with flap. NACA 63A(10)18 with flap. RAE 2815 with flap. 2-D Integral boundary-layer method. Surface-vortex inviscid method. Simple displacement surface.	Capable of calculating flow with no large regions of separation and no significant wake/boundary-layer interactions. Lift within 2 per cent. Drag poor. Converges quickly - 2 to 3 iterations.

Author(s)	Flow and Method	Findings/Comments
Briley and McDonald (1975)	NACA 66_3018 airfoil. 2-D streamfunction - vorticity boundary-layer equations with viscous-inviscid interaction. 2-D Navier-Stokes equations. McDonald-Fish one-equation turbulence model with modifications for separation.	Solutions with the Navier-Stokes equations were compared to those of an interactive procedure with the boundary-layer equations. Results are obtained in small separation bubbles at the leading-edge and are compared with experiments. Boundary-layer equations are not singular at separation and are appropriate for thin separation bubbles. Little difference was found between calculations with the boundary-layer and Navier-Stokes equations for small separation bubbles. Pressure distributions in good agreement with experiment. Mean velocities in reasonable agreement except near re-attachment where the gradients are large or boundary-layer assumptions are inappropriate.
Simpson and Collins (1978)	Flow of Simpson et al (1977). Method of Bradshaw, Feriss and Atwell (1967) for boundary layer. Finite-difference potential flow method with emperical polynomial for separated displacement thickness.	Reynolds normal stresses are important in transport equations for mean momentum and turbulence kinetic energy. Various wall functions were found to be unimportant approaching separation but were in disagreement near detachment. Shape factor is poorly predicted. More data is needed to determine normal stress effects near separation. Flow conditions at intermittent separation can be used in a functional description of the displacement thickness if the distance between intermittent and fully-developed separation is short.

Author(s)	Flow and Method	Findings/Comments
Butter and Williams (1980)	RAE 100 aerofoil. Airfoil with flap and slat. 2-D Integral inverse boundary-layer. Panel method with compressibility correction. Displacement surface (transpiration).	Good pressure distributions otherwise reasonable agreement except near trailing edge. Separation overpredicted. Wake curvature effects important.
Whitefield et al (1981)	Separating flow of Simpson et al (1977). Transonic flow over axisymmetric bump. 18% thick circular-arc airfoil. Body of revolution. Three stores in TER configuration. 3-D Integral inverse boundary-layer. Finite-volume Euler code. Surface-source (transpiration).	Low speed calculation good up to separation. Skin friction agreed downstream of separation whereas other integral quantities did not. Reasonable calculation times (2-6 mins). Practical results for transonic flow.
Veldman (1980)	Dented plate with separation bubble. Quasi-simultaneous method based on triple-deck hierarchy.	Good description and comparison of inverse, direct semi-inverse strategies. Calculate small separation bubbles in 1-20 iterations. Failed to converge above Reynolds number of 4×10^5 because of thick backflow.
Oskam (1980)	NACA 63-009 airfoil. NLR 7301 airfoil with and without flap. 2-D Integral boundary-layer method. Panel method.	Convergence: no separation 3 iterations, with separation 5-6 iterations. Static pressure variation across shear layers near trailing edge needs investigating. Reasonable pressure, lift and drag values without separation. Inlet profiles important.

Author(s)	Flow and Method	Findings/Comments
Leicher (1980)	NACA 4412 airfoil. DO A5 airfoil with flap. DO A4 airfoil with flap or slat BEC-C. Four-element airfoil system. Transonic Al CAST-7 airfoil with and without flap. 2-D Integral inverse boundary-layer method. Panel method (subsonic) and full potential method (transonic).	Pressure under-predicted in separated flow. Separation point and lift variation with with angle of attack adequately predicted. Fair agreement in pressure distribution for large separation bubble and strong trailing edge separation. Velocity fields not presented.
Johnson and Spaid (1981)	Supercritical DSMA 671 airfoil. Method of Arieli and Murphy (1981). Upwind differencing in backflow. Cebeci-Smith turbulence model.	Changes in static pressure and flow angle were small in boundary-layer but large in the wake. Rapid growth just upstream of trailing edge under-predicted. Mean velocities good. Differences in shear stress distribution. Eddy viscosity under-predicted but not the only cause of under-prediction of boundary-layer growth near the trailing edge.
Arieli and Murphy (1980)	Transonic NACA 64A010 airfoil. 2-D Galerkin inverse boundary-layer method. Pressure matching correction.	Equations not elliptic in reverse flow region but parabolic in reverse direction. Comparison with solution of Navier-Stokes equation shows substantial economies in zonal calculations.
Wu and Gulcat (1979)	Wake of a flat plate. Circular cylinder. Streamfunction-vorticity transformation. Boundary-layer equations in attached region. Navier-Stokes equations in detached region.	Boundary conditions difficult, see Wu (1976). Navier-Stokes solution required major part of computer time. Flow patterns adequate. Separation point and coefficients of surface pressure and drag were reasonable.

Author(s)	Flow and Method	Findings/Comments
Cebeci and Schimke (1983)	NACA 66_3018 airfoil. 2-D finite-difference inverse boundary-layer equations. Conformal mapping technique for potential pressure. Cebeci-Smith algebraic eddy-viscosity turbulence model.	Successful prediction of the separation bubble depended on the location and accurate prediction of transition. The procedure which interacts inviscid and boundary-layer equations converged after about 10 iterations. Calculated and measured profiles of mean velocity are in very good agreement. Pressure distributions are in considerable disagreement with measurements in the vicinity of the laminar separation bubble and is attributed to the prediction of transition to turbulent flow in the separation bubble.
Render and Stollery (1983)	NACA 64_3418 airfoil. Experiments also reported with $Re_c = 3.10 \times 10^5$. 2-D Integral momentum and energy equations for the boundary-layer with and without simulation of laminar separation bubbles. Panel method for inviscid flow.	Experimental results obtained for comparison include force and moment measurements and surface pressure distributions. Separation and detachment points were located with visualization. Lift and drag coefficient were less than adequately predicted prior to the occurence of trailing-edge separation. Poorer agreement was found at angles of attack greater than about 6 degrees when turbulent separation occurs more than 5% of chord upstream of the trailing-edge. The location of separation is poorly predicted being too far upstream of its measured location. The influence of laminar separation and reattachment, and hence transition, is of importance to the representation of the trailing-edge separated flow. Inviscid pressure distributions are not corrected for boundary-layer displacement effects and are in poor agreement with measured results.

Author(s)	Flow and Method	Findings/Comments
Bhateley and Bradley (1972)	NACA 23012 airfoil with flap and slat. NACA 64A210 modified airfoil with and without leading-edge slat, or with slat and with or without flap. 2-D Finite-difference boundary-layer. Downstream extension of separation streamline with different approaches including free-streamline model. Distributed-singularity potential flow model. Cebeci-Smith turbulence model. Separation point located from experiment.	Comparison to surface pressures are adequate up to separation. Pressure conditions in separated wake not accounted for and pressures are poorly calculated in separated flow. Displacement thickness under-predicted at trailing edge in all cases. Location of separation streamline ad hoc and separated flow poorly represented.
Maskew, Rao and Dvorak (1980) Maskew and Dvorak (1978)	NACA 0012 modified infinite-swept wing. GA(W)-1 airfoil. NACA 4412 airfoil. 2-D and 3-D Integral boundary layer method. Separated region enclosed with vortex sheets. Panel method. Separation line from experiment for 3-D case and by correlation or zero skin-friction coefficient for 2-D cases.	Pressure distributions in close agreement. Maximum lift values in good agreement otherwise fairly reasonable agreement for variations of lift and drag with angle of attack and Reynolds number. "Problem really for Navier-Stokes equations but not a practical approach for the aerodynamicist".

TABLE 1.2

SUMMARY OF SEPARATED FLOW CALCULATIONS WITH TIME-AVERAGED NAVIER-STOKES EQUATIONS

Author(s)	Flow and Method	Findings/Comments
Rhie and Chow (1982)	NACA 4412 airfoil. NACA 0012 airfoil. 2-D primitive variable. Boundary-fitted orthogonal curvilinear co-ordinate system. 2 Equation k-ε turbulence model.	Agreement is good between experimental and predicted pressure and velocity distributions without separation. With separation, there is good agreement for mean flow but poor for turbulence quantities. Accuracy of the results is highly dependent on resolving the gradients, and on the grid, near the trailing and leading edges. Numerical diffusion likely contributes to these errors.
Hegna (1982)	NACA 0012 airfoil. 2-D primitive variable. Body-fitted orthogonal curvilinear co-ordinate system. Cebeci-Smith turbulence model with ad hoc modifications for separated region.	Pressure distributions are in reasonable agreement except near the trailing edge. Mean velocities are in poor agreement. Lift is under-predicted. Lift-to-drag ratio is moderately well calculated No quantitative turbulence data exists with which to compare results. Solution is sensitive to small changes in leading edge phenomena particularly transition. Numerical accuracy was not evaluated.
Sugavanam and Wu (1982)	Circular cylinder. 12% Thick Joukowski airfoil. 2-D streamfunction - vorticity equations. Time-dependent study. Cebeci-Smith mixing length and combined mixing length/k-ε turbulence models.	In attached flow, pressure and velocity profiles are well predicted with both turbulence models. No comparison was made with experiment for the stalled airfoil case except that calculated oscillations in lift and drag were not observed experimentally. Require improved turbulence models in the transitional and recirculating flow. Additional experimental data needed to establish their validity.

Author(s)	Flow and Method	Findings/Comments
Cebeci, Khalil and Whitelaw (1979)	Flow of Simpson et al (1977). Straight-sided diffusers. Trailing-edge wedges. 2-D Primitive variable. k-ε Turbulence model. Also inverse boundary-layer solution with Cebeci-Smith turbulence model.	Recommend body-fitted co-ordinates. Detailed trailing-edge and diffuser experiments are not available for comparison. Separation point, turbulence kinetic energy mean velocities and integral quantities are in good qualitative agreement with experiment of Simpson et al (1977). Some uncertainty is associated with the downstream boundary conditions of this experiment and with numerical accuracy. Cross-stream pressure gradients must be balanced with corresponding convective terms.
Deiwart (1976)	Symmetric, 18% thick, circular-arc airfoil at transonic speeds. 2-D Compressible primitive variable. Four different zero equation models using algebraic edd-yviscosity equations with and without modifications for separated flow and shock boundary-layer interaction.	Method is capable of simulating basic features of separating transonic turbulent flow fields. Qualitative agreement is good. Quantitative agreement in separated and shock-interaction regions was poor. More detailed experiments are needed to develop models for the interaction and separated regions. Eddy-viscosity models do not seem adequate for representing the complex turbulence phenomena associated with separation.
Shamroth and Gibeling (1980)	NACA 0012 airfoil. 2-D Compressible primitive variable. Body-fitted non-orthogonal co-ordinate system. McDonald-Fish one-equation turbulence model.	Highly-stretched co-ordinate systems are used to emphasize the near-wall and leading-edge regions. Subsonic mean flow and turbulence results are in poor agreement. Lift agrees fortuitously. Grid resolution (numerical errors) affect the results and the turbulence model is deficient. (AIAA paper 79-1543 has good literature review up to 1979.)

Author(s)	Flow and Method	Findings/Comments
Johnson et al (1982)	Transonic axisymmetric bump. 2-D Compressible primitive variable. Variable spaced mesh. Cebeci-Smith and two-equation Wilcox-Rubesin turbulence models. Also 2-D inverse boundary-layer method of Arieli and Murphy (1979).	Separation and shock is predicted too far downstream and reattachment is too far downstream with Cebeci-Smith model. Two-equation model is better in the vicinity of separation and there is little difference elsewhere. Boundary-layer solutions were in good agreement with Navier-Stokes calculations when the C-S model was used.
McGuirk et al (1981)	Confined, axisymmetric baffle of Taylor (1981). 2-D Primitive variable. k-ε turbulence model.	Quantified numerical error and reduce it to acceptable limits. Prediction of longer recirculation, smaller reverse velocities and smaller turbulence kinetic energy than in experiment. Difficulties with turbulence model. Eddy-viscosity hypothesis inappropriate in the initial region downstream of the baffle because the flow is not self-preserving and the normal-stress: normal-strain interaction is not modelled correctly. Streamline curvature effects neglected in turbulence model. Recommend use of Reynolds stress transport equations for turbulence model with demonstrated absence of numerical error.
Habib and Whitelaw (1982)	Wide-angle diffusers of Habib (1980) with and without swirl. 2-D Primitive variable. k-ε Turbulence model. Body-fitted orthogonal curvilinear co-ordinate system.	Mean velocity represented within experimental error without swirl. Less satisfactory results with swirl mainly due to turbulence model. Turbulence kinetic energy is significantly different from measurements due to inability of turbulence model to represent large streamline curvature and rotation. Suggest anisotropic eddy-viscosity. Procedure adequate for many engineering purposes.

Author(s)	Flow and Method	Findings/Comments
Hackman et al (1983)	Backward-facing step. 2-D Primitive variable. k-ε turbulence model. Cartesian and boundary-fitted orthogonal curvilinear co-ordinate system.	Significant errors in the numerical solution of differential equations can influence calculated results more than turbulence model. Upwind differencing is inappropriate in vicinity of recirculation. Recommend skew-hybrid-upwind (vector) differencing which yielded grid independent results with relatively coarse meshes. Mean velocities are in good quantitative agreement with experiment. Pressure recovery is in reasonable agreement. Turbulence stresses are over-predicted due to the turbulence model. Wall function based on the law-of-the-wall are not in agreement with the local production of turbulence kinetic energy in separated region but is not significantly important. Shear layer around recirculation most important to prediction of recirculating zone.
Johns (1980)	Reciprocating flow in engine cylinders. 2-D Primitive variable. Body-fitted orthogonal curvilinear co-ordinate system. k-ε turbulence model.	Body-fitted and orthogonal co-ordinate systems have advantages for numerical accuracy. Calculations are in reasonable qualitative agreement with experiment, but substantial numerical differences exist and are attributable to numerical diffusion, turbulence modelling assumptions and boundary conditions. Solutions independent of grid size and time step, cannot be obtained for economical specifications of these quantities.

Author(s)	Flow and Method	Findings/Comments
Degani and Steger (1983)	Supersonic flow over a ramp. 2-D Primitive variable with finite-difference equation in strongly conservative form for general co-ordinates. Baldwin and Lomax eddy-viscosity model. Also thin, shear layer approximation (TSL) to time-averaged Navier-Stokes equations.	Separation is relatively small and it may be expected that boundary-layer equations should suffice. Little difference between results obtained with TSL and NS equations on a coarse grid. Small discrepancies between TSL and NS results for fine grids are primarily confined to the separated region. Results are not compared with experiment and are likely grid dependent.
Amano (1983)	Axisymmetric abrupt expansion. 2-D Primitive variable. k-ε Turbulence model.	Near-wall boundary conditions, modified to account for the viscous sublayer, have a small influence on the overall prediction of recirculation although the near-wall flow, and hence the value of the Stanton number, is better predicted.
Horstman (1983)	Trailing-edge flow of Viswanath and Brown (1983) 2-D Primitive variable. Algebraic length scale. Two-equation k-ε and k-ω^2 turbulence models.	Results obtained with both two-equation models were in reasonable agreement with each other and experiment but the eddy-viscosity model was in much poorer agreement with experiment. For the two-equation k-ε model the distributions of pressure, displacement and momentum thickness, mean velocity and skin-friction coefficient were in good agreement with experiment. Turbulence shear-stress and kinetic-energy were in reasonable agreement but was slightly under-predicted in the wake. The extent of separated flow was poorly predicted although its dimensions are small. Solutions of the boundary-layer equations were in poor agreement with experiment, and different from solutions of Navier-Stokes equations, because of failure of the boundary-layer procedure to represent the strong viscous-inviscid interaction near the trailing-edge and not because of the neglect of normal stress gradients in the boundary-layer equations.

TABLE 1.3

SUMMARY OF THE RELEVANT WAKE CALCULATIONS

Author(s)	Flow and Method	Findings/Comments
Patel and Scheuerer (1982)	Symmetric and asymmetric wakes of a flat plate and a streamlined body. 2-D Boundary layer finite-difference method of Patankar and Spalding (1972). k-ε turbulence model.	Near and far wakes provided a simple and yet critical test for turbulence modelling but external pressure gradient is neglected. The k-ε model predicts the near wake well but is much less satisfactory for the growth rates and distributions of velocity, shear stress, and turbulence kinetic energy in the far wake. Peaks near the centre-line of very-near wake were not well predicted.
Baker et al (1982)	NACA 63012 airfoil wake. Viscous-inviscid interaction algorithm. 2-D Parabolized time-averaged Navier-Stokes equations. Viscous-corrected potential flow. 2-Equation turbulence model with algebraic equations for Reynolds stresses.	Mean velocity and Reynolds stress distributions were well calculated in near wake. Initial conditions of turbulence kinetic energy and its dissipation rate were critical. Wake calculation depended on representation of the turbulent boundary layers on the airfoil surface. Numerical predictions compare favourably with experimental mean velocities and Reynolds stresses over half of the wake. Detailed comparisons close to the trailing-edge are lacking.

Author(s)	Flow and Method	Findings/Comments
Hah and Lakshminarayama (1982)	NACA 0012 airfoil wake. 2-D Time-average Navier-Stokes equations solved in elliptic form. 2-Equation turbulence model with algebraic equations for Reynolds stresses.	Use of the conventional dissipation equation results in over-prediction of recovery in the wake due to the neglect of the effects of wake curvature. Recommend modified source term in dissipation equation to account for wake curvature. Profiles and decay of mean velocity are well calculated. Reynolds normal and shear stress are reasonably well calculated. The predictions of the intermediate region of the near wake are least accurate but are still in good agreement with experiment.
Waskiewicz et al (1980)	Supersonic wake of a wedge plus flat plate model. 2-D Compressible Navier-Stokes equations in mass-averaged form. Cebeci-Smith turbulence model.	Near wake region is in good agreement with experiment but required ad hoc specification of the relaxation length used to exponentially decay the eddy-viscosity along the length of the wake. Pressure distribution and velocity profiles are in poorer agreement upstream in the very-near wake and recovery to get better agreement downstream seems somewhat fortuitous.
Pope and Whitelaw (1976)	Near wakes of an ellipsoid, flat plate, a disc(baffle), and an annular jet. 2-D Time-averaged Navier-Stokes equations. k-ε and Reynolds stress transport turbulence models.	Without recirculation, turbulence is less important than the boundary conditions at the trailing edge, particularly the cross-stream velocity. Mean velocities are predicted adequately but turbulence normal stresses required the Reynolds stress transport model. Recirculation length and spread of the wake are under-estimated and appears to come from turbulence modelling assumptions in the dissipation equation although numerical accuracy is also suspect.

TABLE 1.4

SUMMARY OF DETAILED EXPERIMENTS IN TURBULENT SEPARATING BOUNDARY LAYERS AND DOWNSTREAM WAKES

Author(s)	Measured Quantities and Techniques	Flow Configuration/Comments
Coles and Wadcock (1979) Wadcock (1978) Wadcock (1980)	$\langle U \rangle$, $\langle V \rangle$, $\langle u^2 \rangle$, $\langle v^2 \rangle$, $\langle uv \rangle$, C_p, intermittency factor and higher order turbulence quantities of U and V. Surface pressure tappings. Flying hot-wire anemometry.	NACA 4412 airfoil at 14 degrees incidence with Re_c of 1.52×10^6. Maximum lift conditions with large separation bubble starting about 85 per cent of chord. Flow control needed for two-dimensionality which was not adequately checked. Flying-wire support mechanism interfered with the external flow. Lack of velocity measurements close to the wall. No w-component information. Higher order turbulence data suspect because less than 1025 samples were used in their ensemble averages.
Nakayama (1983)	$\langle U \rangle$, $\langle V \rangle$, $\langle u^2 \rangle$, $\langle v^2 \rangle$, $\langle uv \rangle$, C_p, and downstream intermittency. Impact probes and surface pressure tappings. Hot-wire anemometry. Laser-Doppler velocimetry.	DSMA 671 airfoil at 12 degrees incidence with Re_c of 1.2×10^6. Small separation bubble starting about 93 per chord. Relatively good two-dimensionality over the centre-span region. Lack of information in the vicinity of incipient detachment and in the backflow very close to the wall. Laminar-to-turbulent transition at 75 per cent of chord.

Author(s)	Measured Quantities and Techniques	Flow Configuration/Comments
Viswanath and Brown (1983)	$\langle U \rangle$, $\langle V \rangle$, $\langle u^2 \rangle$, $\langle v^2 \rangle$ and C_p. Impact probes and surface pressure tappings. Schlieren and shadow-graph visualisation. Laser-Doppler velocimetry.	Flat plate of 0.57 m length with the rear quadrant of an 18%-thick circular arc airfoil attached to the trailing-edge. Very small region of separated flow near the trailing-edge. Regions of recirculating flow extends from 20 mm upstream of the trailing-edge to 4 mm into the wake with a maximum height of 2 mm. The separation bubble closes rapidly in the wake. Few measurements in the region of recirculating flow. Noticeable changes in mean and turbulence fields around separation although the adverse pressure gradient is small. Normal-strain: normal-stress interaction makes a significant contribution to the production of turbulence, and hence the mean flow development, in the vicinity of separation.

Author(s)	Measured Quantities and Techniques	Flow Configuration/Comments
Simpson et al (1981) Simpson et al (1977)	$\langle U \rangle$, $\langle V \rangle$, $\langle u^2 \rangle$, $\langle v^2 \rangle$, $\langle w^2 \rangle$, $\langle uv \rangle$, $\langle u^3 \rangle$, $\langle v^3 \rangle$, $\langle u^2 v \rangle$, $\langle u^4 \rangle$ and $\langle v^4 \rangle$, C_p, C_f and downstream intermittency.	Separation on a flat plate due to the pressure gradient induced by contours of and blowing or suction through the opposite wall.
	Impact probes and surface pressure tappings Hot-wire anemometry. Surface hot-wire skin-friction guage. Laser-Doppler anemometry.	Very large separation in excess of 3 metres in length. Downstream influences on the recirculating flow in the vicinity of detachment are unknown and, for this experiment, have their origins in the three-dimensional region. Measurements not obtained in downstream portion of the separated region. Spanwise diffusion in separated flow occurred so that downstream of about 1 metre from mean streamline detachment, no two-dimensional region was found.
Hastings and Moreton (1982)	$\langle U \rangle$, $\langle V \rangle$, $\langle u^2 \rangle$, $\langle v^2 \rangle$ and C_p.	Separation on a flat plate due to the pressure gradient induced by contours on the opposite wall which was adjusted to give equilibrium velocity profiles.
	Impact probes and surface pressure tappings. Laser-Doppler anemometry.	Lack of potential flow due to the interaction of the roof and floor boundary layers over the test section. Asymmetry in mean flow. Possibly some flow convergence. Uncertainties associated with seeding practice.

Author(s)	Measured Quantities and Techniques	Flow Configuration/Comments
Solignac (1980)	$\langle U \rangle$, $\langle V \rangle$, $\langle u^2 \rangle$, $\langle v^2 \rangle$, $\langle uv \rangle$ and C_p.	Axisymmetric contoured after-body, i.e. annular trailing-edge flow.
	Impact probes. Hot-wire anemometry. Laser-Doppler velocimetry.	Flow measurements in the region of recirculation. No measurements close to the wall in the backflow. Two-dimensionality suspect despite axisymmetry.
Bachalo and Johnson (1979)	$\langle U \rangle$, $\langle V \rangle$, $\langle u^2 \rangle$, $\langle uv \rangle$ and C_p.	Transonic flow over an axisymmetric circular-arc bump on a cylinder.
	Surface pressure tappings. Holograph interferometry. Laser-Doppler velocimetry.	Pressure gradient caused small region of separation near the trailing-edge. Boundary-layer shock interaction farther upstream.
Meier et al (1983)	$\langle U \rangle$, $\langle V \rangle$, $\langle W \rangle$, C_p and C_f.	Three-dimensional boundary-layer and separated flow on a prolate spheroid (body of revolution) at 10 and 30 degrees incidence.
	Surface oil visualization. Impact probes and surface pressure tappings. Pitots used for separated flow. Surface hot-film probes. Laser-sheets with helium bubbles for visualization.	Laminar flow at 10 degrees incidence and turbulent separation at 30 degrees incidence. Flow structure is very complex with vortices and complex separating flow patterns. Turbulence field is not obtained. Large gradients and dimensions of the flow domain make it expensive to obtain measurements even in such a simplified flow.

Author(s)	Measured Quantities and Techniques	Flow Configuration/Comments
Young et al (1978)	$\langle U \rangle$, $\langle V \rangle$, $\langle u^2 \rangle$, $\langle v^2 \rangle$, probability density functions and power spectra. Laser-Doppler velocimetry.	NACA 0012 airfoil at 19.4 degrees incidence with Re_c of 1 x 10^6. Large region of recirculation associated with stall, i.e. separation near the leading edge. Measurements were not obtained close to the wall. Seeding and access difficulties. Two-dimensionality uncertain. Separation was unsteady in the mean and may possibly be associated with laminar bubble-bursting phenomena.
Johnson and Spaid (1981) Spaid and Bachalo (1981) Johnson, Bachalo and Owen (1981) Johnson and Bachalo (1980)	$\langle U \rangle$, $\langle V \rangle$, $\langle u^2 \rangle$, $\langle v^2 \rangle$, $\langle uv \rangle$ and C_p. Impact probe and surface pressure tappings. Holograph interferometry. Laser-Doppler velocimentry.	Supercritical DSMA 671 at M_∞ of 0.72 with small trailing-edge separation. Supercritical DSMA 523 with small pressure-side separation. Supercritical NACA 64A010 with shock-induced stall or leading-edge stall. Supercritical NACA 64A010 at M_∞ of 0.80 with shock/boundary layer interaction without and with either mild separation or stall. These four flow configurations correspond to the four references in the left-hand column. All of these experiments involve a region of supersonic flow.

Author(s)	Measured Quantities and Techniques	Flow Configuration/Comments
Seetharam and Wentz (1979)	<U>, <V>, C_p and some quantitative turbulence turbulence information.	GA(W)-1 airfoil at 18.4 degrees incidence with Re_c of 2.22×10^6.
Seetharam and Wentz (1975)	Impact probes and surface pressure tappings. Hot-wire anemometry. Directionally-sensitive split-film hot-wire anemometry.	Reverse velocities obtained with the split-film probe have large uncertainties. Turbulence quantities are difficult to interpret and may be affected by flow reversals. Near-wall flow is not measured.
Perry and Fairlie (1975)	<U>, <V> and C_p. Impact probes and surface pressure tappings. Directionally-sensitive hot-wire anemometry.	Separating and reattaching turbulent boundary layer over a flat plate with a flexible wall opposite to control pressure gradient. Results in regions of flow reversals are highly uncertain because of the use of stationary hot-wire modified to locate hot-wire wake. Backflow is not investigated close to the wall.

CHAPTER 2

EXPERIMENTAL TECHNIQUES

This chapter describes the experimental techniques and procedures used here and emphasizes their application in the vicinity of a large region of recirculation.

Flow visualization was used to examine the region of boundary layer separation and to indicate the region over which the mean flow may be regarded as two-dimensional. It is discussed in the first section. The measurement of mean pressure with wall tappings and various impact probes is considered in section 2.2 and the principles of hot-wire anemometry are explained in section 2.3. The use of a flying-hot-wire anemometer was required in the vicinity of recirculating flow to avoid the rectification effect associated with a stationary wire and is described in section 2.4 wherein velocity results obtained with pressure-probe and hot-wire methods are compared to those obtained with the flying-wire. The above procedures are used to obtain the measurements of pressure and velocity characteristics presented and discussed in chapter 3. They are compared to calculated results in chapter 5.

2.1 Flow Visualization

The purpose of this section is to describe the present flow visualization techniques which were used to determine the extent of the regions of potential, boundary-layer and recirculating flow and

to determine the degree of two-dimensionality. To achieve these objectives helium bubble tracers, surface oil films, smoke injection, tufts and surface bubbles were used. The reviews by Maltby (1962), Bradshaw (1969), Hinze (1975) and Chang (1976) describe the general aspects of flow visualization as applied to aeronautical and separating flows and the reader is referred to their discussions for alternative visualization techniques.

Helium bubble tracers. The flow is visualized by releasing soap bubbles, filled with helium to balance the weight of the soap, into the upstream flow and following the paths along which they travel. Movement of the bubbles can be used to indicate the instantaneous streamlines away from the wall and to determine if the flow is turbulent or recirculating.

The bubbles were generated by injecting helium into an annular film of soap and were broken away using the friction induced by the airflow of an outer annular jet. The size of the bubbles was controlled by the rotational speed of the peristaltic pump used for the soap, so that they followed the flow and responded to aerodynamic forces. The flow rates were adjusted to generate around 150 bubbles of about 1 mm diameter per minute.

Regions of turbulent flow were identified by unsteady movement of the bubbles and by a marked increase in their spreading rate over that experienced in the potential flow. Turbulent fluctuations were always observed immediately downstream of the nozzle due to the wake of the probe and its supports and because of mixing between the annular jet and the external flow. In the

potential flow,these effects were apparent close to the nozzle whereas the fluctuating motions of the bubbles were larger in the turbulent boundary-layer and turbulence diffusion increased the width of the bubble distribution with downstream distance, particularly in the spanwise direction.

The region of recirculation was identified by observing bubbles which travelled upstream with the reversed flow and by the shift of outer streamlines away from the wall. Some of the bubbles approached the surface and broke so that the surface became wet and modified the surface contours. This was particularly important near the trip wire,used to promote transition,and also near the trailing edge where the soap film tended to build up. Also the small number of bubbles in the near wall region of the recirculating flow made the location of streamline detachment more evident by their absence.

Figure 2.1 shows a series of photographs of helium bubble visualizations which depict an attached boundary layer, turbulent separation at the trailing edge and complete stall for an airfoil with a 250 mm chord. Results of this type were used to help select the angle of attack for the flow configuration of section 3.1. Separation is absent in figure 2.1a but exists in the latter two photographs and the location of mean streamline detachment was deduced from continuous observation. For the flow configuration of section 3.1, photographs were not possible because of the need for flow control vanes on the side wall of the wind tunnel, but the flow was observed to be generally similar in character to the trailing edge separation in figure 2.1b.

Surface oil flow. A surface oil film moves slowly in a manner representative of the intensity and direction of the surface shear stress and streaks in the film indicate the direction of the wall streamlines. The process of separation is dominated by the near wall flow and the location of the separation line, i.e. mean streamline detachment, may be detected where the downstream flow of oil ceases and, for two-dimensional flows, its direction reverses as shown on figure 2.2.

Squire (1961) solved the equations for the motion of a thin oil film under a boundary layer to describe the oil-flow pattern and to determine its effect on the boundary layer flow. The results showed that the oil flow followed the shear stress on the oil surface and the thickness of the oil displaces the boundary layer away from the solid surface. Accurate visualization is obtained with a film thickness less than 0.13 mm in the turbulent boundary layer here and was adhered to in the present study. The location of the separation line is uncertain within about 15 mm, since oil tended to collect around it and the skin friction approached zero.

The surface flow was visualized by observing the motion of a white pigmented-oil mixture over the model surface which was covered by smooth black plastic to keep it clean and to improve the contrast of the oil and the surface. The oil mixture consisted of titanium dioxide powder, medical-grade parafin (kerosene) and silicon oil in the proportions 45, 40 and 15 per cent by volume, respectively, plus a few drops of oleic acid which acted as an emulsifying agent.

The surface was coated with a thin layer of the oil mixture and the tunnel started. In regions where the surface shear stresses were large the oil flowed. In the recirculating region, there was no apparent motion even after 60 minutes and the oil on the surface was gradually diluted with parafin to reduce its viscosity by wiping the surface with a cloth soaked in parafin. This procedure had the additional benefit of reducing the thickness of the oil film in the vicinity of separation.

Figure 2.3 shows the surface oil flow pattern around the base of a circular cylinder for a Reynolds number of 18300, based on the diameter and free-stream velocity. Similar results were obtained for the flow configuration of section 3.1 in the region of attached flow but in the region of recirculating flow the visualization was less certain due to the effects of gravity.

Surface oil flow patterns must be cautiously interpreted and carefully observed during their development if regions of recirculating flow are to be identified. Visualization of the flow approaching separation and in the recirculation region was difficult where the surface shear stresses were small and the results are subject to uncertainties. For the flow configuration of section 3.1 the visualization results were not regarded as conclusive evidence that the mean flow was two-dimensional inside the recirculation bubble, although the two-dimensional features of the separation were correctly demonstrated by the present procedure, and were verified with more quantitative experimental techniques.

Smoke injection. Smoke consists of a suspension of particles or droplets which can be observed in a transparent gas

by the scattering and reflection of light. Oil smoke was used here and was obtained from a pyrotechnic device. Since the smoke diffused within 300 mm of the injecting nozzle, because of turbulence diffusion generated by the boundary layer and probe wake, its range of applicability was limited.

Smoke was injected at the trailing edge of the flow configuration of section 3.1 and filled the recirculation bubble. The instantaneous boundary between upstream and downstream flow along the surface was clearly visible and, as expected, it was unsteady and instantaneously three-dimensional although its mean location appeared to be linear in the spanwise direction. The height of the bubble was also evident and appeared to be two-dimensional over the central region of the flow although it was obscured by turbulence diffusion into the outer flow downstream of the trailing edge. Smoke was retained in the recirculation bubble for less than 2 seconds after injection was stopped and indicated that turbulent fluctuations and the associated turbulence diffusion were large in the separated region.

Tufts and surface bubbles. The region of recirculation was visualized with tufts and soap bubbles on the surface.

Tufts were made from 10 and 25 mm lengths of thin cotton thread and were fixed to the surfaces at their mid-point. The tufts fluctuated due to turbulence and pointed towards the mean separation line except within 20 mm of mean streamline detachment where the fluctuations were so rapid that the flow direction could not be determined regardless of the length of string used.

A soap solution was bubbled onto the surface through holes in the wall. These surface bubbles moved in a similar fashion to the surface oil flow except downstream of separation where they moved up the inclined surface towards the separation line. The bubbles approached within 20 mm of the location of mean streamline detachment and oscillated back and forth over a distance of about 4 mm.

Tufts and surface bubbles confirmed that reversed flow occurred downstream of the separation line identified by surface visualization, and indicated that large fluctuations of velocity occurred inside the region of recirculating flow.

2.2 Pressure Measurements

This section describes the calibration and measurement procedures for impact probes used to quantify the variation of mean values of static pressure and velocity in certain regions of the present flow. The use of pressure probes in subsonic flows has been reviewed, for example by Bryer and Pankhurst (1971), Becker and Brown (1974) and Chue (1975) and is based on the concepts of static pressure, P, total pressure, P_T, and dynamic pressure as given by Bernoulli's equation:-

$$P_T = P + \frac{1}{2}\rho V^2 \qquad (2.1)$$

in which P_T remains constant if viscosity effects are negligible. This equation is used to develop relationships between the pressures

through the sensing holes of the probes and the local values of static pressure, flow direction and velocity around the probe. Impact probes are sensitive to pressure and velocity fluctuations due to turbulence and their calibrations apply over a limited range of flow angle so that they are inappropriate in highly turbulent or reversing flows. They were used in regions of the flow with a predominant flow direction and their use and possible sources of error are discussed here.

Mean pressures are important in the present flow and were measured but fluctuating pressures are of less value since, for example, turbulence kinetic energy budgets balance without fluctuating pressure terms (Bradshaw, Cebeci and Whitelaw, 1981). Also, there is no accepted method for making fluctuating pressure measurements since the probe dimensions must be very small or corrections for spatial resolution conjectured (Bradshaw, 1971).

Surface static pressure. The measurements of static pressure at the wall were made with tappings in the surface and avoids the problems associated with probe disturbances. The observed static pressure can be affected by the diameter of the wall tapping and Shaw (1960) investigated this phenomena in incompressible turbulent boundary layers over smooth walls: accordingly hole diameters of 0.5 mm and a depth to diameter ratio greater than 4 were used here. Burrs around the tappings can affect the pressure reading and were carefully removed. Any errors associated with turbulent fluctuations are likely to be small according to Bradshaw (1969) although the extent of the effect is not precisely known. For free stream velocities less than 30 m/s

the maximum uncertainty due to the cumulative effects of hole dimensions, burrs and turbulence is less than $0.5 \rho U_\tau^2$ which is about 0.35% of the reference dynamic pressure.

Pitot tubes. Pitot tubes can accurately measure total pressure over a limited range of subsonic flow conditions: the flow must be aligned within 10 degrees of the probe axis; viscous effects must be small in the vicinity of the tube; the turbulence intensity must be less than 5 per cent of the undisturbed flow velocity; and the probe must be at least 2 probe diameters from the wall. These criteria are restrictive and this section describes the procedures adopted to correct the total pressures obtained with cylindrical and flattened-end Pitot where the above assumptions do not apply.

A cylindrical Pitot tube was used and had an internal diameter of 0.82 mm and a ratio of the internal over external diameters of 0.66. Correction for viscous effects was not required since the Reynolds number based on the internal diameter always exceeded 100. In regions where there was a gradient of total pressure, the location of the measured pressure was shifted towards the higher total pressure by 15 per cent of the external diameter as suggested by MacMillan (1954a). Within two diameters of the wall an additional correction was applied to increase the total pressure according to the relationship based on the distance from the wall given by Bryer and Pankhurst (1971).

The flattened probe had internal and external heights of 0.31 mm and 0.48 mm, respectively, and a length to diameter ratio of 4.4. The viscosity corrections prescribed by MacMillan (1954b)

were used if the Reynolds number based on the height was less than 1000 and decreased the measured value of total pressure by less than 1 per cent of the local dynamic pressure. No displacement correction for the effects of shear across the flattened probe was applied although the wall proximity correction of Bryer and Pankhurst (1971) was again used closer than two probe heights (1 mm) from the wall.

These corrections were less than the effects of turbulent fluctuations on the mean readings of total pressure. Turbulence effects are reviewed by Hinze (1975) and increase the mean reading of total pressure according to:-

$$\langle P_T \rangle = \langle P \rangle + \frac{1}{2} \langle \rho \rangle \langle V \rangle^2 \{1 + \frac{\langle k \rangle}{\frac{1}{2}\langle V \rangle^2}\} \qquad (2.2)$$

where $\langle k \rangle$ is the mean kinetic energy of the turbulence. The values of $\langle k \rangle$ were obtained with hot-wire anemometry and did not exceed 0.15 of the local dynamic head if the cylindrical-probe results were to be accurate within 1 per cent of dynamic pressure: this level of accuracy requires that the flow is not angled by more than 10 degrees to the probe axis (Bryer and Pankhurst, 1971). Flattened probes have a greater sensitivity to turbulence fluctuations in the transverse plane which results in increased uncertainties in highly turbulent flows. In all cases the Pitot probes were aligned with the mean flow directions by rotating the probe until the maximum total pressure was obtained.

Flow velocity can be obtained from equation 2.2 by combining total and wall pressure measurements provided that the gradient of static pressure is known. This procedure was used in the boundary layer

upstream of the curved section and in the near-wall region where the differences between the local and wall values of static pressure were small.

Wall shear stress, τ_w, can be obtained from a single measurement of velocity using a round pressure probe of diameter, d, lying along the surface and the similarity law (Preston, 1954):-

$$\frac{\Delta p d^2}{\rho \nu^2} = F_{PR}\left(\frac{\tau_w d^2}{\rho \nu^2}\right) \qquad (2.3)$$

where Δp is the difference between the total pressure from the Preston tube and the undisturbed static pressure on the wall. This pressure difference is affected by the close proximity of the probe to the wall and requires calibration such as the chart of Head and Vasanta Ram (1971) used here. This calibration is empirical and requires similarity between the turbulent boundary layer where it was obtained and the measured flow.

Skin friction can also be obtained from velocity profiles if a logarithmic law-of-the-wall is assumed as proposed by Clauser (1954), and is compared in chapter 3 to results obtained with the Preston tube and by extrapolation of the measurements of Reynolds shear stress to the wall (also see the review by Winter, 1979). The extrapolation of hot-wire measurements of <uv> is straightforward and needs no further comment.

The logarithmic law of the wall is given by:-

$$\frac{U}{U_\tau} = \frac{1}{\kappa} \ln\left\{\frac{nU_\tau}{\nu}\right\} + B \qquad (2.4)$$

and can be rearranged by defining the skin friction coefficient, $C_f = \tau_w / \frac{1}{2} \rho U_e^2$, to give:-

$$\frac{U}{U_e} = \left(\frac{C_f}{2}\right)^{1/2} \left[\frac{1}{\kappa} \ln \left\{\left(\frac{C_f}{2}\right)^{1/2} \frac{nU_e}{\nu}\right\} + B\right] \qquad (2.5)$$

which can be compared to experimental velocity profiles on Clauser charts such as figure 3.12. The value of skin friction depends on the values of the constants κ and B which were taken as 0.41 and 5.0 in the present study as recommended by Bradshaw, Cebeci and Whitelaw (1981).

In regions of highly turbulent or reversing flow, pressure probes cannot be used because of the inability to align the probe axis and the instantaneous flow vector, even approximately, and since stationary hot-wires suffer from a similar problem the flying-wire of section 2.4 was required.

Pitot-static probes. Velocity may be obtained from simultaneous measurements of static and total pressure using a Pitot-static probe and equation 2.1. Combining Pitot and static tubes into one instrument poses no special problem since the mutual interference between the total-pressure and static-pressure tappings on the probe is negligible in practice although the probe size is necessarily larger and disturbs the flow to a greater extent.

The Pitot-static probe of the present study was commercially manufactured (Airflows Developments Ltd.) and had a diameter of 2.19 mm and an ellipsoidal nose. When the probe axis was aligned within 10 degrees of the flow direction, equation 2.1 was used to obtain the dynamic pressure to an accuracy better than 1 per cent provided the turbulence intensity is low.

The range of applicability of the Pitot-static probe was limited because the total-pressure and static-pressure holes

are displaced and an error arises in the static pressure reading unless the radius of curvature of the flow is much larger than the length of this displacement. Turbulence affects the total pressure as discussed above and also affects the measured value of static pressure making it high or low by a factor of $\frac{1}{2}\rho(\langle v^2\rangle + \langle w^2\rangle)$ depending on the scale of the turbulence (Hinze, 1975).

The Pitot-static probe was preferred in the outer potential flow and for calibration of hot-wires. It was not used near the surface or in regions with significant turbulence, flow curvature or gradients of pressure and velocity since in these situations the accuracy of its results are inferior to those obtained with the five-hole probe or simple Pitot tube.

Five-hole impact probe. This probe was able to measure the flow angle, static and dynamic pressure simultaneously at the same location although it is larger than the other probes and requires calibration. It is shown diagramatically on figure 2.4 and was constructed from tubing with 0.51 mm inside and 0.82 mm outside diameters so that its maximum cross-stream dimension was 2.58 mm.

The measured pressures from the five tubes were used to obtain the flow angle, θ, dynamic pressure, q, and total pressure, P_T, from the equations (Bryer and Pankhurst, 1971):

$$\theta = K_\theta(P_1 - P_2)/(P_5 - P_m) \tag{2.6}$$

$$q \equiv \frac{1}{2}\rho V^2 = (P_5 - P_m)\{K_A - K_B \log_{10}[(P_5 - P_m)/q_r]\} \tag{2.7}$$

$$\text{and } P_T = P_5 + q(K_1\theta + K_2\theta^2) \tag{2.8}$$

after rotating the probe in yaw to balance the pressures in tubes 3 and 4. The values of K_θ, K_A, K_B, q_r, K_1 and K_2 are constant and were obtained from calibration and P_m is the mean value of the four pressures of the outer tubes (1-4) shown on figure 2.4. The static pressure is obtained from equation 2.1 using the dynamic and total pressures from equations 2.7 and 2.8 respectively.

The constants in equation 2.6-8 are given in table 2.1 and were determined by curve fitting to calibration data obtained in the potential core of a round jet whose velocity was varied over the range 6-30 m/s, with angles of up to 15 degrees between the probe axis and the flow direction. Measurements with these constants were compared to those obtained with impact probes: static and dynamic pressures obtained with the Pitot-static in the free stream agreed within 0.6 and 0.4 per cent of dynamic pressure over the range 7-28 m/s; similar results agreed within 3.4 and 2.9 per cent of dynamic pressure using the wall pressures measured in the attached turbulent boundary layer where cross-stream pressure gradients were around zero. The error in the free-stream measurements arose from the curve fitting procedure while those in the turbulent boundary layer are primarily attributable to velocity gradients although turbulence effects may also have contributed.

The above measurements were repeated with the five-tube probe inclined at angles of up to 15 degrees with the mean flow and agreed within the values given above. The measured angles were correct within 0.2 degrees in the free-stream and 1.7 degrees in the turbulent boundary layer. The latter error is primarily due

to gradients across the probe face and turbulence effects, and the former is attributable to the accuracy of the manometer. The five-tube probe was not used in the region close to the wall since its accuracy decreased rapidly when it approached within 4 mm of the surface.

The discrepancy between measured values in the attached boundary-layer is indicative of the uncertainties expected in the curved boundary-layer and wake of the present flow although it is clear that measurements cannot be made with the five-tube probe in regions where flow reversals occur since the calibration is invalid.

Discussion. The impact probes described here have different limitations which restrict their application to certain regions of the flow. Table 2.2 gives the values of the maximum uncertainty for each pressure probe and the regions of the present flow where they were used.

The Pitot-static probe is preferred in the free stream because it is simpler to use and more accurate than the five tube probe. Cylindrical and flattened-end Pitot tubes were used in the near wall region of the attached boundary layer and the results corrected for the effects of viscosity, turbulence and proximity to the walls. The maximum uncertainty is largest with the five-tube probe in the turbulent boundary layer because no corrections have been applied to account for turbulence or cross-stream gradients: this uncertainty was estimated by comparing to Pitot measurements in a turbulent boundary layer with negligible pressure gradient.

None of these impact probes are capable of measuring reversing flow since they require alignment with the flow direction. This is not applicable to the wall pressure tappings whose readings of static pressure are correct since the tappings are aligned perpendicular to the local direction of the near-wall flow.

2.3 Hot-Wire Anemometry

This section describes the constant-temperature hot-wire anemometry methods used to obtain the velocity characteristics of the present flow outside the regions of reversing flow where the flying-hot-wire of section 2.4 was required. Hot-wire instrumentation and the equations used to interpret and calibrate the signal of a stationary hot-wire are presented.

The principles and practices of hot-wire anemometry are well known and have been reviewed, for example, by Perry (1982), Vagt (1979), Compte-Bellot (1977) and Bradshaw (1969, 1971) and the reader is referred to these and also to the bibliography of Freymuth (1978).

This section is divided into five subsections concerned with the instrumentation; the response equations which convert the cooling velocity into the mean and fluctuating components of the flow velocity; the calibration procedure; the practices used to eliminate or account for the effects of contamination, velocity gradients, walls, and temperature; and the procedures used to measure with a stationary-wire probe.

Instrumentation. Constant-temperature operation of a hot-wire keeps the mean temperature of the wire constant when the velocity, and hence the heat transfer, is changed. Tungsten-platinum wires of 5 μm diameter were used for the heated sensors or the probes (DISA 55P10, 55P11 and 55P61). The anemometers (DISA 55M01) and constant-temperature bridges (DISA 55M10) with an overheat ratio of 1.8 were adjusted to obtain a cut-off frequency in excess of 100 KHz as determined with the square-wave tests recommended by Freymouth (1977).

The hot-wire voltage was converted to a digital signal and recorded by computer in accordance with the recommendations of Gibson (1973). Hot-wire voltage levels were held constant, using sample-and-hold modules (Analogic MP 240), during conversion by an analogue-to-digital converter (DEC AD01) to a 12-bit digital signal, which was accurate to within 1.4 mV. The anemometer voltages were recorded by computer (DEC PDP8E) and, after calibration, gave direct information of the instantaneous wire-cooling velocity. Ensemble averages of the wire-cooling velocity were calculated subsequently for a number of samples large enough that the velocity values and their moments were determinable to a specified statistical accuracy.

Transform equations. Heat transfer and temperature measurements made with hot-wires (Champagne et al, 1967) indicate that they respond to all three components of velocity and their sensitivity must be accounted for when interpreting the measured cooling velocity especially if the hot-wire is inclined to the flow.

The heat transfer from a hot wire depends on Q_{N1}, Q_{N2} and Q_T, the axial, normal and tangential components of the cooling velocity shown on figure 2.5. The effective cooling velocity may be expressed in the form:-

$$Q_{eff} = (Q_{N1}^2 + h_*^2 Q_{N2} + k_*^2 Q_T^2)^{1/2} \quad . \tag{2.9}$$

Rodi (1971) suggested the second term to account for the influence of disturbances due to the prongs and stem, and Muller (1982) has shown h_* to be constant and determined from:-

$$h_*^2 = \{\frac{<Q_{eff}(\psi = 10^o)>^2 - <Q_{eff}(\psi = 0^o)>^2}{<Q>^2 \sin^2(\psi = 10^o) \cos^2(\psi = 10^o)}\} \tag{2.10}$$

which gave typical values of around 1.10. This value has been used here since the pitch angle did not exceed 15 degrees. The importance of tangential cooling on the measured values of the Reynolds stresses was demonstrated by Champagne and Sleicher (1967b). The value of k_* was taken as constant and was obtained from:-

$$k_*^2 = \frac{3<Q_{eff}(\alpha = 45^o)>^2 - 2<Q_{eff}(\alpha = 30^o)>^2}{-<Q_{eff}(\alpha = 45^o)>^2 + 2<Q_{eff}(\alpha = 30^o)>^2} \tag{2.11}$$

which gave typical values of around 0.023.

The instantaneous effective-cooling-velocity of the hot wire which represents the cooling response to the velocity, Q, can be rewritten from equation 2.9 as:-

$$Q_{eff} = <Q> \cos\gamma (\frac{Q_{N1}}{<Q>\cos\gamma})(1 + (\frac{h_*^2 Q_{N2}^2 + k_*^2 Q_T^2}{<Q^2>\cos^2\gamma}) \frac{<Q>^2 \cos^2\gamma}{Q_{N1}^2}\}^{1/2} \tag{2.12}$$

with $<Q>\cos\gamma$ representing the mean axial component, $<Q_{N1}>$, of

the cooling velocity. For convenience, equation 2.12 can be expressed in a more general form as:-

$$Q_{eff} = \langle Q \rangle \cos\gamma (1 + F_1)[1 + F_2(1 + F_1)^{-2}]^{1/2} \qquad (2.13)$$

where $1 + F_1 = Q_{N1}/\langle Q \rangle \cos\gamma$

and $F_2 = (h_*^2 Q_{N2}^2 + k_*^2 Q_T^2)/\langle Q \rangle^2 \cos^2\gamma$

The non-linear term of equation 2.13 which is:-

$$T_* = [1 + F_2(1 + F_1)^{-2}]^{1/2} \qquad (2.14)$$

requires some form of approximation and a binomial expansion may be used for low turbulence-intensity flows. To avoid this restriction the proposal of Ribeiro (1976) that the non-linear term be fitted to curves which represent the response over limited ranges of turbulence intensity and flow angle, has been adopted so that:-

$$Q_{eff} = \langle Q \rangle \cos\gamma \; C_{G1}(1 + F_1 + C_o F_2 + C_1 F_2 F_1 + C_2 F_2 F_1^2) \qquad (2.15)$$

where the non-linear term is approximated in two stages by:-

$H_* = (1 + F_1)^{-1}$ corresponding to $C_{H0} + C_{H1}F_1 + C_{H2}F_1^2$

and T_* corresponding to $C_{G1} + C_{G2}(F_2 H_*^2)$

so that the coefficients of equation 2.15 are:-

$C_i = C_{Hi} C_{G2}/C_{G1}$ for $i = 0, 1, 2.$

The sets of coefficients, C_{Hi} and C_{Gi}, for each wire were determined by linear regression over the required range of turbulence fluctuations. Ribeiro (1976) demonstrated that the

curves could be applied over a wide range of turbulence intensities and experience has shown that the maximum discrepancy between the true and approximated response is less than 0.7% for turbulence intensities less than around 30%. A curve fit can be obtained over any range of turbulence intensity provided the rectification effect, associated with a stationary hot-wire measuring reversals around zero velocity, is avoided.

Calibration. Approximate relations for the cooling of a cylindrical wire have been obtained experimentally for steady incompressible flow with forced convection and are expressed by the familiar King's law equation:-

$$E_* = A_* + B_* Q_{eff}^{n_*} \tag{2.16}$$

that relates the anemometer voltage, E_*, to the effective cooling velocity, Q_{eff}, with the constants, A_* and B_*, and the exponent, n_*, obtained from calibration. The constants, A_* and B_*, depend strongly on the temperature difference between ambient air and the probe sensor, and the exponent, n_*, depends mainly on the local flow pattern around the wire and degree of surfaces contamination due to oxidation or particle deposition. It is generally recognized that equation 2.16 is not universal (Perry, 1982) although it may be applied over a limited range of velocities (Hinze, 1975).

Equation 2.16 has not been used here since single values of A_*, B_* and n_* do not represent the voltage-velocity relationship over a wide range of velocity. Instead the effective cooling velocity of equation 2.9 is obtained from the hot-wire anemometer voltage, E_*, with the explicit equation:-

$$Q_{eff} = A_0 + A_1 E_*^{1/n_*} + A_2 E^{2/n_*} + A_3 E^{3/n_*} \qquad (2.17)$$

which has been applied by Thompson (1981) over the velocity range from 1 to 40 m/s. The exponent, n_*, was taken as 0.5 and reduced in steps of 0.02 if the maximum deviation exceeded 0.15 m/s or if the standard deviation of the error exceeded 0.075 m/s. The reference velocities, which were aligned with the axis of the hot-wire probe, were obtained with a Pitot-static probe located in the potential flow of the wind tunnel for the velocity range from 6 to 35 m/s and overlapped with those obtained with the flying-hot-wire of section 2.4 whose speed was varied between 1 and 13.5 m/s in still air. The coefficients, A_i, were determined by linear regression and required approximately 30 points with increments smaller than 0.5 m/s at the upper and lower limits of the 1 to 35 m/s range. A sample calibration is shown in table 2.3 with the maximum and standard deviations from a curve fit based on the method of least squares.

Practical implications. This subsection examines the factors which affect heat transfer from the hot-wire, other than velocity, and the methods used to control or account for them in the measurements reported in chapter 3.

Velocity gradients along or across the wire can have a significant effect on the measured value of velocity because of averaging of the heat transfer along the wire and have been considered by Gessner and Moller (1971), Ronald (1976) and Perry (1982) for example. In order to reduce the effects of gradient broadening, the magnitude of the mean velocity was determined from a single

wire parallel to the surface (i.e. perpendicular to the velocity gradient) and probes with a length-to-diameter ratio of 200 were used.

Correction for the additional heat loss through conductive walls is important at values of Y^+ less than 6 (Bhatia, Durst and Jovanic, 1982) but no corrections were required here.

The effects of changes in the ambient temperature and drift of the anemometer affect the constants, A_i of equation 2.17, and calibration was repeated if the room temperature changed by more than 1^oC. Also the accuracy of the calibration curve was checked periodically during a set of measurements against the velocity obtained with a Pitot-static probe and recalibration was undertaken if they disagreed by more than 0.3 m/s. After recalibration, velocity measurements were repeated at a previous location to insure that the results with both calibration curves were in agreement.

The presence of a probe inevitably affects the flow field and the effects of the wire supports (pintels) and probe stem are likely to be more significant than one would consider reasonable and are difficult to assess. Vagt (1979) discussed the consequences of aerodynamic disturbances and suggested they may be primarily attributed to the pintels and result in directional sensitivity of the probe as represented by equation 2.9. The use of single values of k_* and h_* in this equation results in errors less than 0.8 and 1.2 per cent of the mean velocity with an angle of incidence less than 15 degrees and is in agreement with the results of Muller (1982).

Contamination of the wire surface by oxidation or particle deposition may also cause the anemometer voltage level to drift. To

prevent this, the tunnel airstream was filtered and the probes were cleaned, by soaking in acetone after about 20 hours of use, unless difficulties in calibration indicated a need for more frequent cleaning due to a build up of dirt. To avoid changes in the oxide layer on the heated surface, probes were burned in prior to measuring by operating them in still air for at least 8 hours when new or after cleaning. These practices coupled with frequent calibration checks, as described above, were used to account for anemometer drift.

The overall accuracy of hot-wire measurements is discussed for a stationary wire in the next subsection and for a flying-wire in section 2.4.

Stationary hot-wire anemometry. This subsection describes the procedures used to measure values of mean velocity and Reynolds stresses with a stationary hot-wire. Two levels of approximation for measuring in two-dimensional mean flow are considered. The simpler method is limited to low turbulence intensities with the probe axis aligned with the flow direction and the more complex method is developed to avoid these restrictions.

Ribiero (1976) has used a curve fitting approach for the hot-wire response equation similar to equation 2.15 and measured for the six Reynolds stresses and the magnitude and direction of the mean flow with seven probe orientations which required the probe axis be aligned with the mean flow. Habib (1980) used the same approach to obtain the mean flow and four non-zero Reynolds stresses in a two-dimensional mean flow with four probe orientations and also required alignment of the probe with the

direction of the mean flow. The first method presented here was used to measure two-dimensional mean flow but without alignment or turbulence intensity restrictions and can readily be extended to three dimensions.

Ensemble averages of the effective cooling velocity, Q_{eff} (normal) from a single wire aligned normal to the mean flow direction, and Q_{eff} (cross, $+\alpha$) and Q_{eff} (cross, $-\alpha$) from a cross-wire arranged with the two wires in the plane of two-dimensional flow, were used to determine the magnitude and direction of the mean cooling velocity, assuming the cosine cooling law. The magnitude and angle of the mean cooling velocity, relative to tunnel co-ordinates are given by:-

$$\langle U \rangle = \langle Q_{eff} \text{ (normal)} \rangle \tag{2.18}$$

$$\theta = \arctan\left\{\frac{\langle Q_{eff} \text{ (cross, } -\alpha)\rangle - \langle Q_{eff} \text{ (cross, } +\alpha)\rangle}{\langle Q_{eff} \text{ (cross, } -\alpha)\rangle + \langle Q_{eff} \text{ (cross, } -\alpha)\rangle}\right\} \tag{2.19}$$

It is advantageous to use the single normal wire to measure the magnitude of the mean velocity since it is subject to smaller gradient broadening effects compared with the cross wire and can measure closer to the surface, although the flow angle must be assumed at distances less than about 1.5 mm where the dimensions of the cross-wire prevent its use.

The Reynolds stresses $\langle u^2 \rangle$, $\langle v^2 \rangle$, $\langle w^2 \rangle$ and $\langle uv \rangle$ may be obtained from the solution of four simultaneous linear equations which represent the cooling response of four hot-wires orientated so that they are sensitive to different components of the velocity fluctuations. The selected orientations of the probe and their

associated sensitivities to the fluctuations and angle of the effective cooling velocities, which appear as the functions F_i in equation 2.15, are shown on table 2.4.

The mean square of the effective cooling velocity for each wire was calculated from:-

$$\langle q_{eff}^2 \rangle = \langle Q_{eff}^2 \rangle - \langle Q_{eff} \rangle^2 \qquad (2.20)$$

and related to turbulence fluctuations with four equations obtained by substituting equation 2.15 into equation 2.20 for each wire orientation and is of the form:-

$$\frac{\langle q_{eff}^2 \rangle}{\langle U \rangle^2} = \cos^2\gamma \left(b_1 \frac{\langle u^2 \rangle}{\langle U \rangle^2} + b_2 \frac{\langle v^2 \rangle}{\langle U \rangle^2} + b_3 \frac{\langle w^2 \rangle}{\langle U \rangle^2} + b_4 \frac{\langle uv \rangle}{\langle U \rangle^2} + \langle P_* \rangle \right) \qquad (2.21)$$

The mean velocity was obtained from equation 2.18 and γ is defined in table 2.4. The coefficients, b_i, are functions of the four sets of coefficients, C_i, of equation 2.15 and the expression for f_i and g_i as defined in table 2.4. The source term, $\langle P_* \rangle$ shown in appendix 2.A, contains third and higher order correlations which could be obtained by solving further equations although they would contain still higher order correlations. Approximation is required to close these equations and that chosen for evaluating the Reynolds stresses was that the probability density function of turbulence fluctuations has a Gaussian behaviour so that odd-order correlations are zero and even-order moments are functions of second order moments only: this is done without appreciable loss of accuracy since the maximum errors in the values of $\langle u_i u_j \rangle$ due to this approximation of the skewness and flatness factors are 0.3% and 0.65% respectively

which were calculated using the values of third and fourth order correlations measured by Simpson et al (1981) in a separating boundary layer.

The Reynolds stresses were obtained by solving the set of four simultaneous equations based on equation 2.21. Initially the term, $\langle P_* \rangle$, is assumed zero and the Reynolds stresses obtained using Gauss-Jordan elimination. This source term is then calculated with these values of the Reynolds stresses and the four simultaneous equations resolved. This procedure is repeated until the Reynolds stresses converge within 0.1% which usually requires from 2 to 9 iterations.

An alternative approach for obtaining the Reynolds stresses is to simplify the four simultaneous equations, based on equation 2.21, by aligning the probe with the flow direction. Alignment was achieved by using the flow angle measured with the five-tube probe of section 2.2 or by balancing the two mean velocities of the cross-wire although at distances closer than 2.5 mm from the surface the flow angle was assumed parallel to the wall. The magnitude of the mean velocity is then obtained from equation 2.18 and the Reynolds stresses obtained from the algebraic equations:-

$$\frac{\langle u^2 \rangle}{\langle U \rangle^2} = \frac{1}{4}\left(\frac{\langle Q_{eff_1}^2 \rangle}{\langle Q_{eff_1} \rangle^2} + \frac{\langle Q_{eff_2}^2 \rangle}{\langle Q_{eff_2} \rangle^2} + \frac{\langle Q_{eff_1} Q_{eff_2} \rangle}{\langle Q_{eff_1} \rangle \langle Q_{eff_2} \rangle}\right) \tag{2.22}$$

$$\frac{\langle v^2 \rangle}{\langle U \rangle^2} = \frac{1}{4}\left(\frac{1 + k_*^2}{1 - 3k_*^2 + 4k_*^4}\right)\left(\frac{\langle Q_{eff_1}^2 \rangle}{\langle Q_{eff_1} \rangle^2} + \frac{\langle Q_{eff_2}^2 \rangle}{\langle Q_{eff_2} \rangle^2} - \frac{\langle Q_{eff_1} Q_{eff_2} \rangle}{\langle Q_{eff_1} \rangle \langle Q_{eff_2} \rangle}\right) \tag{2.23}$$

$$\frac{\langle uv \rangle}{\langle U \rangle^2} = \frac{1}{4}\left(\frac{1 + k_*^2}{1 - k_*^2}\right)\left(\frac{\langle Q_{eff_1}^2 \rangle}{\langle Q_{eff_1} \rangle^2} - \frac{\langle Q_{eff_2}^2 \rangle}{\langle Q_{eff_2} \rangle^2}\right) \tag{2.24}$$

where the subscripts 1 and 2 correspond to the two wires in the vertical plane and angled at ±45 to the mean flow direction. The remaining Reynolds stress may be obtained by rotating the probe by 90^0 around the probe axis.

This approach neglects the higher order terms of $\langle P_* \rangle$ and hence is limited to turbulence intensities less than about 15 per cent of the local mean velocity. It is also worth noting that these equations agree with those obtained by approximating equation 2.12 with a binomial expansion (Champagne and Sleicher, 1967b) and were also used by Ribiero and Whitelaw (1975).

The errors which affect the results obtained with a stationary hot-wire stem from calibration, the approximate treatment of hot-wire response equation and determination of the location of the probe. The maximum deviation between the calibration data and the curve fit was 0.15 m/s and, combined with the error due to interpolation, results in a maximum uncertainty of less than 0.3 m/s. The probe was mounted on a traversing mechanism capable of motion in three orthogonal directions to within 0.02 mm and the position relative to the surface was obtained by measuring the distance between the surface and the wire with gauges and was accurate to within 0.03 mm. The data collection instrumentation has an accuracy of 1.4 mV incurred during the digital conversion process and results in a further possible error of 0.02 m/s.

The sources of inaccuracy in this method to determine the Reynolds stresses are of two types: systematic error in the

approximate form of the response equation and propagation of random error in the measurements. The uncertainty resulting from the approximate nature of the response equation is of order k^2 times Reynolds stresses, and k^4 time third order correlations for mean velocity and Reynolds stresses,respectively. The propagation of random error is not crucial because the quantities to be determined are of the same order and strongly linked to the measured quantities. The overall uncertainties are listed on table 2.5 as a function of flow angle and turbulence intensity together with the statistical error associated with the use of a finite number of samples for the ensemble-averaged quantities.

Summary. The procedures for measuring the velocity characteristics with a stationary hot-wire have been described. For regions with turbulence intensities below 15 per cent, and with the probe axis aligned in the flow direction, algebraic equations were used to transform measurements of wire-cooling velocity into values of mean velocity and Reynolds stresses. An alternative method was used if the turbulence intensity exceeded this value or if the flow was at an angle to the probe. It is more complicated and involves fitting an approximate curve to the response equations for the four wire orientations and solving the resulting simultaneous equations. Calibration curves based on polynomials were used to represent the voltage velocity relation over the velocity range 1-35 m/s. Measurements of mean velocity and Reynolds stresses obtained with both of the methods described above are presented in chapter 3.

2.4 Flying Hot-Wire Anemometry

A flying hot-wire arrangement has been developed for the measurement of the velocity characteristics of the flow around airfoils, and particularly in regions where negative values of instantaneous velocity occur. The mechanism and signal processing system are described and appraised by comparing stationary and flying wire measurements obtained in the trailing edge region of a flap at an angle of attack which leads to upper-surface separation.

The problems associated with the use of hot-wire anemometry in high turbulence intensity and recirculating flows are well known. To overcome the signal rectification which can occur with hot wires, and in parallel with the frequency shifting of laser anemometry, flying hot-wires have been developed and reported by Coles, Cantwell and Wadcock (1978), and by Watmuff, Perry and Chong (1983). This section reports details of the flying-wire instrumentation used to effect the measurements of chapter 3 together with results which allow an appraisal of the technique for use in the separated flow in the vicinity of airfoils at angle of attack.

It is not the purpose of this section to compare the relative advantages of flying-wire, pulse-wire and laser anemometry although each can be used to measure in highly turbulent or recirculating flows. It is useful to note, however, that the two wire-based methods are cheaper and offer the advantage of representing comparatively simple extensions of a well established technique. They have the potential disadvantage of disturbance to the flow but avoid the problem associated with the light-scattering

particles required by laser anemometry. Flying-wire anemometry, in contrast to pulsed-wire anemometry, uses standard hot-wire probes and requires mechanical movements of the probe at a known velocity. Further information on pulsed-wire anemometry can be obtained, for example, from Castro and Cheun (1982) and of laser anemometry from Durst, Melling and Whitelaw (1981).

The remainder of this section is concerned with a detailed description of a flying-wire anemometer and its application to the measurement of the velocity characteristics of the separated flow on the upper surface of an airfoil at high angle of attack. The instrumentation and data acquisition systems are described first and is followed by an outline of the measurement procedure. Results are presented to allow evaluation of the accuracy of the measurements and the problems associated with the use of the instrumenation. The section ends with a summary of the more important conclusions.

Instrumentation and data-acquisition. The path which the flying-wire follows is of considerable importance, and that shown on figure 2.6 was chosen for the present application with the support and drive mechanism mounted externally on the wind tunnel. The mechanism is shown schematically on figure 2.7 and was driven by a motor (Yaskawa PMEE 12 PM11). The location and corresponding velocity of the probe were calculated from the following equations with notation for geometric variables indicated in figure 2.7:-

$$x = \frac{b}{a} r \sin\Omega + \frac{c}{a} \Phi \tag{2.25}$$

$$y = a + r \cos\Omega + \frac{c}{a} r \sin\Omega - (1 - \frac{b}{a}) \Phi \tag{2.26}$$

$$\frac{\partial x}{\partial t} = - \omega r \left[(\cos \Omega) \left(\frac{b}{a} - \frac{c}{a} \frac{r \sin \Omega}{\Phi}\right)\right] \tag{2.27}$$

$$\frac{\partial y}{\partial t} = - \omega r \left[\frac{c}{a} \cos \Omega - \left\{1 - \left(1 + \frac{b}{a}\right) \frac{r \cos \Omega}{\Phi}\right\} (\sin \Omega)\right] \tag{2.28}$$

$$V_p = \left\{\left(\frac{\partial x}{\partial t}\right)^2 + \left(\frac{\partial y}{\partial t}\right)^2\right\}^{1/2} \tag{2.29}$$

with Φ representing the expression $\left[a^2 - (r \sin \Omega)^2\right]^{1/2}$. The angles between the trajectory of the probe and the tunnel centreline and also between the axis of the probe and the centreline were calculated from:-

$$\beta = \arctan \left(\frac{\partial y}{\partial t} / \frac{\partial x}{\partial t}\right) \tag{2.30}$$

and

$$\psi = \arctan (r \sin \Omega / \Phi) \tag{2.31}$$

respectively. To identify the position of the probe, an optical encoder (Digitech DR 1035) was attached to the motor drive and provided a train of 2000 pulses per revolution. The angular shaft velocity was obtained by measuring the time between consecutive encoder pulses using a 10 MHz clock. Table 2.6 contains the essential details of the flying-wire.

The wire starts from its resting position, located outside the boundary layer, and is accelerated at a maximum rate over the region from position 1 to 2 of figure 2.6 where it attains a predetermined velocity of up to 13.5 m/s. This velocity is maintained from location 2 to location 3 while measurements of effective cooling velocity are recorded. The momentum of the wire mechanism carries it back to the rest position 1 where it remains

until any disturbances affecting the region of interest are dissipated after which another series of velocity values may be obtained. The retention of the probe outside the boundary layer and rapid acceleration to a velocity greater than the negative velocities of the flow in the recirculation bubble ensure that the wake of the probe and its holder do not influence the flow prior to the measurement part of the cycle.

Shaft velocity and up to two hot-wire voltages were obtained at each measurement location, and subsequently used to determine the velocity characteristics of the flow. For a sequence of preselected encoder locations, hot-wire voltage levels were held by synchronized sample and hold modules (Analogic MP 240), and recorded by a computer (PDP8E) after conversion to a 12-bit digital signal by an analogue to digital converter (DEC AD01). The anemometer voltages, after calibration, gave direct information of the instantaneous wire-cooling velocity at the required locations. Probe velocity was calculated from equations 2.29 and 2.30 with the time between encoder pulses transferred from hardware while the probe was at rest. Conversion of the hot-wire voltages to effective cooling velocity was also performed at this time using the calibration curve of equation 2.17. Values of probe and effective cooling velocity at each position were ensemble-averaged for a number of sweeps large enough to ensure that the calculated velocity values and their moments were determined to the accuracy specified in table 2.6.

Measurement procedures. The mean velocity and the four non-zero Reynolds stresses of a two-dimensional flow can be obtained

with the flying-hot-wire from the measured characteristics of probe velocity and effective cooling velocity. In order to obtain the Reynolds stresses $\langle u^2 \rangle$, $\langle v^2 \rangle$, $\langle w^2 \rangle$ and $\langle uv \rangle$ of the flow, the mean square of the effective cooling velocity was measured with four different wire orientations which were chosen as follows: a single wire aligned normal to the mean velocity, a cross-wire with its wires located in the plane of the two-dimensional mean flow, and a single wire slanted at 45 degrees to the normal wire with pintels coincident with those of the normal wire. The flying-wire probe cannot be aligned with the net cooling velocity so the mean velocity magnitude and direction were obtained from the effective cooling velocities of the normal wire and cross-wire respectively. Also the hot-wire response equation 2.12 is approximated with the curve fit given by equation 2.15 and was used to determine the characteristics of the fluctuating components of flow velocity after subtraction of the effects of probe motion.

Mean velocity. Ensemble averages of the effective cooling velocity, Q_{eff} (normal) from a single wire aligned normal to the mean flow direction, and Q_{eff} (cross, + α) and Q_{eff} (cross, - α) from a cross-wire arranged with the two wires in the plane of two-dimensional flow, were used to determine the magnitude and direction of the mean cooling velocity, assuming the cosine cooling-law. The magntiude and angle of the mean cooling velocity, relative to tunnel co-ordinates as shown on figure 2.8, are given by:-

$$\langle Q \rangle = \langle Q_{eff} \text{ (normal)} \rangle \tag{2.32}$$

$$\phi = \arctan\left\{\frac{\langle Q_{eff} \text{ (cross, } -\alpha)\rangle - \langle Q_{eff} \text{ (cross, } +\alpha)\rangle}{\langle Q_{eff} \text{ (cross, } -\alpha)\rangle + \langle Q_{eff} \text{ (cross, } -\alpha)\rangle}\right\} - \psi \tag{2.33}$$

with ψ representing the angle of the probe axis relative to the surface or tunnel roof.

The flow velocity was calculated from:-

$$\theta = \arctan\left[\left(\frac{\sin\phi}{\langle V_p\rangle} + \frac{\sin\beta}{\langle Q\rangle}\right)\left(\frac{\cos\phi}{\langle V_p\rangle} - \frac{\cos\beta}{\langle Q\rangle}\right)\right] \tag{2.34}$$

and

$$\langle U\rangle = \pm\left[\langle Q\rangle^2 - \langle V_p\rangle^2 \sin^2(\theta + \beta)\right]^{1/2} - \langle V_p\rangle\cos(\theta + \beta) \tag{2.35}$$

where $\langle V_p\rangle$ and β represent the probe velocity and angle obtained from equations 2.29 and 2.30.

Reynolds stresses. The Reynolds stress $\langle u^2\rangle$, $\langle v^2\rangle$, $\langle w^2\rangle$ and $\langle uv\rangle$ may be obtained from the solution of four simultaneous linear equations which represent the cooling response of four hot-wires orientated so that they are sensitive to different components of the velocity fluctuations. The selected orientations of the probe and their associated sensitivities to the fluctuations and angle of the effective cooling velocities, which appear as the functions F_i in equation 2.15, are shown on table 2.4.

The mean square of the effective cooling velocity for each wire was calculated from equation 2.20 and related to turbulence fluctuations with four equations obtained by substituting equation 2.15 into equation 2.20 for each wire orientation and has the form:-

$$\langle q_{eff}^2\rangle = \langle Q\rangle^2\cos^2\gamma(b_1\langle u_1^2\rangle + b_2\langle u_2^2\rangle + b_3\langle u_3^2\rangle + b_4\langle u_1u_2\rangle + \langle P_*\rangle) \tag{2.36}$$

with $u_i = q_i/\langle Q\rangle$ for $i = 1, 2, 3$.

The mean velocity was obtained from equations 2.32 and γ is defined in table 2.4. The coefficients, b_i, are functions of the four sets of coefficients, C_i, of equation 2.15 and the expressions for f_i and g_i as defined in table 2.4 and P_* is defined in appendix 2.A.

The Reynolds stresses obtained by solving the set of four simultaneous equations based on equation 2.36, represent the fluctuations of the effective cooling velocity and conversion to those pertaining to flow velocity requires subtraction of probe velocity fluctuations. Samples were accepted in the ensemble average only if the probe speed was within 0.3% of its selected value and variations inside this limit resulted in a contribution to the fluctuations of the effective cooling velocity. Ensemble averages of the angular velocity of the motor shaft were used in equations 2.27 and 2.28 to obtain $\langle v_p^2 \rangle$, the mean square of these one-dimensional probe fluctuations. The contribution of the probe fluctuations to the effective cooling velocity for each wire was obtained by substituting the values of $\langle v_p^2 \rangle$, normalised with the cooling velocity $\langle Q \rangle$ and transformed into the co-ordinate system orientated along the cooling velocity, into equation 2.36. These fluctuation effects are added to the source term which then is given by:-

$$\langle P_* \rangle = \langle P_{flow} \rangle + b_1 \langle v_{p1}^2 \rangle + b_2 \langle v_{p2}^2 \rangle + b_4 \langle v_{p1} v_{p2} \rangle + \langle P_{probe} \rangle \qquad (2.37)$$

so that the u_i-fluctuations in equation 2.36 represent the contribution to the effective cooling velocity due to flow fluctuations only. Initially the term, $\langle P_{flow} \rangle$, is assumed zero and the Reynolds stresses obtained using Gauss-Jordan elimination. This source term is then calculated with these values of the Reynolds stresses and the four simultaneous equations resolved. This procedure is repeated until the Reynolds stresses converge within 0.1% which usually requires from 2 to 9 iterations.

The Reynolds stresses of the two-dimensional flow velocity, as shown on figure 2.8, were calculated in boundary layer or tunnel co-ordinates with the equations:-

$$\langle u^2 \rangle = \langle Q \rangle^2 (\cos^2\phi \langle u_1^2 \rangle + \sin^2\phi \langle u_2^2 \rangle - 2\sin\phi \cos\phi \langle u_1 u_2 \rangle) \quad (2.38)$$

$$\langle v^2 \rangle = \langle Q \rangle^2 (\sin^2\phi \langle u_1^2 \rangle + \cos^2\phi \langle u_2^2 \rangle + 2\sin\phi \cos\phi \langle u_1 u_2 \rangle) \quad (2.39)$$

$$\langle w^2 \rangle = \langle Q \rangle^2 \langle u_3^2 \rangle \quad (2.40)$$

$$\langle uv \rangle = \langle Q \rangle^2 (\sin\phi\cos\phi(\langle u_1^2 \rangle - \langle u_2^2 \rangle) + (\cos^2\phi - \sin^2\phi)\langle u_1 u_2 \rangle) \quad (2.41)$$

with $\langle Q \rangle$ and ϕ obtained from equations 2.32 and 2.33.

Preliminary tests. The flying wire was intially tested in still air to verify the calibrated cooling velocity against the encoder-based probe velocity and to determine the delay time at the rest position required to avoid probe interferece effects. The measured cooling velocity was found to be within 0.06 m/s of the probe velocity obtained from the encoder signal and the required delay time was found to be less than 1s although this value was clearly too small to avoid the wake-disturbance effects expected to occur inside the separation bubble. Tests in the recirculating flow showed that a wire velocity of 10 m/s and a rest time of 5s were required to remove the rectification effect and to reduce the wake effect to less than 0.05 and 0.08 m/s of the mean and r.m.s. velocity respectively.

The flying-wire was subsequently used to measure in the potential flow regions above and below the surface where the mean velocity and r.m.s. of velocity fluctuations were known from Pitot tube and stationary hot-wire measurements to be 26 and 0.24 m/s and 14 and 0.15 m/s respectively. Flying hot-wire results obtained

with a calibration between 1 and 40 m/s agreed with these values within 0.2% and 0.8% respectively, and similar results were obtained when the tunnel speed was varied between 7 and 25 m/s and the probe speed varied between 3 and 13 m/s.

Tests in a turbulent separating boundary layer. Measurements of mean and fluctuating velocity have been obtained with the flying hot-wire in the two-dimensional turbulent boundary layer described in chapter 3. Figure 3.1 shows the flow configuration and indicates the regions of potential and attached flow where impact probes, stationary hot-wire and flying hot-wire results were compared. The flying hot-wire was required near separation, where the probability of instantaneous flow reversals increased, and downstream of the location 200 mm from the trailing edge, where mean velocity along the surface was negative.

Measurements were obtained in the near-wall region at s/c of 0.78, i.e. upstream of separation or its influence, with stationary and flying wires and are shown on figure 2.9. The mean velocities agreed within 0.15 m/s with the largest discrepancy occurring between the two hot-wire results in the near wall region where gradient broadening effects are greatest. The Reynolds stresses were obtained by ensemble averaging 1000 samples with the stationary and flying-wire and resulted in agreement with 0.04 m^2/s^2. The results agreed clearly with those of Gibson et al (1983) for a curved boundary layer in that the stabilizing effect of streamwise curvature, which decreases the far wall values, was present and represented a more critical comparison of Reynolds stress measurements since the gradients are larger than in a flat plate boundary layer.

The closest measurement point from the surface was about 0.25 mm with both techniques, and the flow angle was assumed at distances less than 1.5 mm.

In the recirculating flow, the rectification effect associated with the stationary wire at zero velocity results in measurements of mean velocity which are positive, and Reynolds stresses which are smaller compared to those obtained from the flying-wire as shown in figure 2.10. The flying-wire shows that instantaneous flow reversals occur below 0.4 boundary layer thicknesses above the surface which is three times further from the wall than the outer extremity of mean reverse velocities at the same location. As expected, the flying-wire gives rise to higher values of the stresses than does the stationary wire which tends to underestimate the outer maximum and is unable to detect the inner maximum. In the outer region, and as expected from the earlier results, the stationary and flying-wires yield similar results.

The wake measurements of figure 2.11 were obtained downstream of the mean-flow recirculation and, as expected the mean velocity profiles, which are obtained with stationary and flying-wires, are in close accord with a tendency for the flying-wire value to be smaller in the region of minimum velocity. In keeping with this tendency and the finite probability of negative instantaneous velocities, the values of $\langle u^2 \rangle$ and $\langle v^2 \rangle$ obtained with the stationary wire are up to 40% lower than those with the flying-wire. A similar but smaller effect is evident in the vicinity of the stress maxima and maybe associated with the

comparatively high intensities and negative skewness of the $\langle v^2 \rangle$ component. It may also be expected that both wire systems will give rise to low values of stresses in regions of very steep mean velocity gradient where broadening effects are significant: the hot-wire and laser velocimeter results of Nakayama (1983) indicate the magnitude of effects of this type.

Discussion and Summary. The errors which effect the results obtained with the flying-hot-wire stem from calibration, probe velocity measurement, the approximate treatment of the hot-wire response equation, and distortion of the probe moving mechanism. The maximum deviation between the calibration data and the curve fit was discussed in section 2.3 and results in a maximum uncertainty of less than 0.3 m/s. The probe velocity is measured by obtaining the angular velocity of the motor shaft and combining it with equations 2.27 to 2.30, for which the lengths of components are determined within 0.1 mm, the position of encoder pulse is known within 2.5×10^{-6} degrees of the marker pulse, and the time between consecutive pulses is measured within 1 μs, and these represent a maximum error of 0.04 m/s on probe velocity. The position of the probe relative to the surface is obtained by locating the mechanism at bottom dead centre and measuring the distance between the surface and the wire with guages and was accurate to within 0.03 mm. The location of measurement is affected by the finite response time of the sampling logic which delays the acquisition of data by 10 μs after the triggering position is found. This, combined with the maximum frequency response of 100 KHz for the anemometer bridge, gives an added

positional uncertainty of 0.05 mm. The data collection instrumentation has an accuracy of 1.4 mV incurred during the sample-and-hold and digital conversion processes and results in a further possible velocity error of 0.02 m/s. The overall uncertainties are listed on table 2.6 together with the statistical error associated with the use of a finite number of samples for the ensemble-averaged quantities.

The flying-wire was tested and compared to conventional Pitot and stationary hot-wires and the mean velocity value agreed within 0.4% in the regions where all were appropriate. In boundary-layer flow, where the stationary hot-wire is appropriate, the discrepancy between stationary and flying-hot-wire measurements of $\langle U \rangle$, $\langle u^2 \rangle$, $\langle v^2 \rangle$, $\langle w^2 \rangle$ and $\langle uv \rangle$ were less than 0.9, 0.75, 1.2, 1.7 and 0.85% of the maximum value. In a recirculating flow, and in the downstream wake where local intensities exceeds 30%, the rectification effects associated with the stationary wire yielded the expected relation between the two sets of results. The mean velocity values obtained with the stationary wire were high and the Reynolds stresses were lower than those obtained with the flying-wire. The laser-velocimeter measurements of Simpson et al (1977) and Nakayama (1983) confirm similar trends in a separating boundary layer and near wake respectively and indicate velocity and stress results similar to those of figures 2.10 and 2.11 and is discussed in chapter 3 where further results obtained with the flying-hot-wire are presented.

Summary

Experimental techniques have been described for measuring velocity and pressure characteristics and for determining the two-dimensionality of the mean flow. Different devices are applied depending on the nature of the velocity field and chapter 3 indicates which are applied in the potential flow, boundary layer, recirculation region and wake of the present study.

Flow visualization techniques were presented in order to describe the flow patterns and determine the extent of two-dimensional mean flow but have to be verified with quantitative results.

Measurement procedures with impact probes were described and are relatively simple to implement although they are not recommended for regions with flow reversals. A five-tube probe is necessary where the mean flow is curved and it obtains mean values of pressure, velocity and flow angle. A pitot-static probe is preferred in the potential flow. Simple pitots are used in the near-wall region and boundary layer with negligible cross-stream pressure gradient and require wall values of static pressure in order to obtain the flow velocity.

Surface pressure tappings have been described for measuring mean values of static pressure on the wall: the results are valid throughout the regions of attached and separated flow.

Hot-wire anemometry was required to obtain the characteristics of fluctuating velocity, and methods for obtaining the mean and variance of velocity in a two-dimensional flow have been described. Flying hot-wires are used in regions with flow reversals because of the rectification effect associated with a stationary wire around zero velocity.

It is recommended that the flow domain is investigated with measurement techniques in ascending order of difficulty and hence expense; i.e. visualization, impact probes, hot-wires and flying-wires. Further, the more elaborate techniques are recommended only where necessary; for instance, flying hot-wire anemometry is needed in the vicinity of recirculation but not in the inviscid and attached boundary-layer flow.

TABLE 2.1

CONSTANTS OF FIVE-HOLE IMPACT PROBE

K_θ	5.8893 degrees
K_A	1.4757 N/m^2
K_B	0.5637 N/m^2
q_r	472.73 N/m^2
K_1	0.4541×10^{-3} $(degrees)^{-1}$
K_2	2.5218×10^{-3} $(degrees)^{-1}$

Range of validity

angle to probe axis	15 degrees
flow velocity	10-30 m/s

TABLE 2.2

MAXIMUM UNCERTAINTIES FOR PRESSURE PROBES

Potential Flow	
Pitot-static	
mean velocity	0.5% of local velocity
static pressure	1.0% of $\frac{1}{2}U^2$
Five-tube probe	
mean velocity	0.7% of local velocity
static pressure	1.6% of $\frac{1}{2}\rho U^2$
flow angle	0.2 degrees
Attached Turbulent Boundary Layer and Wake	
Negligible cross-stream gradient of static pressure	
Near wall ($y < 10$ mm)	
Circular-end pitot with wall static pressure	
mean velocity	0.7% of local value
Flattened-and pitot with wall static pressure	
mean velocity	0.9% of local value
Far wall (with flow curvature)	
Five-tube probe ($\theta < 15$ degrees)	
mean velocity	1.5% of local value
static pressure	3.4% of $\frac{1}{2}\rho U^2$
flow angle	1.7 degrees
Surface Underneath Boundary Layer (attached and separated)	
wall static pressure	0.35% of $\frac{1}{2}\rho U^2_{ref}$

TABLE 2.3

SAMPLE HOT-WIRE CALIBRATION

HOT-WIRE VOLTAGE	REFERENCE VELOCITY (m/s)	CALCULATED VELOCITY Equation 2.16 (m/s)	Equation 2.17 with n=0.5 (m/s)	Equation 2.17 with n=0.42 (m/s)
.4630	1.420	1.397	1.419	1.411
.4861	1.668	1.663	1.695	1.690
.5127	2.064	2.012	2.051	2.049
.5552	2.684	2.674	2.714	2.715
.5786	3.107	3.099	3.134	3.136
.6072	3.712	3.683	3.705	3.707
.6237	4.080	4.054	4.066	4.068
.6479	4.655	4.645	4.640	4.640
.6677	5.181	5.171	5.148	5.148
.6959	5.964	5.996	5.944	5.941
.7180	6.670	6.704	6.627	6.622
.7435	7.536	7.596	7.487	7.479
.7667	8.409	8.480	8.340	8.330
.7975	9.605	9.760	9.577	9.566
.8144	10.331	10.519	10.313	10.300
.8307	11.058	11.291	11.062	11.050
.8534	12.164	12.435	12.176	12.164
.8716	13.109	13.407	13.126	13.116
.8948	14.366	14.730	14.423	14.415
.9155	15.576	15.983	15.657	15.654
.9277	16.347	16.758	16.422	16.422
.9479	17.666	18.101	17.753	17.758
.9652	18.842	19.312	18.957	18.968
1.017	23.135	23.339	22.997	23.022
1.057	26.580	26.731	26.437	26.467
1.089	29.627	29.811	29.591	29.613
1.03	31.095	31.183	31.005	31.018
1.117	32.553	32.650	32.522	32.522
1.129	33.843	33.920	33.841	33.825
1.142	35.035	35.331	35.310	35.273
Standard deviation (m/s)		.1571	.0686	.0591
Maximum difference				
absolute (m/s)		.470	.175	.139
percentage (%)		2.62	1.62	1.34

TABLE 2.4

PROBE ORIENTATIONS AND SENSITIVITY COEFFICIENTS OF HOT-WIRE

ORIENTATION	PROBE TYPE	EFFECTIVE COOLING VELOCITY	PRIMARY TURBULENCE QUANTITY SENSED	ANGLE	CASE
Parallel to surface	Single normal wire	Q_{eff}(normal)	$\langle q_1^2 \rangle$	0	Case 2
Slanted relative to single normal wire	Single slant wire	Q_{eff}(slant)	$\langle q_1^2 \rangle$, $\langle q_3^2 \rangle$	$+\frac{\pi}{4}$	Case 2
Slanted with wire perpendicular to surface	Cross wire	Q_{eff}(cross, $+\alpha$)	$\langle q_1^2 \rangle$, $\langle q_2^2 \rangle$, $\langle q_1 q_2 \rangle$	$+\frac{\pi}{4}$	Case 1
"	Cross wire	Q_{eff}(cross, $-\alpha$)	$\langle q_1^2 \rangle$, $\langle q_2^2 \rangle$, $\langle q_1 q_2 \rangle$	$-\frac{\pi}{4}$	Case 1

The functions F_1 and F_2 in equation 2.15 are:-

$$F_1 = f_1 u_1 + f_2 u_2 + f_3 u_3$$

$$F_2 = g_0 + g_1 u_1 + g_2 u_2 + g_3 u_3 + g_4 u_1^2 + g_6 u_3^2 + g_7 u_1 u_2 + g_8 u_1 u_3 + g_9 u_2 u_3$$

	CASE 1	CASE 2
γ	$\Delta + \alpha$	$\arccos(\cos\Delta \cos\alpha)$
f_1	1	1
f_2	$-\tan\gamma$	$-\tan\Delta$
f_3	0	$\tan\alpha \sec\Delta$
g_0	$k_*^2 \tan^2\gamma$	$h_*^2 \sec^2\alpha \tan^2\Delta + k_*^2 \tan^2\alpha$
g_1	$2k_*^2 \tan^2\gamma$	$2(h_*^2 \sec^2\alpha \tan^2\Delta + k_*^2 \tan^2\alpha)$
g_2	$2k_* \tan\gamma$	$2(h_*^2 \sec^2\alpha - k_*^2 \tan^2\alpha) \tan\Delta$
g_3	0	$-2k_*^2 \tan\alpha \tan\Delta$
g_4	$k_*^2 \tan^2\gamma$	$h_*^2 \sec^2\alpha \tan^2\Delta + k_*^2 \tan^2\alpha$
g_5	k_*^2	$h_*^2 \sec^2\alpha + k_*^2 \tan^2\alpha \tan^2\Delta$
g_6	$h_*^2 \sec^2\gamma$	$k_*^2 \sec^2\Delta$
g_7	$2k_*^2 \tan\gamma$	$2(h_*^2 \sec^2\alpha - k_*^2 \tan^2\alpha) \tan\Delta$
g_8	0	$-2k_*^2 \tan\alpha \sec\Delta$
g_9	0	$2k_*^2 \tan\alpha \tan\Delta \sec\Delta$

where $u_i = q_i/\langle Q \rangle$ for $i = 1, 2, 3$ and $\Delta = \phi + \psi$.

The angles, α and Δ, are shown on figures 2.5 and 2.8.

TABLE 2.5

MAXIMUM UNCERTAINTIES FOR STATIONARY HOT-WIRE ANEMOMETRY

STATISTICAL ERROR

Maximum uncertainty with a 95% confidence level for measured quantities.

mean velocity	1.3%
variance	3.0%

ESTIMATE OF MAXIMUM UNCERTAINTIES

Method with equations 2.22 - 2.24 which requires probe is aligned with the flow.

	Turbulence Intensity			
	5%	10%	15%	20%
$\langle U \rangle$ (m/s)	0.15	0.16	0.18	0.20
$\langle u^2 \rangle$ (%)	9.3	10.1	15.3	22.3
$\langle v^2 \rangle$ (%)	9.8	10.9	16.1	26.2
$\langle uv \rangle$ (%)	6.3	7.1	11.2	17.0

Method with equations 2.18 - 2.21 using four different probe orientations.

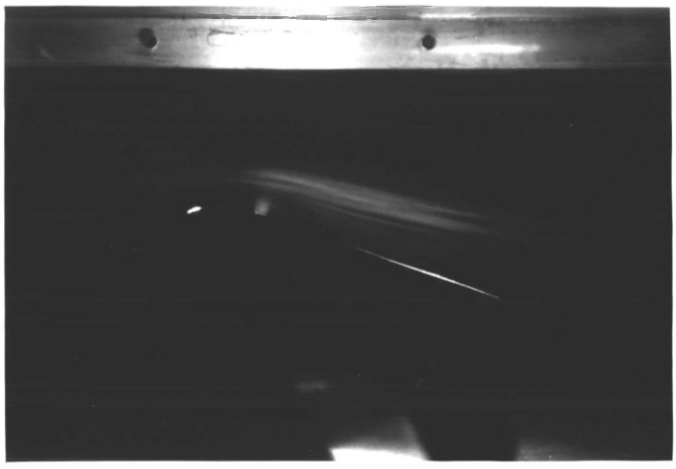
	Flow angle $\langle \theta \rangle$				
	0	5 degrees	10 degrees	15 degrees	20 degrees
$\langle U \rangle$ (m/s)	0.19	0.21	0.24	0.27	0.31
$\langle \theta \rangle$ (degrees)	0.2	0.3	0.3	0.4	0.5
$\langle u^2 \rangle$ (%)	3.0	3.0	3.1	3.1	3.2
$\langle v^2 \rangle$ (%)	10.0	10.1	10.2	10.3	10.6
$\langle w^2 \rangle$ (%)	9.6	10.7	12.4	14.4	17.6
$\langle uv \rangle$ (%)	3.1	4.1	5.9	6.6	8.4

These uncertainties are independent of turbulence intensity and assumes velocity rectification is avoided.

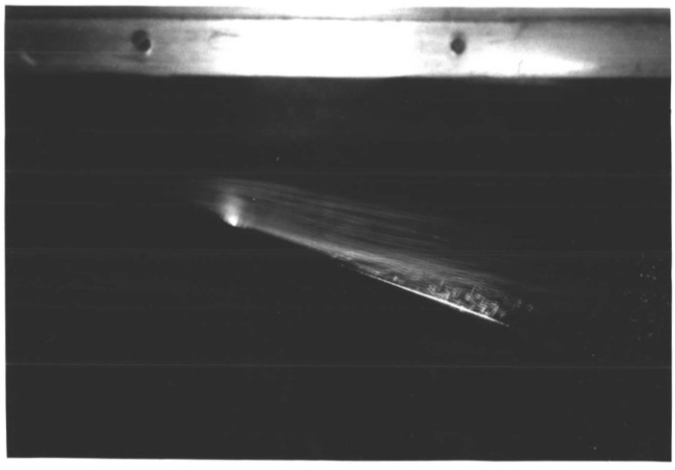
TABLE 2.6

ESSENTIAL DETAILS OF THE FLYING HOT-WIRE ANEMOMETER

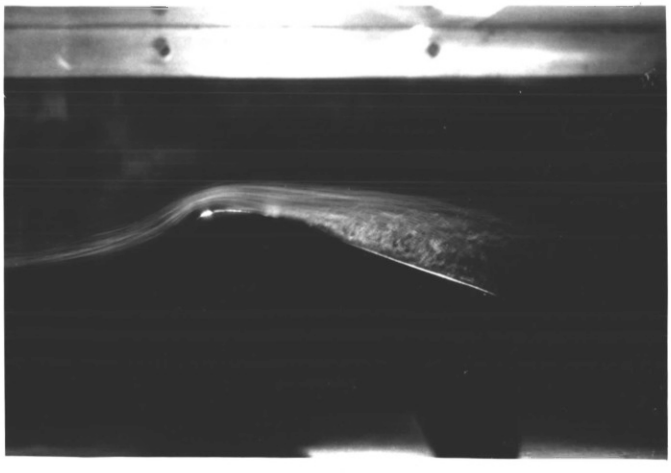
Dimensions:	a	0.160 m
	b	0.357 m
	c	0.127 m
	r	0.04 - 0.06 m
Velocity:	shaft (maximum)	100 rad/s
	probe (maximum)	13.5 m/s
Calibration range:		1-30 m/s
Time in sampling part of cycle		T_S = 0.01 s
Time in dormant part of cycle		T_D = 5 s
Maximum statistical uncertainty with a 95% confidence level for measured quantities:		
	mean velocity	2%
	variance	6%
Maximum uncertainties:	probe speed	0.04 m/s
	flow velocity	0.35 m/s
	flow angle	0.6 degrees
	Reynolds stresses	
	$\langle u^2 \rangle$	7%
	$\langle v^2 \rangle$	20%
	$\langle w^2 \rangle$	23%
	$\langle uv \rangle$	14%



(a)



(b)



(c)

Figure 2.1 Helium bubble visualizations.

(a) Attached boundary layer.

(b) Trailing-edge separation.

(c) Stall.

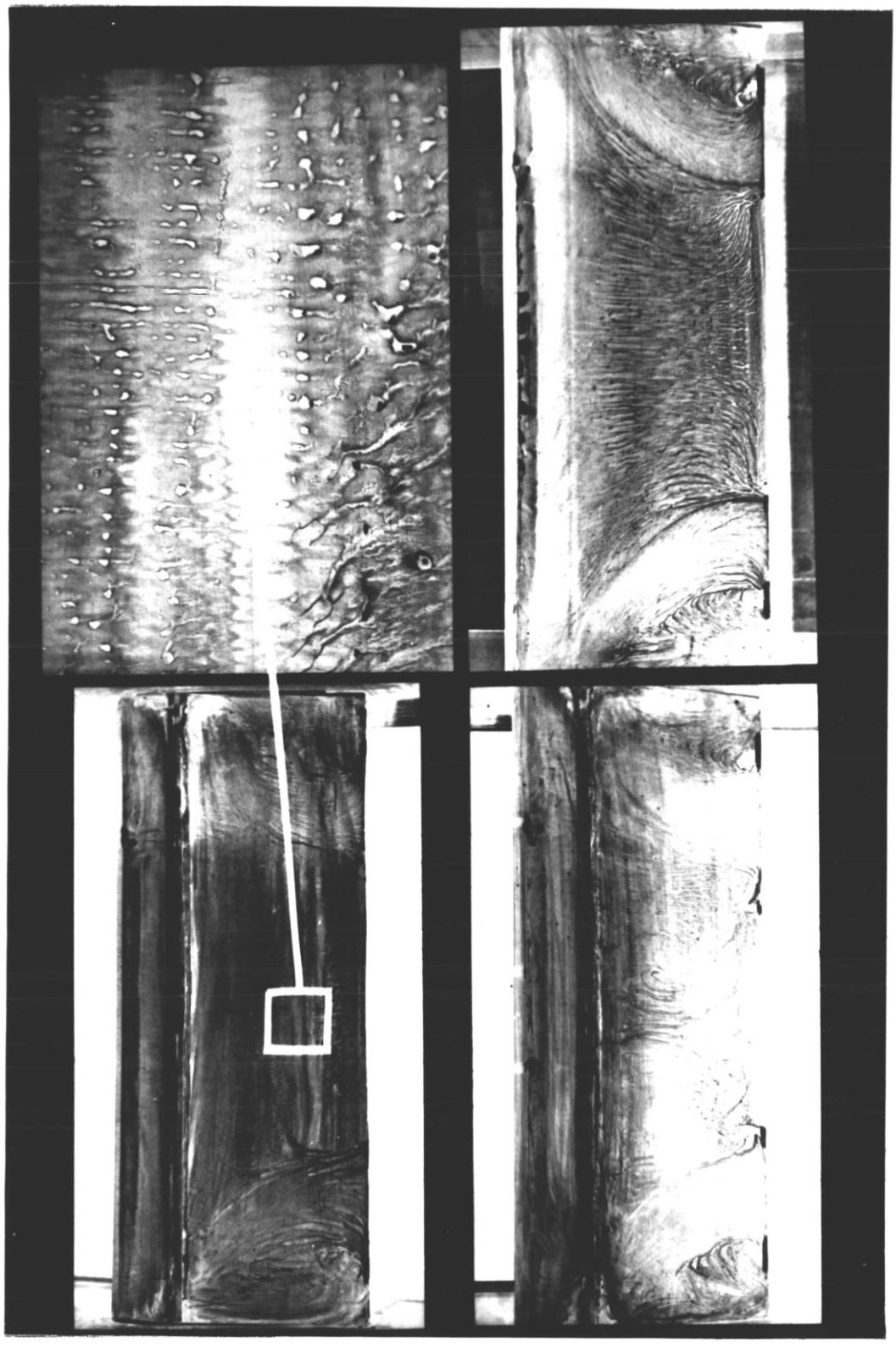


Figure 2.2 Surface oil flow visualization of separation point.

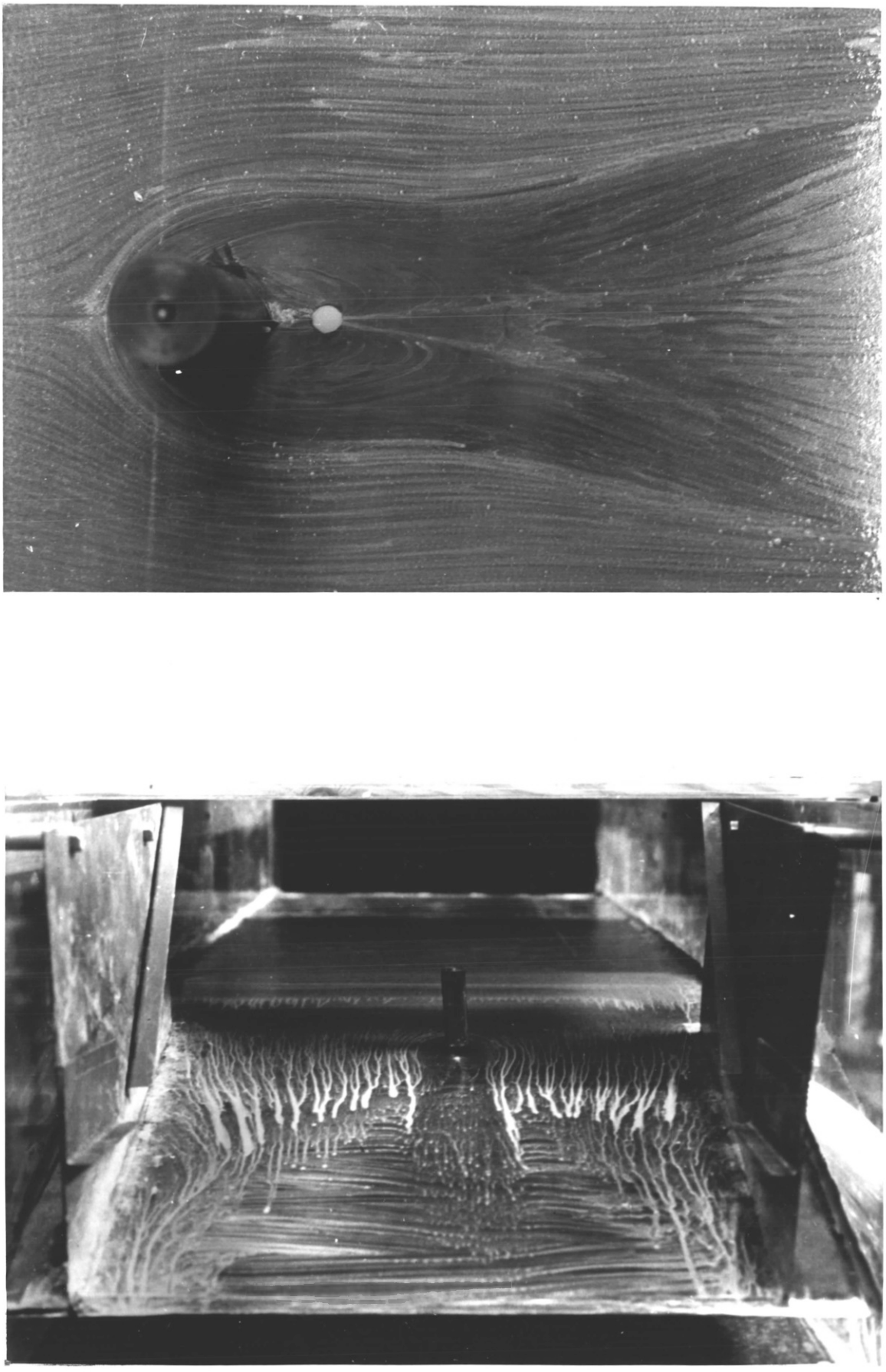


Figure 2.3 Surface oil flow around a circular cylinder.

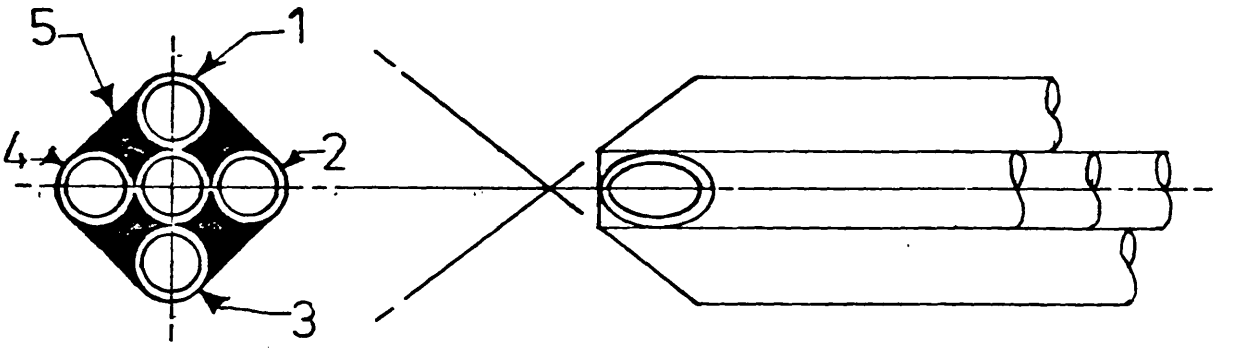
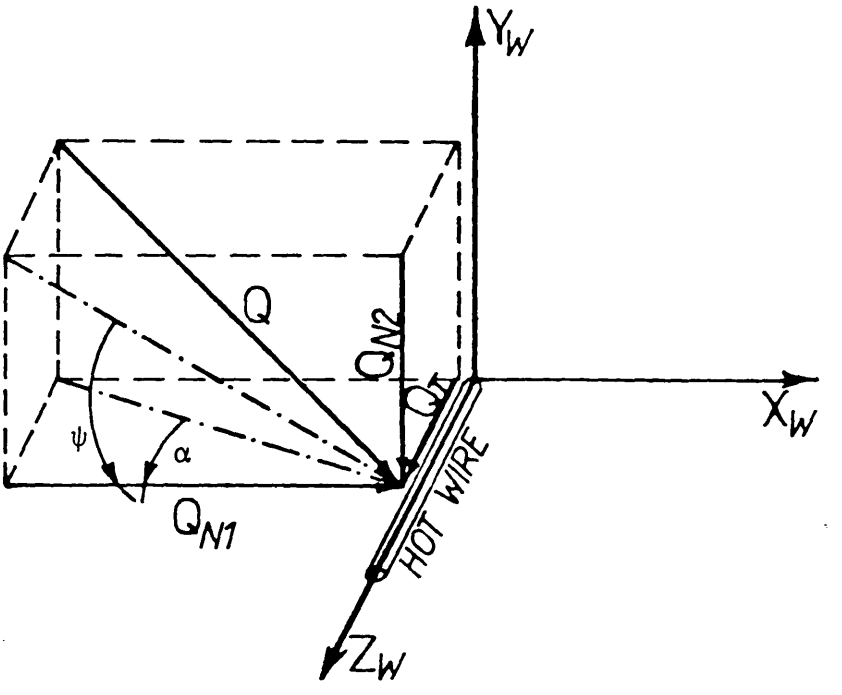


Figure 2.4 Diagram of five-hole impact probe.



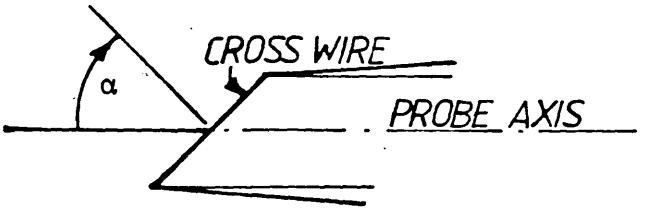


Figure 2.5 Orientation of hot wire.

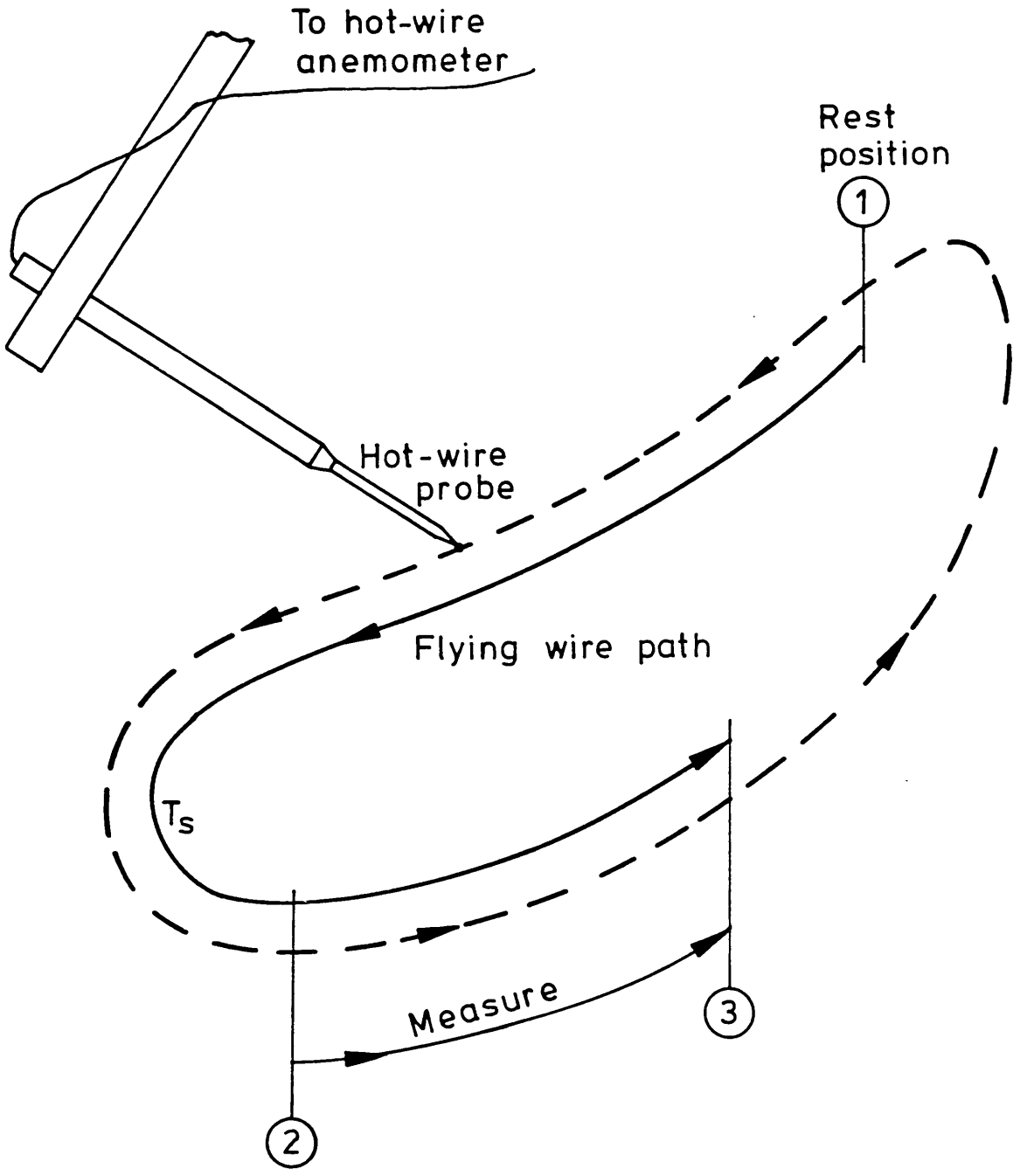


Figure 2.6 Trajectory of flying hot-wire.

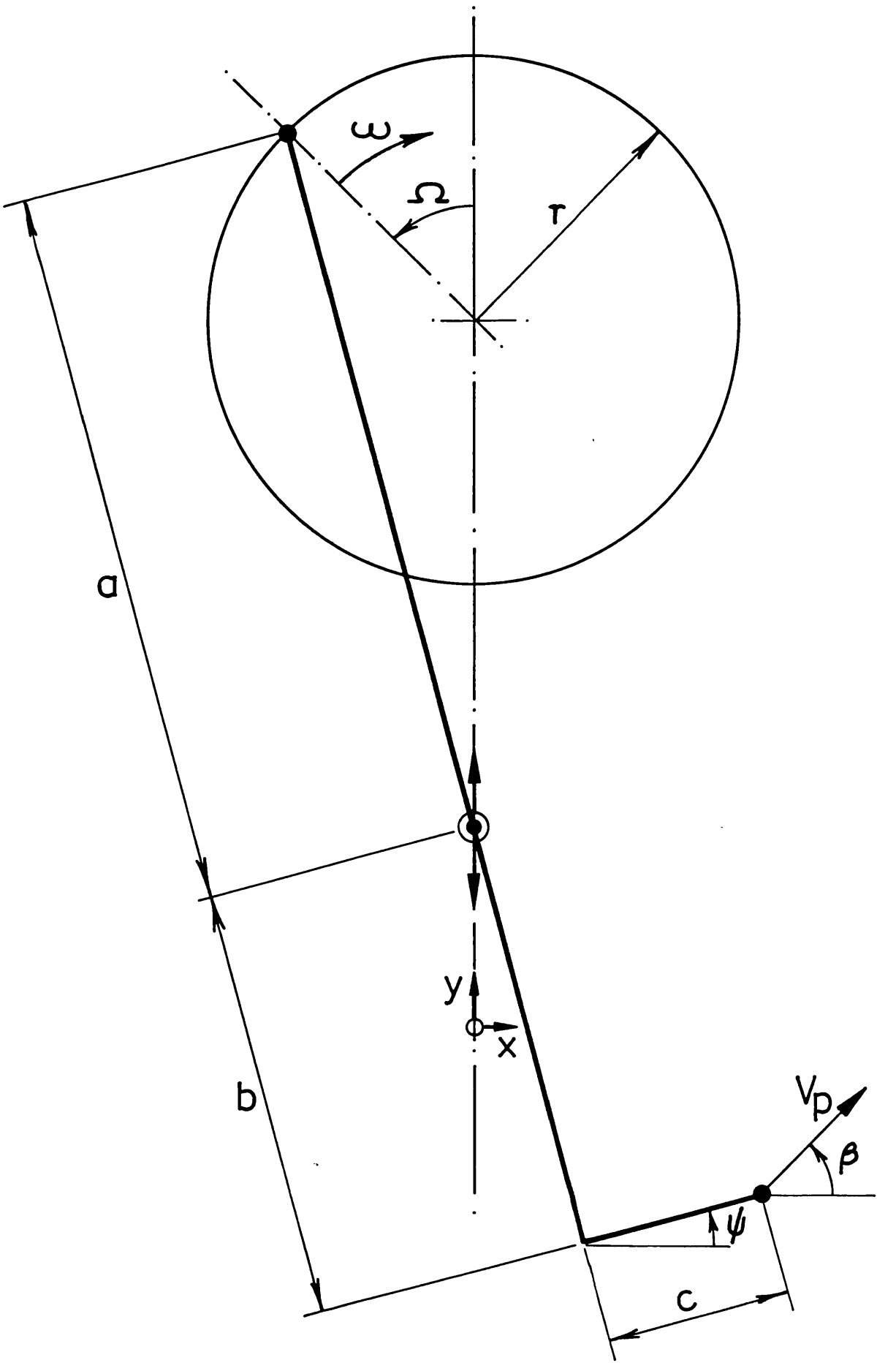
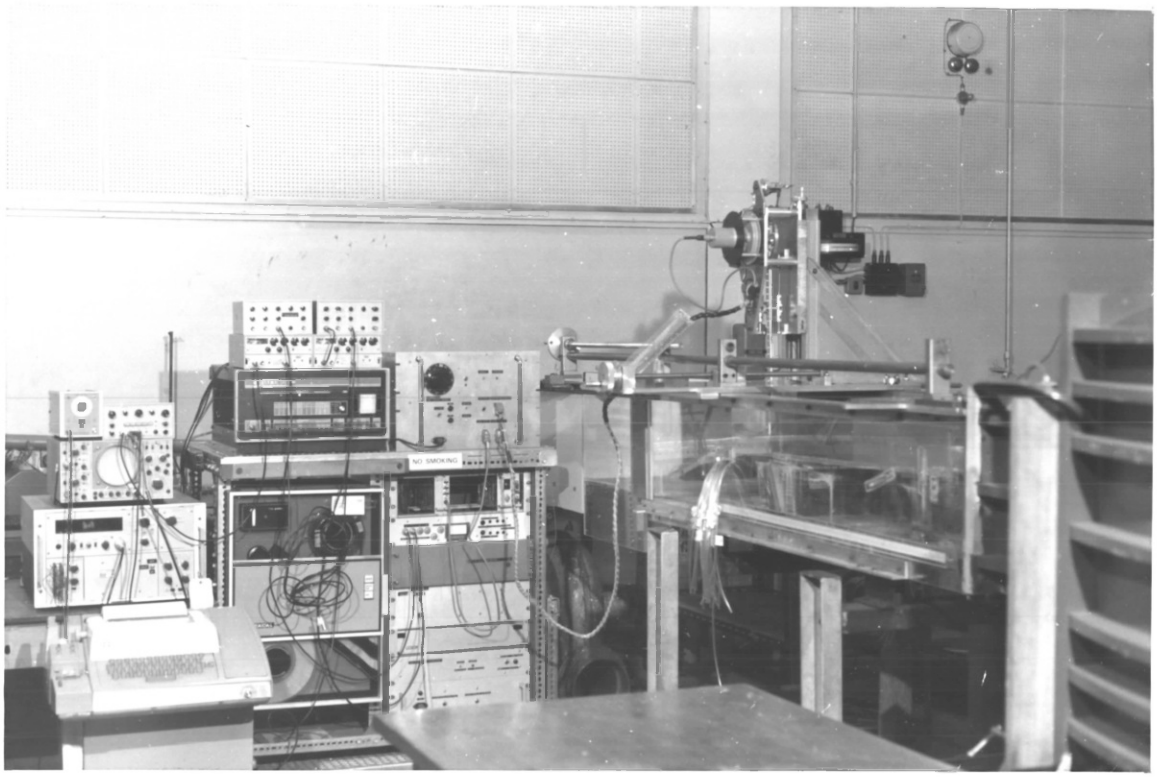


Figure 2.7 Flying-hot-wire mechanism and instrumentation.



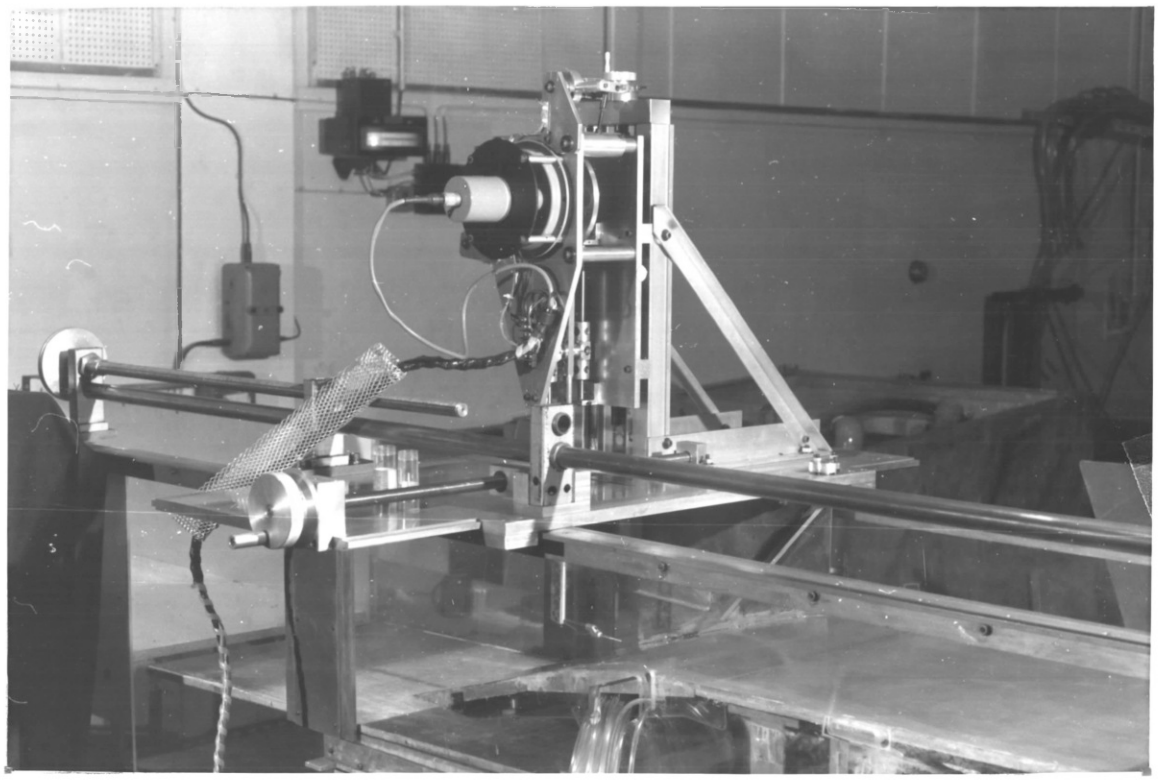


Fig. 2.7 (cont.) (b) Instrumentation.

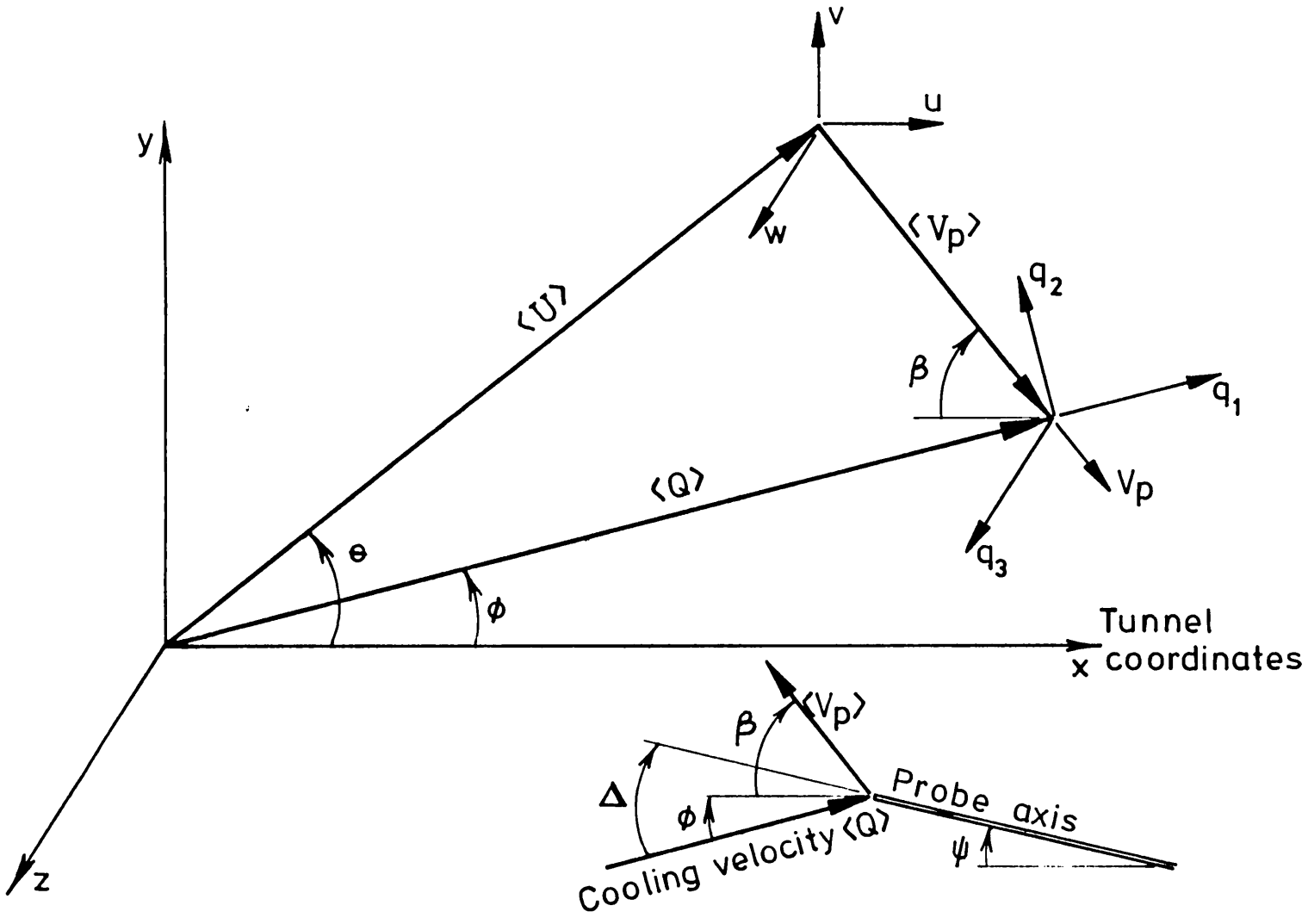


Figure 2.8 Cooling velocity on the flying-hot-wire probe.

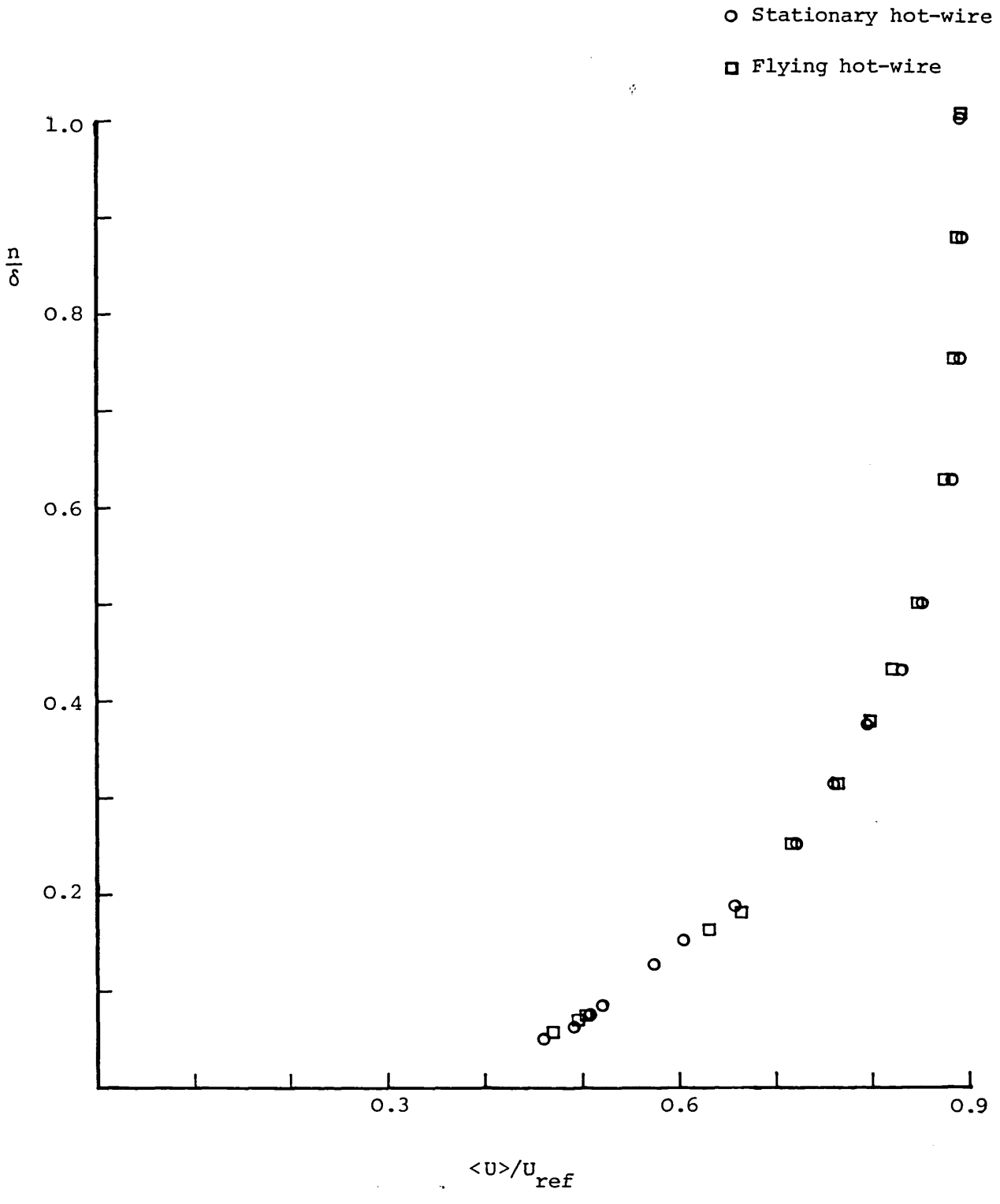


Figure 2.9 Velocity characteristics of the attached boundary-layer flow at s/c of 0.78
(a) Mean velocity.

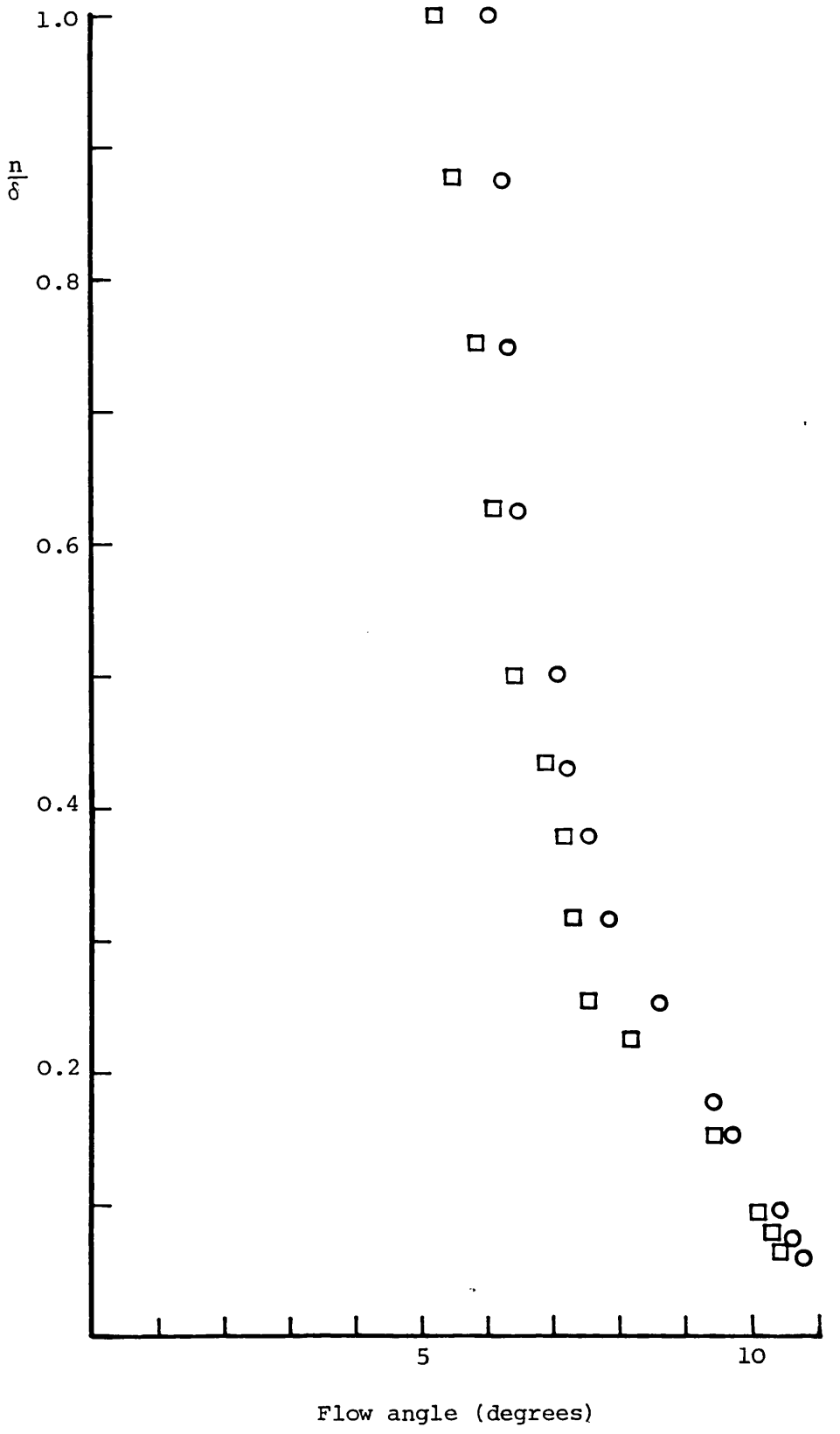


Fig. 2.9 (cont.) (b) Flow angle.

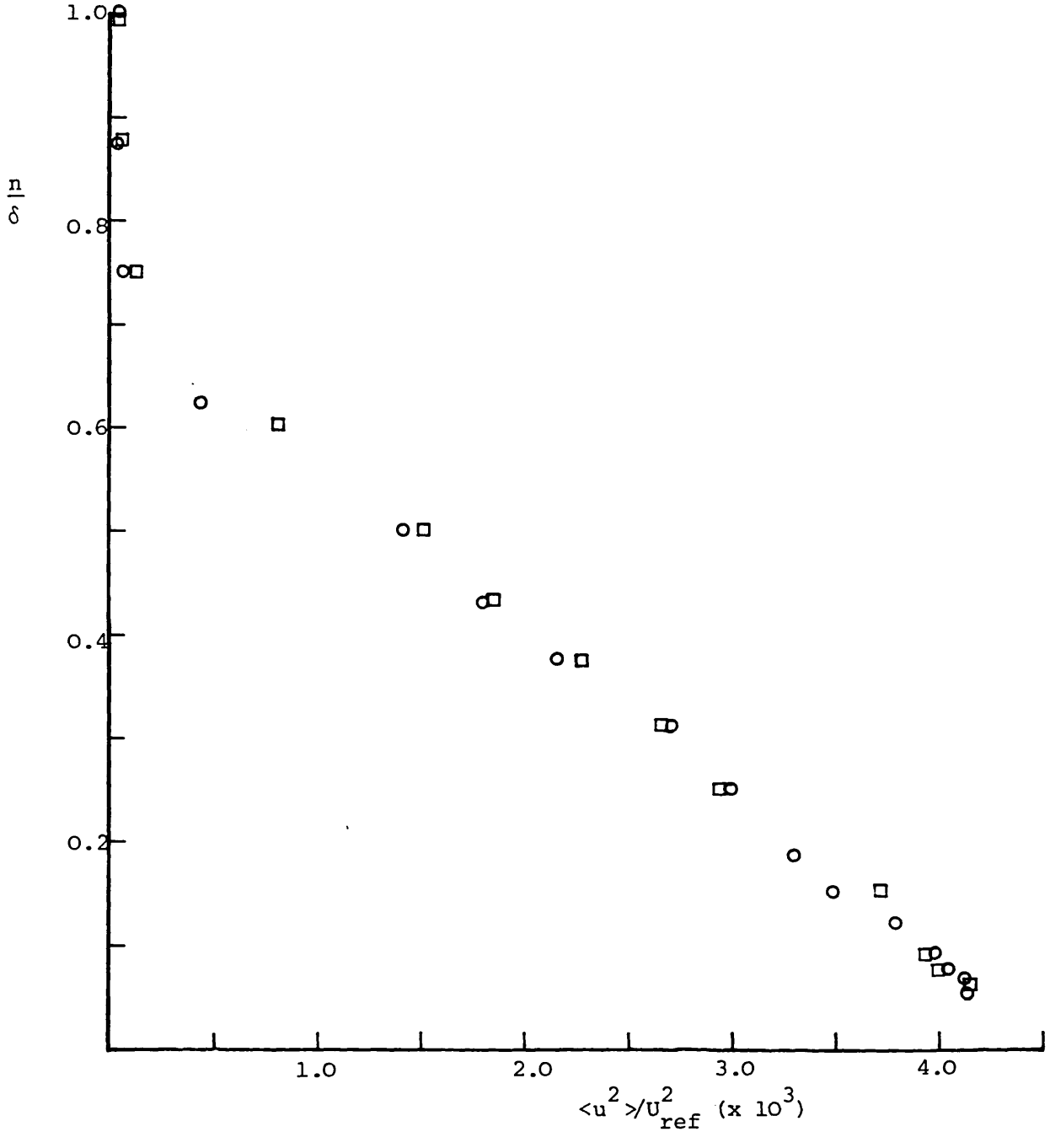


Fig. 2.9 (cont.) (c) Streamwise normal stress.

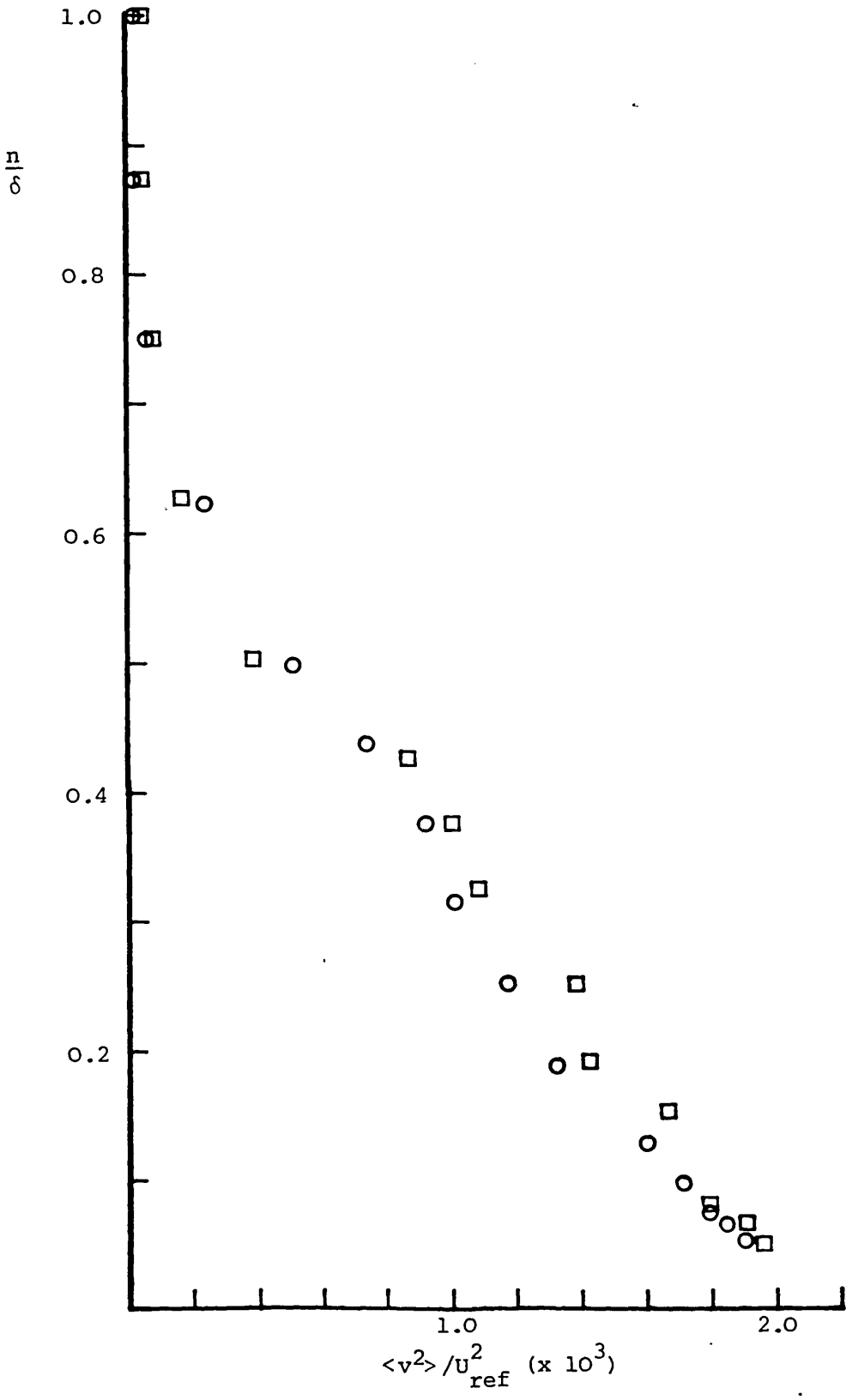


Fig. 2.9 (cont.) (d) Cross-stream normal stress.

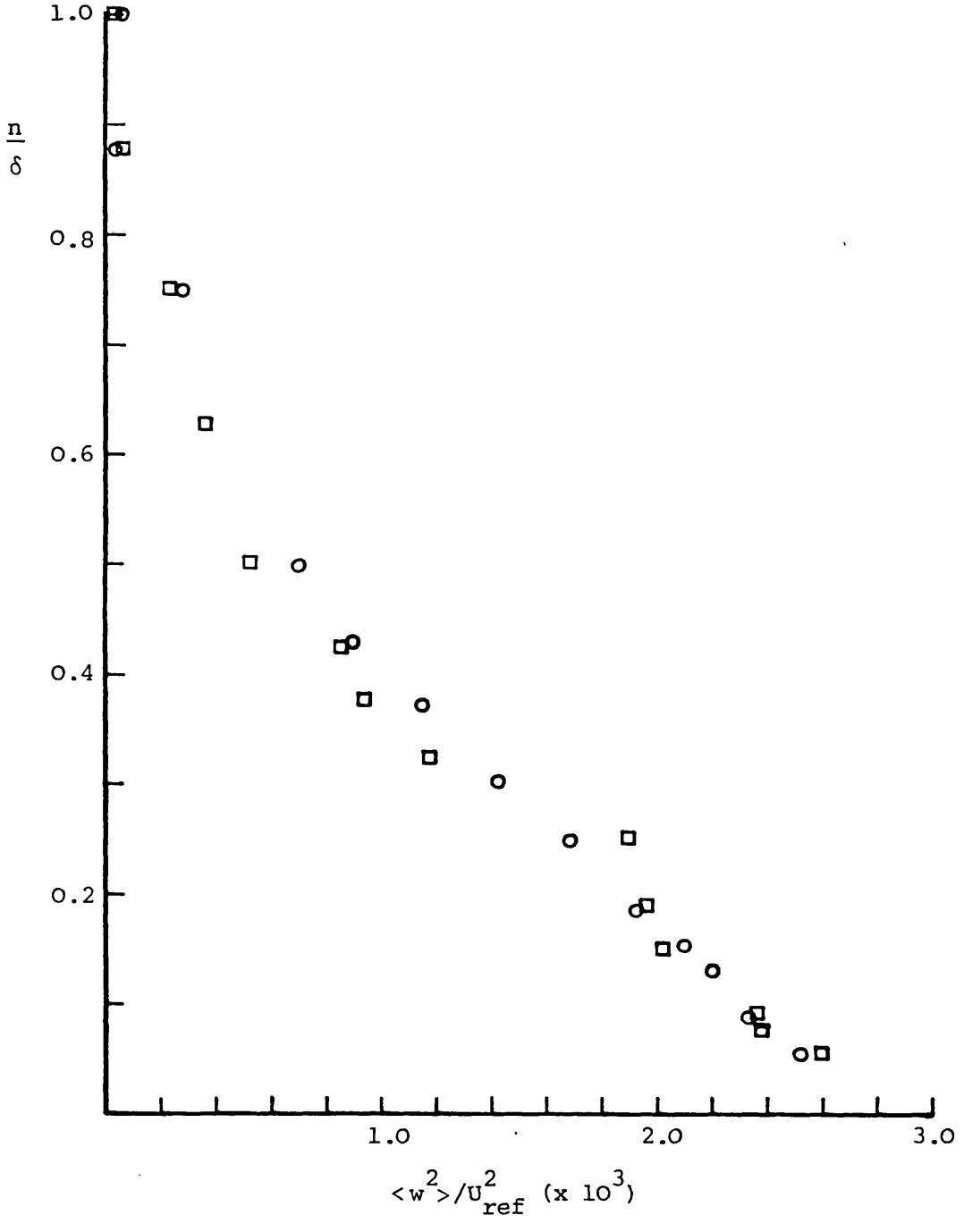


Fig. 2.9 (cont.) (e) Transverse normal stress.

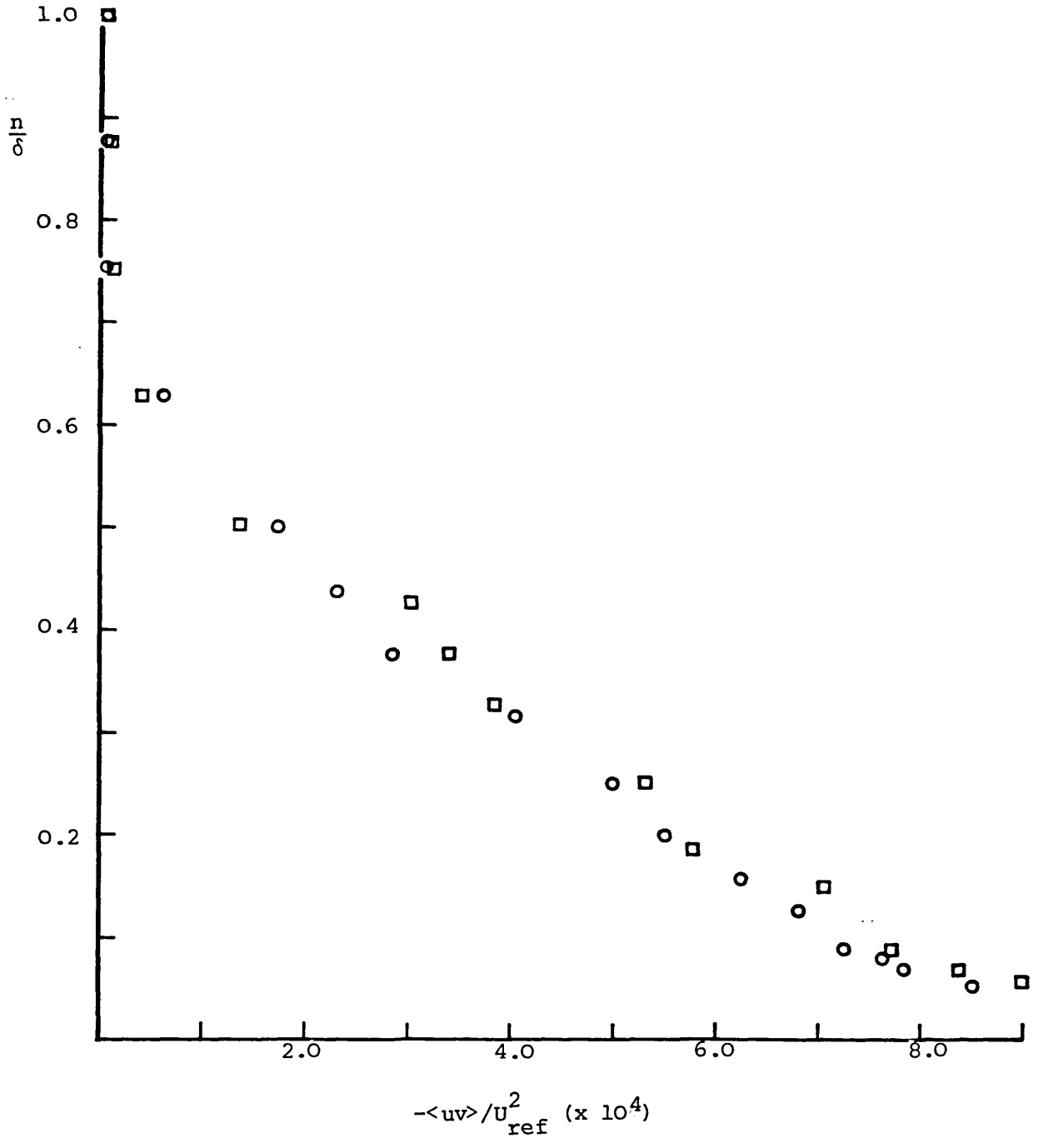


Fig. 2.9 (cont.) (f) Reynolds shear stress.

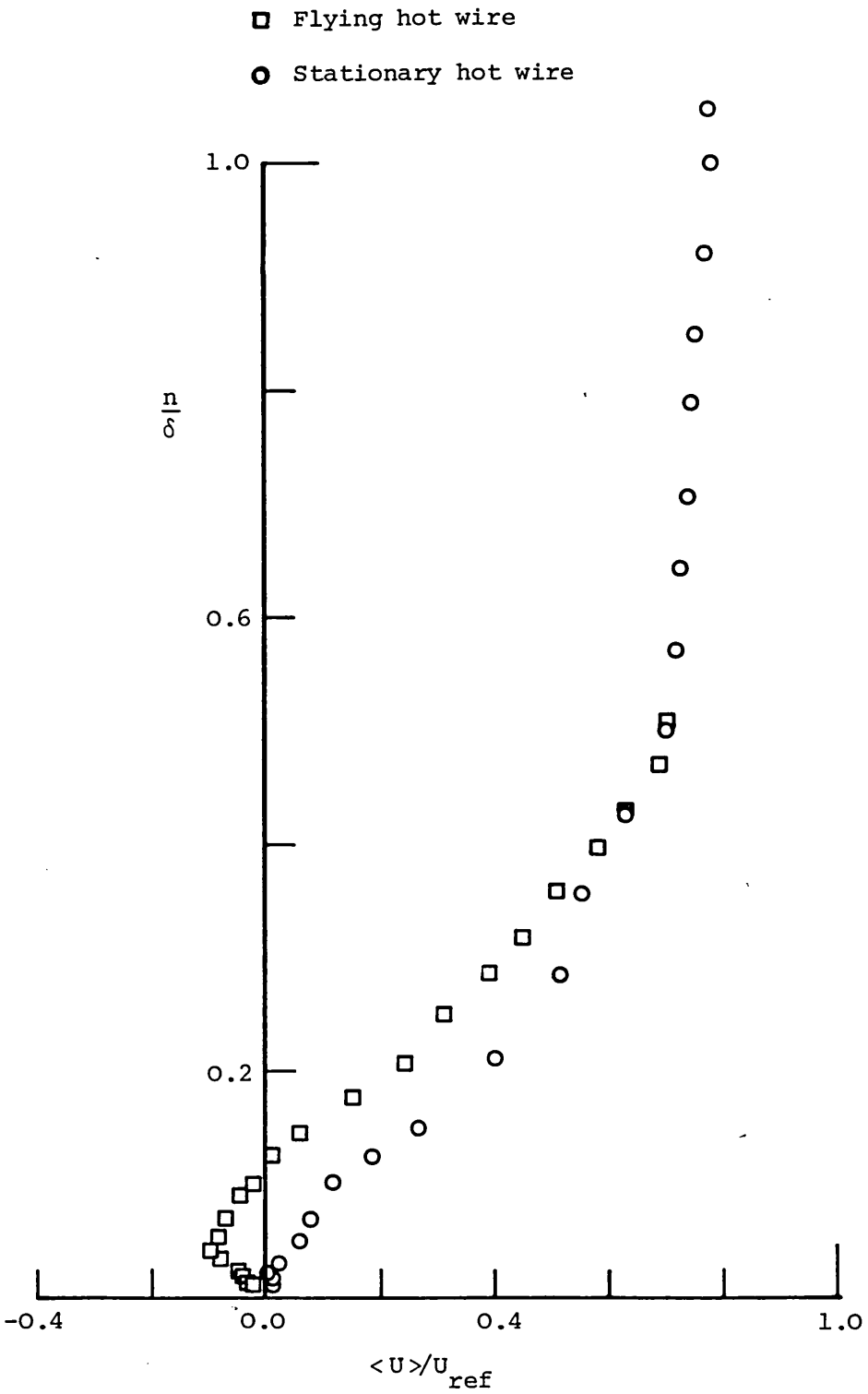


Figure 2.10 Velocity characteristics of the separated boundary-layer flow at s/c of 0.905.

(a) Mean velocity.

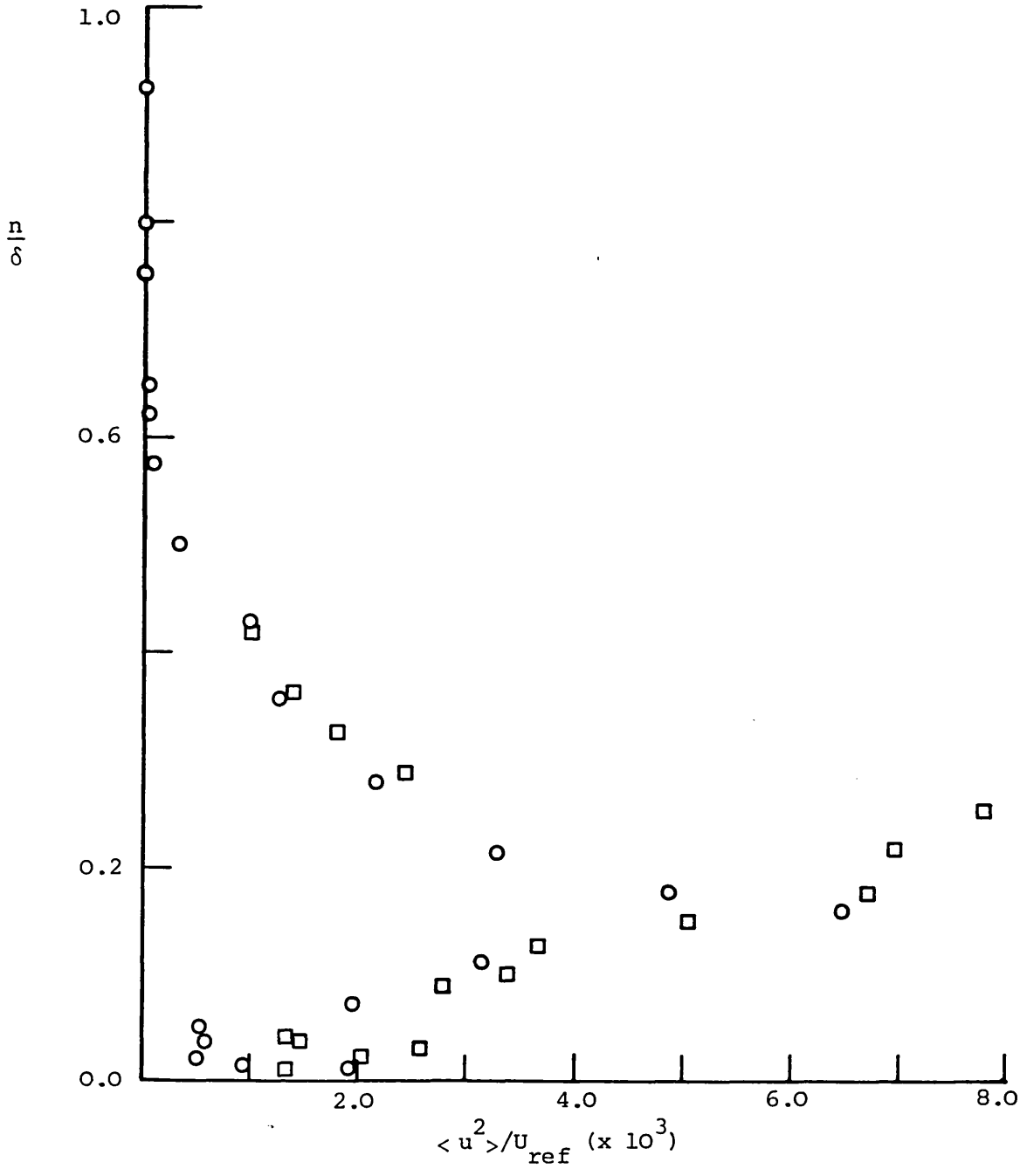


Fig. 2.10 (cont.) (b) Streamwise normal stress.

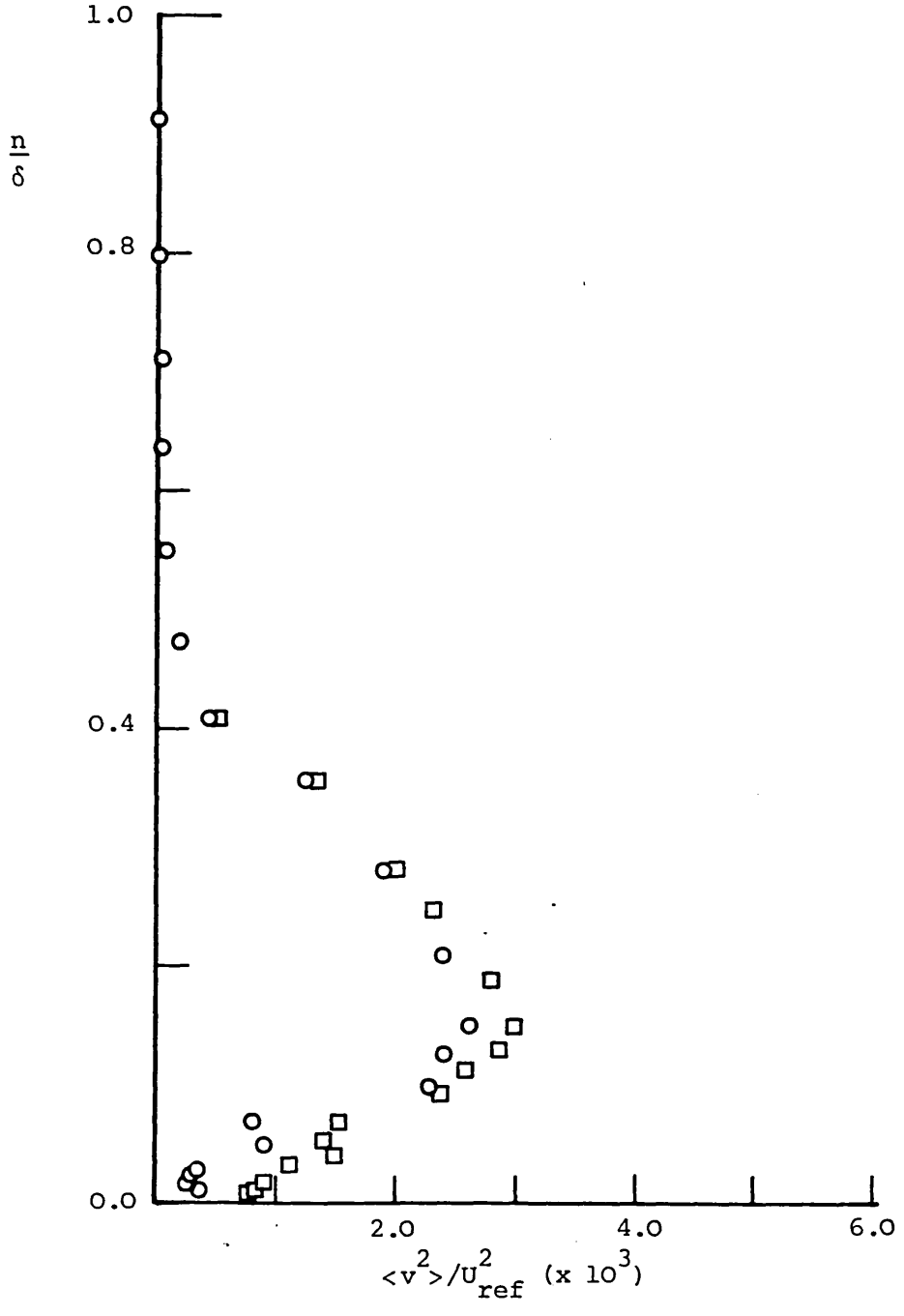


Fig. 2.10 (cont.) (c) Cross-stream normal stress.

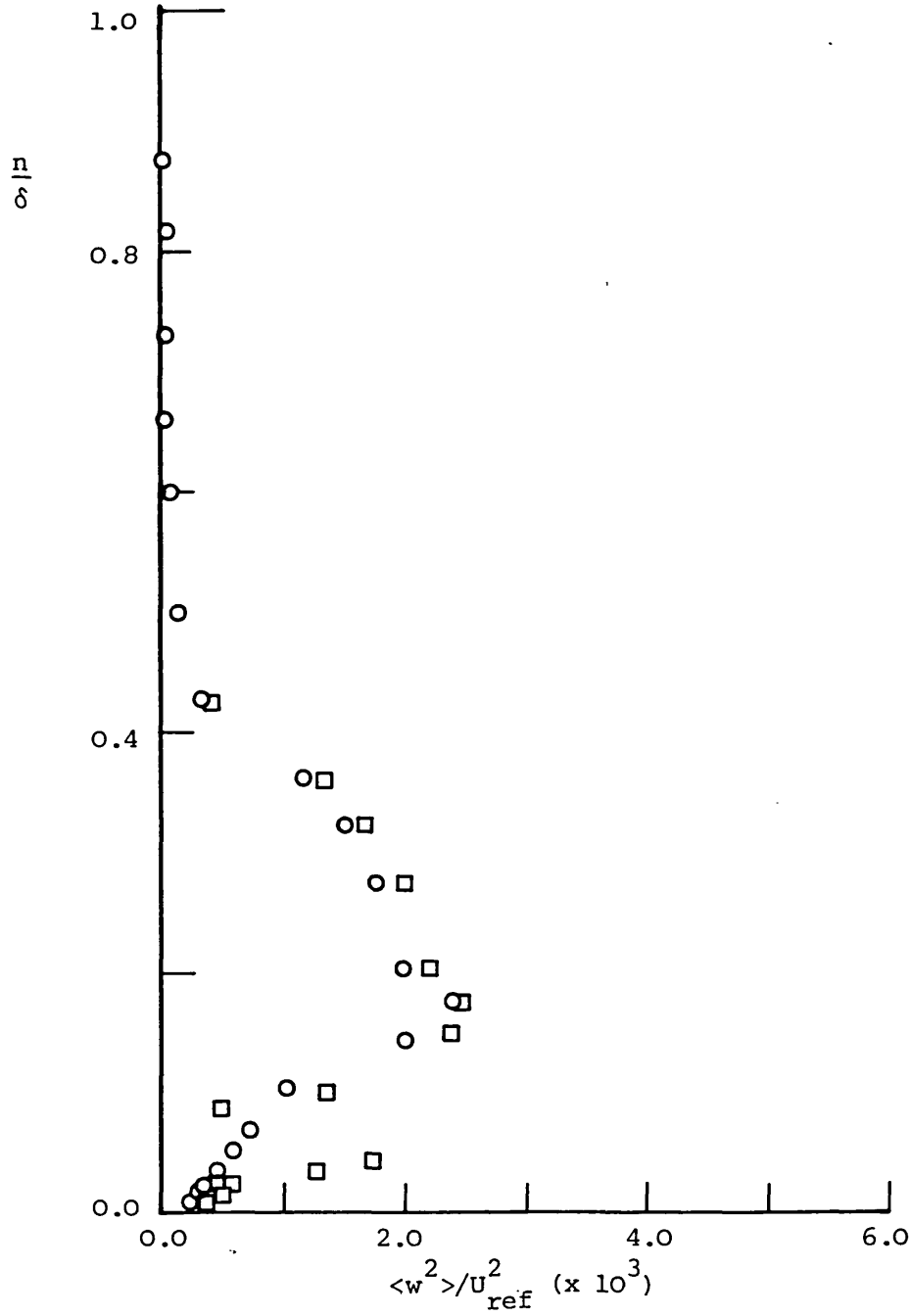


Fig. 2.10 (cont.) (d) Transverse normal stress.

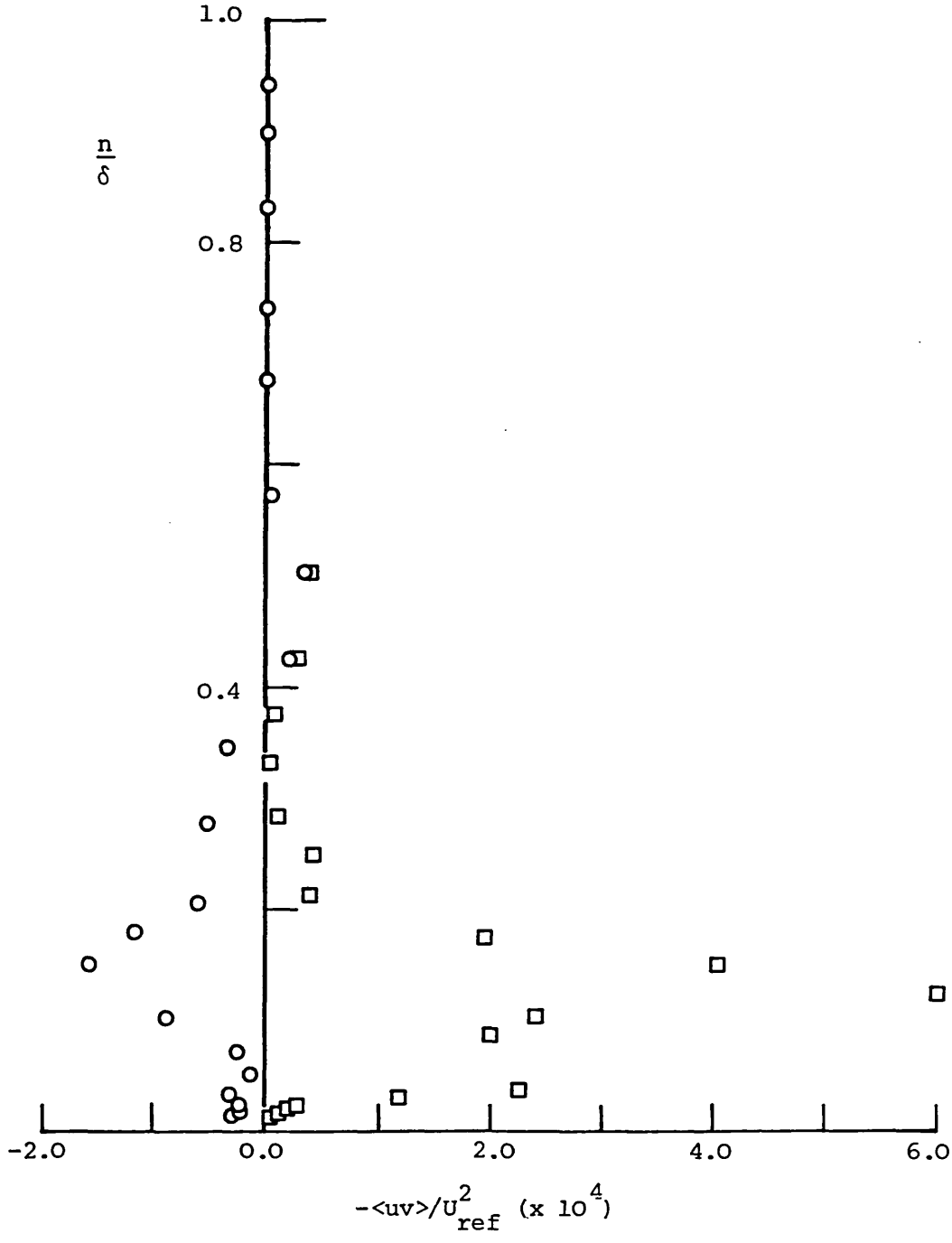


Fig. 2.10 (cont.) (e) Reynolds shear stress.

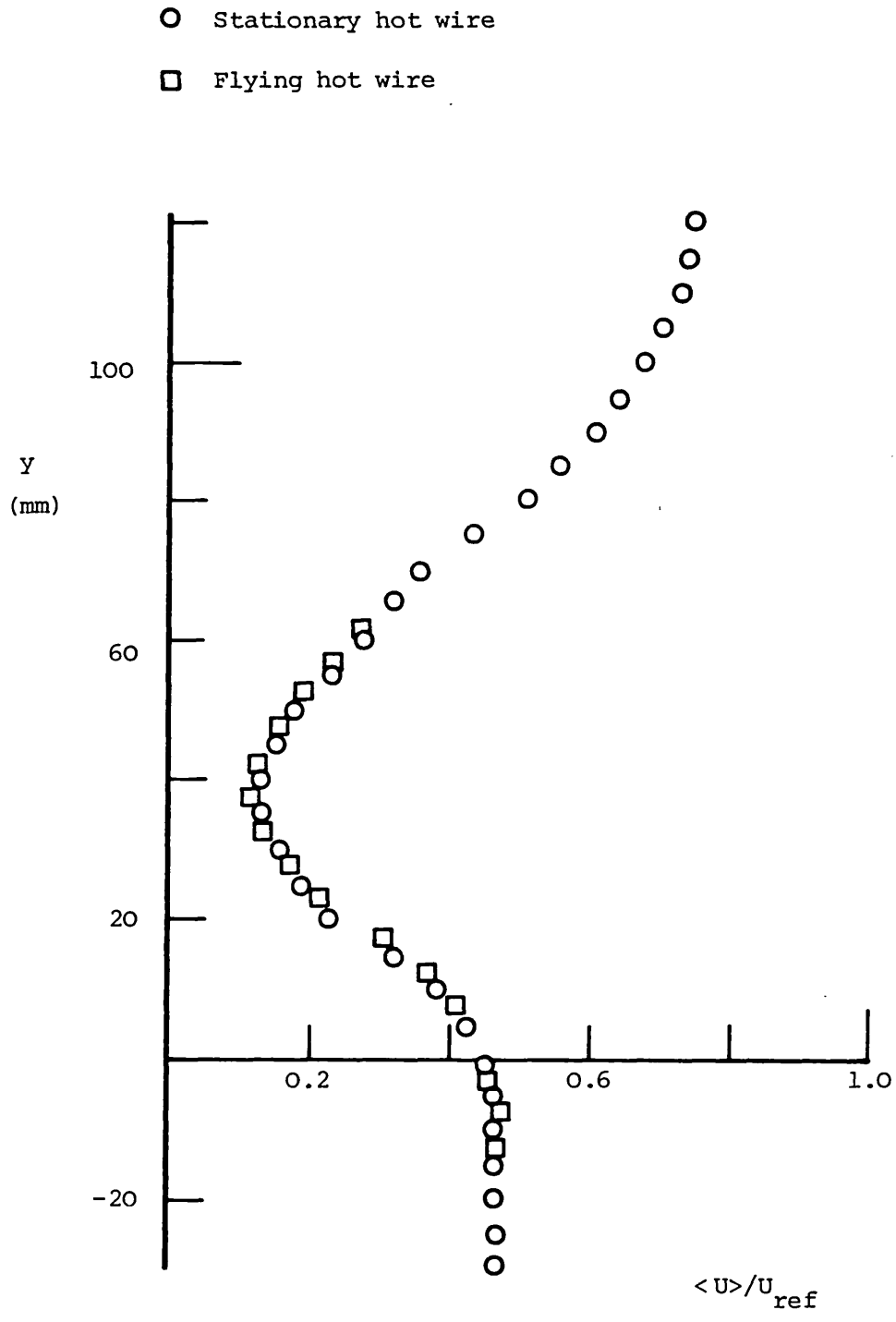


Figure 2.11 Velocity characteristics of the wake at x/c of 0.066.

(a) Mean velocity.

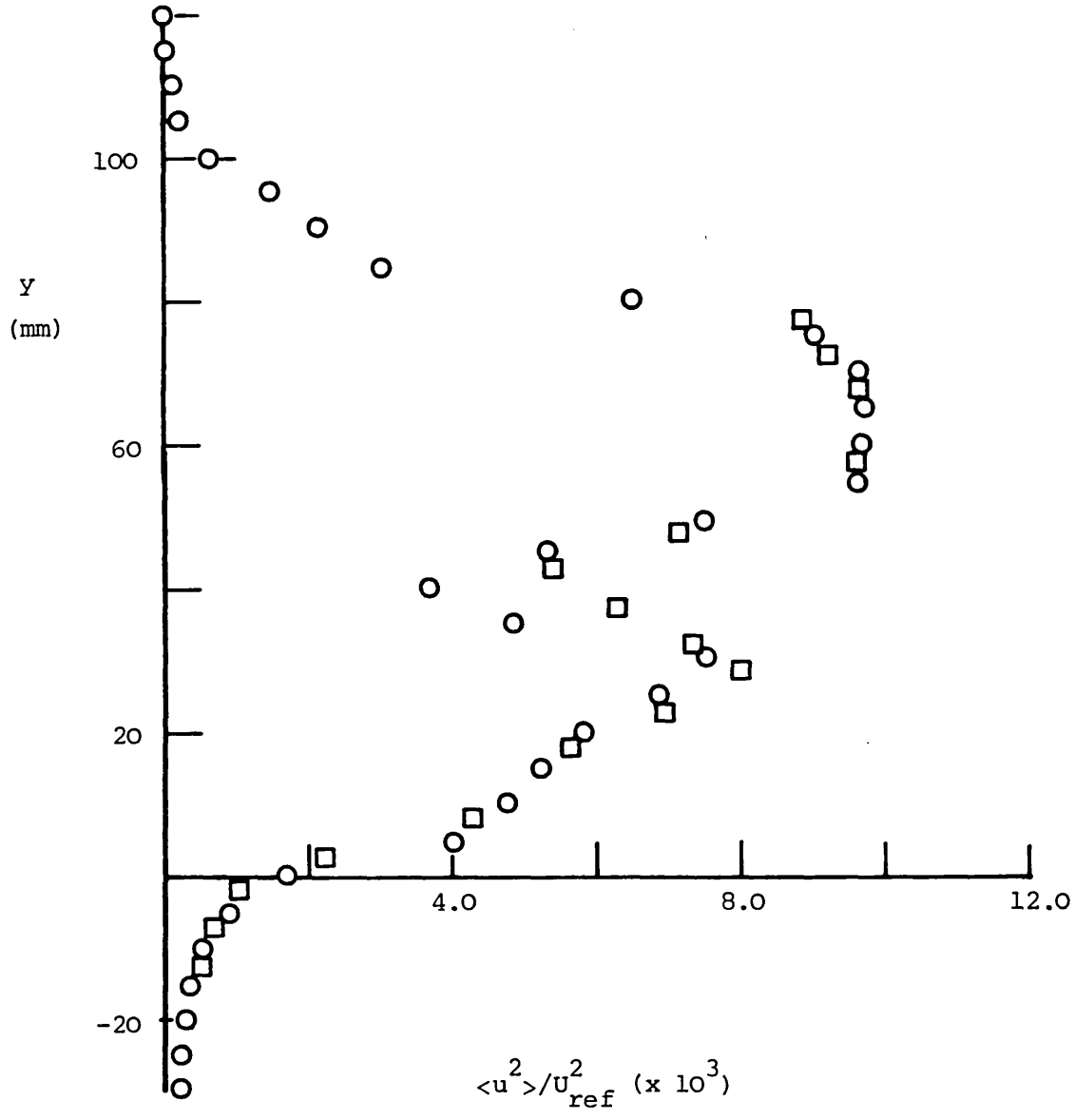


Fig. 2.11 (cont.) (b) Streamwise normal stress.

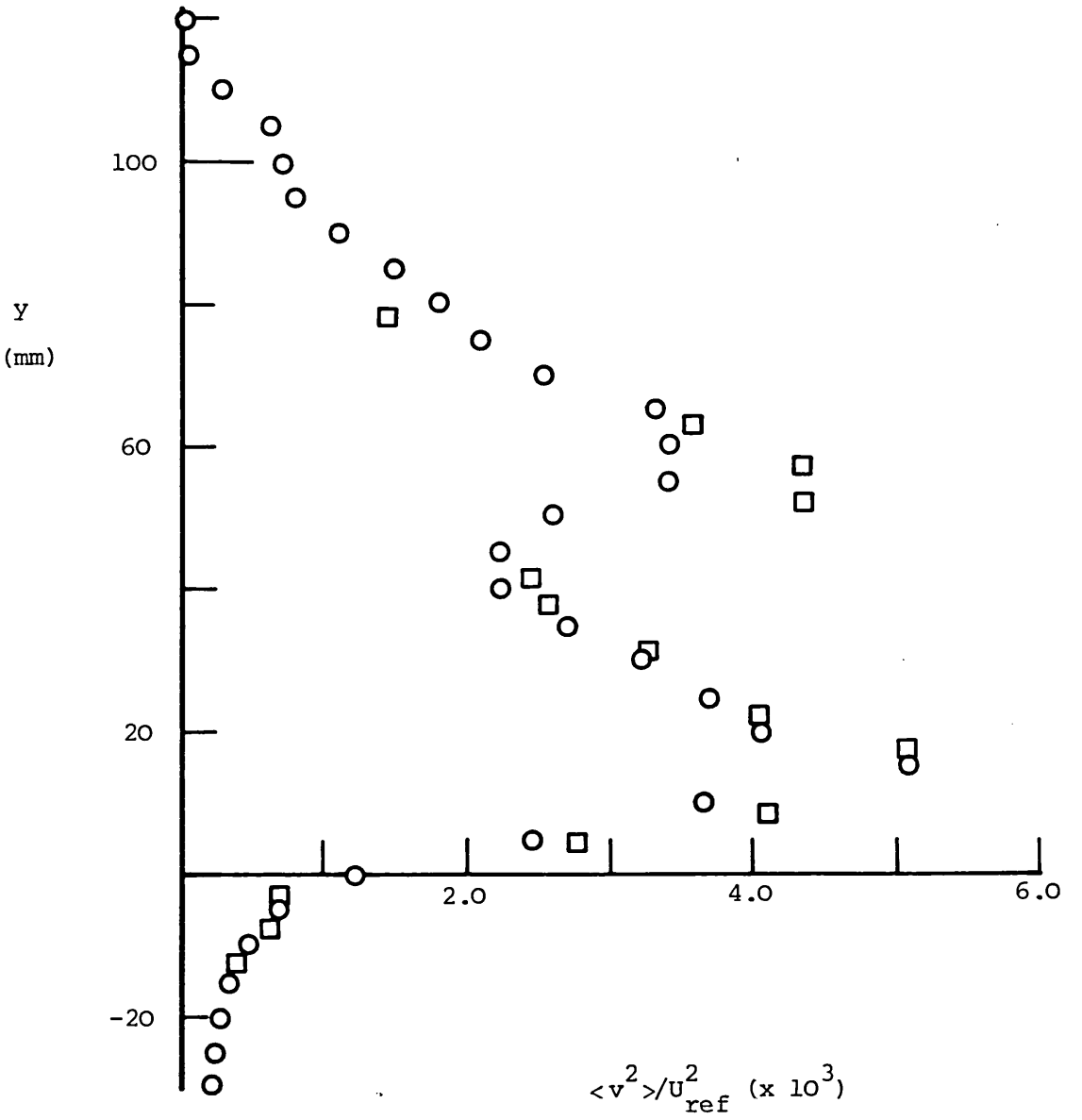


Fig. 2.11 (cont.) (c) Cross-stream normal stress.

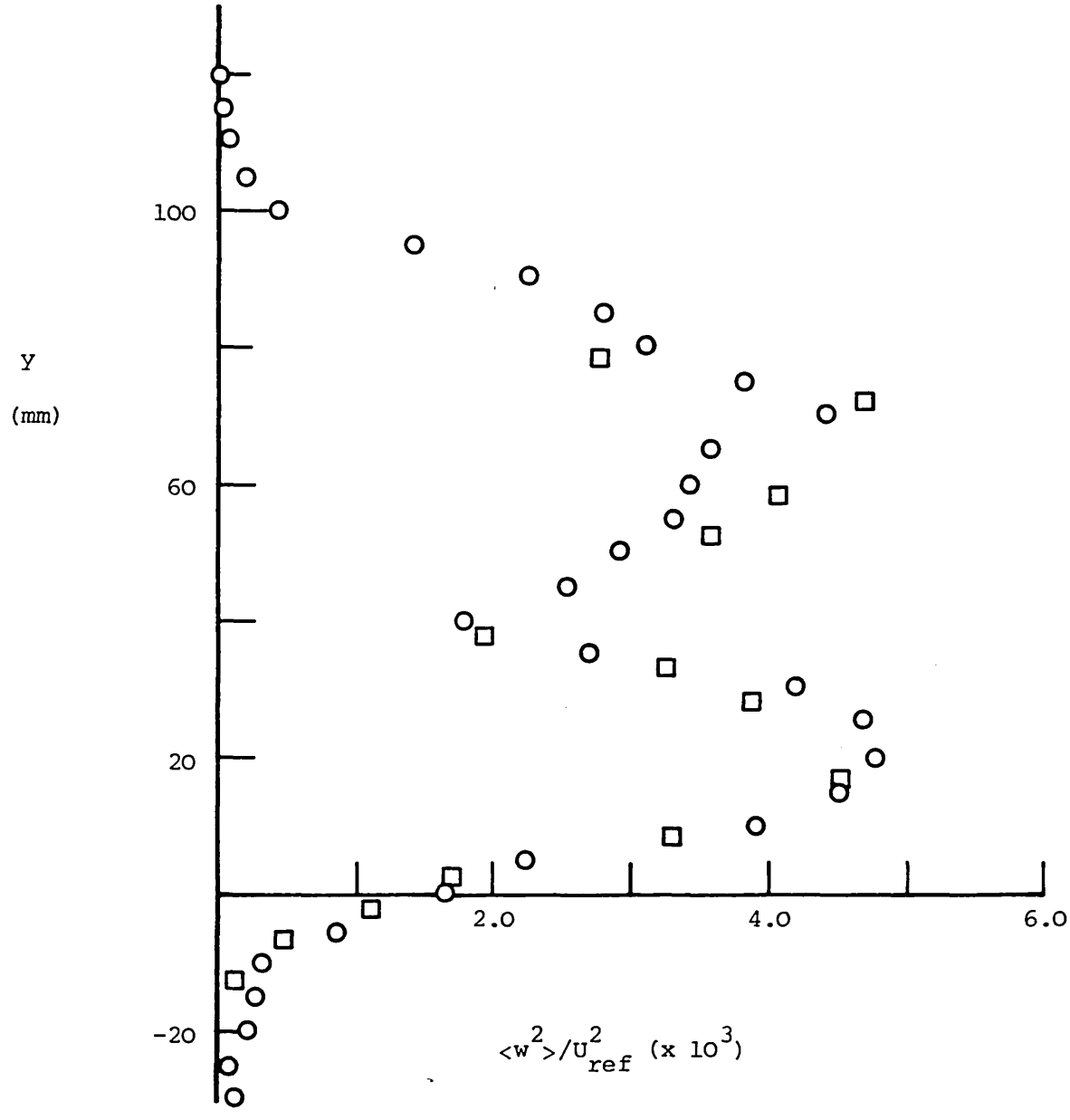


Fig. 2.11 (cont.) (d) Transverse normal stress.

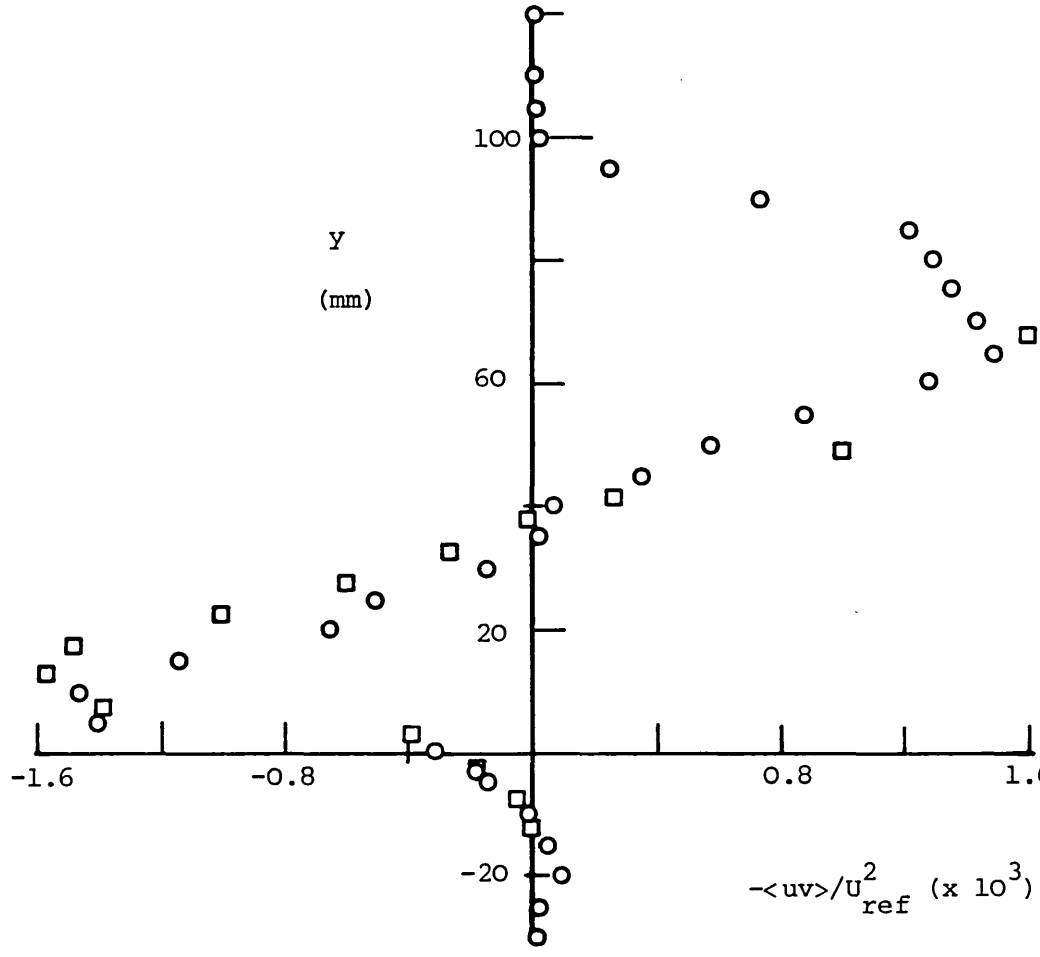


Fig. 2.11 (cont.) (e) Reynolds shear stress.

APPENDIX 2.A

TERMS IN THE HOT-WIRE RESPONSE EQUATION

The approximate equation 2.15 representing the hot-wire response to a cooling velocity results in the following expression for the instantaneous cooling velocity:-

$$
\begin{aligned}
U_{eff} = C_{G1} \langle Q \rangle \cos\phi \{ & a_0 + a_1 u_1 + a_2 u_2 + a_3 u_3 \\
& + a_4 u_1^2 + a_5 u_2^2 + a_6 u_3^2 + \\
& + a_7 u_1 u_2 + a_8 u_1 u_3 + a_9 u_2 u_3 \\
& + a_{10} u_1^3 + a_{11} u_1^2 u_2 + a_{12} u_1^2 u_3 \\
& + a_{13} u_2^3 + a_{14} u_1 u_2^2 + a_{15} u_2^2 u_3 \\
& + a_{16} u_3^3 + a_{17} u_1 u_3^2 + a_{18} u_2 u_3^2 \\
& + a_{19} u_1 u_2 u_3 \\
& + a_{20} u_1^4 + a_{21} u_1^3 u_2 + a_{22} u_1^3 u_3 \\
& + a_{23} u_1^2 u_2^2 + a_{24} u_1^2 u_3^2 + a_{25} u_1^2 u_2 u_3 \\
& + a_{26} u_2^4 + a_{27} u_1 u_2^3 + a_{28} u_2^3 u_3 \\
& + a_{29} u_2^2 u_3^2 + a_{30} u_1 u_2^2 u_3 \\
& + a_{31} u_3^4 + a_{32} u_1 u_3^3 + a_{33} u_2 u_3^3 \\
& + a_{34} u_1 u_2 u_3^2 \} \qquad (2.42)
\end{aligned}
$$

where $u_i = q_i/\langle Q \rangle$ and the coefficients, a_i, are given by:-

$$a_0 = 1 + C_0 g_0$$

$$a_1 = f_1 + C_0 g_1 + C_1 f_1 g_0$$

$$a_2 = f_2 + C_0 g_2 + C_1 f_2 g_0$$

$$a_3 = f_3 + C_0 g_3 + C_1 f_3 g_0$$

$$a_4 = C_0 g_4 + C_1 f_1 g_1 + C_2 f_1^2 g_0$$

$$a_5 = C_0 g_5 + C_1 f_2 g_2 + C_2 f_2^2 g_0$$

$$a_6 = C_0 g_6 + C_1 f_3 g_3 + C_2 f_3^2 g_0$$

$$a_7 = C_0 g_7 + C_1 (f_1 g_2 + f_2 g_1) + 2C_2 f_1 f_2 g_0$$

$$a_8 = C_0 g_8 + C_1 (f_1 g_3 + f_3 g_1) + 2C_2 f_1 f_3 g_0$$

$$a_9 = C_0 g_9 + C_1 (f_2 g_3 + f_3 g_2) + 2C_2 f_2 f_3 g_0$$

$$a_{10} = C_1 f_1 g_4 + C_2 f_1^2 g_1$$

$$a_{11} = C_1 (f_1 g_7 + f_2 g_4) + C_2 f_1 (2 f_2 g_1 + f_1 g_2)$$

$$a_{12} = C_1 (f_1 f_8 + f_3 g_4) + C_2 f_1 (2 f_3 g_1 + f_1 g_3)$$

$$a_{13} = C_1 f_2 g_5 + C_2 f_2^2 g_2$$

$$a_{14} = C_1 (f_1 g_5 + f_2 g_7) + C_2 f_2 (f_2 g_1 + 2 f_1 g_2)$$

$$a_{15} = C_1 (f_2 g_9 + f_3 g_5) + C_2 f_2 (f_2 g_3 + 2 f_3 g_2)$$

$$a_{16} = C_1 f_3 g_6 + C_2 f_3^2 g_3$$

$$a_{17} = C_1 (f_1 g_6 + f_3 g_8) + C_2 f_3 (f_3 g_1 + 2 f_1 g_3)$$

$$a_{18} = C_1 (f_2 g_6 + f_3 g_9) + C_2 f_3 (f_3 g_2 + 2 f_2 g_3)$$

$$a_{19} = C_1 (f_1 g_3 + f_2 g_8 + f_3 g_7) + 2C_2 (f_2 f_3 g_1 + f_1 f_3 g_2 + f_1 f_2 g_3)$$

$$a_{20} = C_2 f_1^2 g_4$$

$$a_{21} = C_2 f_1 (2 f_2 g_4 + f_1 g_7)$$

$$a_{22} = C_2 f_1 (2 f_3 g_4 + f_1 g_8)$$

$$a_{23} = C_2 (f_2^2 g_4 + f_1^2 g_5 + 2 f_1 f_2 g_7)$$

$$a_{24} = C_2 (f_3^2 g_4 + f_1^2 g_6 + 2 f_1 f_3 g_8)$$

$$a_{25} = C_2 (2 f_2 f_3 g_4 + 2 f_1 f_3 g_7 + 2 f_1 f_2 g_8 + f_1^2 g_9)$$

$$a_{26} = C_2 f_2^2 g_5$$

$$a_{27} = C_2 f_2 (2 f_1 g_5 + f_2 g_7)$$

$$a_{28} = C_2 f_2 (2 f_3 g_5 + f_2 g_9)$$

$$a_{29} = C_2 (f_3^2 g_5 + f_2^2 g_6 + 2 f_2 f_3 g_9)$$

$$a_{30} = C_2 (2 f_1 f_3 g_5 + 2 f_2 f_3 g_7 + f_2^2 g_8 + 2 f_1 f_2 g_9)$$

$$a_{31} = C_2 f_3^2 g_6$$

$$a_{32} = C_2 f_3 (2 f_1 g_6 + f_3 g_8)$$

$$a_{33} = C_2 f_3 (2 f_2 g_6 + f_3 g_9)$$

$$a_{34} = C_2 (2 f_1 f_2 g_6 + f_3^2 g_7 + 2 f_2 f_3 g_8 + 2 f_1 f_3 g_9)$$

The constants, C_0, C_1 and C_2, are given in equation 2.15. The expressions for the functions, f_i and g_i are given on table 2.4.

The general expression for second order moments is:-

$$\langle u_{eff}^2 \rangle = \langle U_{eff}^2 \rangle - \langle U_{eff} \rangle^2$$

$$= \langle Q \rangle^2 \cos^2\phi C_{G1}^2 \{b_0 + b_1 \langle u_1^2 \rangle + b_2 \langle u_2^2 \rangle + b_3 \langle u_3^2 \rangle + b_4 \langle u_1 u_2 \rangle + \langle P_* \rangle\}$$

where the coefficients, b_i, are given by:-

$$b_0 = a_0^2 - a_0^2 = 0$$

$$b_1 = a_1^2 + 2a_0a_4 - 2a_0a_4 = a_1^2$$

$$b_2 = a_2^2 + 2a_0a_5 - 2a_0a_5 = a_2^2$$

$$b_3 = a_3^2 + 2a_0a_6 - 2a_0a_6 = a_3^2$$

$$b_4 = 2a_0a_7 + 2a_1a_2 - 2a_0a_7 = 2a_1a_2$$

and the production term $\langle \dot{P}_* \rangle$ is given by:-

$$\begin{aligned}
\langle \dot{P}_* \rangle = {} & p_1\langle u_1^2\rangle\langle u_1^2\rangle + p_2\langle u_1^2\rangle\langle u_2^2\rangle + p_3\langle u_1^2\rangle\langle u_3^2\rangle + p_4\langle u_1^2\rangle\langle u_1u_2\rangle \\
& + p_5\langle u_2^2\rangle\langle u_2^2\rangle + p_6\langle u_2^2\rangle\langle u_3^2\rangle + p_7\langle u_2^2\rangle\langle u_1u_2\rangle \\
& + p_8\langle u_3^2\rangle\langle u_3^2\rangle + p_9\langle u_3^2\rangle\langle u_1u_2\rangle + p_{10}\langle u_1u_2\rangle\langle u_1u_2\rangle \\
& + p_{11}\langle u_1^2\rangle\langle u_1^2\rangle\langle u_1^2\rangle + p_{12}\langle u_1^2\rangle\langle u_1^2\rangle\langle u_2^2\rangle + p_{13}\langle u_1^2\rangle\langle u_1^2\rangle\langle u_3^2\rangle \\
& + p_{14}\langle u_1^2\rangle\langle u_1^2\rangle\langle u_1u_2\rangle + p_{15}\langle u_1^2\rangle\langle u_2^2\rangle\langle u_2^2\rangle + p_{16}\langle u_1^2\rangle\langle u_2^2\rangle\langle u_3^2\rangle \\
& + p_{17}\langle u_1^2\rangle\langle u_2^2\rangle\langle u_1u_2\rangle + p_{18}\langle u_1^2\rangle\langle u_3^2\rangle\langle u_3^2\rangle + p_{19}\langle u_1^2\rangle\langle u_3^2\rangle\langle u_1u_2\rangle \\
& + p_{20}\langle u_1^2\rangle\langle u_1u_2\rangle\langle u_1u_2\rangle + p_{21}\langle u_2^2\rangle\langle u_2^2\rangle\langle u_2^2\rangle + p_{22}\langle u_2^2\rangle\langle u_2^2\rangle\langle u_3^2\rangle \\
& + p_{23}\langle u_2^2\rangle\langle u_2^2\rangle\langle u_1u_2\rangle + p_{24}\langle u_2^2\rangle\langle u_3^2\rangle\langle u_3^2\rangle + p_{25}\langle u_2^2\rangle\langle u_3^2\rangle\langle u_1u_2\rangle \\
& + p_{26}\langle u_2^2\rangle\langle u_1u_2\rangle\langle u_1u_2\rangle + p_{27}\langle u_3^2\rangle\langle u_3^2\rangle\langle u_3^2\rangle + p_{28}\langle u_3^2\rangle\langle u_3^2\rangle\langle u_1u_2\rangle \\
& + p_{29}\langle u_3^2\rangle\langle u_1u_2\rangle\langle u_1u_2\rangle + p_{30}\langle u_1u_2\rangle\langle u_1u_2\rangle\langle u_1u_2\rangle \\
& + p_{31}\langle u_1^2\rangle\langle u_1^2\rangle\langle u_1^2\rangle\langle u_1^2\rangle + p_{32}\langle u_1^2\rangle\langle u_1^2\rangle\langle u_1^2\rangle\langle u_2^2\rangle + p_{33}\langle u_1^2\rangle\langle u_1^2\rangle\langle u_1^2\rangle\langle u_3^2\rangle \\
& + p_{34}\langle u_1^2\rangle\langle u_1^2\rangle\langle u_1^2\rangle\langle u_1u_2\rangle + p_{35}\langle u_1^2\rangle\langle u_1^2\rangle\langle u_2^2\rangle\langle u_2^2\rangle + p_{36}\langle u_1^2\rangle\langle u_1^2\rangle\langle u_2^2\rangle\langle u_3^2\rangle \\
& + p_{37}\langle u_1^2\rangle\langle u_1^2\rangle\langle u_2^2\rangle\langle u_1u_2\rangle + p_{38}\langle u_1^2\rangle\langle u_1^2\rangle\langle u_3^2\rangle\langle u_3^2\rangle + p_{39}\langle u_1^2\rangle\langle u_1^2\rangle\langle u_3^2\rangle\langle u_1u_2\rangle \\
& + p_{40}\langle u_1^2\rangle\langle u_1^2\rangle\langle u_1u_2\rangle\langle u_1u_2\rangle + p_{41}\langle u_1^2\rangle\langle u_2^2\rangle\langle u_2^2\rangle\langle u_2^2\rangle + p_{42}\langle u_1^2\rangle\langle u_2^2\rangle\langle u_2^2\rangle\langle u_3^2\rangle
\end{aligned}$$

$$+ p_{43}\langle u_1^2\rangle\langle u_2^2\rangle\langle u_2^2\rangle\langle u_1u_2\rangle + p_{44}\langle u_1^2\rangle\langle u_2^2\rangle\langle u_3^2\rangle\langle u_3^2\rangle + p_{45}\langle u_1^2\rangle\langle u_2^2\rangle\langle u_3^2\rangle\langle u_1u_1\rangle$$

$$+ p_{46}\langle u_1^2\rangle\langle u_2^2\rangle\langle u_1u_2\rangle\langle u_1u_2\rangle + p_{47}\langle u_1^2\rangle\langle u_3^2\rangle\langle u_3^2\rangle\langle u_3^2\rangle + p_{48}\langle u_1^2\rangle\langle u_3^2\rangle\langle u_3^2\rangle\langle u_1u_2\rangle$$

$$+ p_{49}\langle u_1^2\rangle\langle u_3^2\rangle\langle u_1u_2\rangle\langle u_1u_2\rangle + p_{50}\langle u_1^2\rangle\langle u_1u_2\rangle\langle u_1u_2\rangle\langle u_1u_2\rangle$$

$$+ p_{51}\langle u_2^2\rangle\langle u_2^2\rangle\langle u_2^2\rangle\langle u_2^2\rangle + p_{52}\langle u_2^2\rangle\langle u_2^2\rangle\langle u_2^2\rangle\langle u_3^2\rangle + p_{53}\langle u_2^2\rangle\langle u_2^2\rangle\langle u_2^2\rangle\langle u_1u_2\rangle$$

$$+ p_{54}\langle u_2^2\rangle\langle u_2^2\rangle\langle u_3^2\rangle\langle u_3^2\rangle + p_{55}\langle u_2^2\rangle\langle u_2^2\rangle\langle u_3^2\rangle\langle u_1u_2\rangle + p_{56}\langle u_2^2\rangle\langle u_2^2\rangle\langle u_1u_2\rangle\langle u_1u_2\rangle$$

$$+ p_{57}\langle u_2^2\rangle\langle u_3^2\rangle\langle u_3^2\rangle\langle u_3^2\rangle + p_{58}\langle u_2^2\rangle\langle u_3^2\rangle\langle u_3^2\rangle\langle u_1u_2\rangle + p_{59}\langle u_2^2\rangle\langle u_3^2\rangle\langle u_1u_2\rangle\langle u_1u_2\rangle$$

$$+ p_{60}\langle u_2^2\rangle\langle u_1u_2\rangle\langle u_1u_2\rangle\langle u_1u_2\rangle + p_{61}\langle u_3^2\rangle\langle u_3^2\rangle\langle u_3^2\rangle\langle u_3^2\rangle + p_{62}\langle u_3^2\rangle\langle u_3^2\rangle\langle u_3^2\rangle\langle u_1u_2\rangle$$

$$+ p_{63}\langle u_3^2\rangle\langle u_3^2\rangle\langle u_1u_2\rangle\langle u_1u_2\rangle + p_{64}\langle u_3^2\rangle\langle u_1u_2\rangle\langle u_1u_2\rangle\langle u_1u_2\rangle + p_{65}\langle u_1u_2\rangle\langle u_1u_2\rangle\langle u_1u_2\rangle$$

and the coefficients, p_i, are:-

$$p_1 = 2a_4^2 + 6a_1a_{10}$$

$$p_2 = a_7^2 + 2a_1a_{14} + 2a_2a_{11}$$

$$p_3 = a_8^2 + 2a_3a_{12} + 2a_1a_{17}$$

$$p_4 = 6a_1a_{11} + 6a_2a_{10} + 4a_4a_7$$

$$p_5 = 2a_5^2 + 6a_2a_{13}$$

$$p_6 = a_9^2 + 2a_2a_{18} + 2a_3a_{15}$$

$$p_7 = 6a_1a_{13} + 6a_2a_{14} + 4a_5a_7$$

$$p_8 = 2a_6^2 + 6a_3a_{16}$$

$$p_9 = 2(a_1a_{18} + a_2a_{17} + a_3a_{19} + a_8a_9)$$

$$p_{10} = a_7^2 + 4a_1a_{14} + 4a_2a_{11} + 4a_4a_5$$

$$p_{11} = 15a_{10}^2 + 24a_4a_{20}$$

$$p_{12} = 3a_{11}^2 + 6a_7a_{21} + 6a_{10}a_{14} + 4a_4a_{23}$$

$$p_{13} = 3a_{12}^2 + 6a_8a_{22} + 6a_{10}a_{17} + 4a_4a_{24}$$

$$p_{14} = 24a_4a_{21} + 24a_7a_{20} + 30a_{10}a_{11}$$

$$p_{15} = 3a_{14}^2 + 6a_7a_{27} + 4a_4a_{26} + 4_5a_{23} + 6a_{11}a_{13}$$

$$p_{16} = a_{19}^2 + 2a_{12}a_{15} + 2a_7a_{34} + 2a_8a_{30} + 2a_9a_{25} + 2a_{11}a_{18} + 2a_{14}a_{17}$$

$$p_{17} = 12a_4a_{27} + 16a_7a_{23} + 18a_{10}a_{13} + 18a_{11}a_{14} + 6a_5a_{21}$$

$$p_{18} = 3a_{17}^2 + 4a_6a_{24} + 6a_8a_{32} + 6a_{12}a_{16}$$

$$p_{19} = 4a_4a_{34} + 4a_7a_{24} + 6a_8a_{25} + 6a_9a_{22} + 6a_{10}a_{18} + 6a_{11}a_{17} + 6a_{12}a_{19}$$

$$p_{20} = 12a_{11}^2 + 12a_7a_{21} + 24a_{10}a_{14} + 20a_4a_{23} + 24a_5a_{20}$$

$$p_{21} = 15a_{13}^2 + 24a_5a_{26}$$

$$p_{22} = 3a_{15}^2 + 6a_9a_{28} + 4a_5a_{29} + 6a_{13}a_{18}$$

$$p_{23} = 24a_5a_{27} + 24a_7a_{26} + 30a_{13}a_{14}$$

$$p_{24} = 3a_{18}^2 + 4a_6a_{29} + 6a_{15}a_{16} + 6a_9a_{33}$$

$$p_{25} = 4a_5a_{34} + 4a_7a_{29} + 6a_8a_{28} + 6a_9a_{30} + 6a_{13}a_{17} + 6a_{14}a_{18} + 6a_{15}a_{19}$$

$$p_{26} = 12a_{14}^2 + 18a_7a_{27} + 24a_4a_{26} + 20a_5a_{23} + 24a_{11}a_{13}$$

$$p_{27} = 15a_{16}^2 + 24a_6a_{31}$$

$$p_{28} = 4a_6a_{34} + 6a_8a_{33} + 6a_9a_{32} + 6a_{16}a_{17} + 6a_{17}a_{18}$$

$$p_{29} = 2a_{19}^2 + 4a_4a_{29} + 4a_{12}a_{15} + 5a_5a_{24} + 2a_7a_{34} + 4a_8a_{30} + 4a_9a_{25} + 4a_{11}a_{18} + 4a_{14}a_{17}$$

$$p_{30} = 12a_4a_{27} + 8a_7a_{23} + 12a_{10}a_{13} + 12a_{11}a_{14} + 12a_5a_{21}$$

$$p_{31} = 94a_{20}^2$$

$$p_{32} = 15a_{21}^2 + 24a_{20}a_{23}$$

$$p_{33} = 15a_{22}^2 + 24a_{20}a_{24}$$

$$a_{34} = 192a_{20}a_{21}$$

$$p_{35} = 8a_{23}^2 + 18a_{21}a_{27}$$

$$p_{36} = 3a_{25}^2 + 6a_{21}a_{34} + 6a_{22}a_{30} + 4a_{23}a_{24}$$

$$p_{37} = 72a_{20}a_{27} + 84a_{21}a_{23}$$

$$p_{38} = 8a_{24}^2 + 18a_{22}a_{32}$$

$$p_{39} = 24a_{20}a_{34} + 24a_{21}a_{24} + 30a_{22}a_{25}$$

$$p_{40} = 81a_{21}^2 + 168a_{20}a_{23}$$

$$p_{41} = 15a_{27}^2 + 24a_{23}a_{26}$$

$$p_{42} = 3a_{30}^2 + 4a_{23}a_{29} + 6a_{25}a_{28} + 6a_{27}a_{34}$$

$$p_{43} = 72a_{21}a_{26} + 84a_{23}a_{27}$$

$$p_{44} = 3a_{34}^2 + 2a_{24}a_{29} + 6a_{25}a_{33} + 6a_{30}a_{32}$$

$$p_{45} = 12a_{21}a_{29} + 18a_{22}a_{28} + 16a_{23}a_{34} + 18a_{25}a_{30} + 12_{24}a_{27}$$

$$p_{46} = 68a_{23}^2 + 144a_{20}a_{26} + 126a_{21}a_{27}$$

$$p_{47} = 15a_{32}^2 + 24a_{24}a_{31}$$

$$p_{48} = 18a_{22}a_{33} + 16a_{24}a_{34} + 18a_{25}a_{32}$$

$$p_{49} = 12a_{25}^2 + 24a_{20}a_{29} + 18a_{21}a_{34} + 24a_{22}a_{30} + 20a_{23}a_{24}$$

$$p_{50} = 120a_{20}a_{27} + 108a_{21}a_{23}$$

$$p_{51} = 94a_{26}^2$$

$$p_{52} = 15a_{28}^2 + 24a_{26}a_{29}$$

$$p_{53} = 192a_{26}a_{27}$$

$$p_{54} = 8a_{29}^2 + 18a_{28}a_{33}$$

$$p_{55} = 24a_{26}a_{34} + 24a_{27}a_{29} + 30a_{28}a_{30}$$

$$p_{56} = 81a_{27}^2 + 168a_{23}a_{26}$$

$$p_{57} = 9a_{33}^2 + 12a_{29}a_{31}$$

$$p_{58} = 18a_{28}a_{32} + 16a_{29}a_{34} + 18a_{30}a_{33}$$

$$p_{59} = 12a_{30}^2 + 20a_{23}a_{29} + 24a_{24}a_{26} + 24a_{25}a_{28} + 18a_{27}a_{34}$$

$$p_{60} = 120a_{21}a_{26} + 108a_{23}a_{27}$$

$$p_{61} = 94a_{31}^2$$

$$p_{62} = 24a_{31}a_{34} + 30a_{32}a_{33}$$

$$p_{63} = 5a_{34}^2 + 12a_{24}a_{29} + 12a_{25}a_{33} + 12a_{30}a_{32}$$

$$p_{64} = 12a_{21}a_{29} + 12a_{22}a_{28} + 8a_{23}a_{34} + 12a_{24}a_{27} + 12a_{25}a_{30}$$

$$p_{65} = 20a_{23}^2 + 48a_{20}a_{31} + 48a_{22}a_{32}$$

The expression for the functions, a_i, are given above.

CHAPTER 3

EXPERIMENTAL INVESTIGATION

This chapter presents the measurements of pressure and velocity characteristics obtained in the vicinity of a trailing flap whose angle of incidence results in boundary layer separation, a large region of recirculating flow and a curved downstream wake. A combination of impact, hot-wire and flying-wire probes were used to quantify the flow which is shown to be two-dimensional, steady and incompressible. The flying-wire arrangement was used in the regions of separated and high turbulence-intensity flow.

The objectives of this chapter are to present the measurements and to describe the physical mechanisms of the phenomena associated with two-dimensional separation of the turbulent boundary layer over the surface configuration described in section 3.1. Measurements of the mean flow are presented in section 3.2 and include integral quantities and distributions of mean values of pressure and velocity. The velocity distributions in the near-wall region are examined to determine the extent to which logarithmic law-of-the wall assumptions are valid in and around the region of separated flow: it is important to the calculation method of chapter 4 which requires a knowledge of the near-wall flow to specify the correct boundary conditions. The turbulence is quantified in terms of the Reynolds stresses and the probability of downstream flow, and they are presented in section 3.3. Section 3.4 discusses the implications of the experimental results including the importance of pressure, convection, diffusion

and turbulence in the three main regions of the flow: the curved boundary layer approaching separation, the region of recirculation and the downstream wake.

3.1 Description of the Flow Configuration

The flow configuration is shown on figure 3.1 and comprises a 1035 mm flat plate with a trailing flap located in the working section of the low speed windtunnel described by Crabb et al (1981). The cross-section of the tunnel was 450 x 310 mm and significant regions of potential flow were found in the 250 mm above the trailing edge and in the 60 mm underneath. The flat plate was set at an angle of 1 degree and the flap at 17.5 degrees, both with respect to tunnel co-ordinates, after preliminary experiments to determine the angles which gave rise to the required region of separated flow on the flap.

The boundary layers on the tunnel walls and upper surface of the plate were tripped by 1.5 mm diameter wires located at the start of the flat plate which corresponds to the exit of the 8 to 1 contraction. The trailing flap was 249 mm long and was connected to the flat plate by a radius of 812.5 mm. This arrangement caused the upper-surface boundary layer to separate 187 mm from the trailing edge and gave rise to the characteristic boundaries indicated on figure 3.1. The tunnel exit was located 650 mm downstream of the trailing edge and here the regions of potential flow emanating from

above and below the trailing edge had cross-sections of 190 x 150 mm and 370 x 45 mm respectively.

The flow was investigated from the location of the boundary layer trip on the suction side to the tunnel exit, on the pressure side from 25 mm upstream of the trailing edge to the tunnel exit and in the boundary layers on the roof and floor of the tunnel. In the upstream region of the upper surface, for most of the lower surface and for much of the wake, the flow had a preferred direction and comparatively low turbulence intensities so that it was possible to measure mean values of pressure and velocity with the impact probes of section 2.2 and the velocity characteristics with stationary hot-wire anemometry as described in section 2.3. For the regions of potential flow and away from separation, a Pitot-static probe provided information of the mean velocity and static pressure. Close to separation and where the flow angle deviated from that near the surface of the flap, tunnel roof or floor, the five-tube probe was used to quantify the flow angle, velocity and static pressure as described in section 2.2. Close to the wall a flattened Pitot allowed measurements of mean velocity with reduced blockage and gradient effects. These velocity measurements were confirmed while obtaining turbulence quantities with stationary hot wires using the transform equations which depended on alignment of the probe with the mean velocity as described in section 2.3. The flying-wire arrangement of section 2.4 was selected to obtain the magnitude and direction of the mean flow and the corresponding Reynolds stresses in the region with flow reversals.

Two-dimensionality of the mean flow. The region over which the mean flow was two-dimenaional was established by flow visualization, wall-pressure and local velocity measurements. Passive flow control vanes were used to reduce the growth of secondary flows which occur in the corner of the boundary layer over the curved surface and flap, and can result in premature separation near the side wall. The arrangement is shown on figure 3.2 and was adjusted to maximize the extent over which the mean separation line was two-dimensional.

Measurements of total pressure and of velocity characteristics confirmed that regions of uniform pressure and velocity existed on the upper and lower side of the plate. Table 3.1 gives the mean and r.m.s. values of velocity above the trip and beneath the trailing edge. Figure 3.3 shows a cross-section of the potential flow region at the trailing edge where its width was a minimum.

Visualization of the surface flow was two-dimensional except within 30 mm of the side walls as shown in figure 3.4. This was confirmed by measurements of the near-wall flow with Preston and flattened Pitot tubes which showed variations of less than 1% over this 390 mm and by measurements of wall pressure, mean velocity and Reynolds stresses which were identical, within experimental error, over more than 90% of the tunnel width.

Figure 3.5 shows that the mean separation line was straight and normal to the flow over the central 160 mm of the flap. Hot-wire and flying-wire measurements confirmed that the two-dimensional region narrowed as separation was approached and showed that profiles of mean velocity agreed within 1% of the local values over the central 140 mm (31%) of the tunnel width at the location of mean streamline

detachment. The flying-wire was also used inside the recirculation region to obtain velocity profiles on the centreline and in the 70 mm to either side and mean velocity values agreed within 1.5%.

The momentum integral equation for two-dimensional subsonic flow with significant normal pressure gradient is given by:-

$$\frac{d\delta_2}{ds} + (H + 2)\frac{\delta_2}{\langle U_e\rangle}\frac{d\langle U_e\rangle}{ds} - \frac{1}{\rho\langle U_e\rangle^2}\frac{d}{ds}\left\{\int_0^{\delta}(\langle P\rangle - \langle P_e\rangle)dn\right\} = \frac{C_f}{2} \qquad (3.1)$$

where the subscript e refers to conditions at the edge of the boundary layer, i.e. at the location where the mean velocity reaches 99.5% of its free stream value; the displacement thickness is:-

$$\delta_1 = \int_0^{\delta}(1 - \frac{\langle U\rangle}{\langle U_e\rangle})dn \; ; \qquad (3.2)$$

the momentum thickness is:-

$$\delta_2 = \int_0^{\delta}\frac{\langle U\rangle}{\langle U_e\rangle}(1 - \frac{\langle U\rangle}{\langle U_e\rangle})dn \; ; \qquad (3.3)$$

the shape factor is:-

$$H = \delta_1/\delta_2 \; ; \qquad (3.4)$$

and turbulence quantities are ignored. Terms of this equation were evaluated using the velocity and pressure measurements shown in section 3.2 using second order accurate methods for the integrals and derivatives and using the logarithmic law-of-the-law for the skin friction and velocity variation near the wall. Equation 3.1 was balanced within 6% of the largest term in the regions of the upstream boundary layer approaching separation and the wake, including locations which were 50 mm away from the centreline. The largest

discrepancies occurred in the immediate vicinity of mean streamline detachment and just downstream of the trailing edge and may be attributed largely to variations in the static pressure caused by flow curvature effects associated with separation.

The emphasis of the above discussion has been on the two-dimensional nature of the mean velocity but two-dimensionality of mean turbulence quantities is equally important*. Cross-stream profiles of $\langle u^2 \rangle$, $\langle v^2 \rangle$ and $\langle uv \rangle$ obtained with stationary hot wire anemometry, agreed within experimental error over the central 85% of the tunnel width in the upstream boundary layer, over the central 165 mm above the location of mean streamline detachment, i.e. without flow reversals, and over the central 150 mm downstream of x/c of 0.2 in the wake. The values of Reynolds normal stress, $\langle u^2 \rangle$, obtained with the flying-wire in the recirculating flow agreed within 2% across the flow over the central 130 mm of the tunnel width.

Reference parameters. This subsection presents the parametric data for the present study.

Reference values of velocity, pressure, density and viscosity are shown on table 3.2 and were obtained at the reference location above the trip wire on the suction side and in the region of potential flow.

The reference length, hereafter known as the chord length, was 1.5183 m and represents the distance from the trip wire along the upper surface to the trailing edge. This definition was selected instead of the usual tip-to-root length used with aerofoils because of the shape of the present surface.

*Turbulence is a three-dimensional phenomena but averaged quantities, such as the Reynolds stresses, may vary in a two-dimensional manner.

Flow phenomena are expected to be independent of Reynolds number provided its value is sufficiently large. The present chord Reynolds number of 2.62×10^6 was expected to be large enough to invoke Reynolds number independence and measurements of the non-dimensional pressure distribution on the wall confirmed this over the Reynolds number range from $1.8 - 3.6 \times 10^6$.

3.2 Mean Flow Results

This section presents the mean flow results obtained on the centreline of the tunnel in the boundary layers over the upper surface, tunnel roof and floor and in the wake downstream of the trailing edge.

The skin friction coefficient, wall static pressure coefficient, and free stream values of pressure and velocity are shown on figure 3.6. The skin friction is zero at the location of mean streamline detachment, which can be deduced to have occurred at s/c of 0.879 where the boundary layer thickness was about 75 mm, although intermittent back flow was measured some 40 to 45 mm upstream of this location. The influence of the change in wall curvature at s/c of 0.68 can be seen to have affected the pressure and velocity fields some 5 per cent of chord further upstream. The static pressure coefficient varies between the wall and the free stream from just upstream of the curved section through to the trailing edge. The influence of separation can be seen where the suction-side wall-pressure distribution attains an almost constant value.

Pressure recovery begins near the most upstream location of intermittent backflow and the streamwise pressure gradient is very small from here downstream to the trailing edge.

The distributions of static pressure coefficient,

$$C_p = (\langle P \rangle - \langle P_{ref} \rangle)/(\tfrac{1}{2} \rho \langle U_{ref} \rangle^2) \quad , \tag{3.5}$$

are shown on figure 3.7 across the attached boundary layer and wake. The magnitude of the cross-stream pressure gradient increases as detachment is approached and at s/c of 0.826 achieves a value which is approximately 2.6 times that of the longitudinal pressure gradient. The implications of the pressure gradient are discussed further in section 3.4.

The boundary-layer development is also illustrated on figure 3.6 which shows the momentum thickness and shape factor obtained with equations 3.2-4. The boundary layer grows rapidly as separation is approached with δ_2 and H attaining values of approximately 8 mm and 2.7, respectively, at detachment. Values are presented in and around the separated region although their applicability is limited since terms in the cross-stream momentum equation are important from upstream of detachment through the separated flow.

The distribution of free stream velocity is shown on figure 3.6 in tunnel co-ordinates, x/c. It can be seen that the free stream velocity on the suction side is 1.43 times that on the pressure side. The consequences of this are that velocity gradients are smaller on the pressure-side downstream of the trailing edge and the flow recovers to a plane mixing layer.

The general organization of the mean velocities in the separated region is represented by the vector and streamline plates

of figures 3.8 and 3.9. The streamlines were determined by integrating the mean velocity profiles and show the negative velocity region close to the surface and throughout the length of the bubble. The cross-stream velocity in the separated region is larger than the corresponding streamwise velocity particularly in the regions of flow approaching attachment and after separation of the reverse flow boundary layer: they are small, however, compared with the free stream velocity. The negative flow region extends about 25 mm beyond the trailing edge after which the shear layers which circumvent the recirculation interact and develop into an asymmetric wake.

Profiles of mean velocity and flow angle are shown on figures 3.10 and 3.11 respectively for the region up to separation, in the separated region, and in the wake: it should be noted that the co-ordinate system has changed at the trailing edge to correspond to the tunnel rather than the body although the flow angle is measured relative to the tunnel throughout. The measurements for the attached boundary layer extend to s/c of 0.879 and measurements with a predominant direction in the wake begin at x/c of 0.016 although instantaneous flow reversals were still experienced. The intervening region features the recirculation bubble with its maximum 40 mm width and 210 mm length and negative mean velocities less than 11 per cent of the free stream value. The free shear layer which circumvents the upper boundary of the recirculation region appears to start forming at approximately 7% of chord upstream of the location where the mean streamlines detach from the surface. In the velocity profiles downstream of this and before detachment,

the mean velocity gradient across the flow, $\partial U/\partial n$, decreases and then increases at a distance less than 10 per cent of the boundary layer thickness away from the wall. The corresponding kink in the velocity distribution may occur because the mean flow near the wall is deflected outwards around the region of recirculation. The corresponding flow angles in this region indicate the tendency, towards separation with the rapid increase in flow angle spreading away from the surface as separation is approached. The velocity profiles in the separated region are characterised by the shear layer at the edge of the recirculation bubble which spreads as the strain rate increases with downstream distance and by the reverse flow boundary layer which begins around the trailing edge and continues towards the location of mean streamline detachment. The flow angle is consistent with the larger transverse velocity in the bubble which appear in the vicinity of the trailing edge and of the separation of the reversed-flow boundary layer.

The near-wall flow over the upper surface is depicted on figure 3.12 and confirms that the conventional law-of-the-wall adequately represents the mean velocity distribution in the region prior to separation. The maximum height of the logarithmic region decreases from Y^+ of about 700 on the upstream plate to Y^+ less than 30 at incipient detachment ($\gamma pu < 1.0$). The region of backflow is apparent and its cross-stream dimension increases from its inception at s/c of 0.878 until it extends over about 22 per cent of the boundary layer at the trailing edge. A log-linear velocity distribution also exists in the central backflow between Reynolds numbers, based on the perpendicular distance from the wall, of 600

to 9000. Near the trailing edge where the backflow boundary layer starts to form and in the immediate vicinity of detachment, the log-linear distribution has a different slope and its outer limit is reduced to a value of Reynolds number of 2000.

The standard law-of-the-wall with constants, κ and B of 0.41 and 5.0 respectively, is not appropriate downstream of the location of incipient detachment and in the backflow region. There does seem to be a log-linear variation in the mean-velocity distributions across the reversed boundary layer however the values of skin-friction coefficient based on the standard log-law are an order of magnitude smaller than those obtained by extrapolating the Reynolds shear stress to the wall. With the latter values of c_f, a logarithmic law-of-the-wall can represent the near-wall mean-velocity profiles in the separated region but different log-law constants are required: they change gradually in the vicinity of detachment, from the standard constants above to κ of 1.85 and B of 0.77 which fit the measured velocity distributions over most of the backflow downstream of x/c of 0.90. It should be noted that there is a relatively large uncertainty associated with the near-wall measurements of <uv> because of the small cross-stream dimensions of the log-law and constant Reynolds-stress regions compared to the flying cross-wire probe and because of large mean-velocity gradients close to the wall. This uncertainty, however, does not account for the discrepancy in skin-friction coefficient particularly over the central part of the backflow boundary layer where the values of c_f from extrapolation are about 10 times larger than those from the Clauser chart. Further, the logarithmic region

in the central portion of the backflow would extend over Y^+ of 10 to 172 using the wall shear stress obtained by extrapolating $\langle uv \rangle$ whereas it would be located unreasonably closer, between Y^+ of 3 and 54, if values of C_f from Clauser charts are used. Even with the larger values of C_f, the values of Y^+ are lower than those in the corresponding log-law region of a conventional boundary layer and indicates a decreases in the non-dimensional width of the buffer and viscous layer. The measurements of Simpson et al (1981) and Hastings and Moreton (1982) also show a log-linear region but, in a similar manner, these results do not fit the standard law-of-the-wall. It is also worth noting that the alternative proposal given by Simpson (1983) which gives the reversed mean-velocity profile as a function of the maximum negative velocity and its distance from the wall, did not describe mean-velocity distributions in the present flow.

The free shear layer which circumvents the upper boundary of the recirculation region appears to start forming at approximately 7 per cent of chord upstream of the location where the mean streamlines detach from the surface. In the velocity profiles downstream of this and upstream of detachment, the mean velocity gradient across the flow, $\frac{\partial \langle U \rangle}{\partial n}$, decreases close to the wall and then increases at a distance of about 10 per cent of the boundary layer thickness from the wall. The corresponding inflection point in the velocity profile occurs because the mean flow is deflected outwards around the region of recirculation. Associated with this is the appearance of a maximum in the turbulent shear stress profile and it is also the location where increased production of Reynolds normal stresses

becomes evident as will be discussed in section 3.3. As the location of detachment is approached this inflection point develops into the location of zero mean velocity in the shear layer above the region of backflow.

The wake can be divided into three regions: the very-near wake where negative velocities occur, the near wake where the shear layers from the suction and pressure sides interact and the far wake where recovery to a fully developed plane mixing layer occurs.

The very-near wake extends from the trailing edge to about x/c of 0.07 beyond which flow reversals are not found. Here,the region of reversed mean flow decreases in width until it is no longer evident downstream of x/c of 0.021 which includes about 12 per cent of the length of the recirculation bubble. Also the flow angle indicates that there is entrainment from the outer forward-flowing boundary layers on either side of the bubble as the rear stagnation point is approached. The mean velocity is also small inside this part of the bubble being less than 10 per cent of the free stream velocity on the suction side although the cross-stream component is larger here being as much as 1.5 times the maximum streamwise component. The attached pressure-side boundary layer enters from beneath the trailing edge and has a thickness of 4 mm and a logarithmic region with a skin friction coefficient of 0.00350. A second smaller region of recirculation rotating in the opposite direction to the main recirculation bubble, is apparent between the pressure and suction side shear layers about 18 mm downstream of the trailing edge and balances the vorticity transport equation in association with the beginning of the shear-layer interaction.

Downstream of the location where the two shear layers begin to interact, the shape factor asymtotically approaches 1.0, as was also found by Hah and Lakshminarayana (1982), and the displacement thickness increases with almost constant momentum thickness. Here, the mean flow is in the forward direction and the region with instantaneous flow reversals diminishes until it is no longer apparent downstream of x/c of 0.07. The static pressure variation also decreases with downstream distances and, beyond x/c of 0.66, the difference in static pressure between the suction and pressure side gradually reduces until they are equal at about 20 per cent of chord downstream of the trailing edge. Over this region the distribution of static pressure changes from the double-peaked profile apparent upstream of x/c of 0.15 to a single-peaked profile as a result of interaction of the upper and lower-side shear layers. The mean velocity also recovers here with its minimum value, increasing by about 2.8 times between x/c of .066 and .25 and the maximum gradient of mean velocity decreasing by about 33 per cent.

In the far wake, beyond x/c of 0.25, the mean velocity recovers to a plane mixing layer. The profiles of mean velocity no longer have a distinct minimum and the static pressure becomes constant across the flow in the region downstream of 40 per cent of chord from the trailing edge.

3.3 Turbulence Results

This section presents the Reynolds stresses obtained with hot-wire and flying-wire anemometry in the attached boundary layer, separated region and wake. Discussion of their implications for turbulence-modelling is presented in section 3.4.

Attached boundary layer approaching separation. Reynolds normal and shear stresses were measured in the boundary layer approaching separation and are shown on figure 3.13 normalised with the local wall potential-velocity given by:-

$$U_{pw} = \{2(P_T - P_w)/\rho\}^{1/2} \qquad (3.6)$$

where P_T refers to the total pressure in the free stream and P_W is the static pressure at the wall.

The profiles of Reynolds stresses agree well with those of Klebanoff (1954) in the region downstream of the trip wire and upstream of the location where curvature effects are noticeable, at s/c of 0.60.

Over the curved surface, the measured values of all Reynolds stresses decreased in the outer flow due to the effects of streamwise curvature. They vary in the range between those of Hoffman and Bradshaw (1978) and So and Mellor (1973) whose results were obtained in curved ducts with constant radii of curvature and are shown on figure 3.13 for comparison. Their curvature parameters, δ/R, were 0.01 and 0.18 respectively and bound the present value of 0.03*. The tunnel roof is not curved in the present configuration and results in variations in the flow direction and static pressure through the boundary layer which make exact comparison to curved duct flow impossible.

*Gillis and Johnston (1983) recently presented measurements in curved duct flow, which are in reasonable agreement with the present results, for values of δ/R of 0.05 and 0.10.

This accounts for slight differences in the distributions of Reynolds stresses due to the milder curvature in the outer part of the present boundary layer which has a smaller stabilizing effect than is experienced closer to the wall. As a consequence, the Reynolds stresses decrease more gradually in the outer flow and the turbulence intensities are higher than would be expected in curved duct flow. In contrast, curvature effects are comparable close to the wall and the present distributions of the Reynolds stresses are in reasonable agreement with those in curved ducts at least up to about 75 per cent of chord length where the influence of separation is apparent. Prior to this the turbulence intensities scales with the potential velocity on the wall and decrease in magnitude with downstream distance in the region from the wall outwards to about 65 per cent of the boundary layer thickness: $\langle v^2 \rangle^{1/2}$ is affected most and decreases by up to 50 per cent of its initial value. The azimuthal turbulence intensity, $\langle w^2 \rangle^{1/2}$, decreases almost uniformly with downstream direction at the rate of about 4 per cent per centimetre faster than the potential-velocity at the wall. The value of Reynolds shear stress, which is constant for values of n/δ less than 0.2, decreases in unison with the skin friction coefficient and varies linearly across the central part of the boundary layer until it becomes negligible at a distance of about 80 per cent of the boundary layer thickness from the wall.

The influence of separation is apparent downstream of s/c of 0.75 although mean streamline detachment does not occur until s/c of 0.879. In this region the turbulence intensities increase below n/δ of 0.5 as a result of extra production and decreased

effects of stabilizing curvature associated with the onset of separation and deflection of the mean streamlines outwards around the recirculation bubble. The largest effect is observed in $\langle v^2 \rangle^{1/2}$ again, whose maximum value moves away from the surface and increases by 25 per cent relative to the almost constant value of wall potential-velocity found here and throughout separation. The region of constant Reynolds shear stress which is evident close to the wall upstream of s/c of 0.777, is not apparent here and a maximum value of $\langle uv \rangle$ appears away from the wall and moves progressively outwards as separation is approached. This is an indication of development of the shear layer associated with the streamline that divides the forward and reversed flow. The values of $\langle uv \rangle$ decrease closer to the wall in agreement with the skin-friction coefficient however the maximum values of $\langle uv \rangle$ are larger than those measured in the constant shear stress layer farther upstream. This indicates that there is a decrease in shear stress production close to the wall, as would be expected with lower wall shear stress, although there is increased production, and possibly decreased dissipation, away from the wall in the region associated with deflection of the flow around the recirculation bubble and development of the shear layer in the vicinity of the dividing streamline. Schubauer and Klebanoff (1951) explain qualitatively the mechanism which causes this maximum away from the wall and its association with the prevention of separation in turbulent boundary layer. Above n/δ of 0.5, the effects of stabilizing curvature are similar to those further upstream and the normal stresses continue to decrease at approximately the same rate with downstream distances although they no longer correlate with the

near-wall flow. All of the Reynolds stresses are suppressed to their free stream value beyond about 75 per cent of the boundary layer thickness because of curvature effects which are still important in the outer part of the boundary layer.

Separated flow region. Figure 3.14 shows measured values of the Reynolds stresses in the vicinity of the region of recirculation which were obtained by flying-wire anemometry as described in section 2.4. Instantaneous flow reversals occur close to the wall downstream of s/c of 0.845 and gradually spread outward until s/c of 0.95 where they occur over the inner 55 mm (46%) of the boundary layer. In this region the local turbulence intensity, $\langle u^2 \rangle^{1/2}/\langle U \rangle$, exceeds 0.3 and the region of instantaneous backflow extends 2.1 times further from the wall than the outer extremity of reversed mean velocity.

Positive values of Reynolds shear stress are measured in the near-wall region downstream of s/c of 0.879 which corresponds to the location of mean streamline detachment and zero mean velocity close to the wall. A region of constant turbulent shear stress appears below 3 per cent of the boundary thickness downstream of s/c of 0.96, and was used when extrapolating to obtain the wall shear stress. Between the location of detachment and this point, a region of constant $\langle uv \rangle$ was not detected although it is likely to exist within 2 mm of the wall corresponding to the extent of the log-law region here. Measurements of $\langle uv \rangle$ could not be obtained because the dimensions of the cross-wire prohibit its use so close to the wall.

The distributions of Reynolds shear stress show linear increases from the positive near-wall value to a negative maximum located at about n/δ of 0.25. The positive and negative magnitudes

of <uv> increase gradually with distance along the surface over the inner part of the boundary layer and correspondingly the value at the negative maximum increases by about 4 times over the length of the backflow region to about -1.5 m^2/s^2. The locations of the zero value of <uv> in the inner region correspond to the minima in the mean velocity distributions and moves gradually away from the wall in the backflow region. In the outer part of the boundary layer the turbulent shear stress remains suppressed due to the effects of streamwise curvature and it is negligible outside of n/δ of 0.6.

The profiles of Reynolds normal stresses downstream of s/c of 0.86 show two maxima which correspond approximately with the locations of inflections in the mean velocity profiles: the inner maxima occurs at n/δ of 0.025 and the larger outer maxima appears at around 0.25 except in the region near detachment where it is slightly closer to the wall at s/c of 0.15. The distributions of $\langle u^2 \rangle$ and $\langle v^2 \rangle$ have similar shapes across the outer part of the boundary layer although the magnitude of $\langle v^2 \rangle$ is about 45 per cent of $\langle u^2 \rangle$. The magnutide of the outer maxima increases from 2.6 to 5.5 m^2/s^2 for $\langle u^2 \rangle$ and from 1.2 to 2.5 m^2/s^2 for $\langle v^2 \rangle$ over the backflow region and the location of these maxima corresponds to that of the negative maxima of turbulent shear stress associated with the dividing streamline around the recirculating region. In the near-wall region the values of $\langle v^2 \rangle$ are small as expected with a maximum value of 0.7 m^2/s^2 near detachment before decreasing to 0.23 m^2/s^2, which is less than 15 per cent of $\langle u^2 \rangle$ or $\langle w^2 \rangle$ within the reversed-flow boundary layer.

The distributions of $\langle u^2 \rangle$ and $\langle w^2 \rangle$ are almost identical across the outer 85 per cent of the boundary layer where $\langle u^2 \rangle$ and $\langle w^2 \rangle$ agree within 5 per cent of each other. Closer to the wall the distributions are different with $\langle u^2 \rangle$ generally larger although their values are almost equal at the inner maxima. The cross-stream variation of $\langle w^2 \rangle$ in the near-wall region is greater than that of $\langle u^2 \rangle$ and is similar to $\langle v^2 \rangle$ in that the inner peak is more pronounced. In the reversed boundary from s/c of 0.9 just downstream of detachment to the trailing edge, the profiles and levels of the turbulent normal stresses do not change and are approximately related by the ratios:

$$\langle u^2 \rangle^{1/2} = 2.40 \langle v^2 \rangle^{1/2}$$

$$\langle u^2 \rangle^{1/2} = 1.02 \langle w^2 \rangle^{1/2}$$

$$\langle v^2 \rangle^{1/2} = 0.43 \langle w^2 \rangle^{2}$$

with maximum values of 1.55, 0.27 and 1.48 m^2/s^2 for $\langle u^2 \rangle$, $\langle v^2 \rangle$ and $\langle w^2 \rangle$ respectively in the backflow boundary layer.

The suppression of turbulence fluctuations due to the curvature effects results in free-stream values of the normal stresses above n/δ of 0.6 except near the trailing edge where the flow begins to adjust for convergence and destabilizing curvature associated with the closing of the bubble in the wake.

Downstream wake. The distribution of Reynolds stresses in the wake are shown on figure 3.15 in tunnel co-ordinates. The turbulence structure of the wake is affected by flow curvature and the presence of recirculation and hence it is very complex.

For example, the largest values of Reynolds normal stress are found just downstream of the trailing edge where large increases in the Reynolds stresses on the suction side of the reversed mean flow are found. Over the remainder of the very-near wake the turbulence stresses decrease until instantaneous flow reversals are no longer found downstream of x/c of 0.08. Farther downstream, the shear layers from the suction and pressure sides interact. The Reynolds stresses on the suction side increase with downstream distance whereas they decrease on the pressure side. At the downstream end of this region, at s/c of 0.231, the largest values of Reynolds shear stress are found at the same position as a second set of peak values of the turbulent normal stresses which have values about 80% of the maxima near the trailing edge. This location marks the start of the far wake where the Reynolds stresses diminish and spread outwards with downstream distance although the rate of recovery is more than would be expected in a symmetric wake. The remainder of this section describes the behaviour of the Reynolds stresses in the regions of the very-near, near and far wake which were identified with reference to the mean flow in section 3.2 and with respect to turbulence quantities above.

The very-near wake is characterised by large values of the Reynolds stresses in the shear layers on either side of the region of reversed mean flow. Here, the profiles of Reynolds normal stresses across the wake have two maxima located approximately at the inflection points in the mean velocity distribution. The values of $\langle u^2 \rangle$, $\langle w^2 \rangle$ and particularly $\langle v^2 \rangle$ increase rapidly on the suction side from just upstream of the trailing edge and attain their largest

values in the flow being 7.3, 7.6 and 5.2 m^2/s^2, respectively at x/c of 0.012. These maxima are located in the central part of the upper shear layer and can be attributed to increased production and decreased dissipation associated with convergence and destabilizing curvature of the flow around the downstream end of the recirculating region. Turbulence diffusion is also important here and acts to make the normal stresses constant over about 20 per cent of the wake thickness in the vicinity of their maxima. The values of $\langle v^2 \rangle$ at its central minima increase with downstream distance over the very-near wake whereas the minima of $\langle u^2 \rangle$ and $\langle w^2 \rangle$ remain almost constant at 2.4 and 2.8 m^2/s^2.

The second maxima of the normal stresses occur in the pressure-side shear layer and are smaller than those on the suction side. The pressure-side maxima in $\langle v^2 \rangle$ and $\langle w^2 \rangle$ increase rapidly over the very-near wake changing from their boundary-layer values at the trailing edge to 2.9 m^2/s^2 in $\langle v^2 \rangle$ and to 6.7 m^2/s^2 in $\langle w^2 \rangle$ at x/c of 0.10 where they are almost equal to the maxima on the suction side. In contrast the $\langle u^2 \rangle$-maxima remains almost constant at 4.7 m^2/s^2 although it moves towards the centre of the wake in conjunction with the inflection point in the mean velocity profile. The values of $\langle w^2 \rangle$ change very rapidly at the end of the very-near wake and decrease by as much as 50% over the last 50 mm. Here also, the distributions of $\langle u^2 \rangle$ and $\langle v^2 \rangle$ remain relatively constant in the lower shear layer but their values reduce substantially near the suction-side maxima.

The Reynolds shear stress changes sign at the location of minimum mean velocity and is distributed differently along the

suction and pressure-side shear layers. On the suction side a local maximum value of <uv> of 3.1 m^2/s^2 is found just downstream of the trailing edge and decreases to its lowest value of 1.6 m^2/s^2 by the end of the very-near wake. Smaller values of <uv> are measured in the lower shear layer but, in contrast, they increase from their boundary-layer value at the trailing edge to a maximum of 2.1 m^2/s^2 at x/c of 0.10 which corresponds approximately to the location where the two shear layers collide.

Downstream of this location is the near wake. Here, the smaller maxima associated with the lower shear layer diminish with downstream distance and become indistinguishable beyond x/c of 0.26 in $\langle u^2 \rangle$, 0.20 in $\langle v^2 \rangle$ and 0.25 in $\langle w^2 \rangle$ although negative values of <uv> are found until x/c of 0.41 in the far wake. From the beginning of the near wake at x/c of about 0.10 to its end at x/c of 0.231, all three Reynolds normal stresses increase in the vicinity of the suction-side maxima. This is contrary to what might be expected here since convective and diffusive transport bring in lower levels of the Reynolds stresses than are found in the near wake and the rate of production of turbulence normal stresses is reduced because of decreasing gradients of streamwise and cross-stream mean velocity. In contrast, the rate of dissipation is significantly lowered because of destabilizing curvature and this acts to counterbalance the reducing effects mentioned above so that the turbulence intensities increase over the near wake. The production of Reynolds shear stress is large, however, due to the high Reynolds normal stresses, and <uv> increases by more than 5 fold over the near wake. Its largest value in the flow was measured to be -3.95 m^2/s^2 at the location

of maximum mean velocity gradient in the suction side wake at s/c of 0.231. Local maxima of $\langle u^2 \rangle$, $\langle v^2 \rangle$ and $\langle w^2 \rangle$ of 6.2, 4.9 and 4.6 m^2/s^2, respectively, are also associated with the downstream end of the near wake and represent increases of 49% in $\langle u^2 \rangle$, 61% in $\langle v^2 \rangle$ and 33% in $\langle w^2 \rangle$ above the lowest values of the maxima in their profiles found at the beginning of the near wake some 15 per cent of chord further upstream. These changes in turbulence structure occur before any significant change is apparent in the mean flow.

The effects of destablizing curvature are also important in the outer part of the near wake. The large values of Reynolds stresses associated with the shear layers, which were confined by stabilizing curvature effects upstream, are now able to diffuse toward the central minima and towards the outer extremities of the wake by turbulence diffusion.

In the far wake, downstream of 25 per cent of chord from the trailing edge, the turbulence decays as the flow recovers to a plane mixing layer. A single maximum is observed in the profiles of all four Reynolds stresses. The relative magnitude of the Reynolds normal stresses were found to be:-

$$\langle u^2 \rangle > \langle v^2 \rangle > \langle w^2 \rangle$$

which was also observed by Hah and Lakshminarayama (1982) in the asymetric wake of an aerofoil with attached turbulent boundary layers leaving the trailing edge. Further measurements are required at distances from 45 per cent to at least one chord length downstream of the trailing edge to determine the detailed development of the far wake in the present flow.

3.4 Discussion

This section discusses the physical phenomena implied by the above measurements and their relationship to calculation methods for recirculating flows.

The most important feature of this turbulent separating boundary layer is the free shear layer associated with the dividing streamline. Its development dominates the overall characteristics of the flow in the separated region. Its accurate representation is essential to the successful prediction of recirculation. The largest curvature of the flow around separation is found in the vicinity of this shear layer and the local gradients of cross-stream pressure are correspondingly large. This is especially noticeable near detachment as the mean velocity turns outwards around separation and near the downstream end of the recirculation bubble where it converges towards the centreline. Intense production of turbulence also occurs in this shear layer primarily due to large mean shear although up to 40 per cent of the generation of $\langle u^2 \rangle$ may come from normal stress production (i.e. $(\langle u^2 \rangle - \langle v^2 \rangle)\partial \langle U \rangle / \partial s$). The turbulence is anisotropic in and around recirculation, mainly because of differences in the production rates of Reynolds stresses, and this suggests that turbulence models based on an effective viscosity assumption may be of limited use. This is particularly pertinent on the backflow side of the dividing streamline where the turbulence production due to normal-stress: normal-strain interaction has its largest cross-stream value although the levels of Reynolds stresses here are determined generally by turbulence diffusion from the shear layer above the backflow.

The presence of the separation bubble results in a strong interaction between the potential flow and the boundary layer. The rapid growth of the boundary layer near the onset of separation acts to deflect the flow outwards. The local curvature of the potential flow is reduced and, thus locally, the adverse pressure gradient is relaxed although at different rate than is experienced closer to the wall. The measurements indicate that there is a pressure gradient across the shear layer associated with the dividing streamline since the backflow velocities are small close to the wall inside recirculation and the pressure distributions along the surface and in the potential flow are different. It is necessary, therefore, to solve the cross-stream momentum equation when calculating the recirculation bubble. It also appears likely that a simple interaction method employing the displacement thickness, or an equivalent transpiration velocity, will be inadequate in accounting for the presence of separation. Besides pressure gradient effects described above, the rate of change of displacement thickness near detachment is large so that the local stream function and velocity-potential lines are highly curved and the boundary condition for the solution of the potential-flow equations requires consideration of entrainment into the boundary layer as discussed in section 4.3.

Turbulence diffusion is responsible for transport of energy away from the shear layer and towards the wall which helps to delay the onset of mean streamline detachment. This process can be understood by considering the location of maximum shear stress which develops near the surface and moves progressively away from the wall with downstream distance. The region between the surface and the maximum of $\langle uv \rangle$ receives energy via turbulence

diffusion from the flow beyond the maxima so that the fluid in the near-wall region, although it has insufficient energy of its own, continues to move along the surface towards the region of higher pressure (Schubauer and Klebanoff, 1951). The wall continues to act as a momentum sink for the near-wall flow so that detachment eventually occurs where sufficient energy cannot be received from the outer flow: the instantaneous flow in the forward direction is in balance with that in the reverse direction. In addition to determining the location of detachment, the nature of the free shear layer strongly affects the interaction between the suction-side and pressure-side wakes and, thus, determines the flow pattern at the downstream end of the recirculating region. This is discussed further below.

The reversed-flow boundary layer is significant as a wall boundary condition for calculations although it has less of an effect on the nature of the separation bubble than does the shear layer above it. The fluid in the backflow boundary layer does not always convect from the trailing edge, as there is no location where there was backflow all of the time ($\gamma_{pu} \neq 0.0$), and its flow sometimes originates locally most likely from within the large eddy structures convecting with the outer flow. Velocities in the reversed boundary layer are small and exist primarily because of the streamwise pressure gradient but they cannot sustain a large cross-stream pressure gradient. Turbulence production is apparent in the backflow boundary layer but does not have a predominant effect on the turbulence levels across the centre of the recirculation region. They are determined primarily by turbulence diffusion from the shear layer above since the centre of the bubble

has small velocity gradients, almost as if they exist only to satisfy continuity, and hence local production of turbulence is almost negligible. The effects of the wall are also transmitted by pressure fluctuations rather than by eddy migration alone, and there is confinement of the large eddies by the surface, including in the region downstream of detachment. Viscous effects become smaller near separation, which at least partially accounts for the small height of the viscous sublayer inside the recirculation region, and fluctuations dominate the flow losses. It should be noted that the free-stream flow was steady and the near-wall fluctuations are due to turbulence within the separated boundary layer.

The backflow boundary layer starts to develop near the trailing edge where cross-stream components of mean and fluctuating velocities are significant. The flow pattern and pressure distribution downstream of the trailing edge are important to its initial development and affect the region near detachment via the backflow. The instantaneous flow field divides in this region of rapid distortion downstream of the trailing edge and, accordingly, some of the fluid is pulled forward into the backflow while the remainder convects downstream. The mechanism of this division is likely to be different than that found in the reattaching shear layer of Etheridge and Kemp (1978) and is probably dependent on the turbulence structures in the colliding pressure-side and suction-side wakes. It is worth noting that there was no evidence of low frequency buffeting or characteristic frequencies in the wake, or above the separation bubble, as confirmed by frequency analysis of the linearized signal from a stationary hot-wire aligned normal to the mean flow.

The very-near wake is a critical part of the separation process with the strong interaction between the upper and lower shear layers controlling the downstream extent of the recirculation bubble and the location where the pressure becomes uniform. Closing of the bubble is largely determined by turbulence diffusion of momentum towards the centre of the very-near wake although pressure gradient effects are also important. Cross-stream velocity gradients are decreasing on the suction side but streamwise gradients have their largest values here. Accordingly, the generation rate of turbulence decreases gradually but has a significant contribution from normal-stress: normal-strain production which is dominant in the vicinity of the mean-velocity minimum. Turbulence levels are also reducing as it seems that the dissipation rate is not yet affected by destabilizing curvature so, in the balance, it appears to remain large. Turbulence levels in the pressure-side wake are strongly linked to the mean flow field via turbulence production. The mean-velocity gradients increase with downstream distance and, correspondingly, so do the turbulence intensities.

Gradients of mean velocity decrease with distance farther downstream over the designated near-wake region, however, the turbulence field behaves in a peculiar manner. The turbulence intensities on the pressure side decrease as the strain rate of the mean flow relaxes, as expected, but the turbulence levels on the suction side increase despite locally decreasing gradients of mean velocity. This phenomena is attributable to the destabilizing curvature of the local flow which decreases the rate of dissipation of turbulence. The overall effect of positive values of $\partial V/\partial x$ on a turbulent shear layer with positive $\partial U/\partial x$ is to increase the turbulence intensity by the effects

of destabilizing curvature (Bradshaw, 1973). This is the case here although there is a somewhat greater influence on the turbulence than was measured in the mildly curved mixing layer of Gibson and Younis (1983). This phenomena is similar to that experienced in the flow over a backward facing step measured by Chandrsuda and Bradshaw (1981) where the maximum values of the Reynolds stresses appear in the middle of the shear layer above the location of reattachment. Although the effect of destabilizing curvature seems to be majorly responsible, it appears that there is an additional effect due to the interaction with the pressure-side wake in the present flow.

The influence of pressure gradient is significant in the vicinity of separation. Clearly the pressure balances with turbulence stresses at the location of mean streamline detachment and fixes the position of separation as described by Schubauer and Klebanoff (1951). Comparisons with the experiments of Simpson et al (1981), Coles and Wadcock (1979) and Nakayama (1983) demonstrate how differences in the pressure gradient, and also the curvature of the flow, can affect the mean and fluctuating flow fields. The distributions of Reynolds stresses measured in these experiments are similar to those in the present flow however their magnitudes are different. The Reynolds stresses in the boundary layer immediately upstream of separation are lower with the present configuration because of the larger stabilizing effects of wall curvature. Table 3.3 shows the maximum values of the Reynolds stresses obtained in the boundary layer immediately upstream of separation, in the vicinity of separation and in the wake. The relative increases in the normal stresses as a

result of separation are approximately equal in all of the flows and represent increases of 4, 5 and 6 times the upstream values of $\langle u^2 \rangle$, $\langle v^2 \rangle$ and $\langle w^2 \rangle$, respectively. The turbulence stresses therefore remain lower throughout the separated region of the present flow and is at least partly due to the lower turbulence levels in the upstream boundary layer caused by stabilising curvature. Examination of the Reynolds stress transport equations also shows that the production of turbulence will be lower in the present flow than in those of Coles and Wadcock (1979) and Nakayama (1983). There are two contributory factors: first, the free-stream velocity on the pressure side is less than that on the suction side which means that the cross-stream velocity gradients are smaller in the pressure-side mixing layer. Secondly, the turbulence intensities are lower in the upstream boundary layer as discussed above.

Although the values of the Reynolds stresses are different, the measurements obtained in the present flow are in sensible agreement with the distributions and features measured by Simpson et al (1981) and Wadcock (1980). The distribution of normal stresses are in agreement: there are prominent double peaks in $\langle u^2 \rangle$, $\langle v^2 \rangle$ and $\langle w^2 \rangle$ although $\langle v^2 \rangle$ is smaller here because of curvature. Turbulence length scales are not the same, however, and the processes associated with development of the backflow region are different.

Differences between mechanisms which determine the origin of the backflow may be represented by the ratio of the length of recirculation to the length scale of large-scale turbulence in the boundary layer as is indicated by the ratio, L_N/δ, which relates the length of the negative mean-velocity region to the boundary layer. If this ratio is small, say of order 1, the region of interaction

between the backflow and the outer flow is short and large scale eddies do not necessarily interact strongly with the surface flow; so the streamwise pressure gradient is dominant in the momentum balance close to the wall and the primary source of near-wall flow is convection along the surface from the trailing edge. This is the case in the present flow and in those of Coles and Wadcock (1979) and Nakayama (1983) where L_N/δ is 3.0, 2.9 and 1.2, respectively, and growth of a reversed-flow boundary layer is evident inside the separated region. Flow visualization in the present case also suggests that the backflow comes from downstream of the trailing edge most of the time although it is influenced by local turbulence levels as it moves upstream. In contrast to these flows, the ratio, L_N/δ, in the separating boundary of Simpson et al (1981) is greater than 10* and the backflow would have to travel over 1 m upstream to the point of detachment if it originated at the downstream end of recirculation. This seems unlikely considering the small pressure gradient in the near-wall flow and, for this case, it may be that the backflow is supplied locally as suggested by Simpson et al (1981). Further, the interaction between the backflow and the outer flow occurs over a long distance, relative to the turbulence length scale, so that turbulence diffusion is likely to be more important than pressure in the backflow region. Flow processes near the downstream end of the bubble are also important to the development of the backflow. There may be reattachment in the experiment of Simpson et al (1981) but in the other flows mentioned the rear stagnation point is freely

*This is an approximate value since the downstream end of recirculation is not reported.

located in the wake. This may be a reason for developing a more prominent boundary layer in the reversed flow of the trailing-edge experiments. In summary, the ratios of the recirculation length to the length scale of large-scale turbulence are smaller in the trailing-edge flows mentioned and this indicates that the mechanisms which influence the development of the backflow are dependent more on pressure effects than turbulence diffusion and differ from the processes which determine the backflow in the separating boundary layer of Simpson et al (1981).

The distribution of velocity characteristics in the wake of the present configuration are also in good qualitative agreement with those of Nakayama (1983) although turbulence levels are smaller on the pressure side because of reduced velocity gradients. The initial part of both wakes is dominated by the mixing of the almost stagnant recirculating flow and the high velocity pressure-side flow. The influence of the pressure side boundary is almost negligible. In both flows, the recirculation region extends to about the same non-dimensional distance into the wake, to x/c of 0.07, and the distributions of Reynolds stresses show two peaks: a sharp peak in the pressure-side mixing layer and a broader peak in the upper shear layer. In contrast, the size of the recirculation region over the surface is about 70 per cent larger in the present flow and, accordingly, the viscous-inviscid interaction is greater in the vicinity of separation.

The measurements indicate that the present flow domain can be divided into three regions where simplified versions of the transport equations for mass, momentum and turbulence quantities

can be used to represent the observed flow phenomena. Potential-flow equations can satisfactorily describe a large portion of the flow away from the walls provided appropriate boundary conditions are used to represent the influence of the viscous flow which is particularly near separation. The boundary-layer form of transport equations is adequate in the viscous flow region up to about 7 per cent of chord before detachment where the shear layer associated with the dividing streamline starts to form, although it does seem that the effects of streamwise curvature on the turbulence need to be modelled. Boundary-layer equations are also appropriate in the far wake well downstream of flow reversals. The flow in and around the separated region must be calculated with an elliptic form of the transport equations because the influence of downstream events can propagate upstream via the backflow and the local pressure. There is a distribution of pressure around the streamline dividing forward and reversed flow, and the local values of cross-stream velocity indicate it is necessary to account for pressure, convective and turbulence processes by using the cross-stream momentum equation here.

Turbulence modelling has direct consequences in the calculated results for the viscous flow region and it influences the potential flow through the viscous-inviscid interaction. It is important in determining the magnitude of diffusion terms which make a large contribution to transport in the vicinity of the dividing streamline and have a strong influence on the nature of the separated flow and development of the wake. Streamline curvature acts to change the structure of turbulence, having a stabilizing effect in the upstream boundary layer and a destabilizing effect

in the wake, and its effects on the rate of dissipation of turbulence must be appropriately modelled in order to predict the correct levels of turbulence diffusion. Turbulence transport is not well modelled with an effective viscosity hypothesis if the flow is complex and far from equilibrium. Thus, difficulties may be anticipated in the vicinity of separation since the turbulence is highly anisotropic and there are regions where the dominant production of turbulence kinetic energy occurs via normal-stress: normal-strain interaction. Wadcock (1980) and Simpson et al (1981) show, and it is confirmed in the present flow, that simpler models based on constant eddy-viscosity or mixing-length concepts are inappropriate for separated flows of this type. These authors, Viswanath and Brown (1983) and Delery (1981) emphasize the importance of turbulence normal stresses which are also shown to be important in the present flow. The importance of these effects on the calculated mean values of pressure and velocity is not known and is investigated presently with the calculation methods of chapter 4. The large increases in Reynolds stresses associated with separation in the present flow represents a challenge for turbulence models and calculation methods which are comparable to the difficulties found in the separated flows mentioned above, although it is likely that the effects on the mean flow are somewhat reduced here.

3.5 Concluding Remarks

Measurements of mean values of pressure and velocity have been presented in the two-dimensional regions of boundary-layer, separated and wake flow around the flow configuration shown on figure 3.1. The results depict the rapid growth of the boundary-layer approaching separation and indicate that there is significant cross-stream pressure gradient in the vicinity of the shear layer associated with the dividing streamline. Mean velocity profiles in the near-wall region are found to agree with the logarithmic law-of-the-wall in the region approaching separation. There is a log-linear region in the backflow boundary layer but the standard log-law constants do not apply: there is a variation from the upstream values of κ and B of 0.41 and 5.0 to about 1.85 and 0.77 in the backflow.

The four non-zero Reynolds stresses of two-dimensional flow were measured which required the use of the flying-hot-wire anemometer of section 2.4 in the region with instantaneous backflow. The distributions of Reynolds stresses are complex but are primarily affected by two phenomena: first, streamwise curvature which is stabilizing in the curved boundary layer and destabilizing in the wake and, second, the shear layer around the recirculating flow where there is intense production of turbulence by cross-stream shear augmented by normal-stress: normal-strain interaction. There is an abnormal region in the wake where the Reynolds stresses increase despite decreasing mean-flow gradients and recovery to a plane mixing layer. This phenomena appears to be associated with changes in the rate of turbulence dissipation associated with destabilizing curvature.

Measurements in the present flow are in reasonable agreement with those reported by Nakayama (1983), Viswanath and Brown (1983), Simpson et al (1981) and Coles and Wadcock (1979) in separating turbulent boundary layers. The interaction between the separated viscous and inviscid regions of the present flow is similar in magnitude to that found in Coles and Wadcock (1979) which is larger than in Nakayama (1983) or Viswanath and Brown (1983) and smaller than in Simpson et al (1981). The magnitudes of pressure gradients and turbulence scales are different, as are those representing turbulence production, diffusion and its dissipation rate, although their distributions are similar in these flows. This flow configuration presents comparable difficulties for calculation procedures and turbulence modelling, and represents a further problem with which to verify predicted results.

TABLE 3.1

MEAN AND VARIANCE OF THE FREE-STREAM VELOCITY

	$\langle U \rangle$ (m/s)	$\langle u'^2 \rangle^{1/2}$ (m/s)	$\langle P \rangle^*$ (N/m^2)
Suction side above the trip wire	26.29	0.242	-207.45
Suction side at the trailing edge	20.40	0.244	-42.86
Pressure-side at the trailing edge	14.02	0.151	-42.54

*Static pressure relative to atmosphere

TABLE 3.2

REFERENCE PARAMETERS

Parameter	Symbol	Value
Velocity	U_{ref}	26.29 m/s
Static pressure	P_{ref}	$-207.35\ N/m^2$
Viscosity (kinematic)	μ	18.22×10^{-6} kg/m.s
(dynamic)	ν	$15.221 \times 10^{-6}\ m^2/s$
Density	ρ	$1.197\ kg/m^3$
Temperature	T	20 degrees Celcius
Chord length	C	1.5183 m
Reynolds number	$Re \equiv \frac{U_{ref}C}{\nu}$	2.62×10^6

TABLE 3.3

MAXIMUM VALUES OF REYNOLDS STRESSES AND COMPARISON WITH OTHER EXPERIMENTS

	Maximum values of the Reynolds stresses			
	$\frac{\langle u^2 \rangle}{\langle U_{ref} \rangle^2}$	$\frac{\langle v^2 \rangle}{\langle U_{ref} \rangle^2}$	$\frac{\langle w^2 \rangle}{\langle U_{ref} \rangle^2}$	$\frac{\langle uv \rangle}{\langle U_{ref} \rangle^2}$
Attached boundary layer just upstream of separation	($\times 10^3$)	($\times 10^3$)	($\times 10^3$)	($\times 10^3$)
Simpson et al (1981)	9.5	3.0	3.5	-1.8
Coles and Wadcock (1979)	20	10	-	-7.5
Present	3.7	1.6	1.9	-0.35
Separated Region				
Simpson et al (1981)	40	20	23	-6.0
Coles and Wadcock (1979)	85	55	-	-17.5
Present	10.2	6.3	10.0	-5.2
Wake Region				
Coles and Wadcock (1981)	30	30	-	-7.5
Nakayama (1983)	30	13	-	-10.0
Present	9.0	5.0	5.0	-1.6

TABLE 3.4

PARAMETERS OF THE MEAN FLOW DEVELOPMENT

SUCTION-SIDE SURFACE

$\frac{s}{c}$	U_e (m/s)	$\delta_{.995}$ (mm)	δ_1 (mm)	δ_2 (mm)	H	C_f^* ($\times 10^3$) (Clauser)	C_f^{**} ($\times 10^3$) (<uv>)	$C_{p_{wall}}$	U_{pw} (m/s)
0.372	25.44	19.5	2.64	1.99	1.325	3.30	3.18	0.0078	25.24
0.504	25.24	21.2	3.40	2.56	1.330	2.93	2.86	0.0965	24.98
0.608	25.12	24.2	3.74	2.79	1.340	2.92	2.84	-	-
0.635	25.08	28.3	3.71	2.74	1.354	2.90	2.88	0.0906	25.07
0.649	25.06	31.2	3.72	2.78	1.338	2.94	3.01	0.0892	25.09
0.668	24.98	37.1	3.50	2.65	1.320	3.07	3.08	0.0639	25.43
0.688	24.89	39.2	3.12	2.41	1.296	3.21	3.17	0.0247	25.96
0.695	24.86	43.7	2.97	2.30	1.290	3.30	3.28	0.0130	26.11
0.718	24.79	43.9	3.08	2.35	1.311	3.38	3.43	0.0137	26.10
0.729	24.69	44.8	3.34	2.51	1.330	3.08	2.97	0.0302	25.89
0.743	24.49	45.1	3.54	2.65	1.335	2.87	2.84	0.0452	25.68
0.757	24.29	46.9	3.73	2.78	1.341	2.76	2.79	0.0698	25.35
0.777	23.96	48.1	4.51	3.20	1.410	2.50	2.51	0.1020	24.91
0.784	23.81	51.2	5.64	3.81	1.480	2.14	2.20	0.1350	24.45
0.798	23.51	53.5	6.41	4.16	1.54	1.86	1.89	0.1741	23.89
0.818	23.21	57.6	8.61	4.95	1.74	1.16	1.24	0.2463	22.82
0.826	23.16	59.4	9.26	5.06	1.83	0.57	0.70	0.2650	22.53
0.852	22.49	68.9	15.91	7.21	2.21	0.15	0.44	0.3364	21.41
0.874	22.00	86.2	36.88	11.2	3.29	0.07	0.14	0.3642	20.96
0.885	21.07	111.2	41.95	12.04	3.485	-.0018	-.02	0.3741	20.79
0.905	20.68	137.2	52.35	13.0	3.767	-.028	-.42	0.3826	20.65
0.931	20.66	142.3	65.36	9.22	7.083	-.055	-.84	0.3888	20.55
0.968	20.39	146.8	68.80	10.63	6.473	-.100	-.92	0.3961	20.43
0.994	20.10	136.3	64.80	12.20	5.132	-.090	-.67	0.4060	20.26

*Obtained from Clauser charts with κ and B of .41 and 5.0.

**Obtained by extrapolating Reynolds shear stress to the wall and using the equation:

$$C_f = 2\langle uv\rangle_{wall}/\langle U_e\rangle^2$$

TUNNEL ROOF

$1+\frac{x}{c}$	U_e (m/s)	$\delta_{.995}$ (mm)	δ_1 (mm)	δ_2 (mm)	H	$C_{p_{wall}}$
.370	25.54	2.83	3.83	2.88	1.33	0.1106
.650	24.97	3.71	6.07	4.25	1.42	0.1604
.700	24.89	4.01	7.32	5.08	1.44	0.1846
.750	24.20	4.31	8.43	5.49	1.53	0.2149
.800	24.00	4.62	8.45	5.51	1.53	0.2410
.850	22.98	4.71	9.16	5.70	1.61	0.3121
.900	21.70	4.81	9.73	6.16	1.58	0.3524
.950	20.97	4.97	12.02	7.19	1.67	0.3903
1.00*	20.27	5.18	13.53	7.81	1.73	0.4093
1.066	19.71	5.26	13.21	7.95	1.66	0.4330
1.099	19.70	5.66	13.08	8.04	1.62	0.4495
1.181	19.68	5.76	13.20	7.98	1.65	0.4638
1.230	19.33	6.18	13.86	9.24	1.50	0.4697
1.329	19.30	6.31	13.74	9.15	1.50	0.4827

TUNNEL FLOOR

$1+\frac{x}{c}$	U_e (m/s)	$\delta_{.995}$ (mm)	δ_1 (mm)	δ_2 (mm)	H (mm)	$C_{p_{wall}}$
1.033	13.86	3.31	2.61	1.94	1.34	0.4199
1.066	13.61	3.36	2.62	1.94	1.35	0.4321
1.099	13.42	3.39	2.65	1.95	1.36	0.4302
1.181	13.30	3.40	2.75	1.99	1.38	0.4640
1.230	13.28	3.71	2.96	2.14	1.39	0.4721
1.329	13.24	4.14	3.59	2.51	1.43	0.4820

*Plane of trailing-edge.

WAKE

$\frac{x}{c}$	$U_{e_{upper}}$	$U_{e_{lower}}$	$\delta_{.995}$	δ_1	δ_2	H
.000	(20.50)	14.02				
.040	20.24	13.72	161.3	65.02	21.61	3.01
.066	20.13	13.67	160.4	55.37	20.28	2.73
.099	19.87	13.53	160.2	46.41	20.91	2.22
.132	19.66	13.43	158.1	41.30	21.74	1.90
.181	19.42	13.27	153.6	39.55	21.73	1.82
.231	19.25	13.19	148.0	38.09	21.89	1.74
.329	19.18	13.14	130.6	35.00	21.28	1.65
.395	19.06	13.14	115.3	32.61	21.31	1.53

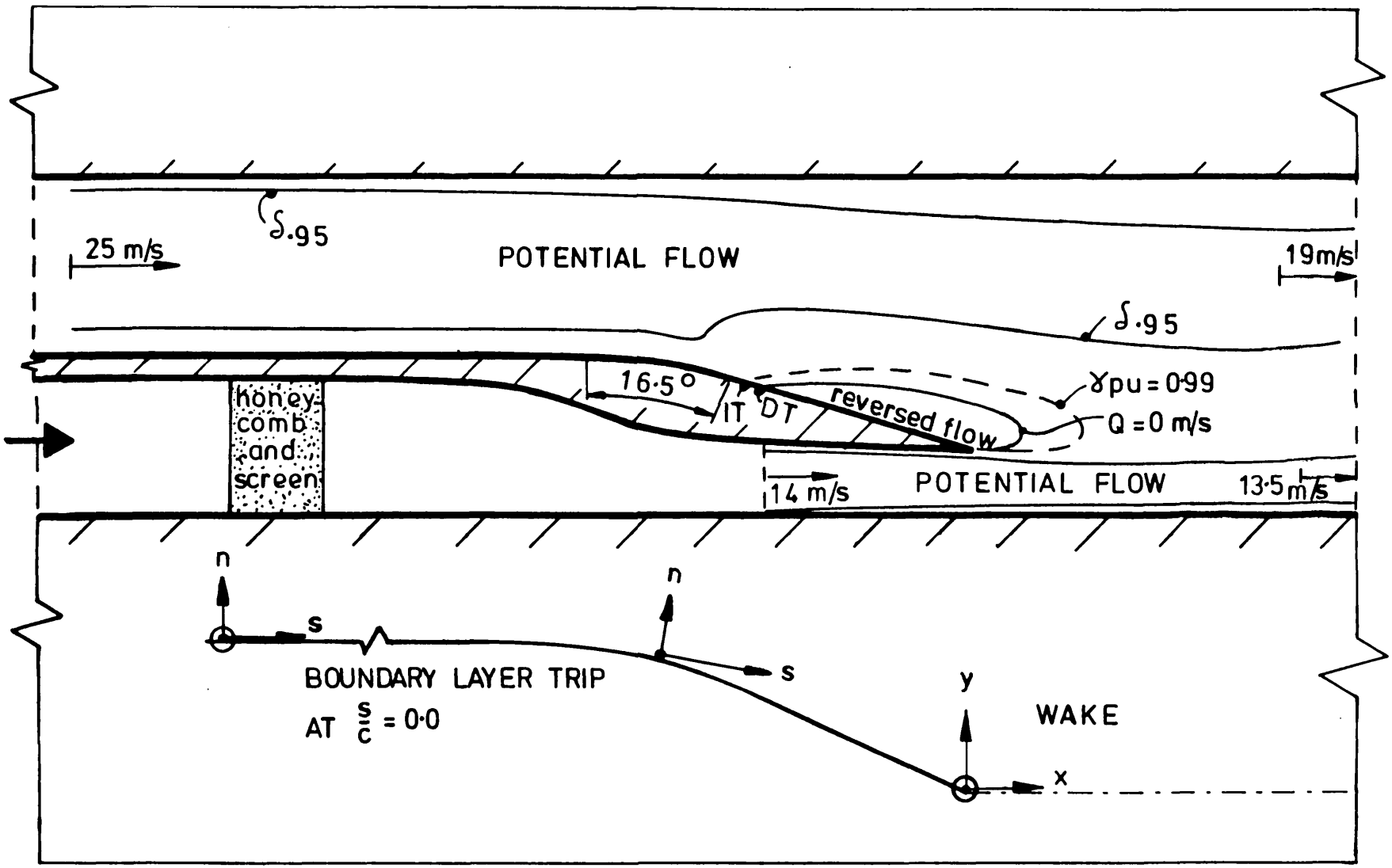


Figure 3.1 Flow configuration.



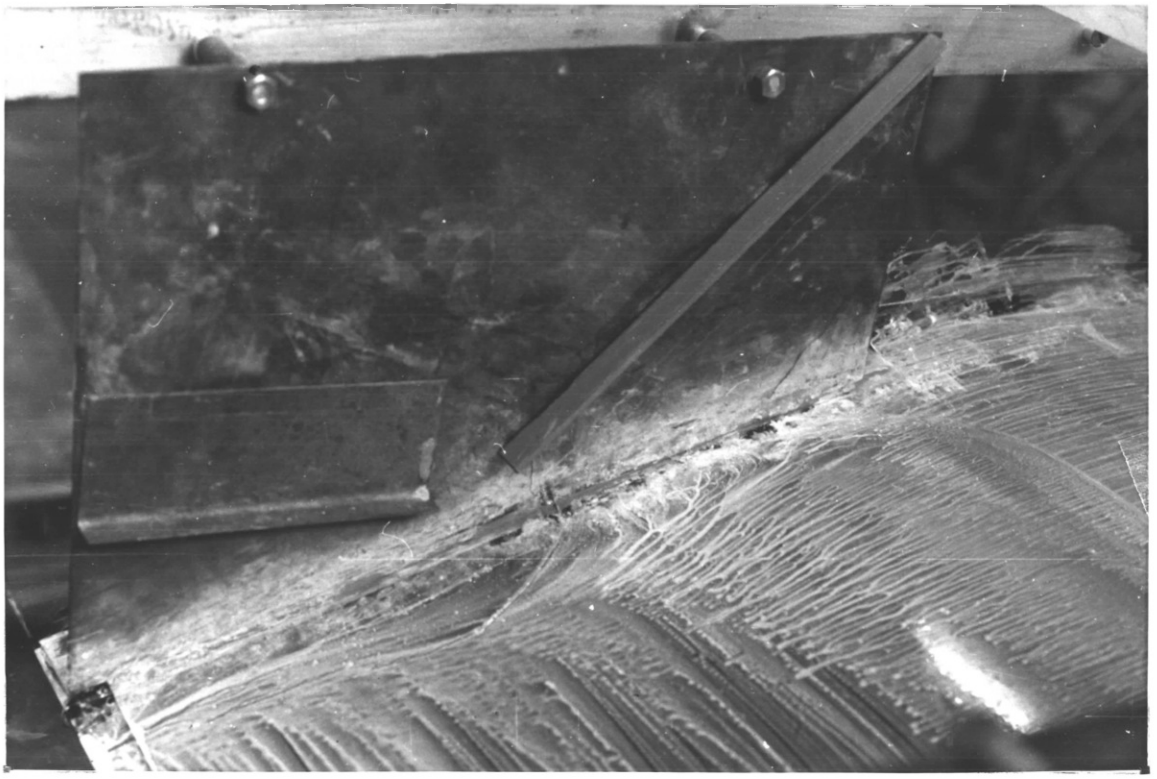


Figure 3.2 Flow control vanes.

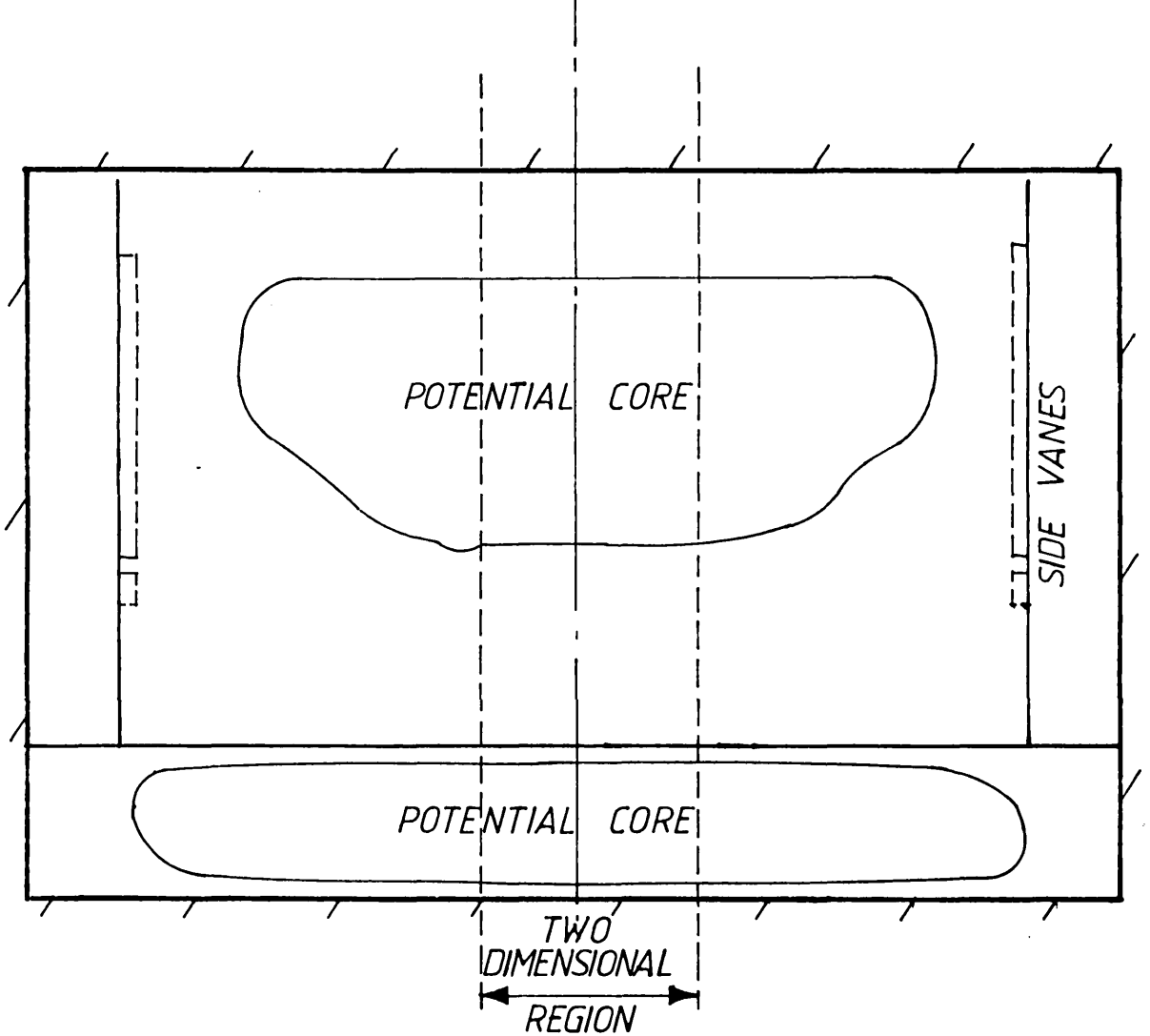


Figure 3.3 Total pressure contours in the plane of the trailing edge.

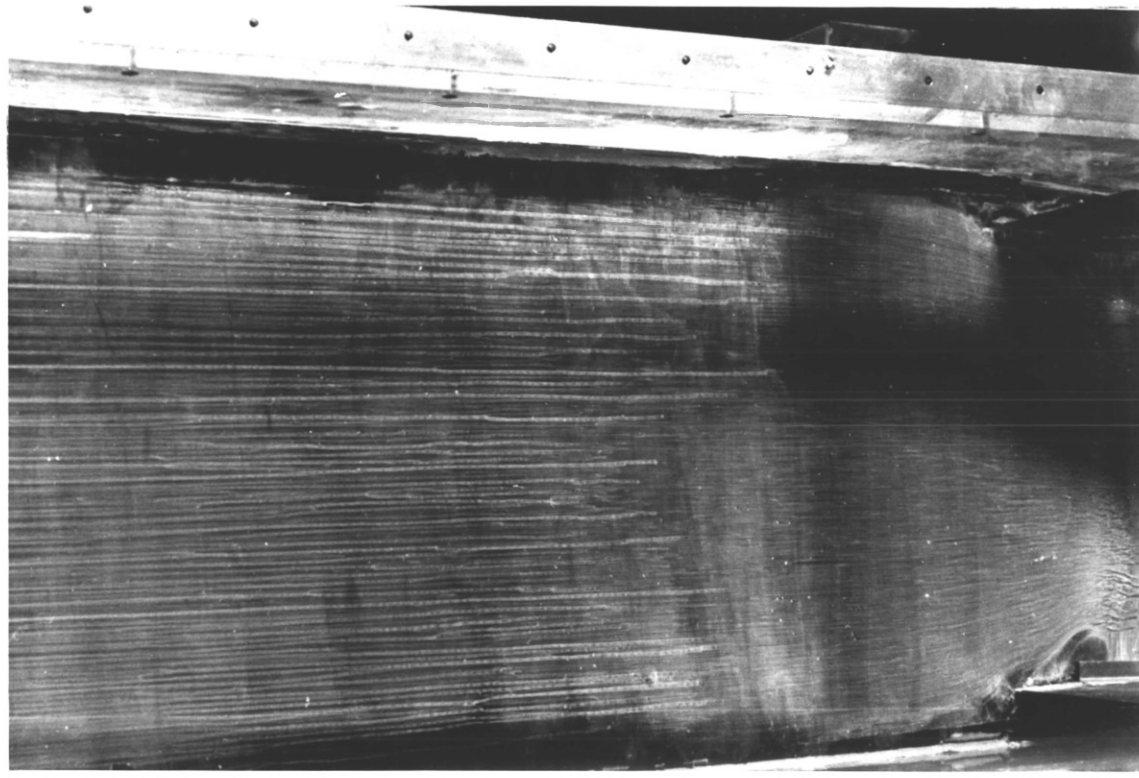


Figure 3.4 Surface flow visualization of the upstream boundary layer.

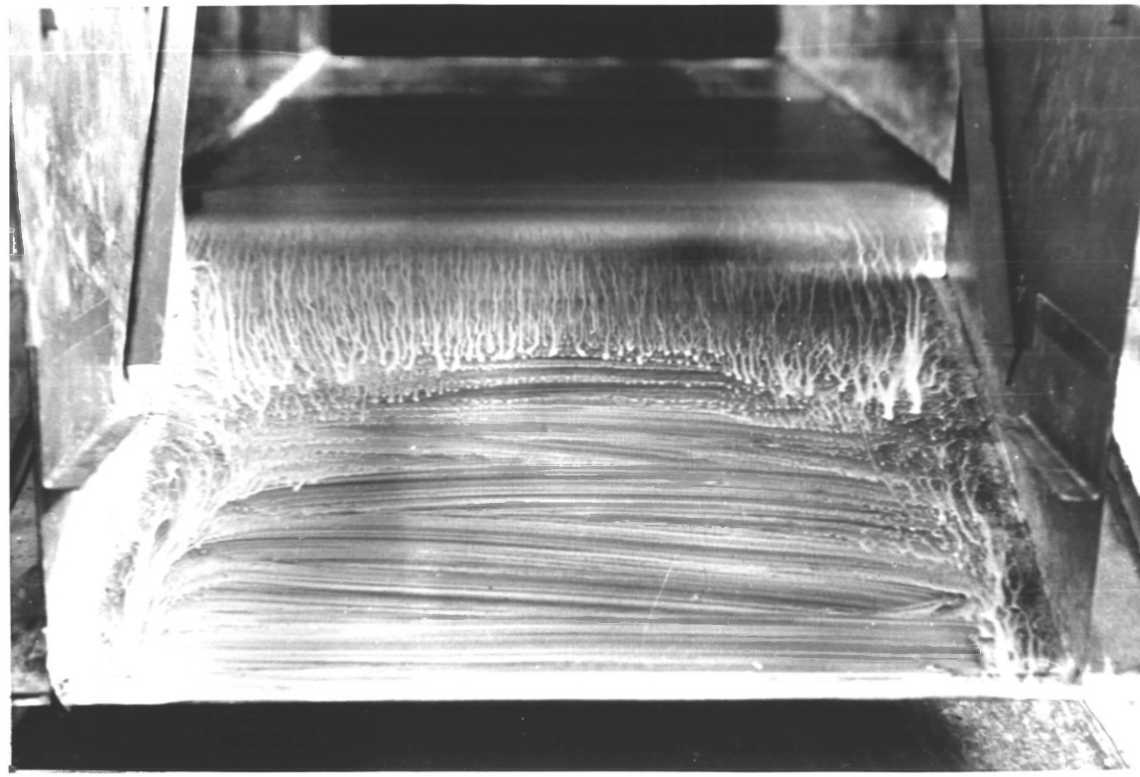


Figure 3.5 Surface flow visualization of the curved boundary layer and separated region.

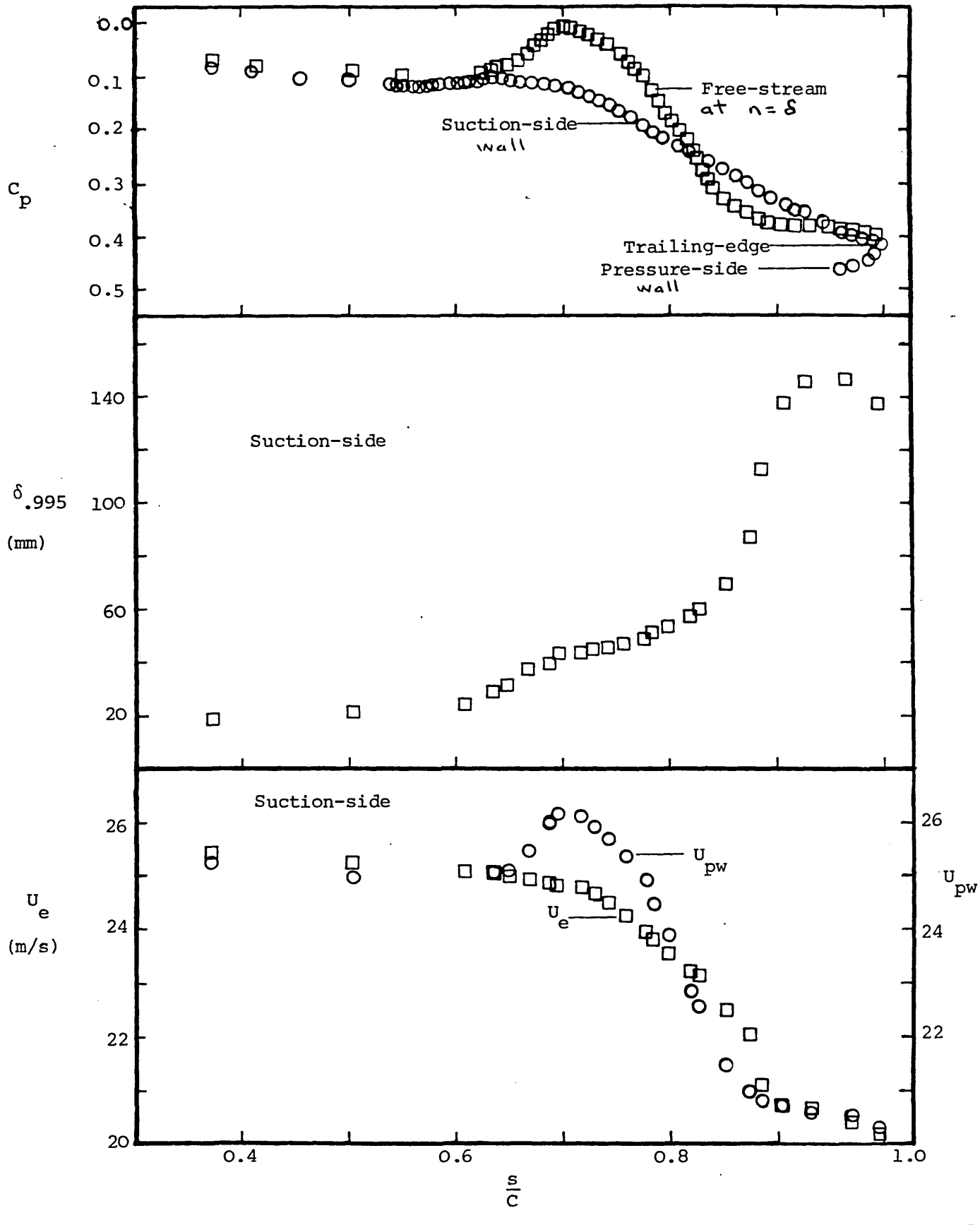


Figure 3.6 Parameters of mean flow development.

(a) Suction-side boundary layer.

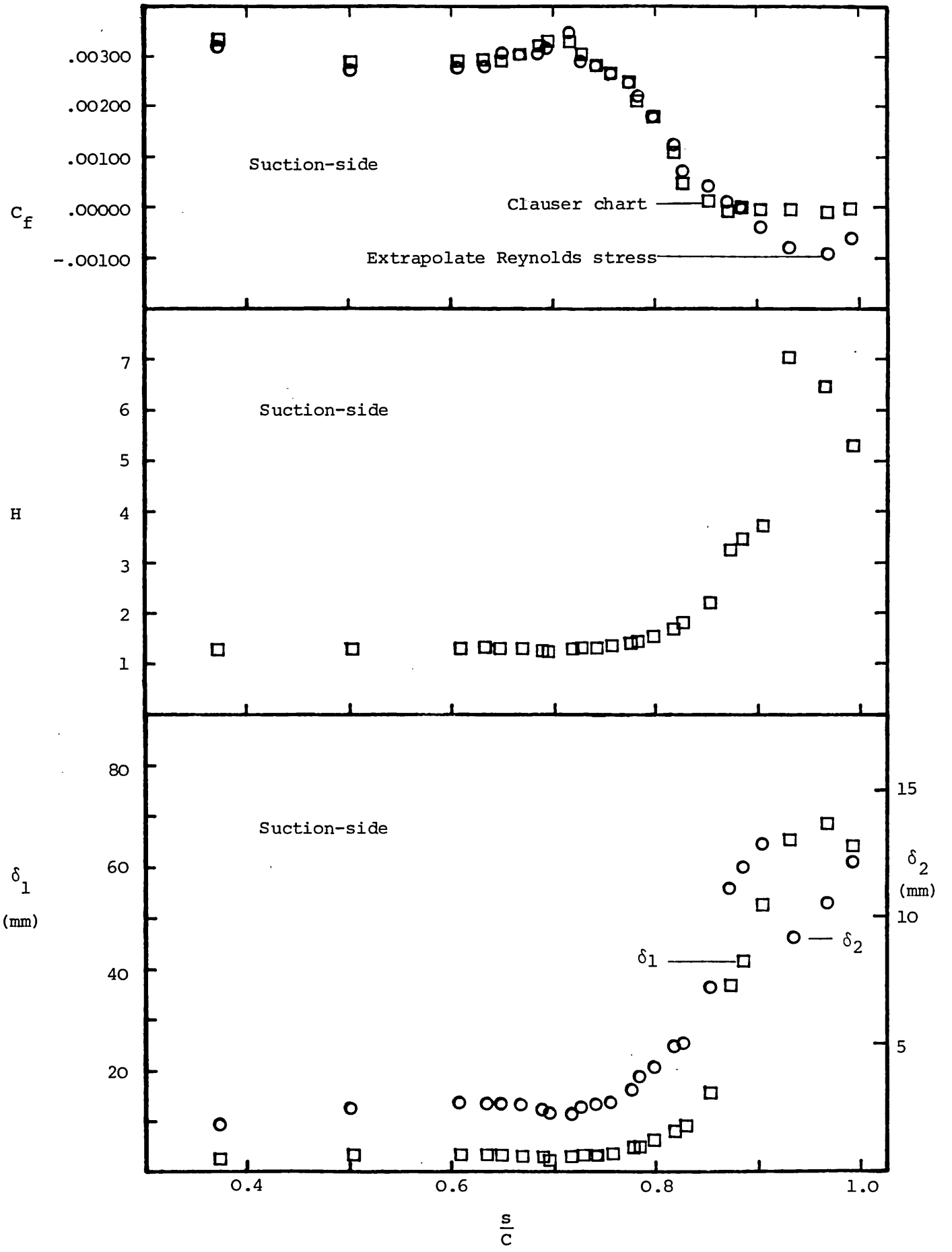


Fig. 3.6 (cont.) Parameters of mean flow development.

(b) Suction-side boundary layer (cont.).

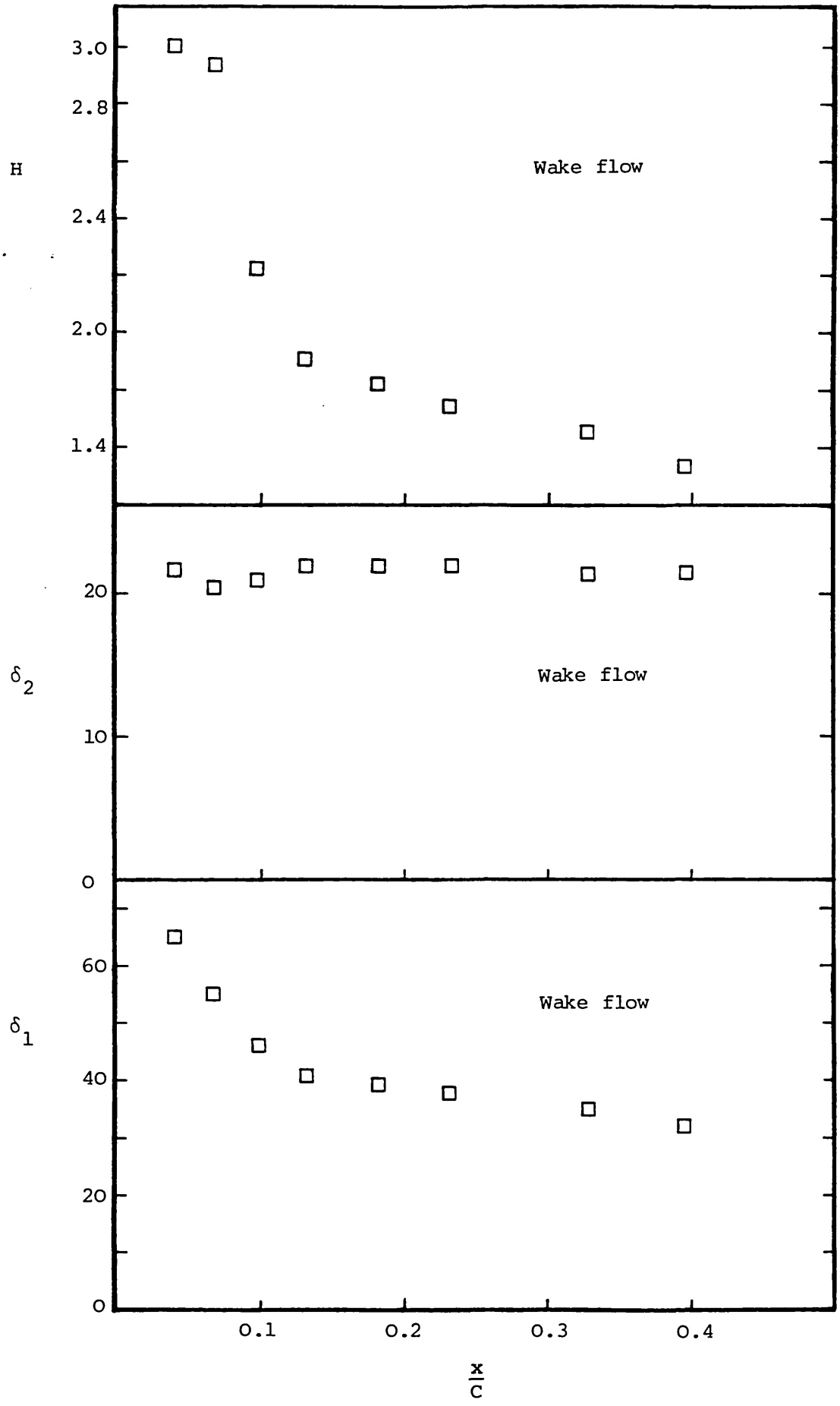


Fig. 3.6 (cont.) Parameters of mean flow development.

(c) Wake flow.

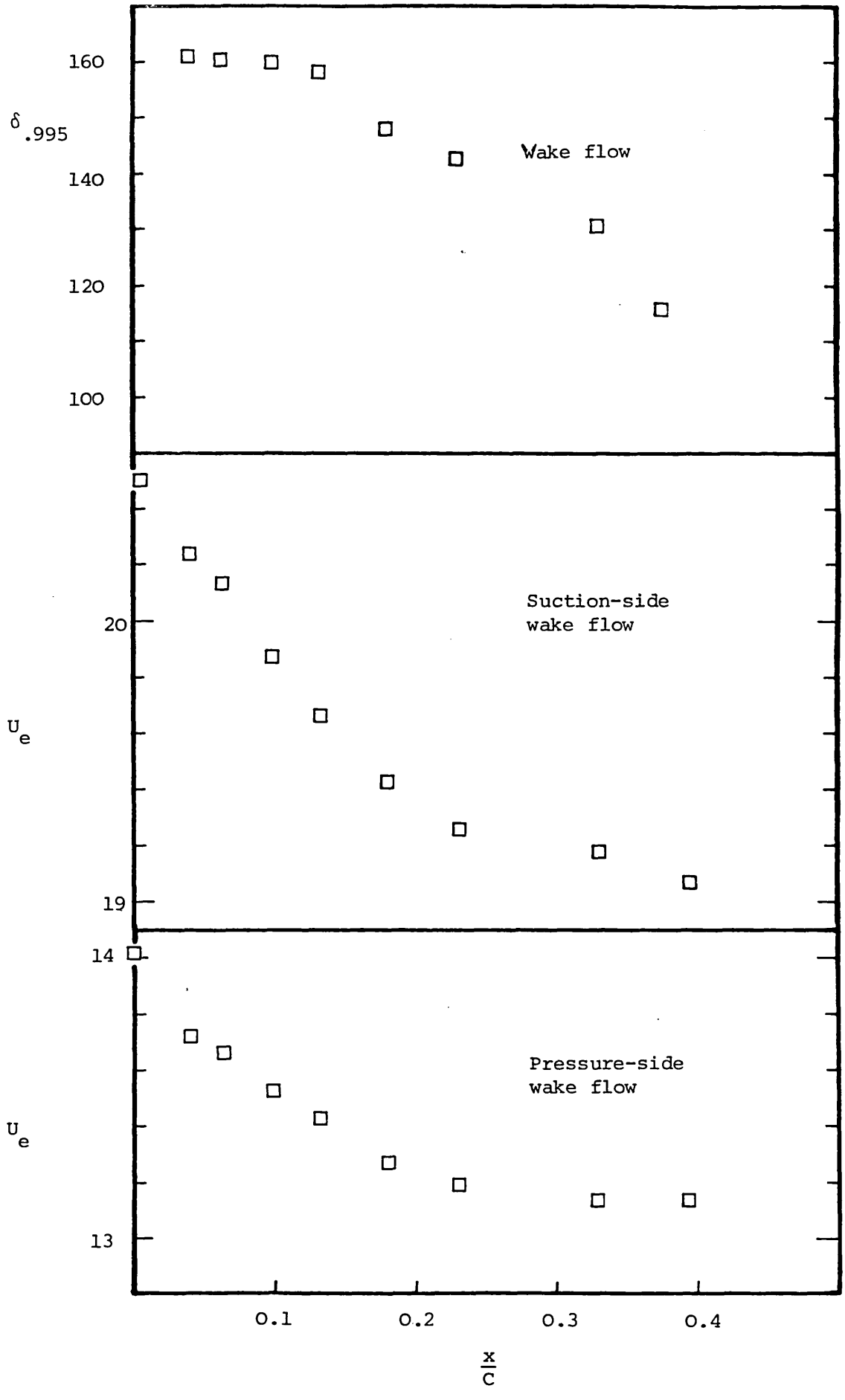


Fig. 3.6 (cont.) Parameters of mean flow development.

(d) Wake flow (cont.).

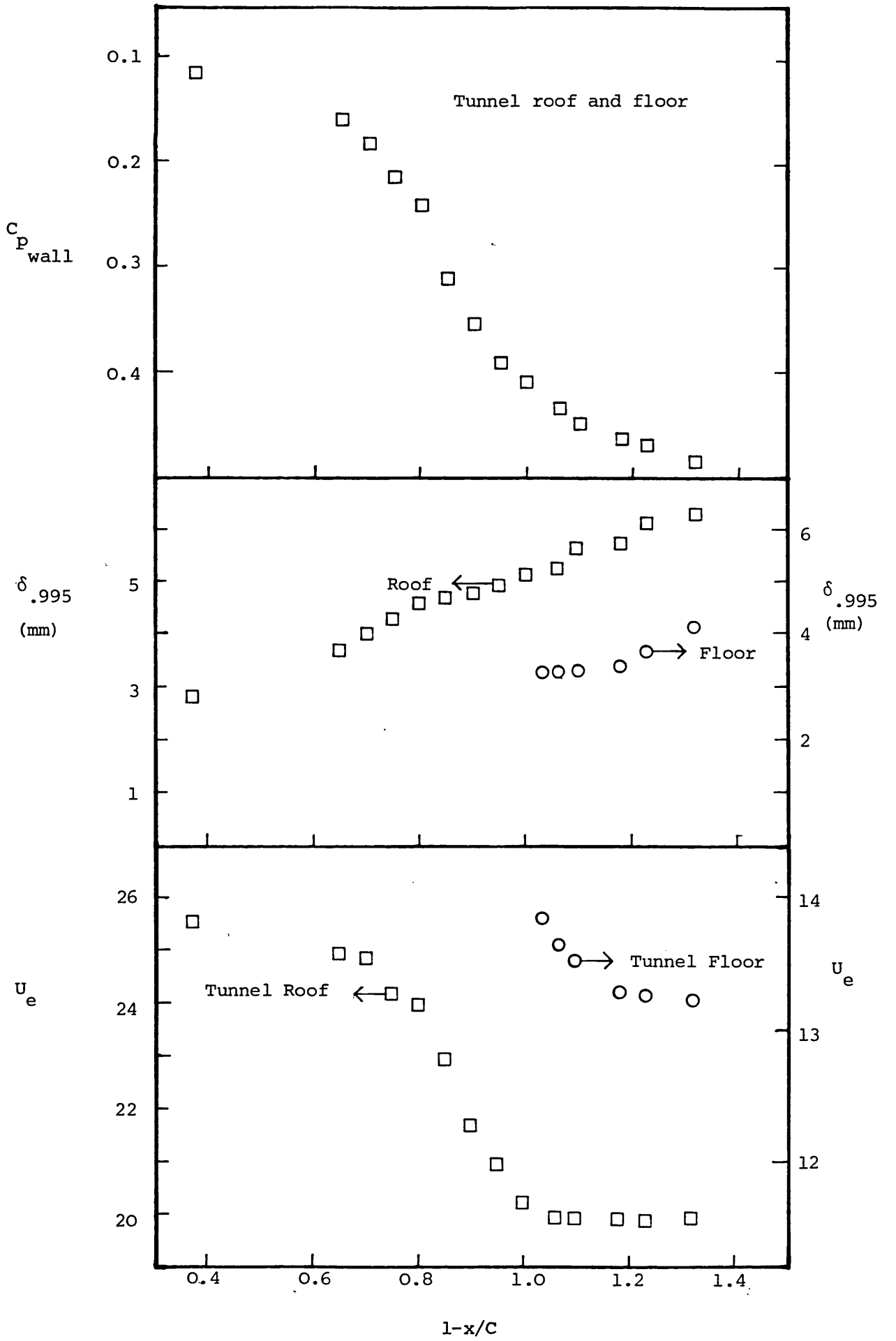


Fig. 3.6 (cont.) Parameters of mean flow development.
(e) Tunnel roof and floor.

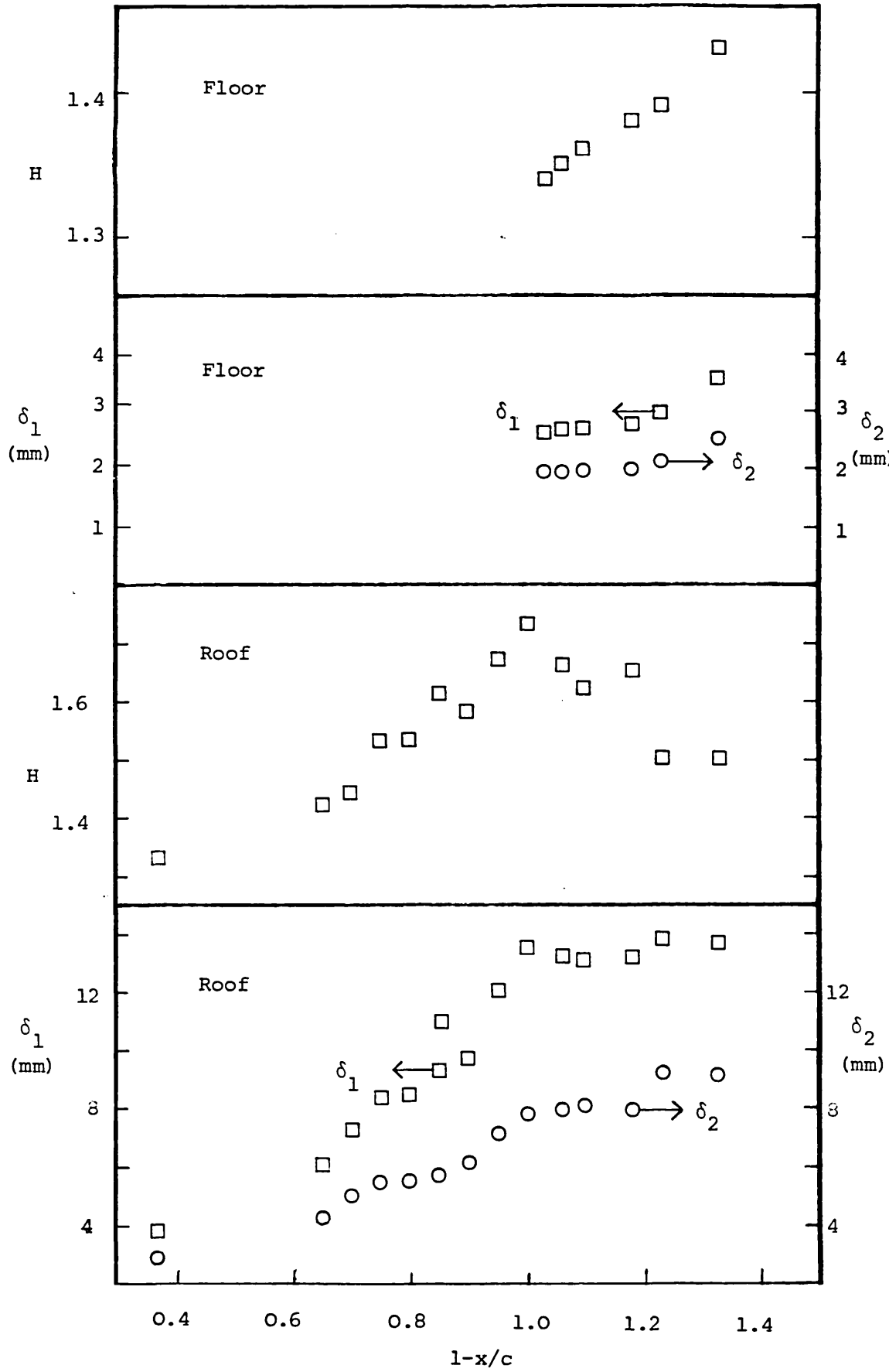
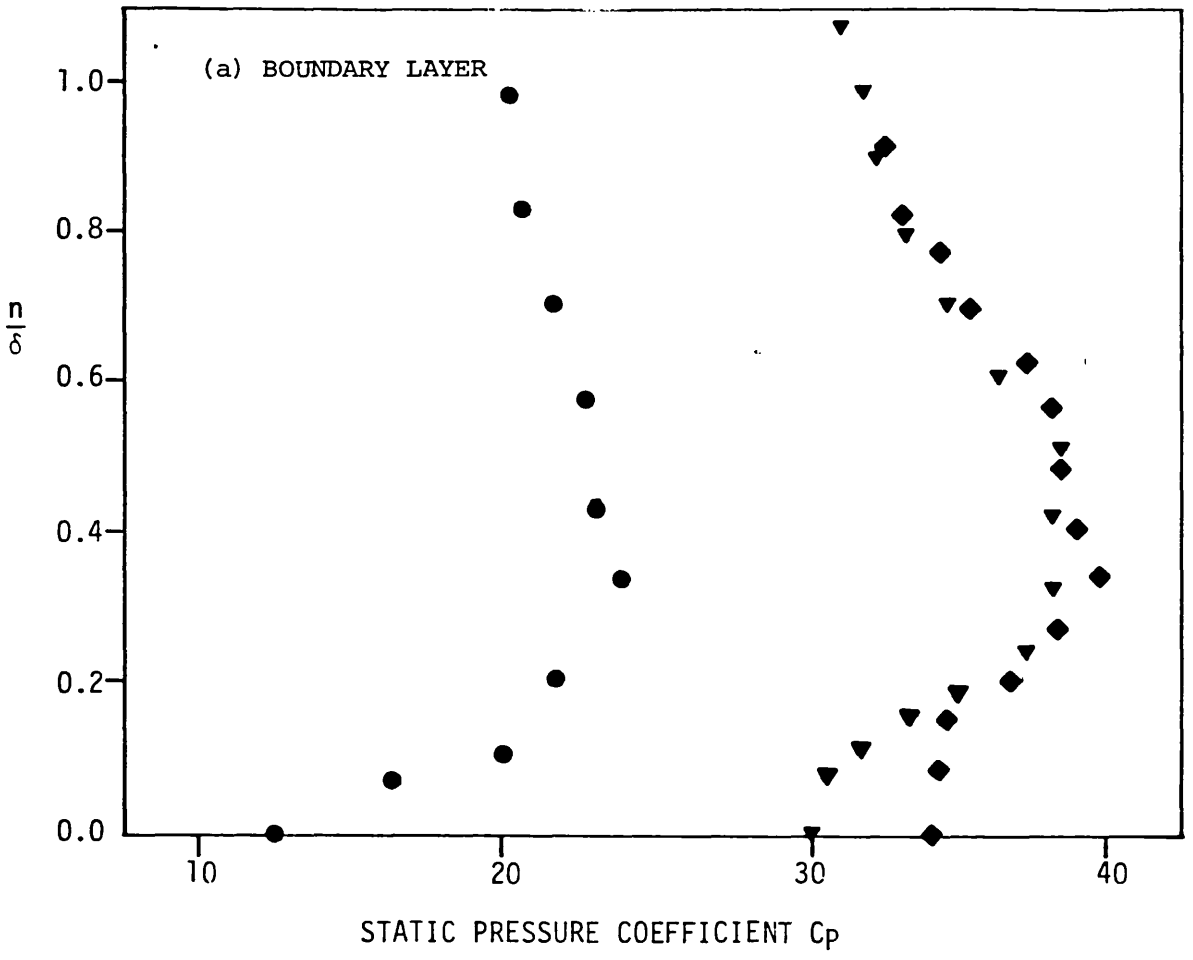


Figure 3.6 (cont.) Parameters of mean flow development.

(f) Tunnel boundary layers.



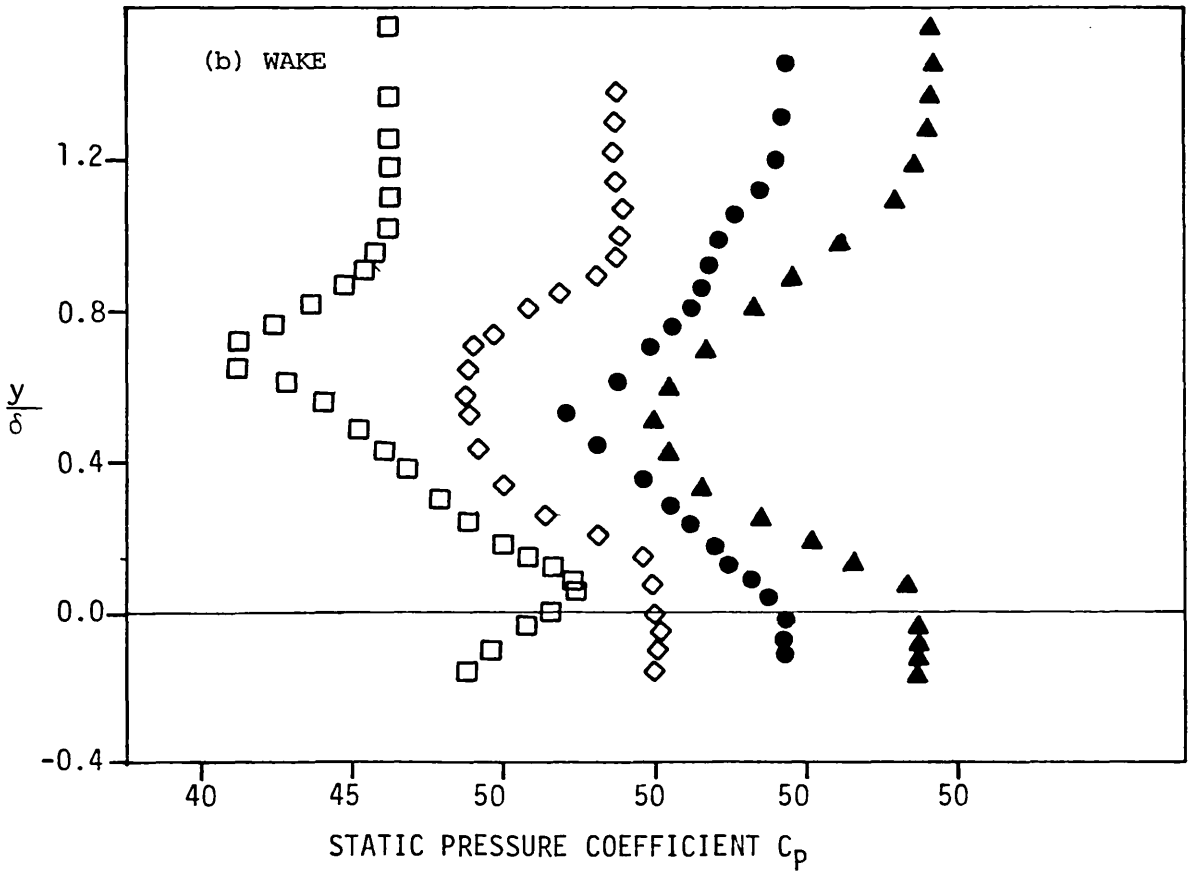


Figure 3.7 Profiles of static pressure coeficient.
(Symbols as in figures 3.10 a and b, respectively.)

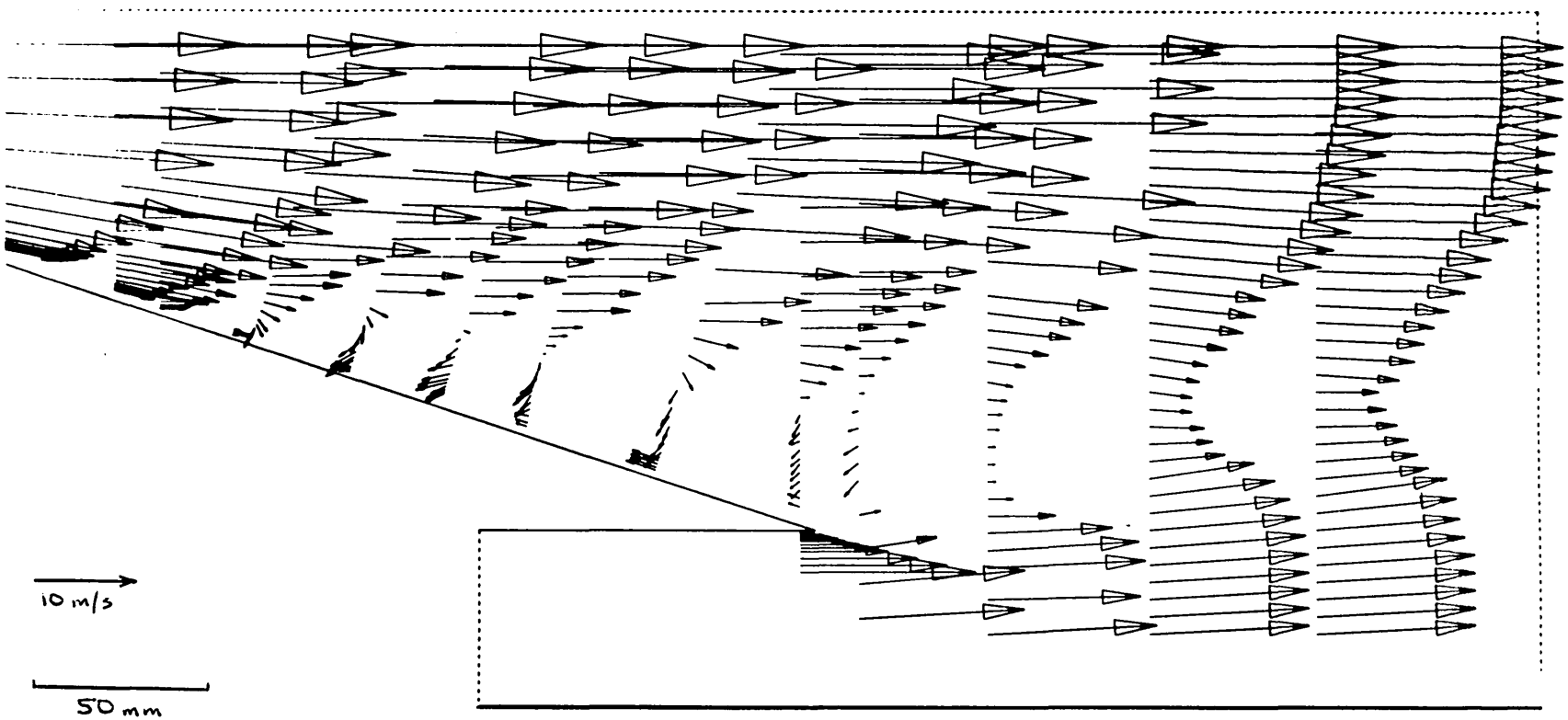


Figure 3.8 Mean velocity vectors in the vicinity of separation.

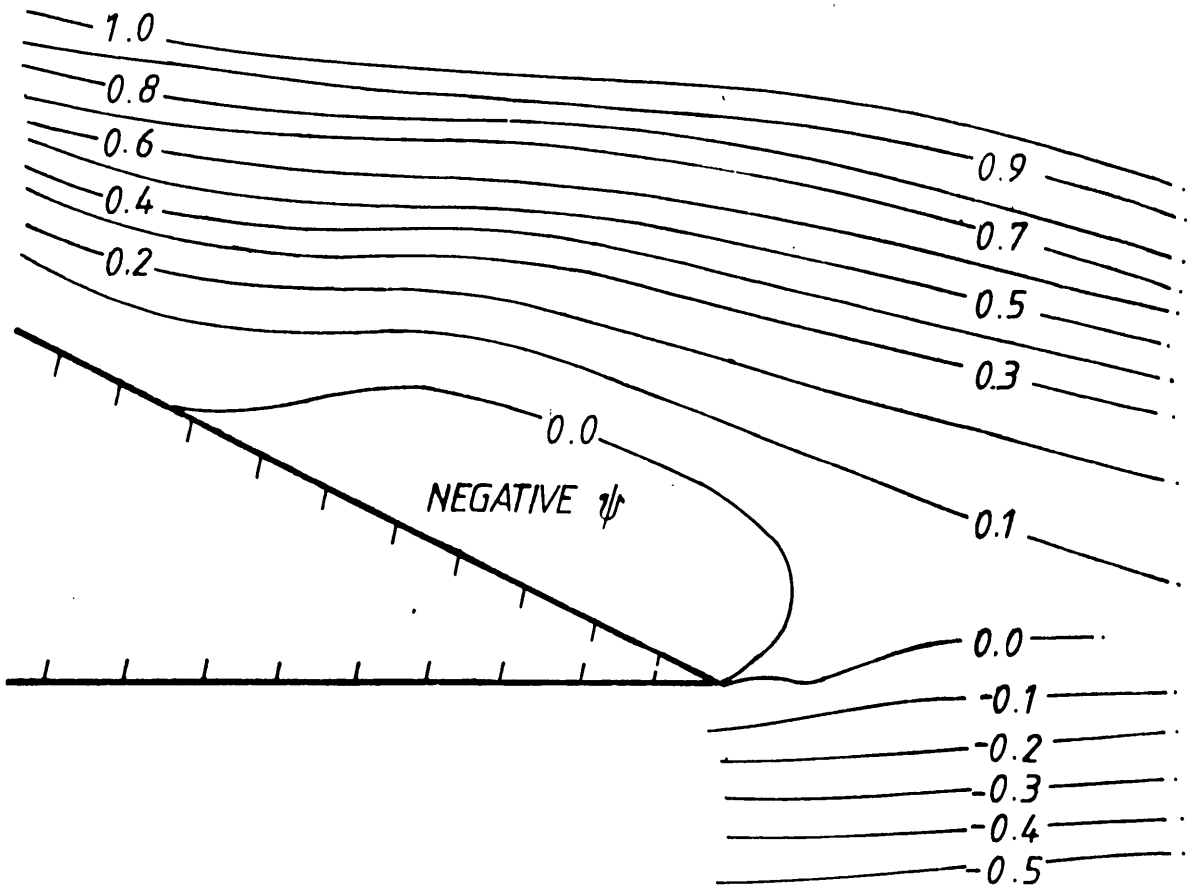


Figure 3.9 Streamlines and probability of downstream flow in the vicinity of separation.

(a) Streamlines.

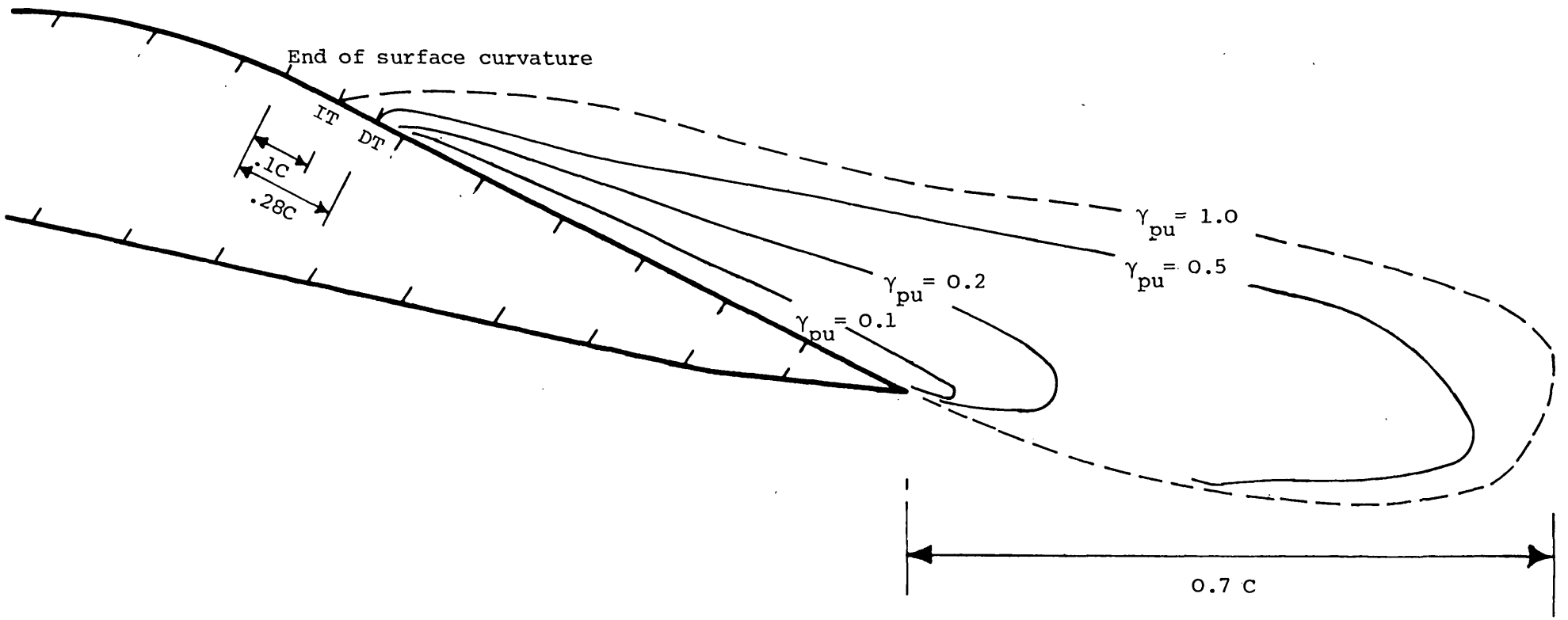


Fig. 3.9 (cont.) (b) Probability of downstream flow.

Figure 3.10 Profiles of mean velocity.

Summary of symbols.

BOUNDARY LAYER

$\frac{s}{c}$	Symbol
0.372	○
0.649	□
0.668	△
0.688	◆
0.695	◇
0.718	×
0.757	+
0.777	●
0.798	■
0.826	▼ ◭
0.839	■
0.852	◆ ▼
0.866	□
0.874	◍
0.886	▽ ▨
0.905	●
0.932	▽
0.955	◈
0.968	▲
0.980	⊗
0.994	◆

WAKE

$\frac{x}{c}$	Symbol
0.000	■
0.006	○
0.050	▼
0.066	○
0.099	▽
0.132	□
0.181	◇
0.231	●
0.329	▲
0.428	■

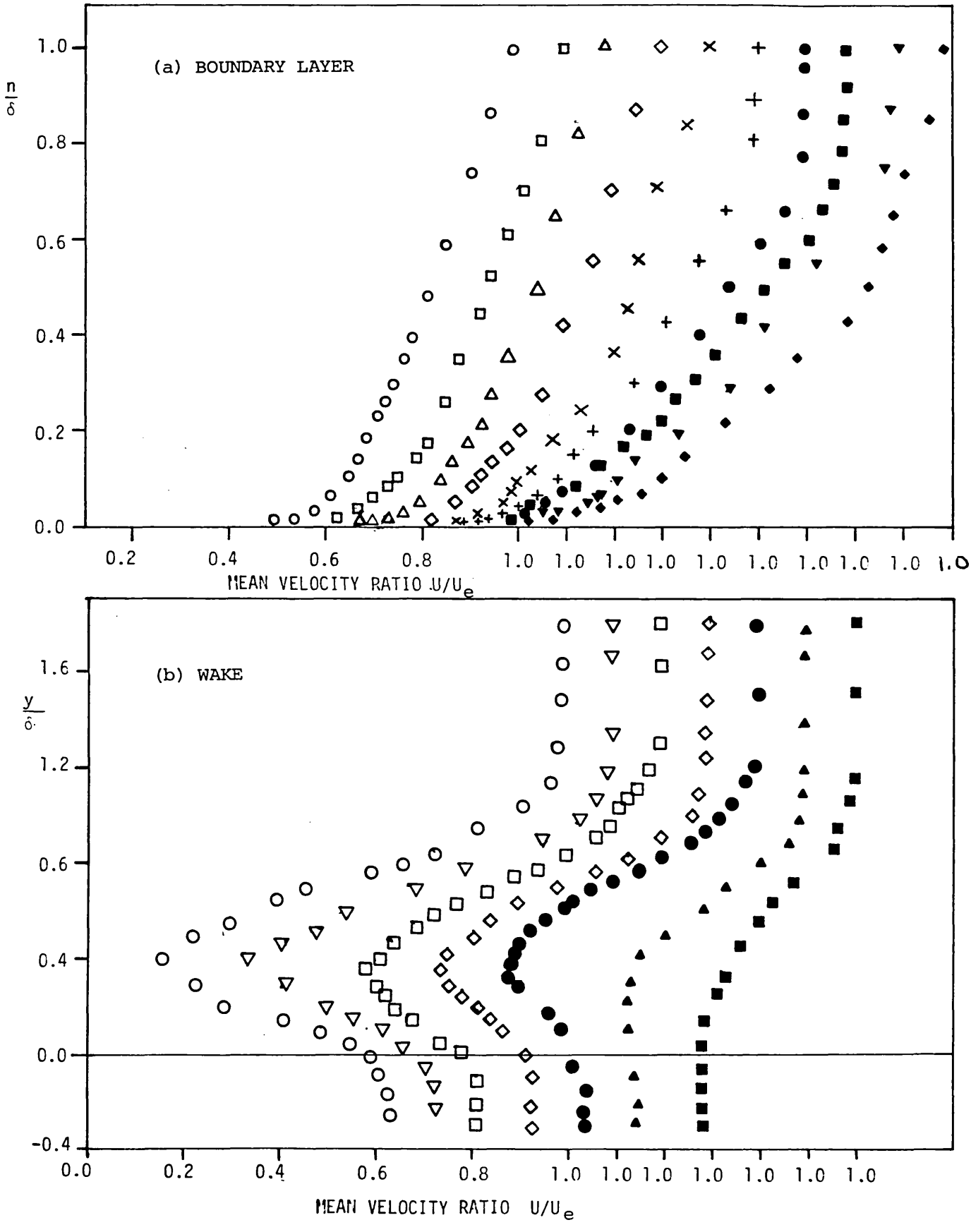
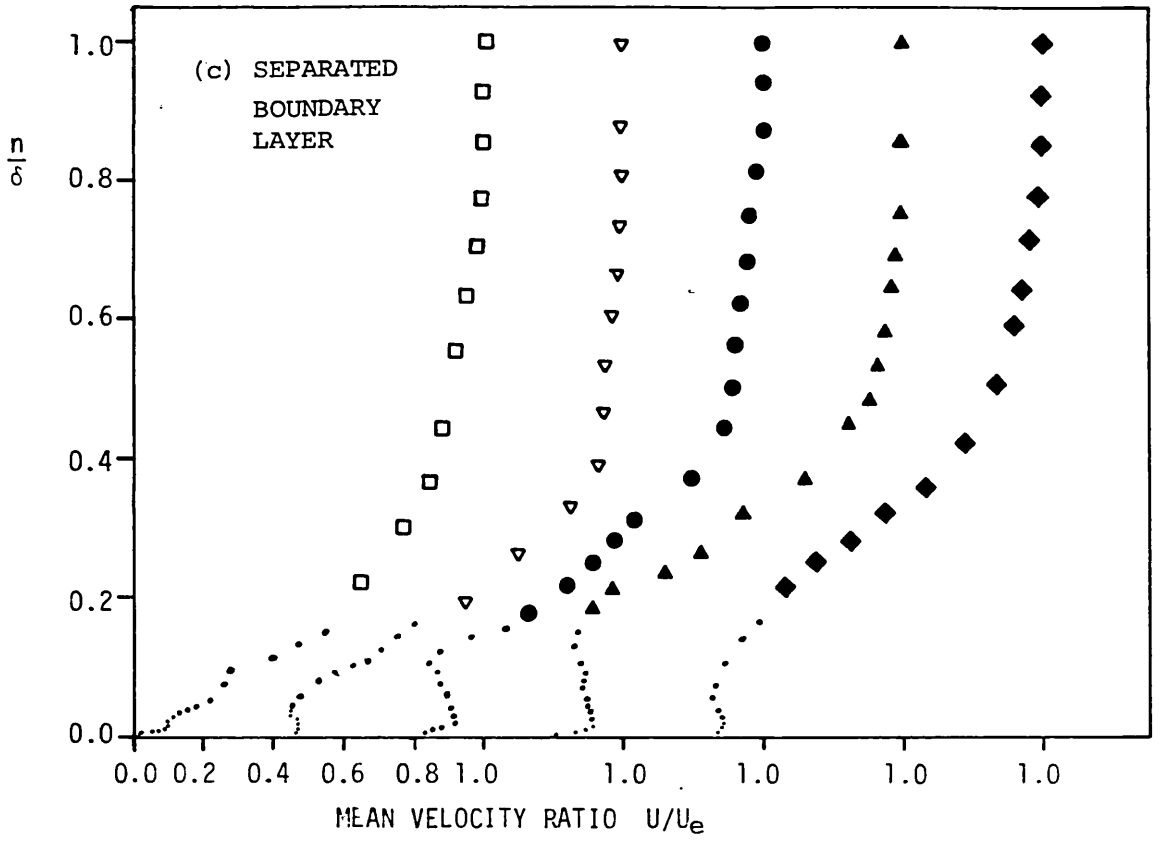


Figure 3.10 Profiles of mean velocity.

(Symbols are shown on previous page.)



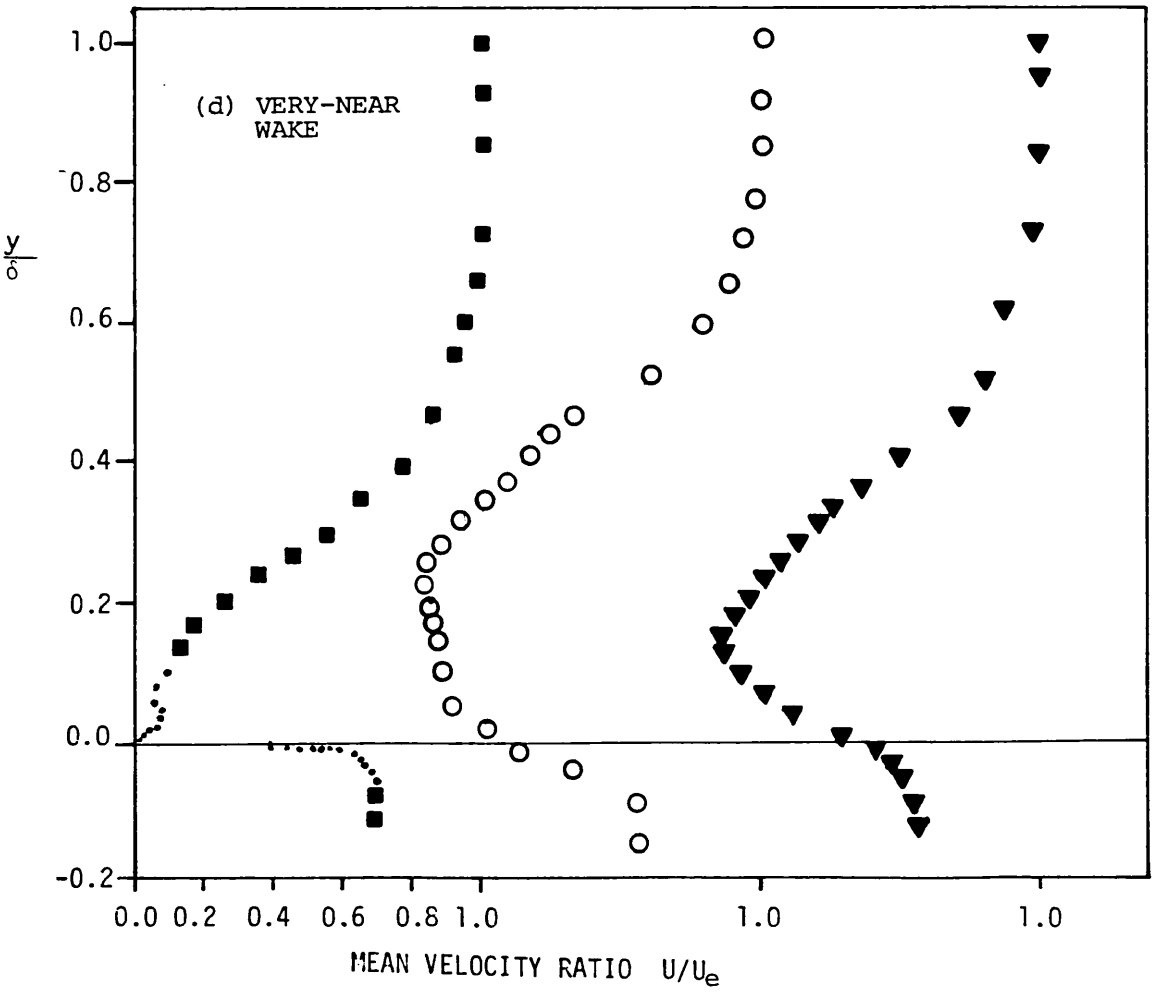


Fig. 3.10 (cont.) Profiles of mean velocity.

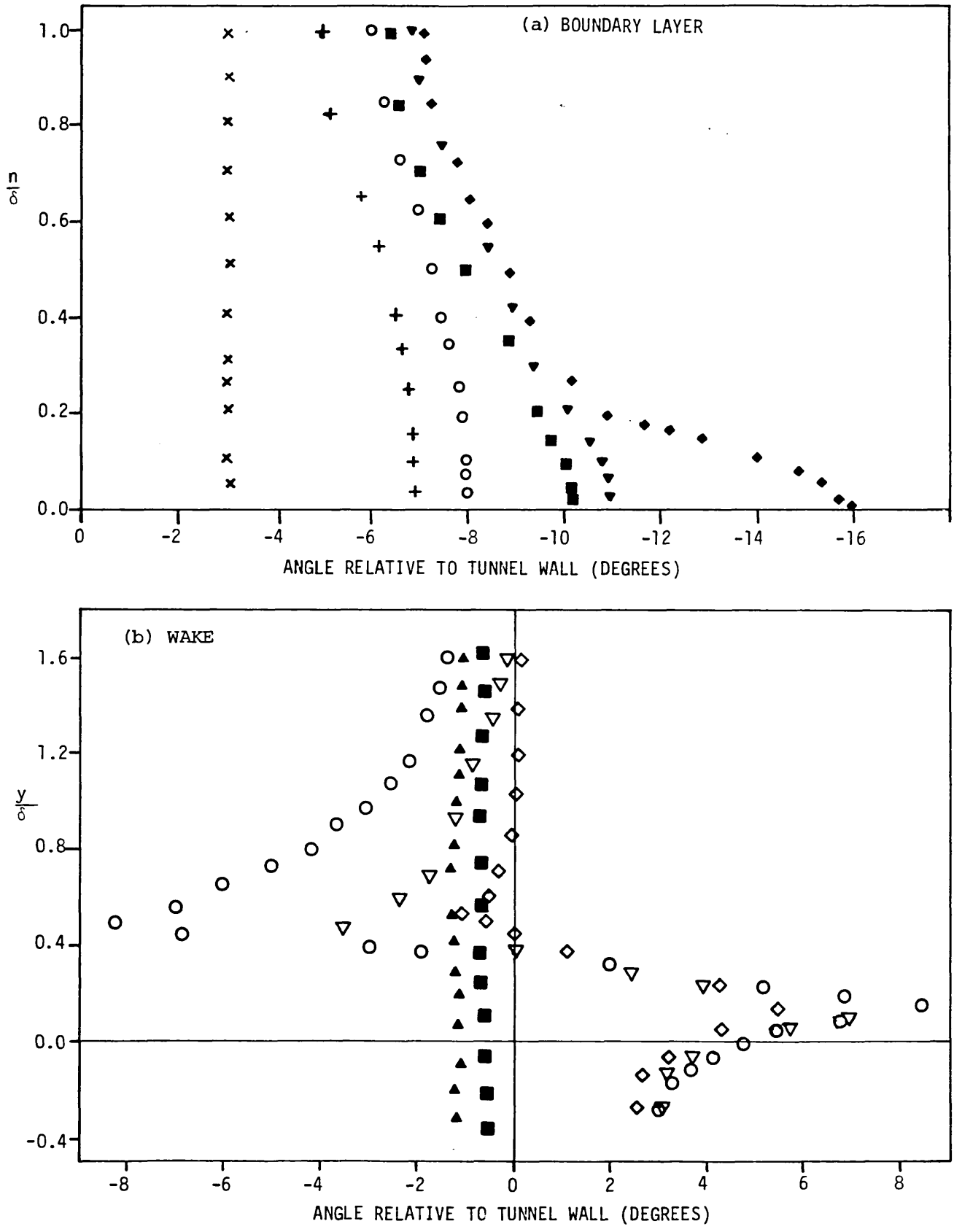


Figure 3.11 Profiles of flow angle.
(Symbols as in figure 3.10)

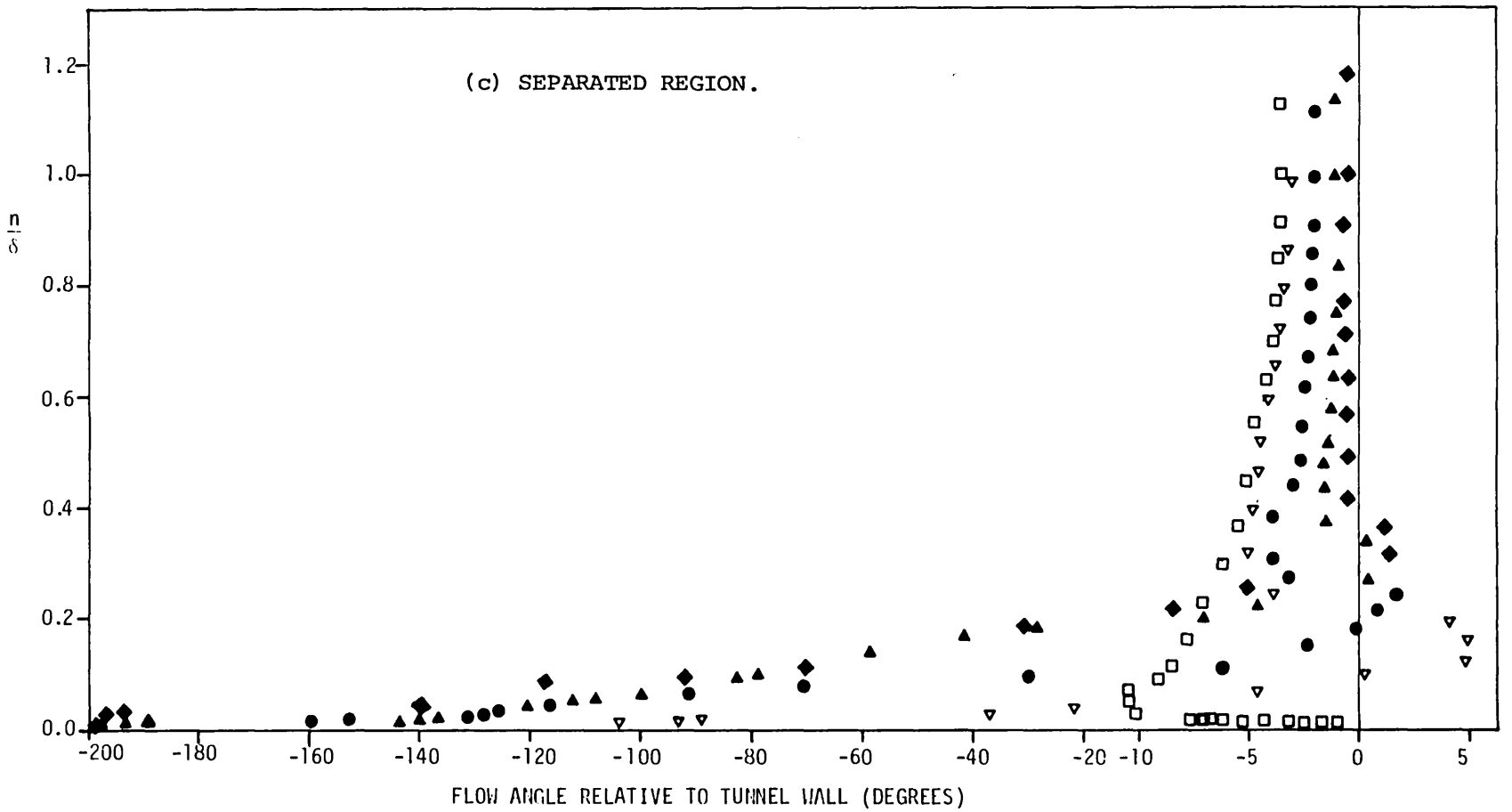


Figure 3.11 (cont.) Profiles of flow angle.

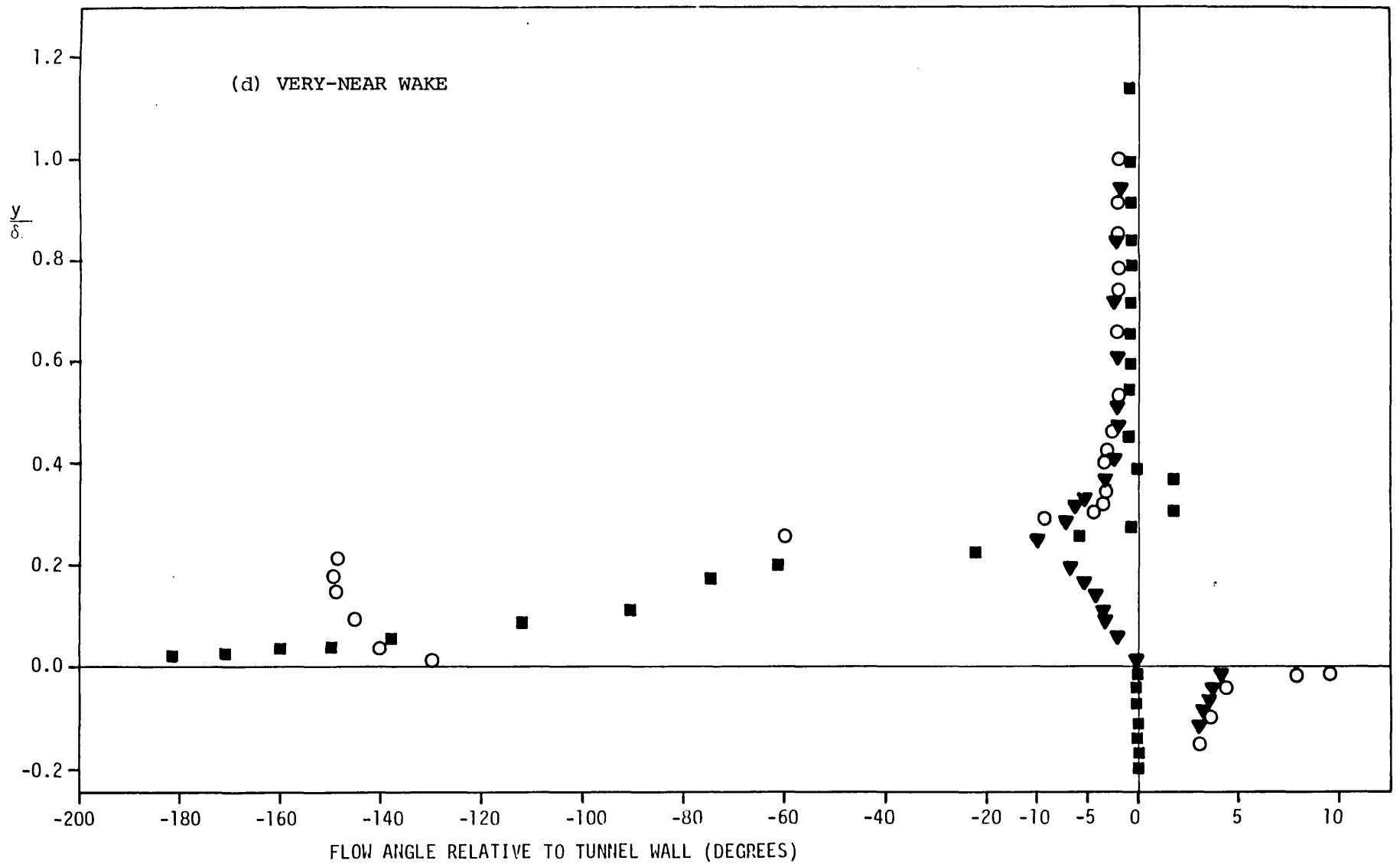


Figure 3.11 (cont.) Profiles of flow angle.

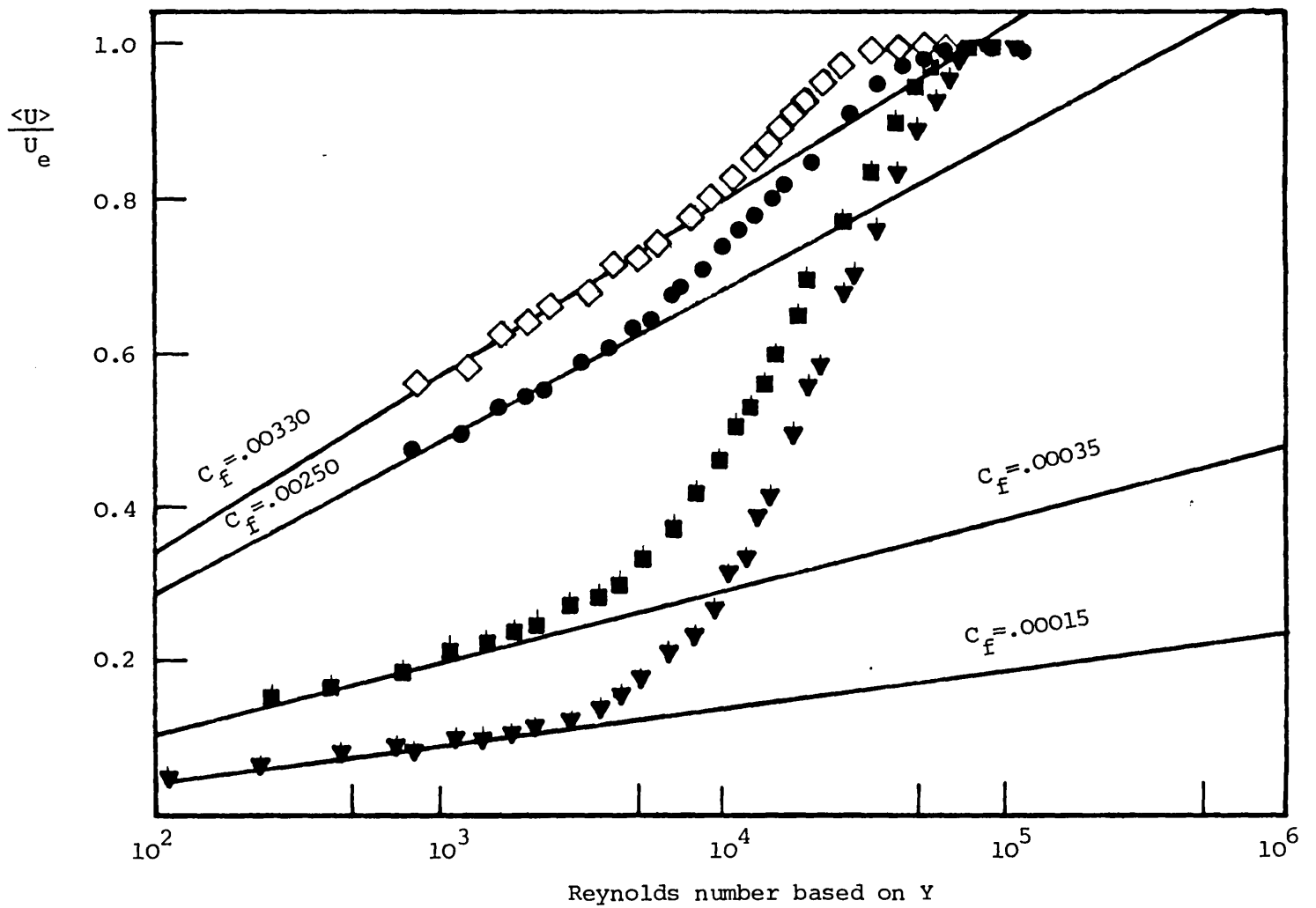
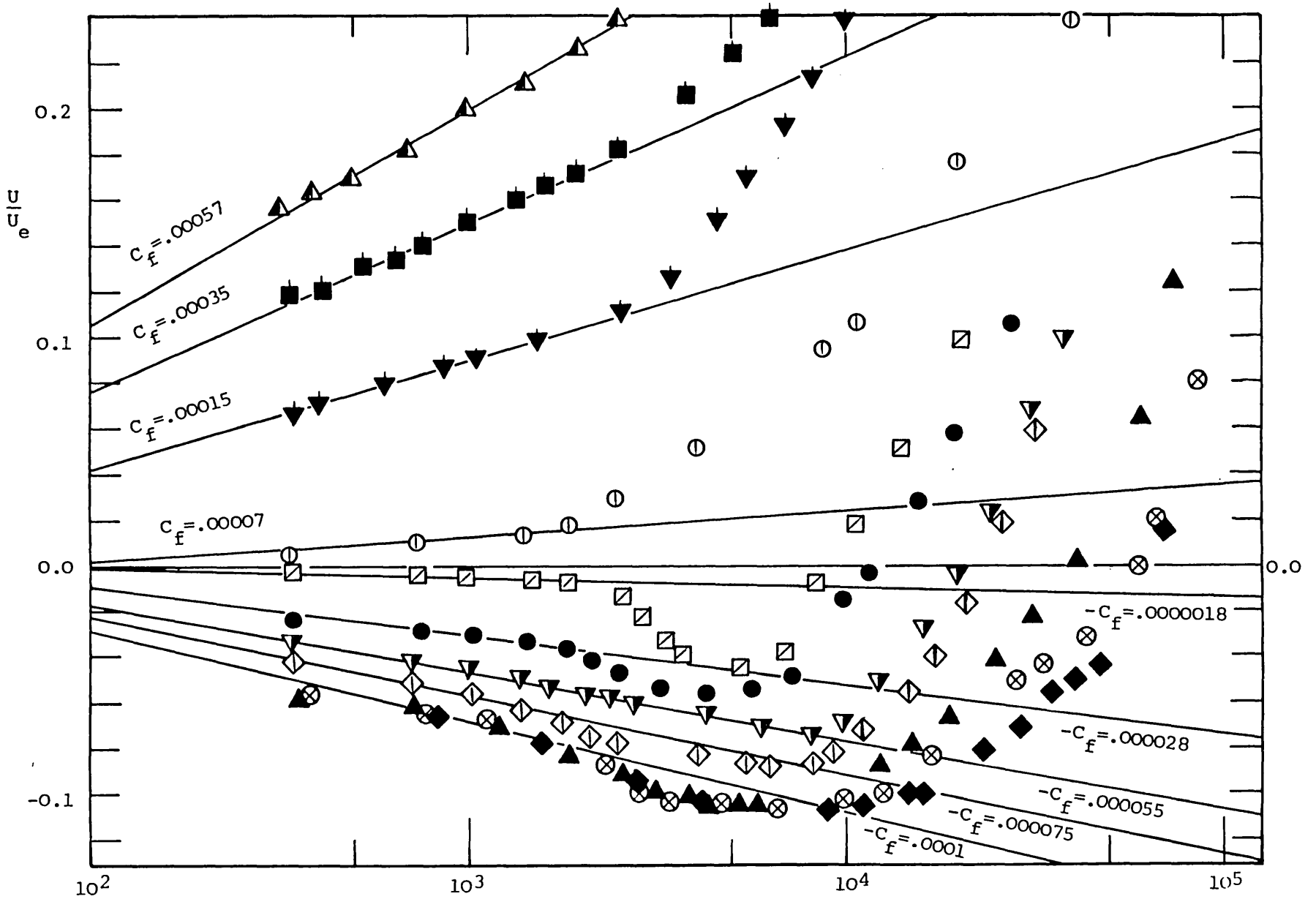


Figure 3.12 Clauser chart. (Symbols as in fig. 3.10)

(a) Upstream boundary layer.



(Symbols as in fig. 3.10)

Figure 3.12 (cont.) Clauser chart. (b) Separated region.

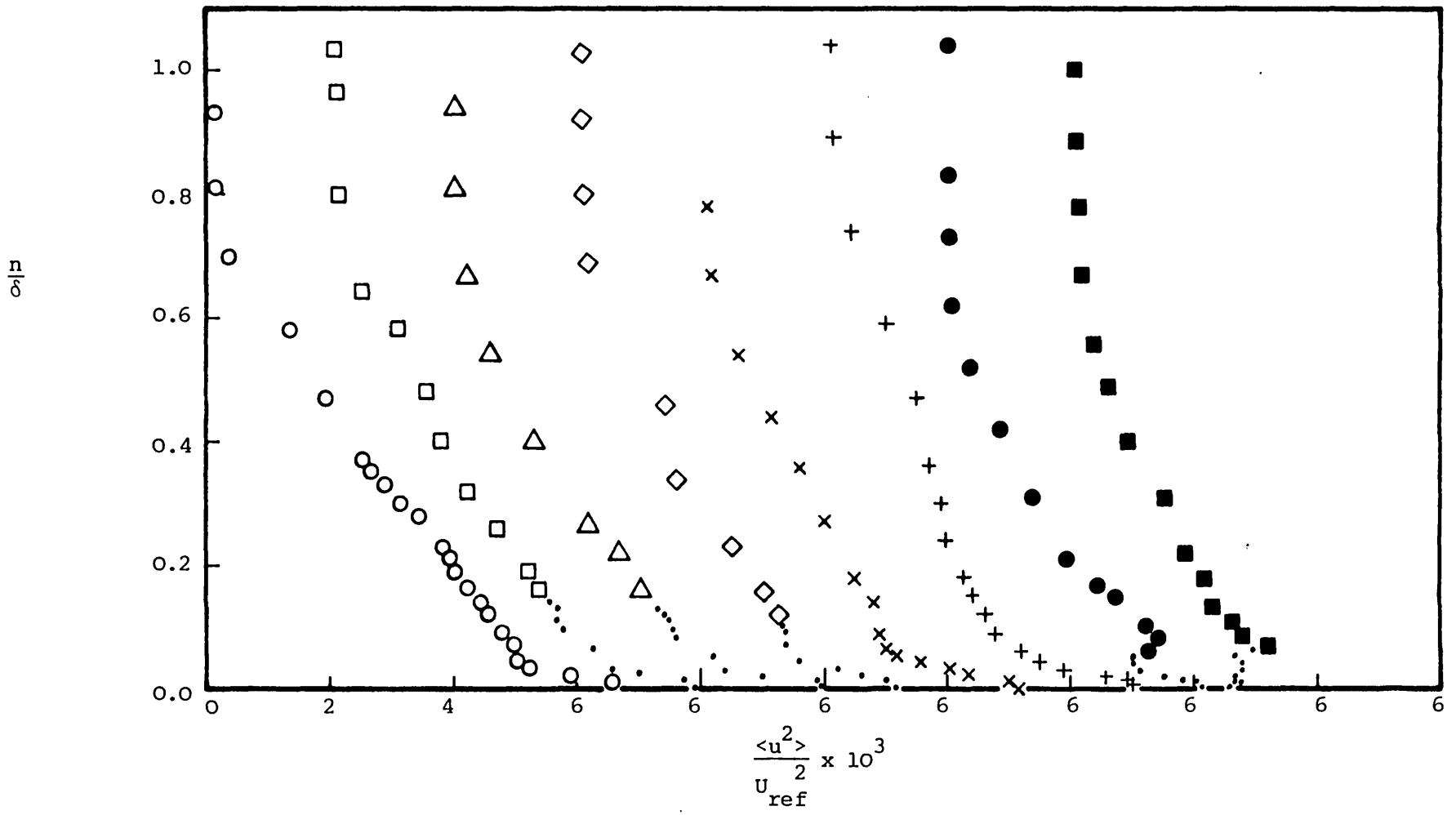


Figure 3.13 Profiles of Reynolds stresses approaching separation.
(Symbols as in fig. 3.10)

(a) Streamwise normal stress.

Note: Plate (e) is non-dimensionalised with U_{pw}.

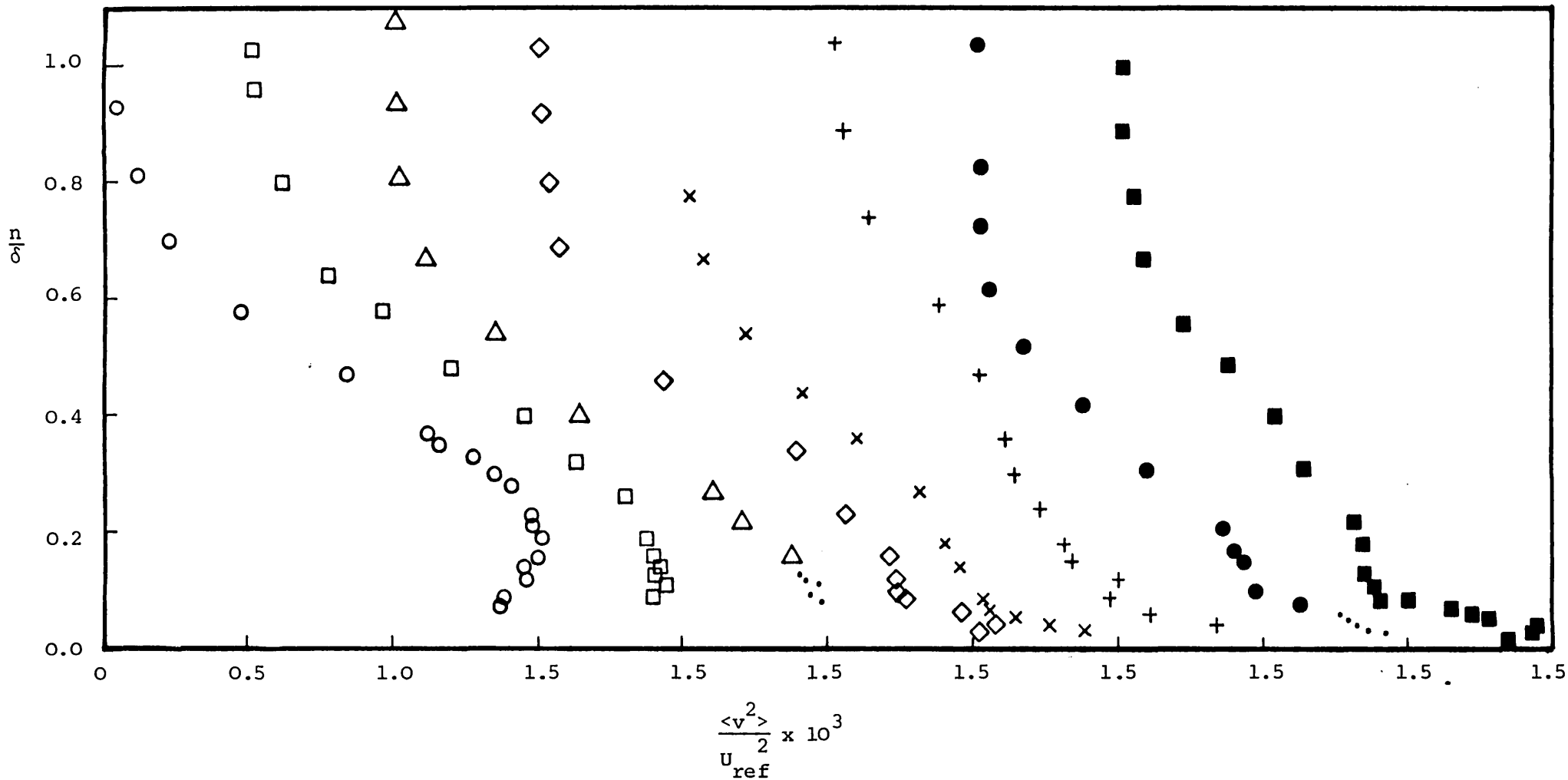


Fig. 3.13 (cont.) (b) Cross-stream normal stress.

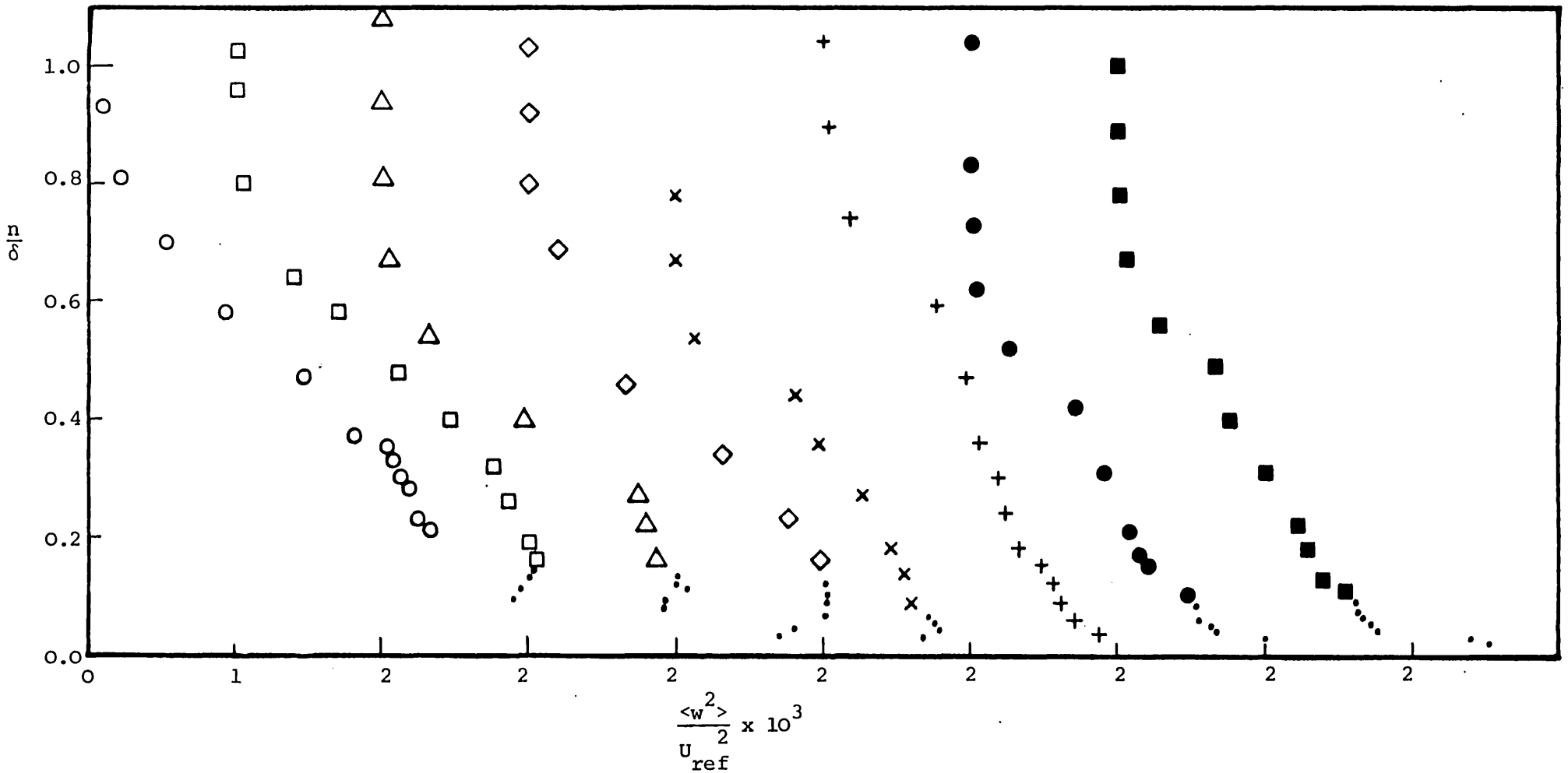


Fig. 3.13 (cont.) (c) Transverse normal stress.

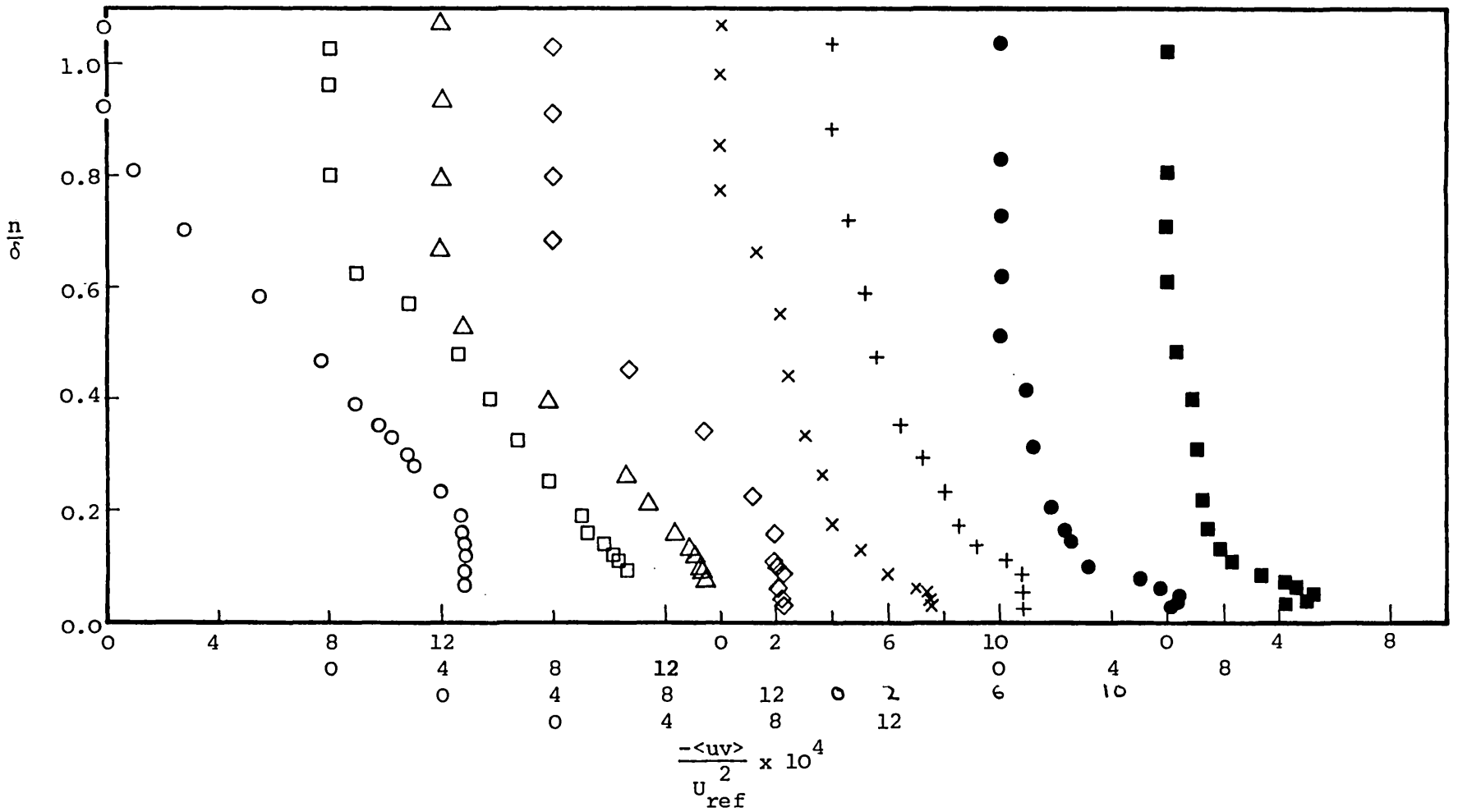


Fig. 3.13 (cont.) (d) Reynolds shear stress.

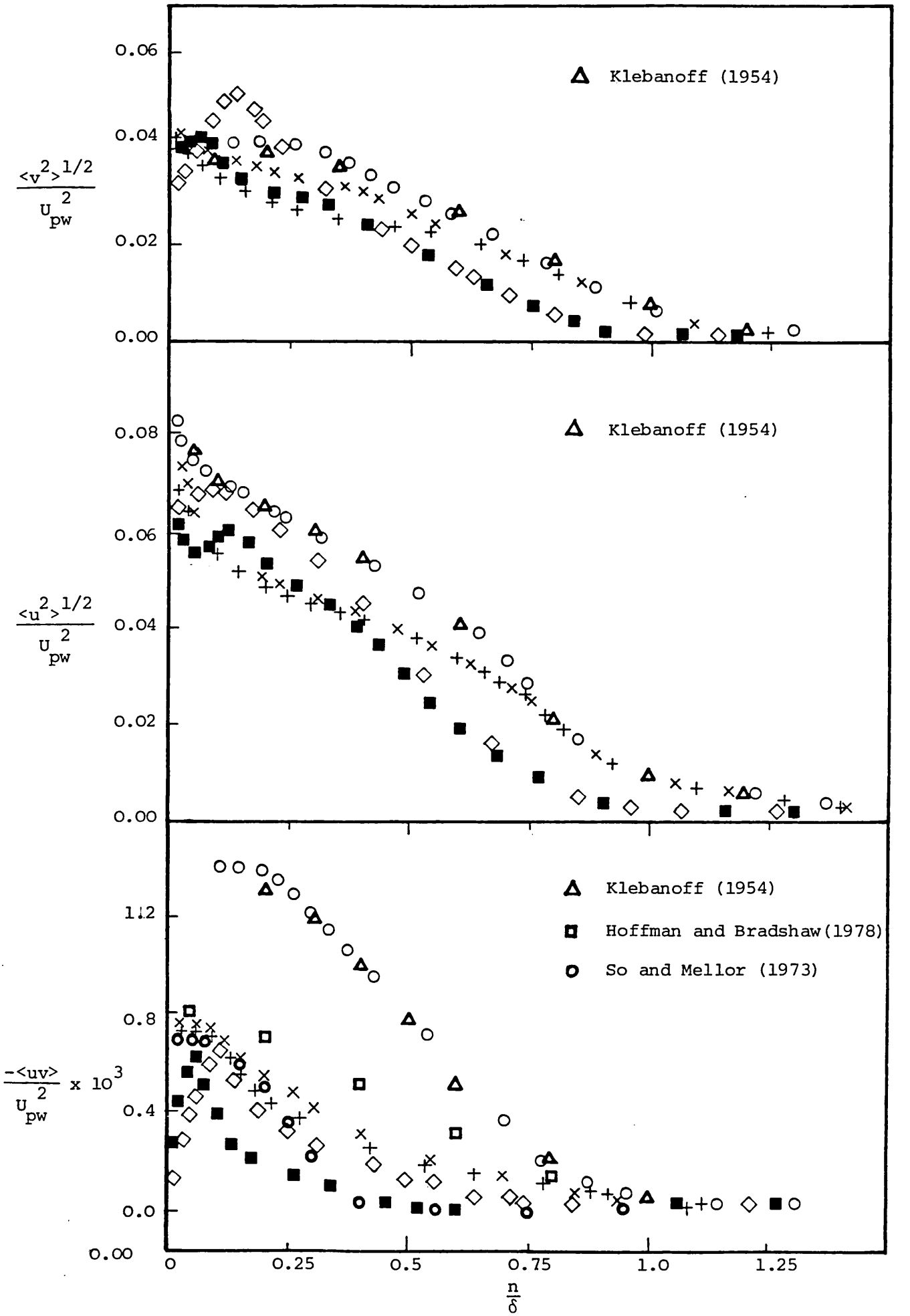


Fig. 3.13 (cont.) (e) Non-dimensionalised with U_{pw}.

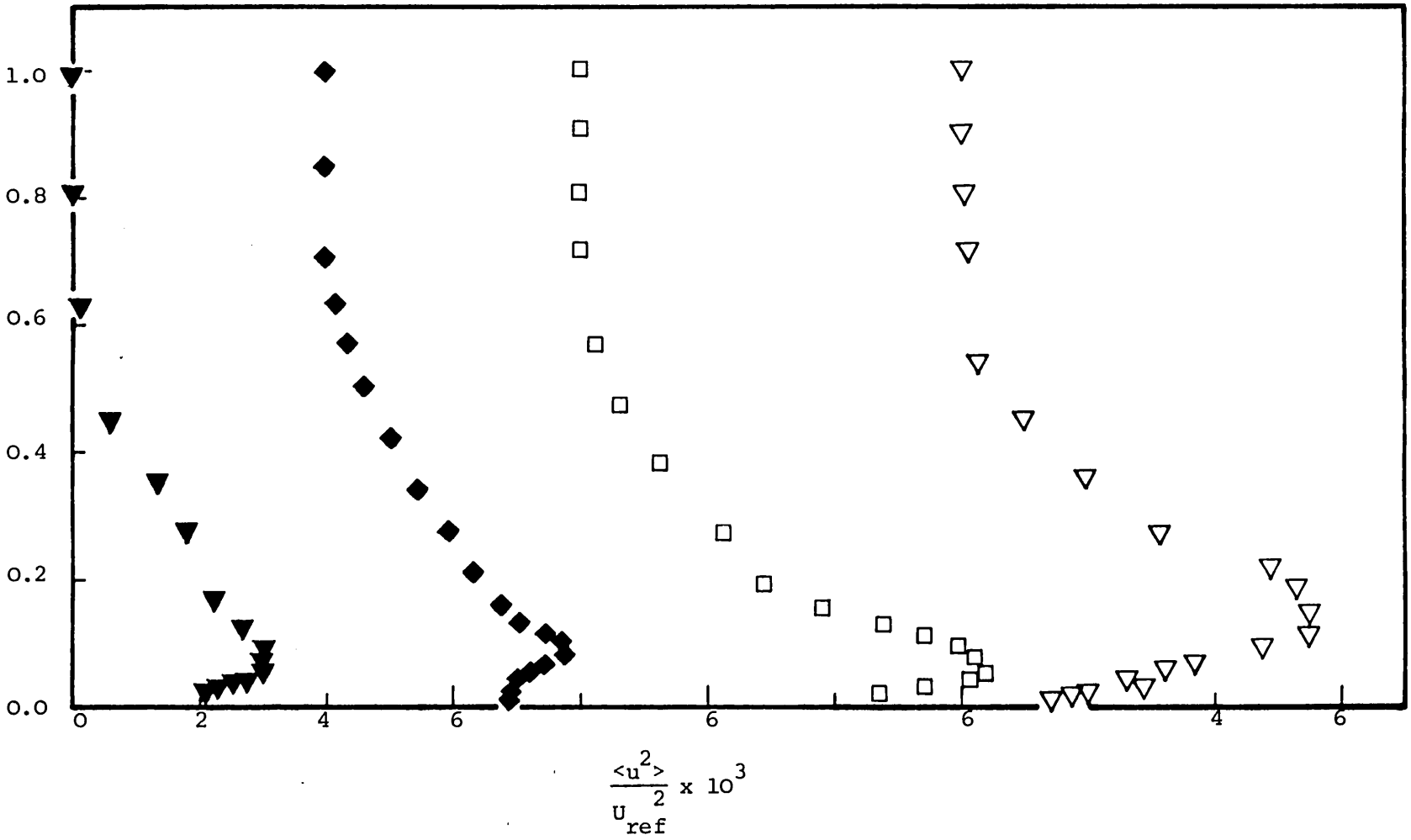


Figure 3.14 Profiles of Reynolds stresses in the vicinity of separation.
(Symbols as in fig. 3.10)

(a) Streamwise normal stress upto detachment.

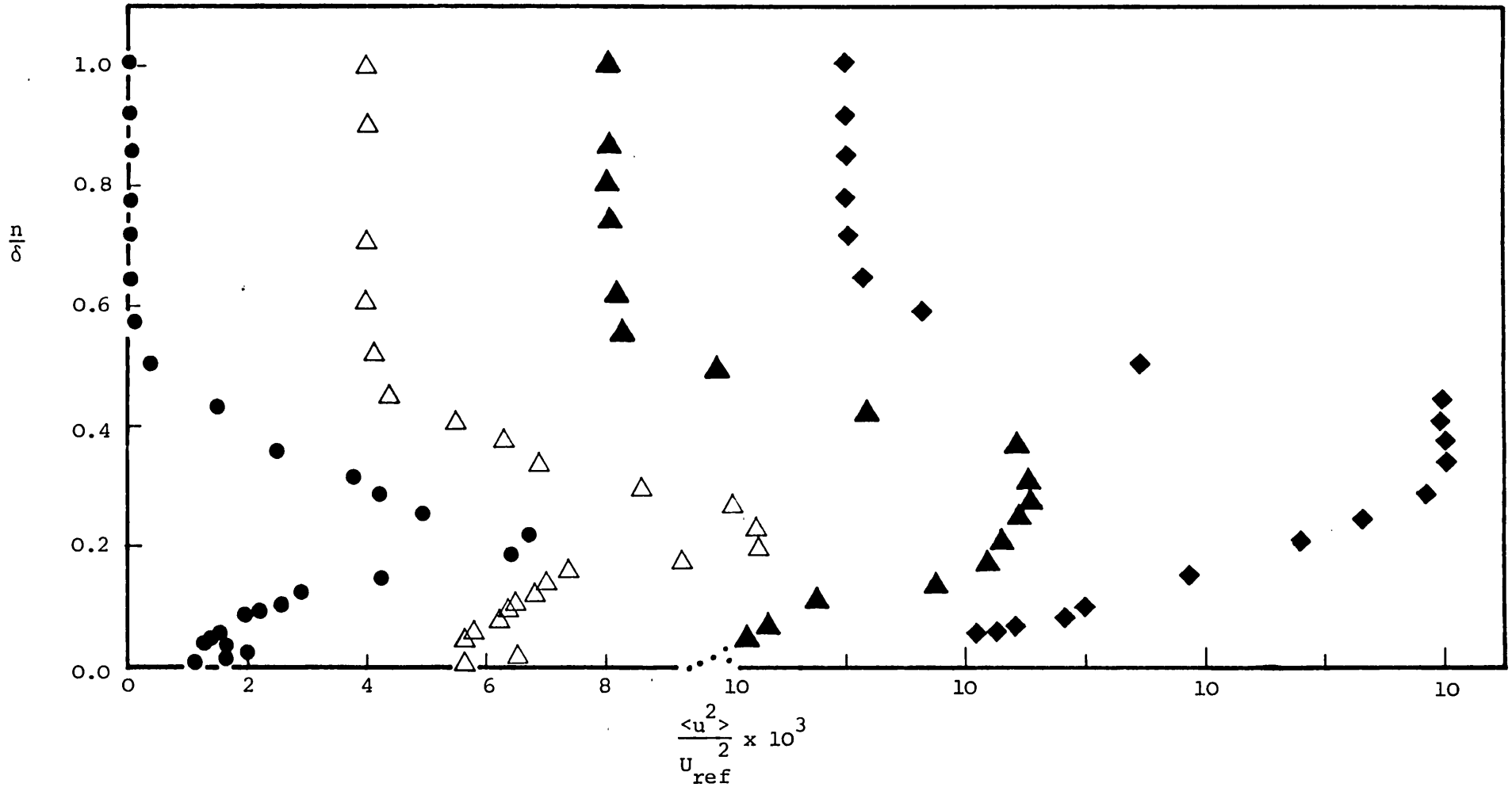


Fig. 3.14 (cont.) (b) Streamwise normal stress downstream of detachment.

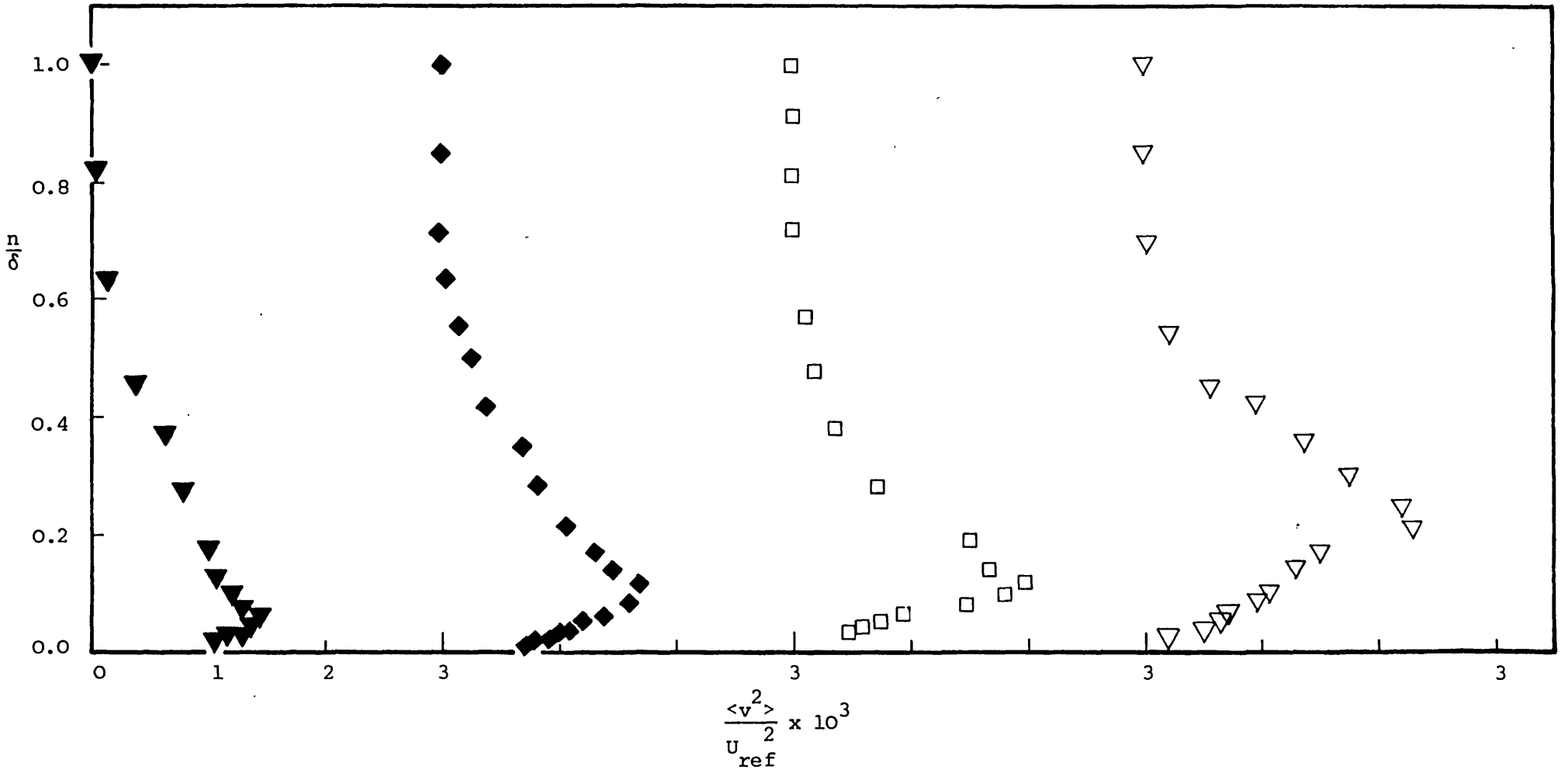


Fig. 3.14 (cont.) (c) Cross-stream normal stress upto detachment.

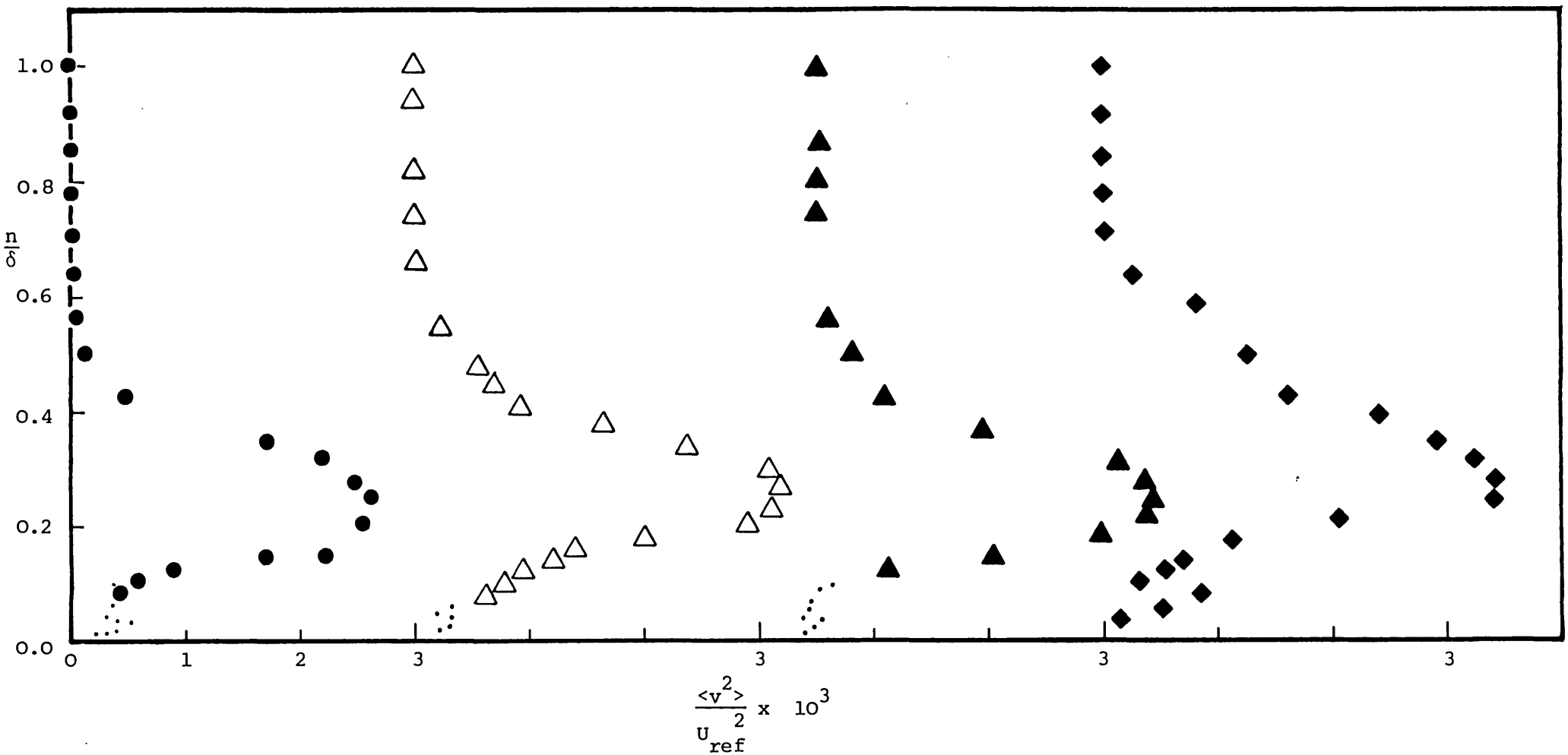


Fig. 3.14 (cont.) (d) Cross-stream normal stress downstream of detachment.

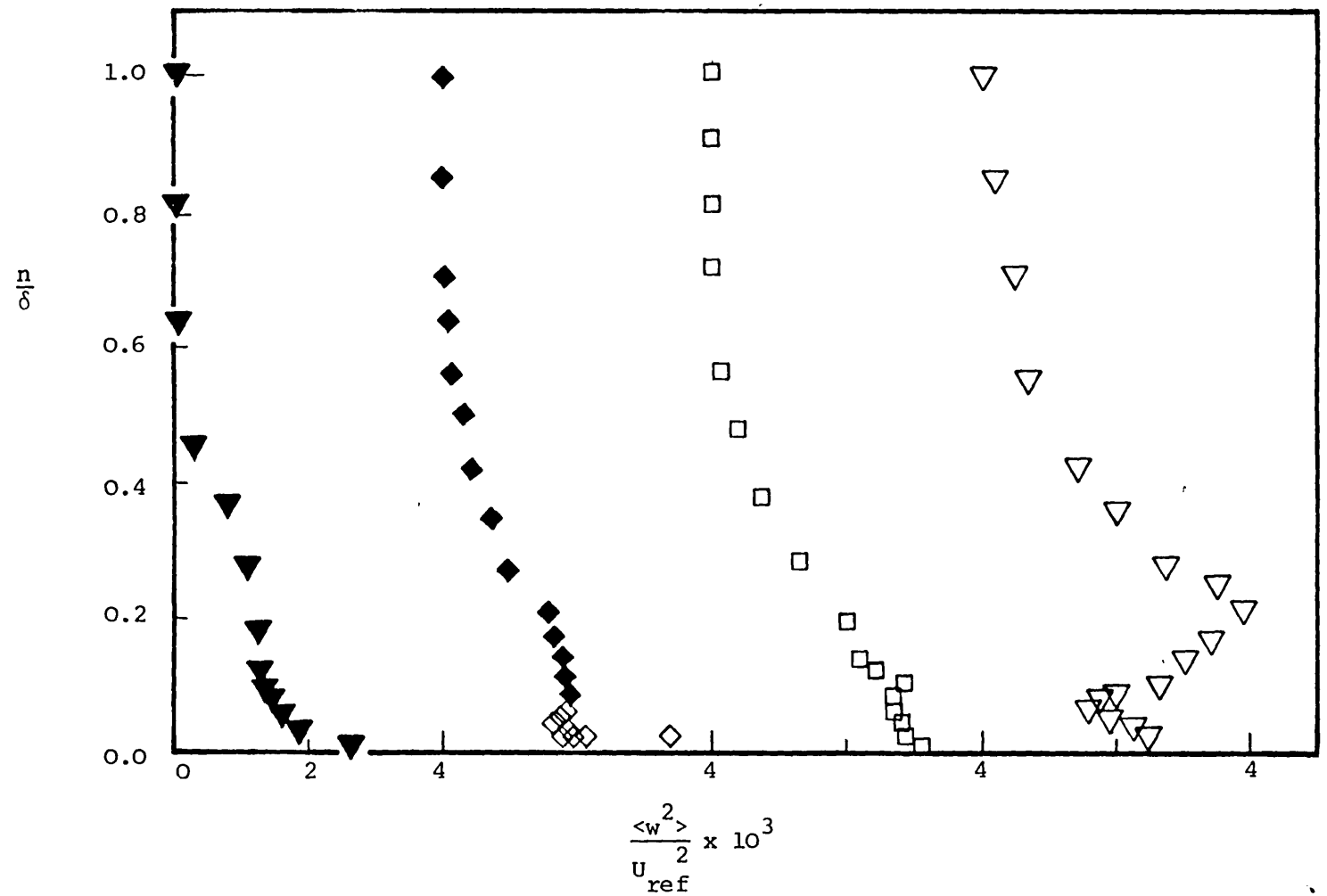


Fig. 3.14 (cont.) (e) Transverse normal stress upto detachment.

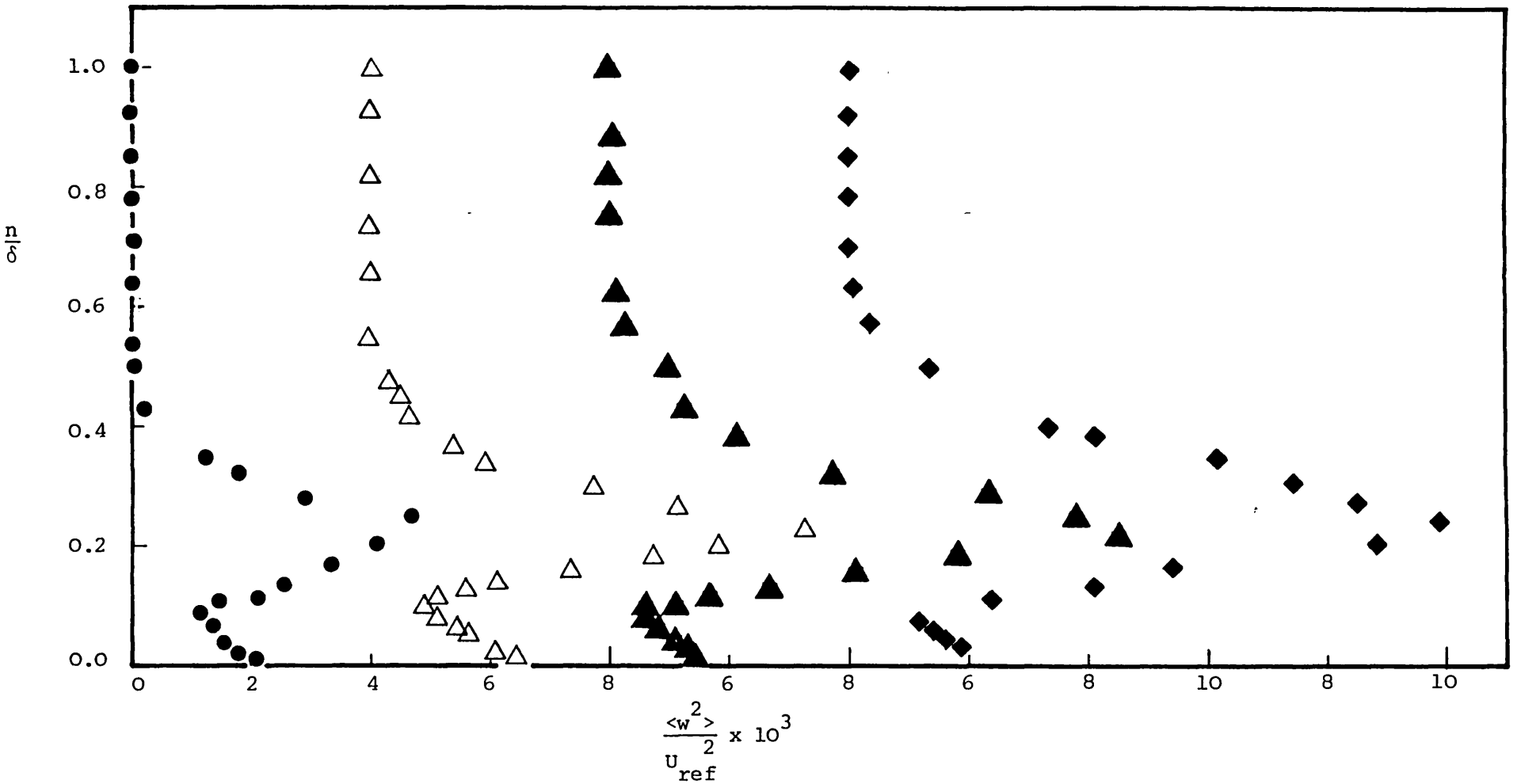


Fig. 3.14 (cont.) (f) Transverse normal stress downstream of detachment.

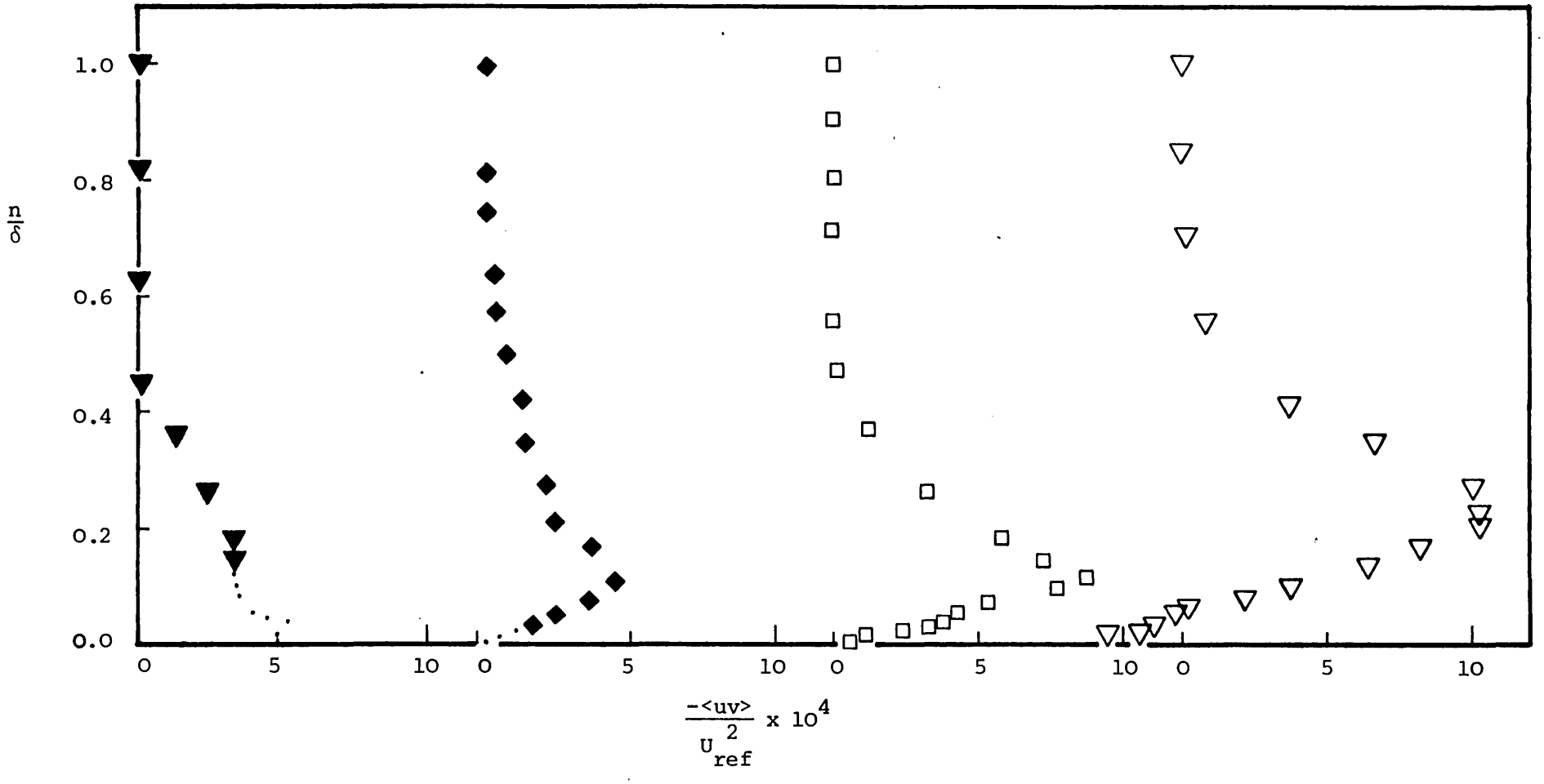


Fig. 3.14 (cont.) (g) Reynolds shear stress upto detachment.

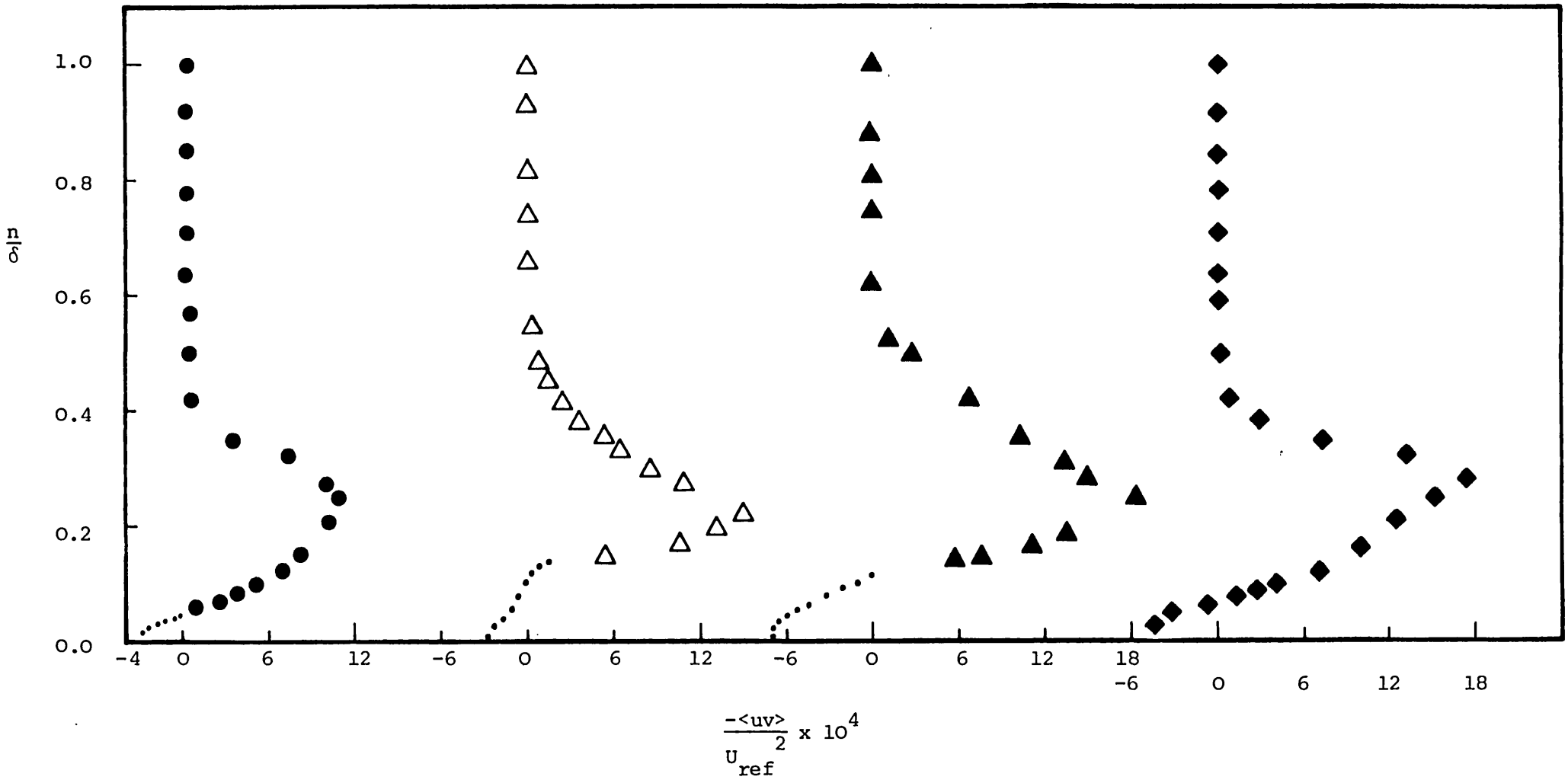


Fig. 3.14 (cont.) (h) Reynolds shear stress downstream of separation.

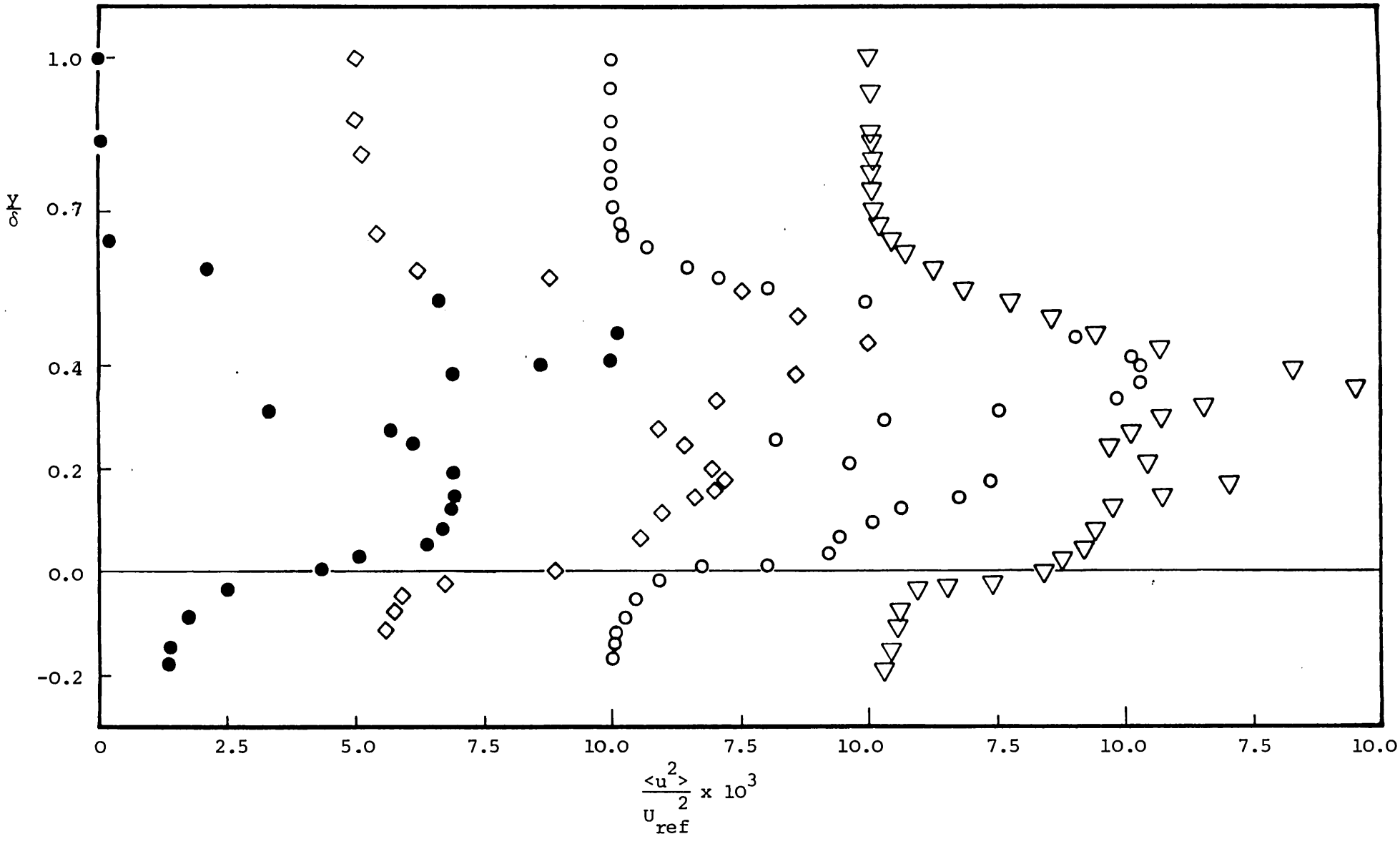


Figure 3.15 Profiles of Reynolds stress in the wake.
(Symbols as in figure 3.10)

(a) Streamwise normal stress in the very-near wake.

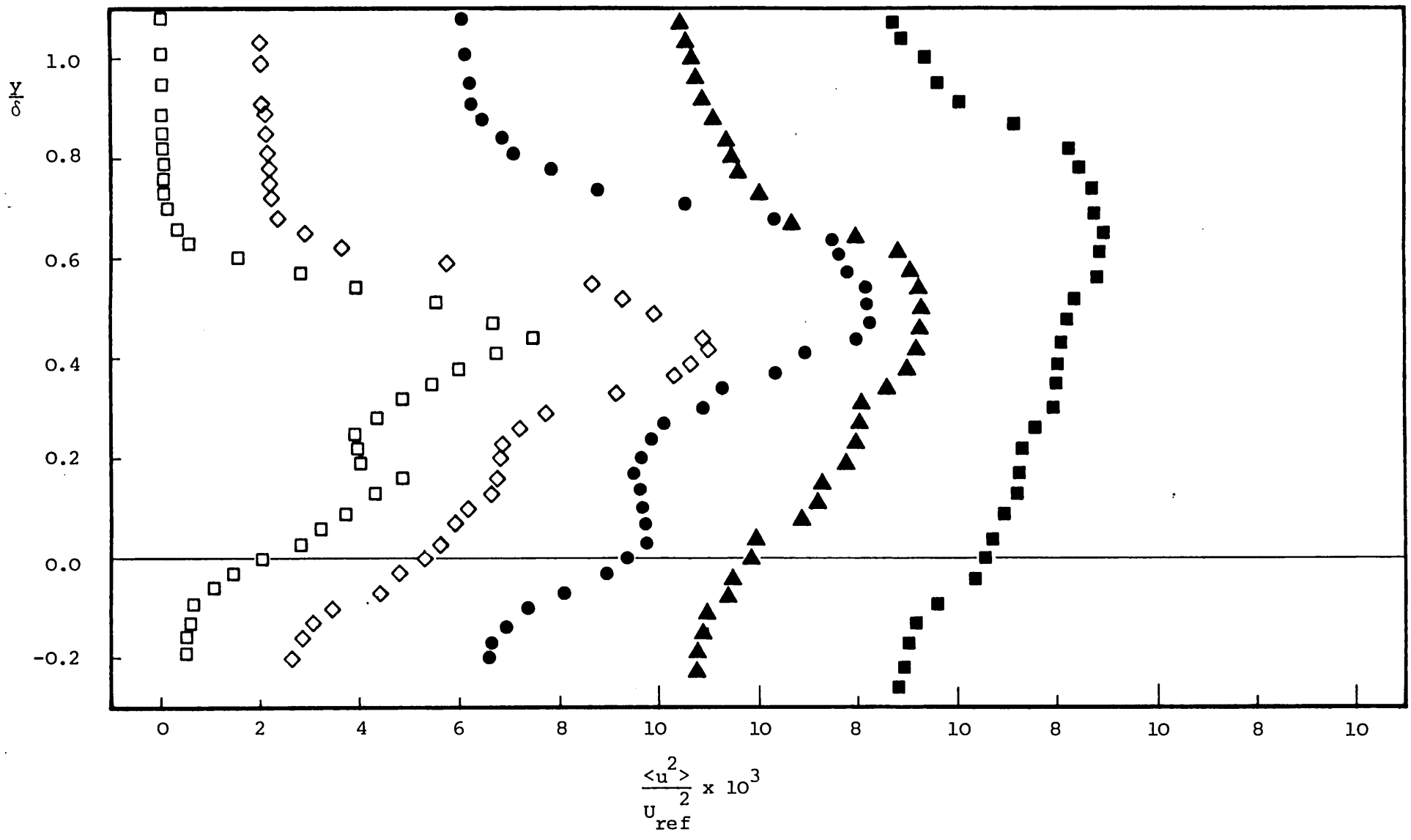


Fig. 3.15 (cont.) (b) Streamwise normal stress in the near and far wake.

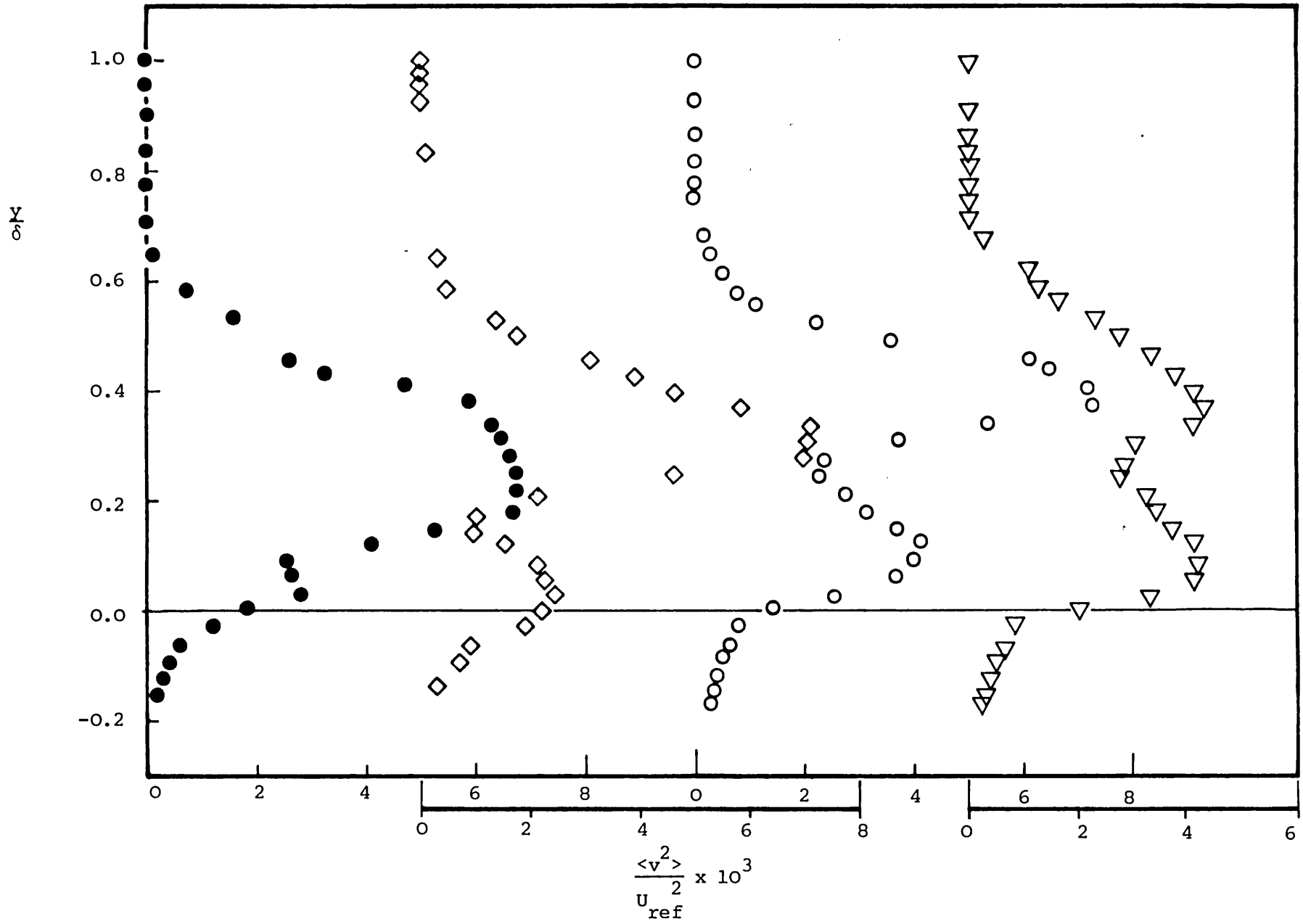


Fig. 3.15 (cont.) (c) Cross-stream normal stress in the very-near wake.

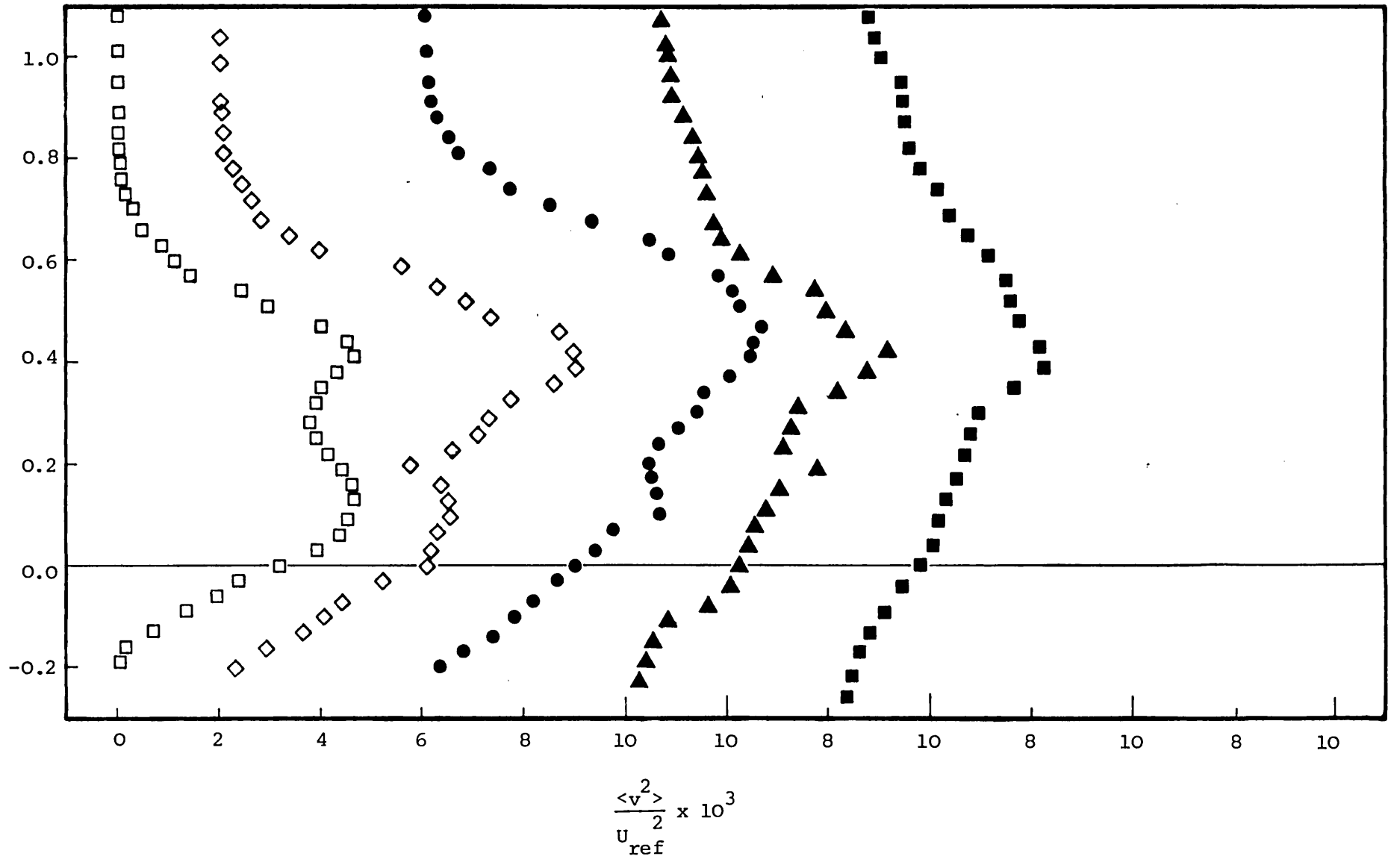


Fig. 3.15 (cont.) (d) Cross-stream normal stress in the near and far wake.

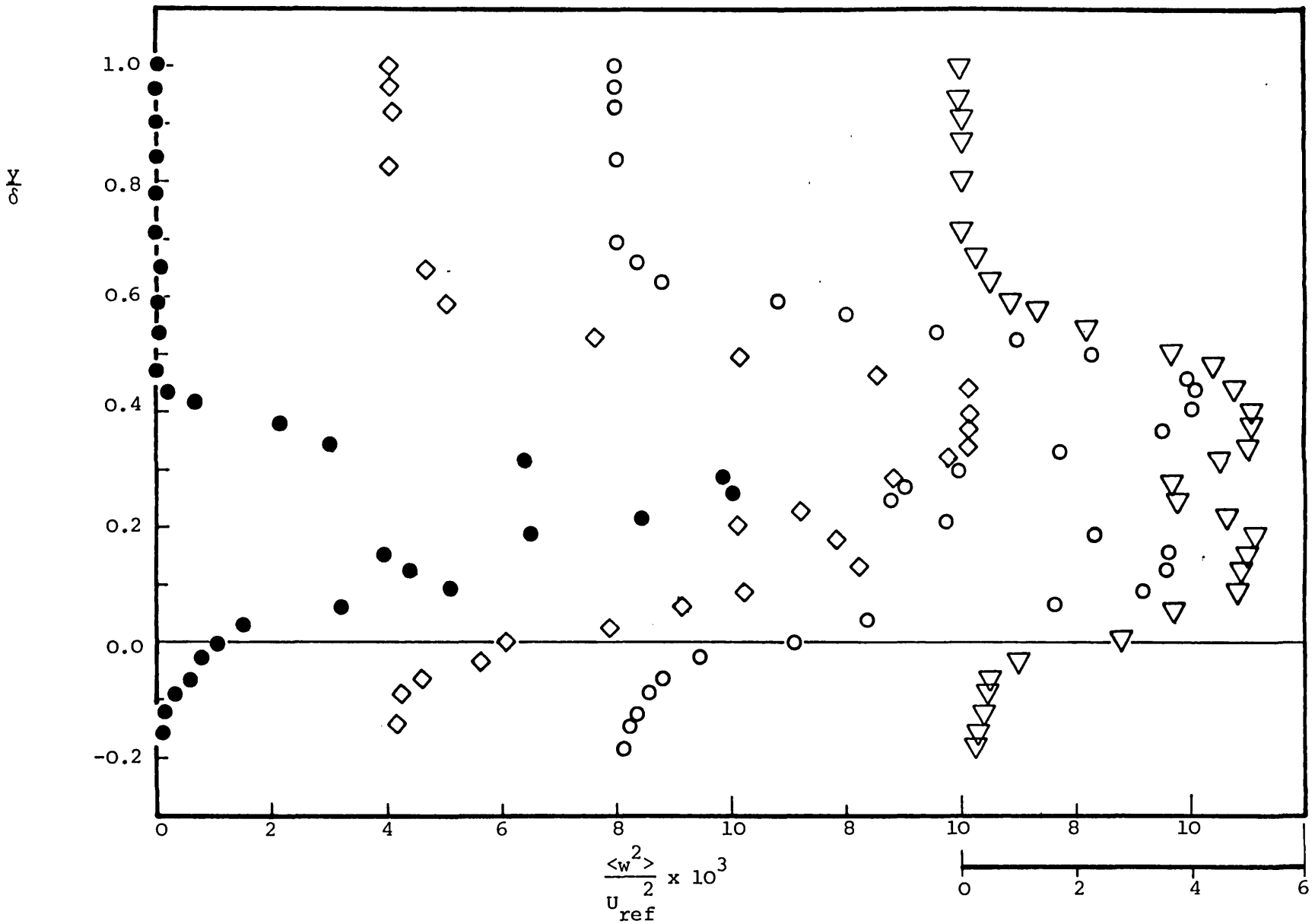


Fig. 3.15 (cont.) (e) Transverse normal stress in the very-near wake.

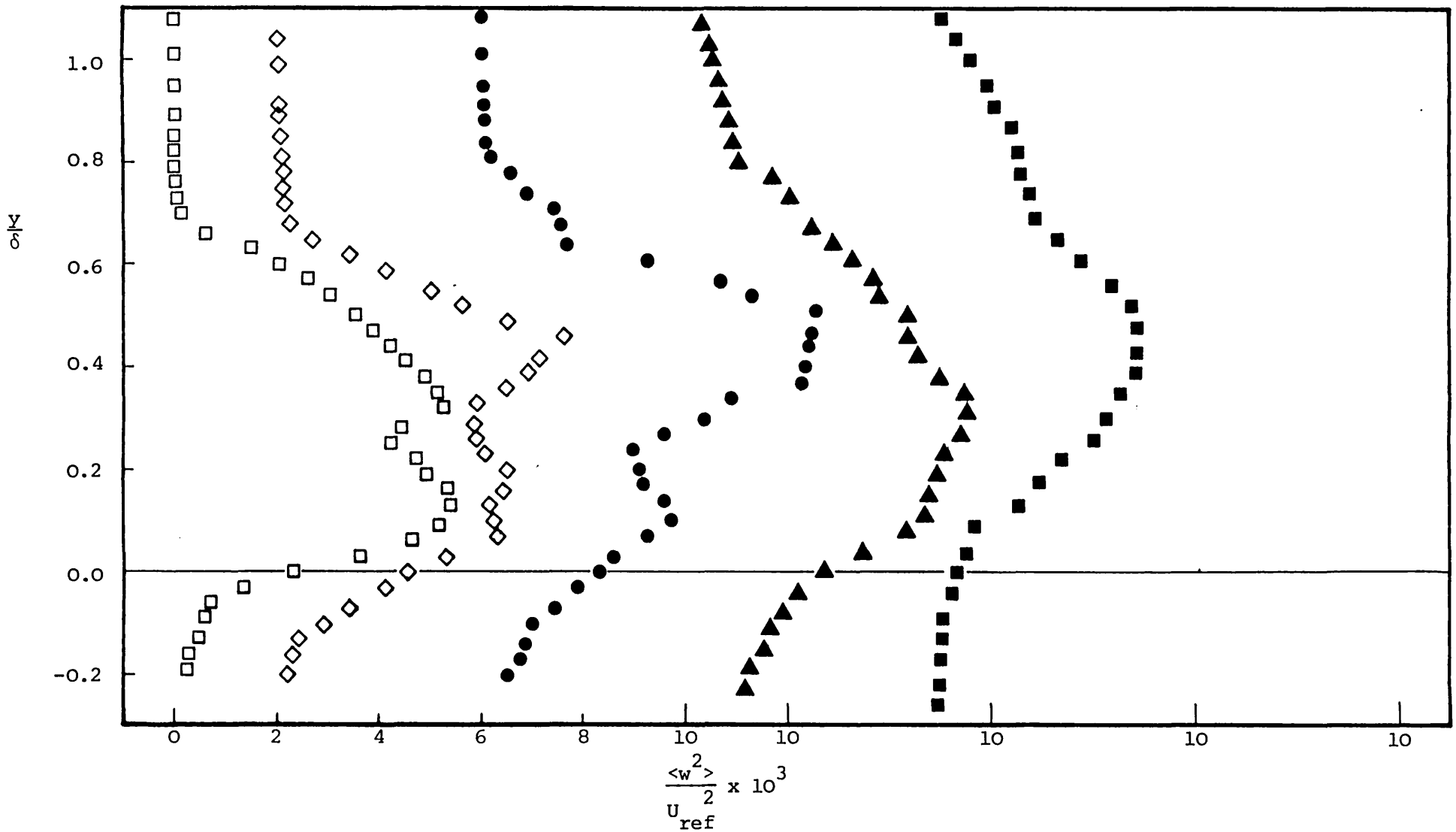


Fig. 3.15 (cont.) (f) Transverse normal stress in the near and far wake.

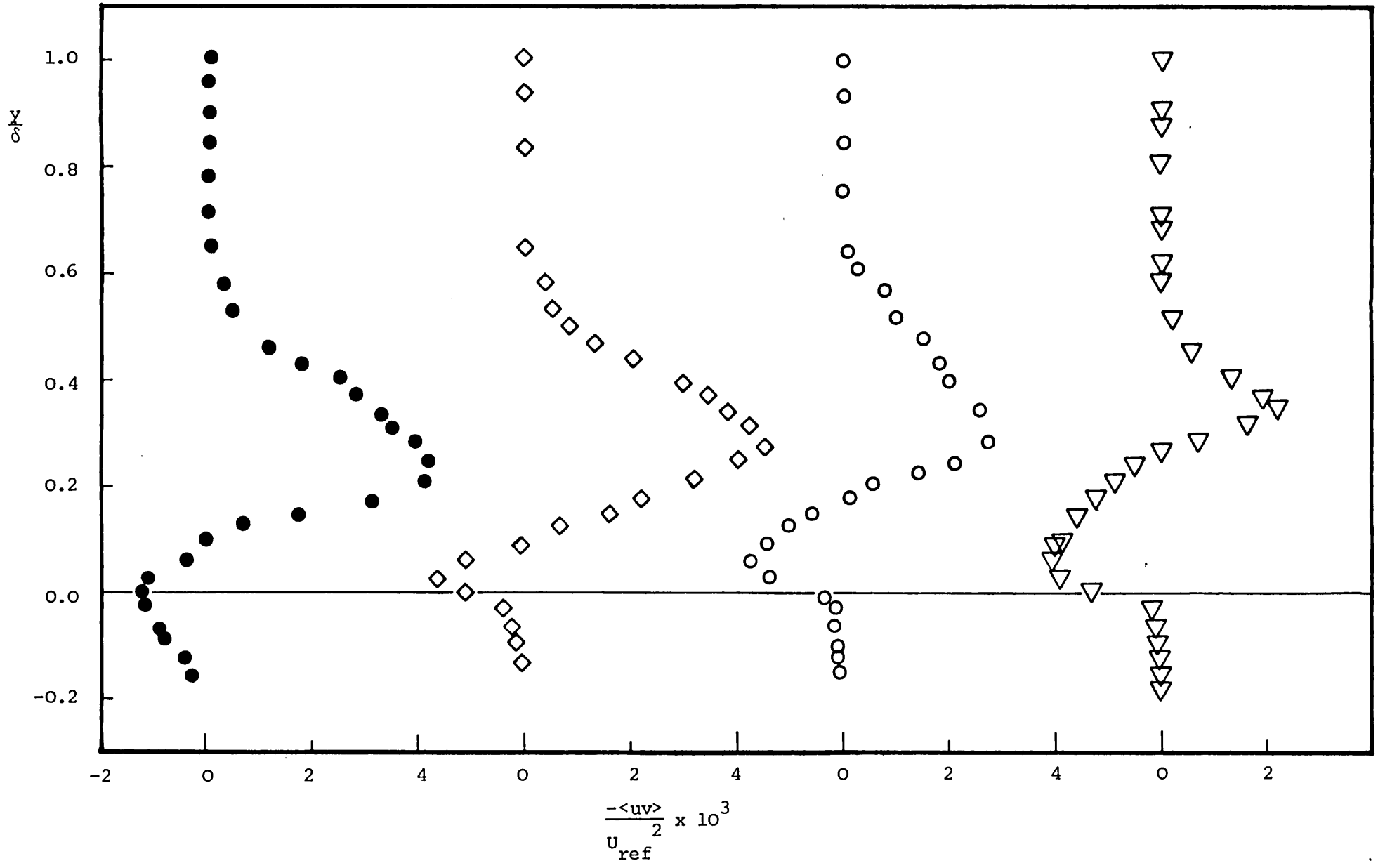


Fig. 3.15 (cont.) (g) Reynolds shear stress in the very-near wake.

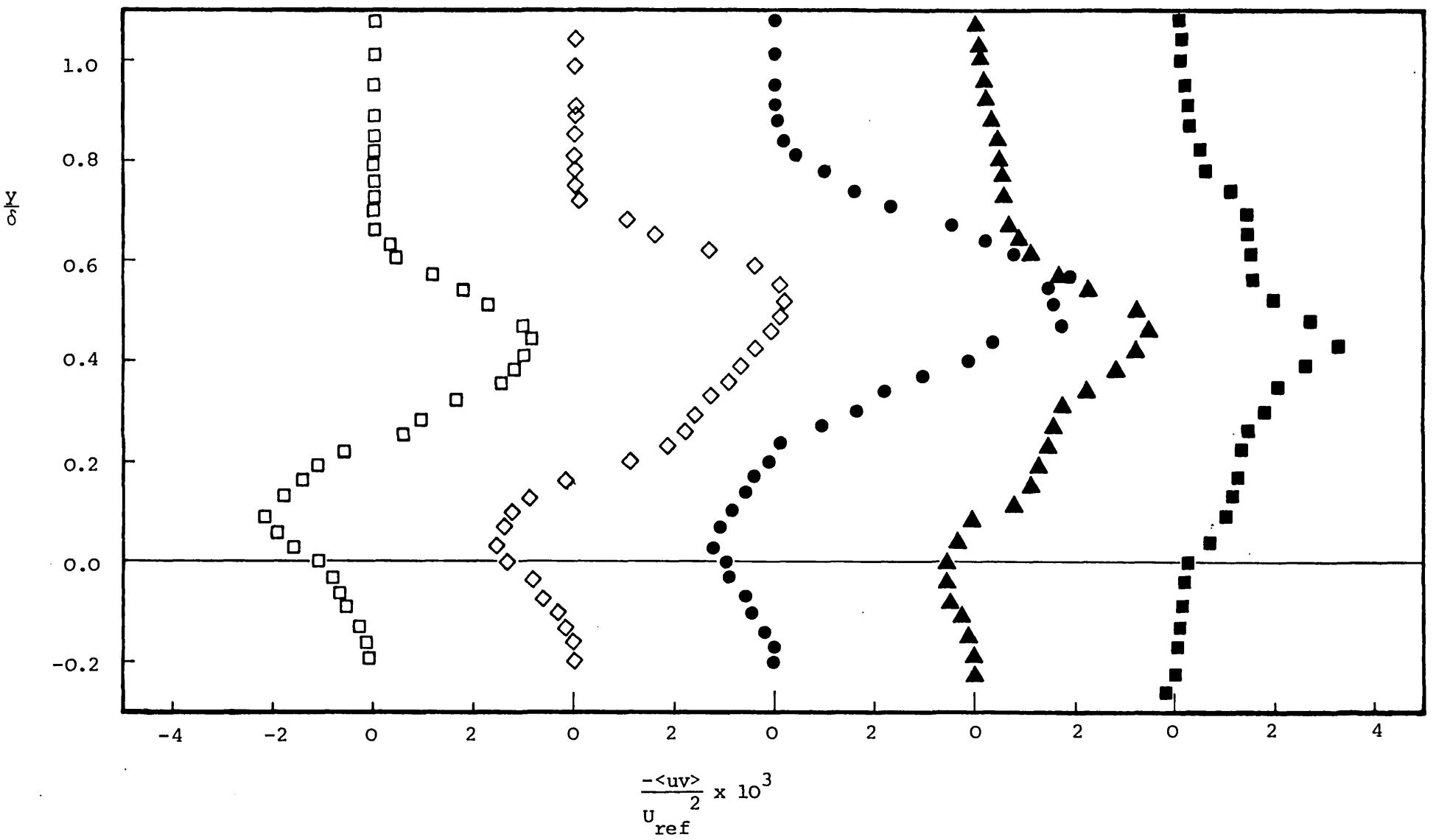


Fig. 3.15 (cont.) (h) Reynolds shear stress in the near and far wake.

CHAPTER 4

CONSERVATION EQUATIONS, TURBULENCE MODELS AND CALCULATION PROCEDURES

This chapter provides a description of the conservation equations used to represent turbulent flows and the solution procedures used to solve them and to obtain the results of chapter 5. The equations have been formulated for steady planar mean flow and are simplified into their potential or inviscid, boundary layer and Reynolds-averaged forms. The boundary conditions and turbulence models required to specify the problem and close the equations, respectively, are described for the calculation procedures which were required to solve the equations for potential, boundary-layer and viscous-recirculating flows.

Section 4.1 describes the transport equations and turbulence models. Each of the three remaining sections deals with a different level of approximation to the instantaneous conservation equations. Section 4.2 describes the solution of the inviscid or potential flow equations to predict the surface pressure distribution and generate orthogonal meshes. In order to determine the influence of viscous effects the boundary layer equations are coupled with the inviscid equations in section 4.3 which describes the methods for solving the boundary layer equations and the viscous-inviscid interaction. This interaction method is expected to predict attached boundary layers and those with small regions of separation. For large regions of separation, however, solution of an elliptic form of the Reynolds-averaged equations is required and section 4.4

describes the procedure which made use of an orthogonal curvilinear mesh. Boundary conditions for solution of the transport equations for mass, momentum and turbulence quantities appear in section 4.5. The chapter closes with summary conclusions and a brief discussion of the evaluation of possible numerical errors.

4.1 Transport Equations and Turbulence Models

It is generally accepted that turbulent flow in simple gases is described by the Navier-Stokes equations which represent the conservative transport of momentum with viscous stresses directly proportional to strain rate. The scale of turbulent motion is sufficiently larger than that of molecular motion to permit the fluid to be treated as a continuum particularly for the subsonic flows considered here. Although the mean flow can in some circumstances be regarded as planar, turbulence is a three-dimensional phenomena and the instantaneous equations which express conservation of mass and momentum in general orthogonal curvilinear co-ordinates are as follows:

Conservation of mass

$$\frac{\partial \rho}{\partial t} + \frac{1}{\ell_1 \ell_2 \ell_3}\left\{\frac{\partial}{\partial \zeta_1}(\ell_2 \ell_3 \rho V_1) + \frac{\partial}{\partial \zeta_2}(\ell_1 \ell_3 \rho V_2) + \frac{\partial}{\partial \zeta_3}(\ell_1 \ell_2 \rho V_3)\right\} = 0 \qquad (4.1)$$

Conservation of momentum - direction 1

$$\frac{\partial(\rho V_1)}{\partial t} + \frac{1}{\ell_1 \ell_2 \ell_3}\left\{\frac{\partial}{\partial \zeta_1}[\ell_2 \ell_3(\rho V_1 V_1 - \tau_{11})] + \frac{\partial}{\partial \zeta_2}[\ell_1 \ell_3(\rho V_1 V_2 - \tau_{12})]\right.$$

$$\left. + \frac{\partial}{\partial \zeta_3}[\ell_1 \ell_2(\rho V_1 V_3 - \tau_{13})]\right\} + \frac{1}{\ell_1}\frac{\partial P}{\partial \zeta_1}$$

(Cont'd)

$$+ \frac{1}{\ell_1 \ell_2} \{ \frac{\partial \ell_1}{\partial \zeta_2} [\rho V_1 V_2 - \tau_{12}] - \frac{\partial \ell_2}{\partial \zeta_1} [\rho V_2 V_2 - \tau_{22}] \}$$

$$+ \frac{1}{\ell_1 \ell_3} \{ \frac{\partial \ell_1}{\partial \zeta_3} [\rho V_1 V_3 - \tau_{13}] - \frac{\partial \ell_3}{\partial \zeta_1} [\rho V_3 V_3 - \tau_{33}] \} = 0 \qquad (4.2)$$

Conservation of momentum - direction 2

$$\frac{\partial (\rho V_2)}{\partial t} + \frac{1}{\ell_1 \ell_2 \ell_3} \{ \frac{\partial}{\partial \zeta_1} [\ell_2 \ell_3 (\rho V_1 V_2 - \tau_{12})] + \frac{\partial}{\partial \zeta_2} [\ell_1 \ell_3 (\rho V_2 V_2 - \tau_{22})]$$

$$+ \frac{\partial}{\partial \zeta_3} [\ell_1 \ell_2 (\rho V_2 V_3 - \tau_{23})] \} + \frac{1}{\ell_2} \frac{\partial P}{\partial \zeta_2}$$

$$+ \frac{1}{\ell_1 \ell_2} \{ \frac{\partial \ell_2}{\partial \zeta_1} [\rho V_1 V_2 - \tau_{12}] - \frac{\partial \ell_1}{\partial \zeta_2} [\rho V_1 V_1 - \tau_{11}] \}$$

$$+ \frac{1}{\ell_1 \ell_3} \{ \frac{\partial \ell_2}{\partial \zeta_3} [\rho V_2 V_3 - \tau_{23}] - \frac{\partial \ell_3}{\partial \zeta_2} [\rho V_3 V_3 - \tau_{33}] = 0 \qquad (4.3)$$

Conservation of momentum - direction 3

$$\frac{\partial (\rho V_3)}{\partial t} + \frac{1}{\ell_1 \ell_2 \ell_3} \{ \frac{\partial}{\partial \zeta_1} [\ell_2 \ell_3 (\rho V_1 V_3 - \tau_{13})] + \frac{\partial}{\partial \zeta_2} [\ell_1 \ell_3 (\rho V_2 V_3 - \tau_{23})]$$

$$+ \frac{\partial}{\partial \zeta_3} [\ell_1 \ell_2 (\rho V_3 V_3 - \tau_{33})] \} + \frac{1}{\ell_3} \frac{\partial P}{\partial \zeta_3}$$

$$+ \frac{1}{\ell_1 \ell_3} \{ \frac{\partial \ell_3}{\partial \zeta_1} [\rho V_1 V_3 - \tau_{13}] - \frac{\partial \ell_1}{\partial \zeta_3} [\rho V_1 V_1 - \tau_{11}] \}$$

$$+ \frac{1}{\ell_2 \ell_3} \{ \frac{\partial \ell_3}{\partial \zeta_2} [\rho V_2 V_3 - \tau_{23}] - \frac{\partial \ell_2}{\partial \zeta_3} [\rho V_2 V_2 - \tau_{22}] \} = 0 \qquad (4.4)$$

The derivation of these equations in general tensor notation is shown by Habib (1980) and, although it is more compact, it is not used here to preserve clarity and to emphasize the last four terms of the momentum equations which are a consequence of co-ordinate curvature. The metric coefficients are defined as:-

$$\ell_i = \left[\left(\frac{\partial x}{\partial \zeta_i}\right)^2 + \left(\frac{\partial y}{\partial \zeta_i}\right)^2 + \left(\frac{\partial z}{\partial \zeta_i}\right)^2\right]^{1/2} \quad \text{for } i = 1, 2, 3 \tag{4.5}$$

relative to the cartesian co-ordinates (x,y,z) so that the incremental length shown on figure 4.1 is given as:-

$$(ds)^2 = (\ell_1 d\zeta_1)^2 + (\ell_2 d\zeta_2)^2 + (\ell_3 d\zeta_3)^2 \tag{4.6}$$

The stress tensor whose components are shown in figure 4.1 are given in general form for incompressible fluid by:-

$$\tau_{ii} = 2\mu \left\{\frac{1}{\ell_i}\frac{\partial V_i}{\partial \zeta_i} + \frac{V_j}{\ell_i \ell_j}\frac{\partial \ell_i}{\partial \zeta_j} + \frac{V_k}{\ell_k \ell_i}\frac{\partial \ell_i}{\partial \zeta_k}\right\} \tag{4.7}$$

and:-

$$\tau_{ij} = \mu\left\{\frac{\ell_j}{\ell_i}\frac{\partial}{\partial \zeta_i}\left(\frac{V_j}{\ell_j}\right) + \frac{\ell_i}{\ell_j}\frac{\partial}{\partial \zeta_j}\left(\frac{V_i}{\ell_i}\right)\right\} \tag{4.8}$$

In most engineering design, the mean flow effects are usually of greatest importance and the instantaneous flow field is of much less direct value. This is fortuitous since present computer limitations do not permit, in general, the microscale of turbulence to be represented in solutions of numerical forms of the equations. The consequencial restriction to the calculation of time-averaged quantities is of considerable advantage since the equations are simplified and solutions can be achieved. Information of the flow behaviour is, however, lost as a result of the averaging

process and is manifest in additional terms that must be determined in order to close the equations. In the case of the momentum equations, the additional terms are second order correlations, the Reynolds stresses, which are apparent when turbulence is important and their representation constitutes the subject of turbulence modelling.

Time-averaging is achieved by dividing the flow variables into mean and fluctuating components according to:-

$$V = \langle V \rangle + v' \tag{4.9}$$

and substituting these into equations 4.1 to 4.4 and time-averaging the resultant equations.

It is expedient to introduce the simplifications appropriate to the present study and to reduce the transport equations 4.1 to 4.4 to the form in which they will be solved. The presented flow is steady, subsonic, planar and at a constant temperature. The density and viscosity are constant and second order correlations involving density fluctuations are presumed negligible. Compressibility and bulk viscosity effects are ignored in the formulation of equations 4.7 and 4.8 and are appropriate assumptions when the Mach number is well below 0.3, as in the present case.

The mean flow in the plane of interest is described in orthogonal curvilinear co-ordinates, as shown on figure 4.2. Two identities which aid the manipulation of the differential equations, and relate the radii of curvature to the metric coefficients, are:-

$$\frac{1}{\ell_1 \ell_2} \frac{\partial \ell_2}{\partial \zeta_1} = \frac{1}{r_2}$$

$$\frac{1}{\ell_1 \ell_2} \frac{\partial \ell_1}{\partial \zeta_2} = \frac{1}{r_1} \,. \tag{4.10}$$

Incorporating the above simplifications in equations 4.1 to 4.4 gives the following conservation equations for incompressible, constant density, planar flow.

Conservation of mass

$$\frac{1}{\ell_1\ell_2\ell_3}\left\{\frac{\partial}{\partial\zeta_1}\left[\ell_2\ell_3\langle\rho\rangle\langle V_1\rangle\right] + \frac{\partial}{\partial\zeta_2}\left[\ell_1\ell_3\langle\rho\rangle\langle V_2\rangle\right]\right\} = 0 \qquad (4.11)$$

Conservation of momentum - direction 1

$$\frac{1}{\ell_1\ell_2\ell_3}\left\{\frac{\partial}{\partial\zeta_1}\left[\ell_2\ell_3(\langle\rho\rangle\langle V_1\rangle\langle V_1\rangle - \langle\tau_{11}\rangle)\right] - \frac{\partial}{\partial\zeta_2}\left[\ell_1\ell_3(\langle\rho\rangle\langle V_1\rangle\langle V_2\rangle - \langle\tau_{12}\rangle)\right]\right\}$$

$$+ \frac{1}{\ell_1}\frac{\partial\langle P\rangle}{\partial\zeta_1} + \frac{1}{r_1}\left[\langle\rho\rangle\langle V_1\rangle\langle V_2\rangle - \langle\tau_{12}\rangle\right] - \frac{1}{r_2}\left[\langle\rho\rangle\langle V_2\rangle\langle V_2\rangle - \langle\tau_{22}\rangle\right] = 0 \qquad (4.12)$$

Conservation of momentum - direction 2

$$\frac{1}{\ell_1\ell_2\ell_3}\left\{\frac{\partial}{\partial\zeta_1}\left[\ell_2\ell_3(\langle\rho\rangle\langle V_2\rangle\langle V_1\rangle - \langle\tau_{12}\rangle)\right] + \frac{\partial}{\partial\zeta_2}\left[\ell_1\ell_3(\langle\rho\rangle\langle V_2\rangle\langle V_2\rangle - \langle\tau_{22}\rangle\right]\right\}$$

$$+ \frac{1}{\ell_2}\frac{\partial\langle P\rangle}{\partial\zeta_2} + \frac{1}{r_2}\left[\langle\rho\rangle\langle V_2\rangle\langle V_1\rangle - \langle\tau_{12}\rangle\right] + \frac{1}{r_1}\left[\langle\rho\rangle\langle V_1\rangle\langle V_1\rangle - \langle\tau_{11}\rangle\right] = 0 \qquad (4.13)$$

The stresses include components of the viscous and Reynolds stress tensors and can be written as:-

$$\langle\tau_{11}\rangle = 2\mu\left[\frac{1}{\ell_1}\frac{\partial\langle V_1\rangle}{\partial\zeta_1} + \frac{\langle V_2\rangle}{r_1}\right] - \langle\rho\rangle\langle v_1'v_1'\rangle \qquad (4.14)$$

$$\langle\tau_{12}\rangle = \mu\left[\frac{1}{\ell_2}\frac{\partial\langle V_1\rangle}{\partial\zeta_2} - \frac{\langle V_1\rangle}{r_1} + \frac{1}{\ell_1}\frac{\partial\langle V_2\rangle}{\partial\zeta_1} - \frac{\langle V_2\rangle}{r_2}\right] - \rho\langle v_1' v_2'\rangle \tag{4.15}$$

$$\langle\tau_{22}\rangle = 2\mu\left[\frac{1}{\ell_2}\frac{\partial\langle V_2\rangle}{\partial\zeta_2} + \frac{\langle V_1\rangle}{r_2}\right] - \langle\rho\rangle\langle v_2' v_2'\rangle \tag{4.16}$$

The conservation equation in the third direction is trivial since, by the definition of two-dimensional mean flow, there is no strain in the ζ_3-direction and:-

$$\tau_{13} = \tau_{23} = 0 \tag{4.17}$$

which implies that:-

$$\langle v_1' v_3'\rangle = \langle v_2' v_3'\rangle = 0 \tag{4.18}$$

The Reynolds stresses, $\langle v_i' v_j'\rangle$, need to be specified or determined in order for the momentum transfer to be completely described in the above equations. Transport equations for these Reynolds stresses can be constructed, as described by Hinze (1975), and the resulting equation in Cartesian co-ordinates with suffix notation used for simplicity, is:-

$$\langle U_\ell\rangle \frac{\partial\langle u_i' u_j'\rangle}{\partial x_\ell} = \Delta_{ij} + P_{ij} + \pi_{ij} + \varepsilon_{ij} \tag{4.19}$$

where the diffusive transport term is:-

$$\Delta_{ij} = \frac{\partial}{\partial x_\ell}\left(\langle u_\ell' u_i' u_j'\rangle\right) + \frac{1}{\langle\rho\rangle}\left(\frac{\partial\langle u_i' p'\rangle}{\partial x_i} + \frac{\partial\langle u_i' p'\rangle}{\partial x_j}\right) \tag{4.20}$$

the stress production term is:-

$$P_{ij} = - \langle u_i' u_\ell' \rangle \frac{\partial \langle U_j \rangle}{\partial x_\ell} - \langle u_j' u_\ell' \rangle \frac{\partial \langle U_i \rangle}{\partial x_\ell} \tag{4.21}$$

the pressure strain term is:-

$$\pi_{ij} = \langle \frac{p'}{\rho} (\frac{\partial u_i'}{\partial x_j} + \frac{\partial u_j'}{\partial x_i}) \rangle \tag{4.22}$$

and the viscous dissipation term is:-

$$\varepsilon_{ij} = - 2 \frac{\mu}{\langle \rho \rangle} \langle \frac{\partial u_i'}{\partial x_\ell} \frac{\partial u_j'}{\partial x_\ell} \rangle \tag{4.23}$$

The reason for expressing the equation in this fashion, and further explanation of the terms, will become apparent once the turbulence model is discussed.

It should be noted that third order correlations appear in this equation and also need to be specified or determined with transport equations in order to close the problem. The transport equation for third order correlations contains fourth order correlations and those for fourth order contain fifth order correlations and so on. The limitless nature of this process suggests that, for engineering problems, some form of approximation is necessary. Further, the number of equations grows rapidly as higher order correlations are considered and experience has shown that reasonable success can be achieved with relatively simple models with the required level of approximation dependent on the nature of the problem. The task of classifying turbulence models is not an objective of the present study and for this the reader is referred to chapter 1 and the texts by Rodi (1980) and Bradshaw, Cebeci and Whitelaw (1981) and Tennekes and Lumley (1972).

The use of zero and one equation models has been explored, for example, by Hegna (1982), Kwon and Pletcher (1983), Bachalo et al (1979),Olson et al (1978), Deiwart (1976) with zero equation models, by Briley and McDonald (1975) and Shamroth and Gibeling (1979) with one equation models, with limited success. The experiences indicated in many historical papers, referred to in the recent reviews by Cebeci, Stewartson and Whitelaw (1983) and Marvin (1982) and in the books of Bradshaw, Cebeci and Whitelaw (1981), Rodi (1980), Fernholz (1979), Launder and Spalding (1972) and Gosman et al (1969), suggest that two equation models represent the minimum level of closure appropriate for separated flows. Two equation models have been used to calculate recirculating flows by many workers, including Cebeci, Khalil and Whitelaw (1977), McGuirk, Taylor and Whitelaw (1981) and many others, and comparisons with zero equations have been favourable (see Johnson et al, 1982, and Sugavanam and Wu, 1982). Marvin (1982) states that Reynolds stress modelling shows little improvement over the two equation approach and the level of improvement is quantified by Habib and Whitelaw (1981) and Habib (1980). The transport of turbulence is important, and particularly so in strong adverse pressure gradients, curved or separated flows, and two-equation or Reynolds stress transport models are generally preferred: they are both used here.

Turbulence Modelling. The two equation model, which involves a turbulent or eddy viscosity assumption, is used to approximate the turbulent transport of momentum in the mean flow equations by replacing the Reynolds stresses with the product of turbulent viscosity, μ_t, and the mean strain rate. The orthogonal curvilinear form of

this approximation (Boussinesq, 1877) may be used to express the Reynolds stresses in terms of mean strain:-

$$-\rho\langle v_i' v_i'\rangle = 2\mu_t \left\{\frac{1}{\ell_i}\frac{\partial\langle V_i\rangle}{\partial\zeta_i} + \frac{\langle V_j\rangle}{\ell_i\ell_j}\frac{\partial\ell_i}{\partial\zeta_j} + \frac{\langle V_k\rangle}{\ell_i\ell_k}\frac{\partial\ell_i}{\partial\zeta_k}\right\} - \frac{2}{3}\rho\, k \qquad (4.24)$$

and

$$-\rho\langle v_i' v_j'\rangle = \mu_t \left\{\frac{\ell_j}{\ell_i}\frac{\partial}{\partial\zeta_i}\left(\frac{\langle V_j\rangle}{\ell_j}\right) + \frac{\ell_i}{\ell_j}\frac{\partial}{\partial\zeta_j}\left(\frac{\langle V_i\rangle}{\ell_i}\right)\right\}$$

The turbulent viscosity, μ_t, is related to the turbulence length scale, ℓ_t, and the velocity scale, v_t, via the relationship (Prandtl, 1925):-

$$\mu_t = \langle\rho\rangle \ell_t v_t \qquad (4.25)$$

Prandtl (1945) also suggested that the velocity scale be represented by the square root of turbulence kinetic energy, which implies local isotropy in the large scale motions,

$$\text{i.e.} \quad v_t = \langle k\rangle^{1/2} = \left[\frac{1}{2}\sum_1^3 \langle v_i' v_i'\rangle\right]^{1/2} \qquad (4.26)$$

The turbulent viscosity is then given by:-

$$\mu_t = \rho\ell_t \langle k\rangle^{1/2} \qquad (4.27)$$

where both k and ℓ_t may be determined from transport equations.

The differential equation for conservation of turbulence kinetic energy may be derived by summing the Reynolds stress equations for $\langle v_i v_i\rangle$. The result for steady planar incompressible flow is:-

$$
\begin{aligned}
I\Big[& \frac{1}{\ell_1\ell_2\ell_3}\Big\{\frac{\partial}{\partial\zeta_1}(\ell_2\ell_3\langle\rho\rangle\langle V_1\rangle\langle k\rangle) + \frac{\partial}{\partial\zeta_2}(\ell_1\ell_3\langle\rho\rangle\langle V_2\rangle\langle k\rangle) \\
II\Big[& + \frac{\partial}{\partial\zeta_1}\Big[\frac{\ell_2\ell_3}{\ell_1}\langle\rho v_1'(k + \frac{p'}{\langle\rho\rangle})\rangle\Big] + \frac{\partial}{\partial\zeta_2}\Big[\frac{\ell_1\ell_3}{\ell_2}\langle\rho v_2'(k + \frac{p'}{\langle\rho\rangle})\rangle\Big|\Big\} \\
III\Big[& + \langle\rho\rangle\langle v_1'v_1'\rangle\Big(\frac{1}{\ell_1}\frac{\partial\langle V_1\rangle}{\partial\zeta_1} + \frac{\langle V_2\rangle}{r_1}\Big) + \langle\rho\rangle\langle v_2'v_2'\rangle\Big(\frac{1}{\ell_2}\frac{\partial\langle V_2\rangle}{\partial\zeta_2} + \frac{\langle V_1\rangle}{r_2}\Big) \\
& + \langle\rho\rangle\langle v_1'v_2'\rangle\Big(\frac{1}{\ell_2}\frac{\partial\langle V_1\rangle}{\partial\zeta_2} - \frac{\langle V_1\rangle}{r_1} + \frac{1}{\ell_1}\frac{\partial\langle V_2\rangle}{\partial\zeta_1} - \frac{\langle V_2\rangle}{r_2}\Big) \\
IV\Big[& - \sum_1^3 \Big\langle\frac{p'}{\ell_i}\frac{\partial v_i'}{\partial\zeta_i}\Big\rangle \\
V\Big[& + \sum_1^3 \mu\Big\langle\Big(\frac{1}{\ell_j}\frac{\partial v_i'}{\partial\zeta_j}\Big)^2\Big\rangle \\
VI\Big[& - \sum_1^3 \frac{1}{\ell_i}\frac{\partial}{\partial\zeta_i}\Big\{\frac{\mu}{\ell_i}\frac{\partial\langle k\rangle}{\partial\zeta_i}\Big\} = 0
\end{aligned}
\tag{4.28}
$$

The meaning of the terms and modelling of the turbulence kinetic energy equation are discussed below and leads to a statement of the modelled form of the k-equation. Term I represents convective transport by the mean motion and requires no further comment.

Term II represents the diffusion by turbulence which is the transport of k by fluctuating velocities. Prandtl (1945), Kolmogorov (1942) and others assume the nature of this term to be diffusive and, neglecting the pressure diffusion part of this term on the basis of measured energy budgets which balance without it (Bradshaw, Cebeci and Whitelaw, 1977), it can therefore be modelled as:-

$$II\left[-\frac{1}{\ell_1\ell_2\ell_3}\{\frac{\partial}{\partial\zeta_1}(\frac{\ell_2\ell_3}{\ell_1}\frac{\mu_t}{\sigma_k}\frac{\partial<k>}{\partial\zeta_1}) + \frac{\partial}{\partial\zeta_2}(\frac{\ell_1\ell_3}{\ell_2}\frac{\mu_t}{\sigma_k}\frac{\partial<k>}{\partial\zeta_2})\}\right. \tag{4.29}$$

where σ_k is a turbulent Prandtl number.

Term III represents the work of deformation of the mean motion by turbulence stresses and acts to generate turbulence kinetic energy. The eddy-viscosity approximation of equations 4.24 is used to replace the Reynolds stresses and the production rate of k is as follows:-

$$G_t = \mu_t\{2(\frac{1}{\ell_1}\frac{\partial<V_1>}{\partial\zeta_1} + \frac{<V_2>}{r_1})^2 + 2(\frac{1}{\ell_2}\frac{\partial<V_2>}{\partial\zeta_2} + \frac{<V_1>}{r_2})^2$$

$$+ (\frac{1}{\ell_2}\frac{\partial<V_1>}{\partial\zeta_2} - \frac{<V_1>}{r_1} + \frac{1}{\ell_1}\frac{\partial<V_2>}{\partial\zeta_1} - \frac{<V_2>}{r_2})^2\} \tag{4.30}$$

Term IV also generates turbulence energy through the interaction of fluctuating pressure and velocities. Little is known about this term although Bray (1974) suggests it is negligible for low Mach number reacting flows; it is neglected here.

Term V represents the viscous dissipation by turbulent motion and is replaced by $<\rho\varepsilon>$, the dissipation rate, ε, being the dependent variable of its own transport equation shown below.

Term VI represents the transport of k by molecular diffusion and may be combined with the modelled form of term II to give:-

$$II + VI\left[-\frac{1}{\ell_1\ell_2\ell_3}\{\frac{\partial}{\partial\zeta_1}(\frac{\ell_2\ell_3}{\ell_1}\frac{\mu_{eff}}{\sigma_k}\frac{\partial<k>}{\partial\zeta_1}) + \frac{\partial}{\partial\zeta_2}(\frac{\ell_1\ell_3}{\ell_2}\frac{\mu_{eff}}{\sigma_k}\frac{\partial<k>}{\partial\zeta_2})\}\right. \tag{4.31}$$

where the effective viscosity, μ_{eff}, is the sum of turbulent and laminar viscosities given by:-

$$\mu_{eff} = \mu_t + \mu \tag{4.32}$$

The final modelled form of the turbulent kinetic energy equation may be written as:

$$\frac{1}{\ell_1\ell_2\ell_3}\{\frac{\partial}{\partial\zeta_1}(\ell_2\ell_3\langle\rho\rangle\langle V_1\rangle\langle k\rangle) + \frac{\partial}{\partial\zeta_2}(\ell_1\ell_3\langle\rho\rangle\langle V_2\rangle\langle k\rangle)$$

$$- \frac{\partial}{\partial\zeta_1}(\frac{\ell_2\ell_3}{\ell_1}\frac{\mu_{eff}}{\sigma_k}\frac{\partial\langle k\rangle}{\partial\zeta_1}) - \frac{\partial}{\partial\zeta_2}(\frac{\ell_1\ell_3}{\ell_2}\frac{\mu_{eff}}{\sigma_k}\frac{\partial\langle k\rangle}{\partial\zeta_2})\}$$

$$- G_t + \langle\rho\rangle\langle\varepsilon\rangle = 0 \tag{4.33}$$

Models have been suggested for the transport of turbulence length scales required by the assumptions of equation 4.27 as a consequence of difficulties in finding generally valid formulae for prescribing or calculating them directly. Length scales in turbulent flow are subject to transport and historic processes in a similar way to the kinetic energy. However, it is not necessary to solve a transport equation directly for the length scale; any combination with k will suffice because the turbulent kinetic energy is known from solution of the k-equation. Several approaches have been tried, see Chambers and Wilcox (1977), Sharma and Patankar (1982) and Coakley (1983), but the most popular has been to solve an equation for the dissipation rate, ε. Experience with various equations has shown that the main difference rests with the representation of diffusion terms in the length scale equation and that near walls the gradient assumption for diffusion with a single constant appears to work better for the dissipation equation than for any other variable (see Launder and Spalding, 1972). The dissipation length scale is then taken as:-

$$\ell_\varepsilon = \langle k\rangle^{3/2}/\langle\varepsilon\rangle \tag{4.34}$$

This length scale represents the eddies which dissipate turbulence kinetic energy and, because of the energy cascade, may be different from the scale of eddies which transfer energy from the mean flow to the turbulence. The length scale in equation 4.27 preferentially represents these large scale motions and thus the turbulence length scale, ℓ_t, is obtained by multiplying the dissipation length scale, ℓ_ε, by an empirical constant according to:-

$$\ell_t = C_\mu \ell_\varepsilon = C_\mu \langle k\rangle^{3/2}/\langle\varepsilon\rangle. \tag{4.35}$$

This equation can also be obtained from dimensional reasoning, see Launder and Spalding (1972). Substitution into equation 4.27 for the turbulent viscosity yields:-

$$\mu_t = \rho C_\mu \langle k\rangle^2/\langle\varepsilon\rangle. \tag{4.36}$$

The differential equation which represents conservation of the dissipation rate is shown below (for the derivation see Watkins, 1977)

$$\text{I}\left[\frac{1}{\ell_1\ell_2\ell_3}\left\{\frac{\partial}{\partial\zeta_1}(\ell_2\ell_3\langle\rho\rangle\langle V_1\rangle\langle\varepsilon\rangle) + \frac{\partial}{\partial\zeta_2}(\ell_1\ell_3\langle\rho\rangle\langle V_2\rangle\langle\varepsilon\rangle)\right.\right.$$

$$\text{II}\left[+ \frac{\partial}{\partial\zeta_1}\left(\frac{\ell_2\ell_3}{\ell_1}\langle\rho\rangle\langle v_1'\varepsilon\rangle\right) + \frac{\partial}{\partial\zeta_2}\left(\frac{\ell_1\ell_3}{\ell_2}\langle\rho\rangle\langle v_2'\varepsilon\rangle\right)\right\}$$

$$\text{III}\left[+ 2\mu\left\{\frac{1}{\ell_\ell}\frac{\partial\langle V_j\rangle}{\partial\zeta_\ell}\frac{1}{\ell_\ell\ell_j}\left\langle\frac{\partial v_i'}{\partial\zeta_\ell}\frac{\partial v_i'}{\partial\zeta_j}\right\rangle + \frac{1}{\ell_\ell}\frac{\partial\langle V_i\rangle}{\partial\zeta_\ell}\frac{1}{\ell_\ell\ell_\ell}\left\langle\frac{\partial v_i'}{\partial\zeta_\ell}\frac{\partial v_i'}{\partial\zeta_\ell}\right\rangle\right\}\right.$$

$$\text{IV}\left[+ 2\mu\left\{\frac{1}{\ell_\ell\ell_\ell\ell_j}\left\langle\frac{\partial v_i'}{\partial\zeta_\ell}\frac{\partial v_j'}{\partial\zeta_\ell}\frac{\partial v_i'}{\partial\zeta_j}\right\rangle + \frac{\mu}{\langle\rho\rangle}\left\langle\left(\frac{1}{\ell_j\ell_\ell}\frac{\partial^2 v_i'}{\partial\zeta_j\partial\zeta_\ell}\right)^2\right\rangle\right\}\right.$$

$$V\left[- 2 \left\langle \frac{\rho\varepsilon}{\ell_j} \frac{\partial v_j'}{\partial \zeta_j} \right\rangle - \frac{\langle\rho\rangle\langle\varepsilon\rangle}{\ell_\ell} \frac{\partial \langle V_\ell \rangle}{\partial \zeta_\ell} \right.$$

$$VI\left[+ \frac{2\mu}{\langle\rho\rangle} \frac{1}{\ell_i} \frac{\partial}{\partial \zeta_i} \left(\frac{1}{\ell_\ell \ell_\ell} \left\langle \frac{\partial v_i'}{\partial \zeta_\ell} \frac{\partial p'}{\partial \zeta_\ell} \right\rangle \right) + \frac{2\mu \partial^2 \langle v_i \rangle}{\ell_\ell \ell_j \partial \zeta_j \partial \zeta_\ell} \left\langle \frac{v_j'}{\ell_\ell} \frac{\partial v_i'}{\partial \zeta_\ell} \right\rangle - S_\mu = 0 \right. \quad (4.37)$$

where S_μ contains terms involving gradients of molecular viscosity, mean density and fluctuating pressure.

Term I represents convective transport of the dissipation rate by mean motion.

Term II describes the transport of ε by the fluctuating velocities and is modelled in the same fashion as the corresponding term in the k-equation.

$$II\left[- \frac{1}{\ell_1 \ell_2 \ell_3} \left\{ \frac{\partial}{\partial \zeta_1} \left(\frac{\ell_2 \ell_3}{\ell_1} \frac{\mu_{eff}}{\sigma_\varepsilon} \frac{\partial \langle\varepsilon\rangle}{\partial \zeta_1} \right) + \frac{\partial}{\partial \zeta_2} \left(\frac{\ell_1 \ell_3}{\ell_2} \frac{\mu_{eff}}{\sigma_\varepsilon} \frac{\partial \langle\varepsilon\rangle}{\partial \zeta_2} \right) \right\} \right. . \quad (4.38)$$

Term III represents the augmentation of the dissipation rate by the mean motion and is modelled after Launder and Spalding (1972) as:-

$$III\left[- C_{\varepsilon 1} \frac{\langle\varepsilon\rangle}{\langle k\rangle} \langle\rho\rangle \langle v_i' v_j' \rangle \frac{1}{\ell_j} \frac{\partial \langle v_i \rangle}{\partial \zeta_j} = - C_{\varepsilon 1} \frac{\langle\rho\rangle\langle\varepsilon\rangle G_t}{\langle k\rangle} \right. . \quad (4.39)$$

Term IV represents the decay of the dissipation rate and is assumed proportional to the dissipation rate itself, divided by the time scale of turbulence, k/ε, after Hanjalic (1970) and the modelled form is:-

$$IV\left[C_{\varepsilon 2} \frac{\langle\rho\rangle\langle\varepsilon\rangle^2}{\langle k\rangle} \right. . \quad (4.40)$$

Term V contains the product of the dissipation rate, and first, the divergence of fluctuating velocity and, secondly, the

divergence of mean velocity. The former is assumed negligible while the latter is zero in incompressible flows.

Terms VI and S_μ are neglected due to the high Reynolds number of the present flow.

The modelled form of the dissipation rate equation is:-

$$\frac{1}{\ell_1\ell_2\ell_3}\{\frac{\partial}{\partial\zeta_1}(\ell_2\ell_3<\rho><V_1><\varepsilon>) + \frac{\partial}{\partial\zeta_2}(\ell_1\ell_3<\rho><V_2><\varepsilon>)$$

$$- \frac{\partial}{\partial\zeta_1}(\frac{\ell_2\ell_3}{\ell_1}\frac{\mu_{eff}}{\sigma_\varepsilon}\frac{\partial<\varepsilon>}{\partial\zeta_1}) - \frac{\partial}{\partial\zeta_2}(\frac{\ell_1\ell_3}{\ell_2}\frac{\mu_{eff}}{\sigma_\varepsilon}\frac{\partial<\varepsilon>}{\partial\zeta_2})\}$$

$$- C_{\varepsilon_1}\frac{<\varepsilon>}{<k>}G_t + C_{\varepsilon_2}<\rho>\frac{<\varepsilon>^2}{<k>} = 0 \quad . \tag{4.41}$$

The values of the empirical constants, C_μ, C_{ε_1}, C_{ε_2}, σ_k and σ_ε are based on extensive examination of free turbulent flows. In grid turbulence the production term, G_t, is zero so that the only constant appearing in the modelled k- and ε-equations is C_{ε_2} whose value is about 1.90 according to Launder, Reece and Rodi (1975) and determined from the measured rate of turbulence decay behind a grid. For local-equilibrium shear layers, where $G_t = <\rho\varepsilon>$, equations 4.30 and 4.36 can be combined to:-

$$C_\mu = (\frac{<v_1'v_2'>}{<k>})^2 \tag{4.42}$$

and measurements of Klebanoff (1954) over plane walls and Meroney and Bradshaw (1975), Muck (1982) and Verriopoulos (1983) over curved walls yields:-

$$\frac{<v_1'v_2'>}{<k>} = 0.3 \tag{4.43}$$

and show that C_μ is 0.09. In the near wall region where the logarithmic law-of-the-wall prevails, production of turbulence energy is approximately balanced by dissipation and convection of dissipation is negligible; the modelled form of the dissipation rate equation reduces to:-

$$C_{\varepsilon 1} = C_{\varepsilon 2} - \frac{\kappa^2}{\sigma_\varepsilon C_\mu^{1/2}} \tag{4.44}$$

where κ is the law-of-the-wall constant and equal to 0.41. This relation fixes $C_{\varepsilon 1}$, or $C_{\varepsilon 2}$, when the other values of the constants are chosen. The diffusion constants σ_k and σ_ε are presumed to be close to unity and they, as well as either $C_{\varepsilon 1}$ or $C_{\varepsilon 2}$, were determined by computer optimization. A sensitivity study has shown that the calculations are most sensitive to the values of $C_{\varepsilon 1}$ or $C_{\varepsilon 2}$; for example Morse (1980) showed that a 5% change in $C_{\varepsilon 1}$ with $C_{\varepsilon 2}$ calculated from equation 4.44 produces a 20% change in the spreading rate of a jet. The value of the constants used by McGuirk et al (1981) in a similar recirculating flow were used for the present study and are given on Table 4.1.

The second type of turbulence model considered here is based on five transport equations for the four non-zero Reynolds $\langle v_1' v_1' \rangle$, $\langle v_2' v_2' \rangle$, $\langle v_3' v_3' \rangle$ and $\langle v_1' v_2' \rangle$ in two-dimensional flow and, ε, the rate of dissipation of turbulence kinetic energy. Equation 4.19 is the exact equation for the transport of Reynolds stresses and modelled forms of the four terms expressed in equations 4.20 - 4.23 are shown below. Cartesian co-ordinates are retained in order to preserve clarity and emphasize the turbulence modelling proposed. The velocities, $\langle U_i \rangle$ and u_i', correspond to the x_i-direction.

The left-hand side of equation 4.19 represents convection of the Reynolds stresses by the mean flow.

The diffusive transport term, Δ_{ij}, is modelled with the simple gradient diffusion proposal of Daly and Harlow (1970). More complex, and theoretically more superior, diffusion models have been developed by Launder et al (1975) but they do not seem to improve predictions (also see Reece, 1977). The modelled form of the diffusion term is

$$\Delta_{ij} = C_t \frac{\partial}{\partial x_\ell} \frac{<k>}{<\varepsilon>} <u_k' u_\ell'> \frac{\partial <u_i' u_j'>}{\partial x_k} \quad . \tag{4.45}$$

All components of the production terms, P_{ij}, are known quantities, obtained from solution of their respective transport equation, and no modelling is required.

The pressure-strain terms, π_{ij}, in the Reynolds stress equation is the only term which does not have a counterpart in the k-equation Recent research has focussed much attention on this term and the approach of Gibson et al (1981) is adopted here. Fluctuating pressures are eliminated from the pressure-strain term via a Poisson equation, as shown by Rotta (1972). As a result, the pressure strain term has two parts which are modelled separately. The first part, $\pi_{ij,1}$, arises from the interaction of fluctuating velocities only and is modelled with Rotta's (1972) proposal as:-

$$\pi_{ij,1} = - C_1 \frac{<\varepsilon>}{<k>}(<u_i' u_j'> - \frac{2}{3} \delta_{ij} <k>) \quad . \tag{4.46}$$

The second part, $\pi_{ij,2}$, arises from the interaction of mean strain and fluctuating velocities and is modelled based on the proposal of Gibson et al (1981) as:-

$$\pi_{ij,2} = - C_2(P_{ij} - \frac{2}{3}\delta_{ij}\frac{G_t}{<\rho>}) \qquad (4.47)$$

where P_{ij} is given by equation 4.21 and G_t is the generation of turbulence kinetic energy, k. Further modelling is required to account for the influence of the wall on the pressure-strain correlation. Gibson et al (1981) suggest that the pressure field is modified close to a rigid wall and that this impedes the transfer of energy from the streamwise direction to that normal to the wall. The observed behaviour of the pressure-strain correlation is generally produced by adding two correction terms which may be written as:-

$$\pi'_{ij,1} = C'_1(\frac{<\varepsilon>}{<k>})(<u'_k u'_m> n_k n_m \delta_{ij} - \frac{2}{3}<u'_k u'_i> n_k n_j$$

$$- \frac{3}{2}<u'_k u'_j> n_k n_i)\ f(\frac{\ell_\varepsilon}{n_i r_i}) \qquad (4.48)$$

$$\pi'_{ij,2} = C'_2(\pi_{km,2} n_k n_m \delta_{ij} - \pi_{ij,2} n_k n_j - \pi_{jk,2} n_k n_i)\ f(\ell_\varepsilon / n_i r_i)$$

where n is the unit vector normal to the surface, r is the position vector, and ℓ_ε is given by equation 4.34. The function, f, is normalised to unity in the near wall region of plane boundary layer flow. The values of the constants, shown on table 4.2, are taken from Gibson et al (1981) which give the values of the stresses levels in a uniform-stress boundary layer to be:-

$$<u'^2_1> = 0.275<k>$$

$$<u'^2_2> = 0.063<k>$$

$$<u'^2_3> = 0.163<k>$$

$$<u'_1 u'_2> = - 0.065<k>$$

Modelling of the dissipation equation remains unchanged from equation 4.41 as do the empirical constants C_μ, $C_{\varepsilon 1}$ and $C_{\varepsilon 2}$ with the exception of the diffusive transport term, term II in equation 4.37, which is modelled after Launder, Reece and Rodi (1975) as:-

$$- C_\varepsilon \frac{\partial}{\partial x_k}\left(\frac{\langle k \rangle}{\langle \varepsilon \rangle} \langle u_k u_\ell \rangle \frac{\partial \langle \varepsilon \rangle}{\partial x_\ell}\right) \tag{4.49}$$

where the value of C_ε is 0.18 suggested by Launder and Morse (1979). The value of C_ε is obtained in local equilibrium flow over a plane wall where convective transport of $\langle \varepsilon \rangle$ is negligible, the energy dissipation rate equals the production rate, and the modelled transport equation for $\langle \varepsilon \rangle$, which combines 4.41 and 4.49, is simplified to (Launder, Reece and Rodi, 1975):-

$$C_\varepsilon = (C_{\varepsilon 1} - C_{\varepsilon 2}) U_\tau^6 / \kappa^2 \langle u_2'^2 \rangle \langle k \rangle^2 \tag{4.50}$$

where U_τ is the wall friction velocity, $(\tau_w/\rho)^{1/2}$.

At high Reynolds numbers, the turbulence is assumed to be locally isotropic and, as a consequence, equal energy is dissipated from each Reynolds normal stress component, $\langle u_i u_i \rangle$. Since there is no dissipation term in the Reynolds shear stress equations, the dissipation term of equation 4.23 is modelled as:-

$$\varepsilon_{ij} = \frac{2}{3} \langle \varepsilon \rangle \delta_{ij} \tag{4.51}$$

where $\langle \varepsilon \rangle$ is obtained by solution of its transport equation 4.41.

This concludes the discussion of turbulence modelling and transport equations. The calculation procedures and associated boundary conditions are discussed in the following sections.

4.2 Inviscid Flow Calculation Procedure

Solutions of the inviscid flow equations for fluid motion are required for two reasons: the surface pressure can be obtained with and without interaction with a boundary layer calculation and, secondly, an orthogonal mesh may be obtained upon which the Reynolds-averaged equations 4.11-13 can be solved.

It may be anticipated that fairly close agreement with observation would be obtained from a theory which, as a simplifying assumption, neglects viscosity. After all, most engineering flows have very high Reynolds numbers and solutions obtained for infinite Reynolds number, thus inviscid, are likely to give a plausible description of the flow patterns. Inviscid flow patterns are initially useful to designers because they give the force and momentum distributions over lifting bodies with unseparated flow and, as is the objective of good design, they have minimum drag forces. It is also not surprising that inviscid theory is in violent disagreement with the observed flow pattern near solid walls where the inviscid flow predicts slip and experiments show that viscous forces are predominant with no slip at the wall (Schlichting, 1968). In section 4.3, viscous effects will be introduced into the solution and their influence on the inviscid flow will be discussed in more detail but presently it is sufficient to indicate that, in order to solve the boundary layer equations, the pressure field is required and can be obtained from solution of the inviscid flow equations.

A comment on using the solution of inviscid flow equations to provide orthogonal meshes is in order, although justification for solving the Navier-Stokes equations in general orthogonal

curvilinear co-ordinates, will be left until section 4.4. One of the intermediate results of an inviscid flow calculation can be the location of the streamlines and velocity potential lines which, by their definition, are orthogonal to one another. Provided that the boundaries for the potential flow solution are coincident with those for solution of the Navier-Stokes equations, then only geometric quantities such as the metric coefficients defined in equation 4.5, are required to formulate the complete equations. Gosman and Johns (1979) argue that it is preferable when solving the inviscid flow equations in finite-difference form to use inverse techniques, which locate the intersections of iso-stream function and iso-potential lines and to avoid the need for the interpolation necessary when the values of stream function and velocity potential are calculated at discrete locations. With the inverse method the geometric quantities associated with the grid are calculated more accurately and the wall pressure can be obtained from one-dimensional momentum and continuity equations which treat the streamlines as slip boundaries.

In the case of two-dimensional, incompressible, inviscid flows, the system of equations 4.11 - 4.13, transformed into Cartesian co-ordinates, is:-

$$\frac{\partial \langle U_i \rangle}{\partial x_i} = 0 \tag{4.52}$$

$$\text{and } \langle U_j \rangle \frac{\partial \langle U_i \rangle}{\partial x_j} + \frac{1}{\langle \rho \rangle} \frac{\partial \langle P \rangle}{\partial x_i} = 0 \tag{4.53}$$

summed for $j = 1, 2$. Examination of the rotational vector, which is zero or constant in inviscid flows, leads to the definition of mean

vorticity:-

$$\Omega = \frac{\partial \langle U_i \rangle}{\partial x_j} - \frac{\partial \langle U_j \rangle}{\partial x_i} \quad . \tag{4.54}$$

Pressure can be eliminated from the calculation by differentiating equation 4.53 for i = 1 with respect to x_2 and for i = 2 with respect to x_1 and, combining with the definition of vorticity above, the vorticity equation for potential flows results:-

$$\langle U_1 \rangle \frac{\partial \Omega}{\partial x_1} + \langle U_2 \rangle \frac{\partial \Omega}{\partial x_2} = 0 \quad . \tag{4.55}$$

This represents convection of vorticity only and shows that the level of vorticity will remain unchanged within the fluid. This is also the necessary condition for the existence of a mean velocity potential, ϕ, which can be defined as:-

$$\langle U_i \rangle = - \frac{\partial \phi}{\partial x_i} \quad . \tag{4.56}$$

Substituting into the continuity equation 4.52 gives the Laplace equation of the velocity potential as:-

$$\frac{\partial^2 \phi}{\partial x_i^2} = 0 \qquad \text{(Summed for i = 1, 2).} \tag{4.57}$$

A mean streamline may be defined as a hypothetical line across which there is no net transport and a mean stream function can be defined with a constant value along a streamline, thus:-

$$\langle U_1 \rangle = - \frac{\partial \psi}{\partial x_2}; \langle U_2 \rangle = \frac{\partial \psi}{\partial x_1} \quad . \tag{4.58}$$

Substitution of these definitions into equation 4.54 gives another Laplace equation for the stream function which is:-

$$\frac{\partial^2 \psi}{\partial x_i^2} = 0 \qquad \text{(Summed for i = 1, 2).} \tag{4.59}$$

Inverse forms of the two Laplace equations (4.57 and 4.59) were obtained by Winslow (1967) using the following general transformations:

$$\frac{\partial \phi}{\partial x_1} = -\frac{1}{J}\frac{\partial x_2}{\partial \psi};\ \frac{\partial \psi}{\partial x_1} = \frac{1}{J}\frac{\partial x_2}{\partial \phi}$$

$$\frac{\partial \phi}{\partial x_2} = -\frac{1}{J}\frac{\partial x_1}{\partial \psi};\ \frac{\partial \psi}{\partial x_2} = -\frac{1}{J}\frac{\partial x_1}{\partial \psi} \tag{4.60}$$

where the Jacobian, J, of the transformation is given by:

$$J = \frac{\partial x_1}{\partial \psi}\frac{\partial x_2}{\partial \phi} - \frac{\partial x_1}{\partial \phi}\frac{\partial x_2}{\partial \psi} \ . \tag{4.61}$$

The inverse equation can be solved numerically to locate the intersections of iso-ϕ and iso-ψ lines and is given by:-

$$\alpha \frac{\partial^2 x_i}{\partial \phi^2} - \beta \frac{\partial^2 x_i}{\partial \phi \partial \psi} + \gamma \frac{\partial^2 x_i}{\partial \psi^2} = 0 \quad \text{for i = 1, 2} \tag{4.62}$$

where α, β, and γ are the quadratic functions:-

$$\alpha = \left(\frac{\partial x_1}{\partial \psi}\right)^2 + \left(\frac{\partial x_2}{\partial \psi}\right)^2$$

$$\beta = \frac{\partial x_1}{\partial \phi}\frac{\partial x_1}{\partial \psi} + \frac{\partial x_2}{\partial \phi}\frac{\partial x_2}{\partial \phi} \tag{4.63}$$

$$\gamma = \left(\frac{\partial x_1}{\partial \phi}\right)^2 + \left(\frac{\partial x_2}{\partial \phi}\right)^2 \ .$$

It should be noted that orthogonality requires satisfaction of the Cauchy-Riemann equations which under general transformation become:

$$\frac{\partial x_1}{\partial \psi} = a \frac{\partial x_2}{\partial \phi} \; ; \; \frac{\partial x_2}{\partial \psi} = - a \frac{\partial x_1}{\partial \phi} \tag{4.64}$$

where a is the aspect ratio given by:-

$$a = \frac{\gamma}{\alpha} \tag{4.65}$$

For an orthogonal mesh which locates the streamlines and velocity potential lines, equation 4.62 reduces to

$$\frac{\partial^2 x_i}{\partial \phi^2} + a^2 \frac{\partial^2 x_i}{\partial \psi^2} = 0 \quad \text{for } i = 1, 2 \tag{4.66}$$

and the central term in equation 4.62 is eliminated by the orthogonality condition. Pope (1978) used the above equation to generate curvilinear-orthogonal meshes and calculated the aspect ratio by integrating the Cauchy-Reimann equations along the boundary in the transformed plane; a was obtained at the boundaries from:-

$$a = - \frac{1}{\Delta x_2} \int \frac{\partial x_1}{\partial \phi} \, d\psi \; ; \; \phi = \text{constant}$$

$$a = \frac{1}{\Delta x_1} \frac{\partial x_2}{\partial \phi} \, d\psi \quad ; \; \phi = \text{constant} \; . \tag{4.67}$$

Boundary conditions are required for both x_1 and x_2 at all locations on the perimeter and these were determined from a specification of the boundary locii and by integrating the appropriate conjugate function represented by equation 4.64.

Gosman and Johns (1979) expressed equation 4.62 in finite-difference form using second-order central differences with constant step sizes, although the values of $\Delta\psi$ and $\Delta\phi$ were different, and it may be written as:-

$$\frac{\alpha(x_{i,E} - 2x_{i,P} + x_{i,W})}{\Delta\phi^2} + \frac{\gamma(x_{i,N} - 2x_{i,P} + x_{i,S})}{\Delta\psi^2} = 0 \qquad (4.68)$$

for i = 1, 2 and where the five point numerical scheme (NSEW-P) is shown on figure 4.3. The associated functions α and γ can also be expressed with central differences as:-

$$\alpha = \left(\frac{x_{1,N} - x_{1,S}}{2\Delta\psi}\right)^2 + \left(\frac{x_{2,N} - x_{2,S}}{2\Delta\psi}\right)^2 \qquad (4.69)$$

$$\gamma = \left(\frac{x_{1,E} - x_{1,W}}{2\Delta\phi}\right)^2 + \left(\frac{x_{2,E} - x_{2,W}}{2\Delta\phi}\right)^2 \qquad (4.70)$$

The result is two equations, for x_1 and x_2, which may be expressed in the form:-

$$A_P x_{i,P} = A_N x_{i,N} + A_S x_{i,S} + A_E x_{i,E} + A_W x_{i,W} \qquad (4.71)$$

where the coefficients are given by:-

$$A_N = A_S = (x_{1,E} - x_{1,W})^2 + (x_{2,E} - x_{2,W})^2$$

$$A_E = A_W = (x_{1,N} - x_{1,S})^2 + (x_{2,E} - x_{2,W})^2 \,. \qquad (4.72)$$

Boundary conditions are required to insure that co-ordinate intersections on the boundaries are linked to internal grid points with a line that is orthogonal to the boundaries. The boundary must first be specified in the physical plane with a discrete or continuous specification of its co-ordinates. Initially the co-ordinates of the intersections on the boundary are guessed and are then refined through subsequent iteration with the equations expressing the orthogonality condition. The method requires that the boundary is continuous and explicit in the first derivative over the region of interest. This is arranged when the boundary is specified as discrete points by fitting

a piecewise parametric cubic polynomial to the boundary co-ordinates (see McConaloque, 1970). Gosman and Johns (1979) propose an iterative equation to express the boundary condition. A straight line is passed from the boundary point through the first internal grid node which for a near horizontal boundary may be expressed by the equations:-

$$x_2^I = -\left(\frac{dy}{dx}\right)_B^{-1} x_1^I + C_* \qquad (4.73)$$

$$x_2^B = -\left(\frac{dy}{dx}\right)_B^{-1} x_1^B + C_*$$

where the superscripts I and B refer to the internal and boundary nodes respectively. The slope of the boundary curve $\left(\frac{dy}{dx}\right)_B$ is obtained with first order accuracy from the equation:-

$$\left(\frac{dy}{dx}\right)_B = \frac{x_2^E - x_2^B}{x_1^E - x_1^B} \qquad (4.74)$$

where the superscript E indicates the estimated value from the previous iteration. After eliminating C_* and x_2^B, the corrected location for the co-ordinate point x_1^B is obtained from the iterative formula:-

$$x_1^B = \frac{x_2^E - x_2^I - x_1^E\left(\frac{dy}{dx}\right)_B - x^I\left(\frac{dy}{dx}\right)_B^{-1}}{-\left(\frac{dy}{dx}\right)_B - \left(\frac{dy}{dx}\right)_B^{-1}} \qquad (4.75)$$

The value of x_1^B may be updated several times with this equation before the internal nodes are recalculated through equation 4.71. Once the value of x_1^B is found the curve describing the boundary is used to obtain x_2^B. For a near vertical boundary, equation 4.75 is replaced by a similar one for x_2^B obtained in an analogous fashion.

The equation set given by 4.71 and 4.75 for x_1 and x_2-directions, is solved in an iterative manner due to non-linearity of the equations and the boundary treatment formulated above. The solution is obtained by forcing the finite-difference equations into tridiagonal matrix form with off-diagonal terms, relating neighbouring lines, evaluated from their most updated values and temporarily taken as known. Equation 4.71 is solved alternatively for the values of x_1 and x_2 and repeatedly along constant-ϕ and constant-ψ lines using the tridiagonal matrix algorithm (TDMA) described by Patankar (1980). After each iteration the values of x_1^B and x_2^B are revised using the boundary value formulae of equation 4.75. The solution for locating the intersections is judged to have converged when the maximum error at any internal intersection is less than 2^o from orthogonal which normally takes between 200 and 400 iterations.

Once the iso-ψ and iso-ϕ lines have been located the geometric parameters for the conservation equations, for example 4.11 - 13, can be obtained in orthogonal co-ordinates. The calculation of the cell-face areas, volumes, arc lengths, radii of curvature and local angle with respect to the x-axis which is coincident with the tunnel roof in the present flow, are based on piecewise parametric cubic polynomial curves fitted between the intersections. The calculation of these geometric parameters with piecewise cubic polynomials has proved to provide an accurate method for the necessary integrations as follows.

The cell face areas of the control volume boundaries, Δa, are computed from the relation:

$$\Delta a_{sw/nw} = \int_{sw}^{nw} \{(\frac{dx_1}{ds})^2 + (\frac{dx_2}{ds})^2\}^{1/2} ds \tag{4.76}$$

where the slash (/) indicates from the point sw to nw on figure 4.4. The arc lengths, ΔS, are obtained in the same fashion at the mid-points of the scalar cells. The values of $\frac{dx_i}{ds}$ are evaluated from the cubic polynomial equation and the limits of integration are defined by the mesh intersections.

The volume, $\forall$, of the region surrounding the point, P, is obtained using the divergence theorem to give the surface integral:-

$$\forall = \S x_2 \frac{dx_1}{ds} ds \tag{4.77}$$

where § indicates integration around the perimeter, sw/nw/ne/se/sw.

The radii of curvature, r_1 and r_2, shown in figure 4.2 are given by equations 4.10 with the ζ_1 and ζ_2-directions coincident with the ψ and ϕ-directions. The metric coefficients, ℓ_1 and ℓ_2, are defined in equation 4.5 and obtained from:-

$$\begin{aligned}(\ell_1)_{sw/nw} &= \{(\frac{\partial x_1}{\partial \psi})^2 + (\frac{\partial x_2}{\partial \psi})^2\}^{1/2}_{sw/nw} = (\frac{\Delta S}{\Delta \psi})_{sw/nw} \\ (\ell_2)_{sw/se} &= \{(\frac{\partial x_1}{\partial \phi}) + (\frac{\partial x_2}{\partial \phi})\}^{1/2}_{sw/se} = (\frac{\Delta S}{\Delta \phi})_{sw/se}\end{aligned} \tag{4.78}$$

Here $\Delta S_{sw/nw}$ corresponds to the arc length along the $\zeta_1 \equiv \psi$ line between grid points sw and nw. The above formula allows a relatively simple finite-difference approximation to be obtained for the mean radii of curvature in terms of the arc lengths joining the vertices which are:-

$$r_1 = \frac{(\Delta S)^2}{\Delta S_{se/ne} - \Delta S_{sw/nw}}$$

$$r_2 = \frac{(\Delta S)^2}{\Delta S_{nw/ne} - \Delta S_{sw/se}} \qquad (4.79)$$

where:-

$$(\Delta S)^2 = \frac{1}{4}(\Delta S_{se/ne} + \Delta S_{sw/nw})(\Delta S_{nw/ne} + \Delta S_{sw/nw}) \qquad (4.80)$$

The pressure field is obtained by solving the one-dimensional streamwise momentum equation for inviscid flow on the orthogonal mesh where the mesh lines ζ_1 and ζ_2 are coincident with iso-ψ and iso-ϕ lines, respectively, which were predicted by the solution of the Laplace equations. The inviscid streamwise momentum equation is obtained by simplifying equation 4.12 to:-

$$\frac{1}{\ell_1 \ell_2 \ell_3}\left\{\frac{\partial}{\partial \zeta_1}(\ell_2 \ell_3 <\rho><V_1><V_1>)\right\} = \frac{1}{\ell_1}\frac{\partial <P>}{\partial \zeta_1} \quad . \qquad (4.81)$$

This equation implies that the velocity, and thus transport, is zero in the direction normal to the streamlines. The ζ_2-direction must be coincident with ϕ-lines and the pressure and potential velocity are obtained by solving 4.81 along stream channels enclosed by the predicted ψ-lines and coincident with the ζ_1-direction as shown on figure 4.4.

Equation 4.81 is manipulated into its finite-difference form using the finite volume approach of Gosman et al (1969) whereby each term of the differential equation is integrated over the surrounding control volume as follows:-

$$\int_{\zeta_{2,n}}^{2,s} \ell_2\ell_3 <\rho><V_1><V_1>\}_W^E \, d\zeta_2$$

$$+ \int_{\forall_P} \ell_1\ell_2\ell_3(S_{V_1})d\zeta_1 \, d\zeta_2 = 0 \qquad (4.82)$$

where the V_1-momentum source term is given by:-

$$S_{V_1} = - \frac{1}{\ell_1} \frac{\partial <P>}{\partial \zeta_1} \, . \qquad (4.83)$$

It is necessary to use upwind differencing because there is no diffusion and is discussed further in Section 4.4. Equation 4.82 can be recast in the following form:-

$$(A_P - S_P)<V_{1,w}> = A_E<V_{1,ww}> + A_W<V_{1,e}> + S_u \qquad (4.84)$$

where

$$A_P = A_E + A_W$$

$$A_W = \max \left[0, \frac{1}{2} <\rho> a_{wsw/wnw}(V_{1,ww} + V_{1,w})\right] \qquad (4.85)$$

$$A_E = \max \left[0, - \frac{1}{2} <\rho> a_{s/n}(V_{1,w} + V_{1,e})\right]$$

$$S_P = 0$$

and $S_u = \Delta a_{sw/nw}(P_P - P_W)$

for the staggered grid shown on figure 4.4*. The values of Δa and $\forall_P$ are calculated from equations 4.76 and 4.77, respectively.

*The slash (/) means from point to point; s to n for example.

The continuity equation may be written as:-

$$\frac{1}{\ell_1\ell_2\ell_3}\{\frac{\partial}{\partial\zeta_1}(\ell_2\ell_3<\rho><V_1>)\} = 0 \tag{4.86}$$

and, after integration, becomes:-

$$\int_{\tau_{2,s}}^{\tau_{2,n}}\{\ell_2\ell_3<\rho><V_1>\}_w^e\, d\zeta_2 = <\rho>\{\Delta a_{se/ne}<V_{1,e}> - \Delta a_{sw/nw}<V_{1,w}>\} = 0 \tag{4.87}$$

This equation can be reformulated in terms of the pressure correction equation, expressed by Chorin (1968), in the following manner. First postulate that the incorrect pressure, P*, was used to calculate the velocity field, V_1^*, and that the result does not satisfy continuity. Postulate secondly that the real pressure and velocity fields, P and V_1, can be obtained by adding a correction to the existing values according to:-

$$\begin{aligned} P &= P^* + P' \\ V_1 &= V_1^* + V_1' \end{aligned} \tag{4.88}$$

where the prime (') denotes the value of the correction. A velocity correction equation may be written as:-

$$V_{1,w}' = \frac{\Delta a_{sw/nw}}{A_p}(P_W' - P_P') = d_w(P_W' - P_P') \tag{4.89}$$

where A_p is given by equation 4.85. Substitute the above equations into 4.87 and the result is the pressure correction equation:-

$$<\rho>\{\Delta a_{se/ne}<V_{1,e}^*> + d_e(P_P' - P_E') - \Delta a_{sw/nw}<V_{1,w}^*> + d_w(P_P' - P_W')\} = 0 \tag{4.90}$$

which can be recast into the form

$$A_P P'_P = A_E P'_E + A_W P'_W + S \tag{4.91}$$

where

$$A_P = A_E + A_W$$

$$A_E = \langle \rho \rangle d_e \Delta a_{se/ne} \tag{4.92}$$

$$A_W = \langle \rho \rangle d_w \Delta a_{sw/nw}$$

$$S = \langle \rho \rangle \Delta a_{sw/nw} \langle V_{1,w}^* \rangle - \langle \rho \rangle \Delta a_{se/ne} \langle V_{1,e}^* \rangle \quad .$$

An iterative solution procedure is required and will give values of approximately zero for the pressure correction, P', when converged.

Boundary conditions are required at the inlet of the solution domain and are taken as the free stream velocity and pressure. At the outlet of the continuity equation is balanced so that mass is conserved.

An iterative solution procedure is adopted because of the non-linear nature of equation 4.84 and due to the formulation of the pressure correction equation. Equations 4.84 and 4.91 are solved alternately using the tridiagonal matrix algorithm. The solution for the pressure was considered converged when the net residual in each stream tube was less than 10^{-5} of the net momentum flux in that tube which required less than 30 iterations.

The pressure at the wall was extrapolated from the field values with a cubic polynomial fit to the pressure nodes at the first three internal nodes.

Errors in the calculated wall pressure arise from the boundary conditions and finite-difference solution procedures used to solve the Laplace and streamwise momentum equations. Gosman and Johns (1979) demonstrate the Laplace equations are solved to approximately second-order accuracy in $\Delta\phi$ and $\Delta\psi$ and that the boundary formulae 4.75 are responsible for the largest contribution to the error. The finite-difference formulation of the streamwise momentum equation will also introduce errors which are dependent on the grid spacing. It is difficult, however, to attribute the errors in the pressure field directly to either of the Laplace or momentum calculation procedures. The overall accuracy may be evaluated by checking that there is no loss of total head along the stream tubes. For a 32 x 32 grid the maximum total head losses were 0.3% and 0.8% of the inlet dynamic head for internal and boundary nodes, respectively, and are not considered important for the present purposes.

The boundary conditions contribute to the error in two ways: through the Laplace equation as discussed above which is minor and, more importantly, through the specification of the boundary at and downstream from the trailing edge. The boundary is specified accurately up to the trailing edge where a dilemma occurs. The shape of the velocity potential and streamline emanating from the trailing edge is not known a priori and must be guessed. This is an implied Kutta condition which fixes the circulation on the surface and clearly affects the surface pressure field upstream. The direct influence of this boundary condition will be investigated with respect to the results discussed in chapter 5.

A technique has been described for generating orthogonal curvilinear meshes to fit simply connected regions with complex surfaces and for the deduction of geometric data required for numerical solution of the orthogonal form of the conservation equations. Furthermore the resultant mesh was used for the numerical solution of the streamwise momentum equation to obtain the static pressure and potential velocity fields. The technique relies on solution of two Laplace equations for the physical locations of the intersection of iso-stream function and iso-velocity potential lines and finite-difference solution of the one-dimensional momentum and continuity equations with the orthogonal co-ordinates taken coincident with the stream function and velocity potential lines.

Regions of recirculation will not be found when the inviscid flow equations are solved and viscous effects must be introduced in order to predict separation. As a result the streamlines obtained from the solution of inviscid flow equations will have transpiration through them. The consequence is that the inviscid streamline must be either moved to their correct location as with the viscous-inviscid interaction method of section 4.3 or allowances made for the cross-flow as in the orthogonal solution procedure of section 4.4. Clearly there will be flow across the inviscid streamlines when a region of recirculation is predicted.

4.3 Viscous-Inviscid Interactive Calculation Procedure

The aerodynamic properties of flows with boundary layers may be calculated using a regional approach with separate solutions for the viscous and inviscid equations interacted via boundary conditions. Viscosity plays an important role only in a thin region in the vicinity of the surface and in the wake, whereas the remaining part of the flow is inviscid in character. The experiences of Thwaites (1955), Kuchemann (1978), Cebeci, Bradshaw and Whitelaw (1981) and others show that lift depends mainly on the inviscid flow and that correction for boundary layer displacement or equivalent blowing velocity is sufficient in many cases. In contrast, the prediction of drag requires accurate representation of the viscous flow and the interaction of the viscous flow with the inviscid flow (Olson et al, 1978). Subdividing the flow field into viscous and inviscid regions permits the computational effort to be focussed on the more demanding region, viscous or inviscid, and may have advantages over solving the viscous equations over the entire domain such as reduction in numerical error or computational expense.

The viscous-inviscid interaction can be regarded as the influence of the boundary layer on the pressure distribution. With weak interactions the viscous effect on the pressure is small and Seebohm and Newman (1975), for example, accounted for it with a non-dimensional displacement thickness, δ_1/C, whose order of magnitude was $|\ln(Re)|^{-1}$ as discussed by Melnik (1980). Stronger interactions occur at the trailing edge or near regions of recirculation, and Melnik and Grossman (1981) and Melnik et al (1983)

found their effect could be an order of magnitude greater on the inviscid flow solution.

Recent work, reviewed by McDonald and Briley (1983), has demonstrated that interactions in the vicinity of small regions of separation may be calculated with the boundary layer equations and a viscous-inviscid interaction. The limit to this approach is not known although it is generally accepted that large regions of separation will not be well represented by boundary-layer equations due to the omission of the cross-stream momentum equation. The present study is concerned with the latter case and with the solution of the time-average Navier-Stokes equations for flows where the region of trailing edge separation is significant. (It also provides information relevant to the application of the Navier-Stokes equations to represent flows without or with small separation.)

It would be inefficient to calculate the entire domain with viscous equations particularly since the interaction is weak in the region upstream of separation and the boundary layer equations are appropriate. An interactive approach should be successful in this region, provided the inviscid flow is resolved, and a very small number of iterations between the solution of the potential flow and boundary layer equations can be expected to suffice (Seebohm and Newman, 1975). This will not be the case close to separation but results from the boundary layer calculation can be used as the upstream boundary conditions for a calculation, based on the Navier-Stokes equations, in the region of strong interaction associated with separation. In this way, the region over which

the elliptic equations are solved, with their greater expense, can be reduced.

Calculations for the weak viscous-inviscid interaction have been performed by the solving of the boundary-layer and inviscid equations coupled through the boundary-layer displacement thickness. An equivalent inviscid flow is defined to be identical to the real flow outside the shear layer by replacing the surface of the body with a displacement surface, which extends into the wake, so that the mass flow between the displacement surface and the edge of the shear layer equals the mass flow in the boundary layer. The inviscid flow equations have been solved inside this boundary to correct the wall pressure for the effects of the boundary layer.

The simplest interactive procedure is as follows. The inviscid-flow equations are solved for the pressure distribution using wall co-ordinates and the boundary-layer equations solved with this wall pressure as a boundary condition. The displacement thickness, δ_1, is then calculated from the viscous solution and the inviscid flow is resolved with a streamline corresponding to the displacement thickness. The pressure obtained along this streamline, is assumed to prevail throughout the boundary layer and is used subsequently as a boundary condition in a second calculation with the boundary layer equations. This process is repeated until the values of wall pressure converge.

This type of interaction has two main restrictions. The streamline taken coincident with the displacement surface is a true streamline in the real fluid only when the displacement effect

on the outer flow is small as pointed out by Veldman (1980), that is to say that the gradients in the inviscid flow solution are negligible inside the boundary layer. Clearly this will not be the case with the strong interaction of the present recirculation region. In this case there will be inflow or outflow across the displacement surface and the boundary conditions must be modified, in the fashion described by Murman and Bussing (1983), to account for this entrainment.

The second restriction is associated with the use of the method of solving the boundary layer equations, which uses wall pressure as a boundary condition. These solutions for steady flow are singular at the location of mean streamline detachment, commonly termed the Goldstein singularity, and arises when the streamwise pressure gradient is specified as a boundary condition and the solution proceeds by forward marching in the streamwise direction. The Navier-Stokes equations have been shown to be regular through separation by Briley (1971), Ghia and Davis (1974) and many others. The presence of the singularity in the solution of the boundary layer equations has also been confirmed by numerical results obtained by Werle and Davis (1972), Klineburg and Steger (1972) and others. It is also clear that this singularity is attributable to the solution algorithm and not the boundary-layer formulation of the equations (McDonald and Briley, 1983).

It is an intuitive conclusion, verified by experience, that direct solution of the boundary layer equations will terminate the calculation at about the location of mean streamline detachment because of the singularity in the solution algorithm.

The influence of strong interaction due to separation was found at least 10 momentum thicknesses, δ_2, upstream of the location of this detachment in the present flow. This region is calculated with the proposed interaction procedure and will verify the extent to which the boundary layer formulation applies in the region approaching separation.

The remainder of this section describes the procedure used to solve the boundary layer equations and that used to introduce the displacement surface into the inviscid flow calculation procedures of section 4.2. The overall solution procedure is shown schematically on figure 4.6 and its implementation described at the end of the chapter.

Solution of the boundary layer equations. The boundary layer equations were solved with the method described by Gibson, Jones and Younis (1981). This method was selected because it had already been used successfully to calculate a range of flows similar to the curved boundary layer region of the present study (see Gibson, Jones and Younis, 1981, Gibson and Younis, 1982, and Younis, 1983). The complete method, turbulence model and results obtained for a number of curved and swirling flows are reported by Younis (1983). The method features solution of the transport equation 4.19 for the Reynolds stresses which have been shown by Younis (1983) to represent the stabilizing influence of convex curvature on the turbulence as is found by experiment see, for example, So and Mellor (1973), Meroney and Bradshaw (1975) and Gibson, Verriopoulos and Vlachos (1983) and the discussion by Bradshaw (1973). Solution procedures with simpler turbulence

models, particularly the k-ε model,were considered but disregarded for the curved boundary layer because they did not offer significant cost advantages and the available corrections for curvature effects such as those of Leschziner and Rodi (1981), Gibson (1978), Launder, Pridden and Sharma (1977) and others, are ad hoc and difficult to extend to three dimensions. For the present case accurate representation of the turbulence field is important where there is a stabilising effect on the turbulence due to longitudinal curvature. Also the results will be used as the upstream boundary conditions for calculation of the separated region with the Navier-Stokes equations which requires an accurate description of the upstream flow.

The transport equations for steady incompressible flow have been simplified to their parabolic boundary-layer form in Bradshaw (1973) by assuming that the only significant shear stresses and diffusional fluxes are caused by gradients in the direction normal to the streamlines and that reverse flow is absent. The resulting boundary-layer equations are given in the s-n co-ordinate system by:-

Continuity

$$\frac{\partial}{\partial s}\langle U_1\rangle + \frac{\partial}{\partial n}\langle hU_2\rangle = 0 \tag{4.93}$$

Streamwise momentum

$$\langle U_1\rangle \frac{\partial \langle U_1\rangle}{\partial s} + h\langle U_2\rangle \frac{\partial \langle U_1\rangle}{\partial n} + \frac{\langle U_1\rangle\langle U_2\rangle}{R}$$

$$+ \frac{1}{\rho}\frac{\partial \langle P\rangle}{\partial s} + h\frac{\partial \langle u_1' u_2'\rangle}{\partial n} + \frac{2\langle u_1' u_2'\rangle}{R} = 0 \tag{4.94}$$

Streamwise Reynolds normal stress

$$<U_1>\frac{\partial<u_1'^2>}{\partial s} + h<U_2>\frac{\partial<u_1'^2>}{\partial n}$$

$$P_{11}\Bigg[+ 2<u_1'u_2'>\left(h\frac{\partial<U_1>}{\partial n} + \frac{<U_1>}{R}\right)$$

$$- \frac{\partial}{\partial n}\left(hC_t\frac{<k>}{<\varepsilon>}<u_2'^2>\frac{\partial<u_1'^2>}{\partial n}\right)$$

$$+ C_1\frac{<\varepsilon>}{<k>}\left(<u_1^2> - \frac{2}{3}<k>\right) + C_2\left(P_{11} - \frac{2}{3}P_k\right) + \pi_{11,1}' + \pi_{11,2}'$$

$$+ \frac{2}{3}<\varepsilon> = 0 \qquad (4.95)$$

Cross-stream Reynolds normal stress

$$<U_1>\frac{\partial<u_2'^2>}{\partial s} + h<U_2>\frac{\partial<u_2'^2>}{\partial n}$$

$$P_{22}\Bigg[+ 4<u_1'u_2'>\frac{<U_1>}{R}$$

$$- \frac{\partial}{\partial n}\left(hC_t\frac{<k>}{<\varepsilon>}<u_2'^2>\frac{\partial<u_2'^2>}{\partial n}\right)$$

$$+ C_1\frac{<k>}{<\varepsilon>}\left(<u_2'^2> - \frac{2}{3}<k>\right) + C_2\left(P_{22} - \frac{2}{3}P_k\right) + \pi_{22,1}' + \pi_{22,2}'$$

$$+ \frac{2}{3}<\varepsilon> = 0 \qquad (4.96)$$

Azimuthal Reynolds normal stress

$$\langle U_1\rangle \frac{\partial\langle u_3'^2\rangle}{\partial s} + h\langle U_2\rangle \frac{\partial\langle u_3'^2\rangle}{\partial n}$$

$$- \frac{\partial}{\partial n}\left(hC_t \frac{\langle k\rangle}{\langle \varepsilon\rangle} \langle u_2'^2\rangle \frac{\partial\langle u_3'^2\rangle}{\partial n}\right)$$

$$+ C_1 \frac{\langle \varepsilon\rangle}{\langle k\rangle}\left(\langle u_3'^2\rangle - \frac{2}{3}\langle k\rangle\right) - \frac{2}{3} C_2 P_k + \pi'_{33,1} + \pi'_{33,2}$$

$$+ \frac{2}{3}\langle \varepsilon\rangle = 0 \qquad (4.97)$$

Reynolds shear stress

$$\langle U_1\rangle \frac{\partial\langle u_1'u_2'\rangle}{\partial s} + h\langle U_2\rangle \frac{\partial\langle u_1'u_2'\rangle}{\partial n}$$

$$P_{12}\Bigg[+ \langle u_2'^2\rangle \left(h \frac{\partial\langle U_1\rangle}{\partial n} + \frac{\langle U_1\rangle}{R}\right) - 2\langle u_1'^2\rangle \frac{\langle U_1\rangle}{R}$$

$$- \frac{\partial}{\partial n}\left(hC_t \frac{\langle k\rangle}{\langle \varepsilon\rangle} \langle u_2'^2\rangle \frac{\partial\langle u_1'u_2'\rangle}{\partial n}\right)$$

$$+ C_1 \frac{\langle \varepsilon\rangle}{\langle k\rangle} \langle u_1'u_2'\rangle + C_2 P_{12} + \pi'_{12,2} + \pi'_{12,2} = 0 \qquad (4.98)$$

Turbulence kinetic energy

$$\langle U_1\rangle \frac{\partial\langle k\rangle}{\partial s} + h\langle U_2\rangle \frac{\partial\langle k\rangle}{\partial n}$$

$$P_k\Bigg[+ \langle u_1'u_2'\rangle \left(h \frac{\partial\langle U_1\rangle}{\partial n} - \frac{\langle U_1\rangle}{R}\right)$$

$$- \frac{\partial}{\partial n}\left(hC_t \frac{\langle k\rangle}{\langle \varepsilon\rangle} \langle u_2'^2\rangle \frac{\partial\langle k\rangle}{\partial n}\right)$$

$$+ \langle \varepsilon\rangle = 0 \qquad (4.99)$$

Rate of dissipation of turbulent kinetic energy

$$\langle U_1 \rangle \frac{\partial \langle \varepsilon \rangle}{\partial s} + h \langle U_2 \rangle \frac{\partial \langle \varepsilon \rangle}{\partial n}$$

$$+ \frac{\partial}{\partial n}\left(h C_\varepsilon \frac{\langle k \rangle}{\langle \varepsilon \rangle} \langle u_2'^2 \rangle \frac{\partial \langle \varepsilon \rangle}{\partial n}\right)$$

$$+ \frac{\langle \varepsilon \rangle^2}{\langle k \rangle} \left(C_{\varepsilon_1} \frac{P_k}{\langle \varepsilon \rangle} - C_{\varepsilon_2}\right) = 0 \qquad (4.100)$$

where

$$h = 1 + \frac{n}{R} \qquad (4.101)$$

and the co-ordinate directions, s and n, the local radius of curvature at the surface, R, the velocity components, U_1, u_1', U_2, u_2' and u_3', are shown on figure 4.5.

The cross-stream momentum equation was simplified to:-

$$\frac{\partial \langle P \rangle}{\partial n} = \frac{\langle \rho \rangle \langle U_1^2 \rangle}{r} \qquad (4.102)$$

where r is the local radius of curvature of the streamlines in the corresponding potential flow. If the streamlines at any s-location are assumed to be locally concentric, the radius of curvature at any location in the profile is given by:-

$$r = n + R \qquad (4.103)$$

and represents a good approximation to the streamlines in the equivalent potential flow defined in section 4.2. At locations where the surface curvature changes discontinuously, the changes are smoothed over a distance of 5 mm with a linear interpolation factor.

The modelled transport equations for turbulence quantities are solved simultaneously with the continuity and momentum equations for the mean flow. The problem is posed as an initial value problem with equations 4.93 - 4.100 in finite-difference form and solved starting from an upstream location where all variables are known by taking steps of ΔS downstream and with boundary conditions provided in the free stream and at the wall. The solution is found using the marching-integration procedure based on the GENMIX program described by Patankar and Spalding (1970).

The upstream boundary conditions were obtained from measured profiles at an inlet location where the cross-stream pressure gradient was negligible. Profiles of the mean velocity, $\langle U_1 \rangle$, and the Reynolds stresses, $\langle u_1'^2 \rangle$, $\langle u_2'^2 \rangle$, $\langle u_3'^2 \rangle$ and $\langle u_1' u_2' \rangle$, are required and were obtained with a stationary hot wire. A Pitot-static probe was also used to verify the mean velocity and to obtain values of the total and static pressure at the inlet. The required dissipation rate was obtained from a mixing length hypothesis.

The outer boundary was located in the free stream where turbulence effects are assumed to be absent and implies the flow is inviscid in nature. The free stream velocity is taken as equal to that corresponding to the local radius of curvature of the surface and the local streamwise pressure gradient, and is obtained by integrating equation 4.102 and combining it with the pressure gradient at the surface. The local values of static pressure are obtained from:-

$$<P>_N = \left[\int_{wall}^{N} \left(\frac{<\rho><U_1>^2}{r}\right)dn\right]_X + \int_0^X \left(\frac{\partial <P>}{\partial s}\right)_{wall} ds + (<P>_{wall})_{ref} \qquad (4.104)$$

where the subscripts X, wall and ref refer to the local streamwise location (s = X), the value at the wall and the reference value, respectively. The free stream velocity is then given by Bernoulli's equation as:-

$$<U_1>_e = \left[2(\{<P_{N=\delta}> + \frac{1}{2}<\rho><U_1>_e^2\}_{ref} - <P_{N=\delta}>)/<\rho>\right]^{1/2} . \qquad (4.105)$$

The flux of turbulence quantities, the dissipation rate, ϵ, and stresses due to laminar and turbulence effects were all taken as negligible.

The wall boundary requires special treatment since the numerical solution of the momentum equation 4.94 is matched to the logarithmic law-of-the-wall. Discussion of the wall functions used to implement this matching is deferred until Section 4.5 although the following comments pertain to the boundary conditions at the wall associated with the Reynolds stress model.

The dissipation in the near wall cell is not zero and is obtained by assuming a linear variation with distance from the wall given by:-

$$<\varepsilon> = u_\tau^3/\kappa n \qquad (4.106)$$

When mean transport and normal stress gradients are neglected, the dissipation equation 4.100 reduces to a simple quadratic equation and is expressed by Gibson et al (1981) as:-

$$<\varepsilon>_w^2 - \frac{C_{\varepsilon 1}}{C_{\varepsilon 2}} P_k <\varepsilon>_w - \frac{C_\varepsilon}{C_{\varepsilon 2}} \frac{<k><u_2'^2>}{n^2} = 0 \quad . \tag{4.107}$$

For local equilibrium flow over a plane wall, the solution of this equation is consistent with the equation 4.50 used by Launder, Reece and Rodi (1975) to establish the model constants and the value of C_ε taken as 0.18 as recommended by Launder and Morse (1979) when used in conjunction with the other constants on table 4.2.

No special treatment is required for the boundary cells of the Reynolds normal stresses provided that the flux through the wall is set to zero and the production terms in the $<u_1'^2>$ and $<k>$-equations have their normal velocity gradients modified to correspond to the logarithmic velocity variation. The method for obtaining the near wall values of streamwise velocity, Reynolds shear stress and production of turbulence energy required use of the assumed logarithmic velocity profile and are discussed in detail in section 4.5. The production of turbulence kinetic energy is important since it appears as a term in the equations for all three normal stresses and the modification to it is the same as that required for the production of $<u_1'^2>$, the streamwise normal stress.

The value of pressure gradient at the wall is required when solving the boundary layer equations and equation 4.104 is used to provide the streamwise pressure gradient away from the wall. The values of pressure are obtained from solution of the inviscid flow equation or from measurements. These values are obtained at discrete locations in the flow which may not coincide

with the s-locations where the boundary layer equations are solved. First order differencing and linear interpolation are used to determine the gradient and values of wall pressure, respectively, when the boundary layer equations are solved at locations between those where pressure is specified.

Only thirty cross-stream nodes were required to resolve the boundary layer which is partly attributable to the use of a wall function based on the logarithmic law. Also, the cross-stream spacing, Δn, was expanded away from the wall with a geometric series as suggested by Bradshaw, Cebeci and Whitelaw (1981) with an expansion factor of 1.14. The forward step size, Δs, is limited by the accuracy to which the streamwise pressure gradient can be determined in the outer flow with equation 4.104 and typical values were between 0.1% and 1% of the boundary layer thickness.

Viscous-inviscid interaction. Returning to the calculation of flow through the entire domain, the viscous-inviscid interaction procedure which couples the boundary layer solution to the inviscid solution is shown schematically on figure 4.6. Initially, surface co-ordinates are used to describe the boundaries and equation 4.66 is solved to locate the streamlines then equation 4.81 is solved, with the streamlines corresponding to the ζ_1-direction, for the wall pressure. Subsequently the boundary layer equations are solved by marching downstream from the location where the measured profiles are provided and using the calculated values of the inviscid wall pressure. The inviscid flow is then corrected for the influence of the boundary by resolving equation 4.66 and 4.81 with a new boundary defined as the displacement surface

above. The displacement surface is located by adding the displacement thickness, given by:-

$$\delta_1 = \int_{wall}^{\delta} \left(1 - \frac{\langle U_1 \rangle}{\langle U_1 \rangle_e}\right) dn \qquad (4.108)$$

to the surface co-ordinates. The new displacement surface represents a streamline in the inviscid flow solution and defines the boundary of the calculation domain for the second solution of the inviscid flow. The pressure obtained from this second solution of the inviscid flow is used as a boundary condition to recalculate the viscous flow with the boundary layer equations and new values of the displacement thickness, δ_1, are obtained with equation 4.108. The process of updating the pressure and displacement thickness is repeated until the overall solution procedure converges which is expected after a few iterations (see Seebohm and Newman, 1975).

The downstream boundary for the inviscid flow is very important and must be supplied from empirical assumptions as discussed in the last section. The problem is compounded when the boundary layer equations are solved because of the Goldstein singularity which prevents even approximate values of the displacements thickness from being obtained in the separated region downstream of the singularity. Similarly the shape of the velocity potential line is not known at the singular point and further empirical interpretation is required with the interaction procedure. Several methods were tried and the degree of success and importance of this downstream boundary condition are evaluated in section 5.2. It should be noted that solution of the boundary layer equation in the inverse mode, which uses the displacement thickness as a boundary condition

instead of wall pressure, would calculate the separated region whether the boundary layer equations applied or not, although the displacement thickness would be erroneous if the boundary layer assumption were invalid.

The methods for solving the boundary layer equations and interacting this viscous solution with the inviscid calculations of the previous section have been described. The location of the downstream boundary when solving for the inviscid flow is identified as important. Section 5.2 will discuss this further and report results obtained with the viscous-inviscid interactive calculation procedure. The presented form of the boundary layer equations exhibits a Goldstein singularity which prohibits solutions in the region of reversed flow. Also the interactive procedure is expected to be limited to regions of weak viscous-inviscid interaction where the coupling boundary condition occurs in a region of small gradients in the equivalent inviscid flow.

4.4 Procedure for Solving Elliptic Transport Equations in Orthogonal Curvilinear Co-ordinates

This section is concerned with the numerical calculation procedure for solving the general transport equations in flows with a region of recirculation. The two-dimensional form of the

time-averaged Navier-Stokes equations 4.11-13 are solved numerically on a general orthogonal-curvilinear, finite-difference grid which was obtained by solving the Laplace equations as described in section 4.2. Closure is obtained with an eddy viscosity hypothesis and modelled forms of the equations representing transport of turbulence kinetic energy and dissipation rate.

The complete partial differential equation which represents instantaneous or time-averaged transport phenomena, are elliptic in nature. Ellipticity is a mathematical classification and depends on the manner in which the highest order derivatives appear in the partial differential equation (see Hornbeck, 1975, and Cebeci and Bradshaw, 1977). With elliptic equations there need not be a dominant direction of flow, unlike the parabolic boundary-layer equations, and disturbances can propagate upstream or downstream as in reversed flow. Boundary conditions are required on a complete contour enclosing the solution domain; elliptic equations pose a boundary-value problem. Since the transport equations are non-linear and, for elliptic problems, the finite-difference equations must be implicit, iterative solution techniques are required and are described in this section.

The finite-difference equations are solved on an orthogonal curvilinear mesh which represents the inviscid flow obtained without any shear layer effects. Orthogonal curvilinear co-ordinates are used because they are more appropriate for the representation of complex boundaries; their flexibility gives a very good approximation of curved boundary surfaces and boundary conditions can be accurately implemented. It is expedient at this point to compare this approach

with alternative schemes that use non-orthogonal or pre-selected shapes for calculation cells, such as with Cartesian or cylindrical systems. These three approaches with non-orthogonal, orthogonal curvilinear or simple shapes for calculation cells differ in three main ways: first, in their ability to represent boundary conditions on complex surfaces; second, in the amount of numerical error they introduce; and, third, in the amount of computational effort, and expense, they incur.

The use of boundary cells which conform to simple shapes such as rectangles, circles or sections thereof, would lead to very uneven distributions of calculation accuracy since some gradients would be much better represented than other; particularly, difficulties would arise when resolving the large gradients found in the wall boundary layers. Figure 4.7 shows the grid which would result if rectangular and curvilinear calculation cells were implemented on a curved boundary and clearly the Cartesian grid would result in errors because of the need to implement the law of the wall boundary condition, discussed in section 4.5, on the velocity component tangent to the surface and would require an excessively large number of nodes to accurately represent stream-wise gradients, in addition to the normal gradients, as is found near separation.

A mesh which is coincident with the inviscid flow solution is advantageous because numerical errors associated with alignment of the grid with the flow direction are reduced. This numerical error manifests itself as false diffusion and Raithby (1976) found that it increases with inclination of the flow direction

to the grid lines being a maximum where the flow vector is inclined at 45 degrees to the cell face. This is discussed further in the subsection on numerical accuracy later in this section but here it is sufficient to point out that numerical error is a minimum, for a particular grid, if the flow vector is aligned with the co-ordinate directions of the calculation mesh. Flow in the outer region is essentially inviscid, in practice, and, if the boundary layer effects are not too strong, it should follow the inviscid streamlines in this region and have minimal numerical diffusion errors.

The implications of a region of recirculation on solution of the equations with an orthogonal grid are primarily twofold: first, streamwise gradients are present which requires small grid spacing in the streamwise direction and is discussed quantitatively in section 5.3 in connection with the grid used for the present study; and, second the flow cannot be aligned with the grid in the vicinity of recirculation since the solution of the potential flow equations does not take any account of separation and the calculated flow is expected to intersect the cell walls at an angle in this region which results in errors associated with numerical diffusion as described above. Also the orthogonality requirement, inherent in the potential-flow solution, must be satisfied by the grid and sometimes results in a non-optimum distribution of grid nodes (see Thompson J.F., 1982). To account for these problems, an overly fine mesh is produced and nodes selected for the elliptic calculation according to the concentrations required to resolve the streamwise and large normal gradients in the wall boundary layer and separated region.

The use of the k-ε turbulence model represents a compromise between an algebraic length scale and a Reynolds stress model. Algebraically specified length scales are generally unsatisfactory in recirculating flows as was discussed in section 4.1. Perhaps the most compelling reason for not using a Reynolds stress model is that, to date, they have not been widely used for predicting recirculating flow except by Pope and Whitelaw (1975) or Habib and Whitelaw (1981) and that the method of solution tended to wash out the effects of the turbulence model, via false diffusion (Whitelaw, 1983). The Reynolds stress equations are also more expensive to solve in their fully elliptic form particularly on an orthogonal curvilinear mesh; the boundary layer equations and related simplifications applied in section 4.3 whereas, for the elliptic equations, the number of computations is greatly increased due to the necessary additional terms associated with streamwise gradients, the solution of the cross-stream momentum equation, and the use of the curvilinear grid which also increases the computer storage requirement. The k-ε model has been used to calculate recirculating flows, for example by Rhie and Chow (1982) Taylor (1981) and Habib (1980), and their results show that reasonable mean flow fields can be predicted despite inaccuracies in the turbulence field.

The remainder of this section deals with the numerical calculation procedure for the solution of the elliptic equations in orthogonal curvilinear co-ordinates. First, the finite-domain equations are obtained by differencing the equations for transport of mass (4.11), momentum (4.12-3), turbulence kinetic energy (4.33)

and dissipation rate (4.41). Special attention is given to the convection terms, which require a hybrid differencing scheme based on a combination of upwind and central differences and to the approximate nature of the solution, which necessitates evaluation of the numerical accuracy. Numerical implementation of boundary conditions is considered at the end of this section and specification of the fluid dynamic aspects of boundary conditions given in section 4.5.

Finite-difference equations. This subsection describes the procedure used to obtain the finite-difference equation which represent the transport equations to be solved. The orthogonal mesh used to obtain the calculation cells for scalar variables is described and integration of the general form of the transport equation is shown. The finite-difference form of the convection and diffusion terms are also obtained in this subsection.

Figure 4.4 illustrates a portion of the computational grid in orthogonal curvilinear co-ordinates. The mutually-orthogonal directions, ζ_1, ζ_2 and ζ_3, are defined with respect to tunnel centreline (x), its vertical perpendicular (y) and azimuthal (z) directions such that the $\zeta_1 - \zeta_2$ plane lies in the x-y plane and the ζ_3-direction is identical with the z-direction. The flow is assumed to be two-dimensional in the x-y plane and, thus, in the ζ_1-ζ_2 plane.

The scalar quantities of pressure, turbulence kinetic energy, dissipation rate and turbulence viscosity are calculated within the finite domain boundary around the points denoted by capitals - NSEWP as shown on figure 4.4. The velocities, V_1 and

and V_2, are displaced in the ζ_1- and ζ_2-directions, respectively, to points on the face of the scalar cell walls in accordance with the procedure first suggested by Harlow and Welch (1965) and subsequently by Caretto et al (1972) and Patankar and Spalding (1972). This staggering has two advantages: the pressure gradient term in both momentum equations can be easily and accurately differenced and the velocities located in a convenient location to calculate the convective fluxes at the scalar cell boundaries. Thus continuity, solved in scalar cells, is balanced with local values of velocity on the cell walls and has a computational advantage over the non-staggered approach, where the velocity in adjacent cells are used, which is unable to predict wavy variations as described by Patankar (1980).

An approximate solution to the partial differential can be found by solving a set of algebraic equations obtained by dividing the entire region into small finite domains within which the variation of the dependent variable is presumed to be known; if the domains are small enough a linear variation is adequate. The transport equations for mean flow and turbulence quantities, denoted by ϕ, can be transformed into the general form:-

$$\frac{1}{\ell_1\ell_2\ell_3}\{\frac{\partial}{\partial\zeta_1}\ [\ell_2\ell_3(<\rho><V_1><\phi> - \frac{\Gamma_\phi}{\ell_1}\frac{\partial<\phi>}{\partial\zeta_1})]$$

$$+ \frac{\partial}{\partial\zeta_2}\ [\ell_1\ell_3(<\rho><V_2><\phi> - \frac{\Gamma_\phi}{\ell_2}\frac{\partial<\phi>}{\partial\zeta_2})]\}$$

$$- S_\phi = 0 \qquad (4.109)$$

where the source term S_ϕ contains the remaining contributions which are different from the convection and diffusion terms. Integration of the general transport equation over the finite domain is described by Gosman et al (1969) and for the variable ϕ located at a point, P, can be expressed as:-

$$F_{\zeta_1}\Bigg[\int_{\zeta_{2,s}}^{\zeta_{2,n}} \ell_2\ell_3(\rho\tilde{V}_1\phi - \frac{\Gamma_\phi}{\ell_1}\frac{\partial\phi}{\partial\zeta_1})_w^e \, d\zeta_2$$

$$F_{\zeta_2}\Bigg[+ \int_{\zeta_{1,w}}^{\zeta_{1,e}} \ell_1\ell_3(\rho\tilde{V}_2\phi - \frac{\Gamma_\phi}{\ell_2}\frac{\partial\phi}{\partial\zeta_2})_s^n \, d\zeta_1$$

$$F_{S_\phi}\Bigg[- \int_{\forall_P} \ell_1\ell_2\ell_3 \, S_\phi d\zeta_1 d\zeta_2 = 0 \qquad (4.110)$$

where the superscript (~) refers to the convection velocity, the other symbols are defined on figure 4.4 and $\forall_P$ represent the cell volume surrounding the point P which has unity depth in the ζ_3-plane and is calculated with equation 4.77. To preserve clarity, the average (<>) and fluctuating (') notation is dropped for the finite domain equations and it should be assumed that all dependent variables are ensemble averaged and independent variables refer to the ζ_1, ζ_2-co-ordinate system unless otherwise stated.

The general transport equation is integrated prior to applying finite-difference approximations in order to preserve conservation relations for the convective and diffusive fluxes. The terms, F_{ζ_1} and F_{ζ_2} of equation 4.110, represent the combined effects of convection and diffusion of ϕ across the cell faces along

the ζ_1- and ζ_2- directions, respectively, and, taking the first term as an example, may be differenced spacially as:-

$$F\zeta_1 \approx \Delta a_{se/ne} \left[\rho \tilde{V}_1 \phi_e - \frac{\Gamma_\phi(\phi_E - \phi_P)}{(\Delta S_1)_{E/P}} \right]_e$$

$$- \Delta a_{sw/nw} \left[\rho \tilde{V}_1 \phi_w - \frac{\Gamma_\phi(\phi_P - \phi_W)}{(\Delta S_1)_{P/W}} \right]_w \qquad (4.111)$$

where the symbols Δa and ΔS represent the cell face areas and are lengths given by, for example:

$$\Delta a_{sw/nw} = (\ell_2 \ell_3 \delta\zeta_2)_{w\text{-face}} \qquad (4.112)$$

$$(\Delta S)_{P/W} = (\ell_1 \delta\zeta_1)_{P \text{ to } W} \qquad (4.113)$$

and are calculated with equation 4.76 . The slash (/) in the subscript indicates evaluation between the points indicated; i.e. P to W in the last equation. The gradient term was differenced as:-

$$\left[\frac{1}{\ell_1} \frac{\partial \phi}{\partial \zeta_1} \right]_e = \frac{\phi_E - \phi_P}{(\Delta S_1)_{E/P}} \qquad (4.114)$$

and the cell Peclet number is defined as:-

$$Pe_e = \frac{(\rho \tilde{V}_1)_e \, \Delta S_{E/P}}{\Gamma_e} \qquad (4.115)$$

and similar equations can be written for the terms on the west face. The cell-boundary diffusivities are evaluated by assuming linear variation between their nearest neighbours so that typically:-

$$\Gamma_e = f_1\Gamma_P + (1 - f_1)\Gamma_E \tag{4.116}$$

where the weighting factor is given by:-

$$f_1 = \frac{\Delta S_{E/e}}{\Delta S_{E/P}} \quad . \tag{4.117}$$

The cell-face values of ϕ may be expressed by defining α according to:-

$$\begin{aligned} \phi_e - \frac{\phi_E - \phi_P}{Pe_e} &= (1 - \alpha_e)\phi_E + \alpha_e\phi_P \\ \phi_w - \frac{\phi_P - \phi_W}{Pe_w} &= (1 - \alpha_w)\phi_P + \alpha_w\phi_W \quad . \end{aligned} \tag{4.118}$$

Equation 4.111 may be expressed with the above definitions as:-

$$F_{\zeta_1} \approx \Delta a_{se/ne}(\rho\tilde{V}_1)_e(\phi_e - \frac{\phi_E - \phi_P}{Pe_e}) - \Delta a_{sw/nw}(\rho\tilde{V}_1)_w(\phi_w - \frac{\phi_P - \phi_W}{Pe_w}) \tag{4.119}$$

or more simply as:-

$$\begin{aligned} F_{\zeta_1} \approx{}& \Delta a_{se/ne}(\rho\tilde{V}_1)_e\,[(1 - \alpha_e)\phi_E + \alpha_e\phi_P] \\ &- \Delta a_{sw/nw}(\rho\tilde{V}_1)_w\,[(1 - \alpha_w)\phi_P + \alpha_w\phi_W]. \end{aligned} \tag{4.120}$$

The differencing approximation used for the source terms in equation 4.110 depends on the variable under consideration and may be represented by:-

$$\int_{\forall_P} S_\phi d\forall = S^\phi_{Ex} + S^\phi_{Im}\phi_P \tag{4.121}$$

in which linearization of the source terms into explicit and implicit form, S_{Ex} and S_{Im} respectively, is anticipated. The finite-difference approximation of these source terms is considered in a following subsection.

The final form of the general transport equation can be written compactly as:-

$$(A_P - S^{\phi}_{Im})\phi_P = A_E\phi_E + A_W\phi_W + A_N\phi_N + A_S\phi_S + S^{\phi}_{Ex} \qquad (4.122)$$

and the coefficients are given by:-

$$\begin{aligned} A_E &= -(1 - \alpha_e)\dot{m}_e \\ A_W &= \alpha_w\dot{m}_w \\ A_N &= -(1 - \alpha_n)\dot{m}_n \\ A_S &= \alpha_s\dot{m}_s \\ A_P &= \alpha_e\dot{m}_e - (1 - \alpha_w)\dot{m}_w + \alpha_n\dot{m}_n - (1 - \alpha_s)\dot{m}_s \end{aligned} \qquad (4.123)$$

where $\dot{m}$ is $\rho\Delta aV$ and the source terms are discussed below.

The above formulation applies directly in the scalar cells of figure 4.4 but the momentum equations require special treatment since they are solved in a control volume which is the central half of two adjacent scalar cells. The convection velocity, $\tilde{V}_1$, of equation 4.111 is obtained by assuming a linear variation between neighbouring values and is typically given as:-

$$\tilde{V}_{1,W} = \left(\frac{V_{1,ww} + V_{1,w}}{2}\right) . \qquad (4.124)$$

The mass flow rate in the ζ_1-direction is:-

$$\dot{m}_W = \rho \Delta a_{wsw/wnw} \tilde{V}_{1,w}$$

and the cell Peclet number is:-

$$Pe_W = \rho \tilde{V}_{1,W} \frac{(\Delta S)_{ww/w}}{\Gamma_W} \quad . \tag{4.125}$$

In the ζ_2-direction, the mass flow rates are obtained from a summation of the various components which, for the south cell-face, is:-

$$\dot{m}_{sw} = \rho \Delta a_{wsw/sw} \tilde{V}_{2,wsw} + \rho \Delta a_{sw/s} \tilde{V}_{2,s} \tag{4.126}$$

and the cell Peclet number is calculated from:-

$$Pe_{sw} = \frac{\dot{m}_{sw}}{\Delta a_{wsw/s}} \frac{(\Delta S)_{wsw/s}}{\Gamma_{sw}} \tag{4.127}$$

where the diffusivity is obtained from a weighted average of the surrounding values according to:-

$$\Gamma_{sw} = f_1 [\Gamma_{SW} f_2 + \Gamma_W (1 - f_2)] + (1 - f_1) [\Gamma_S f_2 + (1 - f_2)\Gamma_p] \tag{4.128}$$

The quantity f_2 is a spatial weighting factor whose specification provides a linear variation of scalar variables between SW to W and S to P, and is defined as:-

$$f_2 = \frac{(\ell_2 \delta \zeta_2)_{P/s}}{(\ell_2 \delta \zeta_2)_{P/S}} \tag{4.129}$$

The transport equation for V_1-momentum can then be written as:-

$$(A_p - S_{Im}^{V_1})V_{1,w} = A_E V_{1,e} + A_W V_{1,ww} + A_N V_{1,nnw} + A_S V_{1,ssw} + S_{Ex}^{V_1} \quad (4.130)$$

where the coefficients are the same as in equation 4.123 except because of the staggered grid, they are evaluated at e, ww, nnw and ssw locations; the mass flow rates are obtained from equation 4.126 and values of α are defined in a similar fashion to equation 4.118 only with the cell Peclet number from equation 4.127. The source terms are integrated over the volume given by:-

$$\forall_{sw} = \frac{\forall_W + \forall_P}{2} \quad (4.131)$$

where $\forall_P$ and $\forall_W$ are the volumes defined by equation 4.77. Similar reasoning is applied to derive the momentum equation in the ζ_2-direction.

Hybrid differencing. The convection velocities, which appear in the coefficients of equations 4.122 and 4.130 as a result of central differencing, carry the dependent variable ϕ into and out of the control volume and special consideration is required when differencing the terms containing values of ϕ. Intuition tells us that if the cell Peclet number, and hence convection, is large the value of the convected quantity, ϕ, should depend strongly on its upstream value and upwind differencing, where the convected quantity equals its value at the nearest upstream node, is a reasonable approximation. However when diffusion is comparable to convection the gradient of the convected quantity can not be approximated as constant, which upwind differencing assumes, and

a higher order approximation, for instance central differencing, is required. Studies by Spalding (1972) and Raithby and Torrance (1974) and Stubley et al (1982), for example, have shown that the use of upwind or central differencing can give erroneous results. The upwind scheme suffers from the problems mentioned above and the central differencing scheme introduces an erroneous influence of downstream values of the convected quantity on the convection fluxes for large Peclet numbers (Stubley, 1982) and causes the A_i-coefficients in equation 4.122 or 4.130 to be negative which gives unphysical solutions for ϕ. A solution is to use a hybrid scheme which takes the advantages of central differencing at low Peclet numbers and upwind differencing at high Peclet numbers and is described below.

Solution of the steady one-dimensional transport equation with only a convective and diffusive term suggest that the variation of the convected quantity ϕ should follow an exponential function so that the value of α in equation 4.118 should typically be:-

$$\alpha_e = - (e^{-Pe/2} - 1)^{-1} \qquad (4.132)$$

and Spalding (1972) has demonstrated that this will reproduce the analytical solution for ϕ_p in one dimension. Exponents are expensive to compute and this scheme is not exact for two-dimensional flows with non-zero source terms. Simplification seems justified and a piecewise fit between central and upwind differencing which approximates this response is used and is given by:-

$$\alpha_e = \begin{cases} \frac{1}{2} + \frac{1}{Pe_e} & \text{for } |Pe| \leq 2 \quad \text{Central Difference} \\ 1 & \text{for } Pe > 2 \\ 0 & \text{for } Pe < -2 \end{cases} \quad \text{Upwind Difference} \qquad (4.133)$$

This scheme ensures stability and gives physically reasonable solutions even on coarse grids by virtue of positive coefficients appearing in the finite-difference equations 4.122 and 4.130 and the coefficient matrix always being diagonally dominant (Roache, 1972).

The accuracy of this scheme can be poor under certain conditions when it is used in multi-dimensional flows. Errors arise when the grid is not aligned with the dominant flow direction and appear as additional diffusion caused by the numerical approximation. Raithby (1976) identified this problem and proposes that higher order schemes, such as skew upwind differencing (Raithby, 1976b), could be used to overcome it. Several schemes have been proposed recently by Leonard (1979), Stubley et al (1980) and Lai (1983) for example, but are presently in their infancy and not well tested. It should be noted that the flow cannot be aligned with the grid a priori in the vicinity of regions of recirculation and substantial errors may arise from numerical diffusion. The evaluation of this possible error is considered later in this section.

Differencing of the source terms. There are several terms in equations 4.11-13, 4.33 and 4.41 which are not accounted for in the finite-difference forms of the convection and diffusion

terms described above. These terms given by equation 4.121 are differenced with variable quantities in S_{Ex} and S_{Im} obtained from values of the previous iteration as shown below.

The source terms, S_ϕ, of the general transport equation 4.109 are shown on table 4.3 for the equations representing transport of mass, momentum, turbulence kinetic energy and dissipation rate. Many of these terms are of similar form and representative examples will be dealt with here.

The pressure gradient terms in the momentum equation are differenced in a straightforward manner according to equation 4.114 and, after integrating over the surface, become typically:-

$$-\int\int \ell_1\ell_2\ell_3\left(\frac{1}{\ell_1}\frac{\partial P}{\partial \zeta_1}\right)d\zeta_1 d\zeta_2 = -\Delta a_{sw/nw}(P_P - P_W) \qquad (4.134)$$

for the V_1-momentum equation 4.130.

The main curvature terms are the centripetal and Coriolis accelerations which have the general forms of $\rho V_i^2/r_k$ and $\rho V_i V_j/r_k (i \neq j)$, respectively, and tend to redistribute energy between the co-ordinate directions. For the ζ_1-direction the terms to be approximated are:-

$$\frac{\rho V_2^2}{r_2} - \frac{\rho V_1 V_2}{r_1} \qquad (4.135)$$

where the constituent parts are given by:-

$$V_2 = \frac{1}{2}\left[f_1(V_{2,wnw} + V_{2,wsw}) + (1 - f_1)(V_{2,n} + V_{2,s})\right]$$

$$r_2 = \frac{1}{2}\left[f_1(r_{2,wnw} + r_{2,wsw}) + (1 - f_1)(r_{2,n} + r_{2,s})\right] \qquad (4.136)$$

where f_1 is defined in equation 4.117. Curvature terms in the ζ_2-direction are similar and are differenced in the same manner.

The higher order curvature terms and all other terms, including those for turbulence quantities k and ε, are differenced by following one of three rules. The first is:-

$$\frac{1}{\ell_1}\frac{\partial\phi}{\partial\zeta_1} = \frac{\phi_e - \phi_w}{(\Delta S)_{e/w}} \tag{4.137}$$

where

$$\phi_w = f_1\phi_W + (1 - f_1)\phi_P \tag{4.138}$$

with f_1 defined by equation 4.117 and ϕ_e treated in a similar expression. The second type is:-

$$\frac{1}{\ell_1}\frac{\partial}{\partial\zeta_1}\left(\frac{1}{\ell_1}\frac{\partial\phi}{\partial\zeta_1}\right) = \frac{1}{(\Delta S)_{e/w}}\left(\frac{\phi_E - \phi_P}{(\Delta S)_{E/P}} - \frac{\phi_P - \phi_W}{(\Delta S)_{P/W}}\right) \tag{4.139}$$

and the third is:-

$$\frac{1}{\ell_1}\frac{\partial}{\partial\zeta_1}\left(\frac{1}{\ell_2}\frac{\partial\phi}{\partial\zeta_2}\right) = \frac{1}{(\Delta S)_{e/w}}\left(\frac{\phi_{ne} - \phi_{se}}{(\Delta S)_{ne/se}} - \frac{\phi_{nw} - \phi_{sw}}{(\Delta S)_{nw/sw}}\right) \tag{4.140}$$

where the values of ϕ at the ne, nw, se and sw-locations are obtained from a weighted average of the surrounding values according to:-

$$\phi_{sw} = f_1\left[\phi_{SW}f_2 + \phi_W(1 - f_2)\right] + (1 - f_1)\left[\phi_S f_2 + \phi_P(1 - f_2)\right] \tag{4.141}$$

The formulation of the curvature terms, with these expressions, is not conservative, although the formulation of convection and diffusion terms in equation 4.110 is conservative, and, hence, this numerical scheme is called weakly conservative. For example, consider the Coriolis term in equation 4.135 whose

counterpart in the ζ_2-direction momentum equation will have different weighting factors applied for V_1 and V_2 in equation 4.136. There is no guarantee that the redistributive action of the Coriolis term in the ζ_1-direction will be exactly accounted for in the ζ_2-direction and thus false sources or sinks may arise solely because of the numerical scheme. For the present case the radii of curvature is large throughout the domain and the resulting error is small for these Coriolis and centripetal accelerations. Higher order source terms are also relatively small.

This completes the discussion of differencing procedures for the equations which must now be solved.

Solution procedure. Finite-difference equations have been constructed above for the transport equations of momentum and turbulence quantities and that for the pressure correction equations is described below and the method used to obtain numerical solutions from them is described here.

The continuity equation is transformed into a pressure correction equation in the same manner as equation 4.91 of section 4.1 except in two dimensions. The velocity components, V_1 and V_2, are corrected in the same fashion as in equation 4.88 for the V_1-component and equations similar to 4.89 will give negligible V_1' and V_2' when the solution is converged.

The procedure for solving the transport equations in finite-difference form is described as follows: the momentum equations are solved starting with a guessed pressure and velocity field; their solution provides the V* velocities of equation 4.88

used to solve the pressure correction equation for P'. The solution of the P'-equation provides the corrections which are substituted back into equations 4.89 and 4.88 to correct the pressure and velocity field such that the latter satisfies continuity. The remaining turbulence equations are then solved and the turbulence viscosity updated. The steps of the iterative cycle, called the SIMPLE algorithm, are:-

1. Guess values of all field variables.
2. Solve the V_1- and V_2-momentum equations with the prevailing pressure field. Conservation of momentum will be satisfied but not continuity.
3. Solve the P'-equation and obtain values of the pressure and velocity corrections.
4. Evaluate new values of V_1, V_2 and P. Continuity is satisfied but not conservation of momentum.
5. Solve the k-equation.
6. Solve the ε-equation.
7. Calculate the turbulent viscosity.
8. Check for convergence: if not attained use prevailing field variables as guessed values and continue from step 2.

The procedure is started with constant values for all field variables except V_1-momentum which is set according to an overall mass balance to assist stability.

The finite-domain formulation constructs a set of simultaneous algebraic equations, of the form of equation 4.122 or 4.130. These algebraic equations are implicit and non-linear since the coefficients, A_i, and source terms, S_{Ex} and S_{Im}, are

functions of the dependent variable ϕ, and must be solved with an iterative method. The equations for nodes along constant ζ_1 or ζ_2 lines can be manipulated into a tri-diagonal matrix by temporarily assuming that values on neighbouring lines are known and temporarily makes A_i,S_{Ex} and S_{Im} constant. The solution is obtained using the Thomas algorithm (Householder, 1964) which is a particular implicit type of Gaussian elimination. Full convergence is not necessary because the approximation of constant coefficients is not correct, and improved values of ϕ, typically taken after 3 iterations, are adequate to obtain convergence of the overall solution with the cyclic procedure described above. Numerical instabilities may occur, however, since the unconverged values of the A_i-coefficients are likely to fluctuate extensively during the initial iterations and underrelaxation was used to suppress large changes in the field values according to:-

$$\phi = \phi_{old} - (1 - T)\phi_{new} \tag{4.142}$$

Values of the underrelaxation parameter for each variable, V_1, V_2, P', k, ε and μ_t are given on table 4.4.

The overall solution was adjudged to be converged when the sum of the absolute value of the normalised residuals in the equations for V_1, V_2 and P' decreased to less than a specified value, usually 0.1 per cent. The residuals were normalized with the net mass flux entering the domain and the reference value of velocity. Additionally the values of velocities, V_1 and V_2, at a representative node were required to change by less than 0.002 m/s on subsequent iterations. It has been found that if both of these

criteria are satisfied the solutions for the turbulence quantities, k and ε, have also converged. Values of all variables at a given location were found to change by less than 0.2% with further iterations once the convergence criteria were satisfied and the maximum imbalance in any cell was less than 0.1% of the largest of the convection, diffusion or source terms.

Numerical accuracy. The numerical accuracy of the solution is dependent on the contributions from round-off errors, residual errors when converged, and approximations associated with the finite-domain volumes and their equations.

The capabilities of the computer used to perform the calculations limits the round-off error because of its finite word size, which was 60 bits on the CDC 6500 used here, and is believed to be negligible. The errors associated with convergence are less than 0.2 per cent as described above.

The errors due to the finite-difference approximations may be divided into two types: those associated with specification of the grid and the others with the finite-difference approximation of the partial differential equations. The grid lines, obtained from the solution of potential flow equations as described in section 4.2, satisfy the orthogonality condition within 1 degree and this error is manifest in the integration used to obtain equation 4.110 which assumes that the mesh lines are orthogonal. It is difficult to quantify this error without adopting an expensive non-orthogonal treatment of the equations (see Demirdzic et al, 1981, and Maliska et al, 1983) and it is likely to be insignificant in the present flow. It is certainly negligible

when compared to the error associated with representing the partial differential equations by finite-difference analogues which is believed to be the limiting factor.

McGuirk, Taylor and Whitelaw (1981) show that the solution of the finite-difference equations corresponds to the exact solution of a partial differential equation which is made of the original equation 4.109 plus additional terms due to the truncated Taylor series expansion for the gradients. With these as the dominant errors, the accuracy of the solution is determined by the relative importance of the added terms arising from the truncated expansion to the other exact terms in the differential equation. In fact, it is the truncation of the hybrid differencing scheme of equation 4.133 which gives most cause for concern.

Taylor series expansions of the variable ϕ about the point P are given by (McGuirk et al, 1981) for one-dimensional flow as:-

$$\rho \frac{U}{2\delta x}(\phi_E - \phi_W) = \rho U\left[\frac{d\phi}{dx} + \frac{1}{3!}\frac{d^3\phi}{dx^3}\delta x^2 + \ldots. + \frac{1}{(2n+1)!}\frac{d^{(2n+1)}\phi}{dx^{(2n+1)}}\delta x^{2n}\right] \quad (4.143)$$

$$\rho \frac{U}{\delta x}(\phi_P - \phi_E) = \rho U\left[\frac{d\phi}{dx} - \frac{1}{2}\frac{d^2\phi}{dx^2} + \ldots + \frac{(-1)^n}{n!}\frac{d^n\phi}{dx^n}\delta x^{n-1}\right] \quad (4.144)$$

where n is an integer. The above equation assumes uniform grid spacing and additional truncation terms are introduced with non-uniform spacing which depend on the mesh expansion. Both uniform

and non-uniform grids were used in the present study but the affect of these additional errors was overshadowed by those considered presently. The approximations of equation 4.143 and 4.144 represent central and upwind differencing, respectively, and it is apparent that the underlined term in the upwind scheme resembles a diffusion term which arises as a consequence only of the numerical scheme. The upwind scheme is applied for cell Peclet numbers greater than |2| and if this solution was used with central differencing to calculate the convection fluxes instead, the finite-difference equation would balance only as:-

$$(A_P^c - S_I^c)\phi_P^u = \Sigma A_i^c \phi_i^u + S_E^c + T \qquad (4.145)$$

where T is the out-of-balance term and the superscripts u and c identify terms evaluated with upwind and central differencing, respectively. This out-of-balance term represents the difference between central and upwind differencing schemes which is, from equations 4.143-4 (McQuirk et al, 1981):

$$T \equiv \rho U\left[\frac{1}{2!}\frac{d^2\phi^u}{dx^2}\,\delta x + \ldots\ldots + \frac{1}{(2n)!}\frac{d^{2n}\phi^u}{dx^{2n}}\,\delta x^{2n-1}\right] \qquad (4.146)$$

and the leading term is the numerical diffusion error. It is plausible that the higher order terms will tend to zero if the solution is suitably well behaved,and that this diffusion error will be the dominant contributor to T and,therefore, here it is considered approximately equal to it.

McGuirk and Rodi (1978) proposed a method for evaluating the local magnitude of numerical diffusion based on equation 4.145

and is applied here as follows. The converged solutions to the finite difference equations are obtained with hybrid differencing. The values of convection, diffusion and source terms are evaluated using central difference approximations and the previous solution which was obtained using upwind differencing in cells where the Peclet number exceeded |2|. The out-of-balance term is obtained from equation 4.145 for each grid node and compared with the largest of the following terms: convection including Coriolis and centripetal accelerations; diffusion including diffusive curvature effects; and pressure gradient or the remaining source terms; all are shown on table 4.5. If T is important, then the grid spacing is reduced locally in the direction in which upwind differencing is being invoked and a new solution calculated. The procedure is repeated until the out-of-balance term is less than a maximum of 10% of the other terms which was selected based on the suggestion of McGuirk (1983). The implication of this error is that the solution is not exact and is dependent on the grid. As will be shown in section 5.3 the error is largest, in relative terms, in the regions of high shear stress where the flow is not aligned with grid, and in the potential flow where diffusion is small and convection balances pressure gradient, although further grid refinement to reduce this error to say 1% would require an excessive number of additional nodes, of the order of 100 times as many, thus making the required computation prohibitively expensive.

The truncation estimation could be performed for all dependent variables but since the major errors occur where the flow is at large angles with the grid lines then testing of the

solutions for V_1, V_2 and one turbulence quantity, usually k, should be sufficient for the purposes of grid refinement.

Boundary conditions. Boundary conditions must be applied for each variable to link the internal grid nodes to those on the boundary. The numerical implementation of the boundary conditions for scalar and velocity cells is considered here. There are three fundamental types of boundary conditions which are used presently: the boundary value is prescribed (Dirchlet), the boundary flux is prescribed (Neumann) and the value at an internal node is prescribed.

The numerical implementation of these conditions for a scalar cell, whose finite-difference equation is given by 4.122, is determined for a west face boundary as an example, and is coincident with the scalar cell-wall as shown on figure 4.7. The Dirchlet condition is prescribed by:-

$$A_W = 0;\ S_{Im} = -A'_W\ ;\ S_{Ex} = A'_W\phi_B \tag{4.147}$$

where ϕ_B is the given value at the boundary and the wall flux coefficient is:-

$$A'_W = \rho\Delta a_{sw/nw}V_{1,B} \tag{4.148}$$

with $V_{1,B}$ being the velocity across the boundary.

The Neumann boundary condition is prescribed by:-

$$A_W = 0;\ S_{Im} = 0;\ S_{Ex} = \dot{q}_B \tag{4.149}$$

where the boundary flux, $\dot{q}_B$, is known and given by, for example:-

$$\dot{q}_B = A_W'\left(\frac{d\phi}{dx}\,\delta x\right)_{x\,=\,B} \tag{4.150}$$

It can be seen for a zero pressure gradient boundary that:-

$$\frac{\partial\phi}{\partial x} = 0; \quad \phi_W = \phi_B = \phi_P \tag{4.151}$$

which is the effect imposed by 4.149 although further direct implementation of 4.151 may be necessary when calculating higher order curvature and other source terms.

Values of the scalar, ϕ_P, may be fixed at an internal node with:-

$$S_{Im} = -\gamma; \; S_{Ex} = \gamma\phi_{fix}; \quad \gamma = 10^{30} \tag{4.152}$$

in the finite-difference equation 4.122.

Implementing the velocity boundary conditions follows the same principles except that the inflow velocity cell has half of the volume of scalar cells adjacent to the boundary as shown in figure 4.7. The Dirchlet boundary condition with a prescribed value for the inflow velocity, $V_{1,B}$, across the boundary is implemented in equation 4.130 with:-

$$A_W = 0; \; S_{Im} = \frac{\rho}{2}\,a_{sw/nw}V_{1,P}; \; S_{Ex} = \frac{\rho}{2}\,a_{sw/nw}V_{1,B}^2 \tag{4.153}$$

using upwind differencing for the convected velocity.

Boundary conditions for velocities parallel to the wall are implemented in the same manner as in scalar boundary cells. Wall boundary conditions are the only exception where the wall shear stress, τ_w, represents an additional momentum flux through the surface and is implemented for a south wall as:-

$$S_{Im} = S_{Im} + a_{ses/e}\left(\frac{\tau_w}{V_{1,P}}\right) \qquad (4.154)$$

and the reason for this formulation will be made clear in section 4.5.

This concludes the discussion of the procedure for solving the full (elliptic) transport equations with an approximate numerical approach based on finite volume equations. The boundary conditions required to complete the specification of the problem are given in the following section and results of a calculation performed for the present flow discussed in chapter 5.

4.5 Viscous Flow Boundary Conditions

In the two preceding sections, calculation procedures for solving differential transport equations were introduced which can only be solved for a particular problem when boundary conditions have been specified. This section provides the conditions required at the various types of boundaries encountered in the present flow when solving the equations for pressure correction, momentum and turbulence quantities. Four types of boundaries are considered: inflow, outflow, wall and free stream boundaries.

Treatment of the boundary conditions for the elliptic and boundary-layer forms of the transport equations used in sections 4.3 and 4.4, respectively, are formulated in the same manner. The parabolic behaviour and hence marching procedure, of the boundary layer equations results in boundary conditions only being required on three sides since conditions at the outflow boundary can not affect the solution. In contrast, the elliptic equations require variables to be specified on the complete boundary encompassing the solution domain. Table 4.6 shows the boundary conditions and their implementation in the calculation procedures for the elliptic and boundary-layer equations. The remainder of this section endeavours to describe the equations and measurements required to effect these conditions.

The solution domain is shown in schematic form on figure 4.8 with the boundary-layer procedure used only in the shaded region. Solution of the conservation equation in their elliptic form is clearly uneconomic in regions where the boundary-layer assumptions are valid and the solution domain shown for the elliptic equations was chosen as a compromise which minimises these regions while

allowing specification of boundary conditions based on experimental knowledge or on the results of the boundary-layer calculation.

Inlet boundary. The upstream boundary conditions include the measured values of $\langle V_1 \rangle$, $\langle V_2 \rangle$, and $\langle P \rangle$ across the flow. Profiles of Reynolds stresses were measured with a stationary hot wire and closely agreed with those of Klebanoff (1954) at S/C of 0.372 where the boundary-layer calculation was started. For the elliptic equations, the inlet boundary was located immediately upstream of the influence of boundary-layer curvature where measurements of all properties, including $\langle V_1 \rangle$, $\langle V_2 \rangle$, $\langle P \rangle$, and $\langle k \rangle$, were determined. The rate of dissipation was obtained with a mixing length hypothesis by approximating equation 4.24 by:-

$$-\langle \rho \rangle \langle v_1' v_2' \rangle = \mu_t \frac{1}{\ell_2} \frac{\partial \langle V_1 \rangle}{\partial \zeta_2} \tag{4.155}$$

and substituting the eddy viscosity from equation 4.36. The dissipation rate then is given by:-

$$\varepsilon = \frac{C_\mu \langle k \rangle^2}{\langle v_1' v_2' \rangle} \left(\frac{1}{\ell_2} \frac{\partial \langle V_1 \rangle}{\partial \zeta_2} \right) \tag{4.156}$$

where the velocity distribution, turbulence kinetic energy and Reynolds shear stress are obtained from measurements.

Detailed knowledge of the lower surface boundary-layer was used as an inlet condition for the flow entering the calculation from beneath the trailing edge. Only the velocity parameters $\langle V_1 \rangle$ and $\langle v_1'^2 \rangle$ were measured with a single normal hot wire in the pressure-side boundary-layer because it had a thickness of only about 5 mm. These velocity values agreed sensibly with Klebanoff (1954) and it was assumed that the remaining Reynolds stresses would also

behave in a similar manner. The wall shear stress was obtained from Clauser charts and the level of turbulence shear stress at the wall set equal to it. The dissipation rate was obtained from equation 4.156.

The accuracy of the velocity measurements used to obtain the inlet profiles is important as is the method of interpolation between measurement locations. The profiles of mean velocity and turbulence correlation were obtained with stationary hot-wire anemometry as described in section 2.3. Measurements were taken so that the increment in mean velocity between cross-stream locations was less than 3 per cent of the free-stream velocity so that steps of less than 0.25 mm were taken close to the wall and increased to 5 mm at the boundary-layer edge. Linear interpolation was used for values required between these locations and for the velocity gradients in equation 4.155. The profiles of eddy viscosity and turbulence dissipation rate were found to vary smoothly and monotonically from their near-wall values to those in the free stream. The affects of interpolation and the accuracy of the mean velocity profiles is likely to be small on the calculation although tests are required particularly for the boundary conditions involving turbulence kinetic energy and its dissipation rate, since they are most uncertain. They are conducted in chapter 5.

The prescribed values at the inflow boundary were introduced into the elliptic calculations with the relations 4.153 for $\langle V_1 \rangle$ and 4.147 for scalars and $\langle V_2 \rangle$. The gradient of the pressure correction was set to zero with relation 4.149 with $\dot{q}_B$ set equal to zero.

With the boundary-layer equations the initial values were set in order to begin marching downstream.

Wall boundary. At the solid boundary the no-slip condition applies so that mean and fluctuating velocities at the wall are zero; however, the dissipation rate is finite and demands special attention.

Two important features distinguish near-wall regions from other parts of the flow: first, very steep gradients prevail normal to the surface for most flow properties and, second, viscous effects can be important so that the effects of molecular viscosity can influence the turbulence field. The presence of the wall influences the eddy structure so that the small scale turbulence is no longer isotropic and the high-Reynolds number turbulence models introduced in section 4.1 are not applicable. It is possible to account for these effects in the framework of the present method by using closely spaced grid nodes to resolve the gradients, but this is expensive, and by modifying the turbulence model so that low Reynolds number phenomena are more appropriately modelled (see Jones and Launder, 1972). This low Reynolds number formulation for the k-ε equations is poorly founded and not well tested and hence it is not used here. Besides the emphasis of the calculation should not be placed, at least initially, on the wall boundary condition.

Calculation through the viscous sublayer is not necessary. The measurements of near-wall velocity profiles in section 3.2 indiciates that the empirical law-of-the-wall holds in sufficient generality so that it can be used to bridge between the wall conditions and the dependent variable outside the viscous sublayer. The semi-empirical relation, given by:-

$$U^+ = Y^+ \tag{4.157}$$

can be used for points in the viscous sublayer and the univeral law-of-the-wall, given by:-

$$U^+ = \frac{1}{\kappa} \ln(EY^+) \tag{4.158}$$

can be used for matching in the inertial sublayer. The dimensionless velocity and distance are defined by:-

$$U^+ = \frac{\langle V_1 \rangle}{U_\tau} \tag{4.159}$$

$$Y^+ = \frac{\rho U_\tau Y}{\mu} \tag{4.160}$$

respectively, with the friction velocity given by:-

$$U_\tau = (\tau_w/\rho)^{1/2} \tag{4.161}$$

where τ_w is the wall shear stress, $\langle V_1 \rangle$ is the mean velocity parallel to the surface and Y is the perpendicular distance from the wall.

The buffer region between the viscous sublayer, below Y^+ of 5, and the inertial region, above Y^+ of 30, may be dispensed with by extending the viscous and inertial layers to a common boundary at Y^+ of 11.63 which is an adequate treatment for engineering purposes.

In the near-wall region the Reynolds stresses are measured to be nearly constant, see section 3.4 for instance, and the wall shear stress, τ_w, will be equal to the near-wall value of Reynolds shear stress so that:-

$$\tau_w \equiv \rho u_\tau^2 = \rho \langle v_1' v_2' \rangle \tag{4.162}$$

The production of turbulence kinetic energy in the near-wall region is then obtained by simplifying term III of equation 4.28 with the additional assumptions of $\langle V_2 \rangle$ and its streamwise gradient being small in the near-wall cells. The cell-faces are taken perpendicular to the

boundary, so that r_2 is infinite, and the generation of turbulence kinetic energy is expressed by:-

$$G_{tw} = \rho(\langle v_1'v_1'\rangle - \langle v_2'v_2'\rangle)\frac{1}{\ell_1}\frac{\partial\langle V_1\rangle}{\partial\zeta_1} + \tau_w\left(\frac{1}{\ell_2}\frac{\partial\langle V_1\rangle}{\partial\zeta_2} - \frac{\langle V_1\rangle}{r_1}\right) \quad (4.163)$$

after invoking continuity. Direct application of the Boussinesq approximation of equation 4.24 would negate any contribution from normal stresses represented by the first term in this equation. In section 3.3 it was observed that $\langle v_1'^2\rangle$ was much greater than $\langle v_2'^2\rangle$ in the vicinity of separation which contrary to the Boussinesq approximation and normal stress production makes an important contribution to G_{tw}. Furthermore, results obtained in the flows of Simpson et al (1977), Nakayama (1983) and Wadcock (1980) show that the production in the near wall may be greater than the contributions from the shear stress production, represented by the second term in equation 4.163, alone. The difference between the normal stresses was accordingly approximated as:-

$$\langle v_1'^2\rangle - \langle v_2'^2\rangle = C_n\langle v_1'^2\rangle \quad (4.164)$$

and the normal stress calculated from equation 4.24 as:-

$$\langle v_1'^2\rangle = \frac{2}{3}\rho k - 2\mu_t\frac{1}{\ell_1}\frac{\partial\langle V_1\rangle}{\partial\zeta_1} \quad (4.165)$$

with a value of C_n obtained from measurements which was typically around 1.0 in the present flow. The generation of turbulent kinetic energy when modified to take some account of normal stress production, takes the form:-

$$G_{tw} = \tau_w \left[\left(\frac{1}{\ell_2} \frac{\partial \langle V_1 \rangle}{\partial \zeta_2} \right)_w - \frac{\langle V_1 \rangle}{r_1} \right] +$$

$$+ \left[\frac{2}{3} \rho k - \mu_t \frac{1}{\ell_1} \frac{\partial \langle V_1 \rangle}{\partial \zeta_1} \right] \frac{1}{\ell_1} \frac{\partial \langle V_1 \rangle}{\partial \zeta_1} \qquad (4.166)$$

and was used here. The velocity gradient was obtained by differentiating equations 4.157 and 4.158 which gives:-

$$\left(\frac{1}{\ell_2} \frac{\partial \langle V_1 \rangle}{\partial \zeta_2} \right)_w = \begin{cases} \dfrac{\rho U_\tau^2}{\mu} = \dfrac{\langle V_1 \rangle}{Y} & \text{for } Y^+ < 11.63 \qquad (4.167) \\ \dfrac{U_\tau}{\kappa Y} = \dfrac{\langle V_1 \rangle}{Y \log(EY^+)} & \text{for } Y^+ > 11.63 \qquad (4.168) \end{cases}$$

As a consequence of nearly constant values of the Reynolds stresses in the near-wall region, convection and diffusion of $\langle v_i' v_j' \rangle$ can be assumed to be negligible which implies that equilibrium prevails. The remaining terms in the turbulent kinetic energy equation are production and dissipation which must balance so that

$$\rho \langle \varepsilon_w \rangle = G_{tw} \ . \qquad (4.169)$$

The production of turbulence kinetic energy is approximated for this equation by considering only the dominant term which is:-

$$G_{tw} = \tau_w \left(\frac{1}{\ell_2} \frac{\partial \langle V_1 \rangle}{\partial \zeta_2} \right)_w \qquad (4.170)$$

so that, by substituting for τ_w from 4.161, equation 4.169 may be expressed as:-

$$\langle \varepsilon_w \rangle = u_\tau^2 \left(\frac{1}{\ell_2} \frac{\partial \langle V_1 \rangle}{\partial \zeta_2} \right)_w \ . \qquad (4.171)$$

Applying the eddy viscosity assumption from equation 4.24 and ignoring terms arising from curvature and streamwise gradients gives the wall gradient as:-

$$\left(\frac{1}{\ell_2}\frac{\partial \langle V_1 \rangle}{\partial \zeta_2}\right)_w = \frac{\tau_w}{\mu_{eff}} \tag{4.172}$$

where μ_{eff} is given by 4.32 and has the values of the laminar viscosity, μ, in the viscous sublayer and the turbulent viscosity, μ_t, in the inertial region. Substituting $\langle\varepsilon\rangle$ from equation 4.36, using τ_w/μ_{eff} from 4.172 for the gradient, and taking the square root of equation 4.171 gives an expression for the friction velocity which is:-

$$U_\tau = C_\mu^{1/4} k^{1/2} \quad . \tag{4.173}$$

The wall value of dissipation rate is then obtained from equation 4.171 by substituting 4.167 and 4.168 and is expressed as:-

$$\langle\varepsilon_w\rangle = \begin{cases} \dfrac{\rho U_\tau^4}{\mu} = \dfrac{\rho C_\mu k^2}{\mu} & \text{for } Y^+ < 11.63 \quad (4.174) \\ \dfrac{U_\tau^3}{\kappa Y} = \dfrac{\rho C_\mu^{3/4} k^{3/2}}{\kappa Y} & \text{for } Y^+ > 11.63 \quad (4.175) \end{cases}$$

where the second term invokes equation 4.173 for the friction velocity.

Alternatively the wall friction can be obtained from equation 4.158 as:-

$$U_\tau = \frac{\kappa \langle V_1 \rangle}{\ln(E\,Y^+)} \quad . \tag{4.176}$$

The wall shear stress is then obtained by multiplying equations 4.173 and 4.176 to give:-

$$\tau_w = \frac{\rho C_\mu^{1/4} k^{1/2} \kappa \langle V_1 \rangle}{\ln(E\ Y^+)} \qquad (4.177)$$

and the value of Y^+ obtained with u_τ from equation 4.173 and expressed as:-

$$Y^+ = \frac{\rho C_\mu^{1/4} k^{1/2} Y}{\mu} \quad . \qquad (4.178)$$

The wall functions were introduced into the elliptic calculation procedure using equation 4.154 and τ_w from equation 4.177 for the V_1-momentum equation. The cross-stream velocity, through the surface, was zero and implemented in 4.153 with $V_{2,B}$ equal to zero for a south cell-face. The gradient of pressure correction was set to zero with equation 4.149 and $\dot{q}_B$ set to zero. The turbulence kinetic energy was taken as zero at the wall according to 4.147 with ϕ_B set to zero and the generation term G_{tw} from equation 4.166. The wall dissipation was set to its value with equation 4.152 and ϕ_{fix} set to $\langle \varepsilon_w \rangle$ obtained from equation 4.169.

The differences when formulating boundary conditions for the Reynolds stress transport equation are that G_{tw} is obtained from equation 4.170 since normal stresses are assumed negligible and $\langle \varepsilon \rangle$ is obtained with equation 4.174 or 4.175 and the additional wall treatment described in section 4.3 by equation 4.107. The other boundary conditions are identical.

Free stream boundary. The boundary layers on the upper and lower surface of the wind tunnel were not calculated and free stream boundary conditions were used which corresponded to the tunnel roof and floor or the measured displacement surface, δ_1 of equation 3.2 added to the surface co-ordinates. The details of the flow in the boundary layers on the tunnel roof and floor are not

important to the separated region provided that their effects on the free stream values of pressure and velocity are represented. Thus, the additional computation expense required to resolve the roof and tunnel boundary layer, is unnecessary.

Along the free-stream boundaries in the elliptic calculation the cross-stream velocity $\langle V_2 \rangle$ was zero and the gradients of $\langle V_1 \rangle$, $\langle k \rangle$, $\langle \varepsilon \rangle$ and P' were set to zero. It should be noted that the velocity $\langle V_1 \rangle$ is allowed to change with downstream distance when the normal velocity $\langle V_2 \rangle$ is zero and its gradient is used to balance the continuity equation 4.11 since $\partial \langle V_2 \rangle / \partial \zeta_2$ may have a non-zero value.

Implementing these conditions in the elliptic code makes use of the treatment described by equation 4.153 only for north or south faces and the value of V_B set to zero. The zero gradient conditions are implemented with equation 4.149 with $\dot{q}_B$ set to zero.

The free stream boundary conditions for the parabolic equations are slightly different. The boundary does not extend to the upper surface of the tunnel and is located by obtaining a value for the entrainment velocity and matching to the free stream conditions immediately outside the boundary layer. The values of free stream velocity are obtained from equation 4.105 and the values of stresses, kinetic energy and dissipation rate of the turbulence were taken as negligible. These assumptions and those for the entrainment rate needed to be tested and the relevant results reported in section 5.2.

Outflow boundary. An outflow boundary was not required for the solution of the boundary layer equations although it is important in the associated potential flow calculation of the pressure as discussed in section 4.3.

The outflow boundary for the solution of the elliptic equation was located far enough downstream of the recirculation region that it did not affect the results: the flow was parabolic in nature at the outlet. The gradients of $\langle V_2 \rangle$, $\langle k \rangle$, $\langle \varepsilon \rangle$ and the pressure correction were set to zero using equation 4.147. The boundary condition for streamwise momentum was implemented by specifying the outlet velocity corrected at every cell with equation 4.153 for an east boundary where the boundary value of velocity is given by:-

$$\langle V_1 \rangle_B = \langle V_1 \rangle_{last} + U_{inc}$$

where the subscripts B and last refer to the velocity at the outlet boundary and in the last V_1-calculation cell, respectively. The value of U_{inc} was obtained by balancing the overall continuity equation and is given by:-

$$U_{inc} = (\dot{m}_{in} - \dot{m}_{last})/\rho A_{out}$$

where $\dot{m}_{in}$ and $\dot{m}_{last}$ are the total mass flow rates at the inlet to the solution domain and at the outlet through the outlet boundary with area, A_{out}. The value of $\dot{m}_{in}$ is calculated by integrating the upstream boundary conditions across the upper and lower entry ports. The value of $\dot{m}_{last}$ is calculated by integrating across the outlet boundary with the velocity of the last V_1-calculation cell. When the solution is converged U_{inc} should have a negligible value and implies that the gradient of $\langle V_1 \rangle$ is zero at the outlet.

4.6 Summary

Calculation procedures have been described to solve the time-averaged transport equations for mass and momentum and employ turbulence modelling based on k-ε and Reynolds stress transport equations. A procedure was also presented to solve the inviscid-flow equations to obtain the pressure distribution and this was coupled with a calculation method based on the boundary-layer equations via an interaction technique using the displacement thickness. The potential-flow solution was also used as an orthogonal curvilinear mesh in a solution procedure for the time-averaged Navier-Stokes equations with the k-ε turbulence model. Results obtained with these methods are presented and compared to experimental results in chapter 5.

The inviscid flow calculation procedure solved the streamwise momentum and continuity equations in finite-difference form on a grid consisting of streamlines and velocity potential lines. The grid was generated inside a body-fitted boundary by solving the potential-flow Laplace equations for the intersections between lines of constant stream function and velocity potential using a finite-difference method. The method used constant values for the spacings between stream function lines and between velocity potential lines so that the locations of nodes in physical space is not fixed a priori. Hence an overly fine grid is generated and calculation nodes are selected from it empirically.

A procedure was described for adding the displacement thickness, which is obtained from a boundary layer calculation, to the surface co-ordinates in order to interact the effects of the viscous boundary layer with those of the potential flow. An existing solution procedure

for the boundary layer equations was described and utilized a Reynolds stress model that was able to account for the influence of streamwise curvature on the turbulence. The scheme can predict the upstream boundary layer but fails at the location of mean streamline detachment because of the Goldstein singularity inherent in the forward-marching formulation. It is also expected that the simplified treatment of the cross-stream momentum equation will be inappropriate upstream of this location because of the strong interaction between the inviscid and viscous flow in the vicinity of separation.

A finite-difference calculation procedure was also described for solving the time-averaged Navier-Stokes equations in orthogonal curvilinear co-ordinates. This procedure can predict regions of recirculation and could be used over the entire flow domain although it would be inefficient where the boundary layer assumptions apply and inaccurate due to numerical diffusion in the inviscid flow. The orthogonal curvilinear formulation was used in order to accurately represent the boundary conditions and has the added benefit of reducing numerical diffusion in the outer inviscid flow since the grid lines here will be approximately aligned with the flow direction. The solution of the potential flow equations used to generate the grid, takes no account of the region of recirculation and the flow is expected to cross the grid lines at an angle near separation. This causes numerical diffusion when upwind differencing is used. This error can be estimated by recalculating terms of the finite-difference equations using central differences and the flow field that was obtained when hybrid differencing was employed. Numerical errors can then be

reduced by refining the grid wherever large imbalances are found.

The k-ε turbulence model was used in the elliptic calculation since it represents the lowest level of closure appropriate to recirculating flow. Further, solving the Reynolds stress transport equations in their elliptic form is computationally expensive, particularly in general orthogonal curvilinear co-ordinates, and offers no guarantee of significant improvement over the k-ε model.

Solutions obtained with all of the above procedures are shown in chapter 5 and the results obtained in the regions of inviscid, boundary-layer and recirculating flow are evaluated.

TABLE 4.1

THE k-ε TURBULENCE MODEL CONSTANTS

CONSTANT	VALUE
C_μ	0.09
$C_{\varepsilon 1}$	1.44
$C_{\varepsilon 2}$	1.92
σ_k	1.0
σ_ε	1.22
κ	0.4187
E	9.793

TABLE 4.2

REYNOLDS STRESS TURBULENCE MODEL CONSTANTS

CONSTANT	VALUE
C_t	0.22
C_1	1.8
C_2	0.6
C_1'	0.5
C_2'	0.3
C_ε	0.18
$C_{\varepsilon 1}$	1.45
$C_{\varepsilon 2}$	1.90
C_μ	0.09
κ	0.41
E	7.768

TABLE 4.3

SOURCE TERMS FOR ORTHOGONAL CURVILINEAR FORM OF TRANSPORT EQUATIONS

VARIABLE ϕ	DIFFUSIVITY Γ_ϕ	SOURCE TERM S_ϕ
$\langle V_1 \rangle$	μ_{eff}	$-\frac{1}{\ell_1}\frac{\partial \langle P \rangle}{\partial \zeta_1}$
		$+\frac{1}{\ell_1 \ell_2 \ell_3}\{\frac{\partial}{\partial \zeta_1}[(\mu_{eff}(\frac{1}{\ell_1}\frac{\partial \langle V_1 \rangle}{\partial \zeta_1}+\frac{2\langle V_2 \rangle}{r_1}))-\frac{2}{3}\langle \rho \rangle \langle k \rangle]$
		$+\frac{\partial}{\partial \zeta_2}[\ell_1 \ell_3 \mu_{eff}(\frac{1}{\ell_1}\frac{\partial \langle V_2 \rangle}{\partial \zeta_1}-\frac{\langle V_1 \rangle}{r_1}-\frac{\langle V_2 \rangle}{r_2})]\}$
		$+\frac{1}{r_1}\{-\langle \rho \rangle \langle V_2 \rangle \langle V_1 \rangle$
		$+\mu_{eff}(\frac{1}{\ell_2}\frac{\partial \langle V_1 \rangle}{\partial \zeta_2}-\frac{\langle V_1 \rangle}{r_1}+\frac{1}{\ell_1}\frac{\partial \langle V_2 \rangle}{\partial \zeta_1}-\frac{\langle V_2 \rangle}{r_2})\}$
		$+\frac{1}{r_2}\{\langle \rho \rangle \langle V_2 \rangle \langle V_2 \rangle$
		$-2\mu_{eff}(\frac{1}{\ell_2}\frac{\partial \langle V_2 \rangle}{\partial \zeta_2}+\frac{\langle V_1 \rangle}{r_2})+\frac{2}{3}\langle \rho \rangle \langle k \rangle\}$

$\langle V_2 \rangle$	μ_{eff}	$-\frac{1}{\ell_2}\frac{\partial \langle P \rangle}{\partial \zeta_2}$
		$+\frac{1}{\ell_1 \ell_2 \ell_3}\{\frac{\partial}{\partial \zeta_1}[\ell_2 \ell_3 \mu_{eff}(\frac{1}{\ell_2}\frac{\partial \langle V_1 \rangle}{\partial \zeta_2} - \frac{\langle V_1 \rangle}{r_1} - \frac{\langle V_2 \rangle}{r_2})]$
		$+\frac{\partial}{\partial \zeta_2}[\ell_1 \ell_3(\mu_{eff}(\frac{1}{\ell_2}\frac{\partial \langle V_2 \rangle}{\partial \zeta_2} + \frac{2\langle V_1 \rangle}{r_2})) - \frac{2}{3}\langle \rho \rangle \langle k \rangle]\}$
		$+\frac{1}{r_1}\{\langle \rho \rangle \langle V_1 \rangle \langle V_1 \rangle - 2\mu_{eff}(\frac{1}{\ell_1}\frac{\partial \langle V_1 \rangle}{\partial \zeta_1} + \frac{\langle V_2 \rangle}{r_1}) + \frac{2}{3}\langle \rho \rangle \langle k \rangle\}$
		$+\frac{1}{r_2}\{-\langle \rho \rangle \langle V_1 \rangle \langle V_2 \rangle + \mu_{eff}(\frac{1}{\ell_2}\frac{\partial \langle V_1 \rangle}{\partial \zeta_2} - \frac{\langle V_1 \rangle}{r_1} + \frac{1}{\ell_1}\frac{\langle V_2 \rangle}{\partial \zeta_1} - \frac{\langle V_2 \rangle}{r_2})\}$
1 (for p')	0	0
k	$\frac{\mu_{eff}}{\sigma_k}$	$G_t - \langle \rho \rangle \langle \varepsilon \rangle$ (for G_t see equation 4.30)
ε	$\frac{\mu_{eff}}{\sigma_\varepsilon}$	$C_{\varepsilon_1}\frac{\langle \varepsilon \rangle}{\langle k \rangle} G_t - C_{\varepsilon_2}\langle \rho \rangle \frac{\langle \varepsilon \rangle^2}{\langle k \rangle}$

TABLE 4.4

UNDER-RELAXATION PARAMETERS

VARIABLE	UNDER-RELAXATION CONSTANT
V_1	0.5
V_2	0.5
P'	0.5
k	0.7
ε	0.7
μ_t	1.0

TABLE 4.5

CONVECTION, DIFFUSION AND SOURCE TERMS OF

MOMENTUM AND TURBULENCE KINETIC ENERGY BALANCE EQUATIONS

BALANCE EQUATION: CONVECTION = DIFFUSION + SOURCE TERMS

V_1 - MOMENTUM BALANCE TERMS

$$\text{Convection} = \frac{1}{\ell_1\ell_2\ell_3}\left\{\frac{\partial}{\partial\zeta_1}(\ell_2\ell_3\langle\rho\rangle\langle V_1\rangle\langle V_1\rangle) + \frac{\partial}{\partial\zeta_2}(\ell_1\ell_3\langle\rho\rangle\langle V_2\rangle\langle V_1\rangle)\right\}$$

$$+ \frac{1}{r_1}\langle\rho\rangle\langle V_2\rangle\langle V_1\rangle - \frac{1}{r_2}\langle\rho\rangle\langle V_2\rangle\langle V_2\rangle$$

$$\text{Diffusion} = \frac{1}{\ell_1\ell_2\ell_3}\left\{\frac{\partial}{\partial\zeta_1}\left(\frac{\ell_2\ell_3}{\ell_1}\mu_{eff}\frac{\partial\langle V_1\rangle}{\partial\zeta_1}\right) + \frac{\partial}{\partial\zeta_2}\left(\frac{\ell_1\ell_3}{\ell_2}\mu_{eff}\frac{\partial\langle V_1\rangle}{\partial\zeta_2}\right)\right.$$

$$+ \frac{\partial}{\partial\zeta_1}\left[\ell_2\ell_3\left(\mu_{eff}\left(\frac{1}{\ell_1}\frac{\partial\langle V_1\rangle}{\partial\zeta_1} + \frac{2\langle V_2\rangle}{r_1}\right)\right) - \frac{2}{3}\langle\rho\rangle\langle k\rangle\right]$$

$$\left. + \frac{\partial}{\partial\zeta_2}\left[\ell_1\ell_3\,\mu_{eff}\left(\frac{1}{\ell_1}\frac{\partial\langle V_2\rangle}{\partial\zeta_1} - \frac{\langle V_1\rangle}{r_1} - \frac{\langle V_2\rangle}{r_2}\right)\right]\right\}$$

$$- 2\frac{\mu_{eff}}{r_2}\left(\frac{1}{\ell_2}\frac{\partial\langle V_2\rangle}{\partial\zeta_2} + \frac{\langle V_1\rangle}{r_2}\right) + \frac{2}{3r_2}\langle\rho\rangle\langle k\rangle$$

$$+ \frac{\mu_{eff}}{r_1}\left(\frac{1}{\ell_2}\frac{\partial\langle V_1\rangle}{\partial\zeta_2} - \frac{\langle V_1\rangle}{r_1} + \frac{1}{\zeta_1}\frac{\partial\langle V_2\rangle}{\partial\zeta_1} - \frac{\langle V_2\rangle}{r_2}\right)$$

$$\text{Pressure gradient} = -\frac{1}{\ell_1}\frac{\partial\langle P\rangle}{\partial\zeta_1}$$

V_2 - MOMENTUM BALANCE TERMS

$$\text{Convection} = \frac{1}{\ell_1\ell_2\ell_3}\left\{\frac{\partial}{\partial\zeta_1}(\ell_2\ell_3\langle\rho\rangle\langle V_1\rangle\langle V_2\rangle) + \frac{\partial}{\partial\zeta_2}(\ell_1\ell_3\langle\rho\rangle\langle V_2\rangle\langle V_2\rangle)\right\}$$

$$- \frac{\langle\rho\rangle}{r_1}\langle V_1\rangle\langle V_1\rangle + \frac{\langle\rho\rangle}{r_2}\langle V_1\rangle\langle V_2\rangle$$

$$\text{Diffusion} = \frac{1}{\ell_1\ell_2\ell_3}\left\{\frac{\partial}{\partial\zeta_1}\left(\frac{\ell_2\ell_3}{\ell_1}\mu_{eff}\frac{\partial\langle V_2\rangle}{\partial\zeta_1}\left(\frac{\ell_1\ell_3}{\ell_2}\mu_{eff}\frac{\partial\langle V_2\rangle}{\partial\zeta_2}\right)\right.\right.$$

$$+ \frac{\partial}{\partial\zeta_1}\left[\ell_2\ell_3\left(\mu_{eff}\left(\frac{1}{\ell_2}\frac{\partial\langle V_1\rangle}{\partial\zeta_2} - \frac{\langle V_1\rangle}{r_1} - \frac{\langle V_2\rangle}{r_2}\right)\right)\right]$$

$$\left.\left. + \frac{\partial}{\partial\zeta_2}\left[\ell_1\ell_3\left(\mu_{eff}\left(\frac{1}{\ell_2}\frac{\partial\langle V_2\rangle}{\partial\zeta_2} + \frac{2\langle V_1\rangle}{r_2}\right)\right) - \frac{2}{3}\langle\rho\rangle\langle k\rangle\right]\right\}\right.$$

$$- \frac{2\mu_{eff}}{r_1}\left(\frac{1}{\ell_1}\frac{\partial\langle V_1\rangle}{\partial\zeta_1} + \frac{\langle V_2\rangle}{r_1}\right) + \frac{2}{3r_1}\langle\rho\rangle\langle k\rangle$$

$$+ \frac{\mu_{eff}}{r_2}\left(\frac{1}{\ell_2}\frac{\partial\langle V_1\rangle}{\partial\zeta_2} - \frac{\langle V_1\rangle}{r_1} + \frac{1}{\ell_1}\frac{\partial\langle V_2\rangle}{\partial\zeta_1} - \frac{\langle V_2\rangle}{r_2}\right)$$

$$\text{Pressure gradient} = -\frac{1}{\ell_2}\frac{\partial\langle P\rangle}{\partial\zeta_2}$$

k - TRANSPORT EQUATION BALANCE TERMS

$$\text{Convection} = \frac{1}{\ell_1 \ell_2 \ell_3} \left\{ \frac{\partial}{\partial \zeta_1} \left(\ell_2 \ell_3 \langle \rho \rangle \langle V_1 \rangle \langle k \rangle \right) + \frac{\partial}{\partial \zeta_2} \left(\ell_1 \ell_3 \langle \rho \rangle \langle V_2 \rangle \langle k \rangle \right) \right\}$$

$$\text{Diffusion} = \frac{1}{\ell_1 \ell_2 \ell_3} \left\{ \frac{\partial}{\partial \zeta_1} \left(\frac{\ell_2 \ell_3}{\ell_1} \frac{\mu_{eff}}{\sigma_k} \frac{\partial \langle k \rangle}{\partial \zeta_1} \right) + \frac{\partial}{\partial \zeta_2} \left(\frac{\ell_1 \ell_3}{\ell_2} \frac{\mu_{eff}}{\sigma_k} \frac{\partial \langle k \rangle}{\partial \zeta_2} \right) \right\}$$

Generation = G_t (see equation 4.30)

Dissipation = $- \rho \langle \varepsilon \rangle$

TABLE 4.6

SUMMARY OF BOUNDARY CONDITIONS

INVISCID CALCULATION

INLET - Velocity potential line (defined)

$$V_1 = U_{ref}; \quad V_2 = k = \varepsilon = 0 \text{ (implied)}$$

OUTLET - Velocity potential line (defined)

$$V_1 = \frac{A_{out}}{A_{in}} U_{ref}; \quad V_2 = k = \varepsilon = 0 \text{ (implied)}$$

where A_{in} and A_{out} are the inlet and outlet areas.

WALL - Streamline (defined)

$$\tau_w = 0; \qquad V_2 = k = \varepsilon = 0 \text{ (implied); slip velocity.}$$

FREE-STREAM - Streamline (defined)

$$\tau_w = 0; \qquad V_2 = k = \varepsilon = 0 \text{ (implied); slip velocity.}$$

BOUNDARY-LAYER CALCULATION

INLET - Measured profiles of $\langle U_1 \rangle$, $\langle u_1'^2 \rangle$, $\langle u_2'^2 \rangle$, $\langle u_3'^2 \rangle$, and $\langle u_1' u_2' \rangle$

$$\langle U_2 \rangle = 0; \quad \varepsilon = C_\mu \langle k^2 \rangle \frac{\partial \langle U_1 \rangle}{\partial n} / \langle u_1' u_2' \rangle$$

OUTLET - Not required because of parabolic formulation.

WALL - Law-of-the-wall

$\langle U_1 \rangle$ uses $\tau_w = \rho U_\tau^2$ with $U_\tau = \dfrac{\kappa \langle U_1 \rangle}{\ln(EY^+)}$; $U_2 = 0$;

$\langle u_1'^2 \rangle = \langle u_2'^2 \rangle = \langle u_3'^2 \rangle = \langle u_1' u_2' \rangle = 0$ at the wall;

$$\langle \varepsilon \rangle_w^2 - \frac{C_{\varepsilon 1}}{C_{\varepsilon 2}} P_k \langle \varepsilon \rangle_w - \frac{C_\varepsilon}{C_{\varepsilon 2}} \frac{\langle k \rangle \langle u_2' \rangle^2}{n^2} = 0 \ ,$$

using $P_k = \langle u_1' u_2' \rangle \dfrac{\partial \langle U_1 \rangle}{\partial y}$.

FREE-STREAM BOUNDARY

$\langle U_1 \rangle_e$ from equation 4.105;

$\langle u_1'^2 \rangle = \langle u_2'^2 \rangle = \langle u_3'^2 \rangle = \langle u_1' u_2' \rangle = \varepsilon = 0$

ELLIPTIC TRANSPORT EQUATIONS

INLET - Measured profiles of $\langle V_1 \rangle$, $\langle V_2 \rangle$, $\langle k \rangle$, $\langle v_1' v_2' \rangle$

$$\varepsilon = C_\mu \langle k \rangle^2 \frac{\partial \langle V_1 \rangle}{\partial \zeta_2} / \langle v_1' v_2' \rangle; \quad \frac{\partial P'}{\partial \zeta_1} = 0.$$

OUTLET - Zero gradient parabolic boundary

$$\frac{\partial \langle V_1 \rangle}{\partial \zeta_1} = 0; \quad \langle V_2 \rangle = 0; \quad \frac{\partial P'}{\partial \zeta_1} = 0; \quad \frac{\partial \langle k \rangle}{\partial \zeta_1} = 0; \quad \frac{\partial \langle \varepsilon \rangle}{\partial \zeta_1} = 0.$$

Note: Overall mass balance applied.

WALL - Law-of-the-wall

$$\langle V_1 \rangle \text{ uses } \tau_w = \frac{C_\mu^{1/4} \langle k \rangle^{1/2} \kappa \langle V_1 \rangle}{\ln(EY^+)}; \quad V_2 = 0; \quad \frac{\partial P'}{\partial \zeta_2} = 0;$$

$$\langle k \rangle \text{ uses } G_{tw} = \tau_w \left[\left(\frac{1}{\ell_2} \frac{\partial \langle V_1 \rangle}{\partial \zeta_1} \right)_w - \frac{\langle V_1 \rangle}{r_1} \right]$$

$$+ \left[\frac{2}{3} \langle \rho \rangle \langle k \rangle - \mu_t \frac{1}{\ell_1} \frac{\partial \langle V_1 \rangle}{\partial \zeta_1} \right] \frac{1}{\ell_1} \frac{\partial \langle V_1 \rangle}{\partial \zeta_1}$$

$$\text{where } \left(\frac{1}{\ell_2} \frac{\partial \langle V_1 \rangle}{\partial \zeta_2} \right)_w = \frac{\langle V_1 \rangle}{Y \ln(EY^+)}; \quad \varepsilon_w = C_\mu^{3/4} \langle k \rangle^{3/2} / \kappa y$$

FREE-STREAM - Streamline with zero gradients

$$\frac{\partial \langle V_1 \rangle}{\partial \zeta_2} = 0; \ \langle V_2 \rangle = 0; \ \frac{\partial P'}{\partial \zeta_2} = 0; \ \frac{\partial \langle k \rangle}{\partial \zeta_2} = 0; \ \frac{\partial \langle \varepsilon \rangle}{\partial \zeta_2} = 0$$

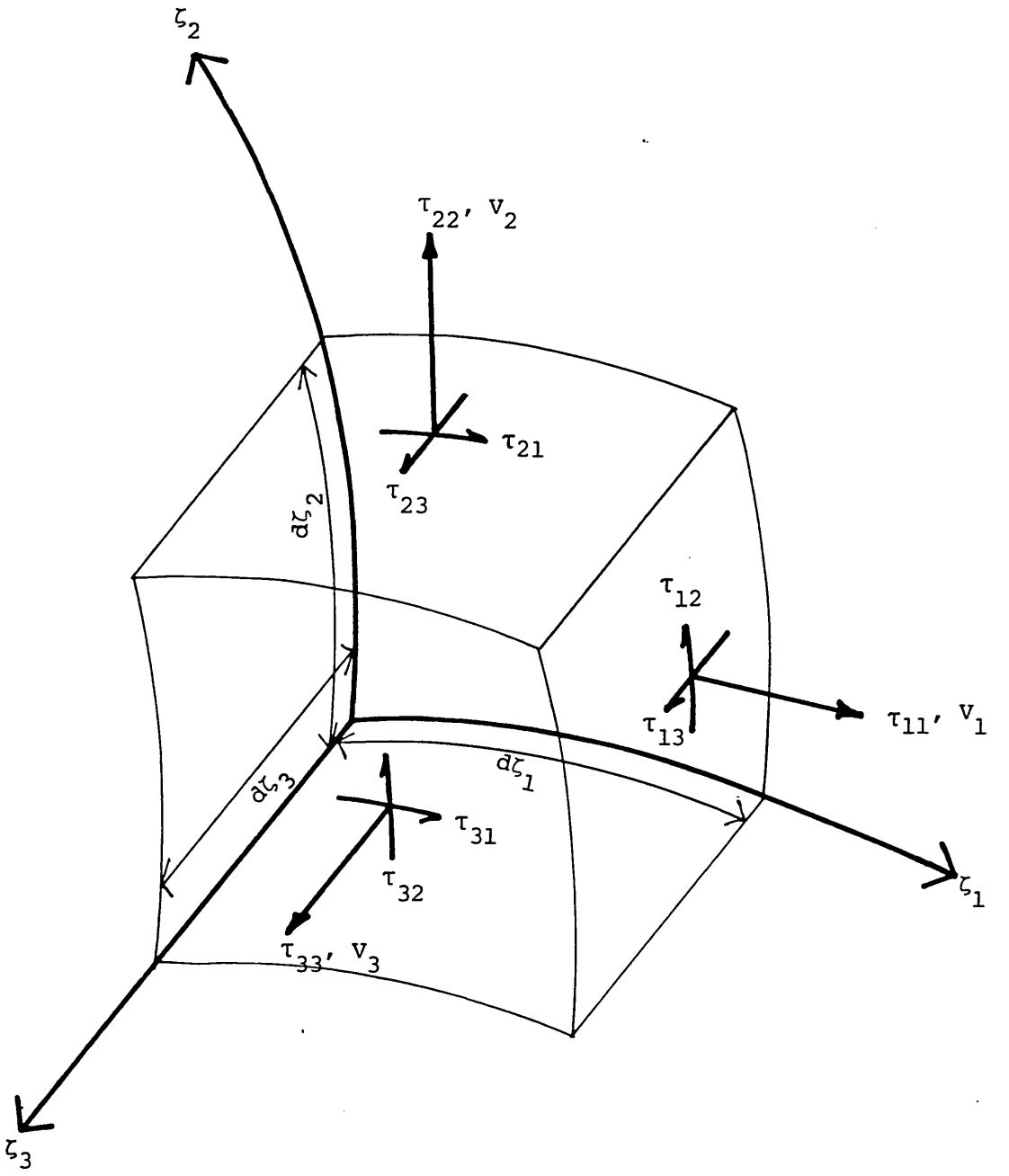


Figure 4.1 Orthogonal curvilinear co-ordinate system.

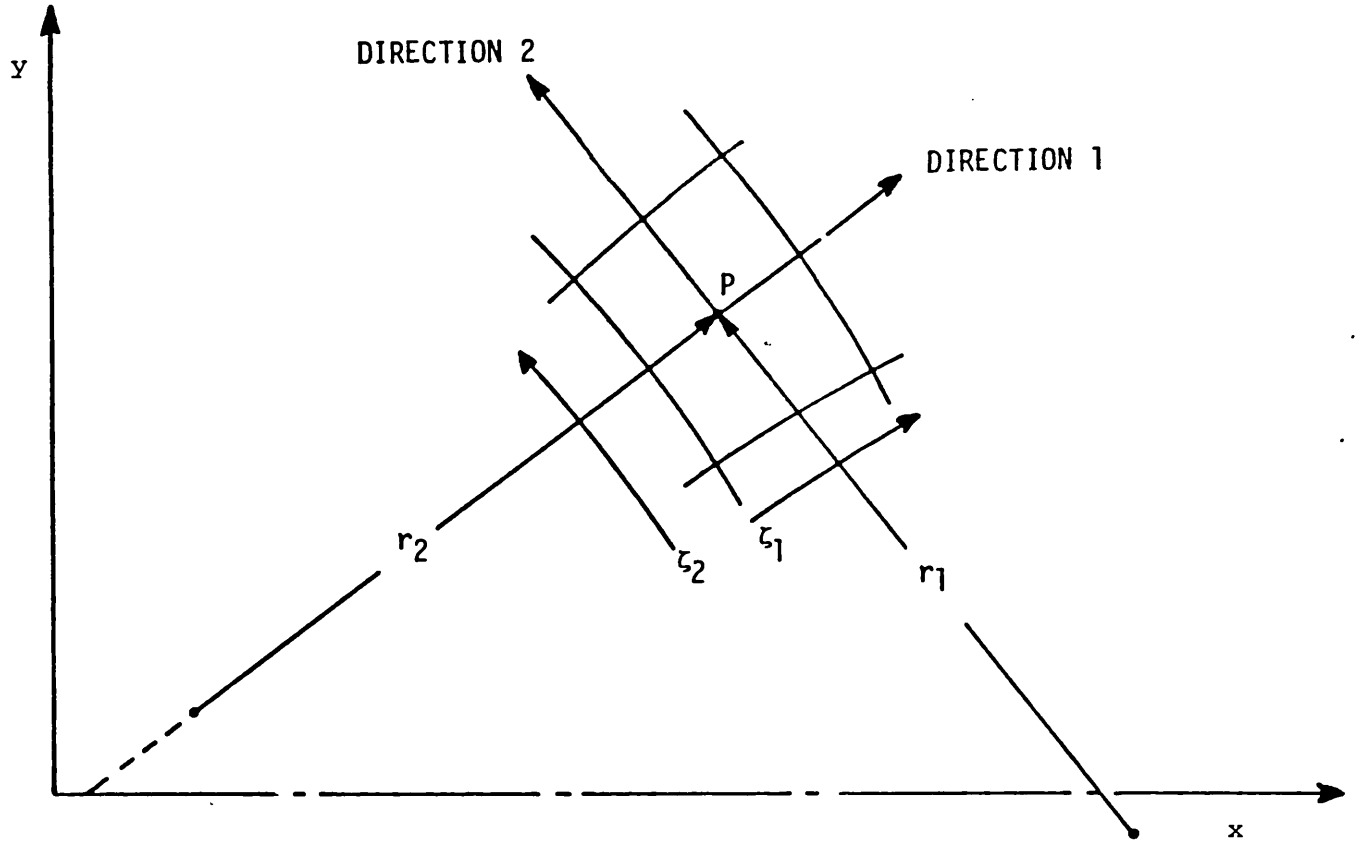


Figure 4.2 Two-dimensional plane of orthogonal-curvilinear co-ordinates.

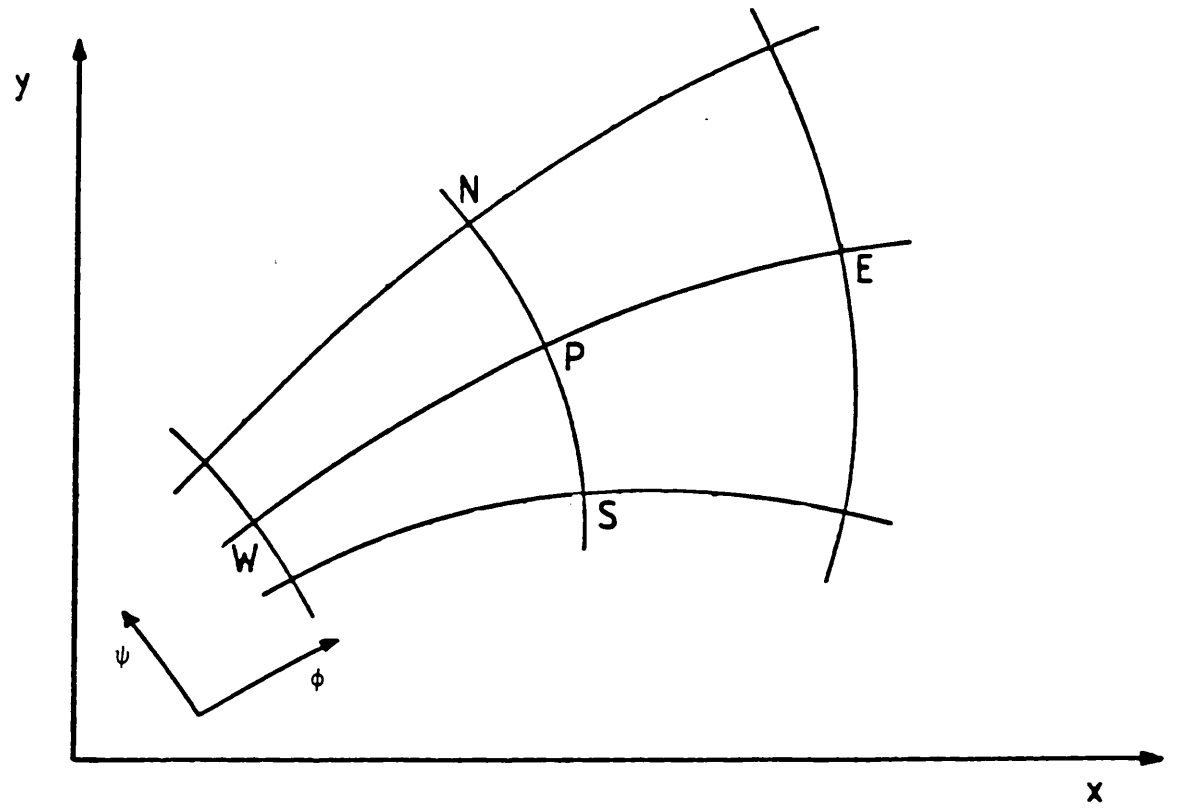


Figure 4.3 Numerical mesh for stream function-vorticity solution.

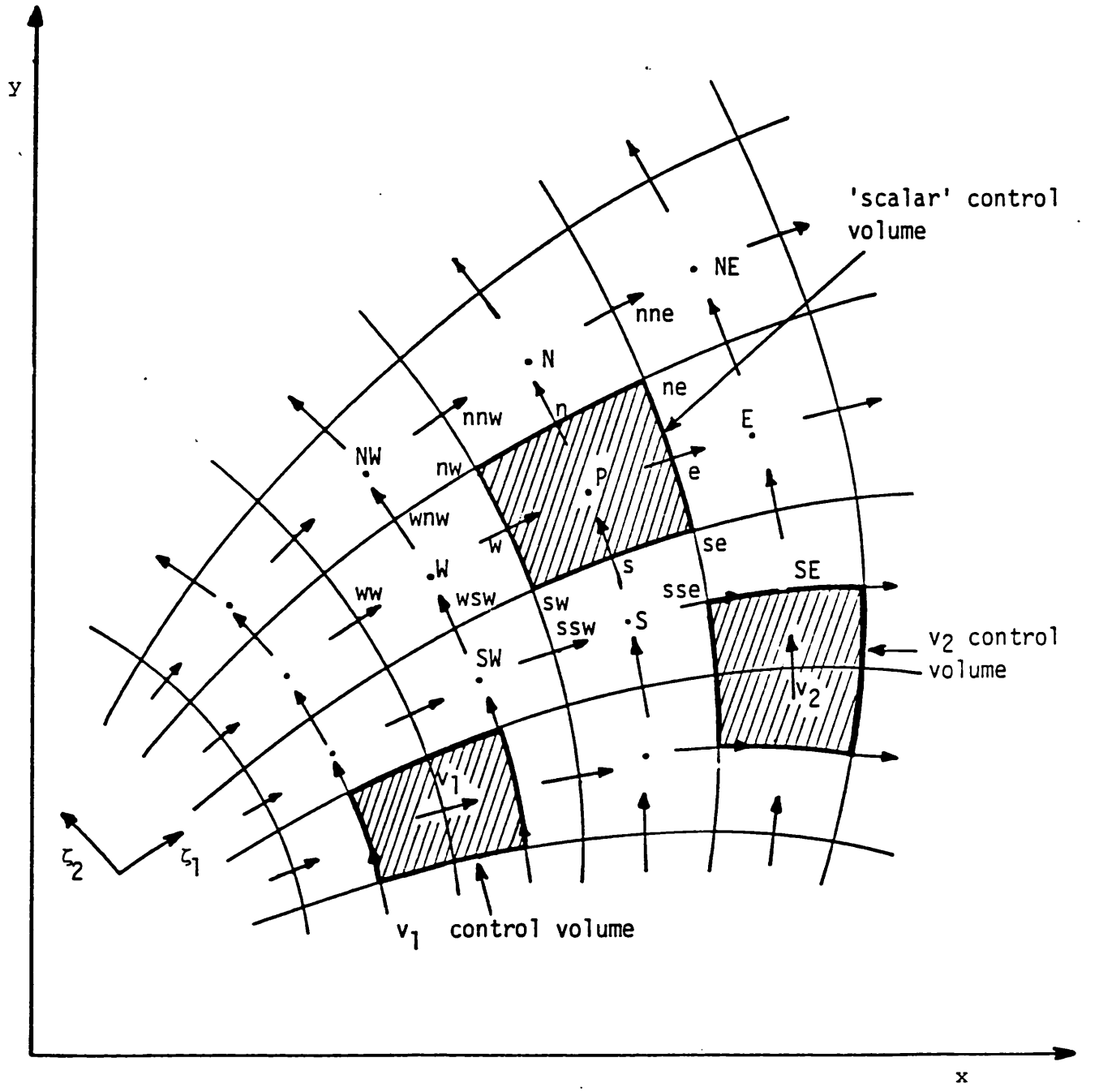


Figure 4.4 Streamline solution mesh.

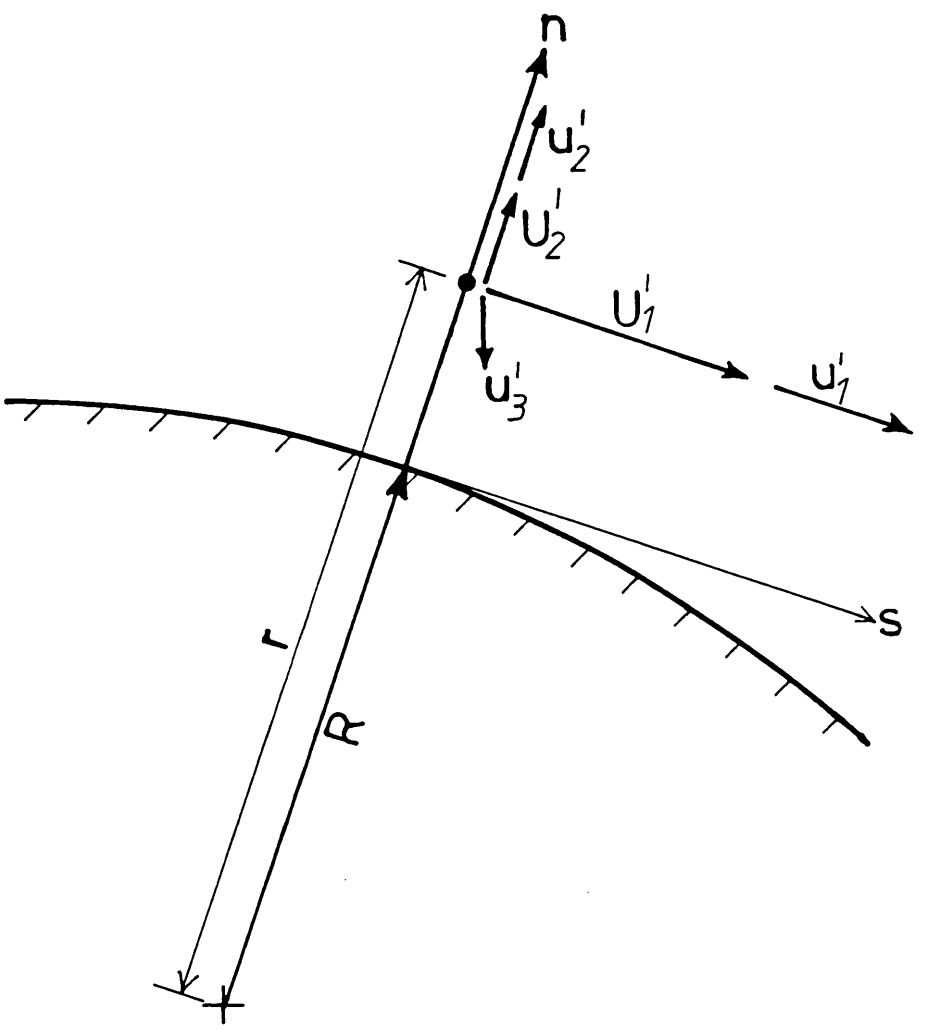


Figure 4.5 s-n Boundary layer co-ordinate system.

FIGURE 4.6

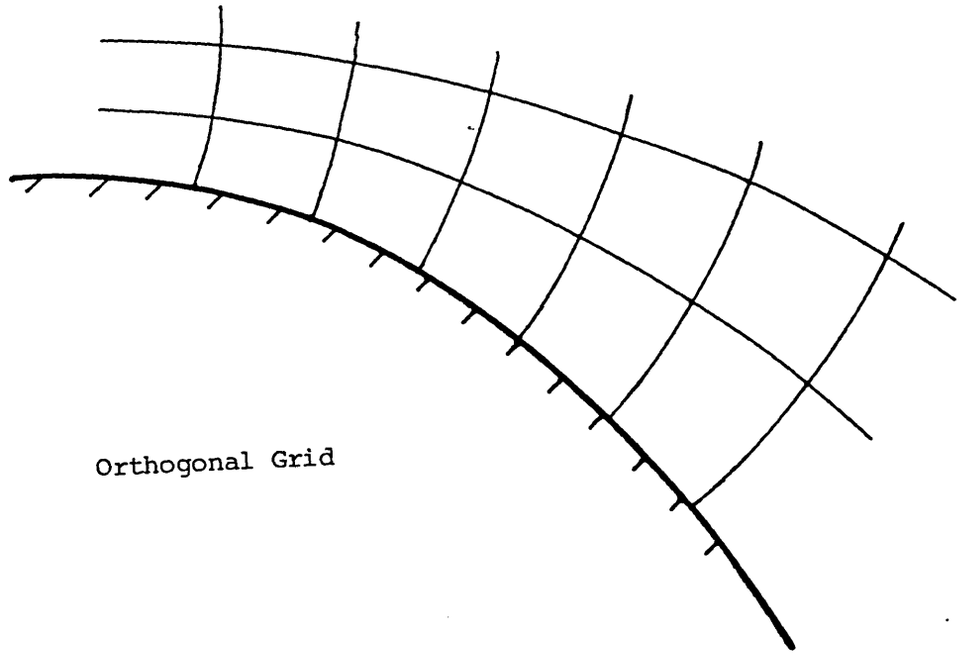
SCHEMATIC OF

VISCOUS-INVISCID INTERACTION PROCEDURE

1. Describe boundaries with surface relations or discrete points
2. Solve equation 4.66 for the location of intersections of iso-stream function and iso-velocity potential lines.
3. Solve streamwise momentum and pressure correction equations to obtain the wall pressure.
4. Solve the boundary-layer equations representing transport of momentum and continuity in the boundary layer.
5. Relocate the boundary streamlines to be coincident with the displacement surface that is described by adding the the calculated displacement thickness to the surface co-ordinates.

5a. Extend the boundary streamlines further downstream, i.e. through the uncalculated separation region, with empirical knowledge if necessary.

6. Repeat the procedure from step 2 onwards until the overall solution of inviscid and boundary-layer equations has converged.



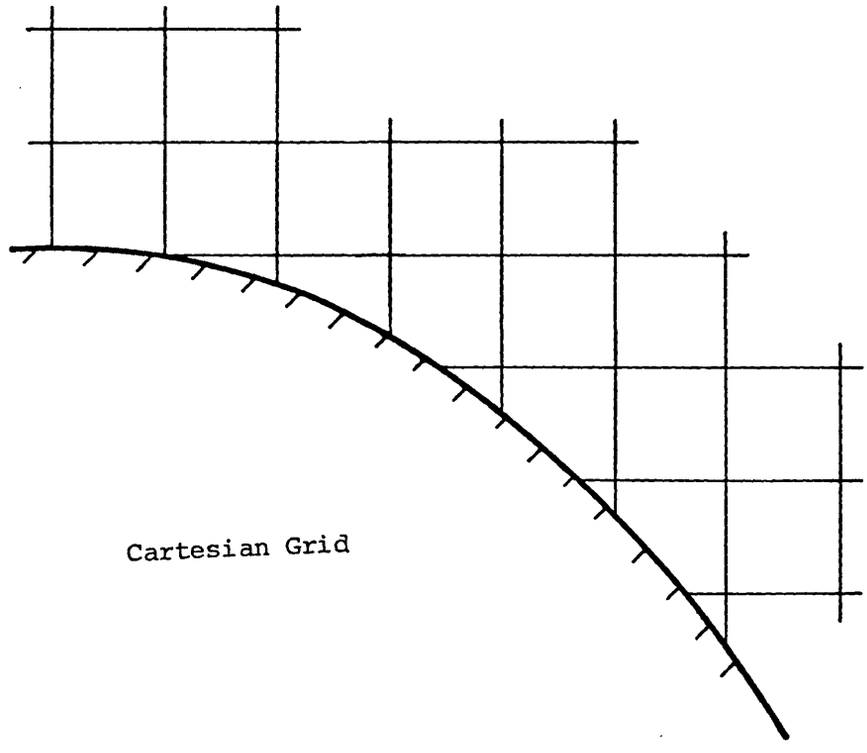


Figure 4.7 Comparison of boundary-cell representation.

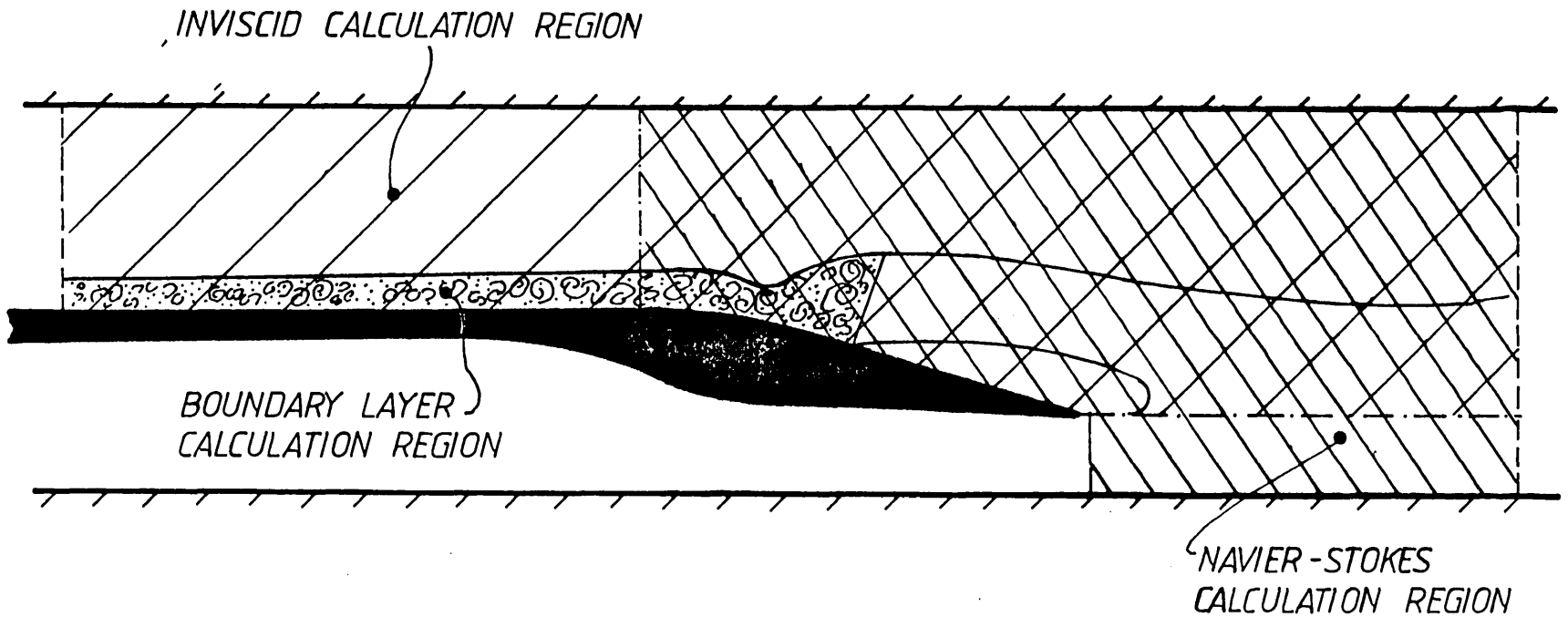


Figure 4.8 Schematic of solution domain.

CHAPTER 5

COMPUTATIONAL INVESTIGATIONS AND COMPARISONS WITH EXPERIMENTAL RESULTS

This chapter presents the results of numerical solution procedures for the inviscid, boundary-layer and elliptic transport equations given in chapter 4. Calculated values of mean pressure, integral quantities, mean velocity, Reynolds stresses and turbulent kinetic energy are compared to the experimental results of chapter 3 and help to quantify the merits of the turbulence model, the numerical scheme, boundary-condition assumptions and the level of approximation present in the transport equations 4.66 for inviscid flow, 4.93-4.99 for boundary-layer flow and 4.11-4.13 for elliptic flow.

The measurements of chapter 3 indicate that the transport equations for mean and turbulence quantities can be simplified to their potential and boundary-layer forms in parts of the flow domain, but not in the vicinity of separation. The application of conservation equations in their elliptic Reynolds-averaged form is clearly uneconomic in regions where these simplifications are valid and the boundaries of the solution domains for potential, boundary-layer and elliptic calculations have been chosen as a compromise which minimizes the calculation effort while allowing specification of boundary conditions, based on experimental knowledge. Accordingly, this chapter has a section dealing with each level of approximation.

Section 5.1 presents the results of inviscid calculations for the potential flow around a circular cylinder, where the pressure distribution is known theoretically, and around the present configuration. Computational results obtained with the boundary-layer equations are

presented in section 5.2 for the region approaching separation. The measured wall-pressure distribution is used initially to examine the boundary-layer approximation and the Reynolds stress turbulence model. The interaction between the viscous and inviscid flow is investigated using the concept of a displacement surface described in section 4.3. Section 5.3 presents calculated results in the region from upstream of separation through the wake which were obtained by solution of the elliptic Reynolds-averaged transport equations in orthogonal curvilinear co-ordinates using the k-ε turbulence model. Mean flow and turbulence quantities are compared to measured values in order to evaluate the overall procedure and separate the effects of numerical accuracy, turbulence modelling and boundary conditions. The discussion of section 5.4 remarks on the appropriate levels of approximation, turbulence modelling, and wall functions required to calculate aerodynamic and separated flows. Implications of the present results are considered with particular attention to the region of recirculation.

5.1 Inviscid Flow

This section presents calculated results obtained with the procedures of section 4.2 for solving inviscid-flow equations. The first part presents results of a test case for the calculation procedure: the potential flow around a circular cylinder is calculated and compared to the theoretical surface-pressure distribution. The

second part presents the potential flow field around the present configuration which is subsequently used in section 5.2 to start the viscous-inviscid interactive procedure described in section 4.3.

Test Case. The potential flow around a cylinder was calculated by solving the Laplace equation (4.66) to obtain the location of stream-function and velocity potential lines and thereby to examine possible problems of relevance to the flow over the geometry of figure 3.1. The cylinder geometry is, of course, a more severe test since it involves a discrete change in surface geometry at the leading edge of the cylinder and thus a singularity in the boundary functions. As discussed in section 4.2, accurate solution of the Laplace equations requires specification of a boundary that is continuous in the first derivative and this requirement is violated at the singular point. A typical result is shown on figure 5.1 which corresponds to the prescription of the constant velocity boundary at 1.5 radii from the centreline of the cylinder and shows that the intersections of the velocity potential and stream-function lines in the vicinity of the singularity on the lower boundary deviate from orthogonality by up to 37 degrees. Similar results were obtained with constant velocity boundaries at 2.5, 5 and 8 radii and showed that the velocity potential lines and streamlines were in reasonable agreement with analytic descriptions of their locations except in the vicinity of the singularity.

The influence of these errors on the local pressure distribution can be quantified from figures, such as figure 5.2, which corresponds to the case of the constant velocity boundary at 5 radii and leads to a value of Cp of -3.04 rather than the exact result of -3.1. Solutions of the potential flow equations were obtained with three grid densities: 24 x 24, 32 x 32 and 48 x 48. The calculated pressure distributions are shown on figure 5.2 and compared to the theoretical distribution given by Schlichting (1968). The agreement is adequate with all of the grids although it is clear that the pressure gradient is represented more accurately with higher concentrations of grid nodes. The distribution of nodes along the surface is not selected a priori since the inverse solution procedure used constant step sizes in streamfunction and velocity potential. The

consequential spacing of nodes in physical space had denser concentrations away from regions with changes in curvature, and hence regions with significant second derivatives in pressure. In order to resolve these regions, a large number of nodes had to appear in regions with smaller gradients and this implies that the mesh-generation procedure makes inefficient use of computer resources.

Errors associated with the location of the streamlines and solution of the streamwise momentum equation, as discussed in section 4.2, manifest themselves as a decrease in total pressure and were found to be 0.5, 0.3 and 0.2 per cent of the inlet dynamic pressure for the 24 x 24, 32 x 32 and 48 x 48 grids, respectively. A further error of about 0.5 per cent of dynamic pressure is associated with numerical approximations in determining the wall-boundary cell and extrapolation of static pressure to the model surface. A higher order differencing scheme for locating intersections with the boundaries, particularly on the curved wall, would reduce this error although at greater expense. The implication of first-order accuracy in equation 4.74 for locating intersections with the boundary is that the orthogonality constraints are less rigidly applied at boundary cells than at internal cells where the second-order accurate scheme of equation 4.72 was used. The latter equation is not applicable at boundary intersections because it would require the use of nodes outside the calculation domain.

Flow configuration of section 3.1. Wall co-ordinates were used to describe the boundary streamlines, without account of any effects of the boundary layer or of separation, and the inviscid equations were solved to give one of the distributions of pressure gradient shown on figure 5.3. The agreement between this calculation and the measurements is adequate up to about s/c of 0.78 where the

process of separation begins to influence the flow. Here the velocity component normal to the surface is about 3 per cent of the local streamwise value in the near-wall region and increases rapidly before detachment to 10 and 15 per cent at s/c of 0.826 and 0.852, respectively.

The influence of numerical approximations and of the downstream boundary condition are both important. Numerical tests demonstrated that grid spacing of less than 8 mm between streamlines and 30 mm between constant velocity-potential lines gave the same results for the calculated pressure and free-stream velocity in the present configuration. This spacing was not adequate when calculating the pressure gradient, as shown on figures 5.3, since the pressure gradient changes rapidly between s/c of 0.65 and 0.86 so that smaller streamwise step lengths are necessary in this region. The required spacing depended on the local curvature of streamlines and velocity-potential lines with the smallest spacing associated with changes in surface curvature. Cell sizes were however difficult to arrange since the distance between nodes was a consequence of the uniform step sizes in velocity potential and stream function as discussed above.

Results were obtained with different downstream boundary conditions to determine their effect on the pressure distribution. Ideally, the downstream boundary should be a velocity-potential line which satisfied the inviscid equation, however this requires knowledge of the mixing process downstream of the trailing edge. Initially, a straight line was taken perpendicular to the tunnel roof at the trailing edge in order to represent the actual velocity-potential line which should be contoured here. Changing the angle of this line by up to 10 degrees from the vertical affected the surface pressure distribution from about 16 per cent of chord upstream of the trailing

edge. To reduce this effect, the outlet boundary was moved downstream to a region where a straight-line approximation adequately represented the velocity potential, or at least did not influence the surface pressure. In practice, this required placement of the boundary streamline beyond 15 per cent of chord downstream of the trailing edge: a horizontal line was used to continue the boundary streamline from the trailing edge downstream to the outlet boundary at x/c of 0.20 where changing the angle of the velocity-potential boundary by up to 10 degrees had negligible effect on the surface pressure. The choice of a horizontal boundary was arbitrary and it was found that the pressure distribution was affected downstream of 90 per cent of chord when its angle was varied between the horizontal and -17.5 degrees: the latter is equivalent to extending the plate further downstream. Although the surface pressure remained the same over more than 90 per cent of the surface with the various downstream boundary conditions, none of the pressure distributions agreed with the measurements downstream of s/c of about 0.78 because of seperation.

The calculated results of figure 5.3 were obtained with a horizontal boundary streamline extending to x/c of 0.20 from the trailing edge where a vertical velocity-potential line was located. Between the plate and the roof, 40 cross-stream nodes were used and resulted in a maximum spacing of 5 mm. Initially 48 streamwise nodes were located between s/c of 0.50 and the outlet, and resulted in spacings of less than 30 mm. Although this was adequate to resolve the pressure distribution, there was an error of up to 25 per cent in the pressure gradient calculated with central differencing. Instead of curve fitting between the predicted nodes, and subsequently calculating the pressure gradient, the longitudinal spacing between nodes was reduced to 10 mm

between s/c of 0.65 and 0.75 and to about 4 mm between s/c of 0.75 and 0.86 by resolving the potential flow equations, i.e. generating a finer mesh, using velocity potential lines obtained from solution with the coarse grid, as the inlet and outlet boundaries. The pressure gradient, shown on figure 5.3, was calculated using central differences between the discrete locations where the surface pressure is obtained.

Summary. Solution of the inviscid-flow equations have been obtained from the Laplace equations in fininte-difference form. The influence of truncation errors, associated with the finite distance between nodes, is significant but can be reduced to acceptable limits. The location and form of the downstream boundary condition is also shown to be important and further work is necessary to determine the best combination of assumptions in separated flows. The inviscid flow calculations are in reasonable agreement with measured results upstream of separation, as expected, and can be used to start the interactive calculation with the boundary layer equations considered in the next section.

5.2 Boundary-Layer Flow and the Viscous-Inviscid Interaction

This section presents results obtained with the solution procedure for the boundary-layer equations as described in section 4.3.

The boundary-layer equations are solved using the measured wall-pressure distribution in order to determine the likelihood of success with this level of approximation of the Navier-Stokes equations

in the region approaching separation and to evaluate the performance of the Reynolds stress turbulence model in the curved boundary-layer.

Secondly, calculated results obtained without prior knowledge of the pressure distribution, are presented. The inviscid-viscous interaction is modelled with a displacement surface and solutions for the potential and boundary-layer flows are revised alternately. This simple method of interaction was expected to be successful in the upstream boundary layer but its ability to represent the flow approaching separation needed to be investigated.

Boundary-layer calculations with measured pressure. The equations appropriate to the boundary layer were solved in the manner described in section 4.3 with the measured wall pressure used to provide the free-stream boundary condition. The upstream boundary conditions included the measurements of mean velocity and Reynolds stresses obtained on the upper plate at s/c of 0.352 as shown on figures 3.10 and 3.13; the required distribution of the rate of turbulence dissipation was obtained using a mixing length hypothesis.

Calculated results were found to agree within 2, 5 and 3 per cent of the measured values of skin friction, shape factor and momentum thickness, respectively, up to x/c of 0.6 and are not presented here. The results obtained further downstream in the curved boundary layer are shown on figure 5.4 and are in reasonable agreement until separation is approached where, for example, the skin friction is under-predicted with its zero value extrapolated to s/c of 0.856 rather than to 0.878 as found by measurement. The calculated momentum thickness is in disaccord with measurements some 10 per cent of chord farther upstream and this location marks the upstream extremity

of the discrepancy betwen calculated and measured results which exists over the region where flow reversals occur. The cross-stream pressure gradient was calculated to be 50 per cent of the value obtained from measurements at s/c of 0.771 and reduces to only 12 per cent of the measured value immediately upstream of detachment: this error is attributable to the simplified form of the cross-stream momentum equation 4.102. The numerical procedure failed to converge downstream of s/c of 0.853.

Profiles of mean velocity and Reynolds stresses are shown on figure 5.5 and are in reasonable agreement in the curved boundary layer and on the trailing flap up to about s/c of 0.845 which corresponds approximately with the upstream extremity of instantaneous flow reversals. The agreement between calculated and measured mean velocities in the near-wall region appears adequate over the curved wall and farther downstream almost to detachment, and is a consequence of using the law-of-the-wall boundary condition which the measurements demonstrate is appropriate. This also accounts for the accurate calculation of skin-friction coefficient up to s/c of 0.85. The mean velocities agree well across the boundary-layer over the curved surface, but are in disaccord with experiments in the outer part of the boundary layer close to separation. Downstream of s/c of 0.845, the cross-stream dimension of the log-linear region does not change rapidly enough with downstream distance and the calculated velocity profiles do not develop the inflection point associated with deflection of flow around the separation bubble. These differences in the calculated velocity distributions are responsible for the under-prediction of momentum thickness and shape factor shown on figure 5.4.

The agreement between calculated and measured Reynolds stresses is reasonable, as shown on figure 5.5, with the stabilizing effects of curvature represented. The agreement is however less satisfactory than with the mean velocities mainly because of the neglect of turbulence production via streamwise gradients although other turbulence modelling assumptions are also likely deficient. The distributions of $\langle u_2'^2 \rangle$ are well calculated and agree within experimental error across most of the boundary layer in the region above the curved surface and up to s/c of 0.845. The values of $\langle u_1'^2 \rangle$, $\langle u_3'^2 \rangle$ and $\langle u_1' u_2' \rangle$, however, are over-predicted by about 1.5, 1.3 and 0.3 m^2/s^2 respectively, i.e. by about 50 per cent, over the inner half of the boundary layer. Evaluation of production terms in the exact transport equations for $\langle u_1'^2 \rangle$ and $\langle u_1' u_2' \rangle$ using experiment results, reveals that the turbulence stress-normal strain interactions, i.e. $\langle u_1'^2 \rangle \partial \langle U_1 \rangle / \partial s$ and $\langle u_1' u_2' \rangle \partial \langle U_1 \rangle / \partial s$, have a reducing effect on production of $\langle u_1'^2 \rangle$ and $\langle u_1' u_2' \rangle$ and that neglect of these negative contributions to the calculated production terms, P_{11} of equation 4.95 and P_{12} of equation 4.98, is mainly responsible for $\langle u_1'^2 \rangle$, $\langle u_3'^2 \rangle$ and $\langle u_1' u_2' \rangle$ being increasingly over-predicted as separation is approached. The predicted levels of Reynolds stresses are highly interdependent and the effect of neglecting turbulence-normal strain interaction is as follows: $\langle u_1 u_2 \rangle$ is over-predicted because its production is calculated to be too large due to the neglect of streamwise gradients of mean velocity, although this is somewhat offset by the over-predicted values of $\langle u_1'^2 \rangle$ used in P_{12}; $\langle u_1^2 \rangle$ is also over-predicted because its production is too large which is the result of a combination of over-predicting $\langle u_1' u_2' \rangle$ and neglecting streamwise velocity gradients; $\langle u_3'^2 \rangle$ is calculated to be too large

because the modelled form of the redistribution pressure-strain correlation, which uses the turbulence kinetic energy and its production rate in its formulation, depends heavily on $\langle u_1 u_2 \rangle$; $\langle u_2'^2 \rangle$ is well calculated since its production is small and normal-strain effects are almost negligible in the $\langle u_2'^2 \rangle$-transport equation. In the outer part of the boundary layer, the calculated values of turbulence intensity are smaller and have larger negative gradients than those in the measurements for two reasons: first, the radius of curvature calculated with equation 4.103 gives smaller values than observed in the present experiment, and this results in over-estimation of the stabilizing effects of curvature on the turbulence in the calculation; secondly, the free-stream turbulence is assumed to be negligible in the calculation. Despite quantitative differences, the qualitative features of the cross-stream and streamwise variations in Reynold stress levels are reasonably well calculated and included the stabilizing effects of streamwise curvature. The calculated Reynolds stresses do not however exhibit the features associated with deflection of flow around the separated region.

Inviscid-viscous interaction. The interactive procedure of section 4.3 is used here to calculate the boundary-layer and potential flow upstream of separation.

Solution of the boundary layer equations with the inviscid wall-pressure calculated in section 5.1 agree satisfactorily with measured values up to s/c of 0.68. Downstream, as shown on figure 5.4, the skin-friction coefficient is under-predicted and the boundary layer grows more rapidly than is measured. This is mainly due to the potential-flow solution which because it assumes that the boundary

layer remains attached, does not predict deflection of the streamlines around separation, and hence the pressure gradient is incorrectly predicted.

The streamlines were corrected to account for viscous effects by obtaining a displacement surface and using it to resolve the inviscid-flow equations and recalculate the wall-pressure distribution. The displacement surface was obtained by adding the displacement thickness, δ_1 of equation 4.108, to the wall co-ordinates and was straightforward up to the calculated location of detachment. The boundary-layer calculation did not give values of displacement thickness downstream of this location and an approximation was required. The initial attempt was to specify a velocity-potential line at the calculated detachment point: it was taken perpendicular to the tunnel roof although measurements indicate it should be contoured. Changing its angle with the roof by up to 10 degrees resulted in different wall pressure distributions in the region from 18 per cent of chord upstream of detachment, and subsequent calculation of the boundary-layer with these pressure distributions resulted in accordingly different distributions of the integral thickness and skin-friction coefficient. The location of separation was always further upstream from that of the first boundary-layer calculation and velocity characteristics were in poorer agreement with experiment.

In an attempt to improve these results, the displacement surface was empirically defined downstream of detachment in accordance with the recommendations of Bhately and Bradley (1972). The displacement surface and downstream boundary were obtained as follows: the wall co-ordinates plus calculated displacement thickness were used up to

calculated detachment; the separation streamline was specified by decreasing the rate of thickening of δ_1 until the flow was tangent to the tunnel roof, in accordance with the flow direction observed in the measurements; its length was extended parallel to the tunnel roof to satisfy the experimentally-observed condition of constant pressure over the separated region; and a velocity-potential line perpendicular to the tunnel roof was located at x/c of 0.20 in accordance with the recommendations of section 5.1. The potential-flow equations were resolved to generate the streamlines shown on figure 5.6 and to obtain the wall pressure which was taken as that on the displacement surface. The streamwise pressure gradient was over-predicted upstream of separation, as shown on figure 5.3, and modification to the shape or angle of the empirical displacment surface above and downstream of the separated region, over a wide range of possibilities reasonably consistent with experimental results, did not improve the calculated pressure gradient in the region approaching separation. The boundary-layer equations were solved with the revised pressure distribution obtained from the potential-flow equations with the displacment surface extrapolated into the separated and wake flow. The location of the boundary-layer separation was found to occur further upstream, as shown on figure 5.4. The agreement between measurements and calculations in the attached boundary layer improved, away from the region of separation, but significant boundary-layer growth occurred too far upstream of detachment when the skin-friction coefficient was under-predicted. It appears that over-prediction of the growth rate of the boundary layer just before separation in the first viscous-flow solution, correspondingly, over-predicts the

blockage effect of separation in the second inviscid-flow calculation and hence the local pressure gradient is larger than that in the experiment and the separation point is calculated too far upstream. Further iterations cause the blockage effect of separation to increase beyond its already over-predicted value and, as a result, the separation point moves further upstream.

The difference between the measured and calculated wall-pressure distributions shows the need for further investigation of the coupling of potential and boundary-layer equations and, more particularly, of the downstream boundary with separation effects incorporated. It appears that in order to predict the flow approaching detachment, at least the blockage effect of the separation bubble must be reasonably well represented. It is unlikely that an empirical function can be developed to describe the streamlines around separation (also see Bhateley and Bradley, 1972) and solution of some form of transport equations is needed to predict separated-flow effects. For instance, inverse procedures can be used to calculate through the separated region although they solve boundary-layer or integral equations which are not appropriate in large regions of recirculation as discussed in chapter 1. This approach will likely be more successful in calculating at least the pressure distribution of the present flow for two reasons: it does not require empirical specification of the boundary streamline provided the use of boundary-layer or integral equations near separation is adequate; and the calculation can be continued into the wake so that the downstream velocity-potential boundary has little influence. More specifically, the boundary-layer equations describe the flow upstream of the location where instantaneous

flow reversals occur and, up to here, the inverse procedure is certainly appropriate as was the present approach to the interaction. Closer to and through the separated region, the boundary-layer equations become increasingly inaccurate, as shown above, so that although inverse procedures can calculate through the region of separated flow, their representation of the blockage effect of separation may not be adequate because they solve inappropriate equations and neglect cross-stream momentum and streamwise gradients. Inverse integral procedures, based on a velocity profile assumption,and discussed in chapter 1, may be more useful provided suitable empirical correlations can be established for the reversed-velocity characteristics. These methods are less general than those based on solution of the Navier-Stokes equations which can represent both the boundary-layer and separated-flow regions as discussed in the next section.

Summary remarks. The results of solutions to the boundary-layer equations with the measured wall pressure, and a simplified form of the cross-stream momentum equation, are in close accord with measurements up to the region where the influence of separation is significant, i.e. at about s/c of 0.845 where instantaneous flow reversals occur. Thereafter, and up to a location very near separation, the wall shear stress is well represented but integral, mean-velocity and turbulent quantities are less well calculated, perhaps due to the simplified form of the cross-stream momentum equation and the neglect of streamwise gradients of mean velocity. The present results demonstrate that simple assumptions about the viscous-inviscid interaction can lead to acceptable results up to the location where the boundary layer thickens rapidly approaching separation, provided

the solution takes into account the displacement thickness of the boundary layer. This is difficult to arrange with a forward-marching procedure for solving the boundary layer equations since its solution has a singularity at detachment and knowledge of the displacement surface downstream of separation, and of the outlet velocity-potential boundary, must be supplied empirically for the potential-flow calculation. Consequently, it appears desirable to evaluate the possibility of solving the steady, two-dimensional form of the Reynolds-averaged equations in the region of and downstream of separation.

5.3 Separated and Wake Flow

This section presents calculated results obtained by solving the two-dimensional Reynolds-averaged momentum transport equations in orthogonal curvilinear co-ordinates, using the method and k-ε turbulence model described in sections 4.4 and 4.1, respectively. The solution domain was chosen to include the curved boundary layer, separated region and wake so that computational expenses were minimised while allowing specification of boundary conditions based on experimental knowledge.

The first part of this section presents calculated mean values of pressure, wall shear stress and velocity in and around the region of recirculation, and compares them to measured results. Numerical assumptions are known to be important and are evaluated using the method described in section 4.4. Calculated profiles of

turbulence kinetic energy are compared to measurements in an assessment of the importance of turbulence modelling in and around the separated region. The influence of boundary conditions, including wall functions, is determined. The section closes with a summary of the more important conclusions.

Calculated mean flow. The results discussed here relate to the region of the flow identified by the solution domain of figure 5.7. Thus, boundary conditions were assigned on all sides of the solution domain, as described in section 4.5, and the finite-difference equations, representing transport of mass, momentum, turbulence kinetic energy and its dissipation rate, solved using the method of section 4.4.

The boundary of the calculation domain was arranged to be coincident with the surface, the tunnel roof, a location upstream of separation selected with experimental knowledge, and extended a short distance downstream of the trailing edge parallel to the tunnel roof. An orthogonal mesh of 48 x 48 nodes was generated within this domain using the method of section 4.2. The 48 x 48 grid was linked to similar but geometric expanding rectangular Cartesian grids which were specified to represent the flow stemming from beneath the lower surface and in the downstream wake. The resulting grid of 60 x 60 nodes implied that solution of the Navier-Stokes equations would be expensive and time consuming. The results obtained below were, as a consequence, obtained with fewer nodes and these were selected with empirical knowledge of the regions of steep gradients and angled streamlines. A typical grid, shown on figure 5.7, comprised 30 x 30 nodes selected from the 60 x 60 mesh originally generated, and led to calculation times of around 850 s and 250

iterations required to achieve a convergence criteria of 0.1 per cent of the maximum residual of any dependent variable including the mass flow of the pressure correction equation.

The calculated mean velocity vectors of figure 5.8 may be compared with the measurements of figure 3.8 and are clearly in good qualitative agreement. As quantified in figure 5.9, mean streamline detachment was calculated to occur at 0.862 rather than the 0.878 of the measurements. The overall size of the calculated reverse-flow region is wider over the first 55 per cent of its length and narrower downstream, by some 10% at the trailing edge, although in the wake it extends to a value of x/c of 0.021 rather than to the 0.016 of the measurements. The calculations also show that the normal momentum is greater than the longitudinal momentum in the vicinity of separation and in the shear layer surrounding the bubble where the normal pressure gradient has its largest values. Within the bubble, the mean velocity has a maximum value of approximately 11% of the free stream velocity and the normal and longitudinal velocities have similar magnitudes with the former being larger at the beginning and end of the reverse flow boundary layer.

The free-stream velocity and wall pressure distributions are shown on figure 5.10. The difference between the measured and calculated velocity distribution is consistent with the discrepancy in the size of the recirculation region which may, in part, be due to the inadequate representation of streamline curvature as discussed previously. The pressure distribution is, of course, very different from that obtained from the Laplace equations in the vicinity of the separation region and is in close accord with measured results except where there are insufficient nodes to represent the streamwise gradients at the start of curvature.

The distribution of skin-friction coefficient of figure 5.10 is also in good agreement with experiment and was obtained with the aid of the wall functions of section 4.5. These wall functions linked the wall to the finite-difference node closest to it and always were located at a value of y^+ less than 56 and greater than 10 with the minimum occurring in the separated region. Further discussion of the effect of wall functions appears below.

It is useful to note that the ratio of $\partial P/\partial y$ to $\partial P/\partial x$ immediately upstream of separation and in the near wake, defines the need for equations which represent both. In addition, the evaluation of measured convection terms showed that the y-momentum was generally greater than the x-momentum in the downstream region of the recirculating flow, and that they had similar magnitudes in the central and upstream regions of separated flow except very close to the wall.

Solution accuracy. The results presented on figures 5.8 to 5.10 and discussed above are encouraging and it is essential to determine the extent to which they depend on the numerical detail of the calculations. A partial answer to this question can be provided on the basis of the limited number of tests referred to in the following pragraph. It is clear from the velocity profiles of figure 5.11 that the calculated wake is wider than it should be and this may be the result of false diffusion associated with numerical inaccuracies discussed in section 4.4. Accordingly, the method of section 4.4 was used to evaluate the numerical error associated with upwind differencing in the solutions for V_1, V_2 and k in each calculation cell. The imbalance term, T of equation 4.145, was determined using a central-differencing approximation whereas the solutions for V_1, V_2 and k were obtained with

upwind-differencing where appropriate, according to the hybrid scheme of equation 4.133, so that the value of this term, T, approximately represents the local levels of numerical diffusion error. The implication of values of T in excess of 10 per cent of the largest transport term, i.e. nett convection, nett diffusion or nett source terms* in the local cell balances, is that numerical error makes a significant contribution to local diffusion and profiles of the dependent variable, for example V_1, V_2 or k spread at a greater rate than is represented by the transport equations; i.e. finite-difference equations have significantly larger diffusion than the differential transport equations from which they were derived.

Values of the out-of-balance term were found to be in excess of 10 per cent of the maximum transport term over a significant part of the flow domain when calculations were obtained on the 30 x 30 grid. The largest out-of-balance terms were found near the front of the recirculation bubble in the shear layer associated with the dividing streamline. Here, the flow deflects around the recirculation region and intersects the grid lines at angles which result in large numerical error, i.e. approaching 45 degrees, because the potential-flow grid lines do not account for separation. The maximum values of T found here are about 120, 160 and 30 per cent of the largest transport terms in the finite-difference equations for V_1, V_2 and k, respectively. The imbalance term is also significant in the near wake where they comprise a maximum of 20, 80 and 45 per cent of the calculated diffusion terms

*Source terms refers to pressure gradient terms in the momentum equations. Turbulence production and dissipation are treated as separate source terms in the k-equation. See section 4.4. for further details.

of V_1, V_2 and k, respectively. The use of a single figure, however, is somewhat misleading since, although these errors are large, they are confined to small regions of the flow in the vicinity of detachment and of closure of the recirculation bubble in the wake. Elsewhere the imbalance term, T, is found to be less than about 30 per cent of the maximum transport term over more than 90 per cent of the calculation domain and less than 10 per cent over more than half of the flow. Numerical error is therefore responsible for some of the enhanced diffusion observed in the calculated velocity characteristics of figure 5.11 and 5.12, particularly between 20 and 40 per cent of the boundary layer thickness, although turbulence modelling assumptions are also likely to be deficient as discussed below.

Numerical diffusion errors are unimportant inside the separation bubble where the cell Peclet numbers were small and central differencing was applied over more than 75% of the recirculation region. The maximum imbalance term, T, was less than 8 per cent of the maximum transport term in the region where upwind differencing was applied immediately around the backflow and directly above the central 60 per cent of the length of recirculating flow, i.e. near the trailing edge. It increased to the larger values given above towards the front and rear of the shear layer around the recirculation region where the flow direction was not alligned with the mesh.

In the outer potential flow, convection balances pressure gradients and the gradients of mean velocity are small, so that the application of the above method would result in small imbalances and an indication of large errors as discussed in section 4.4. Further, the influence of any numerical diffusion would likely be large compared to those of

the local diffusion terms since the levels of viscosity and mean strain rates are small here. Accordingly, calculations were performed to assess the influence of numerical approximation in the inviscid flow regions with the same number of nodes differently located in the solution domain of figure 5.7 and with smaller numbers of nodes. With 30 x 30 nodes, and a greater number located away from the near-flap region, the velocity and pressure fields were very similar and this suggested that, although the cell Reynolds numbers in the free stream had magnitudes up to 10^3, the resulting truncation errors were unimportant. This conclusion was supported by calculations with 20 x 20 nodes which gave very similar velocity and pressure values away from the surface of the flap: even the velocities in the outer region of the recirculation were little changed although the wake was wider with this number of nodes. The distribution of nodes, with concentration away from the flap region, gave rise to different near wall values although the location of detachment was almost the same. In particular, the skin-friction coefficient was altered because the near-wall node was located about twice as far from the wall in the Y^+ region between 24 and 85 in contrast to the 10 to 56 range used earlier. The values of skin-friction coefficient increased along the surface as follows: in the vicinity of detachment, values of C_f increased by about 3×10^{-5} where the near wall node was located between 24 and 50 as opposed to 10 and 26; in the attached boundary layer, C_f increased by about 18×10^{-5} where Y^+ values increased to about 85 from 55; in the backflow, the magnitude of negative skin-friction coefficients increased by 1×10^{-5} where the Y^+ range increased to about 50 to 64 from 28 to 45. Local velocities and pressure coefficients

were also different with the largest changes found in the vicinity of detachment where mean velocity decreased by a maximum of 14 per cent of its local value, which is equivalent to 5 per cent of the reference velocity, and the pressure coefficient changed by less than 3 per cent of reference dynamic pressure in the shear layer associated with the dividing streamline and less than 1.2 per cent on the wall. It is also clear that more nodes or a higher order finite-difference scheme is required to represent the gradients in the shear layer associated with the dividing streamline and in the near wake.

The use of the complete 60 x 60 grid reduced the levels of numerical inaccuracy although numerical diffusion was still important particularly in the vicinity of detachment and near the rear stagnation point. Values of T in the shear layer associated with the dividing streamline decreased by about 30, 25 and 35 per cent but numerical diffusion was still important since levels of T in excess of 75% of the maximum local value of transport terms, were found in the shear layer above the detachment point. Calculations with this 60 x 60 mesh required in excess of 7 times the computational resources of the earlier 30 x 30 grid and also indicated that denser calculation meshes are required to control numerical diffusion within acceptable levels. The generation of and calculation on such grids is prohibitively expensive and, since the 60 x 60 offers only marginal improvements with much greater computational expense, the results of this section were obtained on the 30 x 30 grid of figure 5.7 which was selected from the 60 x 60 grid such that numerical diffusion was minimised, and following the recommendations of Rhie and Chow (1982).

Turbulence results. It is difficult to determine the importance of turbulence-modelling assumptions in the present calculation because of the magnitude of numerical diffusion, but there appears to be reasonable qualitative agreement between the calculated and measured profiles of turbulence kinetic energy, as shown on figure 5.12. Direct evidence of the magnitude of turbulence diffusion terms can be deduced from the present measurements and their qualitative behaviour is in agreement with calculated results which show that they were most important in the vicinity of the edge of the recirculation region and diminish in value towards the free stream, although their influence may be outweighted by numerical diffusion in some regions of the flow and particularly in the wake. Calculated levels of turbulence production were also in reasonable agreement with measured results. The largest production of turbulence occurs in the shear layer associated with the dividing streamline and in the pressure-side mixing layer of the wake. Levels of turbulence kinetic energy in the reversed-flow boundary layer were well calculated as a result of the modified wall production term of equation 4.166. Farther away from the wall, the agreement is less satisfactory because the local levels of production of turbulent kinetic energy are under-predicted, numerical inaccuracies contribute to diffusion, and diffusion by turbulence is over-predicted. The production of k is too small mostly because of numerical diffusion which reduces the local levels of mean-velocity gradient although the over-prediction of turbulence diffusion also contributes. Diffusive transport by turbulence is over-predicted because the stabilizing effects of streamline curvature are neglected in the formulation of the turbulence model. Both also depend on the eddy-viscosity hypothesis

of equation 4.24 and 4.36 which is also deficient as discussed in the next section. It is not possible to separate the effects of numerical diffusion and of over-prediction of turbulence diffusion as a result of turbulence-model assumptions since both act to increase the spreading rate of the mean velocity and turbulence kinetic energy as shown on figures 5.11 and 5.12. The diffusion indicated in these profiles suggests that the differences between calculations and measurements are larger than would be caused by numerical diffusion alone. It appears that the k-ε model in the form used here, tends to over-predict the effects of turbulence diffusion because it neglects the effects of streamline curvature on the turbulence and is in agreement with the results of Hah and Lakshminarayama (1980) and Younis (1983) in non-recirculating flows.

Influence of boundary conditions. The boundary conditions of section 4.5 are inexact and the purpose of this subsection is to examine their influence on the calculated results.

The influence of the location of the roof and floor of the wind tunnel did not appear to be very great since their representation by actual and expanded tunnel co-ordinates led to the same wall-pressure coefficients on the flap and to the same size of the recirculation region. Similarly, the location of mean streamline detachment was always calculated to an accuracy of not less than the distance between grid nodes in the s-direction. The values of free-stream velocity were under-predicted in the wake when surface co-ordinates of the roof and floor were used to locate the free stream boundaries. The blockage effects of the tunnel boundary layers caused the potential flow in the near wake of the experiment to deccelerate less than in the calculation.

Subsequently, the calculation of free-stream velocity was improved, as shown on figure 5.10b, by accounting for the tunnel boundary layers with the experimental displacement surface of the roof and floor boundary-layers used to represent the free-stream boundaries. The downstream end of the recirculation bubble was calculated to be at x/c of 0.19, which was in better agreement with the measurements, and the skin-friction coefficient and wall static pressure changed by less than 1 per cent as the near-wall flow on the suction-side was virtually unchanged.

The influence of the location of the downstream boundary condition was investigated and shown to be negligibly small in the vicinity of the plate and of recirculation.

The inlet boundary conditions for V_1, V_2 and k are obtained from experiment and for ε by estimation, as discussed in section 4.5. The profile of $\langle V_1 \rangle$ is accurately known whereas that of $\langle V_2 \rangle$ is less certain. Accordingly, solutions were obtained with inlet values of $\langle V_2 \rangle$ of zero, 0.05 m/s and with a linear variation of $\langle V_2 \rangle$ from 0.1 m/s to zero between wall and the boundary-layer edge. The most pronounced difference between these solutions was found in the wall pressure distribution whose values changed by less than 4 per cent of dynamic head in the region up to about 4 per cent of chord downstream of the inlet. The calculations with non-zero values of $\langle V_2 \rangle$ showed poorer agreement with experiment than in the zero-velocity case and this may be regarded as a posterior conformation of the validity of the assumption of negligible $\langle V_2 \rangle$.

The inlet boundary was located at s/c of 0.668, upstream of surface curvature, so that the inlet profiles of k and ε did not show the effects of streamwise curvature discussed in chapter 3. Calculations

were performed to test the sensivity of the calculated results to the inlet profiles of k and ε by using values that were half and twice those devised from experiment. The influence of the inlet values of k and ε were observed throughout the calculation domain and, in order to quantify their effect, the changes to the recirculation length and detachment point are shown on table 5.1. It indicates that the size of the backflow changed by as much as 20 per cent and that changes in the dissipation rate had the largest effect. The regional patterns, but not the values, of the mean velocity, turbulence production and diffusion were preserved, partly because the inlet mean velocity field remained the same and so the mean strain rate, which contributes to the levels of turbulence in the vicinity of separation, was not greatly affected. The values of skin-friction coefficient changes in accordance with the different locations of detachment. The values of turbulent viscosity were different throughout the flow and caused the transfer of energy from the mean flow to be smaller if the inlet values of k and ε were under-specified, and larger with over-specified values. This may seem contrary to equation 4.36 when inlet values of ε are changed but, for example, under-specifying ε-values has the overall effect of over-predicting the k-field so that the net result is high turbulent viscosity except very close to the inlet boundary where the k-field is closely related to its inlet values. These results suggest that representation of the turbulence field is important to the location and size of the recirculation region, and implies turbulence modelling is also likely to be influential. The different inlet values of ε affected the spacial distribution of mean flow quantities which suggest that the mixing length hypothesis, or any alternative method for deriving the necessarily approximate inlet values for ε, contributes to the results obtained in the vicinity of recirculation. It

is not possible to recommend the best procedure here because of the influence of numerical diffusion, and further testing is required but with a more accurate numerical scheme.

The calculated values of skin-friction coefficient are, at least in part, due to the use of the law-of-the-wall in regions where it does not strictly apply. Its importance to the results in the vicinity of recirculation was examined by obtaining solutions with different wall boundary conditions in the backflow region. A laminar boundary condition was applied by using equations 4.157, 4.167 and 4.174 and, also, a slip condition of zero wall shear stress was applied by setting τ_w in equation 4.166 to zero. These alternative boundary conditions had very little effect on the solution, as shown on table 5.2. Although these wall functions are radically different, the shear stress in the backflow is small, verified in the experiment, and therefore momentum transfer through the wall is relatively unimportant. Hence, the wall boundary condition does not have a dominant effect on the recirculating flow. Accordingly, the recirculation region was not significantly altered. The values of static pressure coefficient changed by less than 2×10^{-4}, and the turbulence kinetic energy and its dissipation rate remained virtually constant. The latter is a consequence of the dominance of turbulence production in the shear layer associated with the dividing streamline and of turbulence diffusion into the recirculating flow. This confirms, a posteriori, the rational for not emphasizing wall boundary conditions since the law-of-the-wall is applicable in the boundary layer upstream of separation and appears to be of little consequence to the calculation of separated flow.

Summary. The general flow patterns are well calculated and the mean flow results are in accord with measurements in some regions of the flow. In others, significant descrepancies exist and numerical tests indicate that these are due to numerical assumptions although the two-equation turbulence model and related wall functions are also likely to be deficient.

5.4 Discussion and Conclusions

This section discusses the important aspects of calculation procedures for the present recirculating flow: first the approximation of transport equations is considered; secondly, the importance of numerical assumptions are assessed; and, lastly, the role of turbulence modelling, and associated boundary conditions, is discussed.

Approximation of transport equations. It is desirable, and often necessary, to simplify the transport equations for mass, momentum and turbulence quantities to forms which are applicable in only certain regions. The measurements of chapter 3 show the present flow can be divided into regions of inviscid, boundary-layer and separated flow and the calculations of this chapter demonstrate that flow in these regions can be reasonably well calculated using appropriately simplified equations. Initially, it might appear that solution of the complete Reynolds-averaged equations, including a suitable turbulence model, is the most desirable way to calculate the flow through the entire domain. The present results indicate this

is false. Solutions obtained in this manner are likely to have less accurate results, obtained at greater expense, than an approach which divides the flow domain into appropriate regions for solving simplified equations with methods that partition the calculation effort to emphasize the most demanding regions.

The calculation of large regions of potential flow with viscous equations is unnecessary, expensive and can result in numerical errors which introduce false viscosity and destroy the inviscid nature of the solution. For example, results obtained with the solution procedure of section 4.4 are inaccurate in regions of potential flow because of numerical diffusion. There is an aphysical drop in total pressure with downstream distance because, instead of convection processes balancing pressure gradient effects, numerical diffusion plays a dominant role in the momentum balance. Reduction of this error, for example by grid refinement or with higher order differencing schemes, incurs additional computational expense and places the emphasis of the calculation effort on reducing numerical errors in regions of small gradients instead of resolving the larger gradients in the viscous flow. For these regions, simpler methods, such as those of section 4.2 or the panel methods of Hess (1975) and Hunt (1980), are less expensive, more accurate and hence more appropriate although modelling of the viscous-inviscid interaction is required.

The choice between solving the boundary-layer or elliptic Reynolds-averaged equations depends on efficiency of the calculation procedure and applicability of the boundary-layer approximations. Clearly it is worthwhile using the more efficient procedure of section 4.3 to solve the boundary-layer equations wherever possible.

However, the boundary-layer assumptions breakdown, as show in section 5.2, at approximately the upstream extremity of the effects of separation, i.e. at about the farthest upstream location where instantaneous flow reversals are measured, and elliptic equations must be solved farther downstream. Interaction of the solutions of boundary-layer:elliptic equations seems straightforward since their domains can be overlapped and the results from the boundary-layer calculation may be used directly to start elliptic calculations. The latter can continue the calculation downstream through the region of recirculation incorporating streamwise gradients and the cross-stream momentum equation into the solution procedure which are both important as shown in section 5.2 and 5.3.

Numerical assumptions. The influence of numerical approximation was quantified for the three solution procedures for inviscid, boundary-layer and elliptic Reynolds-averaged transport equations. It can be reduced to acceptable levels in the inviscid and boundary-layer solutions, as discussed in sections 5.1 and 5.2, but was important to the solution in the region of recirculation presented in section 5.3.

Numerical errors in the inviscid flow calculation manifest themselves as a drop in total pressure of less than 1 per cent of the wall static pressure. Although the values of wall pressure were well calculated, albeit neglecting separation, the pressure gradient obtained by differentiation using discrete values of pressure, was poorly represented especially in regions with large second derivatives of pressure so that grid refinement was necessary to reduce this error to acceptable limits.

Solutions of the boundary-layer equations were not obtained in the recirculating flow because of the Goldstein singularity in the forward-marching solution procedure. Furthermore, the inability to predict even approximate values of the displacement thickness downstream of separation resulted in failure of the simple viscous-inviscid interaction, as follows: the displacement surface had to be estimated downstream of the singularity; the pressure distribution calculated with this displacement surface overestimated the blockage effect of separation; the separation point moved progressively forward with iteration between the viscous and inviscid solutions.

Numerical errors could not be reduced to acceptable levels in the solution of the elliptic Reynolds-averaged equations in the region of recirculation. Grid densities are required which are so large that they are impracticable for three-dimensional flows. The difficulty arises because of the use of upwind differencing in regions where the flow angle is not aligned with the finite-domain boundaries and resulted in numerical truncation errors of the order of actual diffusive terms for the momentum balances in the vicinity of recirculation. Numerical diffusion is more important than the local influence of turbulence modelling assumptions. Clearly, this is a major problem although recent work suggests that it may be overcome by using higher-order differencing schemes, such as those proposed by Leonard (1979) or Lai (1983), or with flexible grids which can adjust themselves approximately depending on the flow direction (see Ghia and Ghia, 1983): both of these approaches are in their infancy and require further research.

Turbulence modelling and boundary conditions. In view of the influence of numerical diffusion it is difficult to draw conclusions

about the effects of turbulence modelling on the calculation of recirculating flow. The use of a turbulence model based on the Reynolds stress transport equations may have benefits in representing turbulence phenomena in calculations of recirculating flow since it does not rely on the eddy-viscosity assumption used with simpler models, including the k-ε model. The use of an eddy-viscosity assumption depends on on being able to scale the vorticity of eddies involved in cross-stream momentum transfer with the cross-stream vorticity of the mean flow, and on being able to scale the shear stress with any of the Reynolds stresses (Tennekes and Lumley, 1972) so that production equals dissipation with convection balancing diffusion (Bradshaw, 1978). The measurements of chapter 3 show that multiple length scales exist in and around recirculation and, thus, it seems unlikely that an eddy-viscosity model can represent diffusion in the vicinity of separation (also see Simpson et al, 1981). It is useful to quantify the effects of an eddy-viscosity assumption first, considering the advantages of simplicity offered by the k-ε model, although a calculation procedure is needed which does not incur large numerical truncation errors.

The effects of streamwise curvature on the turbulence were reasonably well represented in the boundary-layer calculation of section 5.2 which used a Reynolds stress turbulence model, but were not accounted for in the calculation of section 5.3 with the k-ε model. In view of the importance of the curvature effects in the measured turbulence fields, as discussed in chapter 3, it seems likely that their representation is important to the prediction of recirculating flows. It is not possible to evaluate fully the influence of turbulence modelling, and hence the neglect of curvature effects on the

turbulence, in present results for the separated flow region because of the importance of numerical diffusion. The measurements suggest that turbulence models for recirculating flows are likely to require some account of the effects of streamwise curvature on the turbulence and the importance of these effects needs to be quantified using a more accurate numerical scheme.

Specification of inlet values of velocity, turbulence kinetic energy and its dissipation rate, by calculation or from measurement, is important to the size and position of the recirculation bubble. In contrast, the wall boundary conditions in the backflow does not have much of an influence on the calculated recirculation region as a result of the small values of wall shear stress found here.

In conclusion, it is worthwhile identifying the major impediments to the improvement of turbulence models for recirculating aerodynamic flows: numerical truncation error which suppress the influence of the turbulence model; modelling requirements for the viscous-inviscid interaction; and the lack of experimental results, including turbulence data, in trailing-edge recirculation bubbles. The measurements of chapter 3 contribute to alleviating the latter.

TABLE 5.1

COMPARISON OF RECIRCULATION LENGTH AND DETACHMENT POINT

Inlet Condition	Location of Detachment	Backflow Region	
		Length	Width at Trailing Edge
	s/c	s/c	n/c
Basic	.862	.155	.0161
Half k	.867	.139	.0153
Twice k	.858	.165	.0169
Half ε	.879	.127	.0141
Twice ε	.847	.195	.0179
Measured	.878	.138	.0175

TABLE 5.2

COMPARISON OF THE EFFECTS OF DIFFERENT WALL BOUNDARY CONDITIONS IN THE SEPARATED REGION

Separated Region Boundary Condition (i.e. for $U<0$)	Location of Detachment s/c	Value of s/c of 0.925* V_1 (m/s)	k (m^2/s^2)	C_f (-)
Log-law ($10 < Y^+ < 50$) (nominally 20)	.8622	-1.51	2.60	-2.53×10^{-4}
Laminar ($U^+ = Y^+$)	.8659	-1.35	2.34	-5.1×10^{-5}
Slip condition ($\frac{\partial \langle V_1 \rangle}{\partial \zeta_2} = 0$)	.8621	-1.50	2.60	-2.5×10^{-4}

*Corresponds roughly to the centre of the backflow.

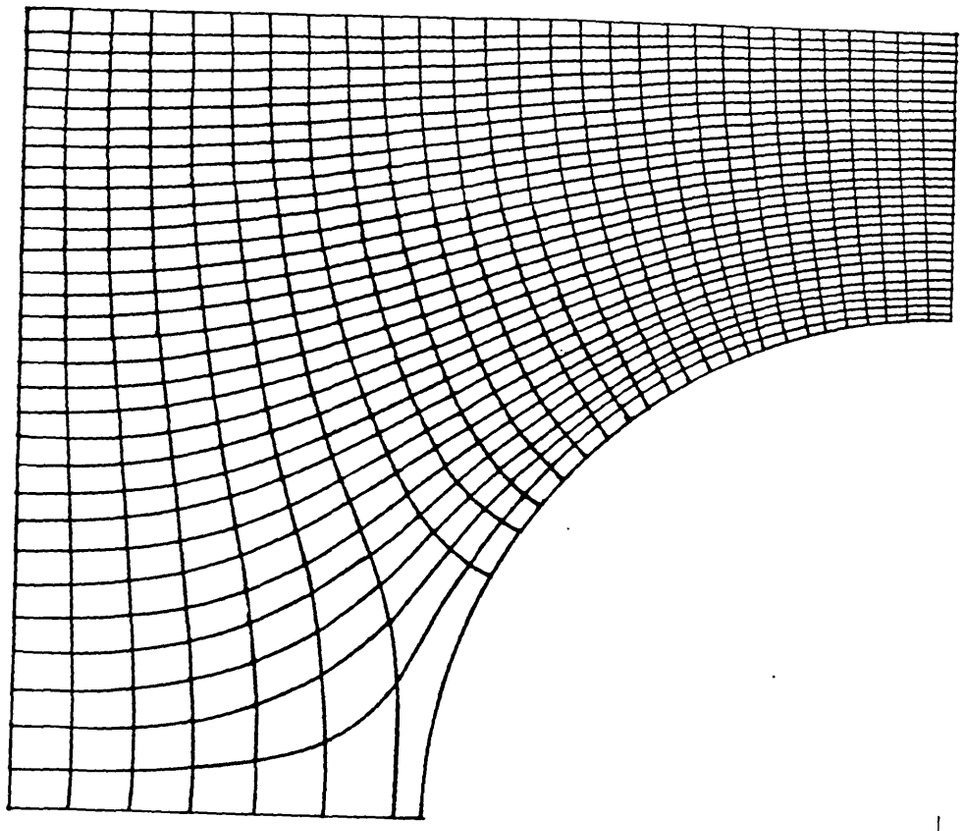


Figure 5.1 Stream-function and velocity-potential lines around a cylinder.

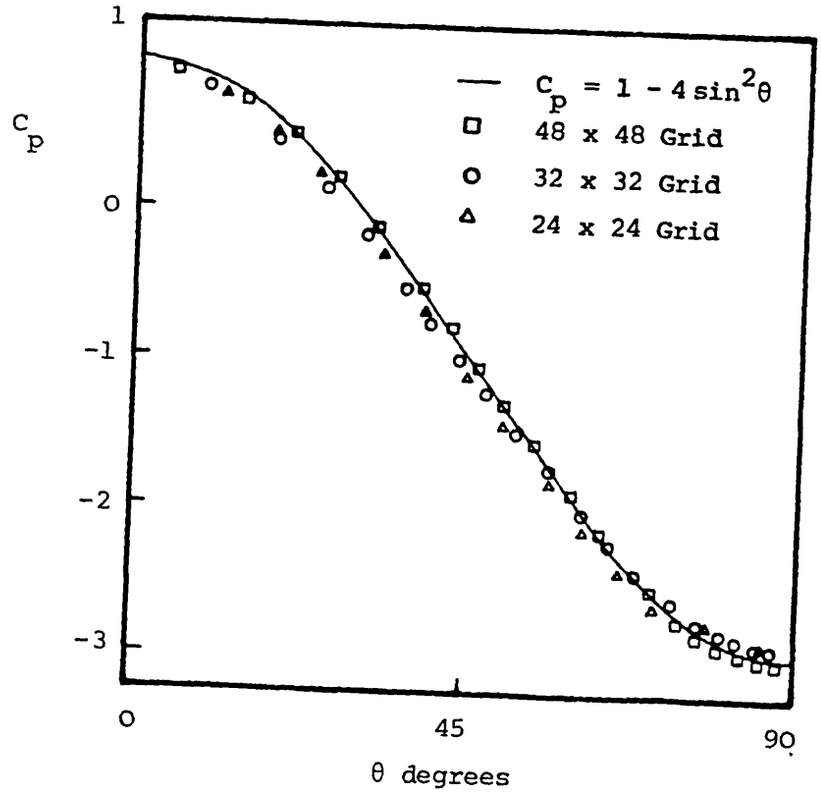


Figure 5.2 Surface pressure distribution on a cylinder.

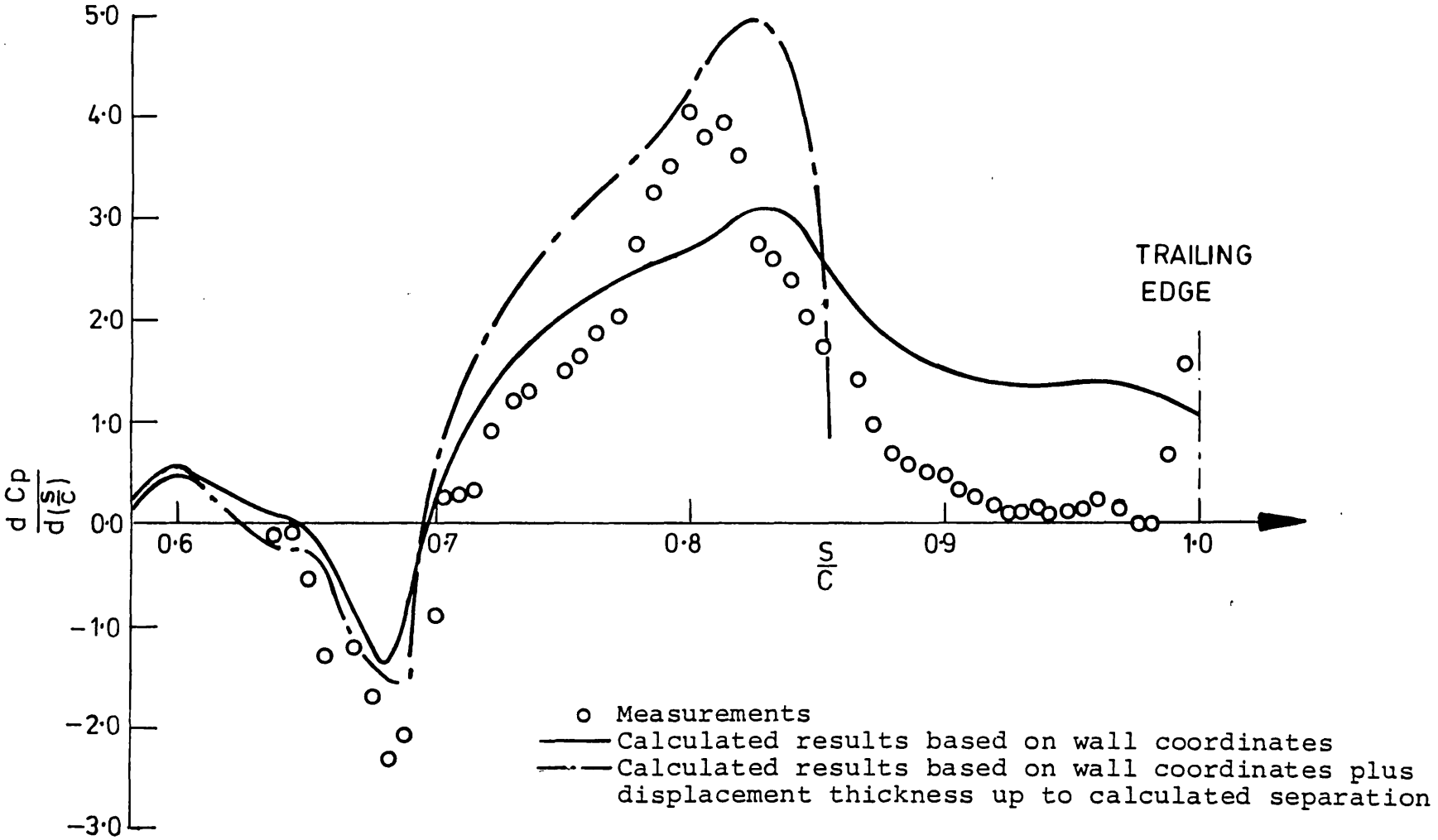


Figure 5.3 Comparison of measured and calculated non-dimensional longitudinal pressure gradient on the upper surface of the plate and flap.

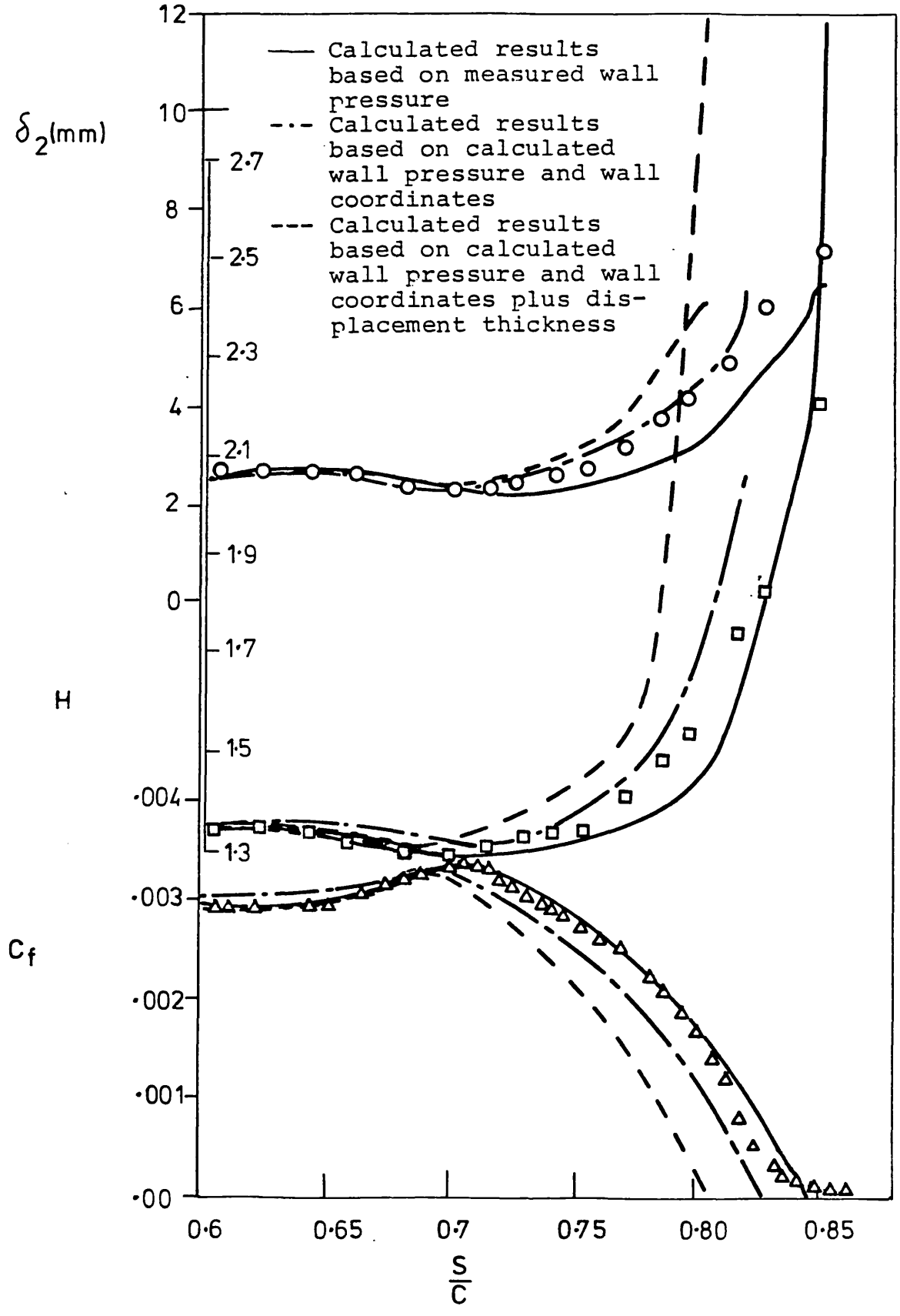


Figure 5.4 Calculated and measured distributions of momentum thickness, shape factor, and skin-friction coefficient in the vicinity of separation.

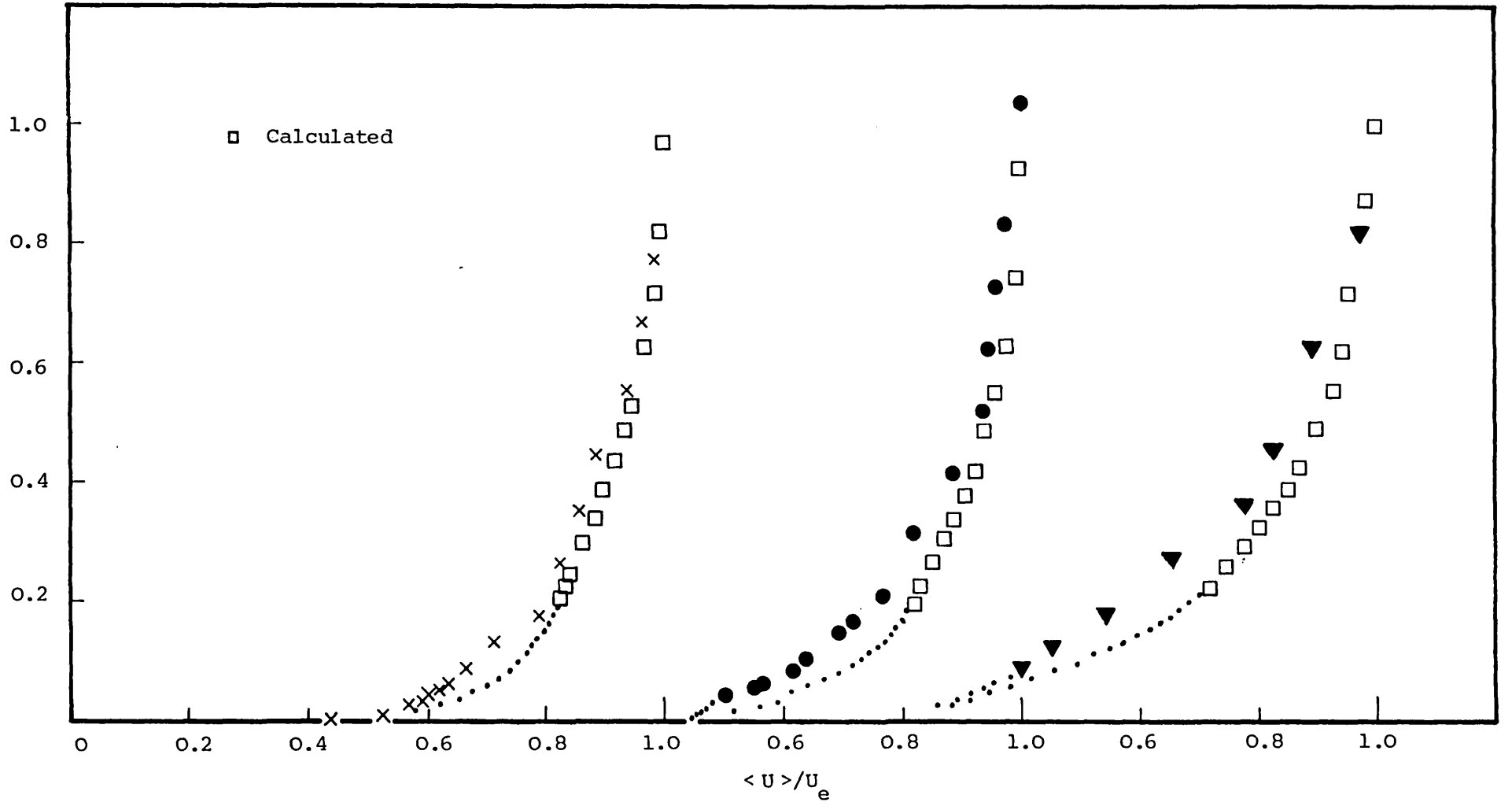


Figure 5.5 Calculated and measured profiles of mean velocity and Reynolds stresses in the boundary layer approaching separation. (Symbols as in fig. 3.10a; □ calclated values from boundary layer calculation procedure.)

(a) Mean velocity.

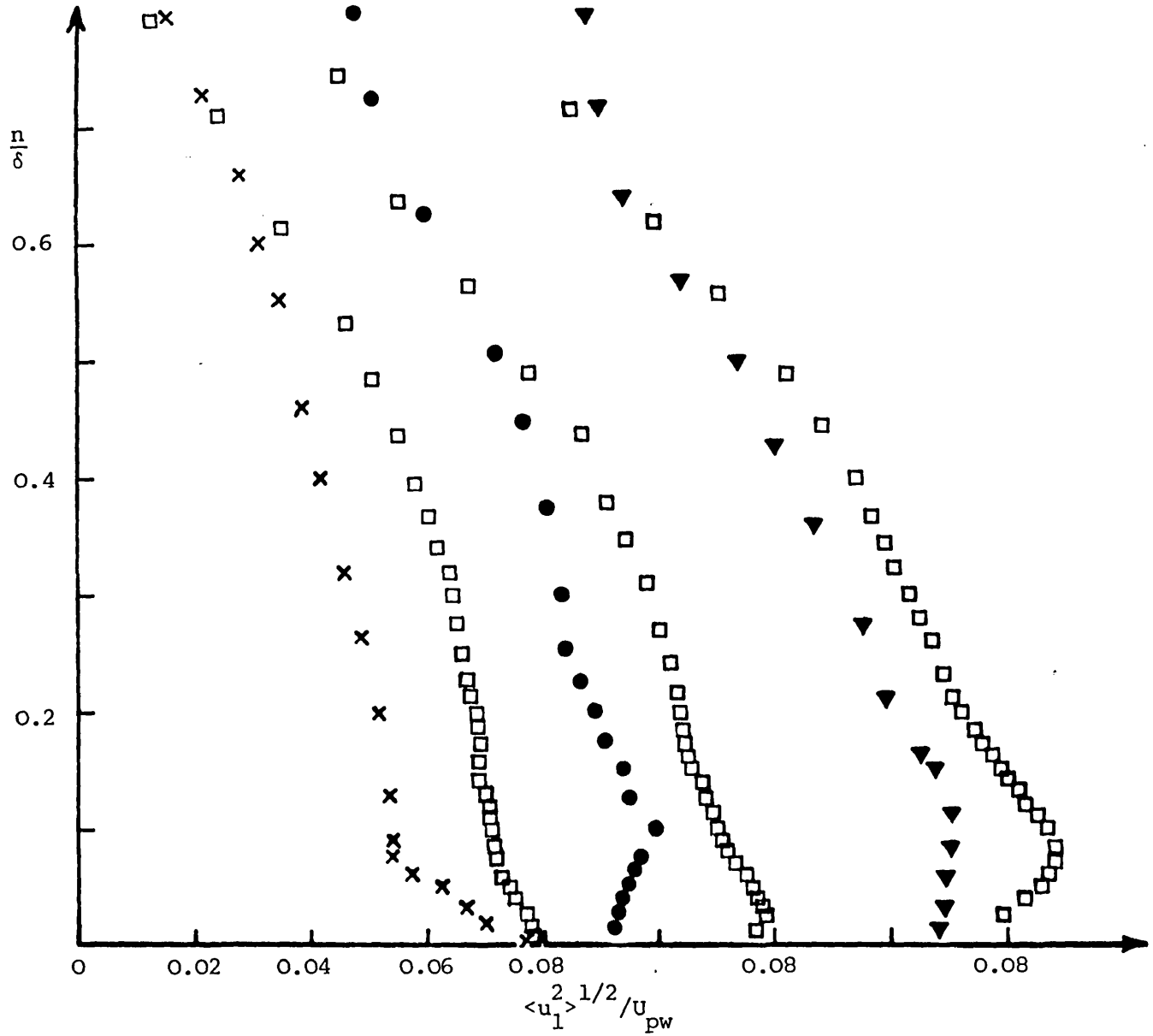


Fig. 5.5 (cont.) (b) Streamwise normal stress.

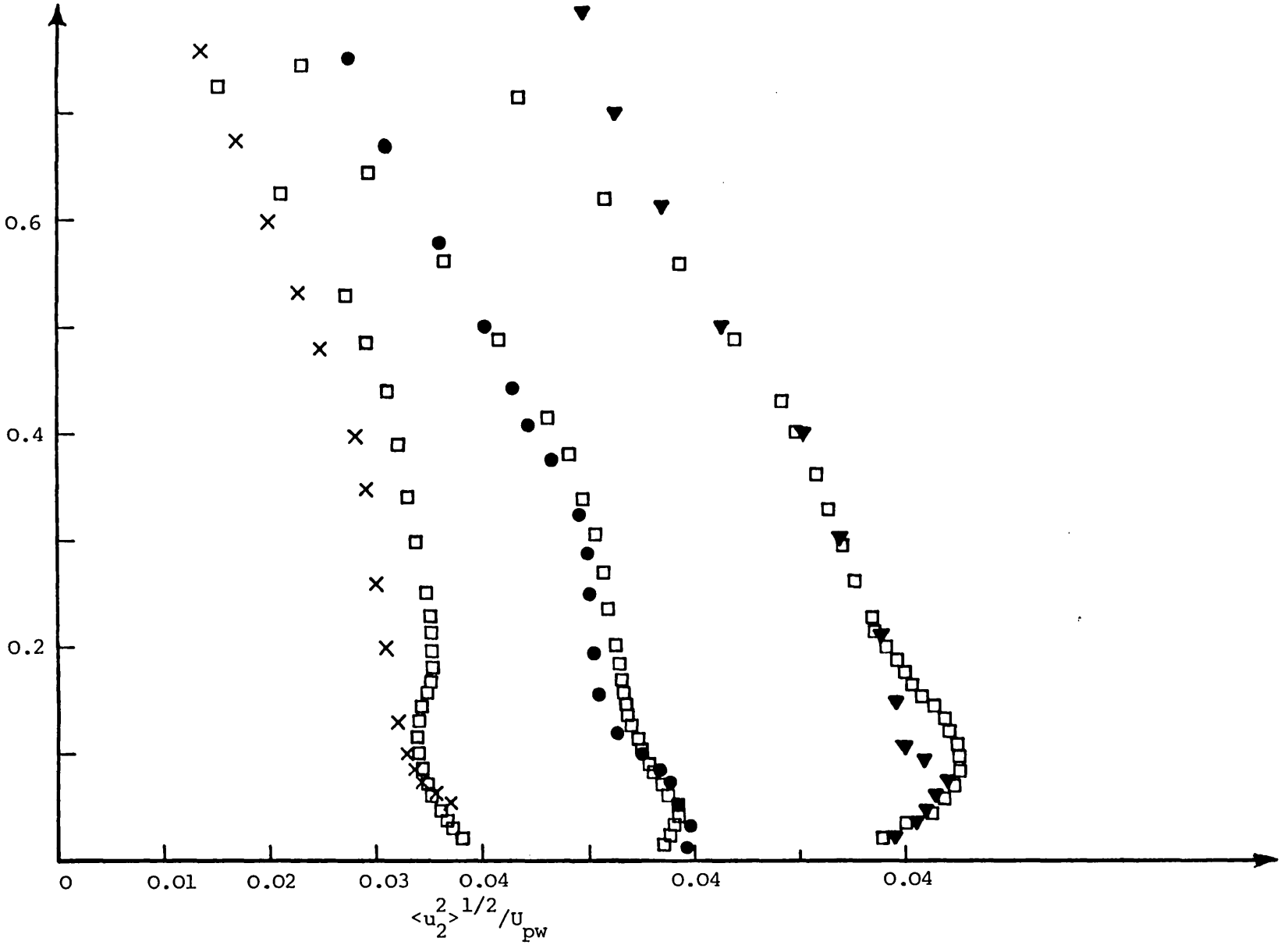


Fig. 5.5 (cont.) (c) Cross-stream normal stress.

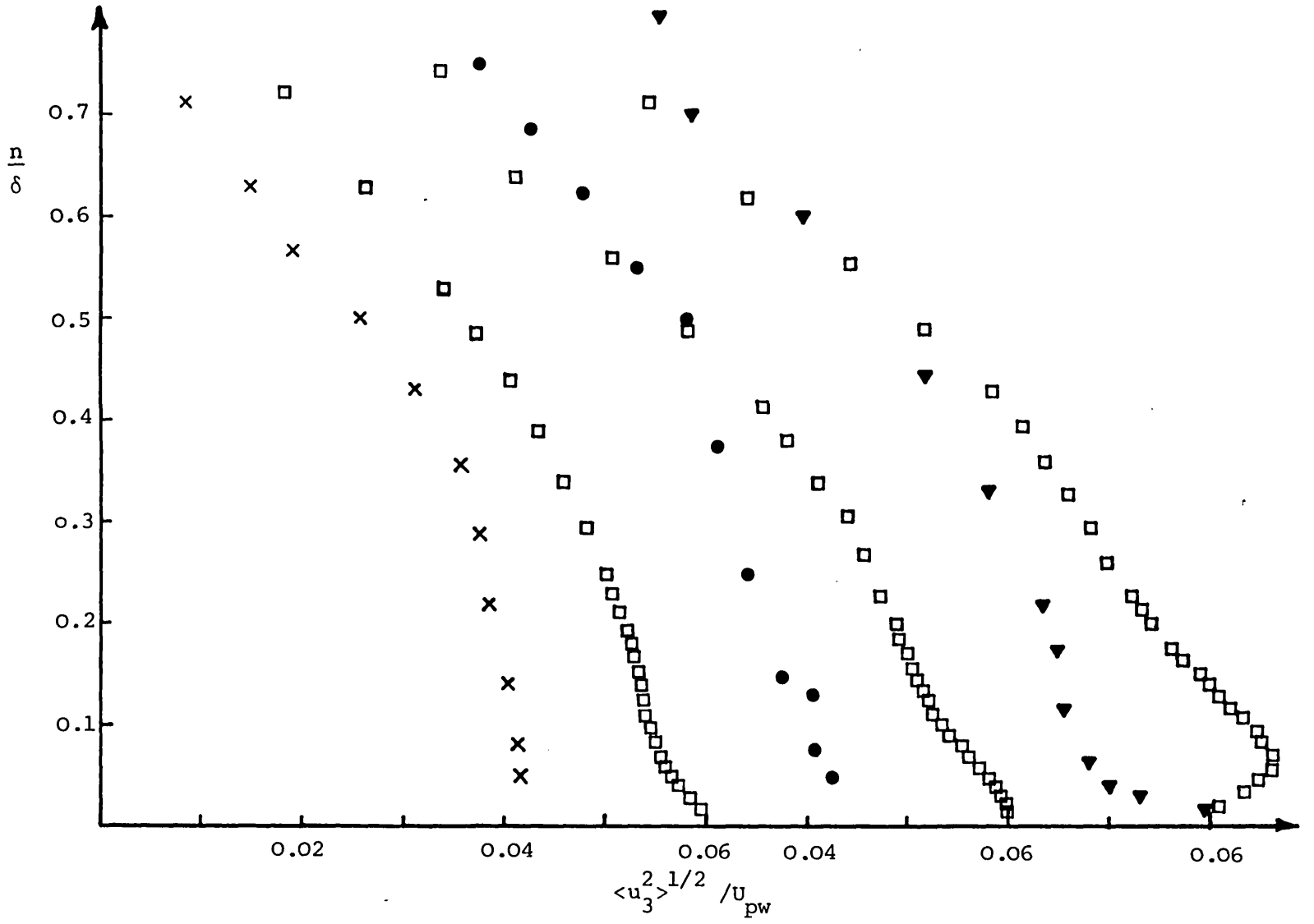


Fig. 5.5 (cont.) (d) Transverse normal stress.

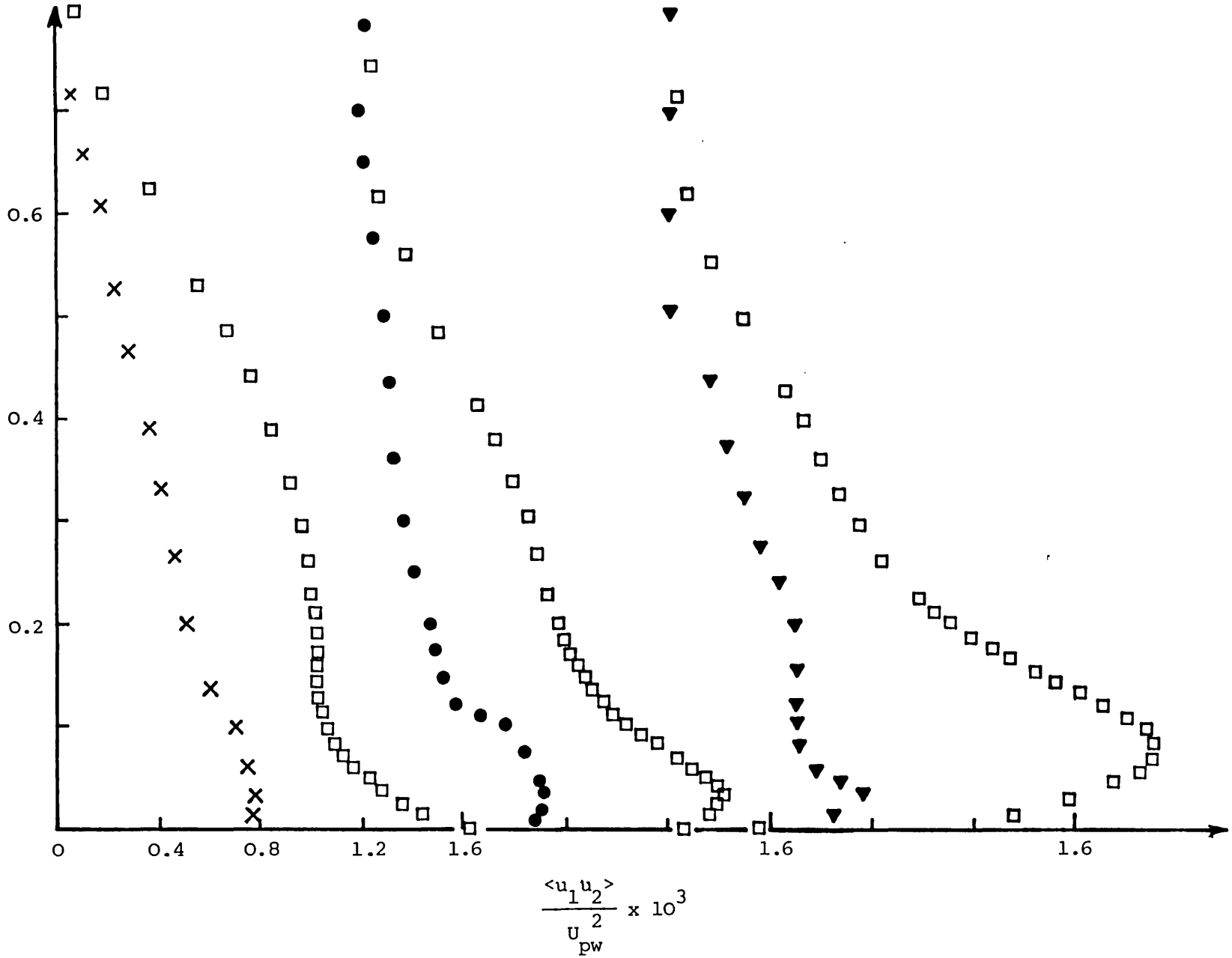


Fig. 5.5 (cont.) (e) Reynolds shear stress.

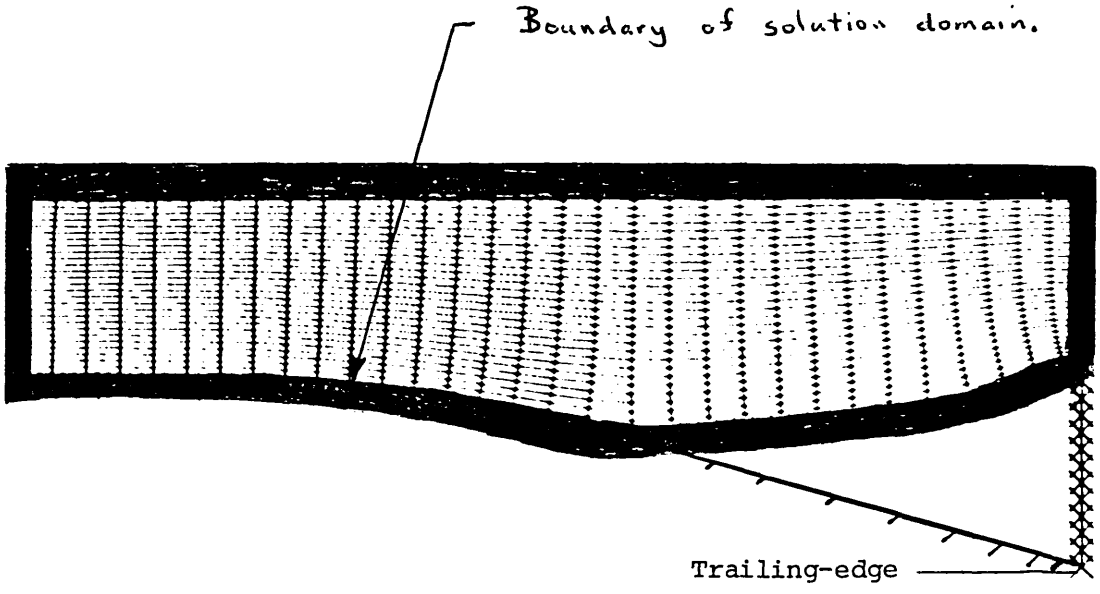


Figure 5.6 Potential flow mesh with the calculated diplacement thickness added to the surface of the plate and flap.

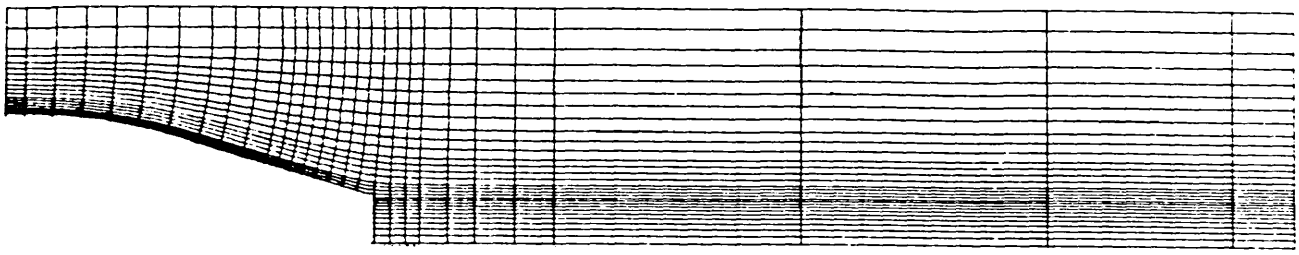


Figure 5.7 Calculation domain and scalar cell faces.

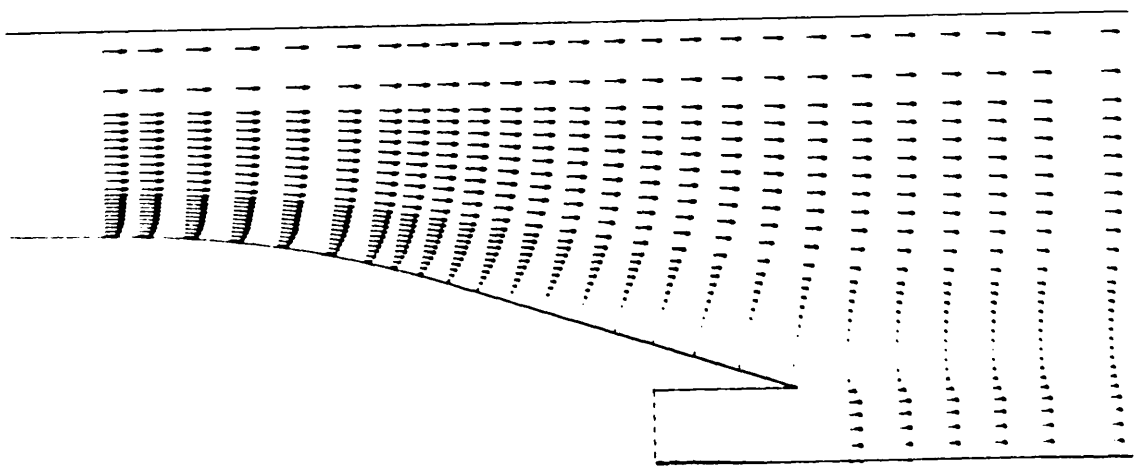


Figure 5.8 Calculated mean velocity vectors.

(a) Overall.

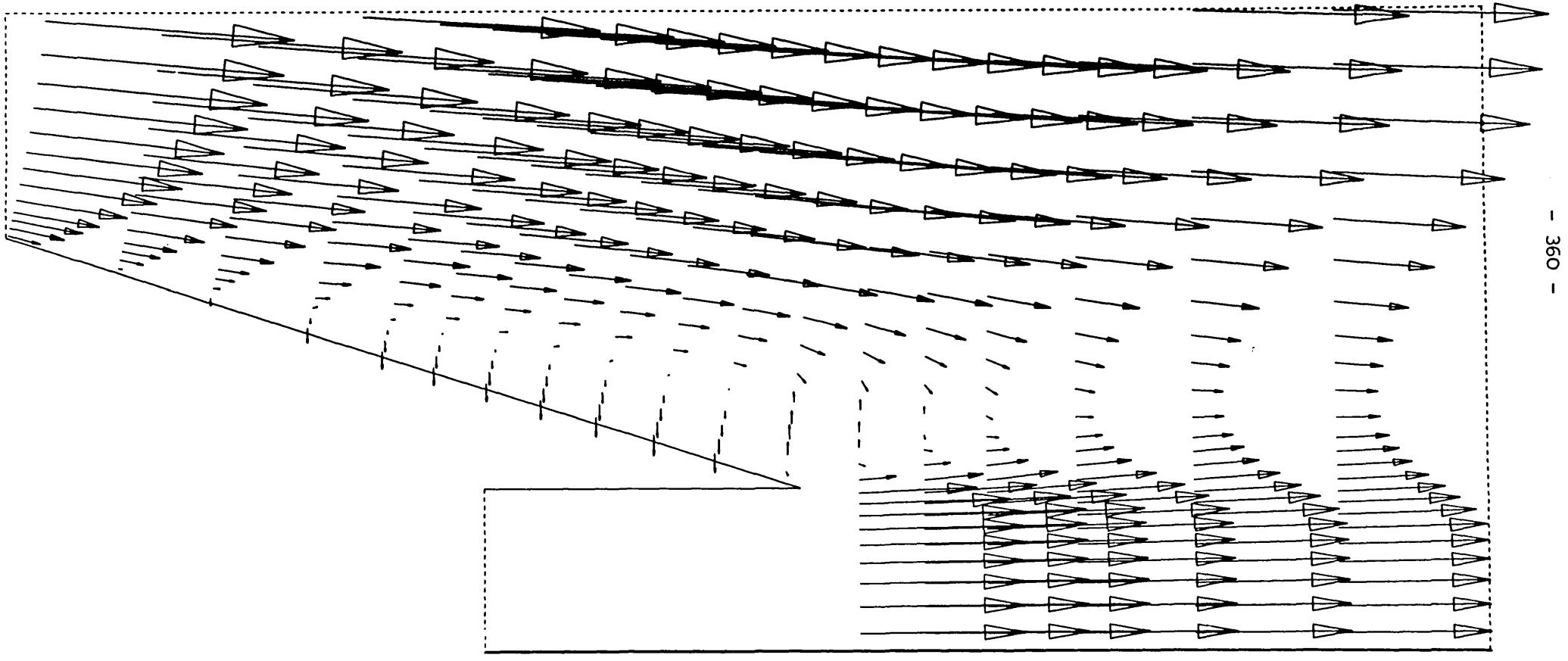


Fig. 5.8 (cont.) (b) Separated region.

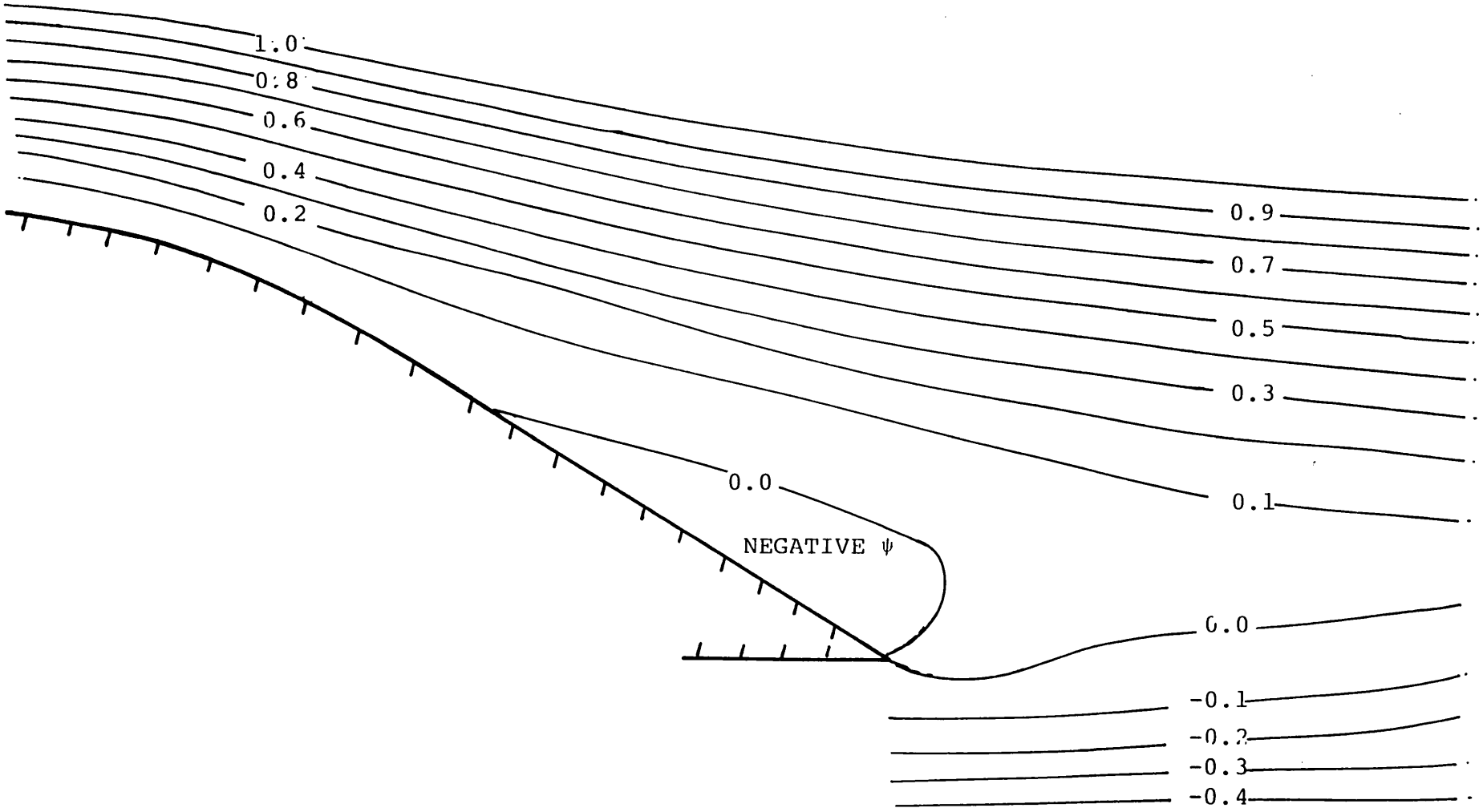


Figure 5.9 Calculated mean streamlines.

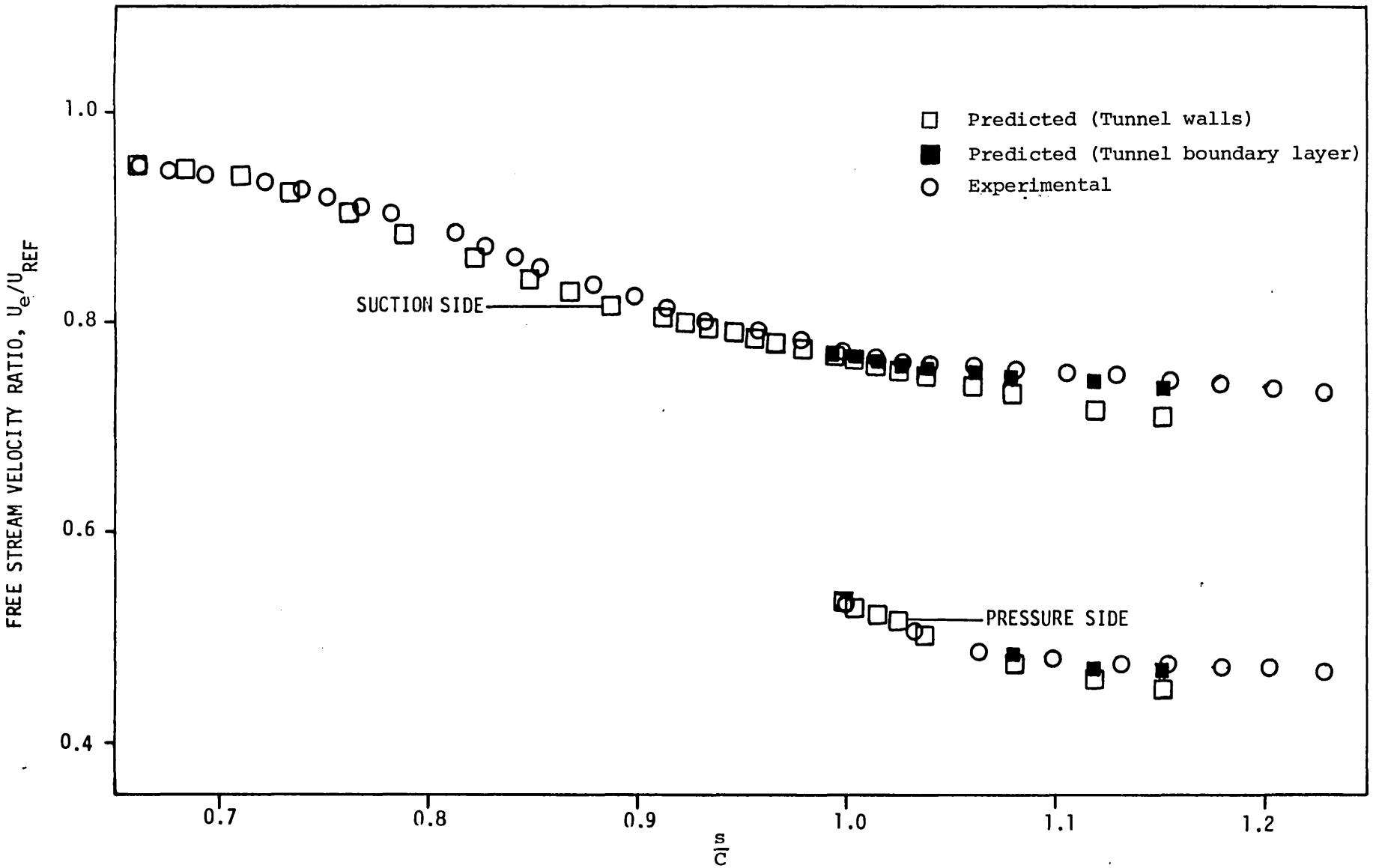


FIGURE 5.10 Calculated and measured distributions of free-stream velocity, surface static pressure and skin-friction coefficient. (a) Free-stream velocity.

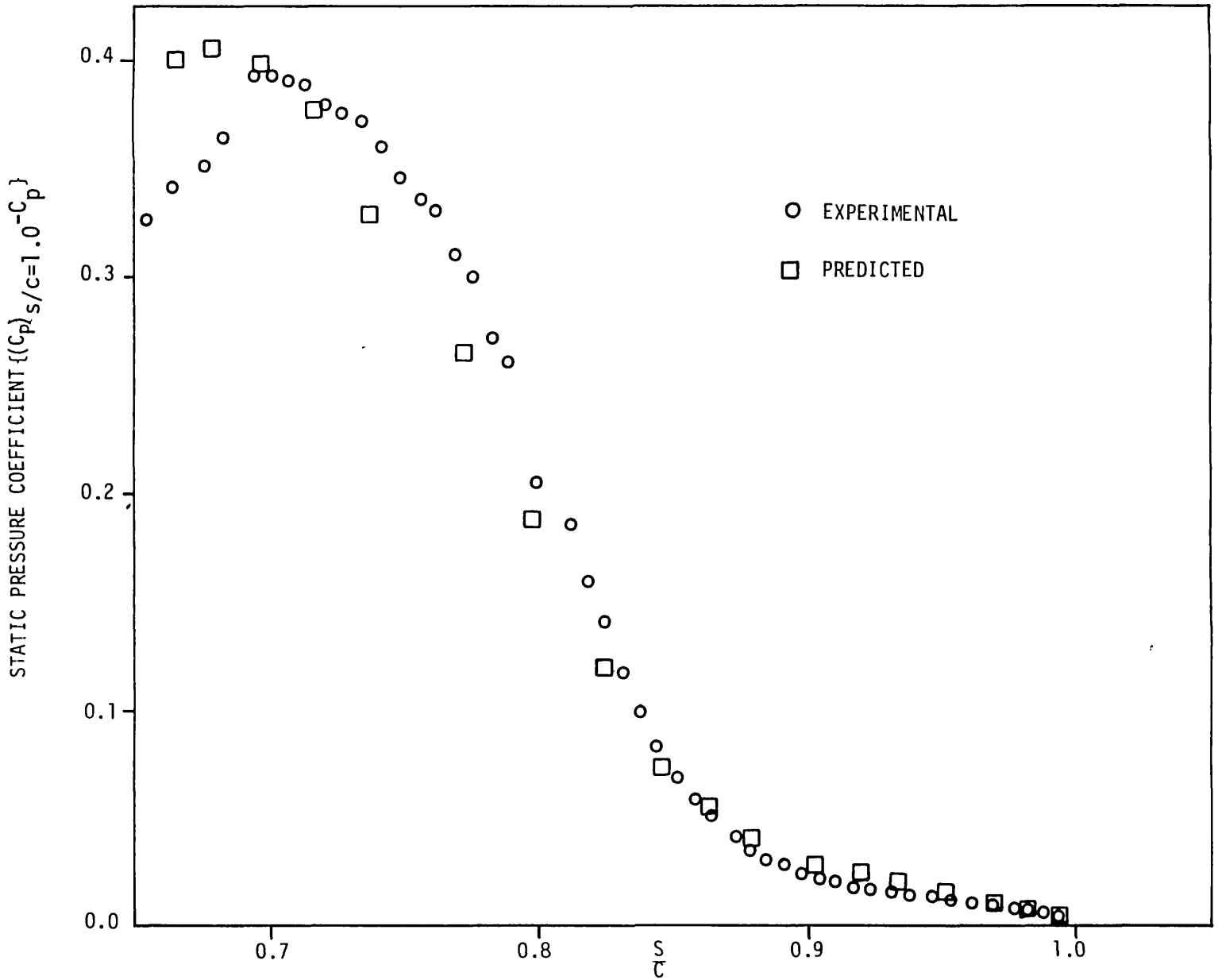


Fig. 5.10 (cont.) (b) Surface static pressure.

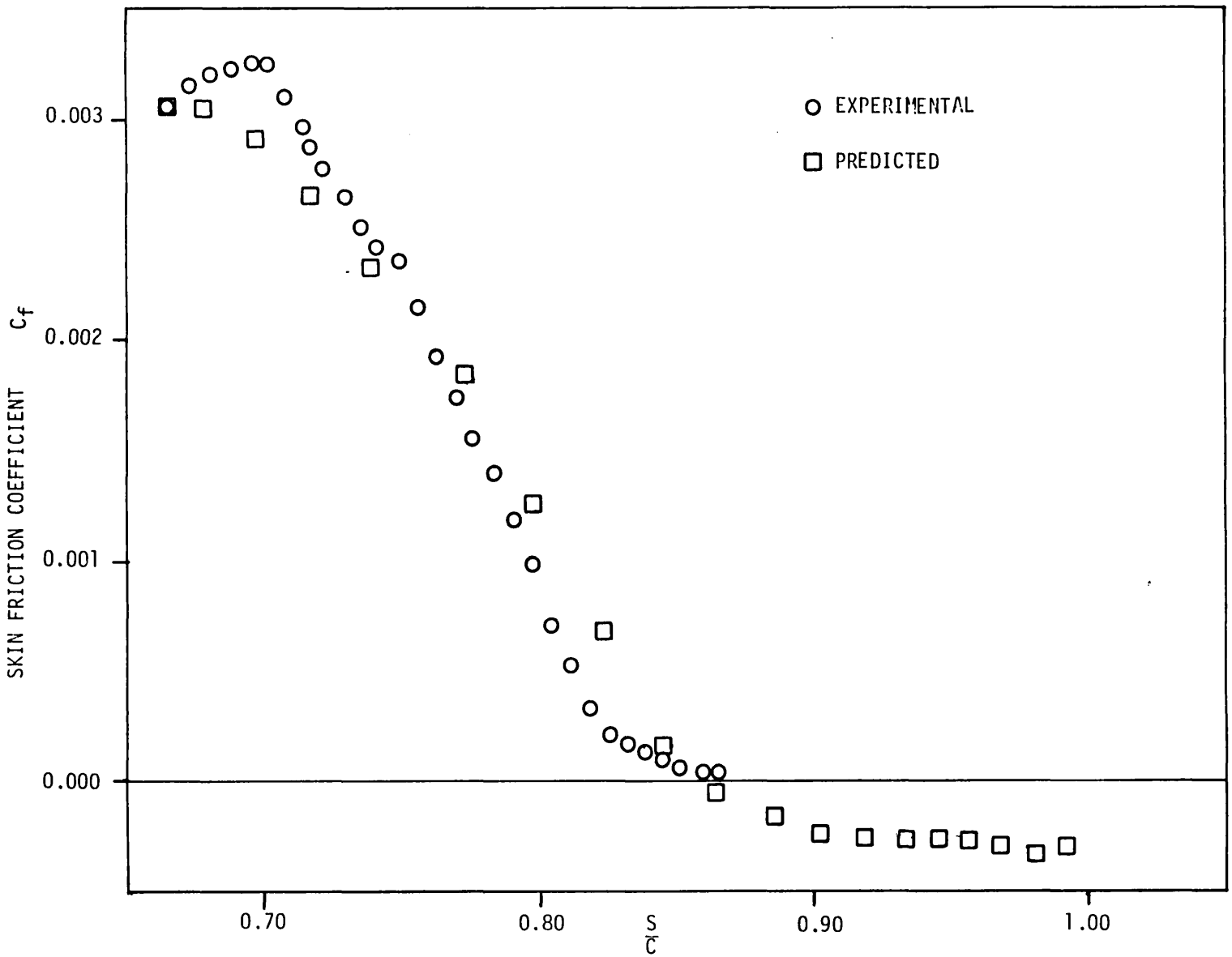
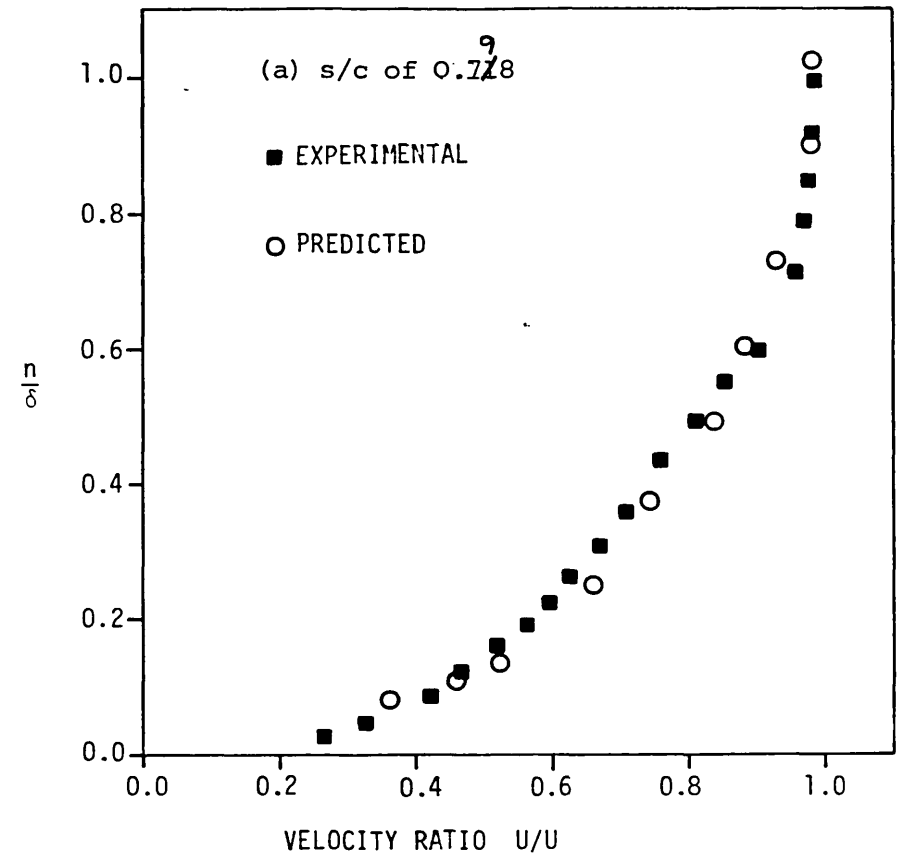


Fig. 5.10 (cont.) (c) Skin-friction coefficient.



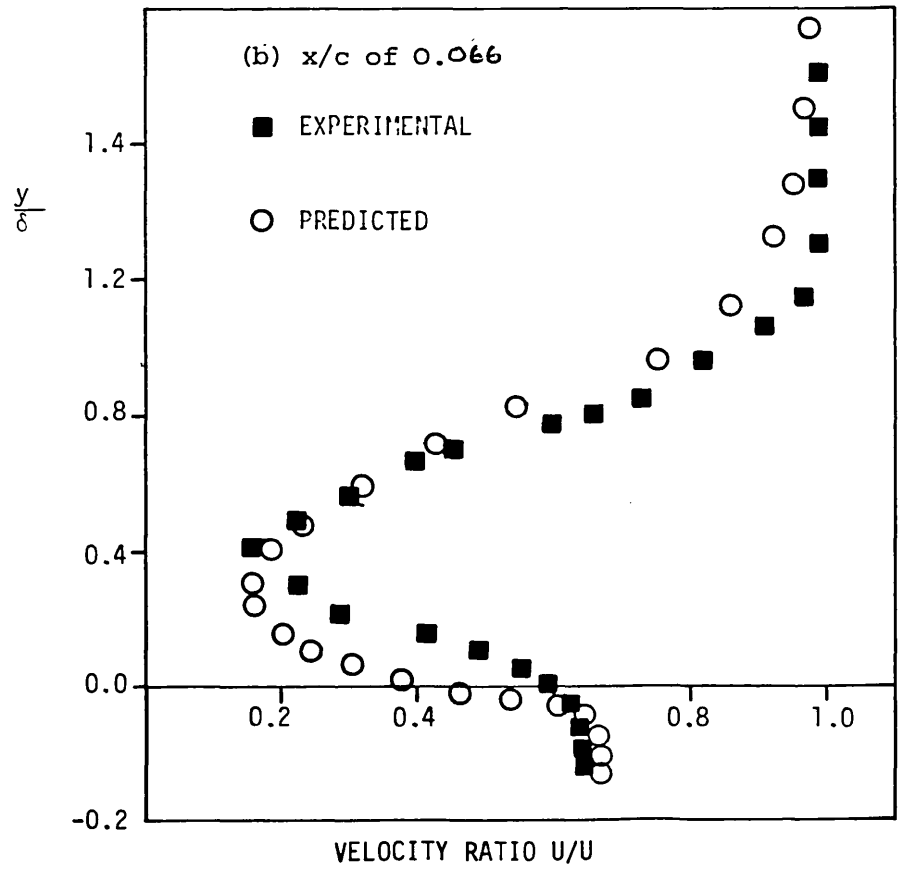
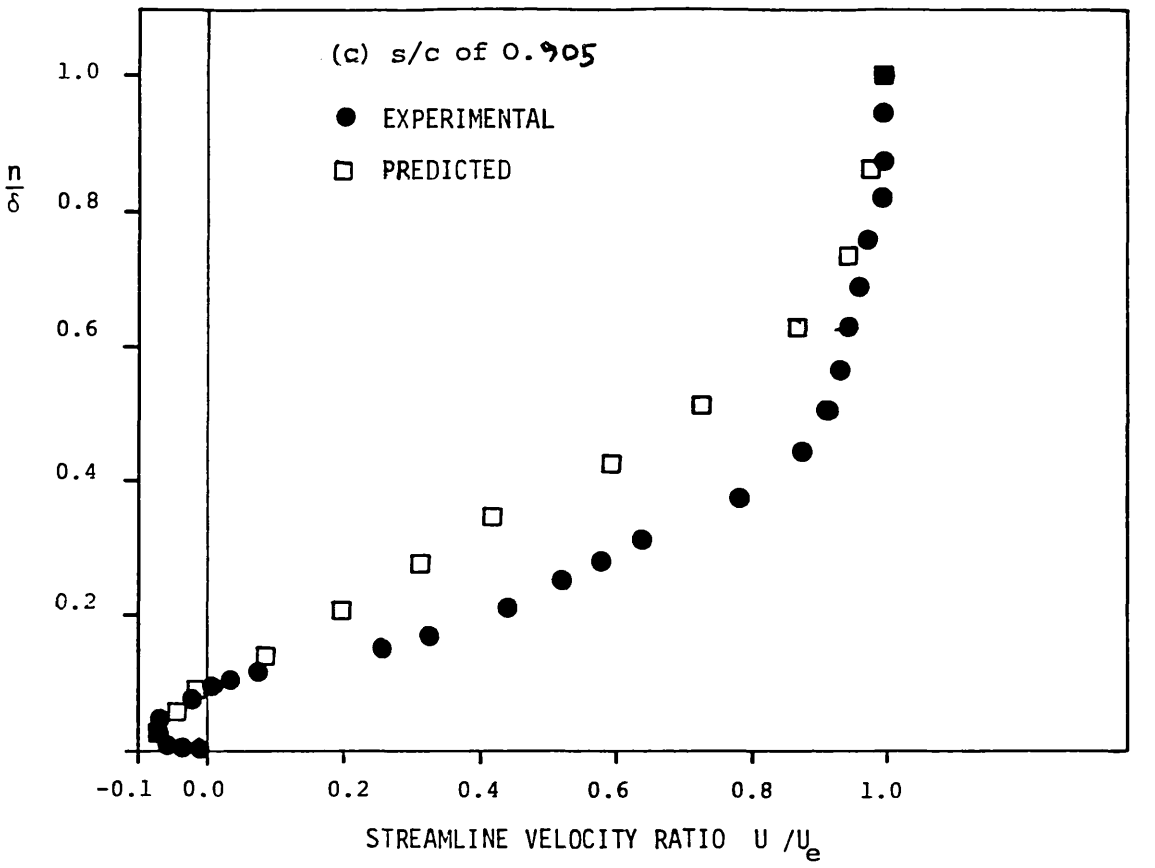


Figure 5.11 Profiles of calculated and experimental mean velocity.



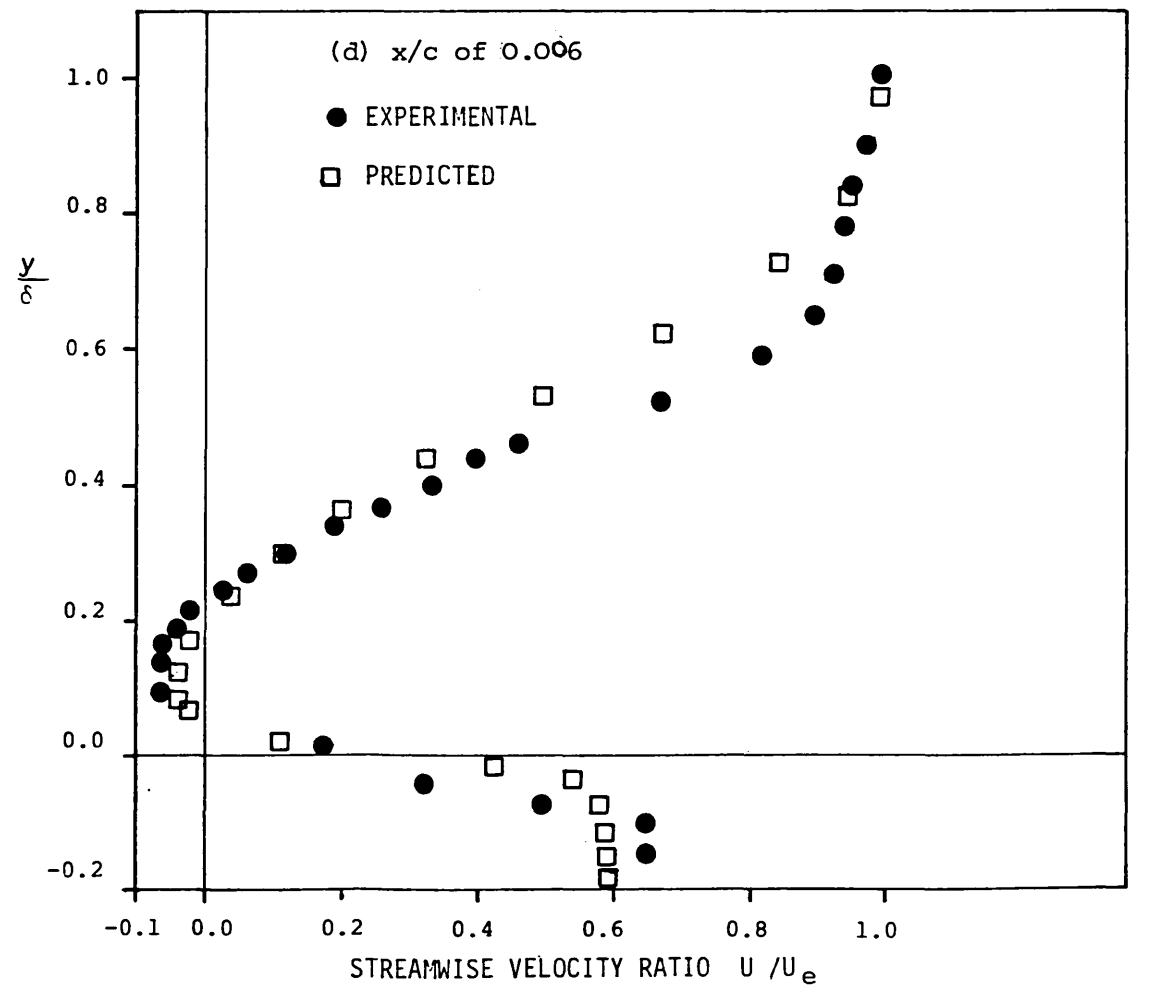
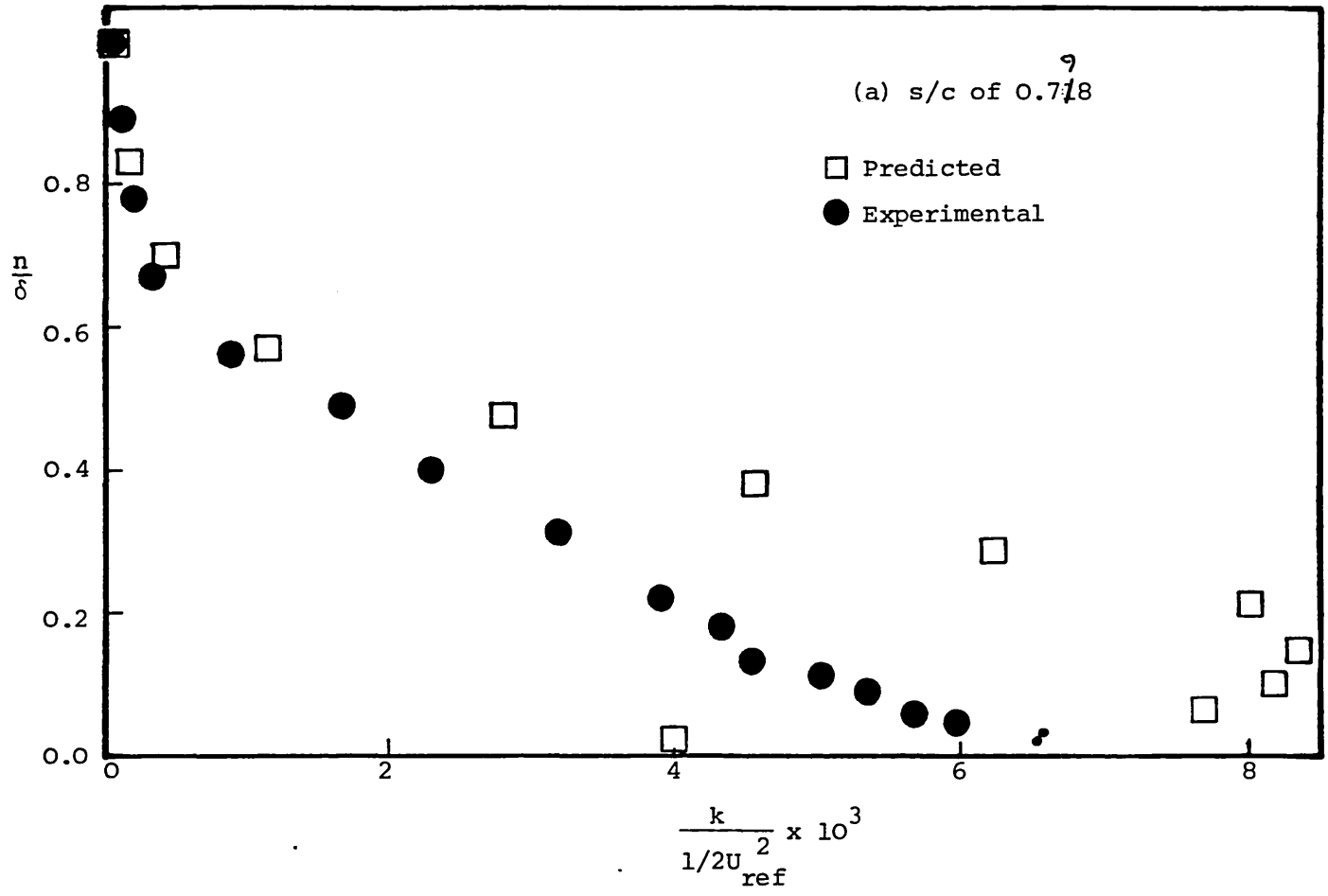


Fig. 5.11(cont.)Profiles of calculated and experimental mean velocity.



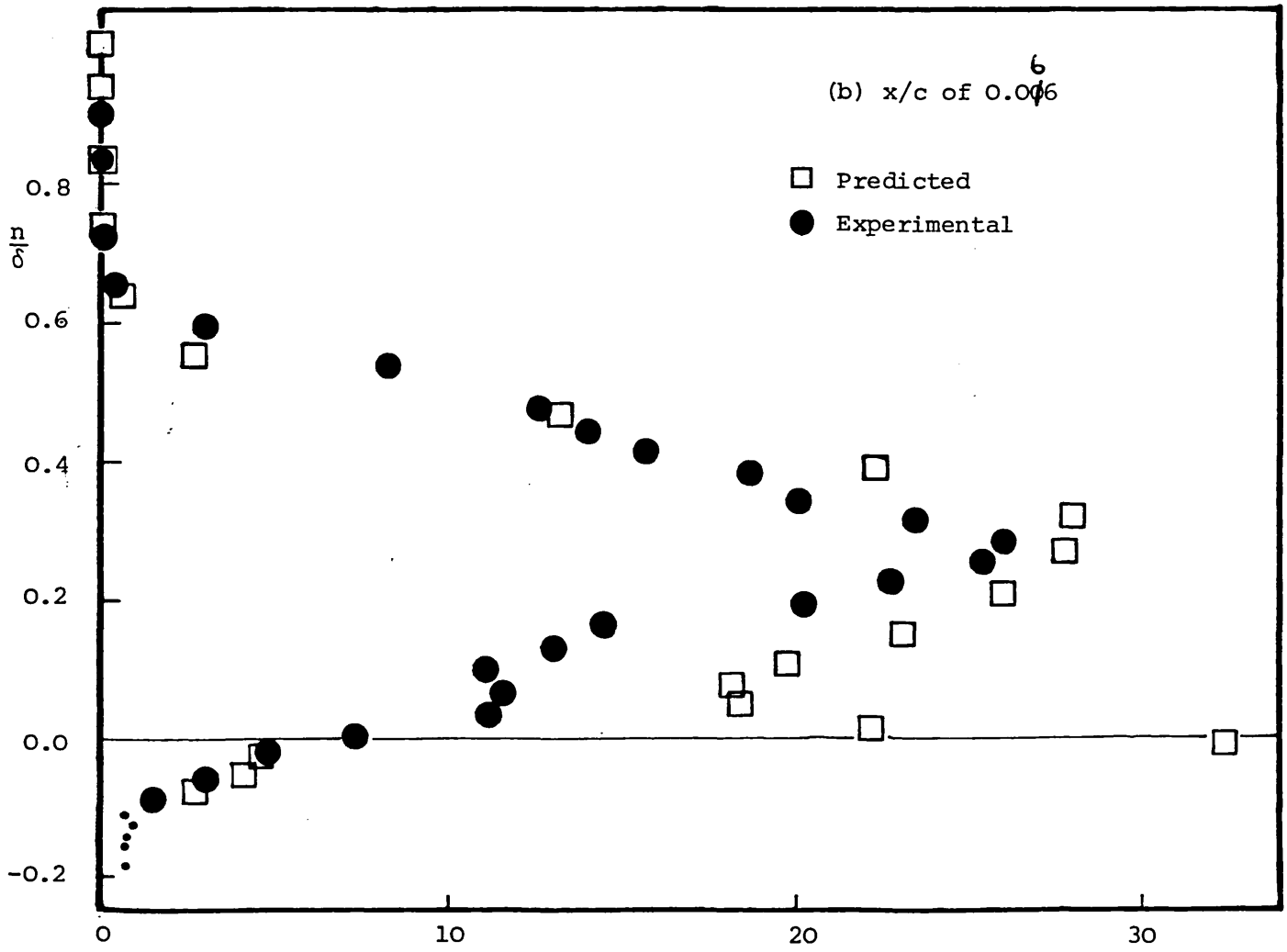
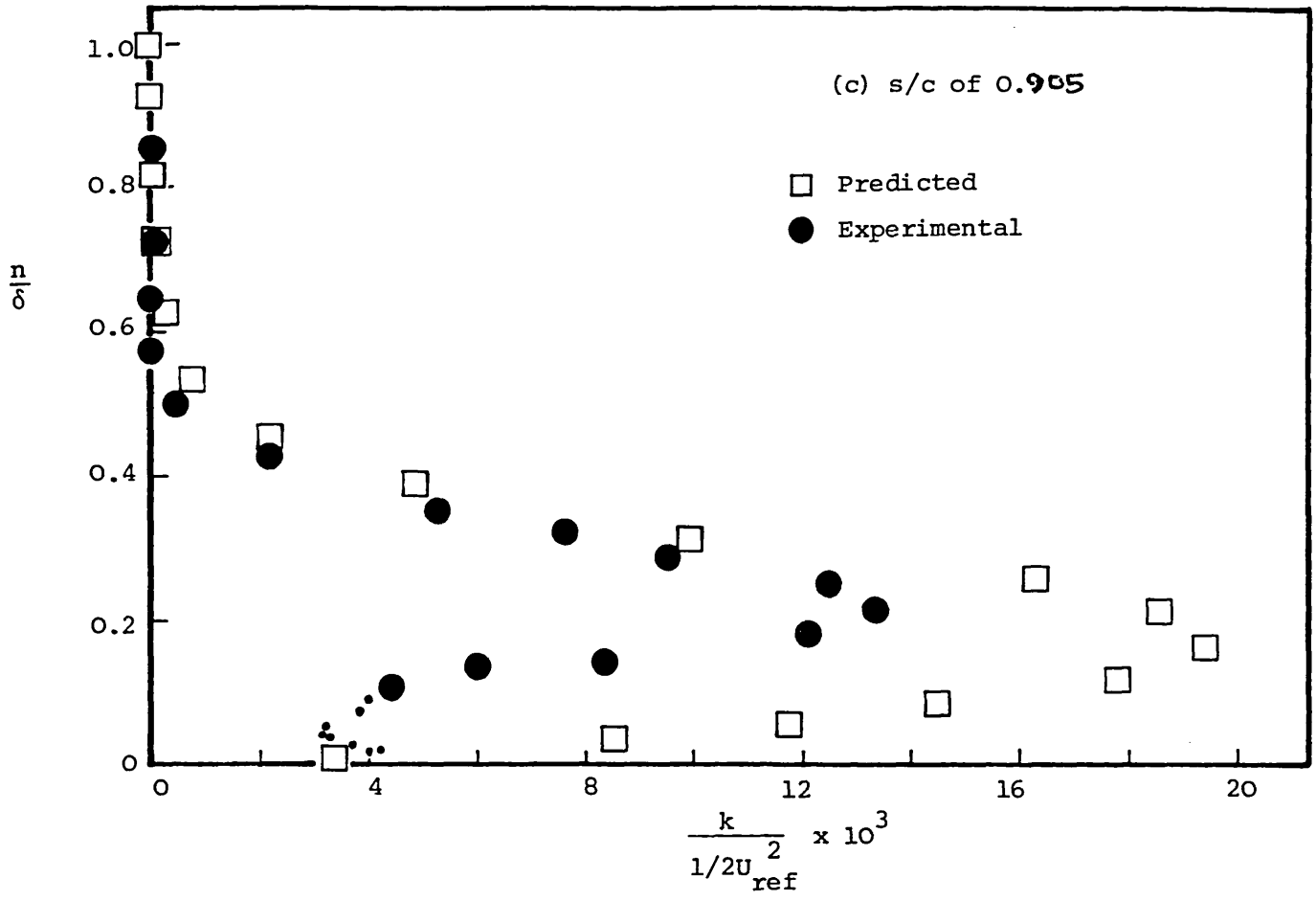


Figure 5.12 Profiles of calulated and experimental turbulence kinetic energy.



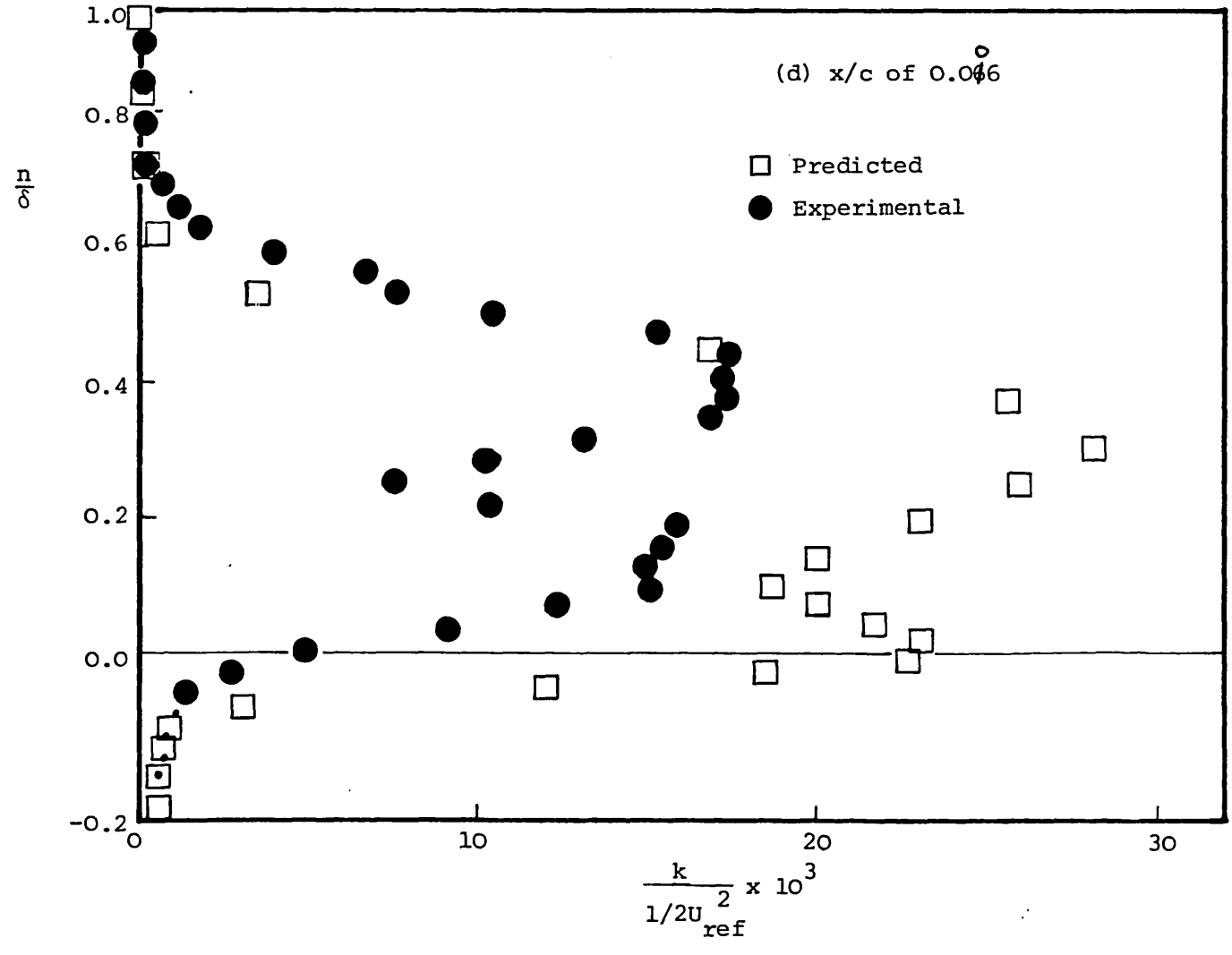


Fig. 5.12 (cont.) Profiles of calulated and experimental turbulence energy.

CHAPTER 6

CLOSURE

This chapter provides a summary of the achievements and conclusions of the present research and makes recommendations for future work. The more important findings of the experimental study are summarized and research with further flow configurations is suggested. The achievements of the computational investigations are also stated and corresponding recommendations made. The first part of this chapter considers the present contribution from experiments and is followed by that from calculations. The chapter closes with suggested improvements and recommendations for further research.

Measurements of pressure and velocity characteristics were made in the flow around a plate extended with a downstream flap to provide turbulent trailing-edge separation that is similar to the two-dimensional separation found on high-lift wings with high aspect ratios. The measurements consist primarily of mean values of pressure, velocity and Reynolds stresses in the potential flow, upstream boundary layer, recirculation region and downstream wake. The experimental procedures feature the use of flying hot-wire anemometry which was required in the vicinity of recirculation where flow reversals were found. The results provide valuable information for testing calculation methods and turbulence models intended for recirculating flows: in particular, they are useful for developing aerodynamic calculation procedures for the flow around the trailing-edge of airfoils near maximum lift, but without the complicating influence of leading-edge phenomena.

The experiments indicate, and verified by calculations, that certain regions of the flow are more important to the successful prediction of the effects associated with separation and they are the subject of the following paragraphs.

The shear layer associated with the dividing streamline is the most important region. Here, the mean flow is diverted around the recirculation region and results in cross-stream momentum and pressure gradients which are greater than can be approximated by boundary-layer equations. Velocity gradients are considerable in both cross-stream and streamwise directions and turbulence production is large. This results in significantly larger values of turbulence stresses throughout this shear layer than would be expected in an attached boundary layer and turbulent diffusion is, consequently, large. Turbulence transport is the main process which balances the pressure gradient in the vicinity of mean streamline detachment, and is important in determining the dimensions of the recirculating region. It is also responsible for the moderately high levels of turbulence stresses found near the centre of the recirculation bubble where turbulence production is insignificant. Turbulence-modelling assumptions are important to the prediction of this shear layer and it is possible that a model using an eddy-viscosity hypothesis may be adequate despite moderate anisotropy of the turbulence field. The present calculations suggest this, but are not completely conclusive because of the influence of numerical truncation errors.

The flow close to the wall has a log-linear distribution of mean velocity across a portion of the boundary layer. The conventional law-of-the-wall describes the near-wall flow upstream

of flow reversals associated with incipient separation. Farther downstream and in the backflow, the log-law constants gradually change although the calculations suggest that this is of little consequence to the mean-flow results, probably because the wall shear stress is very small in and around the recirculation bubble.

Characteristics of the wake were found to be largely dependent on the nature of the recirculating flow upstream. Reynolds stresses are large in the wake because of large levels of turbulence production upstream in the vicinity of recirculation and in the very-near wake, i.e. in the suction-side shear layer and in the pressure-side mixing layer that are found above and below the backflow near the trailing-edge. Correspondingly, turbulence diffusion in the wake is also large and causes the mean flow to recover quickly and the turbulence to approach an isotropic state rapidly although in a highly non-linear manner. To calculate the wake, it is essential to represent mean and turbulence characteristics for the initial development of the wake associated with the backflow because, firstly, the backflow originates mainly in this region and, secondly, development of the remainder of the wake depends heavily on upstream values which are convected downstream and determine the levels of diffusion and turbulence production in the near wake. In the very-near and near wake, curvature of the flow around the downstream end of recirculation destabilizes the turbulence by reducing the local rate of dissipation of turbulence kinetic energy in the vicinity of closure of the bubble. These curvature effects, and those discussed below, have important consequences in that turbulence models require the representation of the effects of significant change in the turbulence structure that is a consequence of the

extra strain, for instance due to curvature, in order to predict the correct levels of turbulence stresses, dissipation, and thus diffusion.

Turbulence in the curved boundary-layer upstream of separation was stabilized as a consequence of streamwise curvature. The measurements showed that the mean flow and turbulence structure were affected and it may be implied that this was caused by an increase in the rate of dissipation of turbulence energy which had the effect of stabilizing the turbulence and, hence, decreasing diffusion. The degree of this effect suggests, and it is confirmed by boundary-layer calculations with the Reynolds stress transport model, that modelling the effects of streamwise curvature is important to the upstream development of the shear layer associated with the dividing streamline, including the location of detachment. In addition, and at least as important in the vicinity of detachment and of the downstream end of recirculation, measurements and calculations indicate that turbulence production by normal-stress: normal-strain interaction may need to be modelled where the turbulence is anisotropic and streamwise gradients are considerable. This suggests that boundary-layer forms of the Reynolds stress transport equation do not represent turbulence phenomena in the region approaching detachment and of recirculating flow so that elliptic forms are required which were also recommended for the mean flow equations discussed above.

Calculations were performed with numerical procedures that solve the Navier-Stokes equations in their inviscid, boundary-layer and elliptic Reynolds-averaged forms, and the results were compared with those of the above experiment. The numerical solution of the Reynolds-averaged two-dimensional, steady, constant property form of the Navier-Stokes equations and equations for the transport of turbulence kinetic

energy and dissipation rate were in reasonable agreement with the experimentally observed mean flow. They showed that the cross-stream momentum equation was important in the vicinity of separation and, specifically, accounted for up to 70 per cent of the momentum transfer in the region where the mean flow converges around the downstream end of recirculation. The calculated values of mean velocity, turbulence kinetic energy and dissipation rate were directly affected by numerical truncation errors which appear as false diffusion. This tended to obscure the influence of turbulence-modelling and boundary-condition assumptions. It was, however, apparent that the use of different boundary conditions on the wall in the region of backflow did not have an appreciable effect on the mean-flow and turbulence results, even within recirculation. It was also evident that there was an additional over-prediction of diffusion by the present formulation of the k-ε turbulence model which was unable to predict the stabilizing effect of streamwise curvature on the turbulence. The influence of this deficiency could not be fully evaluated because it results in extra diffusion of momentum and turbulence energy which can not be distinguished from the false diffusion associated with numerical truncation errors. The numerical procedure for solving elliptic forms of the time-averaged Navier-Stokes equations has additional advantages associated with implicit treatments of the viscous-inviscid interaction and the Kutta condition although the procedure is inefficient in regions where the inviscid or boundary-layer equations are appropriate.

Results obtained with a forward-marching numerical procedure for solving boundary-layer forms of the transport equations for mass, momentum and Reynolds stresses, were in very good agreement with the

experimental mean flow over the curved boundary-layer and upstream of flow reverals. Turbulence levels were reasonably well calculated since the use of the Reynolds stress transport model enabled the representation of the effects of streamwise curvature on the turbulence with appropriate modelling of the pressure-strain correlation and influence of the wall. The boundary-layer calculations did not agree with experiments downstream of the upstream extremity of flow reversals associated with separation, and this is attributable to the neglect of cross-stream momentum and streamwise gradients which both become increasingly significant approaching detachment.

Calculated representation of viscous effects on the inviscid flow, and hence on the surface pressure distribution used in the boundary-layer calculation, was not successful in the vicinity of separation. The boundary-layer approximation failed upstream of separation and over-predicted the rate of boundary-layer growth. As a result, simple account of the viscous flow by adding the displacement thickness to the wall co-ordinates in the inviscid calculation was unable to reproduce the wall pressure gradient. The pressure is over-predicted near separation and the detachment point moves progressively upstream with subsequent iteration between the boundary-layer and inviscid-flow solutions. The present attempt was unsuccessful for three possible reasons and further research is required to determine which are important. First, the simple displacement surface concept may not be appropriate in the vicinity of rapid boundary-layer growth: higher order treatment of the boundary condition to account for large local gradients across the streamlines may be necessary. Secondly, the forward-marching boundary-layer procedure fails to converge

downstream of detachment and empirical specification of the displacement surface was required: inverse methods for calculating the boundary-layer flow would avoid the need to specify the downstream boundary. Lastly, the boundary-layer form of transport equations is invalid in the vicinity of detachment however if this region was smaller than a size yet to be determined, the boundary-layer approximations may be adequate for engineering purposes: inverse techniques are again required to solve for the remainder of the separated flow and additional detailed experiments in smaller regions of separation are needed to define the limits of this approach. Turbulence modelling and wall boundary conditions are of secondary importance compared to the above factors, but it is worth recommending the use of the law-of-the-wall boundary condition, which accurately and efficiently represented the near-wall flow, and use of the Reynolds stress turbulence model which represented the influence of streamwise curvature on the turbulence.

The calculation methods of the present study were able to represent the mean flow around the trailing-edge configuration of figure 3.1 but improvements are needed and are discussed in the following paragraphs.

It seems that the most important deficiency in the calculation of separated and near-wake flow is numerical accuracy of the numerical solution procedure. Truncation errors cause false diffusion in regions where upwind-differencing is applied and the mean velocity is inclined to the calculation mesh, and these errors, although difficult to quantify, can not be ignored. The use of a general curvilinear mesh, which is constructed from the streamlines and velocity-potential lines of the equivalent inviscid flow, helps to improve numerical accuracy in the following two ways: first, the boundary conditions are accurately represented which is of particular importance at the wall

boundary and, secondly, the alignment of the mesh and flow direction is improved especially in regions where viscous effects are small. In contrast, the flow in the vicinity of recirculation has large values of effective viscosity and is deflected around the backflow so that it is not aligned with the inviscid-flow mesh. This misalignment occurs in the vicinity of the important shear layer associated with the dividing streamline, more specifically near detachment and near the rear stagnation point, and results in false diffusion since the velocities here are large enough to require upwind differencing. The accuracy of the calculated result is likely to be adequate for many practical purposes but can usefully be improved, perhaps by the use of higher order approximations. Second-order schemes, such as those of Raithby (1976), Leonard (1979), Lai (1982) and Hackman et al (1983), are possible candidates and need to be quantitatively evaluated for the present flow configuration. The use of adaptive grids, such as those discussed by Ghia and Ghia (1983), are also likely to be beneficial and the present results suggest that pressure gradients are likely to provide an appropriate adaptive criteria.

The present measurements and calculations indicates that diffusion is over-predicted and that this is not due entirely to numerical inaccuracy. The use of an eddy-viscosity hypothesis and the neglect of streamwise curvature effects on the dissipation rate, cannot be fully assessed because of numerical inaccuracies but it does appear that the curvature and diffusion effects would be significant even if numerical diffusion were absent. It is therefore recommended that improvements to the present numerical scheme to reduce numerical truncation errors are followed by an investigation of turbulence

modelling influences in the shear layer associated with the streamline dividing forward and reversed flow and, also, in the curved boundary layer and near wake.

The viscous-inviscid interaction can be modelled with a simple displacement thickness upstream of the influence of separation. Further investigation is needed to determine appropriate procedures farther downstream where the boundary layer grows rapidly as separation is approached, and in the vicinity of recirculating flow and the curved downstream wake. It appears doubtful whether a simple approach will be adequate, at least in the region approaching detachment, because of large gradients in the displacement surface, and hence the equivalent inviscid flow, which leads to the consideration of higher order boundary conditions such as those discussed by Murman and Bussing (1983). Even so, the usual approach has been to solve boundary-layer equations in the viscous flow around airfoils, but significant variations of cross-stream velocity and streamwise gradients that are found in the experiment, and verified in the calculation, indicates that large regions of recirculation must be represented by solutions of less simplified forms of the time-averaged Navier-Stokes equations. Cross-stream momentum can be incorporated by solving its transport equation and this was the practice in the present Navier-Stokes calculations. The importance of streamwise variations of the mean momentum and turbulence stresses in both calculations and experiment, suggests that the local flow properties in the vicinity of recirculation are influenced by events further downstream, and in a manner not accounted for by pressure alone, so that the mathematical property of ellipticity must be represented in the equations used to represent turbulent recirculating flow.

The solution of time-averaged Navier-Stokes equations has advantages over viscous-inviscid interactive calculations which make them attractive for regions of strong viscous-inviscid interaction. Solution procedures for the Navier-Stokes equations, such as that of the present calculation, represent elliptic properties of transport equations that are important in the vicinity of recirculation, as indicated above, whereas interactive calculations retain ellipticity only through the pressure and, in the case of integral methods, velocity-profile assumptions. Also, Navier-Stokes calculations do not require empirical knowledge of or special treatments for the Kutta condition or wake-curvature effects, which are the subject of much uncertainty in interactive calculations, other than those assumptions associated with turbulence modelling and the law-of-the-wall boundary conditions which are less restrictive, and more generally appropriate, than assumptions about the trailing-edge flow discussed by Butter and Williams (1980), for example. In contrast to attached flows, the Kutta-condition and wake-curvature effects are more important in flows with trailing-edge separation because of the corresponding strong viscous-inviscid interaction and appropriate assumptions are difficult to obtain because of the backflow on the suction-side surface. Navier-Stokes calculations incorporate these effects implicitly and, therefore, provide a better representation. In a similar fashion, uncertainty in the boundary condition that couples viscous and inviscid solutions in an interactive calculation does not appear in Navier-Stokes calculations since this boundary condition is implicitly contained in the formulation of the equations although the calculation domain must include the outer potential-flow region. The difficulties with using Navier-Stokes equations for airfoil calculations are primarily associated

numerical inaccuracies and computational efficiency, and in this respect interactive calculations have an advantage provided they can describe the flow appropriately well. Considering present computer constraints, the solution of Navier-Stokes equations over the entire domain is limited to two-dimensional configurations since three-dimensional calculations with them are prohibitively expensive for engineering practice. In the interests of efficiency, the calculation domain could be sub-divided into regions where solutions of inviscid, boundary-layer and Navier-Stokes equations are obtained and coupled with appropriate boundary conditions. For example, solutions of the Navier-Stokes equations could be obtained in a small portion of an airfoil configuration in the vicinity of strong viscoud-inviscid interaction, i.e. near the trailing-edge with or without separation, and coupled to inviscid, boundary-layer or other appropriately simplified versions of transport equations which are used to calculate the remainder of the flow domain. Accordingly, the calculation effort can emphasize the more demanding regions of the flow although appropriate boundary conditions are required to represent the interaction between solutions and could be provided on a matching surface such as that proposed by Maghoub and Bradshaw (1979) and discussed by Bradshaw, Kavanagh and Mobbs (1983). The attributes of this approach with the inclusion of Navier-Stokes calculations for the recirculating flow, needs further investigation to determine the levels of efficiency and accuracy that can be achieved. In summary, solutions of the Navier-Stokes equation provide a more accurate representation of recirculation with less empirical assumptions and are appropriate for a wider range of trailing-edge flow conditions than viscous-inviscid interactive calculations. The latter incur less

computational expense, but the former should be preferred for predicting large regions of trailing-edge separation.

Detailed experiments of the flow around two-dimensional, high-lift airfoil configurations are suggested for further investigation to improve the understanding of separation phenomena and to aid the development of design procedures for airfoils and wings. For airfoils at large angles of attack and trailing plates with separation, improvements to calculation methods, such as those recommended above for numerical accuracy, turbulence modelling, grid generation and interactive procedures, depend in part on obtaining further knowledge from experiments, and specific experiments are suggested in the following paragraphs.

Measurements similar to those in the present flow, are needed on a trailing-edge plate at smaller angles of incidence to assist in determining the size of recirculation region where Navier-Stokes equations are to be preferred to viscous-inviscid interactive procedures. The extent of the separated region is highly dependent on the angle of incidence and decreases of about 1 and 2 degrees from the present 17.5 degrees are likely to provide trailing-edge flows with moderate streamline curvature and a region of instantaneous flow reversals associated with a small region of recirculation and incipient separation, respectively.

Another series of experiments are suggested to investigate the influence of the upstream boundary-layer on separation. Properties of the recirculating flow depend on the distributions of mean and turbulence quantities in the boundary-layer approaching separation and measurements are suggested to quantify this dependence in the flow around a trailing-edge plate with separation. The first set of experiments introduces the wake of an additional plate which interacts with the

suction-side boundary-layer upstream of the trailing-edge plate which is positioned at increasing angles of incidence to promote trailing-edge separation. The aim is to represent the physical characteristics of separating confluent boundary-layers found on the suction-side of advanced high-lift airfoil configurations deploying leading-edge slats and to improve understanding of the physical processes associated with its separation and their implications for the calculation of the recirculating flow. The second set of experiments is intended to assist in determining the importance of streamwise flow curvature on separation processes. The suggested flow configuration comprises a trailing plate with separation preceded by curved surfaces that have curvature parameters δ/R, less than the 0.03 of the present study. It is intended to represent separation on airfoils with shallower curvature over their rear section and to aid the evaluation of turbulence-model assumptions associated with the effects of the extra strain due to curvature on the turbulence structure and, correspondingly, on separation.

Experimental investigations are proposed for a series of flows around similar trailing-edge configurations with initial boundary-layers that resemble those of blown and slotted flaps. These flows, which include investigation of upper-surface separation and the downstream wakes, constitute an extension of the present study to two-element airfoil configurations with a detached trailing flap. The purpose is to assist understanding of the related problems of multi-element airfoils and contributes specifically to the development of design methods for high-lift configurations. A splitter plate with air blown through the surface by an independently controlled fan, and with a downstream detached flap-plate arrangement could be used to establish mean-velocity

distributions closely related to those found on advanced wing designs. Emphasis should be placed on the wake-type profile associated with the slotted-flap arrangement of civil aircraft, high-lift configurations, but measurements also need to be obtained with initial profiles of the wall-jet form found with blown flap arrangements.

In all cases, measurements are required in sufficient detail to enable the evaluation of calculation methods, including turbulence models, and to improve understanding of the physical phenomena of turbulent separated flows. Accordingly, detailed measurements should be obtained to provide boundary conditions for calculations. These experiments have been suggested to assist development of design procedures and calculation method for two-dimensional high-lift airfoil configurations.

The long-term objective is to develop design capability for practical situations, and hence three-dimensional aircraft configurations, but so far the success of calculations has been limited to a small range of conditions, primarily for cruise or nearly two-dimensional configurations. It is advised that extension to three-dimensions be considered during the development of two-dimensional calculation procedures and it is worth noting that the methods of the present study can be extended. Analytical, numerical and experimental investigations of three-dimensional flows are scarce, for example there are no detailed experiments including turbulence data on wings with separation. Three-dimensional separation is likely to have initial mechanisms for separation which are similar to those of two-dimensional flow, but three-dimensional flow structures can be very different. Accordingly, future work needs to encompass measurements in regions of three-dimensional separation, for example to represent separated flows over swept wings, and used to provide understanding of and calculation methods for the flow around aircraft.

NOMENCLATURE

$< >$	time-averaged quantity
A	coefficients of finite-difference equation chapter 4
$A_1 .. A_3$	coefficients of hot-wire voltage-velocity relationship chapter 2
A_*	King's law constant
Δa	cell-face area
$a_1 .. a_{34}$	coefficients in the instantaneous hot-wire response equation
a,b,c,r	dimensions of flying-wire mechanism chapter 2
B	logarithmic law-of-the-wall constant
B_*	King's law constant
$b_1 .. b_4$	coefficients of second order moments in the appropriate equation for hot-wire cooling velocity
C,c	chord length
C_p	static-pressure coefficient
C_f	skin-friction coefficient
C_1, C_2, C_3 C_{H1}, C_{H2}, C_{H3} C_{G1}, C_{G2}	constants in the approximate equation for instantaneous hot-wire cooling velocity
$C_\mu, C_{\varepsilon 1}, C_{\varepsilon 2}$	constants of the k-ε turbulence model
C_t, C_1, C_2 C_μ, C_1', C_2' $C_{\varepsilon 1}, C_{\varepsilon 2}$	constants of the Reynolds-stress turbulence model
d	Preston tube diameter chapter 2 coefficient of finite-difference equation chapter 4
E	logarithmic law-of-the-wall constant
E_*	voltage output of hot-wire anemometer

f	function weighting factor chapter 4
F	function
F_{PR}	Preston-tube similarity function
f_1, f_2, f_3	coefficients of function F_1 of approximate hot-wire response equation
G_t	rate of generation of turbulence kinetic energy; G_{tw} at the wall
$g_1 \cdots g_9$	coefficients of function F_2 of approximate hot-wire response equation
H	shape factor
H_*	function
h_*	constant representing hot-wire sensitivity to normal velocity
K_A, K_B, K_θ K_1, K_2	calibration constants of five-hole impact probe
k	turbulence kinetic energy
k_*	constant representing hot-wire sensitivity to tangential velocity
L_N	length of negative mean velocity region
ℓ	length scale
ℓ_1, ℓ_2, ℓ_3	metric coefficients in ζ_1, ζ_2 and ζ_3-direction
N	designated position from surface, i.e. $n = N$
n	cross-stream boundary-layer co-ordinate perpendicular to surface
n_*	exponent of hot-wire voltage-velocity equation
P	pressure
P'	pressure correction

P_*, P_{flow}, P_{probe}	sum of terms containing third and higher order correlations in approximate hot-wire response equation: general, flow-cooling-velocity, and probe-motion contributions
P_m	mean pressure of tubes 1,2,3 and 4 of five-hole impact probe
$P_1 \ldots P_5$	mean pressures of five-hole impact probe chapter 2
P_{ij}, P_k	rate of production of turbulence kinetic energy chapter 4
Pe	Peclet number
$p_1 \ldots p_{65}$	coefficients of expression for P_*
p'	fluctuating pressure
Δp	difference between Preston-tube and wall pressures
Q	hot-wire cooling velocity
q	dynamic pressure section 2.2 fluctuating component of hot-wire cooling velocity section 2.3 and 2.4
q_r	constant of five-hole impact probe calibration
$\dot{q}$	flux
R	radius of curvature of surface
Re	Reynolds number
r	radius of curvature (pertaining to the flow)
S	source terms in finite-difference equation
ΔS	arc length
s	streamwise boundary-layer co-ordinate parallel to the surface
t	time
T	out-of-balance error term
T_*	non-linear term of hot-wire response equation

U	streamwise velocity component
U_e	velocity at boundary-layer edge
U_i	Cartesian velocity components chapter 4
U_τ	friction velocity
U_1, U_2, U_3	velocity with X_1-direction aligned with the wall (boundary-layer s-n co-ordinates) or tunnel centre-line (wake x-y co-ordinates)
U_{pw}	potential velocity at the wall
u	fluctuating streamwise velocity
u_1, u_2, u_3	normalised fluctuations of hot-wire cooling velocity chapter 2
u_1', u_2', u_3'	fluctuating velocity components of U_1, U_2 and U_3
V	normal velocity component
$\tilde{V}$	convection velocity
V_p	probe velocity
$\forall$	volume
V_1, V_2, V_2	velocity components in ζ_1-ζ_2- and ζ_3-directions
v	fluctuating normal velocity or velocity scale
v_p	fluctuating probe velocity
v_1', v_2', v_3'	fluctuating velocity components of V_1, V_2 and V_3, respectively
w	fluctuating azimuthal velocity (z-direction)
X	designated position along the surface, i.e. $s = X$
x_1, x_2, x_3	Cartesian co-ordinate system
x, y, z	orthogonal co-ordinate system with the x-direction aligned with the tunnel centre-line except in chapter 2 where it may be aligned with the wall (boundary-layer) or tunnel centre-line (wake)

x_w, y_w, z_w	orthogonal co-ordinate system with z_w-direction aligned with the wire and probe pintels in the x_w-z_w plane
Y	distance perpendicular to the surface

Greek Symbols

α	coefficient yaw angle of hot-wire relative to probe axis chapter 2 spacial weighting factor section 4.4
β	coefficient direction of probe velocity chapter 2
Γ	turbulence diffusivity
γ	coefficient angle of mean axial cooling velocity component to mean cooling velocity viewed from the frame of reference on wire chapter 2
γ_{pu}	probability of flow in the downstream u-direction
Δ_{ij}	diffusive transport
Δ	angle of mean flow velocity to the probe axis
δ	boundary-layer thickness
δ_1	displacement thickness
δ_2	momentum thickness
δ_{ij}	Kronecker delta
ε	dissipation rate of turbulence kinetic energy
ε_{ij}	dissipation rate of Reynolds stress components

$\zeta_1, \zeta_2, \zeta_3$	general orthogonal curvilinear co-ordinates
θ	direction of flow velocity
κ	turbulence-model constant
μ	absolute viscosity
ν	kinematic viscosity
π_{ij}	pressure-strain redistribution
ρ	density
Σ	summation
σ	Prandtl number
τ	stress
τ_w	wall shear stress
Υ	under-relaxation factor
Φ	geometric function
ϕ	any dependent variable direction of cooling velocity viewed from frame of reference on the probe chapter 2 velocity potential section 4.2
ψ	pitch angle of hot-wire probe relative to x,y,z-co-ordinates chapter 2 stream function chapter 4
Ω	angular shaft position
ω	angular shaft velocity

Subscripts

B	boundary
e	edge of the boundary-layer
eff	effective
Ex	explicit
flow	pertaining to flow
Im	implicit
i,j,k,ℓ,m	co-ordinate directions in tensor notation chapter 4
k	turbulence kinetic energy
last	last
m	mean
N,S,E,W,P	points-of-the-compass notation
n,s,e,w	for grid points
N1,N2,T	axial, normal and tangential directions of hot-wire cooling velocity relative to probe co-ordinates (x_w, y_w, z_w)
new	new
old	old
PR	Preston tube
p	probe
probe	pertaining to probe
ref	reference
T	total (or tangential see N1)
t	turbulence
V_i	i-direction velocity component
w,wall	wall
ε	turbulence kinetic energy dissipation rate
ϕ	pertaining to ϕ
1,2,3	co-ordinate directions (i.e. V_1, V_2, V_3 for $\zeta_1, \zeta_2, \zeta_3$)
.995	at location of $\langle U \rangle / \langle U_e \rangle = .995$

Superscripts

B	boundary
c	central differencing
I	internal
u	upwind differencing
(')	fluctuating or correction
(+)	non-dimensional
(*)	prevailing, approximate or incorrect value

Mathematical Symbols

Σ	summation
$\int$	integral
∂	partial derivative
d	exact derivative
δ	discrete change
/	i.e. a/b means from location a to b chapter 4
max [,]	maximum value of terms in brackets

REFERENCES

AMANO, R.S. (1983)

A study of turbulent flow downstream of an abrupt pipe expansion.

AIAA J. 21, 1400.

ANDERSON, S.B. (1979)

Historical overview of stall/spin characteristics of general aviation aircraft.

J. Aircraft 16, 445.

ANDREOPOULOS, J. and BRADSHAW, P. (1980)

Measurements of interacting turbulent shear layers in the near wake of a flat plate.

J. Fluid Mech. 100, 639.

ARENA, A.V. and MUELLER, T.J. (1980)

Laminar separation, transition and turbulent reattachment near the leading edge of airfoils.

AIAA J. 18, 747.

ARIELI, R. and MURPHY, J.D. (1980)

Pseudo-direct solution to the boundary-layer equations for separated flow.

AIAA J. 18, 883.

BACHALO, W.D. and JOHNSON, D.A. (1979)

An investigation of transonic turbulent boundary layer separation generated on an axisymmetric flow model.

AIAA paper 79-1479.

BAKER, A.J., YU, J.C.., ORZECHOWSKI, J.A. and GATSKI, T.B. (1982)

Prediction and measurement of incompressible turbulent aerodynamic trailing edge flows.

AIAA J. 20, 51.

BECKER, H.A. and BROWN, A.P.G. (1974)

Response of Pitot probes in turbulent streams.

J. Fluid Mech. 62, 85.

BHATELEY, I.C. and BRADLEY, R.G. (1972)

A simplified mathematical model for the analysis of multi-element airfoils near stall.

AGARD CP 102, 12.1.

BHATIA, J.C., DURST, F. and JOVANOVIC, J. (1982)

Correction of hot-wire anemometer measurements near walls.

J. Fluid Mech. 122, 441.

BOUSSINESQ, J. (1877)

Theorie de l'ecoulement tourbillant.

Mem. Press Acad. Sci. 23, 46.

BRADBURY, L.J.S. (1976)

Measurements with a pulsed-wire and a hot-wire in the highly turbulent wake of a normal flat plate.

J. Fluid Mech. 77, 473. (See also J. Fluid Mech. (1971) 49, 657).

BRADSHAW, P. (1969)

Experimental fluid mechanics. (Second Edition.)

Pergamon Press, Oxford.

BRADSHAW, P. (1971)

An introduction to turbulence and its measurement.

Pergamon Press, Oxford.

BRADSHAW, P. (1973)

Effects of streamline curvature on turbulent flow.

AGARDograph 169.

BRADSHAW, P. (1976)

Turbulence. (Ed. P. Bradshaw)

Springer-Verlag, Berlin.

BRADSHAW, P., CEBECI, T. and WHITELAW, J.H. (1977)

Engineering calculation methods for turbulent flow.

Imperial College, Aero. Tech. Note 77-102.

BRADSHAW, P., CEBECI, T. and WHITELAW, J.H. (1981)

Engineering calculation methods for turbulent flow.

Academic Press, London.

BRADSHAW, P., KAVANAGH, M.J. and MOBBS, D. (1983)

Viscous-inviscid mathcing using higher-order shear-layer equations.

Numerical and Physical Aspects of Aerodynamic Flows: Airfoils.

Springer-Verlag, Berlin.

BRADSHAW, P. and WONG, F.Y.F. (1972)

The reattachment and relaxation of a turbulent shear layer.

J. Fluid Mech. 52, 113.

BRAY, K.N.C. (1974)

Kinetic energy of turbulence in flames.

Univ. of Southampton, AASU report 332.

BRILEY, W.R. (1971)

A numerical study of laminar separation bubbles using Navier-Stokes equations.

J. Fluid Mech. 47, 713.

BRILEY, W.R. and McDONALD, H. (1975)

Numerical prediction of incompressible separation bubbles.

J. Fluid Mech. 69, 631.

BRYER, D.W. and PANKHURST, R.C. (1971)

Pressure-probe methods for determining wind speed and flow direction.

Her Majesty's Stationery Office, London.

BUTTER, D.J. and WILLIAMS, B.R. (1980)

The development of a method for calculating the viscous flow about high-lift aerofoils.

AGARD CP 291, 25.1.

CARETTO, L.S., GOSMAN, A.D., PATANKAR, S.V., POTTER, R. and SPALDING, D.B. (1972)

Two numerical procedures for three-dimensional recirculating flows.

Proc. Int. Conf. on Num. Methods in Fluid Dynamics, Paris.

CARTER, J.E. (1975)

Inverse solutions for laminar boundary-layer flows with separation and reattachment.

NASA TRR 447. Also see AIAA J. 13, 1101.

CASTRO, I.P. and CHEUN, B.S. (1982)

The measurement of Reynolds stresses with a pulsed-wire anemometer.

J. Fluid Mech. 118, 41.

CEBECI, T. (1976)

An inverse boundary-layer method for compressible laminar and turbulent boundary layers.

J. Aircraft, 13, 709.

CEBECI, T. and BRADSHAW, P. (1977)

Momentum transfer in boundary layers.

Hemisphere Publishing Corp., Washington.

CEBECI, T., KELLER, H.B. and WILLIAMS, P.G. (1979)

Separating boundary-layer flow calculations.

J. Comp. Phys. 31, 363.

CEBECI, T., KHALIL, E.E. and WHITELAW, J.H. (1979)

The calculation of separated boundary layers.

AIAA J. 17, 1291.

CEBECI, T. and MEIER, H.U. (1980)

Modelling requirements for the calculation of the turbulent flow around airfoils, wings and bodies of revolution.

AGARD CP 291, 16.1.

CEBECI, T. and SCHIMKE, S.M. (1983)

The calculation of separation bubbles in interactive turbulent boundary layers.

J. Fluid Mech. 131, 305.

CEBECI, T. and SMITH, A.M.O. (1974)

Analysis of turbulent boundary layers.

Academic Press, New York.

CEBECI, T., STEWARTSON, K. and WHITELAW, J.H. (1983)

The calculation of two-dimensional flow past airfoils.

Numerical and Physical Aspects of Aerodynamic Flows: Airfoils.

Springer-Verlag, Berlin.

CHAMBERS, T.L. and WILCOX, D.C. (1977)

Critical examination of two-equation turbulence closure models for boundary layers.

AIAA J. 15, 821.

CHAMPAGNE, F.H. and SLEICHER, C.A. (1967)

Turbulence measurements with inclined hot-wires. Part 2.

Hot-wire response equations.

J. Fluid Mech. 28, 177.

CHAMPAGNE, F.H., SLEICHER, C.A. and WEHRMANN, O.H. (1967)

Turbulence measurements with inclined hot-wires. Part 1.

Heat transfer experiments with inclined hot-wire.

J. Fluid Mech. 28, 153.

CHANDRUSUDA, C. and BRADSHAW, P. (1981)

Turbulence structure of a reattaching mixing layer.

J. Fluid Mech. 110, 171.

CHANG, P.K. (1970)

Separation of flow.

Pergamon Press, Oxford.

CHANG, P.K. (1976)

Control of flow separation.

Hemisphere Publishing Corp., Washington.

CHEVRAY, R. and KOVASZNAY, L.S.G. (1969)

Turbulence measurements in the wake of a thin flat plate.

AIAA J. 7, 1641.

CHORIN, A.J. (1968)

Numerical solution of the Navier-Stokes equations.

Math. Comp. 22, 745.

CHUE, S.H. (1975)

Pressure probes for fluid measurement.

Prog. Aerospace Sci. 16, 147.

CLAUSER, F.H. (1954)

Turbulent boundary layers in adverse pressure gradients.

J. Aeronaut. Sci. 21, 91.

COAKLEY, T.J. (1983)

Turbulence modelling methods for the compressible Navier-Stokes equations.

AIAA paper 83-1693.

COLES, D., CANTWELL, B. and WADCOCK, A. (1978)

The flying hot-wire and related instrumentation.

NASA CR 3066.

COLES, D. and HIRST, E.A. (Ed.) (1968)

Computation of turbulent boundary-layers - 1968.

ASOFR-IFP-Stanford Conference, Volume 2.

Stanford University, California.

COLES, D. and WADCOCK, A.J. (1979)

Flying-hot-wire study of flow past a NACA 4412 airfoil at

maximum lift.

AIAA J. 17, 321.

COMPTE-BELLOT, G. (1977)

Hot-wire and hot-film anemometry.

Measurements of unsteady fluid dynamics phenomena. (Ed. B.E. Richards)

Hemisphere Publishing Corp., Washington.

COOK, P.H., McDONALD, M.A. and FIRMIN, M.C.P. (1979)

Wind tunnel measurements of the mean flow in the turbulent boundary-layer and wake in the region of the trailing-edge of a swept wing at subsonic speeds.

R.A.E. TR 79062.

COOK, N.J. and REDFEARN, D. (1976)

The calibration and use of a hot wire probe for highly turbulent and reversing flows.

J. Ind. Aerodyn. 1, 221.

CRABB, D., DURAO, D.F.G. and WHITELAW, J.H. (1981)

A round jet normal to a cross-flow.

J. Fluids Eng. 103, 142.

DALY, B.J. and HARLOW, F.H. (1970)

Transport equations of turbulence.

J. Phys. Fluids, 13, 2634.

DEGANI, D. and STEGER, J.L. (1983)

Comparison between Navier-Stokes and thin-layer computations for separated supersonic flow.

AIAA J. 21, 1604.

DEIWART, G.S. (1976)

Computation of separated transonic turbulent flows.

AIAA J. 14, 735.

DELERY, J.M. (1981)

Investigation of strong shock turbulent boundary-layer interaction in 2-D transonic flows with emphasis on turbulence phenomena.

AIAA paper 81-1245.

DEMIRDZIC, I.A. (1982)

A finite volume method for computation of fluid flow in complex geometries.

Ph.D. thesis. University of London.

DEMIRDZIC, I., GOSMAN, A.D. and ISSA, R.I. (1981)

A finite-volume method for the prediction of turbulent flow in arbitrary geometries.

7th Int. Conf. Num. Meth. Fluid Dynamics, Stanford.

Springer Verlag, Berlin.

DOWNING, P.M. (1972)

Reverse flow sensing hot-wire anemometer.

J. Phys. E., Sci. Instrum. 5, 849.

DURST, F., MELLING, A. and WHITELAW, J.H. (1981)

Principles and practices of laser-Doppler anemometry. Second Edition.

Academic Press, London.

DURST, F. and RASTOGI, A.K. (1979)

Theoretical and experimental investigations of turbulent flow with separation.

Turbulent Shear Flows I. (Ed. F. Durst et al), 208.

Springer-Verlag, Berlin.

EAST, L.F., SMITH, P.D. and MERRYMAN, P.J. (1977)

Prediction of the development of separated turbulent boundary layers by the lag-entrainment method.

RAE TR-77046.

EATON, J.K. and JOHNSTON, J.P. (1981)

A review of research on subsonic turbulent flow reattachment.

AIAA J. 19, 1093.

ETHERIDGE, D.W. and KEMP, P.H. (1978)

Measurement of turbulent flow downstream of a reward-facing step.

J. Fluid Mech. 86, 545.

FERNHOLZ, H.-H. (1976)

External Flows.

Turbulence. (Ed. P. Bradshaw)

Springer-Verlag, Berlin.

FREYMUTH, P. (1977)

Frequency response and electronic testing for constant-temperature hot-wire anemometers.

J. Phys. E-Sci. Inst. 10, 705.

Also see FREYMUTH, P. (1977)

Further investigation of non-linear theory for constant temperature hot-wire anemometers.

J. Phys. E-Sci. Inst. 10, 710.

FREYMUTH, P. (1978)

A bibliography of thermal anemometry.

TSI Quarterly 4, Issue 4.

GAULT, D.E. (1949)

Boundary-layer and stalling characteristics of the NACA 63-009 airfoil section.

NACA TN 1894. Further see NACA TN 3505 (1955) and NACA TN 3963 (1957).

GESSNER, F.B. and MOLLER, G.L. (1971)

Response behaviour of hot-wires in shear flow.

J. Fluid Mech. 47, 449.

GHIA, U. and DAVIS, R.T. (1974)

Navier-Stokes solutions for flow past a class of two-dimensional semi-infinite bodies.

AIAA J. 12, 1659.

Also see GHIA, K.N., OSWALD, G.A. and GHIA, U. (1983)

A direct method for the solution of unsteady two-dimensional incompressible Navier-Stokes equations. Numerical and Physical Aspects of Aerodynamic Flows: Airfoils.

Springer-Verlag, Berlin.

GHIA, N. and GHIA, U. (Ed.) (1983)

Advances in grid generation.

ASME FED Vol. 5. Proceedings of Appl. Mech. Bioengng. and Fluids Engng Conference, Houston, Texas, June 1983.

GIBSON, C.H. (1973)

Digital techniques in turbulence research.

AGARDograph 174.

GIBSON, M.M. (1978)

An algebraic stress and heat-flux model for turbulent shear flow with streamline curvature.

Int. J. Heat and Mass Transfer, 21, 1609.

GIBSON, M.M., JONES, W.P. and YOUNIS, B.A. (1981)

Calculation of turbulent boundary layers on curved surfaces.

Phys. Fluids, 24, 386.

GIBSON, M.M. and LAUNDER, B.E. (1978)

Ground effects on pressure fluctuations in the atmospheric boundary layer.

J. Fluids Mech. 86. 491.

GIBSON, M.M. and RODI, W. (1981)

A Reynolds-stress closure model of turbulence applied to the calculation of a highly curved mixing layer.

J. Fluid Mech. 103, 161.

GIBSON, M.M., VERRIOPOULOS, C.A. and VLACHOS, N.S. (1983)

Turbulent boundary layer on a mildly curved convex surface: I, Mean flow and turbulence measurements.

Imperial College, Mech. Eng. Report, FS/83/6.

GIBSON, M.M. and YOUNIS, B.A. (1982)

Modelling the curved turbulent wall jet.

AIAA J. 20, 12.

GIBSON, M.M. and YOUNIS, B.A. (1983)

Turbulence measurements in a developing mixing layer with mild destabilising curvature.

Experiments in Fluids, 1, 23.

GILLIS, J.C. and JOHNSON, J.P. (1983)

Turbulent boundary-layer flow and structure on a convex wall and its redevelopment on a flat plate.

J. Fluid Mech. 135, 123.

GOSMAN, A.D. and JOHNS, R.J.R. (1979)

A simple method for generating curvilinear-orthogonal grids for numerical fluid mechanics calculations.

Imperial College, Mech. Eng. Report FS/79/23.

GOSMAN, A.D. and PUN, W.M. (1973)

Calculation of recirculating flows.

Imperial College, Mech. Eng. Report HTS/73/2.

GOSMAN, A.D., PUN, W.M., RUNCHAL, A.K., SPALDING, D.B. and WOFSTEIN, M. (1969)

Heat and mass transfer in recirculating flows.

Academic Press, London.

HABIB, M.A. (1980)

Confined flows with and without swirl.

Ph.D. thesis. University of London.

HABIB, M.A. and WHITELAW, J.H. (1979)

Velocity characteristics of a confined coaxial jet.

ASME J. Fluids Engng. 101, 521.

HABIB, M.A. and WHITELAW, J.H. (1980)

Velocity characteristics of a confined coaxial jet with and without swirl.

ASME J. Fluids Engng. 102, 47.

HABIB, M.A. and WHITELAW, J.H. (1981)

Calculation of confined coaxial-jet flows.

Imperial College, Mech. Eng. Report, FS/81/16.

University of London.

HABIB, M.A. and WHITELAW, J.H. (1982)

The calculation of turbulent flow in wide-angle diffusers.

Num. Heat Transfer, 5.

HACKMAN, L.P., RAITHBY, G.D. and STRONG, A.B. (1983)

Numerical prediction of flows over backward-facing steps.

In press. Also Mech. Eng. report, University of Waterloo, Canada.

HAH, C. and LAKSHMINARAYAMA, B. (1980)

Prediction of two- and three-dimensional asymmetric turbulent wakes, including curvature and rotation effects.

AIAA J. 18, 1196.

HAH, C. and LAKSHMINARAYAMA, B. (1982)

Measurement and prediction of mean velocity and turbulence structure in the near wake of an airfoil.

J. Fluid Mech. 115, 251.

HANJALIC, K. (1970)

Two-dimensional asymmetric turbulent flow in ducts.

Ph.D. thesis. University of London.

Also see HANJALIC, K. and LAUNDER, B.E. (1972)

A Reynolds stress model of turbulence and its application to thin shear flows.

J. Fluids Mech. 52, 609.

HARLOW, F.H. and WELCH, J.E. (1965)

Numerical calculation of time-dependent viscous incompressible flow of fluid with a free surface.

Phys. Fluids, 8, 2182.

HASTINGS, R.C. and MORETON, K.G. (1982)

An investigation of a separated equilibrium turbulent boundary-layer.

Int. Symposium on Applications of Laser-Doppler Anemometry to Fluid Mechanics, Lisbon, Portugal, 11.1.

HEAD, M.R. and VASANTA RAM, V. (1971)

Improved presentation of Preston tube calibration.

Aeronaut. Q. 12, 295.

HEGNA, H.A. (1982)

Numerical solution of incompressible turbulent flow over airfoils near stall.

AIAA J. 20, 29. See also AIAA paper 81-0047.

HESS, J.L. (1975)

Review of integral-equation techniques for solving potential-flow problems with emphasis on the surface-source method.

Comp. Meth. App. Mech. Eng. 5, 145.

HESS, J.L. (1980)

Review of integral-equation techniques for solving potential-flow problems with complicated boundaries.

2nd Int. Sym. Num. Analysis App. Eng. Sci., Montreal.

HINZE, J.O. (1975)

Turbulence. Second Edition.

McGraw-Hill, New York.

HOFFMAN, P.H. and BRADSHAW, P. (1978)

Turbulent boundary layers on surfaces of mild curvature.

Imperial College, Aero. Report 78-04.

HORNBECK, R.W. (1975)

Numerical methods.

Quantum, New York.

HORSTMAN, C.C. (1983)

Prediction of separated asymmetric trailing-edge flows at transonic Mach numbers.

AIAA J. 21, 1255.

HOUSEHOLDER, A.S. (1964)

The theory of matrices in numerical analysis.

Blaisdell, New York.

HUNT, B., MARCHBANK, W.R. and HEWITT, B.L. (1981)

The strengths and weaknesses of computational fluid mechanics in aerodynamic design and analysis.

Part 1 Background and philosophy.

Part 2 Detailed examination of the strength and weaknesses.

C.F.D. Workshop-cum-Seminar, VSSC, Trivandum, India.

JOHNS, R.J.R. (1980)

Prediction of flow in diesel engine cylinders.

Ph.D. thesis. University of London.

JOHNSTON, D.A. and BACHALO, W.D. (1980)

Transonic flow past a symmetric airfoil - Inviscid and turbulent flow properties.

AIAA J. 18, 16.

JOHNSON, D.A., BACHALO, W.D. and OWEN, F.K. (1981)

Transonic flow past a symmetric airfoil at high angle of attack.

J. Aircraft, 18, 7.

JOHNSON, D.A. and HORSTMAN, C.C. and BACHALO, W.D. (1982)

Comparison between experiment and prediction for a transonic turbulent separated flow.

AIAA J. 20, 737.

JOHNSON, D.A. and SPAID, F.W. (1981)

Near wake of a supercritical airfoil at cruise conditions.

AIAA paper 81-1242.

JONES, W.P. and LAUNDER, B.E. (1972)

The calculation of low-Reynolds-number phenomena with a two-equation model of turbulence.

Int. J. Heat and Mass Transfer, 16, 1119.

Also see JONES, W.P. and LAUNDER, B.E. (1972)

The prediction of laminarisation with a two-equation model of turbulence.

Int. J. of Heat and Mass Transfer, 15, 301.

JORGENSEN, F.E. (1982)

Characteristics and calibration of a triple-split probe for reversing flows.

DISA Information 27, 15.

KLEBANOFF, P.S. (1954)

Characteristics of turbulence in a boundary with zero pressure gradient.

NACA TN 3178.

KLINE, S.J., CANTWELL, B.J. and LILLEY, G.M. (Ed.) (1981)

Proceedings of the 1980-81 AFOSR-HTTM Stanford Conference on Complex Turbulent Flows. Volume 1.

Stanford University, California.

KLINE, S.J., MORKOVIN, M.V., SOVRAN, G. and COCKRELL, D.S. (Ed.) (1968)

Computation of turbulent boundary layers - 1968.

AFOSR-IPF-Stanford Conference, Volume 1.

Stanford University Press, Stanford, California.

KLINEBERG, J.M. and STEGER, J.L. (1972)

On laminar boundary-layer separation.

AIAA Paper 74-94.

KOLMORGOROV, A.N. (1942)

Equations of turbulent motion in an incompressible fluid.

IZV Akad. Nuak. SSSR, Ser. Phys., I, 1-2, 56.

(English translations: Imperial College, Mech. Eng. Report ON16, 1968).

KUCHEMANN, D. (1978)

The aerodynamic design of aircraft.

Pergamon Press, Oxford.

KWON, O.K. and PLETCHER, R.H. (1983)

Prediction of subsonic separation bubbles on airfoils by viscous-inviscid interaction.

Numerical and Physical Aspects of Aerodynamic Flows: Airfoils.

Springer-Verlag, Berlin.

LAI, M. (1983)

Numerical analysis of fluid transport phenomena.

Ph.D. thesis. University of London.

LAUNDER, B.E. and MORSE, A.P. (1979)

Numerical prediction of axisymmetric free shear flows with a Reynolds stress closure.

Turbulent Shear Flows I. (Ed. F. Durst et al), 279.

Springer-Verlag, Berlin.

LAUNDER, B.E., PRIDDEN, C.H. and SHARMA, B.I. (1977)

The calculation of turbulent boundary layers on spinning and curved surfaces.

J. Fluids Engng. 99, 231.

LAUNDER, B.E., REECE, G.J. and RODI, W. (1975)

Progress in the development of a Reynolds-stress turbulence closure.

J. Fluid Mech. 68, 537.

LAUNDER, B.E. and SPALDING, D.B. (1972)

Lecture in mathematical models of turbulence.

Academic Press, London.

LAUNDER, B.E. and SPALDING, D.B. (1974)

The numerical computation of turbulent flows.

Comp. Methods Appl. Mech. Eng. 3, 269.

LE BALLEUR, J.-C (1982)

Viscid-inviscid coupling calculations for two-and three-dimensional flows.

VKI lecture series, 1982-04, Comp. Fluid Dyn.

LE BALLEUR, J.-C. (1983)

Numerical viscid-inviscid interaction in steady and unsteady flows.

Numerical and Physical Aspects of Aerodynamic Flows: Airfoils.

Springer-Verlag, Berlin.

LE BALLEUR, J.-C., PEYRET, R., and VIVIAND, H. (1980)

Numerical studies in high Reynolds number aerodynamics.

Computer and Fluids, 8.

LEICHER, S. (1980)

Viscous flow simulation of high lift devices at subsonic and transonic speeds.

AGARD CP 291, 6.1.

LESCHZINER, M.A. and RODI, W. (1981)

Calculations of annular and twin parallel jets using various discretization schemes and turbulent model variants.

J. Fluids Engng. 103, 352.

LEONARD, B.P. (1979)

A stable and accurate convective modelling procedure based on quadratic upstream interpolation.

Comp. Methods Appl. Mech. Eng. 19, 59.

LIEBECK, R.H. (1978)

Design of subsonic airfoils for high lift.

J. Aircraft 15, 547.

LOCK, R.C. (1980)

A review of methods for predicting viscous effects on aerofoils and wings at transonic speeds.

AGARD CP 291.

LYNCH, F.T. (1978)

Recent applications of advanced computational methods in the aerodynamic design of transport aircraft configurations.

11th Congress of ICAS, Lisbon.

MacLENNAN, A.S.M. and VINCENT, J.H. (1982)

Transport in the near aerodynamic wakes of flat plates.

J. Fluid Mech. 120, 185.

MacMILLAN, F.A. (1954a)

Viscous effects on Pitot tubes at low speeds.

J. Royal Aero. Soc. 58, 570. Also A.R.C.R. and M.3028 (1956).

MacMILLAN, F.A. (1954b)

Viscous effects on flattened pitot tubes at low speeds.

J. Royal Aero. Soc. 58, 837.

MAHGOUB, H.E.H. and BRADSHAW, P. (1979)

Calculation of turbulent inviscid flow interactions with large pressure gradients.

AIAA J. 17, 1025.

MALISKA, C.R. and RAITHBY, G.D. (1983)

A method for computing three-dimensional flows using non-orthogonal boundary-fitted co-ordinates.

University of Waterloo, Canada. (In press).

MALTBY, R.L. (1962)

Flow visualisation in wind tunnels using indicators.

AGARDograph 70.

MARVIN, J.G. (1982)

Turbulence modelling for computational aerodynamics. (Invited).

AIAA paper 82-0164.

MASKEW, B. and DVORAK, F.A. (1978)

The prediction of $C_{\ell max}$ using a separated flow model.

J. Amer. Hel. Soc., April, 2.

MASKEW, B., RAO, B.M. and DVORAK, F.A. (1980)

Prediction of aerodynamic characteristics for wings with extensive separations.

AGARD CP 291, 31.1.

MATTICK, A.A. and STOLLERY, J.L. (1981)

Increasing the lift:drag ratio of a flat delta wing.

Aeronaut. J. 85, 379.

McCONALOGUE, D.J. (1970)

A quasi-intrinsic scheme for passing a smooth curve through a discrete set of points.

The Computer Journal, 13, no. 14.

McDONALD, H. and BRILEY, W.R. (1983)

A survey of recent work on interacted boundary layer theory for flow with separation.

Numerical and Physical Aspects of Aerodynamic Flows: Airfoils.

Springer-Verlag, Berlin.

McGUIRK, J.J. (1983)

Private communication.

McGuirk, J.J. and RODI, W. (1978)

A depth-averaged mathematical model for the near field of side discharges into open-channel flow.

J. Fluid Mech. 86, 4.

McGUIRK, J.J., TAYLOR, A.M.K.P. and WHITELAW, J.H. (1981)

The assessment of numerical diffusion in upwind difference calculations of turbulent recirculating flows.

Turbulent Shear Flows 3. (Ed. Bradbury L.J.S. et al).

Springer-Verlag, Berlin.

MEIER, H.U., KREPLIN, H.-P. and VOLLMERS, H. (1983)

Development of boundary layers and separation patterns on a body of revolution at incidence.

Numerical and Physical Aspects of Aerodynamic Flows: Airfoils. Springer-Verlag, Berlin.

MELLOR, G.L. and HERRING, H.J. (1973)

A survey of the mean turbulent field closure models.

AIAA J. 11, 590.

MELNIK, R.E. (1980)

Turbulent interactions on airfoils at transonic speeds - recent developments.

AGARD CP 291, 10.1.

MELNIK, R.E. and GROSSMAN, B. (1981)

On the turbulent viscid-inviscid interaction at a wedge shaped trailing-edge.

Numerical and Physical Aspects of Aerodynamic Flows. Springer-Verlag.

MELNIK, R.E., MEAD, H.R. and JAMESON, A. (1983)

A multi-grid method for the computation of viscid/inviscid interaction on airfoils.

AIAA paper 83-0234.

MERONEY, R.N. and BRADSHAW, P. (1975)

Turbulent boundary layer growth over a longitudinally curved surface.

AIAA J. 13, 1448.

MEULLER, T.J. and BATILL, T.J. (1982)

Experimental studies of separation on a two-dimensional airfoil at low Reynolds numbers.

AIAA J. 20, 457.

MORSE, A.P. (1980)

Axisymmetric free shear flows with and without swirl.

Ph.D. thesis. University of London.

MUCK, K.C. (1982)

Turbulent boundary layers on mildly curved surfaces.

Ph.D. thesis. University of London.

MULLER, U.R. (1982)

On the accuracy of turbulence measurements with inclined hot-wires.

J. Fluid Mech. 119, 155.

MURMAN, E.M. and BUSSING, T.R.A. (1983)

On the coupling of boundary layer and Euler equation solutions.

Numerical and Physical Aspects of Aerodynamic Flows: Airfoils.

Springer-Verlag.

NAKAYAMA, A. (1983)

Measurements of attached and separated turbulent flows in the trailing-edge regions of airfoils.

Numerical and Physical Aspects of Aerodynamic Flows: Airfoils.

Springer-Verlag.

OLSON, L.E., JAMES, W.D. and McGOWAN (1978)

Theoretical and experimental study of the drag of single- and multi-element airfoils.

AIAA paper 78-1223. Also J. Aircraft (1979), 16, 462.

OLSON, L.E. and ORLOFF, F.L. (1981)

On the structure of turbulent wakes and merging shear layers of multi-element airfoils.

AIAA paper 81-1238.

ORLOFF, K.L. and OLSON, L.E. (1982)

High-resolution LDA measurements of Reynolds stresses in boundary layer and wakes.

AIAA J. 20, 624.

OSKAM, B. (1980)

Computational aspects and results of low speed viscous flow about multi-component airfoils.

AGARD CP 291, 19.1.

PATANKAR, S.V. (1980)

Numerical heat transfer and fluid flow.

McGraw-Hill, Washington.

PATANKAR, S.V. and SPALDING, D.B. (1970)

Heat and mass transfer in boundary-layers. (2nd Edition)

Intertext, London.

PATANKAR, S.V. and SPALDING, D.B. (1972)

A calculation procedure for heat, mass and momentum transfer in three-dimensional parabolic flows.

Int. J. Heat Mass Transfer, 15, 1787.

PATEL, V.C. and BAEK, J.H.

Calculation of boundary-layers and separation on a spheroid at incidence.

Numerical and Physical Aspects of Aerodynamic Flows: Airfoils.

Springer-Verlag, Berlin.

PATEL, V.C. and SCHEUERER, G. (1982)

Calculation of two-dimensional near and far wakes.

AIAA J. 20, 900.

PERRY, A.E. (1982)

Hot-Wire Anemometry.

Oxford University Press, New York.

PERRY, A.E. and FAIRLIE, B.D. (1975)

A study of turbulent boundary-layer separation and reattachment.

J. Fluid Mech. 69, 657.

POPE, S.B. (1978)

The calculation of turbulent recirculating flows in general orthogonal co-ordinates.

J. Comp. Phys. 26, 197.

POPE, S.B. and WHITELAW, J.H. (1976)

The calculation of near-wake flows.

J. Fluid Mech. 73, 9.

POT, P.J. (1979)

A wake boundary layer mixing experiment.

Turbulent Shear Flows II. (Ed. Bradbury et al)

Springer-Verlag, Berlin. Also see NLR TR 79063 U (1979).

PRANDTL, L. (1925)

Bericht uber Untersuchungen zur ausgenbildeten Turbulenz.

ZAMM, 5, 136.

English Translation: Spalding, D.B. (1980)

Imperial College, Mech. Eng. Report HTS/TN/80/1.

PRANDTL, L. (1945)

Uber ein Neus Formelsystem fur die Ausgebildete Turbulenz.

Nachrichten von der Akad. der Wissenschaft in Gottingen.

PRESTON, J.H. (1954)

The determination of turbulent skin friction by means of Pitot tube.

J. Royal Aeronaut. Soc. 58, 109.

PRESTON, J.H., SWEETING, N.E. and COX, D.K. (1945)

The experimental determination of the boundary-layer and wake characteristics of a Piercy 12/40 aerofoil, with particular reference to the trailing-edge region.

ARC R & M 2013. Also see ARC R & M 1998 (1943).

RAITHBY, G.D. (1976a)

A critical evaluation of upwind differencing applied to problems involving fluid flow.

Comp. Meth. Appl. Mech. Eng. 9, 75.

RAITHBY, G.D. (1976b)

Skew upwind differencing schemes for problems involving fluid flow.

Comp. Meth. Appl. Mech. Eng. 9, 153.

RAITHBY, G.D. and TORRENCE, K.E. (1974)

Upstream-weighted differencing schemes and their application to elliptic problems in fluid flow.

Computers and Fluids, 2, 191.

RAMAPRIAN, B.R., PATEL, V.C. and SASTRY, M.S. (1982)

The symmetric turbulent wake of a flat plate.

AIAA J. 20, 1228.

REECE, G.J. (1976)

Development and applications of a generalised Reynolds-stress model of turbulence.

Ph.D. thesis. University of London.

RENDER, P.M. and STOLLERY, J.L. (1983)

A comparison between the predicted and experimental characteristics of a NACA 63_3418 aerofoil at low Reynolds number.

Numerical and Physical Aspects of Aerodynamic Flows: Airfoils.

Springer-Verlag, Berlin.

REYNOLDS, W.C. (1976)

Computation of turbulent flows.

Annual Review of Fluid Mechanics, 8.

RHIE, C.M. and CHOW, W.L. (1982)

A numerical study of the turbulent flow past an isolated airfoil with trailing edge separation.

AIAA paper 82-0998. Also AIAA J. (1983), 21, 1525.

RIBEIRO, M.M. (1976)

The turbulence structure of free jet flows with and without swirl.

Ph.D. thesis. University of London.

RIBEIRO, M.M. and WHITELAW, J.H. (1975)

Statistical characteristics of a turbulent jet.

J. Fluid Mech. 70, 1.

ROACHE, P.J. (1972)

Computational fluid dynamics. (Revised printing, 1982).

Hermosa, Albequerque.

RODI, W. (1971)

A new method for analysing hot-wire signals in highly turbulent flow and its evaluation in a round jet.

Imperial College, Mech. Eng. Report ET/TN/B/10.

Also DISA Information (1975), 17, 9.

RODI, W. (1980)

Turbulence models and their application in hydraulics -

A state of the art review.

Int. Association for Hydraulic Research - Publication, Delft.

RODGERS, E.J., WENTZ, Jr., W.H. and SEETHARAM, H.C. (1979)

Instrumentation, techniques and data reduction associated with airfoil testing programs at Wichata State University.

NACA CP 2045, 539.

RONALD, M.C. (1976)

Shear effects in hot-wire measurements.

J. Fluids Engng. 98, 771.

ROTTA, J.C. (1972)

Turbulente Stromungen.

Teubner, Stuttgart.

SCHLICHTING, H. (1968)

Boundary-layer theory. 6th Edition

McGraw-Hill, New York.

SCHUBAUER, G.B. and KLEBANOFF, P.S. (1951)

Investigation of separation of the turbulent boundary-layer.

NACA Report 1030.

SEEBOHM, T. and NEWMAN, B.G. (1975)

A numerical method for calculating viscous flow round multiple-section aerofoils.

Aeronaut. Q. 26, 176.

SEETHARAM, H.C. and WENTZ, Jr., W.H. (1975)

Experimental studies of flow separation on a two-dimensional airfoil at low speeds.

NASA CR 2560.

SEETHARAM, H.C. and WENTZ, Jr., W.H. (1977)

Experimental investigation of subsonic turbulent separated boundary-layers on an airfoil.

J. Aircraft, 14, 51. Also see J. Aircraft, 14, 95 (1977) and NASA CR 2884 (1977).

SHAMROTH, S.J. and GIBELING, H.J. (1979)

The prediction of the turbulent flow field about an isolated airfoil.

AIAA paper 79-1543.

SHAMROTH, S.J. and GIBELING, H.J. (1980)

Navier-Stokes solution of the turbulent flow field about an isolated airfoil.

AIAA 18, 1409. Also see NASA CR 3183 (1979).

SHARMA, R.N. and PATANKAR, S.V. (1982)

Numerical computations of wall-jet flows.

Int. J. Heat Mass Transfer, 25, 1709.

SHAW, R. (1960)

The influence of hole dimensions on static pressure measurements.

J. Fluid Mech. 7, 550.

SIMPSON, R.L. (1981)

A review of some phenomena in turbulent flow separation.

J. Fluids Engng. 103, 520.

SIMPSON, R.L. (1983)

A model for the backflow mean velocity profile.

AIAA J. 21, 142.

SIMPSON, R.L. and COLLINS, M.A. (1978)

Prediction of turbulent boundary layers in the vicinity of separation.

AIAA J. 16, 289.

SIMPSON, R.L., CHEW, Y.-T. and SHIVAPRASAD, B.G. (1981)

The structure of a separating turbulent boundary-layer.

Part 1. Mean flow and Reynolds stresses.

J. Fluid Mech. 113, 23.

Part 2. Higher-order turbulence results.

J. Fluid Mech. 113, 53.

Part 4. Effects of periodic free-stream unsteadiness.

J. Fluid Mech. (1983), 127, 219.

Also see SHILOH, K., SHIVAPRASAD, B.G. and SIMPSON, R.L. (1981)

Part 3. Transverse velocity measurements.

J. Fluid Mech. 113, 75.

SIMPSON, R.L., STRICKLAND, J.H. and BARR, P.W. (1977)

Features of a separating turbulent boundary layer in the vicinity of separation.

J. Fluid Mech. 79, 553.

SMETANA, F.O., SUMMEY, D.C., SMITH, N.S. and CARDEN, R.K. (1975)

Light aircraft lift, drag and moment prediction - a review and analysis.

NASA CR 2523.

SMITH, A.M.O. (1972)

Aerodynamics of high-lift airfoil systems.

AGARD CP 102, 10.1.

SMITH, F.T. (1983)

Interacting flow theory and trailing-edge separation - no stall.

J. Fluid Mech. 131. 219.

SO, R.M.C. and MELLOR, G.L. (1973)

Experiment on convex curvature effects in turbulent boundary layers.

J. Fluid Mech. 60, 43.

SOLIGNAC, J.-L. (1980)

Experimental study of the separation at the trailing-edge of an axisymmetric contoured after-body.

Rech. Aerosp. No. 1980-3, 65.

SPAID, F.W. and BACHALO, W.D. (1981)

Experiments on the flow about a supercritical airfoil, including holographic interferometry.

J. Aircraft, 18, 287.

SPALDING, D.B. (1972)

A novel finite-difference formulation for differential expressions involving both first and second derivatives.

Int. J. Num. Meth. Engng. 4, 551.

SQUIRE, L.C. (1961)

The motion of a thin oil sheet under the steady boundary-layer on a body.

J. Fluid Mech. 11, 161.

STEGER, J.L. (1978)

Implicit finite-difference simulation of flow about arbitrary two-dimensional geometries.

AIAA J. 16, 679.

STREET, C.L. (1982)

Viscous-inviscid interaction for transonic wing-body configurations including wake effects.

AIAA J. 20, 915. Also AIAA paper 81-1266.

STUBLEY, G.D., RAITHBY, G.D. and STRONG, A.B. (1980)

Proposal for a new discrete method based on an assessment of discretization errors.

Numer. Heat Transfer 3, 411.

STUBLEY, G.D., RAITHBY, G.D., STRONG, A.B. and WOOLNER, K.A. (1982)
Simulation of convection and diffusion processes by standard finite-difference schemes and by influence schemes.
Comp. Meth. App. Mech. Eng. 35, 153.

SUGAVANAM, A. and WU, J.C. (1982)
Numerical study of separated turbulent flow over airfoils.
AIAA J. 20, 464.

SWAFFORD, T.W. (1983)
Analytical approximation of two-dimensional separated turbulent boundary-layer velocity profiles.
AIAA J. 21, 923.

TANI, I. (1964)
Low-speed flows involving bubble separations.
Prog. Aeronaut. Sci. 5, 70.
MacMillan, New York.

TAYLOR, A.M.K.P. (1981)
Confined, isothermal and combusting flows behind axisymmetric baffles.
Ph.D. thesis. University of London.

TAYLOR, A.M.K.P. and WHITELAW, J.H. (1983)
Velocity characteristics in the turbulent near wakes of confined axisymmetric bluff bodies.
J. Fluid Mech. To be published.

TENNEKES, H. and LUMLEY, J.L. (1972)
A first course in turbulence. 5th printing, 1978.
MIT Press, Cambridge, Mass.

THOMPSON, B.E. (1981)
Preliminary evaluation of flying-hot-wire instrumentation.
Imperial College, Mech. Eng. Report FS/81/23.

THOMPSON, J.F. (1982)

Numerical grid generation. (Ed. J.F. Thompson)

Elsevier Science Publ. Co. Inc.

THWAITES, B. (1955)

Incompressible aerodynamics.

Clarendon Press, Oxford.

VAGT, J.-D.(1979)

Hot-wire probes in low speed flow.

Prog. Aerospace Sci. 18, 271.

VAN DEN BERG, B. (1981)

Role of laminar separation bubbles in airfoil leading-edge stalls.

AIAA J. 19, 553.

VLEDMAN, A.E.P. (1980)

The calculation of incompressible boundary-layers with strong viscous-inviscid interaction.

AGARD CP 291, 12.1.

VERRIOPOULOS, C.A. (1983)

Effects of convex curvature on heat transfer in turbulent flow.

Ph.D. thesis, University of London.

VISWANATH, P.R. and BROWN, J.L. (1983)

Separated trailing-edge flow at a transonic Mach number.

AIAA J. 21, 803.

VISWANATH, P.R., CLEARY, J.W., SEEGMILLER, H.L. and HORSTMAN, C.C. (1980)

Trailing-edge flows at high Reynolds number.

AIAA J. 18, 1059.

WADCOCK, A.J. (1978)

Flying-hot-wire study of two-dimensional turbulent separation on an NACA 4412 airfoil at maximum lift.

Ph.D. thesis. California Institute of Technology, Pasadena.

WADCOCK, A.J. (1980)

Simple turbulence models and their application to boundary layer separation.

NASA CR 3283.

WASKIEWICZ, J.D., SHANG, J.S. and HANKLEY, W.L. (1980)

Numerical simulation of near wakes utilizing a relaxation turbulence model.

AIAA J. 18, 1440.

WATKINS, A.P. (1977)

Flow and heat transfer in piston cylinder assemblies.

Ph.D. thesis. University of London.

WATMUFF, J.H., PERRY, A.E. and CHONG, M.S. (1983)

A flying hot-wire system.

Experiments in Fluids, 1, 63.

WENTZ, Jr., W.H. and SEETHARAM, H.C. (1977)

Split-film anemometer measurements on an airfoil with turbulent separated flow.

Proc. 5th Biennial Sym. on Turbulence.

University of Missouri-Rolla.

WERLE, M.J. and DAVIS, R.T. (1972)

Incompressible laminar boundary layers on a parabola at angle of attack: a study of the separation point.

J. Appl. Math. 7.

WHITEFIELD, D.L., SWAFFORD, T.W. and JACOCKS, J.L. (1981)

Calculation of turbulent boundary-layers with separation and viscous-inviscid interaction.

AIAA J. 19, 1315.

WHITELAW, J.H. (1981)

Recirculating flows, laser-Doppler anemometry and calculation methods.

Proc. 8th Canadian Cong. Appl. Mech., Moncton, 97.

WHITELAW, J.H. (1983)

Private communication.

WINSLOW, A.M. (1967)

Numerical solution of quasilinear Poisson equation in a non-uniform triangular mesh.

J. Comp. Phys. 2, 149.

WINTER, K.G. (1979)

An outline of the techniques available for the measurement of skin friction in turbulent boundary layers.

Prog. Aerospace Sci. 18, 1.

WOOD, D.H. and BRADSHAW, P. (1982)

A turbulent mixing layer constrained by a solid surface.

Part 1. Measurements before reaching the surface.

J. Fluid Mech. 122, 57.

WU, J.C. (1976)

Numerical boundary conditions for viscous flow problems.

AIAA J. 14, 1042.

WU, J.C. and GULCAT, U. (1981)

Separate treatment of attached and detached flow regions in general viscous flow.

AIAA J. 19, 20.

WU, J.C. and SAMPATH, S.J. and ELSEMAN, P.R. (1978)

The prediction of the turbulent flow field about an isolated airfoil.

NACA CR 2969.

YOUNG, A.D. (1981)

Windtunnel corrections for high angle of attack models.

AGARD report no. 692.

YOUNG, W.H., MEYERS, J.F. and HOAD, D.R. (1978)

A laser velocimeter flow survey above a stalled wing.

NASA TP 1266.

YOUNIS, B.A. (1983)

On modelling the effects of streamline curvature on turbulent shear flows.

Ph.D. thesis. University of London.

YU, J.C. (1981)

Mean-flow and turbulence measurements in the vicinity of the trailing-edge of an NACA 63_1-012 airfoil.

NASA TP 1845.